FORMERLY ACTA GEODAETICA, GEOPHYSICA ET MONTANISTICA ACADEMIAE SCIENTIARUM HUNGARICAE

Acta Geodaetica, Geophysica et Montanistica Hungarica

VOLUME 18, NUMBERS 1–2, 1983

Akadémiai Kiadó, Budapest

AGGM 18 (1–2) 1–220 (1983) HU ISSN 0374-1842

ACTA GEODAETICA, GEOPHYSICA et MONTANISTICA HUNGARICA
A Quarterly Journal of the Hungarian Academy of Sciences

Acta Geodaetica, Geophysica et Montanistica (AGGM) publishes original reports on geodesy, geophysics and minings in English.

AGGM is published in yearly volumes of four numbers by

AKADÉMIAI KIADÓ

Publishing House of the Hungarian Academy of Sciences
H-1054 Budapest, Alkotmány u. 21.

Manuscripts and editorial correspondence should be addressed to

AGGM Editorial Office
H-9401 Sopron P.O. Box 5

Subscription information

Orders should be addressed to

KULTURA Foreign Trading Company
H-1389 Budapest P.O. Box 149

INSTRUCTIONS TO AUTHORS

Manuscripts should be sent to the editors (MTA Geodéziai és Geofizikai Kutató Intézete, AGGM Editorial Office, H-9401 Sopron, P.O.Box 5, HUNGARY). Only articles not submitted for publication elsewhere are accepted.

Manuscripts should be typewritten in duplicate, double-spaced, 25 lines with 50 letters each. The papers generally include the following components, which should be presented in the order listed.

1. Title, name of author(s), affiliation, dateline, abstract, keywords
2. Text, acknowledgements
3. References.
4. Footnotes
5. Legends
6. Tables and illustrations

1. The *affiliation* should be as concise as possible and should include the complete mailing address of the authors. The *date of receipt* of the manuscript will be supplied by the editors. The abstract should not exceed 250 words and should clearly and simply summarize the most important methods and results. 5–10 significant expressions describing the content are used as *keywords*. Authors may recommend these keywords.

2. The *text* should be generally in English and as short and clear as possible. From Hungarian authors papers are also accepted in Hungarian.

The section heading should *not* be underlined or in capitals.

Please note that underlining denotes special types:

— single underlining: italics
— double underlining: bold-face roman

ACTA GEODETICA, GEOPHYSICA et MONTANISTICA HUNGARICA

A Quarterly Journal of the Hungarian Academy of Sciences

VOLUME 18

Akadémiai Kiadó, Budapest
1983

AUTHOR INDEX

KEYWORD INDEX

CONTENTS

EDITORIAL NOTE

The name of Acta Geodaetica, Geophysica et Montanistica Academiae Scientiarum Hungaricae has been abbreviated to *Acta Geodaetica, Geophysica et Montanistica Hungarica.*

Acta Geodaetica, Geophysica et Montanistica Hungarica is a journal of the Hungarian Academy of Sciences. The change does not affect the status and editorial policy of the journal.

Acta Geodaet., Geophys. et Montanist. Hung. Volume 18 (1—2), pp. 1—8 (1983)

PROFESSOR LAJOS HOMORÓDI
1911—1982

Less than one year passed between the festive scientific session held at the Hungarian Academy of Sciences on the occasion of the 70th birthday of Professor Lajos Homoródi, full member of our Academy — where he himself delivered a lecture in good health and at the height of his creative power — and January 22, 1982, when after short suffering he left us for ever.

His death means a serious loss for the scientific life in Hungary and within that, for geodesy. In his person the Section of Geosciences and Mining of the Hungarian Academy of Sciences lost one of its most active members, chairman of the Geodetic Scientific Committee, member of the Hungarian National IUGG Committee, member of the IAG Section of IUGG, and member of the editorial board of this journal.

Excellent practical sense was very favourably combined in him with scientific interest and inclination to intensive research work. Thus from a practical, later managing engineer of the State Surveying he turned into an outstanding scientist and a Member of the Academy.

His gift for technical literature developed already in his youth, the fruit of which was a rich choice of foreign-language papers in different *Actas* of the Academy as well as publications in Hungarian in the journals of the Section, further in *Geodézia és Kartográfia*, in *Periodica Polytechnica* and in a number of other journals. He was one of the most fruitful specialist authors on geodesy in Hungary. His works include the first, and till today only, Hungarian text-book on geodesy as well as several university lecture notes, about 60 scientific papers and more than 140 actual reviews.

His excellent ability to see and select the crux of the matter, his sharp logic, his mastery as lecturer, his interesting university lectures raised him among the most outstanding university professors. The Technical University of Budapest lost in him a former Head of the Department of Photogrammetry, a former Director of the Institute for Geodesy, Surveying and Photogrammetry, a former scientific Vice-Rector and a former Dean of the Faculty for Civil Engineering.

Throughout his life his working capacity was almost limitless. He held active and highly responsible leading posts simultaneously in several national and international scientific organizations and boards. He was a founding member and for nearly twenty years chairman of the Hungarian Society for Geodesy and Cartography. At the same time he successfully worked as vice-chairman and chairman of Commission 2 (Professional Education) of FIG (Federation International des Geometres) for six years, further in the International Society for Photogrammetry (ISP) and in the International Union of Geodesy and Geophysics (IUGG). Besides, he took part in the work of several scientific boards, committees and councils.

His death leaves a gap in the Hungarian scientific life which will be difficult to fill for a long time. We will keep his memory.

The board of editors

The scientific publications of Professor Lajos Homoródi

A) Books, lecture notes

1. Geodesy. Lecture notes. Budapest, 1948.
2. Geodesy I–III. University lecture notes. Budapest, 1953—1954.
3. Geodesy I–II. University lecture notes. Budapest,1960—1961.
4. Geophysics. University lecture notes. Budapest, 1960.
5. Mapping—City surveying. Notes of a special-engineer course. Tankönyvkiadó, Budapest, 1962.
6. "Basic concepts" and "Primary triangulation". In: *Handbook of Geodesy and Surveying*, Vol. 1. Közgazdasági és Jogi Kiadó, Budapest, 1975.
7. Photogrammetry I. (Co-author: Mrs. Gy Domokos) University lecture notes. Tankönyvkiadó, Budapest, 1966.
8. Modern tendencies in geodesy. (Co-author: P Biró) Notes for a special engineer course. Tankönyvkiadó, Budapest, 1966.
9. Geodesy. University text-book. Tankönyvkiadó, Budapest, 1966.

10. Photogrammetry II. (Co-author: Mrs. Gy. Domokos) University lecture notes. Tankönyvkiadó, Budapest, 1967.
11. Photogrammetry II. University lecture notes. Tankönyvkiadó, Budapest, 1973.
12. Photogrammetry II. Tankönyvkiadó, Budapest, 1975.
13. Geodetic control networks. University lecture notes. Tankönyvkiadó, Budapest, 1980.

B) Scientific papers

1. The unit of time. *Technika*, Budapest, 1937.
2. Geophysical exploration methods. *Technika*, Budapest, 1938.
3. The accuracy of the prism range finder type Oltay—Süss. *Geodéziai Közlöny*, 16 (1940), 13–38.
4. The accuracy reached in the angular measurements of the new traverses of the city surveying in Budapest. *Geodéziai Közlöny*, 18 (1942), 41–52.
5. The accuracy reached in the distance measurements of the new traverses of the city surveying in Budapest. *Geodéziai Közlöny*, 18 (1942), 83–94; 118–127.
6. Error sources of exact distance measurements with rods. *Geodéziai Közlöny*, 20 (1944), 6–39; 70–96.
7. Development and present state of the works of the National Surveying. *Geodéziai Közlöny*, 23 (1947).
8. Test of circle graduation. *Geodéziai Közlöny*, 23 (1947).
9. The reliability of the excentricity elements determined indirectly. *Földméréstani Közlemények*, 2 (1950), 15–24.
10. Calculation of the excentricity elements determined indirectly. *Földméréstani Közlemények*, 2 (1950), 87–97.
11. Operations in geodesy in the USSR. *Földméréstani Közlemények*, 3 (1951), 1–11.
12. The application the Laplace-equations in the adjustment of the primary triangulation network. *Földméréstani Közlemények*, 3 (1951), 93–101.
13. The new formulae of the International Association of Geodesy for determining the accuracy of leveling. *Földméréstani Közlemények*, 3 (1951), 137–141.
14. Investigations of the geodetic datum of our new triangulation network. *Földméréstani Közlemények*, 4 (1952), 1–10; 61–71.
15. The influence of the variation in the dimensions of the ellipsoid on the results of the adjustment of a triangulation network. *Földméréstani Közlemények*, 4 (1952), 134–145; 185–193.
16. Datum and orientation of our old triangulation networks. *Földméréstani Közlemények*, 5 (1953), 1–18.
17. Reduction of the base lines onto the ellipsoid. *Földméréstani Közlemények*, 5 (1953), 117–131.
18. High capacity computers. *Földméréstani Közlemények*, 6 (1954), 55–63.
19. La reduction des bases géodésiques sur l'ellipsoide. *Acta Technica*, 1954.
20. National triangulation and local control systems. *Geodézia és Kartográfia*, 7 (1955), 82–98.
21. The error-ellipse and the error of a point. *Geodézia és Kartográfia*, 8 (1956), 5–16.
22. The test of the circle graduation of a theodolite. *Geodézia és Kartográfia*, 9 (1957), 19–24.
23. Old stations in the new control network. *Geodézia és Kartográfia*, 9 (1957), 133–145.
24. The renewal of the fourth order triangulation network. *Geodézia és Kartográfia*, 9 (1957), 218–239.
25. Determination of the movement and deformation of big buildings by surveying method. *Geodézia és Kartográfia*, 10 (1958), 26–35.
26. Problems in connection with our new map projection system. *Geodézia és Kartográfia*, 11 (1959), 99–110.
27. Die Deutung des Punktfehlers. *Acta Technica*, 1959.
28. Problems in connection with the utilization of the results of the new geodetic triangulation in Hungary. *ÉKME Tudományos Közleményei*, Budapest, 1960.
29. The reorganization of the professional education of civil engineers for geodesy and surveying. *Geodézia és Kartográfia*, 12 (1960), 181–190.
30. Artificial earth satellites in the service of geodesy. *Geodézia és Kartográfia*, 13 (1961), 94–105.
31. The absolute orientation of our new geodetic triangulation network. *ÉKME Tudományos Közleményei*, Budapest, 1961.
32. Investigation of the Earth 's crustal movements. *Geodézia és Kartográfia*, 14 (1962), 300–302.

33. The situation of the science geodesy and the trend of its development. *Geodézia és Kartográfia*, 15 (1963), 110–114.
34. The reform of the professional education of civil engineers for geodesy and surveying. *Geodézia és Kartográfia*, 15 (1963), 170–175.
35. Deduction of local control networks from the new geodetic triangulation network. *Geodézia és Kartográfia*, 15 (1963), 247 257.
36. Tasks and problems of the professional education of civil engineers with respect to the reformed curriculum. *Magyar Építőipar*, 1967.
37. Is the mark "sufficient" really sufficient? *Pedagógiai Közlemények*, 1967.
38. Twenty years. *Geodézia és Kartográfia*, 20 (1968), 1.
39. Remarks to the paper "Technical school for surveyors". *Geodézia és Kartográfia*, 20 (1968), 133–136.
40. From astrogeodesy to panel surveying. *Geodézia és Kartográfia*, 20 (1968), 261–265.
41. Investigation of the accuracy of geodetic triangulations with deduced angles. *Geodézia és Kartográfia*, 20 (1968), 406–413.
42. Geodetska delatnost u NR Madjarskoj. *Geokarta*, 1968.
43. Loránd Eötvös and the geodesy. *Geodézia és Kartográfia*, 21 (1969), 81–86.
44. Again about the geodetic triangulation with deduced angles. *Geodézia és Kartográfia*, 21 (1969), 244–247.
45. Untersuchungen der Genauigkeit der mit abgeleiteten Winkeln vollzogenen Triangulierung. *Acta Geod., Geoph., Mont. Hung.*, 4 (1969), 425–439.
46. 25 years of professional education of civil engineers for geodesy and surveying. *Geodézia és Kartográfia*, 22 (1970), 178–182.
47. The problems of the professional education of civil engineers for geodesy and surveying at home and abroad. *Geodézia és Kartográfia*, 23 (1971), 249–256.
48. Photogrammetry, settlement-development, protection of environment. *Acta Geologica*, 17 (1973).
49. Terrestrial and aerial triangulation. *MTA X. Oszt. Közleményei*, 1974.
50. Some problems of the professional education and postgraduate training of surveyors in Hungary. *Geodézia és Kartográfia*, 26 (1974), 243–247.
51. A special photogrammetric problem. *Geodézia és Kartográfia*, 26 (1974), 255–260.
52. The basis of aerial triangulation. *Geodézia és Kartográfia*, 27 (1975), 25–32.
53. Ergebnisse und Anwendungsbereiche der Aerotriangulation in Ungarn. *Periodica Polytechnica*, 19 (1975).
54. The development of photogrammetry at home and abroad. *Műszaki Tervezés*, 1975.
55. The new curriculum of the branch geodesy and surveying at the Technical University, Budapest. *Geodézia és Kartográfia*, 29 (1977), 164–168.
56. Einige Erfahrungen über die mehrstufige Ausbildung von Vermessungsfachleuten. Berichte des XV. Kongresses der FIG, Stockholm, 1977.
57. Three decades of Geodézia és Kartográfia. *Geodézia és Kartográfia*, 30 (1978), 397–399.
58. The study curriculum for civil engineers for geodesy and surveying. *Geodézia és Kartográfia*, 31 (1979), 254–257.
59. Photogrammetrische Arbeiten für nicht-topographische Zwecke in Ungarn. *Int. Archiv für Photogrammetrie*, Hamburg, 23 B5 (1980).
60. Eine besondere photogrammetrische Aufgabe. *Int. Archiv für Photogrammetrie*, Hamburg, 23 B5 (1980).
61. Die Anfänge der Vermessungsingenieurausbildung in Ungarn. Mitteilungen d. Geod. Inst. der TU Graz. Festschrift K Hubeny. 1980.

C) Reviews

1. Hundred years photography. *Vasárnap*, Arad, 1937, 411–412.
2. Rutherford. *Vasárnap*, Arad, 1937, 423–424.
3. The birth of the sunbeam. *Vasárnap*, Arad, 1937, 254–255.
4. The earthquake. *Vasárnap*, Arad, 1938, 265–266.
5. The dowsing rod and its successors. *Vasárnap*, Arad, 1938, 284–285.
6. Natural sciences and free will. *Vasárnap*, Arad, 1938, 470–471.

7. The common adjustment of the European geodetic triangulation networks. *Az Állami Földmérés Közleményei*, 1 (1949), 97–100.
8. The General Assembly of IUGG in Oslo. *Az Állami Földmérés Közleményei*, 1 (1949), 133–136.
9. Atomic clock: a new time keeper. *Földméréstani Közlemények*, 2 (1950), 148–151.
10. The improvement of distance measurement by the interference of light-rays. *Geodézia és Kartográfia*, 2 (1950), 64.
11. Two new theodolites for primary geodetic observation. *Földméréstani Közlemények*, 2 (1950), 148–151.
12. New and modern surveying instruments. *Földméréstani Közlemények*, 3 (1951), 85–86.
13. The 1951 General Assembly of the Hungarian Academy of Sciences. *Földméréstani Közlemények*, 3 (1951), 48–49.
14. The General Assembly of IUGG in Bruxelles. *Földméréstani Közlemények*, 4 (1952), 115.
15. The Congress for Geodesy and Geophysics in Budapest. *Geodézia és Kartográfia*, 4 (1952), 171–176.
16. Leveling experiences in France. *Földméréstani Közlemények*, 4 (1952), 178–181.
17. Triangulation with infrared rays. *Földméréstani Közlemények*, 4 (1952), 230–232.
18. Triangulation with electromagnetic rays. *Földméréstani Közlemények*, 4 (1952), 235–237.
19. Conquering of giant mountains. *Geodézia és Kartográfia*, 6 (1954), 68.
20. The leveling refraction. *Geodézia és Kartográfia*, 8 (1956), 250–251.
21. A new leveling rod for underground and night observations. *Geodézia és Kartográfia*, 8 (1956), 331–332.
22. The Geodetic Congress of the Hungarian Academy of Sciences. *Geodézia és Kartográfia*, 9 (1957), 64–68.
23. International course for distance-measurements in Munich. *Geodézia és Kartográfia*, 9 (1957), 81–82.
24. About the invention of triangulation. *Geodézia és Kartográfia*, 10 (1958), 65.
25. The European uniform triangulation network. *Geodézia és Kartográfia*, 10 (1958), 65–66.
26. The electric eye in the praxis. *Geodézia és Kartográfia*, 10 (1958), 67.
27. Conference about the Text-book of Geodesy and about the journal Geodézia és Kartográfia. *Geodézia és Kartográfia*, 10 (1958), 75–78.
28. Polish proposals to the standardization of the works in geodesy surveying and cartography. *Geodézia és Kartográfia*, 10 (1958), 153–154.
29. Meeting on the professional education of surveyors in Dresden. *Geodézia és Kartográfia*, 11 (1959), 210–215.
30. International Conference on Geodetic Calculations in Cracow. *Geodézia és Kartográfia*, 11 (1959), 298–299.
31. Geodesy and its related sciences before UN. *Geodézia és Kartográfia*, 12 (1960), 209–211.
32. Geodesy at the liberation festivities of the Technical University for Civil Engineering and Communication. *Geodézia és Kartográfia*, 12 (1960), 212.
33. An interesting French innovation. *Geodézia és Kartográfia*, 12 (1960), 213.
34. The Congress of IUGG. *Geodézia és Kartográfia*, 12 (1960), 288–292.
35. New definitions of the astronomical unit. *Geodézia és Kartográfia*, 14 (1962), 116–117.
36. Criticism on "Geodézia és Geofizika". *Geodézia és Kartográfia*, 14 (1962), 207–210.
37. Geodesy in the service of artificial satellites. *Geodézia és Kartográfia*, 14 (1962), 302–303.
38. The international organization of geodesy is 100 years old. *Geodézia és Kartográfia*, 14 (1962), 303–304.
39. Scientific conference on recent crustal movements in Leipzig. *Geodézia és Kartográfia*, 14 (1962), 380–381.
40. The 3rd Congress of Yugoslavian surveyors. *Geodézia és Kartográfia*, 15 (1963), 65.
41. A geodetic artificial satellite. *Geodézia és Kartográfia*, 15 (1963), 66.
42. The education of engineer-teachers in the GDR. *Geodézia és Kartográfia*, 15 (1963), 66.
43. Large-scale mapping of Japan. *Geodézia és Kartográfia*, 15 (1963), 131.
44. To the 100 years anniversary of the birth of Radó Kövesligethy. *Geodézia és Kartográfia*, 15 (1963), 222.
45. The key of symbols in our large-scale maps. (Co-author: I Novotny) *Geodézia és Kartográfia*, 15 (1963), 290–292.
46. Training practice of surveying students abroad. *Geodézia és Kartográfia*, 15 (1963), 292–293.
47. Some data about the content of Volume 14 of our journal. *Geodézia és Kartográfia*, 15 (1963), 293–294.
48. The accuracy of the topographic maps. *Geodézia és Kartográfia*, 15 (1963), 370–373.
49. Conference on surveying of mines in Pécs. *Geodézia és Kartográfia*, 15 (1963), 377.
50. The problems of engineering surveying at the FIG. *Geodézia és Kartográfia*, 15 (1963), 389.
51. International colloquium on photogrammetry in Dresden. *Geodézia és Kartográfia*, 15 (1963), 459–460.

52. A new gravimeter for marine observations. *Geodézia és Kartográfia*, 16 (1964), 292.
53. Triangulation with distance measurements in the Pacific area. *Geodézia és Kartográfia*, 16 (1964), 292.
54. A new electronic distance meter. *Geodézia és Kartográfia*, 16 (1964), 458.
55. Clairaut (1713—1765). *Geodézia és Kartográfia*, 17 (1965), 138.
56. HIFIX: a new electronic instrument in surveying. *Geodézia és Kartográfia*, 17 (1965), 141–142.
57. Fermat (1601—1665). *Geodézia és Kartográfia*, 17 (1965), 201.
58. The situation of our literature on geodesy and surveying. *Geodézia és Kartográfia*, 18 (1966), 40–46.
59. Altimeter working on the laser-principle. *Geodézia és Kartográfia*, 18 (1966), 58.
60. Conference on the shape of the Earth and on refraction in Vienna (Co-author: P Biró) *Geodézia és Kartográfia*, 19 (1967), 299–300.
61. Congress of the IAG. *Geodézia és Kartográfia*, 20 (1968), 136–138.
62. The 18th Conference of the Polish Geodetic Society. *Geodézia és Kartográfia*, 20 (1968), 143.
63. A new photogrammetric plotter. *Geodézia és Kartográfia*, 20 (1968), 145.
64. Connection of the Azores to the European tringulation net. *Geodézia és Kartográfia*, 20 (1968), 219–220.
65. Technical practice and exchange of foreign experiences. *Geodézia és Kartográfia*, 20 (1968), 291–292.
66. Cosmic triangulation above the Caribean See. *Geodézia és Kartográfia*, 20 (1968), 295–296.
67. The number of surveyors in the Federal Republic Germany. *Geodézia és Kartográfia*, 20 (1968), 292–293.
68. Some data of taking photos from the Moon. *Geodézia és Kartográfia*, 20 (1968), 303.
69. A new objective. *Geodézia és Kartográfia*, 20 (1968). 304.
70. Upper Mantle Project. *Geodézia és Kartográfia*, 20 (1968), 304.
71. Instrument for the measurement of electric aerial contact lines. *Geodézia és Kartográfia*, 20 (1968), 375.
72. Dr. István Rédey. *Geodézia és Kartográfia*, 20 (1968), 458.
73. The 4th Congress of Yugoslavian surveyors. *Geodézia és Kartográfia*, 21 (1969), 140.
74. Suomen Geodettinen Laitos. *Geodézia és Kartográfia*, 21 (1969), 375–376.
75. Expenses of surveying. *Geodézia és Kartográfia*, 21 (1969), 462.
76. The number of surveyors and cartographists in the FRG. *Geodézia és Kartográfia*, 21 (1969), 462.
77. A new law about the mine-surveying service. *Geodézia és Kartográfia*, 22 (1970), 211.
78. Some data on the situation of the world survey. *Geodézia és Kartográfia*, 22 (1970), 375–376.
79. Scientific session at the Academy. *Geodézia és Kartográfia*, 23 (1971), 47.
80. Reports on the sessions of the Photogrammetric Sub-Committee of the Geodetic Scientific Committee of the Hungarian Academy of Sciences. *Geodézia és Kartográfia*, 23 (1971), 296–297.
81. Conference on the training of surveyors in Dresden. *Geodézia és Kartográfia*, 23 (1971), 298–299.
82. Conference on land registers in Yugoslavia. *Geodézia és Kartográfia*, 23 (1971), 299–300.
83. To the memory of two Finnish scientists. *Geodézia és Kartográfia*, 24 (1972), 125–127.
84. The Institute for Geodesy, Surveying and Photogrammetry at the Technical University of Budapest. *Geodézia és Kartográfia*, 24 (1972), 136–137.
85. The economical importance of city-surveys. *Geodézia és Kartográfia*, 24 (1972), 144.
86. The Union of Technical Societies and the Society for Geodesy and Cartography in figures. *Geodézia és Kartográfia*, 24 (1972), 292–293.
87. The 12th Congress of the International Society for Photogrammetry. *Geodézia és Kartográfia*, 24 (1972), 371–372.
88. Géza Hankó (obituary). *Geodézia és Kartográfia*, 25 (1973), 121–122.
89. Days of hydrosurveying in Baja. *Geodézia és Kartográfia*, 25 (1973), 292–293.
90. The GEOPLANE 300. *Geodézia és Kartográfia*, 25 (1973), 387.
91. 25 years "Geodézia és Kartográfia". *Geodézia és Kartográfia*, 25 (1973), 401–404.
92. Days of Hungarian Geodesy in Vienna. *Geodézia és Kartográfia*, 26 (1974), 67–68.
93. Information about the Conference on Technical Education in Székesfehérvár. *Geodézia és Kartográfia*, 26 (1974), 280–282.
94. The 14th FIG Congress. (Co-authors: Gy Gabos, I Joó) *Geodézia és Kartográfia*, 27 (1975), 63–68.
95. Opening talk at the festive session to the 30th anniversary of the liberation of our country. *Geodézia és Kartográfia*, 27 (1975), 153–154.
96. Awarding doctor honoris causa at the Technical University, Budapest. *Geodézia és Kartográfia*, 27 (1975), 216.
97. Dr. Gertrud Láng (obituary). *Geodézia és Kartográfia*, 27 (1975), 219.

98. Artificial satellites launched in 1973. *Geodézia és Kartográfia*, 27 (1975), 221.
99. Information about the 13th International Photogrammetric Congress. *Geodézia és Kartográfia*, 27 (1975), 223–224.
100. Report on the yearly assembly of IAG, 1975. (Co-authors: Gy Alpár, F Halmos, I Joó) *Geodézia és Kartográfia*, 28 (1976), 57–64.
101. Remarks to the paper of G. Vagács: About the parallax. *Geodézia és Kartográfia*, 28 (1976), 145–146.
102. The Fifth Congress of the Yugoslavian Surveyors and Technicians. *Geodézia és Kartográfia*, 28 (1976), 148.
103. The African surveying conference. (Co-author: F Raum) *Geodézia és Kartográfia*, 28 (1976), 452–453.
104. The Geodetic Society of the GDR 25 years old. *Geodézia és Kartográfia*, 28 (1976), 453–454.
105. The Congress of the International Society for Photogrammetry. *Geodézia és Kartográfia*, 28 (1976), 449–451.
106. Reports of the Department of Geodetic Science of the Ohio State University. *Geodézia és Kartográfia*, 28 (1976), 475–476.
107. The Congress of ISP. (Co-authors: J Gebry, M Gerencsér, B Kovács, O Rádai) *Geodézia és Kartográfia*, 29 (1977), 129–136.
108. The new curriculum of civil engineers for surveying at the University of Dresden. *Geodézia és Kartográfia*, 29 (1977), 138.
109. Willem Schermerhorn (obituary). *Geodézia és Kartográfia*, 29 (1977), 206–207.
110. Artificial satellites launched in 1974. *Geodézia és Kartográfia*, 29 (1977), 292–293.
111. The leading staff of UGGI. *Geodézia és Kartográfia*, 29 (1977), 293–294.
112. The Union of Technical Societies and the Society for Geodesy and Cartography in figures. *Geodézia és Kartográfia*, 29 (1977), 295–296.
113. The 15th Congress of IAG. (Co-authors: Á Detrekői, F Halmos, F Raum) *Geodézia és Kartográfia*, 29 (1977), 368–370; 455–460.
114. The National Surveying in Sweden. *Geodézia és Kartográfia*, 29 (1977), 461.
115. An anniversary. *Geodézia és Kartográfia*, 29 (1977), 464.
116. The artificial satellites launched in 1975. *Geodézia és Kartográfia*, 30 (1978), 311–312.
117. The 6th Conference of Special Committe of ISP. *Geodézia és Kartográfia*, 30 (1978), 470.
118. The session of the Council of ISP. *Geodézia és Kartográfia*, 30 (1978), 470–471.
119. Remarks to the paper: The teaching of economics and management principles. *Geodézia és Kartográfia*, 31 (1979), 192–194.
120. The artificial satellites launched in 1976. *Geodézia és Kartográfia*, 31 (1979), 220–221.
121. A new French technical society. *Geodézia és Kartográfia*, 31 (1979), 460.
122. The General Assembly of the Hungarian Academy of Sciences in 1980. *Geodézia és Kartográfia*, 32 (1980), 279–280.
123. The General Assembly of the Polish Geodetic Society. *Geodézia és Kartográfia*, 32 (1980), 396.
124. The artificial satellites launched in 1977. *Geodézia és Kartográfia*, 33 (1981), 66–67.
125. Commemoration to Prof. Buchholz at the Technical University Dresden. *Geodézia és Kartográfia*, 33 (1981), 68–69.
126. The artificial satellites launched in 1978. *Geodézia és Kartográfia*, 33 (1981), 138–141.
127. The 14th Congress of ISP. (Co-author: P Winkler) *Geodézia és Kartográfia*, 33 (1981), 219–220.
128. The work of Committee VI at the 14. Congress of ISP. *Geodézia és Kartográfia*, 33 (1981), 224–225.
129. Commemoration to the 25th anniversary of founding the Society. *Geodézia és Kartográfia*, 33 (1981), 237–240.
130. The General Assembly of the Hungarian Academy of Sciences. *Geodézia és Kartográfia*, 33 (1981), 367–369.
131. The education of surveying engineers in Switzerland. *Geodézia és Kartográfia*, 34 (1982), 45–47; 116–118.
132. The XVI. Congress of FIG. *Geodézia és Kartográfia*, 34 (1982), 50–53.
133. The Technical Society and our Society in figures. *Geodézia és Kartográfia*, 34 (1982), 63–64.
134. The XVIth Congress of the International Association of Surveyors (FIG). The meetings of the commissions. (Co-authors: Á Detrekői and T Lukács) *Geodézia és Kartográfia*, 34 (1982), 125–130.

135. Control of bridge structure elements by photogrammetry. *Geodézia és Kartográfia*, 34 (1982), 139–140.
136. The anniversary of the founding of the Polish Photogrammetrical Society. *Geodézia és Kartográfia*, 34 (1982), 140.
137. Opinions about the technical education in the FRG. *Geodézia és Kartográfia*, 34 (1982), 140.

Acta Geodaet., Geophys. et Montanist. Hung. Volume 18 (1—2), pp. 9—14 (1983)

SOME PROBLEMS OF GEODYNAMICS AND METHODS FOR THEIR SOLUTION[1]

A A IZOTOV[2]

Central Research Institute for Geodesy, Photogrammetry and Cartography, Moscow

[Manuscript received October 15, 1980]

Inner and outer forces influencing the present evolution of the Earth can be detected and interpreted by the effects caused in the Earth's crust and surface (change of the rotation velocity, polar motion, earth tides, vertical and horizontal crustal movements, movements of lithospheric plates). The most urgent problems are in this field the connection of physico-chemical processes in the Earth's interior with tectonic phenomena, interaction between continental and oceanic parts of the crust, the development of oceanic trenches and their effect on the crustal evolution, present and past continental movements.

In the framework of the International Geodynamics Project the problems are approached from a geological–geophysical point of view. These methods, however, cannot yield accurate numerical data on these movements. Global geokinetic processes could be studied most easily by satellite geodetic and astronomic methods. The author discusses such methods and proposes to establish a mixed commission of astronomers-geodesists and geologists-geophysicists which should outline the problems to be solved by common efforts.

Keywords: crustal movements; geodynamics; geokinetics; plate tectonics; polar motion; satellite geodesy; spherical astronomic

Some basic ideas of geodynamics emerged already at the end of the last century. They were connected with the dynamics of the rotation of the Earth, namely, it has been found that measured and theoretical periods of the polar motion differ from each other. These problems have been closely connected ever since their emergence with Earth tides, with the inner construction of the Earth, and with the investigation of geodynamic processes in the interior and at the surface.

In the last decades, the problems of geodynamics met deep interest in many branches of the geosciences and they are the subject of extended researches. These investigations are carried out partly in the framework of national programs, partly in international cooperations with the collaboration of scientists from many countries. Such an international project was from 1961 on "The Upper Mantle and Its Effect on the Evolution of the Earth's Crust", reorganized since 1975 into the "International Geodynamic Project", suggesting a wider program for researches in this field.

[1] Paper presented at the Conference "The role of geosciences in the prospection of energy sources", Sopron, October 15, 1980

[2] 125 167 Moscow A—167, Ul. Viktorenko 211 kv 18

Geodynamics is separate branch of geosciences with its own field of research. It consists of two Greek words: "γεοσ" is Earth, and "δυναμισ" is force; this two words well describe the content of the branch of science. Evidently the inner and outher forces were considered by the founders as the subject of their investigations, as they act in the interior of the Earth and in the surrounding space and influence its evolution.

The Earth is a planet of the solar system and it is under the action of the gravitational forces exerted by other members of this system, mainly by the Sun and the Moon. They together bring about the Earth tides. In addition in the Earth's interior there are own gravitational forces which influence differentiation and mass movements. But the most important fact is that the Earth is yet in an active phase of inner physico-chemical and physico-mechanical processes which cause changes in its stress distribution, and result in material movements in deep layers as well as in the Earth's crust.

Inner and outer forces which influence the present evolution of the Earth can be detected and understood by a study of effects and phenomena caused in the Earth's crust and at the surface. This means that the study of geokinetic processes has utmost importance for the study and solution of many geodynamic problems. Such geokinetic effects can be immediately measured and observed. They include variations of the rotational velocity of the Earth polar motion, Earth tides, vertical and horizontal crustal movements, including also the drift of great lithospheric plates.

The changes of the Earth's rotation were studied so far by the astronomic observation of the changes in the longitude of observatories of the world time service network. The long-term observations led to the conclusion that the rotation of the Earth has seasonal, longer periodic and even secular changes. In the results and consequently in the scientific conclusions deduced from them, however, many contradictions have appeared, not yet being clarified. Thus e.g. by using the results of the European and North-American stations of the time service, different values are obtained for the change of the Earth's rotation.

The results of the observation of the longitudes in the observatories of the time service are also used in the study of the polar motion. For this purpose astronomical observations in five stations of the International Polar Motion Service have been used for more than 80 years. On the basis of the latitude observations, the main components of the polar motion have already been determined. The same data show that the North-Pole has also a secular wandering in the direction of Greenland with a velocity of 10 cm/year, but the whole wandering is a little dubious.

Some contradictions and doubts in connection with the non-uniform rotation and the polar motion can be due to movements of the astronomical observation stations in consequence of the drifts of the lithospheric plates. Meanwhile there are no reliable data on the stability or possible motion of these stations, as their relative situation has not been determined in a uniform geodetic system of coordinates, and they are not controlled by regular repetitive measurements. In addition, it is supposed for all temporary and permanent astronomical regular latitudinal and longitudinal observations that the vertical conserves its original position at all stations in spite of its temporary changes in the Earth's interior and surface due to material movements. That means that on the basis of exclusively astronomical latitude- and longitude determinations it is very difficult to reach unambiguous and clear conclusions about the geokinetic phenomena to be studied.

Researches of the vertical crustal movements by geodetic methods resulted in the conclusion that positive and negative height changes with values of 3—5 mm/year are possible even inside of lithospheric plates. The studies of the horizontal crustal movements have at present only a local character, as they are carried out only on tectonically active areas. Thus, the direction and velocity of the regional horizontal movements of the Earth's crust are not yet well understood.

It is evident that the vertical and horizontal movements of the Earth's crust are the components of its own deformation caused by the same geodynamic processes in the Earth's crust and in the layers below it. Nevertheless, geodetic investigations result in independent determinations of these components without any connection between them. In addition it is supposed in the study of the vertical crustal movements that the gravity field of the Earth does not change in time. Naturally these suppositions do not allow to get a complete picture on the realistic deformations of the Earth's crust and on the geodynamic processes provoking them.

Earlier purely astronomic measurements made for the verification of the hypothesis on the drift of the continents did not yield any conclusive results.

The latter can be explained by the unadequateness of technics and methods of the astronomical observations in the near past for determining small-scale variations in the position of sites at the Earth's surface. This is why the continental drift is even now severely discussed, and neither its opponents nor its supporters possess sufficient data to convince about their point of view.

As it is known the international programs mentioned resulted in a survey of the mid-ocean ridges and deep sea trenches, and it was recognized that the inner structure of the Earth's crust is different below continents and oceans, etc. These discoveries resulted in a revival of old theories on the mobility of the Earth's crust and new hypotheses were made about the Earth's inner structure and development. The actual problems of this field are: physico-chemical processes in the Earth's interior, their connection with tectonic phenomena, interaction between continental and oceanic parts of the crust, mechanism of the deep oceanic trenches and their effect on the evolution of the Earth's crust, continental drift at present and in the historic past.

The present International Geodynamic Project proposes the solution of these problems by geologic-geophysical means. But these methods, even if they are the most uptodate ones, do not allow a numerical determination of the present drift rate of continents and lithospheric plates. Further, this project does not include a study of the geokinetic phenomena such as non-uniform rotation of the Earth, polar motion, although they can be the consequences, sometimes even the causes of tectonic processes.

The mentioned presently active geokinetic phenomena can be detected only by regularly repeated astronomical-geodetic observations in some points of the Earth's surface in a uniform and invariable system of coordinates. By a determination of the relative position of these points in different epochs, numerical data can be collected on the studied phenomena, further on their temporal and spatial changes. The same data enable to reach very important, but non-unambiguous conclusions about the geodynamic processes causing these geokinetic variations.

It is evident that the study of geokinetic phenomena as the drift of continents necessitates repeated geodetic-astronomical measurements during rather long time spans in not very long time intervals. Therefore, they can be studied most easily in a network of permanent geodetic-astronomical stations (or in geodynamic stations or observatories). The basis for such a network could be the station network of the International Polar Motion Service and the latitude observatories of the International Time Service. Naturally, it is advisable to extend this network by other existing or newly established stations in order to include the most interesting zones and areas of the Earth's surface. Such stations would be necessary not only in continents, but also in oceanic areas, using for this purpose suitable islands.

For the establishment of the geodynamic station network and for the determination of the changes of the coordinates of the stations both classical and modern satellite methods of geodetic-astronomical observations are to be used. Both methods will find applications according to their theoretical properties. It would be necessary to solve one and the same problem by several methods in order to obtain results which are free of the characteristic errors of the different methods.

The most important task of every geodynamic station is to carry out regular latitude and longitude determinations by classical methods. These methods have developed to a very high level, thus the error of latitude and longitude determinations from yearly series do not surpass 0.01″ or 0.3 m. Classical astronomical methods can be used for these purposes as they enable the independent determination of latitude and longitude which are then independent from all other stations.

In order to eliminate the effect of the changes of the vertical on the determinations latitude and longitude, high precision gravimetric investigations are to be carried out around every geodynamic station in certain time intervals. Uptodate gravimetric instruments and methods enable the determination of the relative value of the gravity acceleration with an error not greater than 0.05 mgal. This accuracy enables already a rather accurate determination of the changes of the vertical at the geodynamic stations.

In addition it is advisable to carry out high precision measurements of the gravity acceleration with absolute methods at all geodynamic stations. At present this is already possible as there are ballistic gravimeters at disposal which enable the absolute measurement of the gravimetric field with a precision of some 10^{-2} mgals. These instruments enable the study of the temporal variations of the Earth's gravity field and to collect new data for the explanation of geodynamic processes in the Earth's interior and at its surface.

The theory of the continental drifts could be controlled by very high precision classical geodetic measurements, including repeated levelings and triangulations. But such measurements are, especially when they cover wide areas, very expensive and time-consuming, even within one cycle of the measurements. Therefore, classical geodetic measurements can only be used at present for the study of local and partly of regional crustal movements.

For the study of the global geokinetic phenomena the most advantageous methods and technical means are satellite geodetic and astronomical measurements. They enable a very accurate positioning of points on the Earth's surface even with very long distances between them, and seas and oceans can be traversed as well. These methods are at the same time both organisatorically and technically more simple and operative than classical geodetic methods.

Continental drifts and polar motion can also be studied by laser location of the Moon, by observing laser mirrors on its surface. As it is known the observation of the distance to a laser mirror on the Moon's surface during one night enables the determination of the radius of the latitudinal circle of a station with an error of 10 cm. Such measurements made during one month enable already a similarly high precision determination of the distance of the station from the equatorial plane of the Earth. Measuring the transit times of the same laser mirror on the Moon's surface through the meridians of a number of stations, in knowledge of the right ascension of the laser mirror, the geocentric longitudes of the stations can also be measured. Naturally the laser location of the Moon necessitates the exact knowledge of the geocentric coordinates of the laser mirrors, the shape parameters of the Moon, its physical libration and movements along its path. Besides, this method necessitates high power telescopes, therefore it can only be realized at greater astronomic observatories.

It seems that the geometric methods of the space geodesy are more adaptable for a study of the continental drifts. It is sufficient for this purpose to carry out regular measurements to a satellite with laser ranging equipment and to carry out synchronous photographic measurements. These measurements and observations enable in all cases the determination of the relative position of terrestrial stations in a system of coordinates connected with the gravity centre of the Earth and its rotation axis. According to computations, the present level of cosmic geodesy enables the determination of the distance of surface stations with errors of 10–20 cm using satellites in altitudes of 4–5 thousand km provided with laser mirrors and observations made with laser telescopes. For the study of the continental drift, and even more for that of the changes of the rotation velocity of the Earth, the VLBI-method can also be used which has been developed in the Soviet Union and in the US. That means the synchronous observation of an extragalactic radio source using two radio telescopes at great distances from each other. Its utilization is enabled by etalon frequencies of high phase stability; portable radio telescopes have already been manufactured or will be produced in the near future. A survey of the possibilities of the VLBI shows that the determination of the relative position of observing stations with errors of 10 cm can be reached and the changes of the length of the day can be measured with an error of less than one tenth of ms.

There are other radiotechnical methods for the solution of geodetic problems by satellite observations too. Among them the most sympathetic and perhaps most advantageous method is the Doppler-method which has been used already for a number of purposes. It is partly used for the tasks of the International Polar Motion Service. It can also be applied for the temporal tracing of the relative spatial position of geodynamic stations.

It is clear that researches for the solution of geodynamic problems shall be continued and intensified in the future. These programs have to include the study of the presently known geokinetic phenomena by geodetic-astronomical methods which are based on the observation of the artificial satellites of the Earth. In this connection, working plans for the study of the Earth environment should include the needs of geodynamic investigations, too.

The tools and methods of the geodetic-astronomical observations and measurements are continuously improving in accuracy. Thus e.g. it can already be hoped that repeated geodetic-astronomical measurements can be used for the control and monitoring of the present drift of continents during the lifetime of a scientific generation.

Naturally, the organization of the geodetic-astronomical measurements for the solution of geodynamic problems raises many technical questions, too. This problem should be studied by a team consisting of geodetico-astronomists and geologico-geophysicists in order to enable the start of such measurements in the near future. This is necessary to conclude the discussion of theories and to begin with proven facts and unambiguous scientific conclusions in connection with problems which are of great interest for the modern geosciences.

Acta Geodaet., Geophys. et Montanist. Hung. Volume 18 (1—2), pp. 15—27 (1983)

ENTWICKLUNGSTENDENZEN IN DER LANDESVERMESSUNG[1]

K RINNER[2]

Technische Universität, Graz

[Eingegangen am 15. Oktober 1980]

National Survey stands for the creation of the basis of geodetic operations required in national, regional, and continental areas. It is observed that these fundamentals are not settled definitions but depend on requirements and theories and on available technologies. From the present point of view these are systems of terrestrial control points and navigation satellites as well as maps and digital models for conveyance of land informations and geodetic observatories where the connection to higher systems is exercised.

In the following the historical development of geodesy is considered first. Then kind and accuracy of measured variables, models, and procedures as well as education are discussed. A view to the future shows the activities in geodesy in developing countries as well as in countries with geodetic tradition. Finally it is pointed out that the tasks of national survey are completed neither in theory nor in practice and that a period begins which is marked by a broader offer of geodetic informations and by the measurement of the influence of time variations.

Als „Landesvermessung" wird die Schaffung von Grundlagen für die Durchführung der im nationalen, regionalen und kontinentalen Bereichen erforderlichen geodätischen Operationen bezeichnet. Dabei wird beachtet, daß diese Grundlagen nicht feststehende Begriffe sind, sondern von Anforderungen und Theorien und von den verfügbaren Technologien abhängig sind. Aus der derzeitigen Sicht sind diese flächenförmig angeordnete vermarkte Systeme von terrestrischen Kontrollpunkten und von Navigationssatelliten sowie Kartenwerke und digitale Modelle zur Vermittlung von Landinformationen und Geodätische Observatorien in welchen der Anschluß in übergeordnete Systeme erfolgt.

In der Folge wird erst die geschichtliche Entwicklung der Geodäsie betrachtet. Sodann erfolgt eine Diskussion über die Art und die Genauigkeit der Meßgrößen, über Modelle und Verfahren sowie über die Ausbildung. In einem Ausblick in die Zukunft wird die Tätigkeit in den geodätischen Entwicklungsländern sowie in den Ländern mit geodätischer Tradition betrachtet. Schließlich wird festgestellt, daß die Aufgaben der Landesvermessung weder in der Theorie noch in der Praxis abgeschlossen sind und eine durch die Erweiterung des geodätischen Informationsangebotes und die Erfassung von zeitlichen Veränderungen gekennzeichnete Epoche beginnt.

Keywords: control points; digital models; geodetic observatories; history of geodesy; national survey; navigation satellites

[1] Vortrag abgehalten am 15. Oktober 1980 an der Konferenz „Die Rolle der Geowissenschaften in der Erkundung der Energiequellen" in Sopron

[2] A-8010 Graz, Rechbauer Str. 12

1. Was ist Landesvermessung?

Die geodätischen Aufgaben werden in allen Teilen der Welt in gleicher Weise gestellt. Immer ist es ihr Ziel, geometrische und andere Informationen über die Erdoberfläche und die darauf befindlichen materiellen Organismen und natürlichen und künstlichen Objekte zu ermitteln. Immer interessieren zeitliche Veränderungen dieser Größen und immer ist eine geeignete Darstellung und Interpretation der Information erforderlich. Einteilung und Bezeichnung der verschiedenen geodätischen Operationen sind jedoch in verschiedenen Teilen der Welt verschieden. Aus diesem Grund muß erst die Frage beantwortet werden: Was ist Landesvermessung?

Nach dem Sinn des Wortes könnte als Landesvermessung die Summe aller geodätischen Operationen in einem Land (nationaler Bereich) bezeichnet werden. Tatsächlich erfolgt jedoch eine fachliche Beschränkung auf geodätische Operationen, welche Grundlagen hiefür schaffen und eine geographische Erweiterung auf zusammengehörige Regionen oder Kontinente. Die Begriffe Landes-, Regional- und Kontinentalvermessung sind daher in fachlicher Hinsicht analog. Hinsichtlich der Organisation ihrer Durchführung sind sie jedoch von gegebenen nationalen oder übernationalen Gegebenheiten abhängig. Ganz allgemein werden durch die Landesvermessung selbständige geodätische Einheiten geschaffen, die zu regionalen oder kontinentalen Vermessungssystemen zusammengefügt werden und mit dieser einen Bestandteil des endgültig angestrebten Weltsystems bilden. Die Schaffung dieses ist jedoch Aufgabe der Erdmessung.

Wegen der großen Bedeutung der geodätischen Aktivitäten für die Wirtschaft, die technische Erschließung, die Wissenschaft und die Verwaltung werden die Hauptaufgaben der Landesvermessung in der Regel im staatlichen Bereich durchgeführt und nur Teilbereiche privaten Büros übertragen.

Nach dem bisher Gesagten ist es Aufgabe der Landesvermessung (= LV), Grundlagen für die Durchführung der im nationalen, regionalen und kontinentalen Bereich erforderlichen geodätischen Operationen zu schaffen. Dabei muß beachtet werden, daß Grundlagen nicht feststehende Begriffe sind, sondern von den Anforderungen, den Theorien und den verfügbaren Technologien abhängig sind. Aus derzeitiger Sicht sind dies folgende Operate:

- — Flächenförmig angeordnete und vermarkte Systeme von terrestrischen Kontrollpunkten (Festpunktfelder) für die Bestimmung der Lage, der Höhen und von Schwerewerten, deren zeitliche Veränderungen routinemäßig bestimmt werden sollen. Diese Systeme werden durch Navigationssatelliten hoher Genauigkeit ergänzt und kontrolliert.
- — Topographische und thematische Kartenwerke, Pläne, Verzeichnisse und digitale Modelle zur Vermittlung von Landinformationen, die in möglichst kurzen Intervallen dem aktuellen Zustand angepaßt werden.

— Geodätische Observatorien, in welchen der Anschluß der LV an übergeordnete, geodätische Systeme und die Mitarbeit an überregionalen Projekten erfolgt, sowie Testfelder in welchen neue Verfahren und Technologien den besonderen Bedürfnissen des Landes (Region oder Kontinent) angepaßt werden.

Tendenzen für die weitere Entwicklung der LV hängen von allgemeinen Zielsetzungen und Aufgaben der Geodäsie, sowie von Entwicklungen der Technologie der geodätischen Instrumente ab. Es ist daher notwendig, erst diese zu betrachten.

2. Blick in die Entwicklung der Geodäsie

Wie jede naturwissenschaftliche Disziplin erfüllt auch die Geodäsie wissenschaftliche und praxisorientierte Aufgaben und Anwendungen. Als Wissenschaft obliegt ihr einmal die Bestimmung der geometrischen, der gravimetrischen und der Orientierungsparameter der Erde, also eine Aufgabe, welche der Geophysik zuzuzählen ist. Außerdem muß sie Theorien, Verfahren und Technologien für den Einsatz bei der Durchführung von technischen Projekten bereitstellen und ist daher auch ein Teil der Ingenieurwissenschaften. In der praktischen Anwendung liefert die Geodäsie einerseits Daten, die als Grundlage für Theorien und Aussagen anderer Geodisziplinen Verwendung finden, und nimmt anderseits an der Planung, Durchführung und Kontrolle von technischen Projekten teil, welche der wirtschaftlichen Erschließung dienen, trägt zur Bodenordnung bei und stellt für die Verwaltung bedeutsame Informationen bereit.

In allen Funktionen werden geodätische Aussagen aus Meßgrößen mit Hilfe mehrfach kontrollierter überbestimmter Modelle abgeleitet und können daher in jeder Funktion als Fundament für die Aussagen anderer Disziplinen Anwendung finden. Fundamentale Aufgaben der wissenschaftlichen Geodäsie sind:

— die Bestimmung der geometrischen Form, der Orientierung und der Strukturparameter, des Schwerefeldes der Erde in einem inertialen Bezugssystem,

— die Bestimmung der zeitlichen Veränderungen der geometrischen und Orientierungsparameter sowie der zeitlichen und räumlichen Veränderungen der Strukturparameter des Schwerefeldes,

— die Darstellung der Ergebnisse in zeitabhängigen Erdmodellen durch die Raumpositionen eines Fundamentalsystems von Kontrollpunkten, die geometrischen und physikalischen Parameter eines Erdellipsoids, Parameter der Polbewegung und die Parameter von bekannten, dynamischen Phänomenen (Erdgezeiten, Krustenbewegung, Plattentektonik),

— die Durchführung analoger Aufgaben für die Bestimmung der geometrischen Form der Orientierung und des Schwerefeldes des Mondes und der übrigen Planeten des Sonnensystems.

Dazu kommen wichtige Aufgaben, welche die praktische Anwendung der geodätischen Operate betreffen. Es sind dies:

— die Bestimmung und Erhaltung von nationalen und regionalen Systemen von geodätischen Kontrollpunkten für die Position und die Schwere sowie die Ermittlung ihrer zeitlichen Veränderungen,
— die Anfertigung von grundlegenden topographischen und thematischen Land- und Seekarten, Verzeichnissen und digitalen Modellen, durch welche geometrische und andere Informationen über die Oberfläche der Erde auf den Kontinent und unterhalb der Meere vermittelt werden,
— die Einrichtung von Datenbanken, in welchen die ermittelten Informationen gespeichert sind und die Vereinigung dieser zu einem Landinformationssystem, das möglichst viele geometrische, juridische, physikalische, geologische, land- und forstwirtschaftliche, hydrologische und andere Daten über das betrachtete Gebiet enthält,
— die Absteckung von technischen Projekten in der Natur und Überwachung der plangerechten Ausführung und
— die Bestimmung der zeitlichen Veränderungen von Objekten und ihrer Umwelt zufolge der Durchführung von technischen Projekten oder von Naturereignissen, Ermittlung von Prognosen für den weiteren Verlauf.

Aus Voraussetzung für die Durchführung der geodätischen Aktivität kommt dazu die Ausbildung des Nachwuchses in die einschlägigen, mathematischen, physikalischen und ingenieurwissenschaftlichen Theorien sowie in die Technologie der Meßinstrumente und in den Verfahren der Messung, Berechnung und Analyse.

Die geodätischen Aussagen werden aus Meßgrößen mit Hilfe von mathematischen und physikalischen Modellen abgeleitet, welche sich den in der Natur vorliegenden Verhältnissen möglichst gut anschmiegen. Die Genauigkeit der Aussage hängt von der Genauigkeit der Meßgrößen, von der Güte der benutzten Modelle und Verfahren und von der im konkreten Fall vorliegenden Konfiguration der Bestimmungsgleichungen ab. Eine Steigerung der Genauigkeit kann durch Verbesserung aller drei genannten Faktoren erfolgen.

2.1 *Meßgrößen*

Geodätische Meßgrößen sind geometrische Verbindungsparameter zwischen Meß- und Zielpunkten (Richtung und Winkel, Strecken und Streckendifferenzen, trigonometrische Höhenunterschiede), physikalische Parameter des Schwerefeldes

(Beschleunigungen, Gradienten, Potentialdifferenzen), Frequenzen (Zeit, Dopplereffekt), Interferenzen, Beschleunigungen, Druck, Temperatur usw., sowie durch Photogrammetrie, Radargrammetrie und durch andere Verfahren der Fernerkundung vermittelte Information.

Geometrische Meßgrößen, die aus Zustandsgrößen (Richtung, Frequenz, Phase, Intensität) von Licht- und elektrischen Wellen abgeleitet werden, sind durch die Refraktion beeinflußt. Ihre derzeit etwa $\pm(1$ bis $10)\cdot 10^{-6}$ betragende Genauigkeit zwischen terrestrischen Punkten kann durch Dispersionsmessungen (zwei-Farben-Laser) und Mikrowelle um ein bis zwei Zehnerpotenzen gesteigert werden. Bei Messungen nach Punkten außerhalb der Atmosphäre nimmt der innerhalb dieser verursachte Refraktionseffekt bei Richtungsmessungen proportional mit der Entfernung zu, bei der Entfernungsmessung aber ab. In der Entfernungsmessung nach weit entfernten Satelliten werden daher hohe Meßgenauigkeiten im cm-Bereich erwartet.

Physikalische Meßgrößen können im allgemeinen mit höherer Genauigkeit bestimmt werden als geometrische. Bei Zeit-(Frequenz) Messungen wird eine relative Genauigkeit von $\pm 1\cdot 10^{-13}$ bei Dopplerfrequenzen $\pm 10^{-12}$ erreicht. Aus bestimmten physikalischen Meßgrößen (Geschwindigkeit, Beschleunigung) lassen sich geometrische (Strecken) durch Integration bestimmen. Aus Potentialdifferenzen (Nivellement, Schweremessung) abgeleitete Höhendifferenzen sind ein bis zwei Zehnerpotenzen genauer als trigonometrische. Für die Bestimmung von ellipsoidischen Höhen werden aber mehrfach ungenauer bestimmbar (Undulationen, Anomalien, Mittelwerte von Pegel) benötigt.

Der Betrag des Schwerevektors kann mit einer Genauigkeit von (1 bis $10)\cdot 10^{-9}$ bestimmt werden, die Richtung (aus astronomischen Messungen) mit einer Genauigkeit von etwa $1\cdot 10^{-6}$ je Richtungskomponente, eine Steigerung ist wegen der schlecht erfaßbaren Refraktion nicht absehbar. Änderungen von Richtung und Betrag des Schwerevektors lassen sich durch Pendel- und Gravimetermessungen mit einer Genauigkeit von (1 bis $10)\cdot 10^{-9}$ ermitteln.

Die Genauigkeit der photogrammetrischen Information wird durch Verbesserung der optischen und photographischen Abbildung und durch Digitalisierung der Informationen gesteigert. Analoges gilt auch für die Radargrammetrie und andere am Beginn der Entwicklung stehende Verfahren der Fernerkundung.

Ein Ausblick in die Zukunft läßt erkennen, daß neben der Erhöhung der Genauigkeit auch eine Erweiterung in der Art und Anzahl der geodätischen Informationen zu erwarten ist. Außerdem wird der Meßvorgang durch die Automation und die Möglichkeit, diesen auch von und nach Raumfahrzeugen auszuführen mit geringeren Kosten und in kürzerer Zeit erfolgen können.

2.2 *Modelle und Verfahren*

Für die Bestimmung von 2D und 3D Positionen von Punkten stehen nach wie vor die klassischen Verfahren der Triangulation und Trilateration, sowie des geometrischen und trigonometrischen Nivellements zur Verfügung. Diese sind durch die Entfernungsmessung mit elektromagnetischen Wellen, sowie durch die Automation der Meß- und Rechenvorgänge effektiver geworden und lassen sich in kürzerer Zeit, mit größerer Genauigkeit (in kleineren Systemen von 1 bis 2 km Ausdehnung im sub-Millimeterbereich) und größerer Wirtschaftlichkeit durchführen.

Zu diesen Verfahren kommt die Positionsbestimmung mit Hilfe von Satelliten, nach oder von welchen Meßgrößen (Richtungen, Entfernungen und Dopplerfrequenzen) bestimmt werden. Dabei muß unterschieden werden, ob Satelliten nur als Hochziele (Ziel- oder Standpunkte) dienen (geometrische Verfahren), oder ob auch die durch die Bewegungsgesetze vorliegenden Informationen mitbenutzt werden (dynamische Verfahren). Im ersten Fall lassen sich nur die Positionen der Meß- und Zielpunkte, in letzteren zusätzlich auch die Strukturparameter des Schwerefeldes bestimmen.

Praktische Bedeutung haben Verfahren erlangt, die von bekannten Bahndaten ausgehen und als Meßdaten integrierte Dopplerfrequenzen benutzen. Ein Beispiel hiefür ist das Navy Navigation Satellite System = NNSS, bei dem erst die Bahndaten (Ephemeriden) aus Dopplermessungen auf Stationen mit bekannten Positionen oder einem bekannten Modell des Schwerefeld abgeleitet und dann die Bestimmung der Positionen von Neupunkten aus integrierten Dopplerfrequenzen ermittelt werden. Ein Nachfolgesystem (GPS = Global Positioning System) höherer Genauigkeit wird installiert. Bei diesen Systemen haben die in Funktion der Zeit angegebenen Raumpositionen der Satelliten die Funktion von Kontrollpunkten, von welchen mit Hilfe der Meßdaten die Positionen der Neupunkte durch Einfach- oder Mehrfach-Punkteinschaltung bestimmt werden können. Die absolute Genauigkeit dieser Positionsbestimmung liegt derzeit im Meter-Bereich, die relative ist um eine Größenordnung besser.

Für die genaue Bestimmung der Verbindungsvektoren von weit entfernten Punkten stehen auch Verfahren mit Laser Entfernungen und interferometrischen Daten zur Verfügung. Diese werden in globalen und regionalen Versuchsnetzen (in Europa EROS, VLBI und EDOC) erprobt und mit bekannten Daten verglichen. Die bisherigen Ergebnisse lassen Genauigkeiten im cm-Bereich erwarten.

Die Bestimmung der Parameter des Schwerefeldes erfolgt durch terrestrische Messungen der Schwerebeschleunigung und ihrer Gradienten, durch entsprechende Messungen in Raumfahrzeugen und aus geometrischen Meßdaten, welche nach, von und zwischen Raumfahrzeugen ermittelt werden.

Strukturparameter des Schwerefeldes, Orientierungsparameter der Erde (Polschwankungen, Rotationsgeschwindigkeit, Krustenbewegung und Positionen der terrestrischen Meßpunkte werden in einem Iterationsprozeß bestimmt. Die Kombination verschiedener terrestrischer und Satellitenverfahren und die Verwendung verschiedener Meßmittel und Meßgrößen läßt die Ausschaltung systematischer Einflüsse erwarten.

Für die Gewinnung globaler Werte werden Beobachtungseinrichtungen in stationären Observatorien benötigt (globales Testnetz). Für die Verdichtung und die Verfeinerung werden transportable Laserstationen und interferometrische (VLBI) Geräte entwickelt. Die genannten Aufgaben können nur in internationaler Zusammenarbeit gelöst werden. Jedes Land kann und soll dazu durch Errichtung von entsprechend ausgerüsteten geodätischen Labors (Geo-Stationen) beitragen und sich mit diesen an der Forschung beteiligen.

In die so geschaffenen Grundlagen können die regionalen und nationalen Festpunktfelder für die Lage, Höhe und Schwere eingebunden werden. Durch die moderne Technologie für die Datengewinnung (Messung) und Datenverarbeitung (Berechnung) in Verbindung mit der Automation von Messung, Berechnung und Darstellung kann die Neubestimmung und Strukturanalyse der Festpunktfelder in kürzerer Zeit und mit höherer Genauigkeit als bisher erfolgen. Außerdem werden durch Anwendung statistischer Verfahren numerisch belegte Hinweise für die Interpretation der Ergebnisse erhalten. Daraus folgt die Möglichkeit zeitabhängiger Veränderungen der geometrischen Form, des Schwerefeldes und der Orientierung der Erde durch geodätische Verfahren zu bestimmen und zur Erfassung von geodynamischen Phänomenen beizutragen.

Von besonderer Bedeutung sind die am Beginn ihrer Entwicklung stehenden inertialen Meßverfahren, bei welchen auf kreiselstabilisierten Plattformen die Beschleunigungskomponenten der Bewegung eines Trägerfahrzeuges (Auto oder Flugzeug) vom Start zum Zielpunkt gemessen werden. Durch zweifache Integration folgen daraus die Koordinatenunterschiede der Verbindungsstrecke, außerdem kann die Schwerebeschleunigung gemessen werden. Mit Hilfe eines Computers werden die Meßdaten mit Normalwerten verglichen und Lotabweichungen und Schwereanomalien ermittelt. Bei inertialen Meßverfahren können daher die Informationen über die Raumposition und über Schwerewerte in einem Arbeitsgang ermittelt werden. Wegen auftretender Gänge in den Meßeinrichtungen sind die Verfahren derzeit nur für die Interpolation zwischen etwa 100 km entfernten Punkten geeignet. Die erreichbare Genauigkeit liegt derzeit für Koordinatenunterschiede im Dezimeterbereich, Verbesserungen können erwartet werden. Es kann angenommen werden, daß Inertialverfahren in Zukunft an Bedeutung gewinnen.

Für die Beschaffung von Detailinformationen über geometrische und andere Eigenschaften der Erdoberfläche stehen die leistungsfähigen Verfahren der Photogrammetrie, der Radargrammetrie und andere Verfahren der Fernerkundung zur Verfügung. Diese werden durch Verbesserung der Abbildung (Auflösung und Geometrie) und durch die Digitalisierung genauer, vollständiger und wirtschaftlicher. Die Verarbeitung zu thematischen Karten, Verzeichnissen und digitalen Modellen wird automatisiert, die Kartographie wird in den Prozeß der bisherigen Auswertung einbezogen. Auf dem Weg von der Datengewinnung durch die Aufnahme zum bisherigen Endprodukt der Karte werden digitale Modelle eingeschaltet.

Die erzielten Fortschritte in der Gewinnung geodätischer Aussagen haben naturgemäß auch die Auswirkungen auf die ingenieurgeodätischen Anwendungen. Sie stellen einen wertvollen Beitrag zur Rationalisierung und Kontrolle von bestehenden und der Entwicklung neuer Verfahren dar, welche für die Planung, Durchführung und Überwachung von technischen Projekten von großer Bedeutung sind.

Für die praktische Anwendung ist die Optimierung der geodätischen Operationen in Bezug auf vorgegebene Zielstellungen von Bedeutung. Dabei soll die Frage nach dem optimalen Meßaufwand bei vorgegebener Genauigkeit bestimmter Daten, oder nach der maximal erreichbaren Genauigkeit bei vorgegebenem Meßaufwand beantwortet werden. Die Theorien hiefür sind bekannt, leistungsfähige Computer ermöglichen die numerische Berechnung, oder das numerische Experiment. Als Ergebnis der Optimierung liegen Hinweise für die optimale Anordnung und Gewichtung von Messungen und für die Orientierung von Systemen vor. Doch muß beachtet werden, daß dabei auch Fragen einer geodätischen Kosmetik eine Rolle spielen. Eine wichtige ingenieurgeodätische Aufgabe liegt in der Erstellung von Genauigkeitsprognosen für bestimmte geodätische Daten, z.B. für Durchschlagsfehler unterirdischer Bauwerke.

Ein Ausblick in die Zukunft zeigt, daß die Geodäsie durch die Entwicklung neuer Technologien, durch den Computer, durch die Automation und durch die Verwendung von Satelliten als Ziel und Träger von Meßinstrumenten leistungsfähiger geworden ist und dieser Trend noch anhält. Die Geodäsie kann daher zusätzlich zu den bisherigen statischen Aufgaben der Beschreibung bestehender Zustände neue Aufgaben übernehmen, welche die Veränderungen und den Trend dieser sowie die Vermehrung der Information, also dynamische Vorgänge betreffen. Sie entwickelt sich damit zu einem Informationssystem über bestimmte Zustände und deren Veränderungen der Erde und ihres Außenraumes im Großen und im Kleinen und wird in Zukunft mit erhöhter Aussagekraft und Leistung Grundlagen für die wirtschaftliche Erschließung, für die Überwachung, Verwaltung, für die Kontrolle unserer Umwelt und für wissenschaftliche Forschung liefern.

2.3 *Ausbildung*

Für jede Disziplin ist die Ausbildung der Nachwuchskräfte eine wichtige Aufgabe. Dies gilt besonders in Zeiten des Umbruches, in denen neue Möglichkeiten und Verfahren entstehen und althergebrachte Anschauungen den Wert verlieren. Die Ausbildung soll weniger die Anwendung, als die Grundlagen betreffen und soll der Erkenntnis entsprechen, daß nichts praktischer ist, als eine gute Theorie. Sie muß künftige Führungskräfte in die Lage versetzen, das leistungsfähige Instrument der

Automaten für die Messung und die Berechnung voll einzusetzen und mit Hilfe verfeinerter Modelle eine bessere Anpassung an die Wirklichkeit zugewinnen. Die Ausbildung muß von der Erkenntnis ausgehen, daß im Zeitalter der Automaten für die Messung und Zeichnung sowie für die kartographische Verarbeitung, vor allem 2 Gruppen von Führungskräften gebraucht werden: Geodätische Manager, welche Automaten und Techniker einsetzen und die gewonnenen Ergebnisse richtig bewerten können und Wissenschaftler, welche beitragen, die Verfahren, sowie die Meß- und Rechenautomaten zu entwickeln und die erhaltenen Ergebnisse zu analysieren.

Wegen der großen Bedeutung der Ausbildung und den verschiedenartigen Anforderungen, welche hiebei mitwirken, haben alle internationalen Vermessungsorganisationen Kommissionen und Arbeitsgruppen gebildet, welche Vorschläge hiefür ausarbeiten sollen. In der nächsten Zeit ist unter Mitwirkung der UNESCO eine gemeinsame Tagung dieser Kommissionen beabsichtigt. Bei dieser soll das Ziel verfolgt werden, gemeinsame Grundlagen für die in verschiedenen Regionen unserer Welt bestehenden Aufgaben der Ausbildung zu formulieren und den einzelnen Ländern in Form von Modellen zur Verfügung zu stellen.

3. Ausblick in die LV

Nach den Betrachtungen im ersten Abschnitt besteht für jedes Land die Notwendigkeit eine LV einzurichten, welche die Herstellung der vermessungstechnischen Grundlagen für die wirtschaftliche Erschließung und für die Verwaltung, sowie die routinemäßige Mitarbeit an wissenschaftlichen Projekten durchführen soll. Zu ihren Aufgaben gehört die Bestimmung der Festpunktfelder für die Position und für die Schwerewerte, die Herstellung grundlegender Kartenwerke und digitaler Modelle für Landinformationen und die Einrichtung und der routinemäßige Betrieb von wissenschaftlichen Observatorien und Testnetzen.

Für die Durchführung dieser Aufgaben stehen außer den klassischen Geräten und Verfahren neue, leistungsfähige, weitgehend automatisierte Meßgeräte und Computer zur Verfügung. Durch die Entfernungsmessung mit elektromagnetischen Wellen, durch die Benutzung von Satelliten als Ziele und Träger von Meßeinrichtungen, durch Inertialverfahren und durch die Automation können mehr und auch neue Informationen in wesentlich kürzerer Zeit erhalten werden als bisher. Durch die Möglichkeiten der automatischen Berechnung lassen sich daraus mit Hilfe von verfeinerten Modellvorstellungen in kürzerer Zeit, mit größerer Genauigkeit und Zuverlässigkeit und in größerer Allgemeinheit verbesserte Aussagen ableiten.

Dadurch wird die Leistungsfähigkeit der LV in der Bestimmung von Festpunkten und in der Ermittlung von Landinformationen wesentlich erhöht. Die LV kann daher nicht nur die bisherigen statischen Aussagen über einen bestimmten Zustand einfacher ermitteln, sie ist auch in der Lage, durch Wiederholung der nunmehr genaueren Operationen in kurzen Zeiträumen zeitabhängige Phänomene meßtechnisch zu erfassen und Vorhersagen über den weiteren Verlauf mitzuteilen.

In fast allen Ländern der Welt gibt es daher Ämter und Organisationen, welche für die Durchführung der LV zuständig sind. Mit der regionalen und kontinentalen Vermessung, also der Zusammenfassung einzelner LV zu größeren Einheiten befassen sich naturgemäß internationale Arbeitsgruppen und Organisationen.

Der Zustand einer LV hängt vom Zustand der technischen und kulturellen Entwicklung des Landes ab, ebenso die Maßnahmen, welche zur Erreichung der gestellten Ziele erforderlich sind. Es muß daher zwischen der LV in Ländern mit geodätischer Tradition und Ländern unterschieden werden, welche erst am Beginn ihrer technischen Entwicklung stehen.

3.1 *Länder mit geodätischer Tradition*

In geodätischen Traditionsländern sind in der Regel Festpunkte vorhanden. Die Genauigkeit ihrer Parameter ist aber als Folge der in vielen Jahrzehnten erfolgten Entstehung und Überarbeitung nicht homogen und oft unzureichend. Hier besteht die Aufgabe durch ergänzende und Neumessungen und Berechnungen eine Verbesserung der Genauigkeit der Parameter (2D-Koordinaten, Höhen und Schwerewerte) zu erreichen.

Für relative 2D Positionen kommt hiefür die Messung von Laser-Entfernungen und Richtungen zwischen bisher nachgeordneten Punkten (niederer Ordnung) in Betracht, weil in diesen der Einfluß der Refraktion weitgehend erfaßt werden kann. Die Ausschaltung systematischer Einflüsse und der Anschluß an übergeordnete Systeme kann mit Daten (Entfernungen, Richtungen, Positionen) erfolgen, die für mehrere Hundert km von einander entfernte Punkte mit Hilfe von Satelliten abgeleitet werden. Bei der Berechnung kann die bisherige Hierarchie der Systeme erster, zweiter usw. Ordnung wegfallen, und eine gemeinsame Behandlung aller Meßdaten bei Einführung entsprechender Gewichte erfolgen.

Die durch Potentialdifferenzen definierten Höhen werden durch Nivellement und Schweremessungen erhalten. Zur Bestimmung von trigonometrischen (ellipsoidischen) Höhen werden zusätzlich Undulationen des Geoides oder Höhenanomalien benötigt. Diese lassen sich nach bekannten terrestrischen oder aus Satellitenverfahren ermitteln. Als Ergebnis werden ellipsoidische 3D Koordinaten (Länge, Breite, Höhe oder XYZ) und Nivellementhöhen für alle Festpunkte angestrebt, damit terrestrische und Satellitendaten unmittelbar verwendet werden können.

Schwerewerte werden in der LV für die Reduktion von Meßgrößen, für die Bestimmung von Lotabweichungen und Undulationen, für die Ermittlung von Höhen, als Strukturparameter des Schwerefeldes, für geophysikalische Aufgaben und als Ausgangsdaten für die Lagerstättenforschung benötigt. Da die Aussagekraft von der

Genauigkeit der Schweredaten abhängt, besteht das Bestreben, diese durch Einsatz der absoluten Schweremessung mit Hilfe von transportablen Frei-Fallgeräten zu erhöhen. Es liegt daher die Aufgabe vor, innerhalb der LV ein Grundsystem nullter Ordnung einzurichten, an welches bestehende und neue Gravimetermessungen angeschlossen werden können.

Die LV wird in Zukunft mehr als bisher mit der Bereitstellung von Landinformationen beschäftigt sein. Zusätzlich zum Grundstücks- und Grenzkataster, welche geometrische Informationen über die Einteilung, Bebauung, sowie die land- und forstwirtschaftliche Nutzung vermitteln, werden die juridischen Informationen des Grundbuches, die hydrologischen und geologischen und andere technischen Informationen aus den zuständigen Katastern, sowie die Vermittlung soziologischer Informationen, Aufgabe der LV sein. Als Endziel zeichnet sich ein Landinformationssystem (LIS) ab, in welchem für bestimmte Flächeneinheiten möglichst viele Informationen enthalten sind, die abgerufen und in beliebiger Form dargestellt werden können. Dadurch leistet die LV einen wertvollen Beitrag zur Verbesserung und zur weiteren Entwicklung der Bodenordnung und damit der Verwaltung, Überwachung und Verbesserung der Lebensbedingungen.

Als Grundlage für die technische Planung und für wissenschaftliche Untersuchungen wird ein möglichst genaues digitales Geländemodell für jedes Land benötigt. Die Anfertigung und die laufende Berichtigung dieses Modelles ist ebenfalls Aufgabe der LV.

Für grundlegende topographische und thematische Karten besteht im Zuge der wirtschaftlichen Erschließung, der Planung und Durchführung technischer Projekte, für Aufgaben des Verkehrs, der Verwaltung und andere technische Aufgaben ein zunehmendes Bedürfnis. Der Inhalt der Karten wird aber nicht mehr wie bisher ausschließlich graphisch vermittelt werden, hiefür werden digitale Speicher und Dateien angefertigt, aus denen gewünschte Informationen in gewünschter, manipulierter Form dargestellt werden können. Ein wichtiges Informationsmittel sind Orthophotos und Radargramme, die in zunehmendem Maße als Grundrißinformation für Kartenwerke Anwendung finden.

3.2 *Geodätische Entwicklungsländer*

In Entwicklungsländern sind in der Regel unzureichende geodätische Grundlagen vorhanden. Aufgabe der LV ist es daher, diese möglichst rasch bereitzustellen. Dabei spielt in der ersten Phase die benötigte Zeit die wesentliche Rolle, die angestrebte Genauigkeit und Vollständigkeit braucht erst in späteren Phasen erreicht werden. In diesen Fällen liegt naturgemäß ein ideales Anwendungsgebiet für neue Verfahren vor, mit welchen der erstrebte Endzustand in aufeinander aufbauenden Phasen wie ein lebendiger Organismus geschaffen werden soll.

Unabhängig von den praktischen Bedürfnissen sollen aber schon von Anfang an auch wissenschaftliche Bedürfnisse der LV beachtet und gefördert werden. Denn dadurch kann die Anwendbarkeit von Ergebnissen der Forschung außerhalb des Landes geprüft, der für die Entwicklung der Geodäsie erforderliche nationale Beitrag erbracht und der Anschluß an übernationale geodätische Systeme gesichert werden.

Als Kontrollpunkte für die Positionen kommen in der ersten Entwicklungsphase die Satelliten eines operativen, präzisen Navigationssystems in Betracht. Dies sind derzeit die beiden Versionen (broadcast und precise des US-Navy Navigation Satellite System = NNSS), die in absehbarer Zeit durch das leistungsfähigere Global Positioning System (GPS) ergänzt werden. Auch andere Nationen diskutieren oder erproben derartige Systeme. Es kann daher angenommen werden, daß in Zukunft eine große Zahl von Satelliten mit bekannten Bahndaten als Kontrollpunkte der LV zur Verfügung stehen. Die Raumpositionen (kartesische oder ellipsoidische Koordinaten) der Punkte eines terrestrischen Festpunktefeldes können daraus durch Messung von geodätischen Daten (Entfernungen, Richtungen, Dopplerfrequenzen) nach oder von diesen Satelliten-Kontrollpunkten erfolgen. Dabei muß zwischen Verfahren zur Bestimmung der relativen und der absoluten Positionen unterschieden werden. Erstere können derzeit mit einer Genauigkeit von etwa $\pm 0{,}2$ m, letztere um eine Zehnerpotenz ungenauer bestimmt werden.

Die Verdichtung wird in der ersten Entwicklungsphase vor allem durch Inertialverfahren erfolgen und durch die wesentlich weniger leistungsfähigen terrestrischen Verfahren der Triangulierung und Polygonierung ergänzt werden. Für die Kontrolle und Verbesserung werden in einer zweiten Phase der Entwicklung Verfahren der Stellartriangulation, der 3D-Polygonierung und kombinierten Triangulation und Trilateration, sowie Satellitenverfahren mit mobilen Laser und interferometrische Verfahren zur Verfügung stehen. Dabei sollten auch die Geo-Stationen und die Testfelder des Landes benutzt werden. Das Festpunktefeld für die Schwerewerte kann auf ein System absoluter Schwerepunkte gestützt und durch Gravimetermessungen verdichtet werden. Erste Informationen über die Topographie und andere Eigenschaften des Landes werden durch Informationssatelliten vermittelt. Diese können durch photogrammetrische und Radaraufnahmen aus Flugzeugen und auch durch terrestrische Verfahren ergänzt werden. Die Verarbeitung zu topographischen und thematischen Karten wird durch die Digitalisierung der Information und Programmen zur Manipulation weitgehend automatisiert werden. Das Orthophoto und das digitale topographische Modell werden bereits in einem frühen Entwicklungsstadium vorliegen. Mit fortschreitender wirtschaftlicher Entwicklung und der damit verbundenen technischen Aufschließung wird als Grundlage für eine Bodenordnung die Anfertigung von Grundkataster, Grundbuch und anderen Katastern erforderlich sein. Dabei besteht aber die Möglichkeit, gleich von Anfang an, ein allgemeines Landinformationssystem zu planen, dieses aber erst im Zuge der Entwicklung langsam auszuführen.

3.3 *Abschließende Bemerkungen*

Die LV hat die ihr in der Vergangenheit übertragene Aufgabe für die Bodenordnung, Verwaltung und Planung weitgehend erfüllt. Festpunktefelder für die horizontale Lage, für Höhen und für Schwerewerte liegen in vielen Ländern vor, Katastraloperate für Grundstücke und andere Daten und grundlegende Kartenwerke sind entweder vorhanden oder in Bearbeitung. Manchmal wird daher die Meinung vertreten, daß in Zukunft die LV nur mehr konservierende Aufgaben zu erfüllen habe und die inzwischen entwickelten präzisen und automatischen Geräte für die Messung, Berechnung, Analyse und Kartierung gar nicht mehr richtig ausgenutzt werden können. Diese Meinung ist aber nicht richtig. Denn in der Zwischenzeit sind neue Aufgaben entstanden, welche vor allem zeitliche Veränderungen, also dynamische Zustände feststellen sollen und die nun zusätzlich zu den bestehenden, statischen Aufgaben aktuell geworden sind. Diese erfordern eine Erhöhung der Genauigkeit der geodätischen Aussage und eine Verminderung der Zeit für ihre Gewinnung und Interpretation. Dazu kommt eine Vermehrung des Inhaltes der geodätischen Informationen und der geodätischen Aussagen durch die Fernerkundung aus Flugzeugen und aus Satelliten, die digitale Speicherung der Informationen und die Möglichkeit ihrer Manipulation sowie die Mitteilung in thematischen Karten, Verzeichnissen und anderen Darstellungen. Die Geodäsie entwickelt sich nunmehr zu einem Informationssystem für technische Planungen, für die Verwaltung und auch für die Überwachung unserer Umwelt.

Die LV beschreitet damit einen Weg, der vom zentralen Vermessungsamt zur Informationszentrale für geodätische, physikalische, geologische, land- und forstwirtschaftliche, juridische, soziologische und andere Parameter unseres Landes führt. Die bisherigen geodätischen Meßdaten werden durch allgemeinere Informationen ergänzt. Zusätzlich zu Koordinatenverzeichnissen, Plänen und Karten kommen nun digitale Modelle mit oben genannten Parametern. Die LV wird damit ein tragendes Element und Instrument eines übergeordneten Landinformationssystems.

Daraus folgt, daß die Aufgaben der LV weder in der Theorie noch in der Praxis abgeschlossen sind. Eine neue durch die Erweiterung des geodätischen Informationsangebotes und die Erfassung von zeitlichen Veränderungen gekennzeichnete Epoche beginnt. Die Anwendung neuer Verfahren der Meß- und Rechentechnik, der Datengewinnung, Speicherung, Manipulation und Darstellung und neue wissenschaftliche Erkenntnisse stehen bereit. Für die LV bestehen daher neue Möglichkeiten und Verpflichtugen. Es ist zu hoffen, daß alle damit befaßten Personen in den Ämtern, Labors und Büros und die in den Regierungen Verantwortlichen diese Aufgabe erkennen und ihre Bewältigung in Angriff nehmen. Dazu gehört neben dei instrumentellen und personellen Ausstattung aber auch ein enger Kontakt mit den Forschungsstellen an den Universitäten, der Industrie und der Verwaltung.

Acta Geodaet., Geophys. et Montanist. Hung. Volume 18 (1—2), pp. 29—46 (1983)

ON THE ADJUSTMENT OF GYROTHEODOLITE OBSERVATIONS

ABDELHAMID KAMAL HASSAN[1]

Geodetic and Geophysical Research Institute of the Hungarian Academy of Sciences, Sopron

[Manuscript received September 20, 1981]

The paper presents the results of the adjustment calculations for the observations of a gyrotheodolite type MOM Gi-B2. The purpose of the study was to evaluate some aspects of different orders best fitting curves to the observations. Three sets of reversion points observed with the three measuring techniques of the amplitude method were used in the measurements. The three sets of observations were adjusted to get the order of the curve which show the best fitting for both the left and the right reversion points of different sets with minimum corrections. The mean of the gyroscope swings were calculated from the adjustment results of both the right and the left reversion points. The damping factor was also calculated from the same results on the basis of the theoretically exact equation of a damped simple harmonic motion which describes the damping factor. Finally a comparison was made between the obtained results. The results are shown in Tables and illustrated with diagrams.

Keywords: adjustment of gyrotheodolites; amplitude method; damping; drift of gyrotheodolites; gyrotheodolites; MOM Gi-B2; reversion point

1. Introduction

In a pendulous gyroscope used for finding the direction of the meridian, the horizontal movement of the spinning axis of the gyroscope is that of a damped simple harmonic motion. The direction of the meridian can be calculated from a number of successive turning points of the spinning gyroscope. This problem has been investigated by many authors starting with the famous formula derived by Schuler (1932) of Göttingen.

The paper presents a study for the adjustment of the gyrotheodolite observations (of the amplitude method). The adjusting procedures are based on the best fitting curve. The purpose of the study is to evaluate their aspects in the case of the gyrotheodolite observations to find to what extent it fits. The adjusting calculations were made for the right and the left reversion points separately on the assumption that the observations are stochastically independent and observed with equal precision. The mean of the gyroscopic swingings (the rest position) and the initial amplitude of the swings were calculated from the adjustment results of both the right and the left reversion points

[1] Permanent address: Banha University, Faculty of Engineering, Cairo, Egypt

Table I. Results of the adjustment

Observation set	Order of the adjusting model	μ_{Y_R}	μ_{Y_L}	α_N	μ_{α_N}	α_0	μ_{α_0}	f	μ_f
SET 1	1st order	±9.65″	±8.48″	212° 40′ 02.92″	±2.83″	1° 40′ 35.68″	±2.83″	3.71×10^{-5}	$\pm6.6\times10^{-6}$
	2nd order	±9.58″	±8.61″	212° 40′ 04.33″	±2.83″	1° 40′ 39.23″	±2.83″	5.17×10^{-5}	$\pm2.7\times10^{-5}$
	3rd order	±4.49″	±4.82″	212° 40′ 04.71″	±1.45″	1° 41′ 02.06″	±1.45″	8.84×10^{-5}	$\pm3.6\times10^{-5}$
SET 2	1st order	±4.56″	±4.32″	46.80″	±1.38″	38′ 10.50″	±1.38″	6.10×10^{-5}	$\pm8.6\times10^{-6}$
	2nd order	±4.65″	±4.23″	48.53″	±1.38″	38′ 09.30″	±1.38″	1.00×10^{-4}	$\pm3.5\times10^{-5}$
	3rd order	±2.52″	±2.95″	47.78″	±0.86″	37′ 58.35″	±0.86″	1.99×10^{-4}	$\pm5.7\times10^{-5}$
SET 3	1st order	±5.80″	±3.46″	28.80″	±1.28″	24′ 00.75″	±1.28″	1.66×10^{-4}	$\pm1.5\times10^{-5}$
	2nd order	±1.76″	±2.26″	31.73″	±0.63″	24′ 10.65″	±0.63″	2.88×10^{-4}	$\pm2.5\times10^{-5}$
	3rd order	±1.50″	±2.18″	33.60″	±0.58″	24′ 11.55″	±0.58″	4.28×10^{-4}	$\pm6.2\times10^{-5}$

after the reduction to the instant of release of the spinning gyroscope. The damping factor was calculated from the same results on the basis of the expansion of the exponential function which describes the damping factor.

The gyrotheodolite observations used in the investigation were measured with the usual techniques of the amplitude method, namely: observations with automatic and manual following, SET 1, observations with automatic following only, SET 2, and observations without following, SET 3. The observations were made in the geodetic laboratory of the Geodetic and Geophysical Research Institute of the Hungarian Academy of Sciences, Sopron. The used gyrotheodolite was of the type MOM Gi-B2.

The observations of the three sets were long series (56 reversion points) to give results clear enough to enable a good comparison between the adaptability of different adjusting models.

A comparison was made between the adjusting results of the three sets in Table I and in Figs 4–9. The azimuth of the observed reference direction was calculated using the rest position obtained after the adjustment and the reduction to the instant of release. A comparison was then made between the calculated azimuths to know which adjusting model gives better results. The results are shown in Table II.

Table II. Calculated azimuths and their accuracies

Observation set	Order of the adjusting model		
	1st order	2nd order	3rd order
SET 1	287° 55′ 14.55″ ± 3.50″	287° 55′ 13.14″ ± 3.50″	287° 55′ 12.76″ ± 2.51″
SET 2	287° 55′ 12.61″ ± 2.47″	287° 55′ 10.88″ ± 2.47″	287° 55′ 11.63″ ± 2.23″
SET 3	287° 55′ 17.39″ ± 2.42″	287° 55′ 13.89″ ± 2.15″	287° 55′ 11.66″ ± 2.13″

2. The mathematical model used in the adjustment

The right hand and left hand reversions were adjusted separately three times. The mathematical model used in the first adjustment is that of the first order best fitting curve i.e. the best fitting straight line as follows,

$$Y_i = A + BX_i\,, \tag{1}$$

where Y_i = the adjusted value of the reversion points read on the horizontal circle or in the autocollimator,

i = the order of the observations,

A = the initial Y-value of the fitted line, and

B = the slope of the fitted line.

Equation (1) was applied with both the right and the left reversion points separately; for the right reversions points $i = (1, 3, 5, \ldots n-1)$ and for the left ones $i = (2, 4, 6, \ldots n)$,

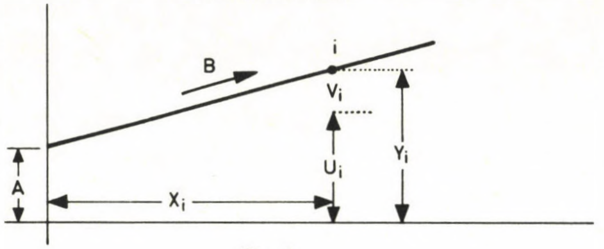

Fig. 1.

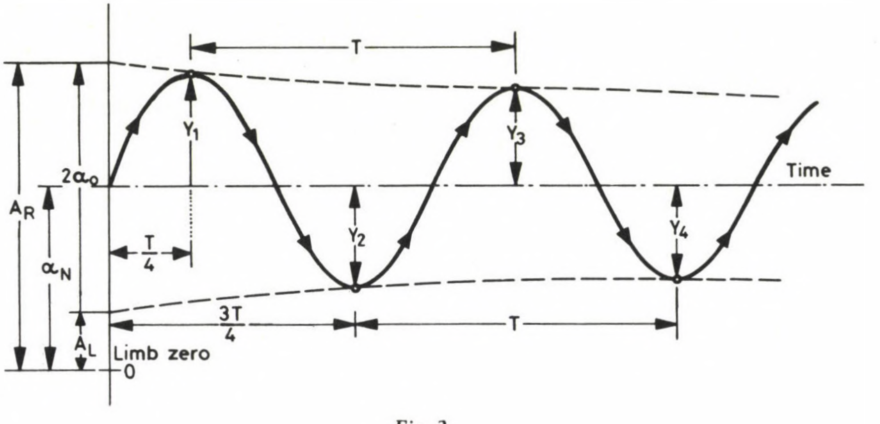

Fig. 2.

where n is the number of the reversion points of each set. The X-axis in Fig. 1 represents the time intervals between the reversion points which are equidistant with the time of a complete swing (T), Fig. 2. In the adjustment, T is supposed to be error-free as it can be measured with a high accuracy at the positions of the reversion points.

2.1 *Formation of the observation equations*

In Eq. (1) Y_i is replaced by the observed reversion points U_i and their residuals (correction) V_i, that is,

$$U_i + V_i = A + BX_i\,. \tag{2}$$

Applying Eq. (2) for the right reversions we get,

$$\begin{aligned} U_1 + V_1 &= A_R + B_R X_1 \\ U_3 + V_3 &= A_R + B_R X_3 \\ &\vdots \\ U_{n-1} + V_{n-1} &= A_R + B_R X_{n-1}\,. \end{aligned}$$

And for the left reversions we obtain the following:

$$\begin{aligned}
U_2+V_2&=A_L+B_LX_2\\
U_4+V_4&=A_L+B_LX_4\\
&\vdots\\
U_n+V_n&=A_L+B_LX_n\,.
\end{aligned}$$

The matrix-form for both the right and the left reversions (using continuous indices in both cases) is,

$$\begin{pmatrix}U_1\\U_2\\\vdots\\U_m\end{pmatrix}+\begin{pmatrix}V_1\\V_2\\\vdots\\V_m\end{pmatrix}=\begin{pmatrix}1 & X_1\\1 & X_2\\\vdots & \vdots\\1 & X_m\end{pmatrix}\cdot\begin{pmatrix}A\\B\end{pmatrix}\qquad\text{or}$$

$$\underset{(m,\,1)}{\mathbf{U}}+\underset{(m,\,1)}{\mathbf{V}}=\underset{(m,\,2)}{\mathbf{C}}\cdot\underset{(2,\,1)}{\mathbf{X}}$$

where $\mathbf{U}$ = vector of the observations (right or left reversion point),
$\mathbf{V}$ = vector of the residuals,
$\mathbf{X}$ = vector of the unknowns,
$\mathbf{C}$ = coefficient matrix of the unknowns, and
m = number of the right or the left reversions.

In case of applying a second order curve the coefficient matrix $\mathbf{C}$ and the vector of the unknowns $\mathbf{X}$ will be as follows:

$$\underset{(m,\,3)}{\mathbf{C}}=\begin{pmatrix}1 & X_1 & X_1^2\\1 & X_2 & X_2^2\\\vdots & \vdots & \vdots\\1 & X_m & X_m^2\end{pmatrix},\qquad\underset{(3,\,1)}{\mathbf{X}}=\begin{pmatrix}A\\B\\C\end{pmatrix},$$

and for a third order curve, $\mathbf{C}$ and $\mathbf{X}$ are,

$$\underset{(m,\,4)}{\mathbf{C}}=\begin{pmatrix}1 & X_1 & X_1^2 & X_1^3\\1 & X_2 & X_2^2 & X_2^3\\\vdots & \vdots & \vdots & \vdots\\1 & X_m & X_m^2 & X_m^3\end{pmatrix},\qquad\underset{(4,\,1)}{\mathbf{X}}=\begin{pmatrix}A\\B\\C\\D\end{pmatrix}.$$

If the order of the curve is denoted by K, then the general dimensions of $\mathbf{U}$, $\mathbf{V}$, $\mathbf{C}$, and $\mathbf{X}$ are

$$\underset{(m,\,1)}{\mathbf{U}} + \underset{(m,\,1)}{\mathbf{V}} = \underset{(m,\,K+1)}{\mathbf{C}} \cdot \underset{(K+1,\,1)}{\mathbf{X}} . \tag{3}$$

2.2 Solution for the unknowns and the residuals

The adjustment was solved according to the basic idea of the method of least squares, i.e., the sum of the calculated corrections for the observations must be a minimum i.e. $\mathbf{V}^T\mathbf{P}\mathbf{V} = \min$, where $\mathbf{P}$ is the weight matrix of the observations. For the system of Eq. (3), the normal matrix $\mathbf{N}$ (Detrekői 1977) is,

$$\mathbf{N} = \mathbf{C}^T\mathbf{P}\mathbf{C} .$$

The adjustment was made on the assumption that the observations are independent and of equal precision, then $\mathbf{N}$ is

$$\underset{(m,\,m)}{\mathbf{N}} = \underset{(K+1,\,m)}{\mathbf{C}^T} \cdot \underset{(m,\,K+1)}{\mathbf{C}} . \tag{4}$$

The solution for the vector of unknowns is:

$$\underset{(K+1,\,1)}{\mathbf{X}} = -\underset{(K+1,\,K+1)}{(\mathbf{C}^T \cdot \mathbf{C})^{-1}} \underset{(K+1,\,1)}{(\mathbf{C}^T \cdot \mathbf{U})} \tag{5}$$

and for the vector of the residuals:

$$\underset{(m,\,1)}{\mathbf{V}} = \underset{(m,\,K+1)}{\mathbf{C}} \cdot \underset{(K+1,\,1)}{\mathbf{X}} + \underset{(m,\,1)}{\mathbf{U}} . \tag{6}$$

The adjusted values of the reversion points are

$$Y_i = U_i + V_i . \tag{7}$$

2.3 Check of the calculations

The calculations were checked by computing the value [VV] by two methods; the first using the calculated vector of the residuals, and the second using the calculated vector of the unknowns, being in a matrix form as follows:

$$[VV] = \mathbf{V}^T\mathbf{V}, \qquad \text{and} \qquad [VV] = \mathbf{U}^T\mathbf{C}\mathbf{X} + \mathbf{U}^T\mathbf{U} .$$

The value of $[VV]$ with the two methods agreed with high accuracy. The mean square error of the unit weight for the adjusted reversions is calculated as follows:

$$\mu_0^2 = \frac{[VV]}{m-(K+1)}. \tag{8}$$

The covariance matrix of the unknowns $Q_{(x)}$ is calculated as the inverse of the normal matrix $\mathbf{N}$,

$$\mathbf{Q}_{(x)} = \mathbf{N}^{-1}$$

i.e. (9)

$$\mathbf{Q}_{(x)} = \mathbf{C}^T\mathbf{C}^{-1}.$$

The mean square error matrix $\mathbf{M}$ of the unknowns is calculated as follows:

$$\mathbf{M} = \mu_o^2 \mathbf{Q}_{(x)}. \tag{10}$$

3. Calculations of the main elements of the observations

The main elements of each set of reversion points are the mean position of the swings (the rest position) α_N, the amplitude of the swings α_o, and the damping coefficient f.

Starting with the formula of slowly damped monofrequential periodic swingings (the case of gyroscopic swingings in the plane), (Halmos 1977),

$$y_i = \alpha_N + \alpha_o \sin \frac{2\pi}{T} t_i \cdot e^{\left(-\frac{f}{2} t_i\right)} + K \tag{11}$$

where y_i = the momentaneous position of the gyroscope axis in the time t_i,
α_N = the mean position of the swings (the rest position),
α_o = the initial amplitude of the swings,
f = the damping coefficient,
K = a constant deviation from the gyro-north (due to the band torsion),
T = the time of a complete swing.

The constant K will be taken into consideration when calculating the gyro-azimuths.

For the first and second reversions, i.e. the first right and first left reversions (Y_{R1}, Y_{L1}), the times t_i are $\frac{T}{4}$ and $\frac{3T}{4}$, Fig. 2, and Eq. (11) will be:

$$Y_R = \alpha_N + \alpha_o \sin \frac{\pi}{2} e^{\left(-\frac{f}{8} T\right)},$$

$$Y_L = \alpha_N + \alpha_o \sin \frac{3\pi}{2} e^{\left(-\frac{3f}{8} T\right)}$$

Using the first three terms of the expansion of the exponential function we get:

$$Y_R=(\alpha_N+\alpha_o)-\left(\frac{\alpha_o f}{8}\right)T+\left(\frac{\alpha_o f^2}{128}\right)T^2-\left(\frac{\alpha_o f^3}{3072}\right)T^3,$$
$$Y_L=(\alpha_N-\alpha_o)+\left(\frac{3\alpha_o f}{8}\right)T-\left(\frac{9\alpha_o f^2}{128}\right)T^2+\left(\frac{27\alpha_o f^3}{3072}\right)T^3. \tag{12}$$

Referring to Eq. (1), its generalized form is:

$$Y_i=A+BX_i+CX_i^2+DX_i^3. \tag{13}$$

Applying Eq. (13) for the right and left reversions we get the following:

$$Y_R=A_R+B_RX+C_RX^2+D_RX^3$$
$$Y_L=A_L+B_LX+C_LX^2+D_LX^3 \tag{14}$$

comparing Eqs (12) and (14) and considering that X represents T, as mentioned before, we obtain,

$$A_R=\alpha_N+\alpha_o, \qquad A_L=\alpha_N-\alpha_o,$$
$$B_R=-\frac{\alpha_o f}{8}, \qquad B_L=\frac{3\alpha_o f}{8},$$
$$C_R=\frac{\alpha_o f^2}{128}, \qquad C_L=-\frac{9\alpha_o f^2}{128}, \tag{15}$$
$$D_R=-\frac{\alpha_o f^3}{3072}, \qquad D_L=\frac{27\alpha_o f^3}{3072}.$$

where A_R, B_R, C_R and D_R are the elements of the vector of unknowns calculated as in Eq. (6) for the right hand reversions and A_L, B_L, C_L and D_L for the left hand reversions.

From Eqs (15) we get α_N and α_o as follows:

$$\alpha_N=\frac{A_R+A_L}{2} \tag{16}$$

$$\alpha_o=\frac{A_R-A_L}{2}. \tag{17}$$

The mean square errors of α_N and α_o are,

$$\mu^2_{\alpha_N} = \frac{1}{4}(\mu^2_{A_R} + \mu^2_{A_L}) \tag{18}$$

and

$$\mu^2_{\alpha_o} = \frac{1}{4}(\mu^2_{A_R} + \mu^2_{A_L}). \tag{19}$$

As the gyrotheodolite swingings are slight and linearly damped, therefore only the linear terms of the exponential are retained, therefore the damping coefficient f is calculated from B_R and B_L of Eqs (15) as follows:

$$f = \frac{4(B_R + B_L)}{\alpha_o} \tag{20}$$

and its mean square error is,

$$\mu^2_f = \frac{16}{\alpha^2_o}\left(\mu^2_{B_R} + \mu^2_{B_L} + \frac{B^2_R + B^2_L}{\alpha^2_o}\mu^2_{\alpha_o}\right)$$

The numerical value of $\frac{B^2_R + B^2_L}{\alpha^2_o}\mu^2_{\alpha_o}$ is an insignificant value and can be neglected, therefore μ_f will be:

$$\mu^2_f = \frac{16}{\alpha^2_o}(\mu^2_{B_R} + \mu^2_{B_L}). \tag{21}$$

For each set of observations f was calculated twice, once using only the linear terms from Eqs (15), and then using all the terms of Eqs (15). The two values agreed with a negligible difference; this proves that the damping is linear.

4. Reduction of α_N and α_o to the instant of release

On the assumption that the drift existing in the rest position is linear, it is possible to reduce α_N and α_o to the instant of release of the spinning gyroscope when no drift was yet present. The reduction is made according to (Gregerson et al. 1971), as follows:

$$\begin{aligned} A_R &= 1.75\ Y_1 - 0.75\ Y_3 \\ A_L &= 2.25\ Y_2 - 1.25\ Y_4 \end{aligned} \tag{22}$$

where $Y_1, \ldots Y_4$ (Fig. 3) are the adjusted reversion points. The values of α_N and α_o reduced to the instant of release can be then calculated as in Eqs (16) and (17) but using A'_R and A'_L.

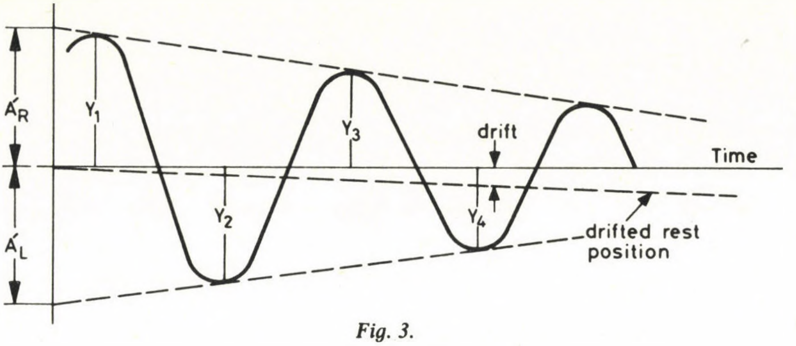

Fig. 3.

5. Computer program

The calculations were made by the help of the computer HP 2100A of the Geodetic and Geophysical Research Institute of the Hungarian Academy of Sciences, Sopron. The program "GYFIT" was used in the calculations. The Schuler means of the reversion points before and after the adjustment were calculated using the convolution coefficients 1/4, 1/2, 1/4.

The program "GYFIT" included the subroutine "POLI" with which the right hand and the left hand reversion points were adjusted using first, second and third order interpolations. The list of the subroutine "POLI" is shown in Table III and the whole program can be found in the computer center of the institute.

Table III

SUBROUTINE "POLI"

```
      SUBROUTINE POLI (N, K, C, SZORAS, SZIGMA)
      DIMENSION A(256),B(16),C(16),MUN1(17),MUN2(17),SZORAS(16)
      DIMENSION SUM(30)
      COMMON Y(600)
      XN=N
      SUM(1)=N*(N+1.0)/2.0
      SUM(2)=N*(N+1.0)*(2.0*N+1.0)/6.0
      SUM(3)=(N*(N+1.0)/2.0)**2
      SUM(4)=N*(N+1.0)*(2.0*N+1.0)*(3.0*N**2+3.0*N-1.0)/30.0
      SUM(5)=XN**2*(XN+1.0)**2*(2*XN**2+2*XN-1)/12.0
      SUM(6)=XN*(XN+1.0)*(2*XN+1.0)*(3.0*XN**4+6.0*XN**3-3*N+1.)/42.
      SUM(7)=XN**2*(N+1.)**2*(3*XN**4+6*XN*(3-XN**2-4*XN+2.)/24.
      SUM(8)=XN*(XN+1)*(10.*XN**7+35.*XN**6+(XN-1.)*(25.*XN**4
     1 -17.*XN**2+3.))/90.
      KK=K+1
      IF(K.GT.4) GO TO 53
      A(1)=N
      DO 54 J=1,K
```

Table III (contd)

```
 54 A(J+1)=SUM(J)
    DO 55 I=1,K
    DO 55 J=1,KK
    IJ=I*KK+J
    JI=I-1+J
 55 A(IJ)=SUM(JI)
    GO TO 56
 53 IF(K.LE.4) GO TO 100
    IJ=2*K
    DO 57 I=9,IJ
    SUM(I)=0.
    DO 57 II=1,N
 57 SUM(I)=SUM(I)+FLOAT(II)**I
    DO 58 J=1,K
 58 A(J+1)=SUM(J)
    A(1)=N
    DO 59 I=1,K
    DO 59 J=1,KK
    IJ=I*KK+J
    JI=I-1+J
 59 A(IJ)=SUM(JI)
 56 CONTINUE
    CALL MINV(A,KK,DET,MUN1,MUN2)
    IF(DET.EQ.0.0) STOP 777
    DO 62 I=1,KK
 62 B(I)=0.0
    DO 64 J=1,N
    B(1)=B(1)+Y(J)
    DO 64 I1=1,K
    B(I1+1)=B(I1+1)+FLOAT(J)*I1*Y(J)
 64 CONTINUE
    DO 66 I=1,KK
    C(I)=0.0
    DO 66 J=1,KK
    LL1=(J-1)*KK+I
    C(I)=C(I)+A(LL1)*B(J)
 66 CONTINUE
    SZIGMA=0.
    DO 67 J=1,N
    S=C(1)
    DO 65 H1=1,K
 65 S=S+FLOAT(J)**I1*C(I1+1)
    S=Y(J)-S
 67 SZIGMA=SZIGMA+S*S
    SZIGMA=SZIGMA/(N-KK)
    DO 68 I=1,KK
    J=(I-1)*KK+I
 68 SZORAS(I)=SQRT(SZIGMA*A(J))
    SZIGMA=SQRT(SZIGMA)
100 CONTINUE
    RETURN
    END
```

6. Summary of the results

The results of α_N, α_o and f with their accuracies are tabulated in Table I, where the results obtained for the three sets adjusted with three adjusting models are shown. From the tabulated results we notice the following:

1. For sets 1 and 2, the accuracy of Y_R, Y_L, α_N, α_o and f obtained from applying adjusting models 1 and 2 closely agreed but they are not the best, while at set 3, their accuracies obtained from the adjusting models 2 and 3 nearly agree and are better than the accuracy obtained from model 1. Generally, at the three observation sets, the accuracy obtained from the third order adjusting models are the best, see Table I.

2. Considering the results obtained from the third order model for the three sets, it is clear that the damping coefficient f of the first set is the smallest and that of the third set is the largest. The ration between $f_1:f_2:f_3$ is nearly equal to 1:2:4.

3. From the results of the three sets it is clear that the accuracies obtained for the third set are generally the best showing that the observation technique without following is better than the others and has the best internal accuracy, that because errors due to the secondary vibrations caused by the operations on the instrument are avoided. This is also clear from Figs 4–9 which show the corrections for the reversions and of the Schuler means for the three sets; in the diagrams the numbers 1, 2 and 3 have the following meanings:

1: diagrams concerning the 1st order adjustment model,
2: diagrams concerning the 2nd order adjustment model,
3: diagrams concerning the 3rd order adjustment model.

4. The azimuth of the direction connecting the instrument station and the collimator was calculated using α_N obtained from the adjustment and reduced to the instant of release. A comparison is made between the calculated azimuths of the three sets. The results are shown in Table II. It is clear that the azimuths calculated using α_N of the third order model for the three sets are the nearest to each other and have better accuracies than the others.

7. Conclusions

Gyrotheodolite observations of the amplitude method can be adjusted using several mathematical models presented by many authors considering that the oscillations of the spinning gyroscope has the character of a simple harmonic motion of the linearly damped form. The paper presented an investigation for the adjusting results of the gyrotheodolite observations obtained using an adjusting model utilizing interpolation curves of different orders and at the same time based on the formula of the simple harmonic motion (gyrotheodolite swinging).

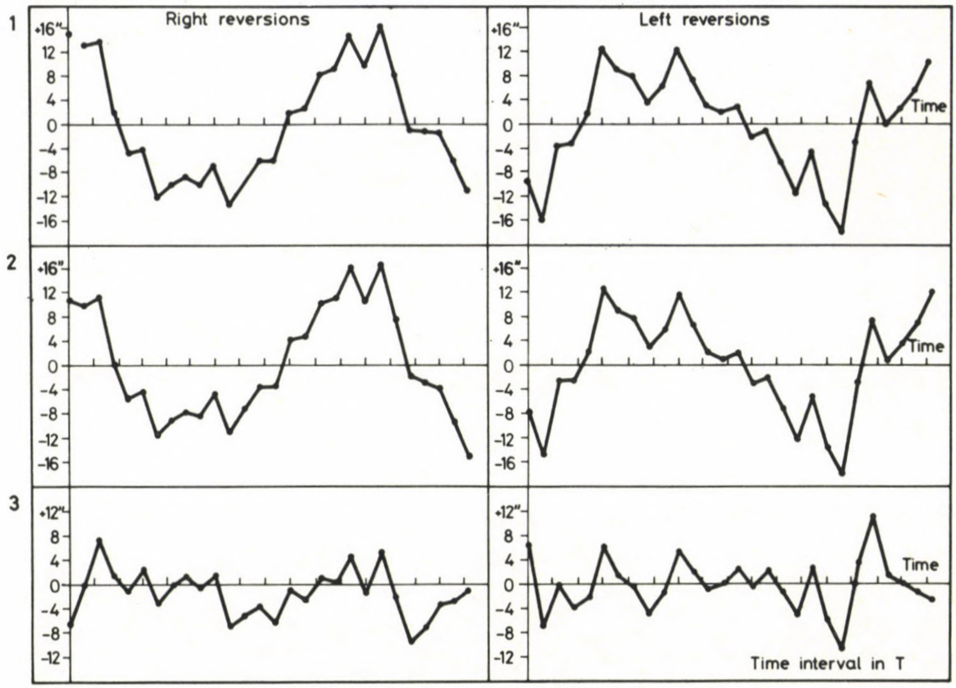

Fig. 4. Errors in the observations of (set 1)

The results of the investigation showed the following:

1. For gyrotheodolite observations of the amplitude method observed with the previously mentioned three observation techniques, a third order interpolation suits the adjustment of the observations with the minimum corrections, Figs 4–6, see Table I.

2. The Schuler means of the reversion points adjusted with a third order interpolation has the minimum corrections if compared with those of the other order interpolations, Figs 7–9.

3. The accuracy of the results of α_0 and α_N obtained from the adjustment using the third order interpolations are generally the best, Table I although the accuracies obtained from other order interpolations agreed.

4. Considering the results of the third order interpolation, the observations of the third set (measuring technique of the amplitude method without following) showed better internal accuracy than the other measuring techniques; that for the reasons mentioned before, see Table I.

5. Gyro-azimuths calculated using the adjusting results of the third order interpolation from the three sets are the nearest to each other and have the best accuracy, see Table II.

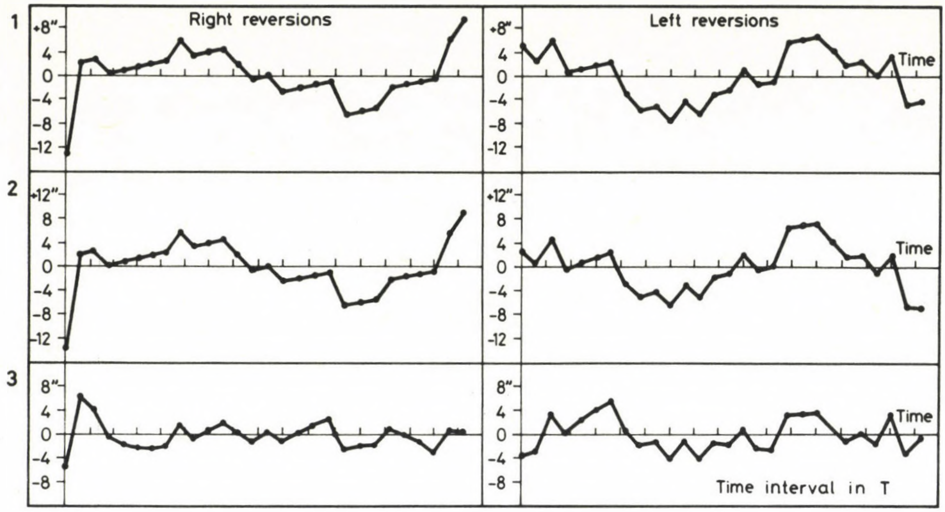

Fig. 5. Errors in the observations of (set 2)

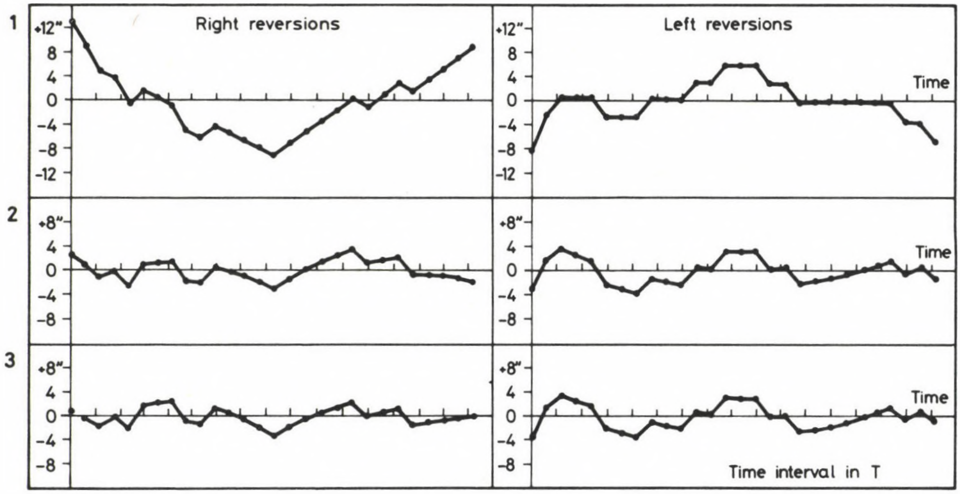

Fig. 6. Errors in the observations oı (set 3)

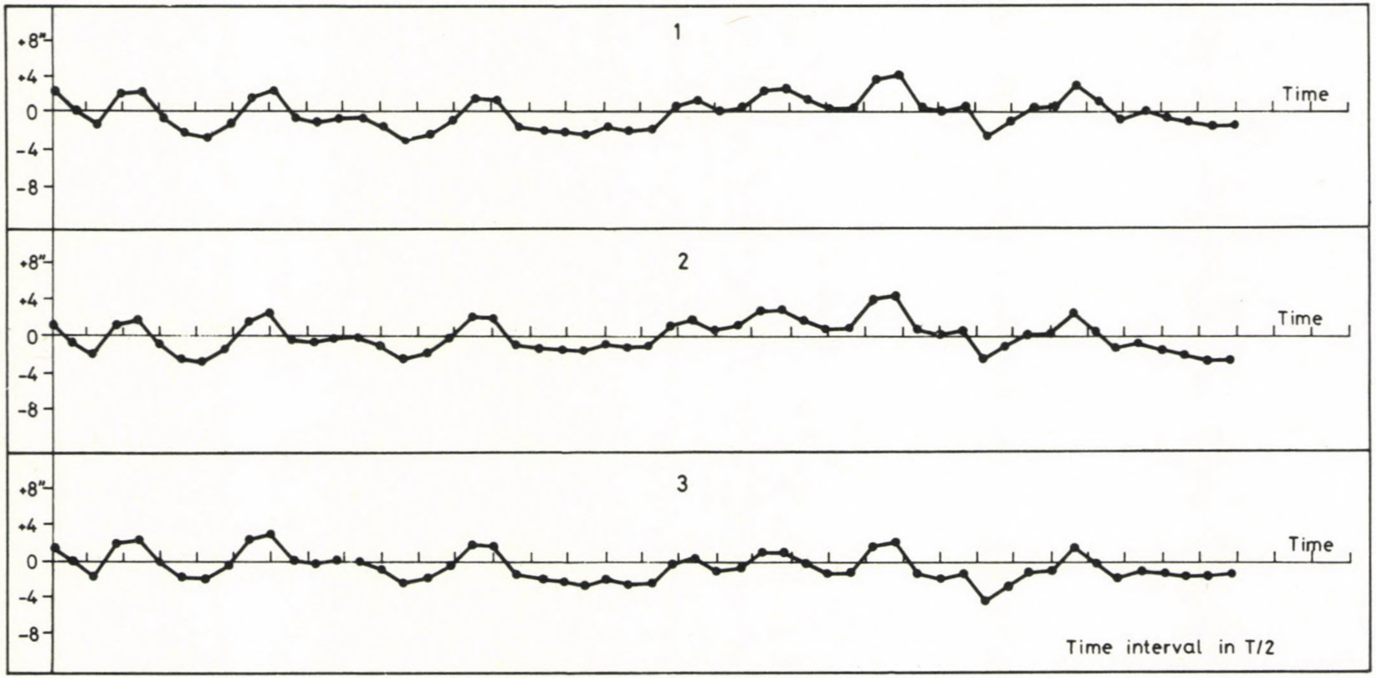

Fig. 7. Corrections for the Schuler means (set 1)

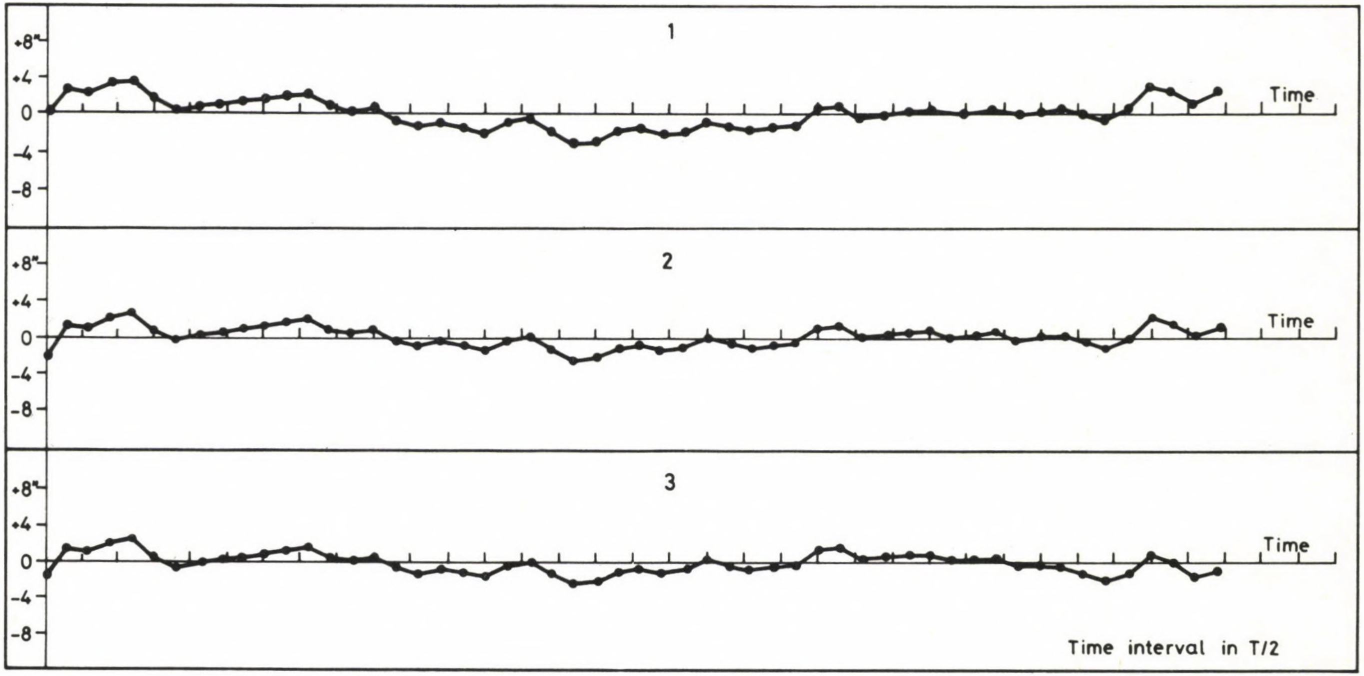

Fig. 8. Corrections for the Schuler means (set 2)

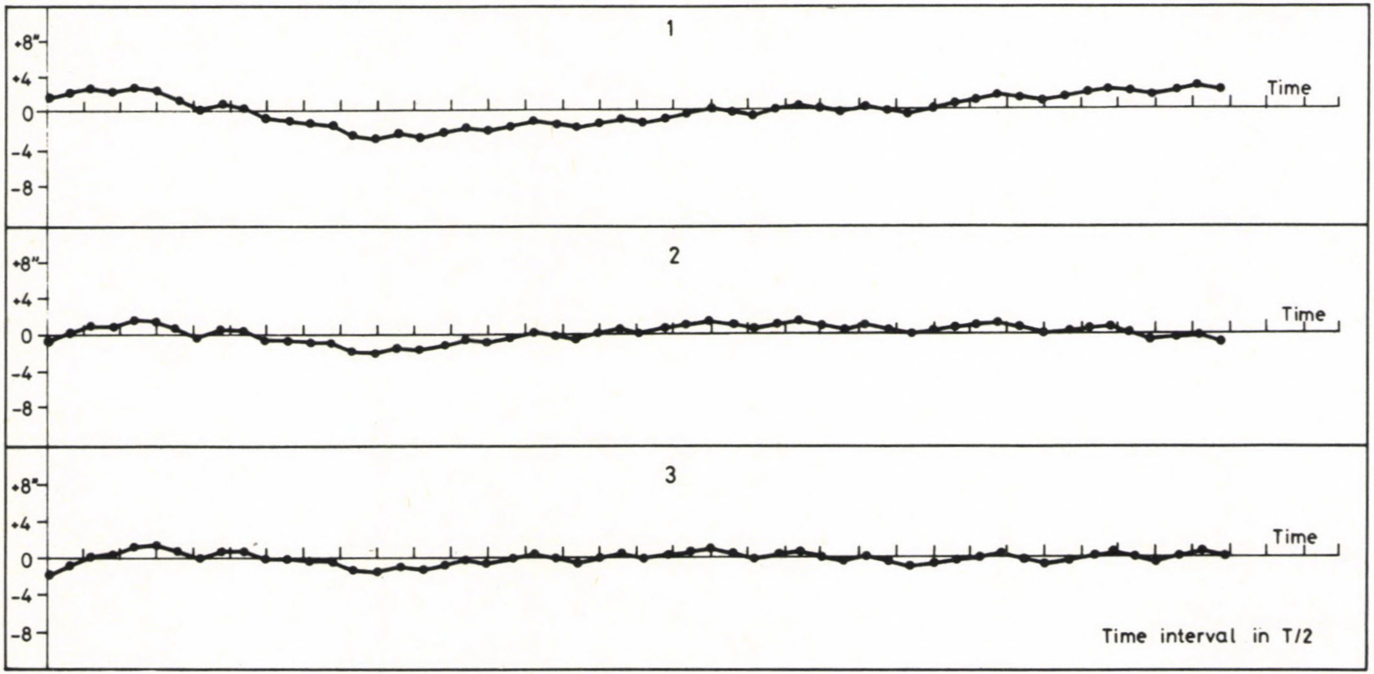

Fig. 9. Corrections for the Schuler means (set 3)

6. Gyrotheodolite observations of the amplitude method measured without following (set 3) are damped more than the observations with following, and the observations with automatic and manual following (set 1) are of the smallest damping coefficient, the ratio $f_1:f_2:f_3$ is nearly equal to 1:2:4.

Acknowledgements

The help of Mr. J Závoti in the preparation of the "POLI" program is gratefully acknowledged. Also I should like to thank Mrs. I Fleischhacker for the typing of the paper.

References

Abdelhamid K H. Halmos F 1981: Results of evaluation and methods of azimuth determination with new and old gyrotheodolites. Paper presented at the XVI. FIG Congress, Commission No. 6., Montreux, Switzerland.

Bennett G G 1970: The least squares adjustment of gyrotheodolite observations. Unisurv. Report, No. 12, 1968, University of New South Wales, Australia.

Detrekői Á 1977: Adjusting calculation. (in Hungarian) Tankönyvkiadó, Budapest.

Gregerson L F, Vanicek P, Symonds G R 1971: Report from experiments with gyroscope equiped with electronic registration. Paper presented at the IAGA Congress in Moscow.

Halmos F 1968: Methodological and accuracy investigations of gyrotheodolite azimuth determinations. *Geodézia és Kartográfia*, 20, 7–19.

Halmos F 1977: Theoretical and practical problems of the use of gyrotheodolites in geodesy. MTA GGKI Kiadványa. No. 6.

Lauf G G 1967: Adjustment and precision of gyrotheodolite observations. A paper presented at the third South African National Survey Conference, Johannesburg.

Schuler M 1932: Die Berechnung der Gleichgewichtslage von gemessenen Schwingungen auf Grund der Fehlertheorie. *Zeitschrift für Angewandte Math. und Mech.* 12, 152–156.

Acta Geodaet., Geophys. et Montanist. Hung. Volume 18 (1—2), pp. 47—58 (1983)

EVALUATION OF THE DRIFT IN THE GYROTHEODOLITE OBSERVATIONS AND ITS INFLUENCE ON GYRO-AZIMUTHS OF THE AMPLITUDE METHOD

ABDELHAMID KAMAL HASSAN[1]

Geodetic and Geophysical Research Institute of the Hungarian Academy of Sciences, Sopron

[Manuscript received September 20, 1981]

In this paper the drift in the gyrotheodolite observations is evaluated. The gyrotheodolite used in the investigation is an old one of the type MOM Gi-B2. The amplitude method with its three measuring techniques was applied. The investigation was made for the data obtained from the adjustment of three observation sets, each consisting of 56 reversion points. For each set, the rest position of the oscillations was calculated and reduced to the instant of release where no drift is yet active, and again calculated as the Schuler mean of the last three adjusted reversion points where the cumulative drift in the observations is greatest. The two values of the rest position where then compared to calculate the drift in the rest position of the swings. The gyro-azimuths were calculated using the two values of the rest position to evaluate the influence of the drift on the azimuths. The results are tabulated and illustrated with diagrams.

Keywords: amplitude method; azimuth determination; drift of gyrotheodolites; geodetic instrument; gyrotheodolites; MOM Gi-B2

1. Introduction

In gyrotheodolite observations with the amplitude method (reversion points) there exists a drift phenomenon. The paper deals with the evaluation of this drift in order to determine its influence on the gyro-azimuths calculated from the observations.

The instrument used in the investigation was of the type MOM Gi-B2, it is the same instrument used in the investigation presented by Abdelhamid (1982b) for which the study of the systematic errors due to drift resulted in a value of about 2″ per each value for the drift rate in the calculated independent azimuths. In this paper the drift effect on gyro-azimuths calculated from long independent measurements is studied. Three sets (each of 56 reversion points) were investigated; the first set was observed with both automatic and manual follow-ups for the swinging spinning gyroscope, the second set with automatic following only, while the third one was observed without following. The observations of the three sets were adjusted according to Abdelhamid (1982a), the obtained adjustment results were used in the calculation of the rest position

[1] Permanent address: Banha University, Faculty of Engineering, Cairo, Egypt.

of the oscillations after the reduction to the instant of release when no drift-effect is yet active. The rest position was calculated again using the adjusted values of the last three reversion points. Both values of the rest position were then corrected for the torsion of the suspension band to get the gyro-norths. These gyro-norths were compared with each to find to what extent the second value deviates from the first one. Using the observation data of each set (calibration data and the geodetic sights) and both values of the gyro-north, the gyro-azimuths were calculated and were also compared with each other. Finally a comparison was made between azimuth results of the three sets to calculate a drift ratio for the three sets. The final results are shown in Table IV.

2. The gyrotheodolite measurements

The gyrotheodolite observations were made in the geodetic laboratory of the Geodetic and Geophysical Research Institute of the Hungarian Academy of Sciences, Sopron. The Instrument was mounted on a heavy steel mount placed on a concrete pillar established especially for precise measurements. The gyrotheodolite was centered above the point of intersection of a cross etched on a brass plate fixed rigidly on the concrete pillar. A stabilized *D.C.* supply unit was used for feeding the generator of the gyrotheodolite, this unit comprises regulator circuits for keeping the required voltage constant. This precaution was taken to avoid disturbances due to changes in the voltage when using a 12 V accumulator. A collimator was placed in a fixed position on another concrete pillar near the gyrotheodolite pillar, Fig. 1, for making a geodetic sight. The use of the collimator increases the reliability of the geodetic sights because the cross hairs of the collimator where sharply viewed and are considered as if being far at infinity from an optical point of view. For measuring the swing time T a stop watch with two pointers was used to make it possible to measure the times of $\frac{1}{2}$, 1, $1\frac{1}{2}$, ... n swings separately, and at the same time to measure the time of the whole swings.

Before starting the observations, the gyroscope was let to swing without spinning for about one hour to eliminate smaller band torsions and deformation, also the gyroscope was let to spin before the measurements for about one hour to reach a heat equilibrium to avoid shifts in the equilibrium position. The zero point position of the band was regulated to be as small as possible (it was lass than ± 1 scale division) to make the disturbing effects and torsions symmetrical to the zero position (the rest position) along the whole swinging part (Halmos 1968, 1977).

Three sets of gyrotheodolite observations were measured with the prementioned techniques, each set included the following:

a) pointing to the reference object (the collimator) and reading of the horizontal circle $I_{(b)}$ with the two faces,

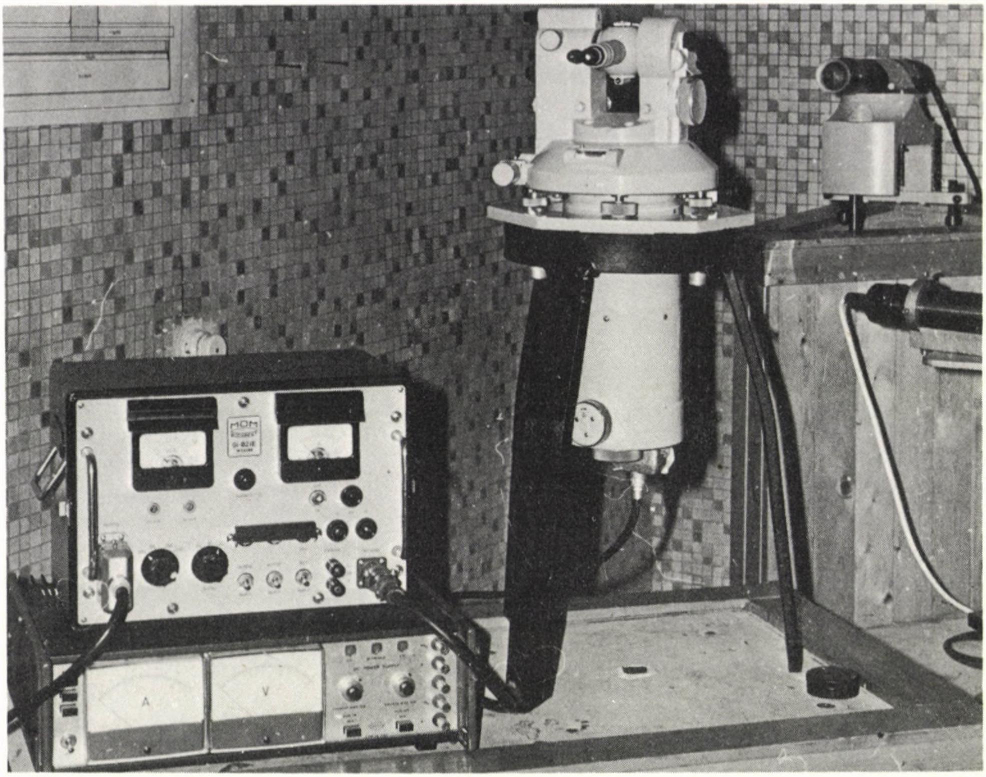

Fig. 1.

b) determination of the torsion free-position of the band (the zero point) $u_{o(b)}$ from 4 reversion points read in the autocollimator with nonspinning, free swinging gyroscope, at the same time, the time of the free swing t was measured and recorded,

c) at each set, 56 reversion points were observed with spinning gyroscope, the transit times of the reversion points as well as the time elapsed with 56 reversion points (T_n) were measured and recorded as mentioned before,

d) the torsion-free position of the band $u_{o(a)}$ was determined again after the measurements with the spinning gyroscope,

e) the reference object was sighted again and the horizontal circle reading $I_{(a)}$ was recorded too.

The observation data of the three sets are shown in Table I.

Table I. Summary of the observation data

Observation data	SET 1	SET 2	SET 3
Date	May 8, 1980	May 13, 1980	May 20, 1980
Time	12.30h – 17.00h	11.15h – 15.45h	8.30h – 12.40h
Temp.	22° C	22° C	22° C
I_b	50° 23′ 31.50″	170° 23′ 02.50″	290° 12′ 46.20″
$u_{0(b)}$	– 1.00 s.d.	+ 0.19 s.d.	+ 0.65 s.d.
t	1^m 14.9^s	1^m 14.9^s	1^m 14.9^s
No. of Rev.	56	56	56
α_M	–	332° 38′ 56″	92° 28′ 50″
T	9^m 33^s 70	9^m 33^s 30	8^m 44^s 71
T_n	$262^{(T_f)}$ 57.20	$262^{(T_f)}$ 45.20	$240^{(T_{wf})}$ 29.70
$u_{0(a)}$	– 1.85 s.d.	+ 1.44 s.d.	– 0.22 s.d.
$I_{(a)}$	50° 23′ 34.00″	170° 23′ 04.50″	290° 12′ 47.70″

3. The applied methods for calculating the azimuths

Using the gyrotheodolites of type MOM Gi-B2, the gyro-azimuth can be calculated from the observations by two main methods; the amplitude method (or reversion points method) and the transit time method. In this research the amplitude method with its three measuring techniques mentioned in 2.*C* was used. According to the size of the amplitude of the swings these techniques can be classified into large amplitude and small amplitude ones, the first belongs to the large amplitude ones, where the reversions of the gyroscopic swings are read on the horizontal circle of the theodolite in degrees units, while the second and the third use small amplitudes and the reversions are read in the autocollimator in units of scale divisions (amplitude of the swings is less than 40′). For more details about applying these measuring techniques and about the advantages and disadvantages of each, we refer to Halmos (1977). In this paper only the used calculating formulae are mentioned.

The general formula for the calculation of the gyro-azimuth (Halmos 1977) is

$$A = I - No + \Delta\,, \tag{1}$$

where A = the azimuth to be determined,
I = the horizontal circle reading when sighting the reference object,
No = the horizontal circle reading of the torsion-free rest position, and
Δ = the instrument constant determined in the calibration.

The gyro-North (No) is obtained after applying the torsion correction as follows:

$$No = No' + \Delta No'\,, \tag{2}$$

where No' = the torsioned rest position of the axis of the spinning gyroscope,
$\Delta No'$ = the torsion correction in seconds of arc.

The torsion correction is calculated in same manner for the three methods as follows:

$$\Delta No' = Cu_o \tag{3}$$

where the factor C is calculated as follows:

$$C = K\left(\frac{T_f^2}{T_{wf}^2} - 1\right) = \text{constant} \tag{4}$$

where u_o = the torsion-free position of the suspension band (the zero point)
K = the value of one scale division of the autocollimator in arc seconds,
T_f, T_{wf} = the swing times of followed and unfollowed oscillations respectively.

u_o is calculated according to Schuler (1932) from the reversion points (u_i) of the nonspinning, free swinging gyroscope read in the autocollimator.

The determination of No' differs with the different techniques, in the first measuring technique, No' is calculated directly according to Schuler (1932) from the reversion points of the spinning gyroscope, followed automatically and read on the horizontal circle of the theodolite (with manual following).

In the second technique, No' is calculated as follows:

$$No' = \alpha_M + Kn'_o, \tag{5}$$

where α_M = the horizontal circle reading of the preliminary orientation of the instrument and
n'_o = the rest position of the oscillations.

The value n'_o is calculated according to Schuler (1932) from the reversion points n_i of the spinning gyroscope, followed automatically only, and read in the autocollimator.

In the third technique, as no following is made during the swinging motion, the torsion effect is taken in the value n'_o twice therefore No' is calculated as follows:

$$No' = \alpha_M + Kn'_0 - Cn'_0 \tag{6}$$

where α_M, K, n'_0 have the same meaning as in Eq. (5), the only difference is that the motion of the spinning axis of the gyroscope is observed without following. For more details about the observation methods we refer to Halmos (1977).

4. Summary of the calculations and results

Table II shows the calculations for the three sets. The calculations were repeated twice for each set in columns 1 and 2. Columns 1 show the calculations using $I_{(b)}$ and $u_{o_{(b)}}$ with the rest position α_N reduced to the instant of release as described by Abdelhamid (1982b) where no drift is present yet, while in columns 2, the calculations

Table II. The calculations of the gyro-azimuths ($A = I - \mathrm{No} + \Delta$)

SET 1			SET 2			SET 3		
$\mathrm{No} = \mathrm{No}' + cu_0$			$\mathrm{No} = \alpha_M + kn'_0 + cu_0$			$\mathrm{No} = \alpha_M + kn'_0 - cn'_0 + cu_0$		
	1	2		1	2		1	2
No′	212° 40′ 04.71″	212° 39′ 39.42″	α_M	332° 38′ 56.00″	332° 38′ 56.00″	α_M	92°28′ 50.00″	92° 28′50.00″
—	— —	— —	kn'_0	+47.78″	+35.41″	kn'_0	+33.60″	+05.88″
—	— —	— —	—	— —	— —	cn'_0	+06.53″	+01.15″
cu_0	+05.83″	+10.84″	cu_0	−01.11″	−08.44″	cu_0	−03.79″	+01.29″
No	212° 40′ 10.54″	212° 39′ 50.26″	No	332° 39′ 42.67	332° 39′ 22.97″	No	92° 29′ 26.34″	92° 28′ 58.32″
I	50° 23′ 31.50″	50° 23′ 34.50″	I	170° 23′ 02.50″	170° 23′ 04.50″	I	290° 12′ 46.20″	290° 12′ 47.70″
−No	212° 40′ 10.54″	212° 39′ 50.26″	−No	332° 39′ 42.67″	332° 39′ 22.97″	−No	92° 29′ 26.34″	92° 28′ 58.32″
Δ	90° 11′ 51.80″	90° 11′ 51.80″	Δ	90° 11′ 51.80″	90° 11′ 51.80″	Δ	90° 11′ 51.80″	90° 11′ 51.80″
A	287° 55′ 12.76″	287° 55′ 35.54″	A	287° 55′ 11.63″	287° 55′ 33.33″	A	287° 55′ 11.66″	287° 55′ 41.18″

were made using $I_{(a)}$, $u_{o_{(a)}}$ and the rest position obtained from the last three reversion points (after the adjustment from the observation errors) where the whole drift in the set occurs. The instrument constant used in the calculations ($\Delta = 90°\ 11'\ 51.80''$) was determined from the calibration data of the instrument made at the Bánfalva observatory in Sopron, Table III shows a summary of the calibration results. The values of the constant shown in the table are corrected for the drift as described by Abdelhamid (1981). The C-factor used in the calculations is $C = -5.86''$/one scale division, it was calculated according to Eq. (4) using the mean values of T_f and T_{wf} shown in Table I.

Table III. Summary of the calibration results

Date	indep. measts.	Δ	V
May 12, 1980	mean of 7 determs.	90° 11′ 52.36″	0.56″
June 18, 1980	mean of 7 determs.	90° 11′ 52.10″	0.30″
June 19, 1980	mean of 7 determs.	90° 11′ 53.23″	1.43″
June 23, 1980	mean of 6 determs.	90° 11′ 51.76″	−0.04″
June 25, 1980	mean of 7 determs.	90° 11′ 53.84″	2.04″
June 26, 1980	mean of 8 determs.	90° 11′ 49.30″	−2.50″
June 27, 1980	mean of 7 determs.	90° 11′ 52.21″	0.41
June 30, 1980	mean of 8 determs.	90° 11′ 50.34″	−1.46″
July 1, 1980	mean of 8 determs.	90° 11′ 51.06″	−0.74″
Mean value of 9 days measurements		90° 11′ 51.80″	0.00

μ of the instrument constant: $\pm 0.47''$

Table IV: Results of the drift in the rest positions, the gyro-norths and the gyro-azimuths

Sets		SET 1	SET 2	SET 3
α_N	1	212° 40′ 04.71″	47.78″	33.60″
	2	212° 39′ 39.42″	35.41″	05.88″
$d\alpha_N$		−25.29″	−12.37″	−27.72″
$d\alpha_N$/6 rev.		− 2.7″	− 1.3″	− 3.0″
No	1	212° 40′ 10.54″	332° 39′ 42.67″	92° 29′ 26.34″
	2	212° 39′ 50.26″	332° 39′ 22.97″	92° 28′ 58.32″
dNo		−20.28″	−19.70″	−28.02″
dNo/6 rev.		− 2.2″	− 2.1″	− 3.0″
A	1	287° 55′ 12.76″	287° 55′ 11.63″	287° 55′ 11.66″
	2	287° 55′ 35.54″	287° 55′ 33.33″	287° 55′ 41.18″
dA		+22.78″	+21.70″	+29.52″
dA/6 rev.		+ 2.5″	+ 2.4″	+ 3.2″

In Table IV a comparison is made between the two values of each of the rest positions α_N, the gyro-norths No and the gyro-azimuths A of the three sets, rows 1 show the values free from the drift while rows 2 show the values loaded with the whole drift present in the set. The differences between the two rows ($d\alpha_N$, dNo, dA) indicate drifts in α_N, No and A. The drift per 6 reversion points was also calculated and tabulated. Figures 2–4 show the Schuler mean diagrams for the observed and the adjusted reversion points of the three sets. The drift in the rest positions $d\alpha_N$ is clear; it is the difference between the first and last values of the Schuler mean.

As shown in Table IV the drift in the rest position of the reversion points of set 3 is the largest and that of set 2 is the smallest. These drifts cannot be taken as a base for any comparison, because the torsion corrections are not yet applied. After applying the torsion corrections and other reductions (Table II), the gyro-norths were obtained, their values can then be taken as a base for the comparison. The drifts in No of sets 1 and 2 closely agree after applying the torsion corrections. In set 3 the drift is nearly the same after applying the torsion correction.

Comparing the gyro-azimuths A of the three sets (Table IV), the values in rows 1 agree with high accuracy, these azimuths were calculated using the rest positions reduced to the instant of release, $u_{o(b)}$ and $I_{(b)}$ i.e. azimuths free from the drift. This shows that the three techniques of observations have nearly the same accuracy after the adjustment and applying the reductions. When comparing the azimuths in rows 1 and 2 we get the effect of the drift in the gyro-norths on the gyro-azimuths (the drift in the gyro-azimuth dA). Comparing dA of the three sets, we find that dA at sets 1 and 2 agree and have smaller values than dA at set 3. This means that the gyrotheodolite reversion points observed with following have a smaller drift amount than those observed without following, the drift ratio obtained was nearly 2:3. The drift per 6 reversions in set 1 has nearly the same value as that evaluated by Abdelhamid (1982b) for the same instrument used for repeated azimuth determinations with independent starts.

5. Conclusions

In gyrotheodolite observations of the used instrument, there is a clear drift; a tendency for the rest position of the oscillations to decrease. This phenomenon affects the calculated gyro-azimuths. The results of the paper showed that the three measuring techniques of the amplitude method have nearly the same accuracy for the gyro-azimuths calculated after the adjustment and the reduction to the instant of start (drift-free values). The evaluated drift in the three sets showed that the reversion points of the spinning gyroscope observed with following have smaller drifts than those observed without following and the obtained drift ratios are nearly 2:3.

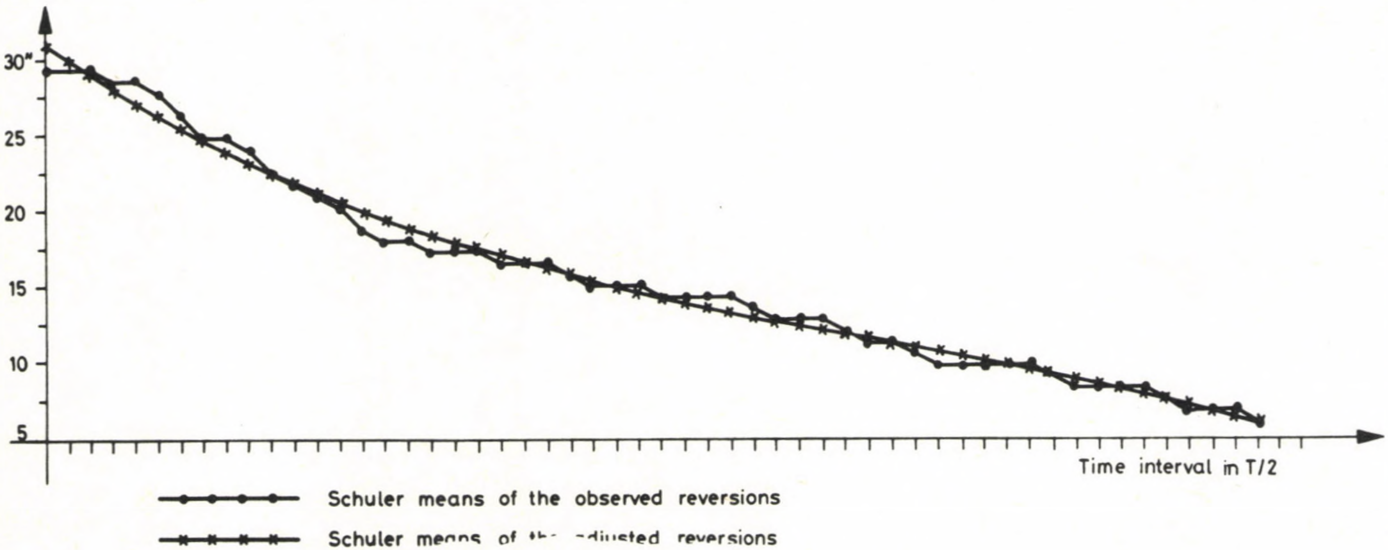

Fig. 2. Schuler mean diagrams for observations with both the automatic and manual following (set 1)

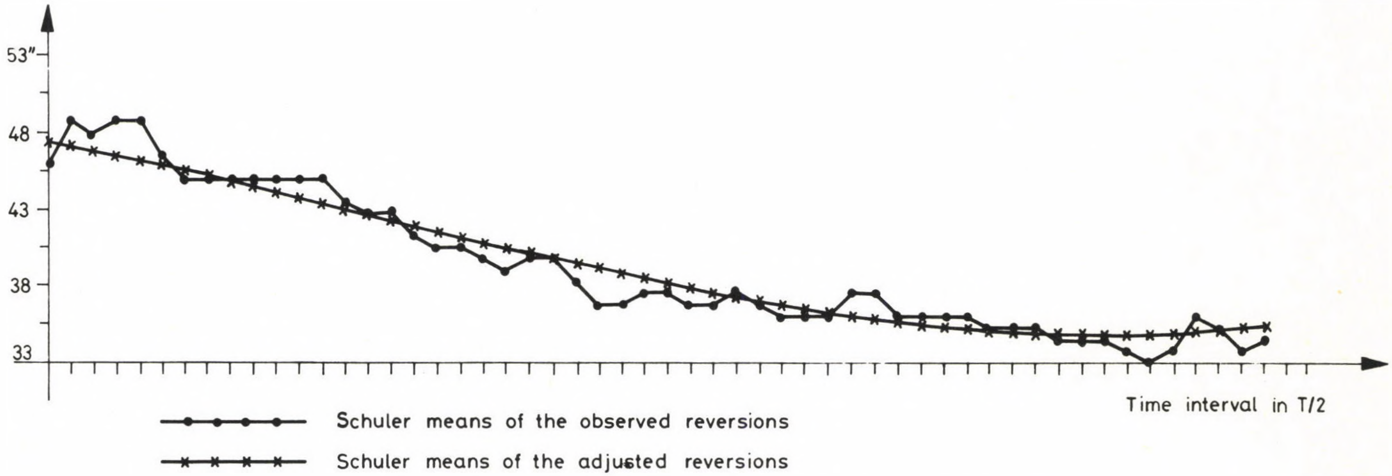

Fig. 3. Schuler mean diagrams for observations with the automatic following only (set 2)

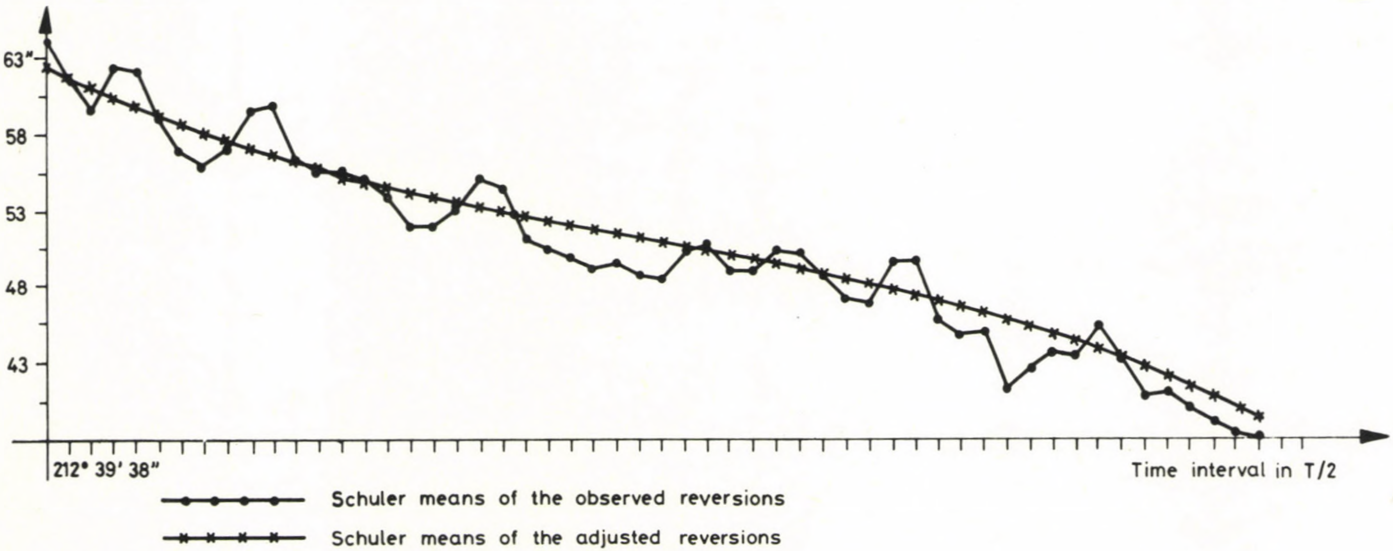

Fig. 4. Schuler mean diagrams for observations without following (set 3)

References

Abdelhamid K H 1982a: On the adjustment of the gyrotheodolite observations. *Acta Geod., Geoph., Mont. Hung.* (in press)

Abdelhamid K H 1982b: Comparison between result of the gyro-azimuths determined with old and new gyrotheodolites. *Acta Geod., Geoph., Mont. Hung.* (in press)

Abdelhamid K H, Halmos F 1981: Results of evaluation and methods of azimuth determination with new and old gyrotheodolites. Paper presented at the XVI. Congress of the FIG Committee No. 6, Montreux, Switzerland.

Bennett G G 1970: The least squares adjustment of gyrotheodolite observations. Unisurv. Report, University of New South Wales, Australia, No. 12, 1968.

Gregerson L F, Vanicek P, Symonds G R 1971: Report from experiments with gyroscope equiped with electronic registration. Paper presented at the IAG Congress in Moscow.

Halmos F 1968: Methodological and accuracy investigations of gyrotheodolite azimuth determinations. *Geodézia és Kartográfia*, 20, 87–92.

Halmos F 1972: Systematic and random errors of the direction measurements with gyrotheodolites. MOM Review No. 4, 24–32.

Halmos F 1977: Theoretical and practical problems of the use of gyrotheodolites in geodesy. MTA GGKI Kiadványa. No. 6.

Lauf G G 1967: Adjustment and precision of gyrotheodolite observations. A paper presented at the third South African National Survey Conference, Johannesburg.

Schuler M 1932: Die Berechnung der Gleichgewichtslage von gemessenen Schwingungen auf Grund der Fehlertheorie. *Zeitschrift für Angewandte Math. und Mech.*, 12, 152–156.

Acta Geodaet., Geophys. et Montanist. Hung. Volume 18 (1—2), pp. 59—65 (1983)

SIMPLE DETERMINATION OF THE CONVERGENCE OF THE MERIDIANS FOR THE AREA OF EGYPT

ABDELHAMID KAMAL HASSAN

Banha University, Faculty of Engineering, Cairo, Egypt

GY SZÁDECZKY-KARDOSS

Geodetic and Geophysical Research Institute of the Hungarian Academy of Sciences, Sopron

[Manuscript received February 23, 1981]

The paper presents a simple computation method for the determination of the convergence of the meridian for the area of Egypt, i.e. for the territory enclosed between the geographical latitudes of 22°–32° north of the equator. The method is valid for the Hayford 1909 ellipsoid, and the equations are suitable to be used for the Universal Transversal Mercator (UTM) projection system. A numerical example is given to illustrate the practical use of the attached table. The presented formula gives the convergence of meridian with an accuracy of 0.1 second of arc which is suitable for geodetic computation tasks. The table of coefficients facilitates the execution of practical computations. With these, the computation work is considerably shortened and made suitable for rapid use to complete the up-to-date gyrotheodolite measurement for the orientation purposes.

Keywords: convergence of meridian; coordinate system; Egypt; Gauss–Krüger coordinates; Hayford ellipsoid; North Africa; meridian arc distance; Universal Transversal Mercator (UTM)

The results of azimuths measurements with gyrotheodolites show that the gyro-azimuth is the same as the astronomical azimuth but it can be used in the orientation of higher order geodetic networks only after applying a correction due to the convergence of the meridian and other reductions. Therefore it is necessary to know the convergence of the meridian in orde. to enable its being taken into account when computing the final values of the azimuths measured astronomically or with the gyrotheodolite.

In the present paper a simple method is given for the determination of the convergence of the meridian for the Universal Transversal Mercator projection system (UTM) in the area of Egypt ($\varphi = 22$N to 32N).

The calculations are based on the Hayford 1909 ellipsoid. A table containing the coefficients for the computations is given. This table can be used easily in any measuring stations if the UTM x and y coordinates are known to the nearest 5 meters; this gives an accuracy of 0.1 second of arc for the convergence of the meridian. Besides, the computational relations are uniform and valid for bandwidths up to 6° UTM, only they require the knowledge of a few coefficients. Therefore the computations can be

Table I

x_0	C_{01}	C_{11}	C_{03}	C_{21}	C_{13}
3550 km	+2024.52	+70.72	−0.230	+0.689	−0.013
3500	1989.33	70.04	0.224	0.671	0.012
3450	1954.48	69.38	0.218	0.653	0.012
3400	1919.95	68.73	0.212	0.635	0.012
3350	1885.74	68.11	0.206	0.618	0.011
3300 km	+1851.84	+67.50	−0.200	+0.601	−0.011
3250	1818.24	66.90	0.195	0.585	0.011
3200	1784.93	66.33	0.190	0.569	0.010
3150	1751.90	65.77	0.185	0.554	0.010
3100	1719.16	65.22	0.180	0.539	0.010
3050	1686.68	64.69	0.175	0.525	0.010
3000 km	+1654.47	+64.17	−0.170	+0.510	−0.009
2950	1622.51	63.66	0.165	0.496	0.009
2900	1590.80	63.18	0.161	0.483	0.009
2850	1559.33	62.70	0.156	0.470	0.009
2800	1528.10	62.24	0.152	9.457	0.008
2750	1497.09	61.79	0.148	0.444	0.008
2700km	+1466.31	+61.35	−0.144	+0.432	−0.008
2650	1435.74	60.92	0.140	0.420	0.008
2600	1405.38	60.51	0.136	0.408	0.008
2550	1375.23	60.11	0.132	0.397	0.008
2500	1345.27	59.71	0.128	0.386	0.008
2450	1315.51	59.33	0.125	0.375	0.008
2400km	+1285.94	+58.97	−0.121	+0.364	−0.007

easily carried out in the measuring station to give a complete evaluation for the measured azimuth, and also they can be easily programmed for computers.

The general formula for the computation of the convergence of the meridians (μ) in the UTM system (Tárczy-Hornoch–Hristov 1968, p. 52) can be simplified as follows:

$$\mu = C_{01}\Delta y + C_{11}\Delta x\Delta y + C_{21}\Delta x^2\Delta y + C_{03}\Delta y^3 + C_{13}\Delta x\Delta y^3 \tag{1}$$

where

$$\Delta x = 10^{-5}(x - x_o) \tag{2}$$

$$\Delta y = 10^{-5}y\,. \tag{3}$$

In the equation, x and y are the UTM coordinates (in meters) of the measuring station whose μ value is required, and x_o is the x coordinate of a reference point of a latitude φ. The numerical values of the coefficients are in Table I.

In Eq. (1) the coefficients are:

$$C_{01} = \frac{10^5 \rho}{N_0} t_0 \tag{4}$$

$$C_{11} = \frac{10^{10} \rho}{N_0^2} (1 + t_0^2 + \eta_0^2) \tag{5}$$

$$C_{21} = \frac{10^{15} \rho}{N_0^3} t_0 (1 + t_0^2 - \eta_0^2 - 2\eta_0^4) \tag{6}$$

$$C_{03} = \frac{10^{15} \rho}{3N_0^3} t_0 (-1 - t_0^2 + \eta_0^2 + 2\eta_0^4) = -\frac{1}{3} C_{21} \tag{7}$$

$$C_{13} = \frac{10^{20} \rho}{3N_0^4} (-1 - 4t_0^2 - 3t_0^4 - 2t_0^2\eta_0^2 + 3\eta_0^4 - 10t_0^2\eta_0^4) \tag{8}$$

where $\eta_0^2 = e'^2 \cos^2 \varphi_0$

$N_0 = \dfrac{C}{\sqrt{1+\eta_0^2}}$ = (the curvature in the prime vertical)

$t_0 = \tan \varphi_0$ (φ_0 = the latitude of the point x_o)

$\rho = 206\,264.806$

$e'^2 = 0.006\,768\,170$ (the 2nd numerical excentricity of the Hayford 1909 ellipsoid)

$C = \dfrac{a^2}{b} = 6\,399\,936.608\ m$ (for the Hayford 1909 ellipsoid),

The x_o interval used in the calculation of the coefficients is 50 km for practical purposes. According to the UTM projection system, the territory of Egypt extends between $x_o = 2400$ km and $x_o = 3550$ km, therefore the calculations are made for 24 reference points.

For the determination of the coefficients we have at first to compute the corresponding geographical latitude (φ_0) from the UTM coordinate (x_o) (the points with the coordinate x_o are on the central meridian of each UTM coordinate system). This task can be solved with several methods, in the following a method proposed in this paper is used. Starting with the data of another ellipsoid (Krassowski 1940), the φ_0 value corresponding to the UTM x_o values can be found partly at Tárczy-Hornoch and Hristov (1968, p. 346), partly they were computed to complete the Krassowski ellipsoid tables. The difference between the meridian arc distances (ΔB) for the two ellipsoids (Krassowski minus Hayford) was calculated using the following formula:

$$\Delta B = -1.675\,577\,0\varphi_1 + 141.7031 \sin\varphi_1 \cos\varphi_1 -$$
$$-1.194\,74 \sin\varphi_1 \cos^3\varphi_1 + 0.009\,41 \sin\varphi_1 \cos^5\varphi_1 \qquad (9)$$

where ΔB = the difference between the meridian arc distance of the points with the same x_o value on the two ellipsoids.

φ_1 = the latitude (φ_0) corresponding to the x_o value referring to the Krassowski ellipsoid.

It was found from the calculations that at $x_o = 3550$ km $\Delta B = +9.635$ m, while for $x_o = 2400$ km $\Delta B = +11.969$ m, and the greatest value of ΔB is $+12.076$ m for $x_o = 2600$ km.

Having computed ΔB, this value of φ_0 is calculated according to Szádeczky-Kardoss (1963) as follows:

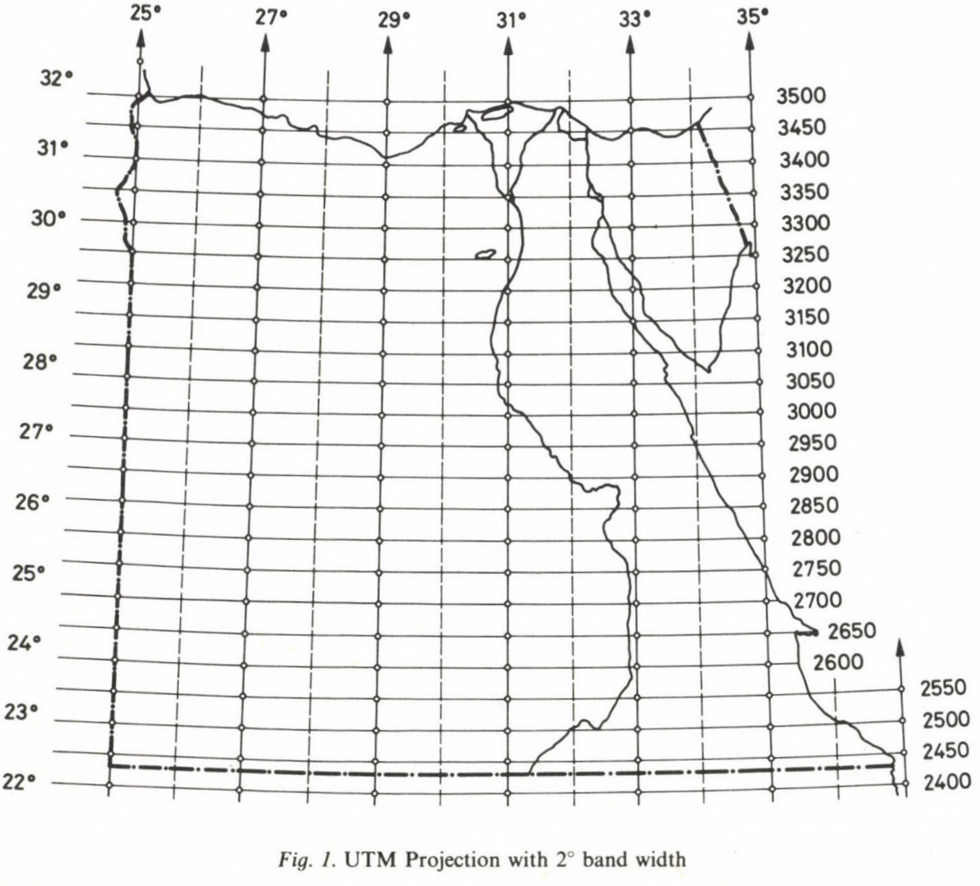

Fig. 1. UTM Projection with 2° band width

$$\varphi_0 = \varphi_1 + 3600\left[\frac{\Delta B}{U_1} - \frac{U_2}{U_1}\left(\frac{\Delta B}{U_1}\right)^2\right] \tag{10}$$

where

$$U_1 = 111\,136.54 - 563.429(2\cos^2\varphi_1 - 1) + \\ + 2.383\cos^2\varphi_1(4\cos^2\varphi_1 - 3) \tag{11}$$

$$U_2 = 19.667\sin\varphi_1\cos\varphi_1\,. \tag{12}$$

Control calculation was made and it showed that the maximum difference between the given x_o coordinate and the x_o value obtained from the computed φ_0 is smaller than 0.003 m.

The coefficients $C_{01}\ \ldots\ C_{13}$ are then calculated according to Eqs 4–8 using the last φ_0 values. The results are tabulated in Table I.

In the UTM projection there exist coordinate systems with bandwidths of 2^0, 3^0 and 6^0 (y-intervals at the equator). For the case of Egypt we show the three systems with their reference points in Figs 1–3. Control calculations were made for the coefficients

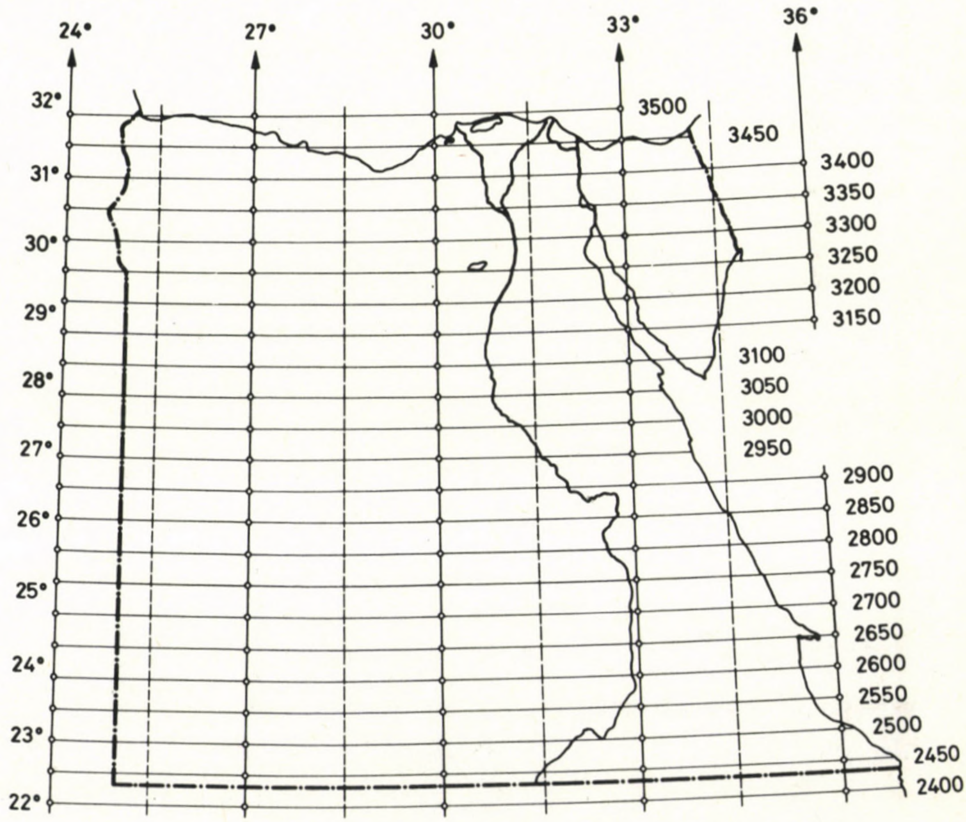

Fig. 2. UTM Projection with 3° band width

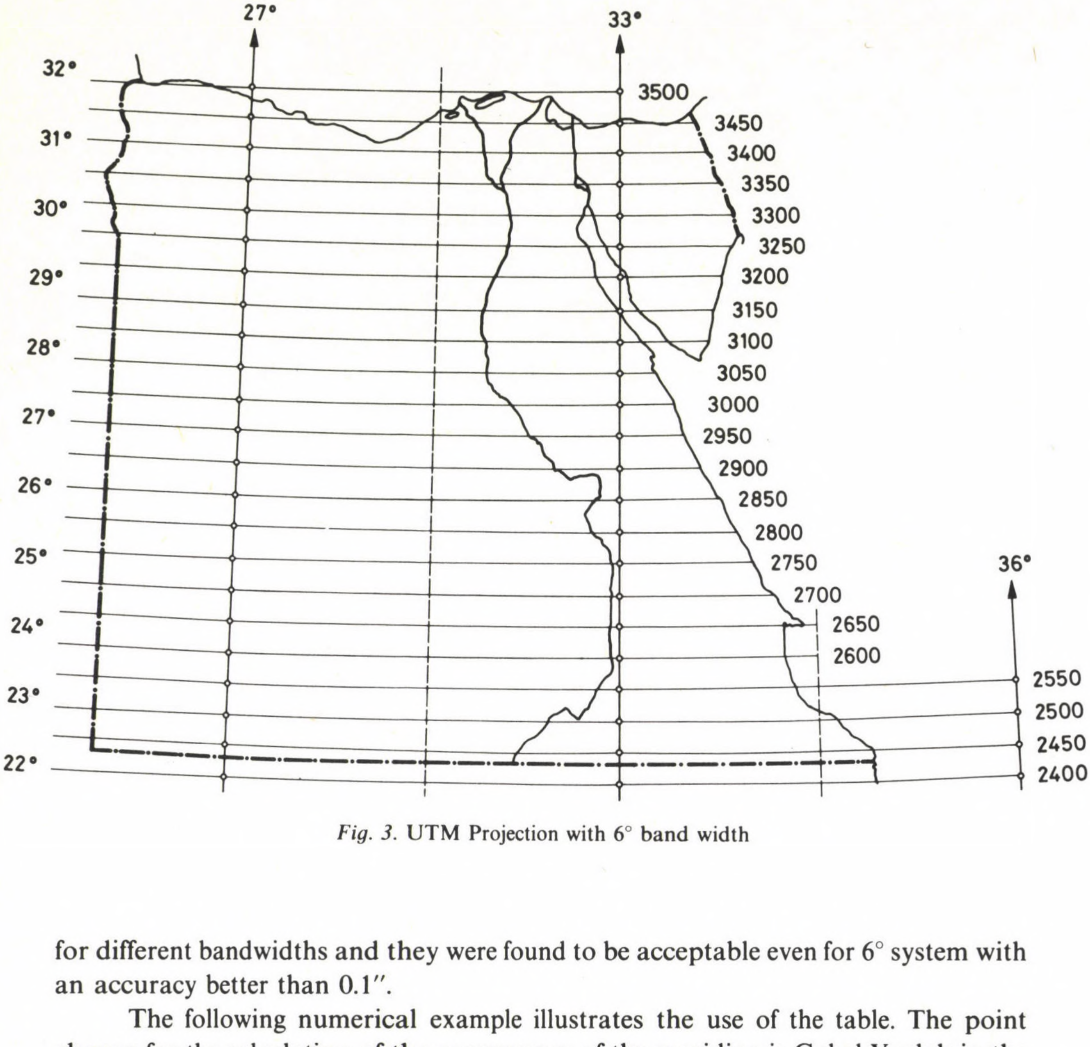

Fig. 3. UTM Projection with 6° band width

for different bandwidths and they were found to be acceptable even for 6° system with an accuracy better than 0.1″.

The following numerical example illustrates the use of the table. The point chosen for the calculation of the convergence of the meridian is Gabal Yaalak in the Sinai peninsula whose UTM coordinates in the 2° system are:

$$x = +3\,368\,163.64 \text{ m}$$

$$y = + \quad 25\,725.63 \text{ m}\,.$$

The central meridian of the UTM projection system is 33° E. The used reference point is $x_o = 3350$ km. According to Eqs 2 and 3,

$$\Delta x = +0.181\,636$$

$$\Delta y = +0.257\,256\,.$$

For the chosen reference point, the values of the coefficients are:

$$C_{01} = +1885.74\ , \quad C_{11} = +68.11\ , \quad C_{03} = -0.206$$
$$C_{21} = +\ \ 0.618, \quad C_{13} = -\ \ 0.011.$$

Substituting in Eq. (1) for Δx, Δy and the above coefficients, we get μ as follows:

$$\mu = +485.13 + 3.18 - 0.003 + 0.005 = 488.318'' = +8'08.3''$$

References

Halmos F, Szádeczky-Kardoss Gy 1967: Die einfache Bestimmung der Meridiankonvergenz bei verschiedenen Projektionen. *Acta Geod. Geoph. Mont. Hung.*, 2, 351–366.

Halmos F, Szádeczky-Kardoss Gy 1968: Die geodätische Umrechnung der Kreiseltheodolitmessungen. *Acta Geod., Geoph., Mont. Hung.*, 3, 23–43.

Szádeczky-Kardoss Gy 1956: Notes on computation of distances along meridional sections. *Publications of the Faculties of Mining and Geotechniques*, Sopron, 19, 165–173.

Szádeczky-Kardoss Gy 1963: Földrajzi koordináták számítása ellipszoidos ívhosszakból (The Computations of the Geographical Coordinates from Ellipsoidical Arc Length). Új mérési és számítási eljárások a geodéziában, Budapest, 1–10.

Tárczy-Hornoch A, Hristov V K 1968: Tables for Krassowski-Ellipsoid (between the 25th and 40th parallels). Akadémiai Kiadó, Budapest

Acta Geodaet., Geophys. et Montanist. Hung. Volume 18 (1—2), pp. 67—70 (1983)

PROBLEMS OF FIELD DATA COLLECTION IN GEODETIC MEASUREMENTS

GY MENTES[1]

Geodetic and Geophysical Research Institute of the Hungarian Academy of Sciences, Sopron

[Manuscript received March 26, 1982]

The paper deals with problems of the development of data collection systems for geodetic field measurements. The advantages of the semi-automatic and automatic data collection equipments are described in details together with the most important demands against such systems. At last the construction of a new intelligent data collection system is described which eliminates the disadvantages of earlier data collection systems.

Keywords: field data collection; digital instrument; surveying instruments; geodetic instrument

The automatization of geodetic field measurements is an old problem. The idea that after the pointing to the station all further processes should be carried out automatically by the instrument, has already emerged at the beginning of the sixties. The development of the microcomputers and of the electronics made this more and more practicable. Nevertheless at present the majority of the geodetic instruments have either traditional, non-digital output, or digital output without complete automatization. The results of the field measurements are then processed at all geodetic firms on up-to-date computers. A close connection between the central computer and the traditional field instruments can only be realized by field data collection systems which enable an immediate input of the field data into the computer.

The application of field data collectors seems at present due to rather high prices more expensive than to keep the minutes as traditionally. If one takes into account, however, the advantages of the automatic or semi-automatic data collecting then it is evident that the higher price will be quickly amortized in use. The most important advantages of the field data collection systems are:

1. The shortening of the time of the data management which appears in two factors:

— quick data input and storage,

— collected data can be transmitted to the computer for processing without keyboard-work.

[1] H-9401 Sopron, Pf. 5, Hungary

2. Reduction of the possible error sources due to less manual transcription of data. Errors are naturally at the first input both in on-line and off-line operations possible, but the subsequent processes of the data transfer and manipulation have strongly decreased error possibilities in the former case.

3. Data are available immediately in computer-readable form. In order to use all these advantages during the field-work, the field data collection system has to meet the following demands:

— The work of the surveyor working in the field should be simplified. This condition is automatically fulfilled if the data collector is connected to the digital output of the instrument. In such a case the surveyor has only to introduce additional informations through the keyboard to the buffer. If the data collector is used in off-line operation, i.e. if it is connected with an instrument without digital output, then the input of these data through the keyboard do not mean always a simplification for the surveyor, even it can mean a surplus work. This surplus work will, however, be paid back later when the data input into the computer is less extensive and the error sources are reduced.

— Keeping the minutes should be simplified. This demand can be fulfilled both in on-line and off-line operations if the data collector needs the data in form which corresponds to the character of the surveying work (leveling, distance measurement, etc.). In such a case the errors of the minute taking are also reduced.

— The data collector could be connected to a computer. This is necessary in order to simplify data transmission and to reduce error sources there.

— The data carrier of the data collector should be exchangeable. In case of field works far from the site of the processing, in long campaigns this is an inevitable demand.

— The data collector should be universal, i.e. the same type of the data collector could be used for surveying works of different kinds. As it has already been mentioned the errors of the data input decrease if the data collector needs the data in a format corresponding to the actual surveying field work, therefore the format of the data collector must be programable for the task prescribed by the producer or by the user.

— The data collector should be "intelligent", thus it should be capable to re-arrange and to correct data, to retrieve them according to a prescribed format, etc.

Present surveying data collection systems fulfil most of the demands listed above. Such are e.g. the data collector of the electronic theodolite Kern ET2 (Aeschliman 1979), the data collector Geomemo produced by Geotechnica (1978) and AGA Geodat (1979).

A common feature of all these data collection systems is that data are stored in a semi-conductive type memory which can store them for a certain time after the switch-out of the instrument depending on the type of the instrument. The semi-conductor memory cannot be, however, exchanged in case of any of these data collectors, therefore if the memory is full (after the measurement at 200–500 points) data must be transferred immediately to a computer or to an intermediate data base (e.g. magnetic cassette). That means that in case of a several days long campaign far from the site of the processing the surveyor has to carry with him a cassette recorder data collection system, too. All the types have the common disadvantage that they are made for one or a few special tasks, therefore the format with which the data collector is manufactured is not an optimum one in case of other tasks. This could be avoided if the format of the data collector could be programmed by the user itself (including number of characters, character of the functions, length of a data block and their content, etc.) according to the actual problem.

The scheme of a data collector which fulfils all the demands listed earlier can be seen in Fig. 1. The system has a microprocessor construction enabling a versatile use of the apparatus.

Data input is possible either manually through the keyboard, or completely automatically through the serial input interface (interfaced to a given instrument). In addition, a semi-automatic operation is also possible. In such a case the measurement results are transferred immediately from the measuring instrument, while additional informations (e.g. serial number of the measurement, etc.) are transmitted by the keyboard. For data control, correction, etc. the 16 character alphanumeric display displays the values together with their identifying code.

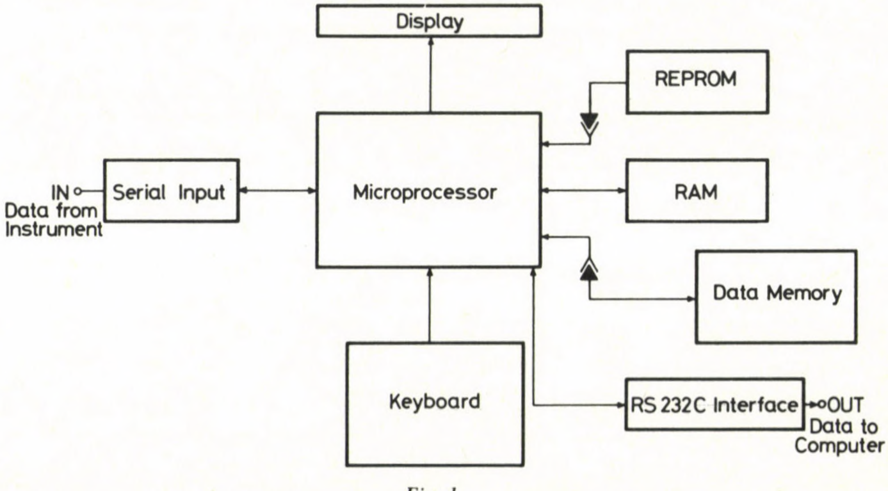

Fig. 1

The microprocessor needs and handles data and data blocks in a format stored in the REPROM-memory. This REPROM-memory can be taken out from the data collection system and according to the demands of the user, it can be reprogrammed on an other apparatus by the user itself.

Data are collected in a 4 Kbyte semi-conductor memory which can store all the data after switching out of the power for unlimited time. The data storage unit is a separate one with a capacity of 4 Kbyte. According to experiences this is sufficient for the storage of the results of measurements of one day. This memory is, however, exchangeable, therefore data should not be stored in an intermediate data carrier even in case of several days long campaigns. The content of these exchangeable storage units can be transmitted to the computer through the RS 232C type interface of the data collecting system.

As it can be seen from all this, it is advantageous to increase the intelligence and the versatility of the field data collection systems for sake of economy of the application of these systems. For such a development the technical conditions are already given.

References

Aeschliman H 1979: Ein Gerätesystem für die automatische Registrierung von Messwerten. Kern und Co. AG Werke für Präzisionsmechanik, Optik und Elektronik, Aarau, Schweiz 350d 8.79-Fa

AGA Geodat 120, AGA Geotronics AB, 1979

The Geomemo Data Collection System, Geotechnica GmbH., 1978

Acta Geodaet., Geophys. et Montanist. Hung. Volume 18 (1—2), pp. 71—81 (1983)

QUICK ZONE-TO-ZONE TRANSFORMATION IN THE GAUSS–KRÜGER PROJECTION

I HAZAY[1]

Technical University, Budapest

[Manuscript received May 4, 1982]

The Gauss–Krüger projection is used in many countries and there are several methods for zone-to-zone transformations for its adjacent zones. These methods are generally rather tedious. The author found lately an immediate connection which radically simplifies the problem. Neither arc-to-chord reductions, nor scale factors are necessary as the difference between the data of the two zones can be easily determined. The connection is based on the double value of the y coordinates at the border meridian.

The method can also be used for the connecting systems of any oblique Mercator (cylindrical) projection of the sphere, and the method is in this case even simpler due to the less complicated curvature of the sphere; here the connection refers to the distance of the two y axes.

Keywords: arc-to-chord reduction; conform transversal cylinder; ellipsoidic computations; Gauss–Krüger coordinates; projections; scale factor; Universal Transversal Mercator coordinates

I

The conform transversal cylinder projection of the ellipsoid — which generally called Gauss—Krüger projection in Central Europe — is used in many countries both for small and large scale representations. The zone-to-zone transformation of points is often necessary, and for this purpose several different methods are available. The author himself has constructed several such methods. A part of them is used in practice, an other part remained a theoretical possibility. In recent investigations, I found an immediate connection which radically reduces the problem and yields a result with an error of $2-3$ mm. A pre-condition of its use is that points should be available with a density of $50-60$ km having known coordinates in both systems. The connection is based on the double value of the y coordinates of the border meridian: $\eta = 2y_0$. With simple functions of this quantity both the grid bearing and the distance can be immediately transformed. The method can also be used for any oblique conform cylinder projection of the sphere and in this case it is even simpler due to the simpler curvature of the sphere.

The steps of the transformation are presented at first for the simpler case, i.e. for the sphere. Here the connection is based instead of η on the distance ξ of the images of the two tangential circles, i.e. of the x-axes.

[1] H-1111 Budapest, Műegyetem rkp. 3, Hungary

According to the known formula for cylinder projection of the arc-to-chord reduction (subscript m refers to the midpoint of the connecting line, Δy and Δx are the differences of the corresponding coordinates):

$$\Delta_1 = +ax_{m1}\Delta y_1 - b(\Delta x_1 \cdot \Delta y_1)$$

$$\Delta_2 = +ax_{m2}\Delta y_2 - b(\Delta x_2 \cdot \Delta y_2).$$

With the required computational accuracy Δy_2 can be substituted by Δy_1 in the first term, therefore one gets:

$$\Delta_1 - \Delta_2 = -a(x_{m2} - x_{m1})\Delta y_1 - b(-\Delta x_1 \cdot \Delta y_1 + \Delta x_2 \cdot \Delta y_2).$$

The second term can be neglected (in the following example its value is some 10^{-4} seconds of arc). The values of the line midpoint x_m differ in their sign, thus their difference ξ is well approximated by the distance of the two y-axes.

Thus one has:

$$\Delta_1 - \Delta_2 = +a\xi \cdot \Delta y_1 = \gamma \cdot \Delta y_1 .$$

Especially for the computation of the scale factor it should be taken into account that the image of the y-axis of system 2 is in system 1 a curved line (Fig. 1).

In Hungary the projectional distance of the y-axes along the x-axes is in the northern and central system $\xi_0 = 1.74\,494$ (in units of 100 km). The shortening due to the curvature (ε) is if y is also expressed in units of 100 km:

y	1	2	3 (100 km)
ε	21	85	193 (m)

If ξ is computed from ξ_0 according to this, then at first the factor

$$\gamma = a\xi$$

is to be determined, where a is the value corresponding to the Gaussian sphere with a radius of $R = 6\,378\,512.966$ m valid for Hungary:

$$a = \frac{\rho''}{2R^2} = 25.3487 .$$

The difference of the arc-to-chord reductions in the two projection systems for a line section connecting two points (with subscripts referring to the projection) is obtained as a product:

$$\Delta_1 - \Delta_2 = \gamma \cdot \Delta y_1$$

where Δy_1 is the projection of the distance in the direction y in system 1 (in units of

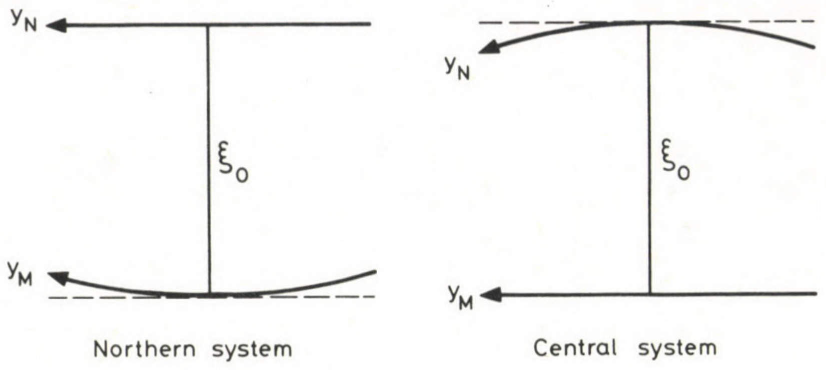

Fig. 1.

100 km). In Hungary the value of γ between the two systems changes from 44.18 to 44.23. In most cases the arithmetic mean can be used, but in more accurate computations one has to use:

$$\gamma = 44.232 - 0.0054\, y_{m1}^2$$

where the sign of γ is identical with the sign of the coordinates x in system 1 directed towards system 2.

According to the formula of the scale factor:

$$m_1 = 1 + ex_{m1}^2 + f \cdot \Delta x_1^2 + gx_{m1}^4$$

$$m_2 = 1 + ex_{m2}^2 + f \cdot \Delta x_2^2 + gx_{m2}^4$$

where

$$e = \frac{1}{2R^2} = 122\,894 \cdot 10^{-9}; \qquad f = \frac{1}{24R^2} = 10241 \cdot 10^{-9}.$$

The difference of the last terms can be omitted due to the small value of the factor $g = 25 \cdot 10^{-10}$, and as the value f is also small, the approximation $\Delta x_1^2 = \Delta x_2^2$ can also be accepted.

$$m_2 - m_1 = e(x_{m2}^2 - x_{m1}^2)$$

$$x_{m2}^2 = (\xi - x_{m1})^2 = \xi^2 - 2\xi x_{m1} + x_{m1}^2$$

$$m_2 - m_1 = e(\xi^2 - 2\xi x_{m1}) = \alpha - \beta x_{m1}.$$

α is always positive, and the sign law of β is identical with that of γ.

Taking into account the change of ξ with y_{m1}, and using the well approximating functions for Hungary one gets:

$$\alpha = 0.000\,373\,825 + (4 - y_{m1}^2)92 \cdot 10^{-9}$$

$$\beta = 0.000\,428\,676 + (4 - y_{m1}^2)53 \cdot 10^{-9}.$$

The first terms refer to the place $y = 2.00000$ and correspond rather well to the mean values.

Table I

	Projection 1	Projection 2	2−1
y_A	−74 251.204	− 74 261.392	
x_A	+55 238.915	−119 229.557	
y_B	−88 639.519	− 88 643.740	
x_B	+76 128.193	− 98 333.325	
δ_{AB}	325° 26′ 28.811″	325° 27′ 40.853″	+1′ 12.042″
Δ	−2.269″	+4.093″	+6.362″
μ_A	+0° 45′ 3.226″	+0° 43′ 57.547″	−1′ 5.679″
t	25 365.046 m	25 367.389 m	+2.343 m
Δy	−0.14 388	−0.14 382	
Δx	+0.20 889	+0.20 896	
y_m	−0.81 446	−0.81 453	
x_m	+0.65 684	−1.08 782	

Let us see an *example*. There are two points with known coordinates in both systems. All data and the projectional values are summarized in Table I, thus they can be compared with the results of the new method. The notations are the generally accepted ones: δ is the grid bearing, Δ the arc-to-chord reduction, μ the convergence of the map meridian, t the distance of the two points in the projection, $\Delta y = y_B - y_A$, and x_m and y_m the coordinates of the midpoint of the line. The last three have been expressed as generally usual in projection transformations, in units of 100 km.

Let us suppose at first that the coordinates are known in both systems. In that case $z = \mu_1 - \mu_2$ can be easily determined in both end points (The subscripts 1 and 2 refer, as everywhere in the following, to systems 1 and 2). E.g. in point A one has:

$$\Delta_1 - \Delta_2 = \gamma \cdot \Delta y_1 = +(44.228)(-0.14388) = -6.363''$$

(γ has been interpolated!).

According to a known formula:

$$z = \delta_2 - \delta_1 + \Delta_1 - \Delta_2 .$$

Thus in our case:

$$\begin{aligned} \delta_2 - \delta_1 &= +0^\circ\ 1'\ 12.042'' \\ \Delta_1 - \Delta_2 &= \quad\quad -\ 6.363'' \\ \hline z_A &= +\quad 1'\ \ 5.679'' \end{aligned}$$

If point B is taken as origin, then Δy changes its sign,therefore its orientation constant will be:

$$\begin{aligned} \delta_2-\delta_1 &= +0^\circ\ 1'\ 12.042'' \\ \Delta_1-\Delta_2 &= +\ 6.363'' \\ \hline z_B &= +\ 1'\ 18.405''. \end{aligned}$$

If in system 2 only the data of point A are known, and B is to be computed, then according to the formula

$$\delta_2=\delta_1+(\Delta_2-\Delta_1)+z_A$$

one gets:

$$\begin{aligned} \delta_1 &= 325^\circ\ 26'\ 28.811'' \\ -(\Delta_1-\Delta_2) &= +\ 6.363'' \\ z_A &= +\ 1'\ 5.679'' \\ \hline \delta_2 &= 325^\circ\ 27'\ 40.853''. \end{aligned}$$

In many cases z is already known, but if not, it can be easily determined from the line leading from A to a point C, known in both projections by means of the previously described method. It is to be known that the value of z is theoretically constant in any point, but the accuracy of the computed values depends naturally on the level of correspondence of the points known in both systems.

Let us continue now with the transformation of the distance:

$$m_2-m_1=\alpha-\beta x_{m1}\,.$$

In the present *example:*

$$\begin{aligned} \alpha &= 0.000\,374\,132 \\ \beta &= 0.000\,428\,853 \\ \text{and being:}\quad x_{m1} &= +0.65\,684 \end{aligned}$$

$$\begin{aligned} \alpha &= 374\,132\cdot 10^{-9} \\ \beta x_{m1} &= 281\,688\cdot 10^{-9} \\ \hline m_2-m_1 &= +92\,444\cdot 10^{-9} \end{aligned}$$

$$dt=t_2-t_1=(m_2-m_1)t_1=-2.345\text{ m}\,.$$

Now being both δ_2 and t_2 known, the coordinates of the point B can be determined by polar point positioning from the coordinates of point A in system 2. The example shows that the differences from the correct values are only some 10^{-3} seconds of arc, and millimeters, respectively.

The example shows further that for the transformation neither arc-to-chord reductions, nor scale factors are necessary, and only one grid bearing and one distance is to be computed, if z is know. If z must also be determined, than two additional grid bearings are to be computed (without distances). The transformation itself consists only of a few multiplications and additions.

II

The transformation between *two neighborous zones of the conform transversal cylinder projection of the ellipsoid* is theoretically identical with the previous case. As the image of the tangential meridian is here the x axis, and the distance of the original meridian of the two systems has the direction y, for the computation of the transformation factors the distance $\eta = 2y_0$ is to be used instead of the previous distance ξ, where y_0 is the coordinate y at the place x of the border meridian.

With respect to the more complicated curvature of the ellipsoid the interpolation of the coefficients α and β — if more accurate results are necessary — can be carried out by using linear and quadratic differences, and even γ is to be interpolated (linearly) in every case. Its sign follows the sign of the y-values. Considering that the difference between Δx_1 and Δx_2 cannot be neglected due to the stronger rotation, the γ values are to be interpolated to the average of the values x_{m1} and x_{m2}, and their multiplicator will be the weighted mean of Δx_1 and $\Delta x_2(\Delta x)$. These values are, however, not known for the zone 2, therefore a well fitting value for them is to be determined. If the convergence of the map meridian in the connecting point is approximately μ_0, then

$$\lambda = \Delta y_1 \tan \mu_0$$

by denoting approximative values by parantheses:

$$(x_m) = x_{m1} + \lambda \qquad (x_2) = \Delta x_1 + 2\lambda\,.$$

The weights of the values Δx_1 and (Δx_2) are obtained according to the values of the y_m. The weight of Δx_1 is $y_{m1} : \eta$. The remaining part of the unit represents then the weight of (Δx_2) (see the *example*, too). Then the difference of the two arc-to-chord reductions will be:

$$\Delta = \gamma(\Delta x)\,.$$

The numerical values are given here for the *Krassowski-ellipsoid*. The value of $\tan \mu_0$ in the 3°-zone system for the area of Hungary can be determined from the following formula:

$$\tan \mu_0 = 0.01913 - 29(52 - x_0) \cdot 10^{-5}$$

where x_0 is the coordinate of the connecting point in units of 100 km. The other factors can be determined from the following well fitting functions for the area of Hungary, taking into account that the factors a and e also depend on the coordinate x:

$$\text{If} \quad \overline{\Delta x} = 52.00\,000 - x_m \qquad \text{and} \qquad \overline{\Delta x_1} = 52.00\,000 - x_{m1} \, ,$$

then

$$\eta = 2.28 + 0.04\,\overline{\Delta x}$$

$$\gamma = 57.90 + 0.98\,\overline{\Delta x}$$

$$\alpha = 0.000\,641\,383 + (21\,603\,\overline{\Delta x_1} + 30\,\overline{\Delta x_1^2}) \cdot 10^{-9}$$

$$\beta = 0.000\,561\,402 + (9518\,\overline{\Delta x_1} - 60\,\overline{\Delta x_1^2}) \cdot 10^{-9} .$$

The neglection of $\bar{\Delta} x_1^2$ means only an error of some mm.

The signs of the different factors can be found in Table II depending on whether the transformation is made from the eastern half-zone into the western one or vice versa, from the western half-zone into the eastern one. The sign of λ can also be obtained from the rule that the line section from the connecting point is rotating in positive sense, if transforming from the eastern half-zone to the western one, and in the negative sense, if the transformation is made from the western half-zone into the eastern one. This rule must be especially cared for very strongly if the endpoint of the line section in the zone 1 lies outside of the border meridian. In such cases the sign rule can be sometimes opposite to the generally valid one.

The computations are presented again by an example in which in addition to the connecting point A, the other endpoint of the line section is known in both systems.

Transformations are generally necessary only in a zone of a width of 40 – 50 km from the border meridian. Therefore, it is advantageous to use a connecting point on the border meridian (which has known coordinates in both systems). Hazay and Tárczy-Hornoch (1951) published the coordinates of the points of the border meridian in the area of Hungary for each 5′ for $\varphi = 45°\ 30'$ to $48°\ 40'$ (here φ denotes geographic

Table II

Factors	From Western half-zone to Eastern half-zone	From Eastern half-zone to Western half-zone
y_1	–	+
Δ for the computation of z	–	–
Δ for the computation of δ_2	+	+
λ	–	+
α	+	+
β	–	+
z	–	+

latitude). For the points of the border meridian one has $x_1=x_2$; $y_1=-y_2$ and the orientation constant z is $2\mu_1$, as $\mu_1=-\mu_2$ (in the table, the sine and cosine of this value is given, thus one has not to compute the value of z!).

Tárczy-Hornoch and Hristov (1959 and 1966) published the data of the connecting points on the border meridian for each 30′ for $\varphi=25°$ to 55°.

In order to illustrate the general method of the transformation the connecting point in the example does not lie on the border meridian, but inside of zone 1. The data are contained in Table III.

Table III

	Zone 1	Zone 2	2−1
y_A	+92 607.699	−137 646.164	
x_A	5 153 416.682	5 154 272.296	
y_B	+60 000.000	−168 904.753	
x_B	5 188 400.000	5 190 479.880	
δ_{AB}	317° 0′ 46.600″	319° 11′ 43.549″	+2° 10′ 56.949″
Δ	−7.247″	+13.586″	+20.833″
μ_A	−0° 52′ 31.501″	+1° 18′ 4.611″	+2° 10′ 36.112″
t	47 823.578 m	47 833.967 m	+10.389 m
Δy	+0.326 08	−0.312 59	
Δx	+0.349 83	+0.362 08	
y_m	+0.763 04	−1.532 75	
x_m	51.709 08	51.723 76	

$$\tan\mu_0=0.01\,913+29(0.32\,608)10^{-5}=0.01\,904$$

$$\lambda=0.01\,904\Delta y_1=0.00\,621$$

$$(x_m)=+51.70\,908+0.00\,621=51.71\,529$$

$$(\Delta x_2)=+0.34\,983+0.01\,242=+0.36\,225$$

$$\overline{\Delta x}=52-(x_m)=+0.28\,471$$

$$\overline{\Delta x_1}=52-x_{m1}=+0.29\,092$$

$$\overline{\Delta x_1^2}=0.08\,463$$

$$\gamma=57.90+0.98\overline{\Delta x}=58.179$$

$$\eta=2.29 \qquad y_{m1}:\eta=0.333$$

$$\Delta x=0.333\Delta x_1+0.667(\Delta x_2)=+0.35\,811$$

$$\Delta_2-\Delta_1==\gamma\cdot\Delta x=+20.834$$

$$\begin{aligned} \delta_2-\delta_1 &= +2°\ 10'\ 56.949'' \\ -\Delta &= \underline{\qquad\quad -20.834''} \\ z_A &= +2°\ 10'\ 36.115'' \end{aligned} \qquad \begin{aligned} \delta_1 &= 317°\ \ 0'\ 46.600'' \\ \Delta &= +\qquad\ \ 20.834'' \\ z_A &= \underline{+2°\ 10'\ 36.115''} \\ \delta_2 &= 319°\ 11'\ 43.549'' \end{aligned}$$

$$\begin{aligned} \alpha = \ & 0.000\,641\,383 \\ & \qquad\ 6\,285 \\ & \underline{\qquad\qquad\ 2} \\ & 0.000\,647\,670 \end{aligned} \qquad \begin{aligned} \beta = \ & 0.000\,561\,402 \\ & \qquad + 2\,769 \\ & \underline{\qquad -\quad 5} \\ & 0.000\,564\,166 \end{aligned}$$

$$\begin{aligned} \alpha &= 647\,670 \cdot 10^{-9} \\ \beta y_{m1} &= \underline{430\,481 \cdot 10^{-9}} \quad (-) \\ m_2-m_1 &= 217\,189 \cdot 10^{-9} \end{aligned}$$

$$dt = t_1(m_2-m_1) = +10.387 \text{ m}.$$

Let us now transform bach the distance (now one has

$$\overline{\Delta x}_1 = +0.27\,624; \qquad \overline{\Delta x}_1^2 = 0.07\,631 \qquad \text{and} \quad y_{m1} = -1.53\,275)$$

$$\begin{aligned} \alpha = \ & 0.000\,641\,383 \\ & \qquad\ 5\,968 \\ & \underline{\qquad\qquad\ 2} \\ & 0.000\,647\,353 \end{aligned} \qquad \begin{aligned} \beta = \ & 0.000\,561\,402 \\ & \qquad + 2\,629 \\ & \underline{\qquad -\quad 5} \\ & 0.000\,564\,026 \end{aligned}$$

$$\begin{aligned} \alpha &= 647\,353 \cdot 10^{-9} \\ \beta y_{m1} &= \underline{864\,511 \cdot 10^{-9}} \quad (-) \\ m_2-m_1 &= -217\,158 \cdot 10^{-9} \end{aligned}$$

$$dt = t_2(m_2-m_1) = -10.387 \text{ m}.$$

The transformation factors between the 2° wide zones for Hungary are the following:

$$\tan \mu_0 = 0.01\,275 - 19(52 - x_0)10^{-5}$$

$$\eta = 1.52 + 0.03\overline{\Delta x}$$

$$\gamma = 38.60 + 0.65\overline{\Delta x}$$

$$\alpha = 0.000\,285\,007 + (9603\overline{\Delta x}_1 + 11\overline{\Delta x}_1^2)10^{-9}$$

$$\beta = 0.000\,374\,235 + (6346\overline{\Delta x}_1 - 45\overline{\Delta x}_1^2)10^{-9}$$

In the present case again $\overline{\Delta x}=52.00\,000-x_m$; $\overline{\Delta x}_1=52.00\,000-x_{m1}$ and x_0 is the coordinate of the connecting point.

The transformation factors for 6° wide zones are for the area of Hungary

$$\tan\mu_0=0.03\,826-19(52-x_0)10^{-5}$$

$$\eta=4.57+0.08\overline{\Delta x}$$

$$\gamma=115.85+1.97\overline{\Delta x}$$

$$\alpha=0.002\,568\,248+(86\,490\overline{\Delta x}_1+120\overline{\Delta x}_1^2)10^{-9}$$

$$\beta=0.001\,123\,404+(19\,038\overline{\Delta x}_1-130\overline{\Delta x}_1^2)10^{-9}$$

As it can be seen from the example, the transformation between the zones of the ellipsoidic cylinder projection needs somewhat more computations than the transformation between spheric systems. The method is, however, significantly simpler than the method described by Hazay and Tárczy-Hornoch (1951) or any other proposed method.

In Hungary the longest meridian zone has a length of about 3°, i.e. it is short. This enabled to find for all transformation factors a well approximating function. For longer meridian arcs this is not more true, therefore in areas having greater lengths in x-direction the meridian arc must be split into sections, and the approximating functions are to be determined separately for these sections.

The factors to be determined are:

$$\gamma=a\eta \qquad \alpha=e\eta^2 \qquad \beta=2e\eta\,.$$

III

The coordinates of the point on the projection 2 can be determined not only by polar positioning, but also by intersection. If the bearings in system 2 are computed in both systems from several known points, one has all data necessary for the intersection. It is also possible that the bearings computed in system 1 will be reduced with the difference of the arc-to-chord reduction $\Delta_2-\Delta_1$, and the same will be done for one or several orientation directions from the control points; thus "measurement series" will be produced which can be oriented in system 2. (Naturally if the intersection is chosen the transformation of the distances is not necessary. The computation of the differences of the arc-to-chord reductions means then not more than a single product.)

References

Fasching A 1914: Manual of surveying. Budapest

Hazay I 1951: Zur Umrechnung der Gauss—Krügerschen Koordinaten von einem Projektionsstreifen in den benachbarten. *Acta Technica*, 1, No. 2, 55–73.

Hazay I—Tárczy-Hornoch A 1951: Computation of the Gauss—Krüger coordinates. Budapest

Hazay I 1955: Terrestrial projections. Budapest

Hazay I 1969: Projections. Budapest

Hazay I 1975: Umrechnung zwischen den Gauss—Krüger Projektionsstreifen durch Transformation der Richtungswinkel. *Periodica Polytechnica*

Hristow W K 1943: Die Gauss—Krügerschen Koordinaten auf dem Ellipsoid. Leipzig

Jordan-Eggert 1948: Handbuch der Vermessungskunde. Band III. S Stuttgart

Tárczy-Hornoch A—Hristov W K 1959: Tables for Krassowski-Ellipsoid. Budapest, I. 1959; II. 1968.

Tárczy-Hornoch A—Szádeczky-Kardos Gy 1959: Transformation between two zones of the Gauss—Krüger projection zones with the help of two connecting points. *Geodézia és Kartográfia*, 11, 81–86.

Acta Geodaet., Geophys. et Montanist. Hung. Volume 18 (1—2), pp. 83—96 (1983)

SOURCE PARAMETERS OF SEVERAL EARTHQUAKES RECORDED AT THE SEISMIC STATION KAŠPERSKÉ HORY

D PROCHÁZKOVÁ

Geophysical Institute, Czechosl. Acad. Sci., Prague

[Manuscript received June 23, 1981]

The paper discusses some methodical questions of the source parameters determination and presents numerical values of the source parameters for several earthquakes.

Keywords: coda waves; earthquake sources; P waves; seismic source parameters; seismic station Kašperské Hory; S waves

Introduction

There are many dependences describing the seismic regime, however, for the prediction of earthquakes they are not yet sufficient. To obtain further information we must find other parameters describing the source properties of individual shocks, in addition to geographical coordinates, depth, time of origin and magnitude. Earthquake source parameters could serve as an important data base for the generalization and synthesis in seismology. Routine determination and reports of source properties enable a new level of understanding in many seismological studies. This is made possible now by digitally recorded seismic data and computer programs.

The dislocation theory, provided that the mechanism of the earthquakes can be characterized by a double couple, offers the following parameters:

1. the seismic moment, determining the strength of a source and representing the mechanical moment of one couple from the double couple;

2. the source dimension, representing the radius of an equivalent circular source area;

3. the stress drop, expressing the difference of the shear stresses on the fault surface before and after the shock;

4. the average of the relative displacement at both sides of a fault;

5. the energy emitted from the focus in form of seismic waves; etc.

The importance of source parameters in many seismological studies necessitates to analyse and to compare the different methods used and their reliability.

Methodical questions of source parameters determination

Theoretical researches of the earthquake source made it possible to use the amplitude spectra of the P and S waves for the determination of the source parameters, Table I. M_0 denotes here the seismic moment, r the source dimension, $\Delta\sigma$ the stress drop, u the average displacement across the fault, E the energy emitted from the focus in the form of seismic waves, ρ the density of the medium, v the propagation velocity of the corresponding phase, R the hypocentral distance, $R_{\vartheta\Phi}$ the radiation pattern for a wave type, Ω_0 the long-period spectral amplitude, f_0 the corner frequency and μ the shear modulus in the source region.

Table I

	Brune (1968, 1970) Hanks, Wyss (1972)	Sharpe [Fučík, Rudajev, 1979]
$M_0=$	$4\pi\rho v^3 R\Omega_0/R_{\vartheta\varphi}$	$8\pi^2\mu v_P R\Omega_0$
$r=$	$v_P/(\pi f_0)2.3v_S/(2\pi f_0)$	$v_P/(\sqrt{3}\pi f_0)$
$\Delta\sigma=$	$7\,M_0/(16\,r^3)$	$M_0/(\pi r^3)$
$u=$	$M_0/(4\pi\mu r^2)$	
$E=$	$\Delta\sigma M_0/(2\mu)$	$\pi r^3\Delta\sigma^2/(2\mu)$

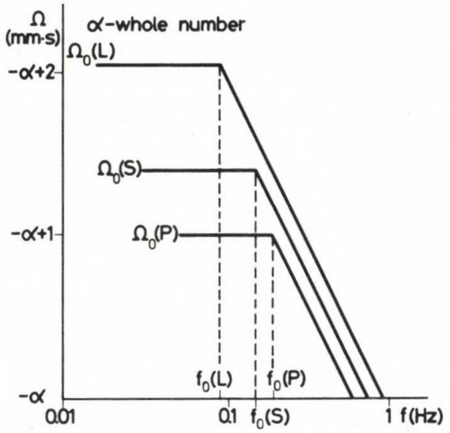

Fig. 1. Average of the amplitude spectra; relative positions of the long-period levels and of the corner frequencies for P, S and surface waves are shown

In the case of stronger especially shallow earthquakes, the record of the group of surface waves, among them mainly of the Rayleigh waves, is evident and clear; similarly the amplitude spectra are clear, too. On the basis of the amplitude spectra of the P, S and surface waves of about 30, mostly European earthquakes recorded by the broad-band seismograph FBV at the seismic station Kašperské Hory in the period 1974–1979 a comparison of the investigated waves was made. Figure 1 shows the average form of

Table II

dt – sampling period, SL – sample length, D_c – epicentral distance, L – surface waves, * – incomplete data

1. Japan 30.7° N, 138.4° E, $H=22^h05^m23.5^s$ GMT, November 29, 1974, $m=6.1$, $D_c=86.3°$ (ISC); d$t=1.28$ s

L: NS	–	$\Omega_0=0.260$ mm s	$f_0=0.060$ Hz	SL = 21.57 m
EW	–	$\Omega_0=0.190$ mm s	$f_0=0.075$ Hz	SL = 22.72 m
Z	–	$\Omega_0=0.170$ mm s	$f_0=0.080$ Hz	SL = 21.33 m
		$\Omega_0=0.364$ mm s	$f_0=0.072$ Hz	

$M_0=7.99\cdot10^{17}$ N m, $r=11.39$ km, $\Delta\sigma=0.238$ MPa, $u=0.163$ m, E$=3.18\cdot10^{12}$ J, $M_W=5.9$, $M(M_0)=5.7$, $M(E)=5.1$

2. Iran 33.39° N, 57.43° E, $H=15^h\,35^m\,56.6^s$ GMT, September 16, 1978, $h=N$, $M=7.4$, $m=6.5$, $D_c=37°$ (NEIS); d$t=0.2954$ s for body waves, d$t=0.8185$ s for surface waves

P: NS	–	$\Omega_0=0.004$ mm s	$f_0=0.163$ Hz	SL = 0.89 m
EW	–	$\Omega_0=0.022$ mm s	$f_0=0.136$ Hz	SL = 0.85 m
Z	–	$\Omega_0=0.024$ mm s	$f_0=0.163$ Hz	SL = 0.85 m
		$\Omega_0=0.033$ mm s	$f_0=0.154$ Hz	
S: NS	–	$\Omega_0=0.220$ mm s	$f_0=0.056$ Hz	SL = 1.94 m
EW	–	$\Omega_0=0.451$ mm s	$f_0=0.063$ Hz	SL = 1.90 m
Z	–	$\Omega_0=0.213$ mm s	$f_0=0.063$ Hz	SL = 2.05 m
		$\Omega_0=0.545$ mm s	$f_0=0.061$ Hz	
L: NS	–	$\Omega_0=1.763$ mm s	$f_0=0.053$ Hz	SL = 22 m
EW	–	$\Omega_0=1.664$ mm s	$f_0=0.058$ Hz	SL = 16.66 m
Z	–	$\Omega_0=1.680$ mm s	$f_0=0.067$ Hz	SL = 20.99 m
		$\Omega_0=2.949$ mm s	$f_0=0.059$ Hz	

	P	*S*	*L*	*mean value*	*unit*
M_0	$2.48\cdot10^{18}$	$8.14\cdot10^{18}$	$2.77\cdot10^{18}$	$4.46\cdot10^{18}$	N m
r	12.4	21.31	13.9	15.87	km
$\Delta\sigma$	0.572	0.370	0.454	0.465	MPa
u	0.427	0.475	0.380	0.427	m
E	$2.37\cdot10^{13}$	$5.03\cdot10^{13}$	$2.10\cdot10^{13}$	$3.17\cdot10^{13}$	J

$M_W=6.4$, $M(M_0)=6.2$, $M(E)=5.8$

3. Romania 45.83° N, 26.72° E, $H=19^h\,21^m\,54.1^s$ GMT, March 4, 1977, $h=86$ km, $m=6.1$, $D_c=9.49°$ (ISC), $N=7.2$ (NEIS); d$t=0.3002$ s

P: NS	–	$\Omega_0=$ 0.175 mm s	$f_0=0.133$ Hz	SL = 0.49 m
EW	–	$\Omega_0=$ 0.730 mm s	$f_0=0.100$ Hz	SL = 0.47 m
Z	–	$\Omega_0=$ 0.712 mm s	$f_0=0.100$ Hz	SL = 0.55 m
		$\Omega_0=$ 1.035 mm s	$f_0=0.111$ Hz	
S: NS	–	$\Omega_0=$ 2.016 mm s	$f_0=0.050$ Hz	SL = 0.73 m
EW	–	$\Omega_0=$ 2.412 mm s	$f_0=0.035$ Hz	SL = 0.68 m
Z	–	$\Omega_0=$ 5.668 mm s	$f_0=0.035$ Hz	SL = 0.62 m
		$\Omega_0=$ 6.481 mm s	$f_0=0.040$ Hz	

Table II (contd)

L:	NS –	$\Omega_0 = 3.555$ mm s	$f_0 = 0.103$ Hz	SL = 5.30 m
	EW –	$\Omega_0 = 9.618$ mm s	$f_0 = 0.048$ Hz	SL = 6.62 m
	Z –	$\Omega_0 = 12.346$ mm s	$f_0 = 0.051$ Hz	SL = 7.11 m
		$\Omega_0 = 16.049$ mm s	$f_0 = 0.067$ Hz	
coda :	NS –	$\Omega_0 = 0.225$ mm s	$f_0 = 0.158$ Hz	SL = 10.73 m
	EW –	$\Omega_0 = 0.327$ mm s	$f_0 = 0.150$ Hz	SL = 10.66 m
	Z –	$\Omega_0 = 0.448$ mm s	$f_0 = 0.141$ Hz	SL = 10.65 m
		$\Omega_0 = 0.599$ mm s	$f_0 = 0.150$ Hz	

	P	S	L	*mean value*	*unit*
M_0	$2 \cdot 10^{19}$	$2.48 \cdot 10^{19}$	$3.87 \cdot 10^{19}$	$2.78 \cdot 10^{19}$	N m
r	17.2	32.5	12.24	17.65	km
$\Delta\sigma$	1.729	0.318	9.286	3.778	MPa
u	1.792	0.622	6.845	3.0086	m
E	$5.77 \cdot 10^{14}$	$1.32 \cdot 10^{14}$	$6 \cdot 10^{15}$	$2.24 \cdot 10^{15}$	J

$M_W = 6.9$, $M(M_0) = 6.8$, $M(E) = 7.1$

4. Greece 40.76° N, 23.27° E, $H = 23^h\,34^m\,11.4^s$ GMT, May 23, 1978, $h = 10$ km, $m = 5.7$, $M = 5.6$, $D_c = 10.8°$ (NEIS); $dt = 0.151$ s for body waves, $dt = 0.303$ s for surface waves

P :	NS –	$\Omega_0 = 0.0023$ mm s	$f_0 = 0.165$ Hz	SL = 0.63 m
	EW –	$\Omega_0 = 0.0027$ mm s	$f_0 = 0.144$ Hz	SL = 0.53 m
	Z –	$\Omega_0 = 0.0030$ mm s	$f_0 = 0.161$ Hz	SL = 0.73 m
		$\Omega_0 = 0.0046$ mm s	$f_0 = 0.157$ Hz	
S :	NS –	$\Omega_0 = 0.008$ mm s	$f_0 = 0.065$ Hz	SL = 0.77 m
	EW –	$\Omega_0 = 0.011$ mm s	$f_0 = 0.084$ Hz	SL = 0.53 m
	Z –	$\Omega_0 = 0.004$ mm s	$f_0 = 0.110$ Hz	SL = 0.58 m
		$\Omega_0 = 0.0142$ mm s	$f_0 = 0.086$ Hz	
L:	NS –	$\Omega_0 = 0.672$ mm s	$f_0 = 0.093$ Hz	SL = 8.20 m
	EW –	$\Omega_0 = 0.578$ mm s	$f_0 = 0.108$ Hz	SL = 7.41 m
	Z –	$\Omega_0 = 0.675$ mm s	$f_0 = 0.106$ Hz	SL = 7.56 m
		$\Omega_0 = 1.1141$ mm s	$f_0 = 0.102$ Hz	

	P	S	L	*mean value*	*unit*
M_0	$1.01 \cdot 10^{17}$	$6.20 \cdot 10^{16}$	$3.06 \cdot 10^{17}$	$1.56 \cdot 10^{17}$	N m
r	12.17	15.12	8.04	11.78	km
$\Delta\sigma$	0.0247	0.0079	0.2590	0.0972	MPa
u	0.018	0.007	0.125	0.050	m
E	$4.17 \cdot 10^{10}$	$4.53 \cdot 10^{9}$	$1.32 \cdot 10^{12}$	$4.55 \cdot 10^{11}$	J

$M_W = 5.4$, $M(M_0) = 5.2$, $M(E) = 4.6$

Table II (contd)

5. Greece 40.74° N, 23.23° E, $H=20^h\,03^m\,21.0^s$ GMT, June 20, 1978, $h=3$ km, $m=6.1$, $M=6.4$ (NEIS), $D_c=11°$; $dt=0.14745$ s for body waves, $dt=0.34188$ s for surface waves

P: NS	–	$\Omega_0=0.0141$ mm s	$f_0=0.177$ Hz	SL = 0.44 m
EW	–	$\Omega_0=0.0066$ mm s	$f_0=0.217$ Hz	SL = 0.39 m
Z	–	$\Omega_0=0.0116$ mm s	$f_0=0.226$ Hz	SL = 0.43 m
		$\Omega_0=0.0194$ mm s	$f_0=0.207$ Hz	
L: NS	–	$\Omega_0=4.67$ mm s	$f_0=0.089$ Hz	SL = 9.18 m
EW	–	$\Omega_0=0.763$ mm s	$f_0=0.142$ Hz	SL = 9.36 m
Z	–	$\Omega_0=1.89$ mm s	$f_0=0.130$ Hz	SL = 10.85 m
		$\Omega_0=5.0954$ mm s	$f_0=0.120$ Hz	

	P	*L*	*mean value*	*unit*
M_0	$4.34 \cdot 10^{17}$	$1.43 \cdot 10^{18}$	$9.32 \cdot 10^{17}$	N m
r	9.23	6.83	8.03	km
$\Delta\sigma$	0.2429	1.9748	1.1089	MPa
u	0.135	0.812	0.474	m
E	$1.76 \cdot 10^{12}$	$4.72 \cdot 10^{13}$	$2.45 \cdot 10^{13}$	J

$M_W=5.9$, $M(M_0)=5.7$, $M(E)=5.7$

6. Yugoslavia 41.96° N, 19.02° E, $H=02^h\,10^m\,20.3^s$ GMT, April 9, 1979, $h=10$ km, $m=5.3$, $M=4.9$ (NEIS), $D_c=8.4°$; $dt=0.1434$ s

P: NS	–	$\Omega_0=0.000\,19$ mm s	$f_0=0.473$ Hz	SL = 0.57 m
EW	–	$\Omega_0=0.000\,07$ mm s	$f_0=0.596$ Hz	SL = 0.62 m
Z	–	$\Omega_0=0.000\,09$ mm s	$f_0=0.562$ Hz	SL = 0.54 m
		$\Omega_0=0.000\,21$ mm s	$f_0=0.544$ Hz	
S: NS	–	$\Omega_0=0.000\,57$ mm s	$f_0=0.200$ Hz	SL = 0.52 m
EW	–	$\Omega_0=0.000\,72$ mm s	$f_0=0.266$ Hz	SL = 0.52 m
Z	–	$\Omega_0=0.000\,31$ mm s	$f_0=0.316$ Hz	SL = 0.48 m
		$\Omega_0=0.000\,97$ mm s	$f_0=0.261$ Hz	
L: NS	–	$\Omega_0=0.011\,1$ mm s	$f_0=0.117$ Hz	SL = 6.05 m
EW	–	$\Omega_0=0.016\,7$ mm s	$f_0=0.115$ Hz	SL = 5.81 m
Z	–	$\Omega_0=0.005\,3$ mm s	$f_0=0.141$ Hz	SL = 5.69 m
		$\Omega_0=0.020\,74$ mm s	$f_0=0.124$ Hz	

	P	*S*	*L*	*mean value*	*unit*
M_0	$3.54 \cdot 10^{15}$	$3.25 \cdot 10^{15}$	$4.37 \cdot 10^{15}$	$3.72 \cdot 10^{15}$	N m
r	3.51	4.98	6.61	5.03	km
$\Delta\sigma$	0.036	0.012	0.007	0.018	MPa
u	0.008	0.004	0.003	0.005	m
E	$2.13 \cdot 10^{9}$	$6.51 \cdot 10^{8}$	$5.11 \cdot 10^{8}$	$1.10 \cdot 10^{9}$	J

$M_W=4.4$, $M(M_0)=4$, $M(E)=3$

Table II (contd)

7. Yugoslavia 42.10° N, 19.21° E, $H=06^h\,19^m\,44.1^s$ GMT, April 15, 1979, $h=10$ km, $m=6.2$, $M=6.9$ (NEIS), $D_c=8.2°$; $dt=0.1456$ s

P : NS	–	$\Omega_0=0.0028$ mm s	$f_0=0.282$ Hz	SL = 0.59 m
EW	–	$\Omega_0=0.0024$ mm s	$f_0=0.355$ Hz	SL = 0.52 m
Z	–	$\Omega_0=0.0021$ mm s	$f_0=0.316$ Hz	SL = 0.58 m
		$\Omega_0=0.0042$ mm s	$f_0=0.318$ Hz	
S : NS	–	$\Omega_0=0.0047$ mm s	$f_0=0.216$ Hz	SL = 0.46 m
EW	–	$\Omega_0=0.0298$ mm s	$f_0=0.209$ Hz	SL = 0.58 m
Z	–	$\Omega_0=0.0037$ mm s	$f_0=0.366$ Hz	SL = 0.49 m
		$\Omega_0=0.0304$ mm s	$f_0=0.280$ Hz	
L: NS*	–	$\Omega_0=0.0660$ mm s	$f_0=0.126$ Hz	SL = 2.33 m
EW*	–	$\Omega_0=0.0389$ mm s	$f_0=0.126$ Hz	SL = 1.94 m
Z*	–	$\Omega_0=0.0269$ mm s	$f_0=0.079$ Hz	SL = 2.45 m
		$\Omega_0=0.0812$ mm s	$f_0=0.110$ Hz	

	P	S	L	*mean value*	*unit*
M_0	$7 \cdot 10^{16}$	10^{17}	$1.69 \cdot 10^{17}$	$1.13 \cdot 10^{17}$	N m
r	6.01	4.64	7.45	6.03	km
$\Delta\sigma$	0.142	0.440	0.180	0.254	MPa
u	0.051	0.123	0.081	0.085	m
E	$1.66 \cdot 10^{11}$	$7.35 \cdot 10^{11}$	$5.08 \cdot 10^{11}$	$4.70 \cdot 10^{11}$	J

$M_W=5.3$, $M(M_0)=5.1$, $M(E)=4.6$

8. Yugoslavia 42.32° N, 18.68° E, $H=14^h\,43^m\,06.0^s$ GMT, April 15, 1979, $h=10$ km, $m=5.7$, $M=5.6$ (NEIS), $D_c=7.9°$; $dt=0.1464$ s,

P : NS	–	$\Omega_0=0.00025$ mm s	$f_0=0.794$ Hz	SL = 0.57 m
EW	–	$\Omega_0=0.00008$ mm s	$f_0=0.631$ Hz	SL = 0.62 m
Z	–	$\Omega_0=0.00015$ mm s	$f_0=0.631$ Hz	SL = 0.53 m
		$\Omega_0=0.00030$ mm s	$f_0=0.685$ Hz	
S : NS	–	$\Omega_0=0.00053$ mm s	$f_0=0.422$ Hz	SL = 0.52 m
EW	–	$\Omega_0=0.00098$ mm s	$f_0=0.562$ Hz	SL = 0.52 m
Z	–	$\Omega_0=0.00057$ mm s	$f_0=0.398$ Hz	SL = 0.52 m
		$\Omega_0=0.00127$ mm s	$f_0=0.461$ Hz	
L: NS	–	$\Omega_0=0.0434$ mm s	$f_0=0.141$ Hz	SL = 7.00 m
EW	–	$\Omega_0=0.0638$ mm s	$f_0=0.124$ Hz	SL = 5.41 m
Z	–	$\Omega_0=0.0225$ mm s	$f_0=0.158$ Hz	SL = 6.08 m
		$\Omega_0=0.08038$ mm s	$f_0=0.141$ Hz	

Table II (contd)

	P	S	L	*mean value*	*unit*
M_0	$4.84 \cdot 10^{15}$	$4.06 \cdot 10^{15}$	$1.62 \cdot 10^{16}$	$8.37 \cdot 10^{15}$	N m
r	2.79	2.82	5.82	3.81	km
$\Delta\sigma$	0.0981	0.0797	0.0362	0.0713	MPa
u	0.016	0.014	0.013	0.014	m
E	$7.93 \cdot 10^{9}$	$5.40 \cdot 10^{9}$	$9.79 \cdot 10^{9}$	$7.71 \cdot 10^{9}$	J

$M_W = 4.6$, $M(M_0) = 4.3$, $M(E) = 3.4$

9. Yugoslavia 42.33° N, 18.76° E, $H = 03^h\ 30^m\ 34.8^s$ GMT, May 12, 1979, $h = 10$ km, $m = 4.8$, $M = 4.9$ (NEIS), $D_c = 7.9°$; $dt = 0.1464$ s

P : NS	–	$\Omega_0 = 0.000\,14$ mm s	$f_0 = 0.636$ Hz	SL = 0.69 m
EW	–	$\Omega_0 = 0.000\,04$ mm s	$f_0 = 0.794$ Hz	SL = 0.54 m
Z	–	$\Omega_0 = 0.000\,05$ mm s	$f_0 = 0.891$ Hz	SL = 0.58 m
		$\Omega_0 = 0.000\,15$ mm s	$f_0 = 0.774$ Hz	
S : NS	–	$\Omega_0 = 0.000\,36$ mm s	$f_0 = 0.447$ Hz	SL = 0.57 m
EW	–	$\Omega_0 = 0.000\,41$ mm s	$f_0 = 0.794$ Hz	SL = 0.57 m
Z	–	$\Omega_0 = 0.000\,09$ mm s	$f_0 = 0.906$ Hz	SL = 0.51 m
		$\Omega_0 = 0.000\,55$ mm s	$f_0 = 0.716$ Hz	
L: NS	–	$\Omega_0 = 0.003\,29$ mm s	$f_0 = 0.158$ Hz	SL = 5.17 m
EW	–	$\Omega_0 = 0.004\,15$ mm s	$f_0 = 0.163$ Hz	SL = 3.63 m
Z	–	$\Omega_0 = 0.004\,81$ mm s	$f_0 = 0.200$ Hz	SL = 5.75 m
		$\Omega_0 = 0.007\,15$ mm s	$f_0 = 0.174$ Hz	

	P	S	L	*mean value*	*unit*
M_0	$2.42 \cdot 10^{15}$	$1.76 \cdot 10^{15}$	$1.44 \cdot 10^{15}$	$1.87 \cdot 10^{15}$	N m
r	2.47	1.82	4.71	3.00	km
$\Delta\sigma$	0.0707	0.1285	0.0061	0.068	MPa
u	0.011	0.014	0.002	0.009	m
E	$2.86 \cdot 10^{9}$	$3.78 \cdot 10^{9}$	$1.47 \cdot 10^{8}$	$2.70 \cdot 10^{9}$	J

$M_W = 4.2$, $M(M_0) = 3.8$, $M(E) = 3.1$

the amplitude spectra, the general relation of the long-period levels and of the corner frequencies of the P, S and surface waves. The slope of the spectrum beyond the corner frequency is approximately the same for all types of waves, it is equal to 2 or is sometimes a little more.

If the seismic moment is computed on the basis of surface waves with the same formula as for body waves and using the phase velocity of the surface waves numerical results summarized in Table II are obtained. In average M_0 (surface waves): M_0 (body waves) = 10 for shallow and M_0 (surface waves) = M_0 (body waves) for intermediate earthquakes. Using these relations the numerical results obtained on the basis of the surface waves can be compared directly with those obtained on the basis of body waves.

The relationship for the computation of the source dimension by means of the amplitude spectra of the surface waves was statistically derived on the basis of data in Table II. In agreement with Brune's relationships for the P and S waves, the relationship was supposed to have the form $r = cv_L/f_0$ (r is the source dimension, v_L the

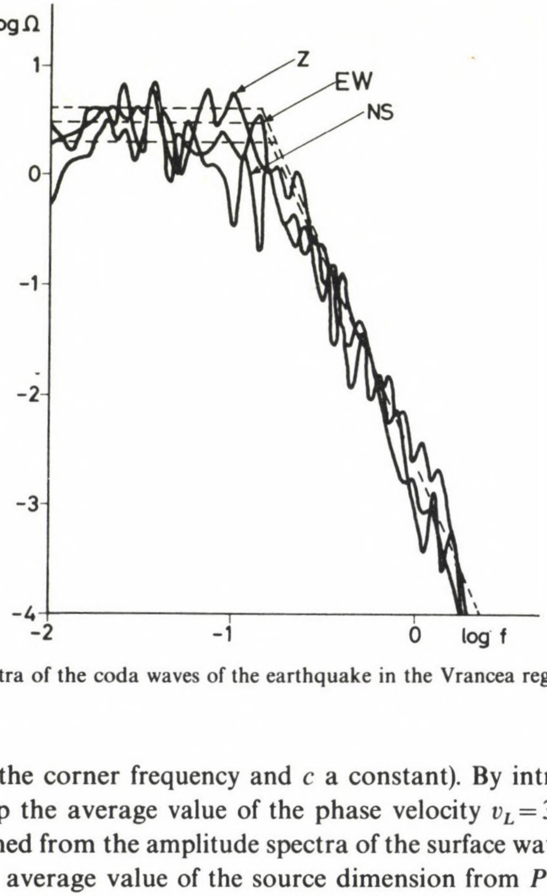

Fig. 2. Amplitude spectra of the coda waves of the earthquake in the Vrancea region of March 1, 1977

phase velocity, f_0 the corner frequency and c a constant). By introducing into this general relationship the average value of the phase velocity $v_L = 3$ km/s, the corner frequency f_0 obtained from the amplitude spectra of the surface waves and the source dimension r as the average value of the source dimension from P and S waves, the numerical value of the constant c is obtained. On the basis of the numerical values in Table II one has in average $c = 0.273$ (± 0.047).

Figure 2 shows amplitude spectra of the coda waves. It is interesting to note that the long-period spectrum level is clear. Rautian and Khalturin (1978), Aki and Patton (1978) and others supposed the coda waves as transverse waves. For individual focal regions they compiled connections with body waves and used the coda waves for the source parameters determination. It is necessary in near future to derive such a relation for Europe.

It should be reminded that numerical values of the source parameters depend on the computational formula. The factors in relation to the values determined by the

Sharpe model are given in Table III. The discrepancies between individual formulas can be comprehensibly seen in the concrete computations.

In the computation of the source parameters one has to take into account the following:

Table III

	r	$\Delta\sigma$	M_0
Brune	1.74	1.37	4.9
Kasahara	0.60		
Hanks, Wyss	2.04		
Sharpe	1.00	1.00	1.00

a) For the computation of the amplitude spectra several numerical methods can be used; it is generally known that the resulting spectra can differ not only in the numerical values but also in the form (Gutowski et al. 1978). For computation of the source parameters, the FFT and Fillon methods are practicable in most cases, whereas methods using narrow windows are not practicable because they give accurate spectrum values only in a narrow frequency interval near the centre of the time window [Båth 1974].

b) Seismic waves and their spectra depend on the azimuth between the seismic station and the fault, on the geological structure in the region of the source and under the seismic station, on the properties of the medium in which the waves propagate and on the recording instrument. The instrumental response can be corrected by the relation: $\Omega_E(f)=\Omega_C(f)/H(f)$, where $\Omega_C(f)$ is the computed amplitude spectrum, $H(f)$ is the amplitude-frequency response of the instrument and $\Omega_E(f)$ is the corrected spectrum. Realistic spectrum records can be obtained only using broad-band instruments.

Figure 3 shows the influence of the inelastic attenuation of seismic waves on the amplitude spectrum according to the formula $\Omega_F/(f)=\Omega_D(f)\exp(D\pi F/Qv)$, where $\Omega_F(f)$ is the spectrum radiated from the focus, $\Omega_D(f)$ the spectrum at a hypocentral distance D, v the wave velocity and Q the attenuation coefficient. The Figure shows schematically, that numerical values in the amplitude spectra do not change practically up to 0.1 Hz i.e. numerical values of the long-period levels are nearly constant. However, the numerical value of the corner frequency may change; its shift to higher values causes an apparent decrease of the source dimension; the magnitude of the shift of the corner frequency depends on the hypocentral distance, on the wave velocity and on the attenuation coefficient.

Theoretical calculations show that the orientation of the fault with respect of the direction source — seismic station practically does not influence the long-period spectral values, but there is an influence on the corner frequency. The lowest corner frequency is observed in the direction in which the fracture is spreading i.e. in principle

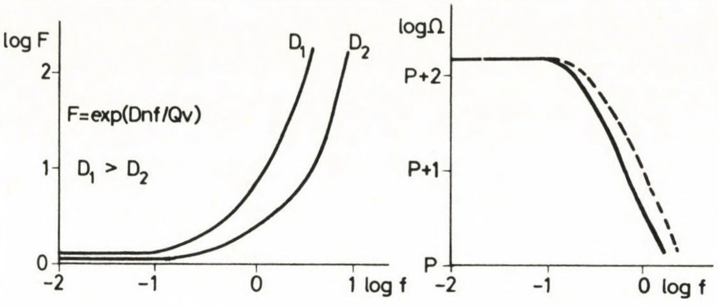

Fig. 3. Schematic picture of the influence of the inelastic attenuation on the amplitude spectra

the azimuthal variation of the amplitude spectra should provide information on how a fault propagetes. According to the results of Lander (1979) and others it seems that in epicentral distances greater than 20° the amplitude spectra become smoother and do not show any azimuthal variations.

c) The sampling period must be sufficiently small in order to conserve the highest frequencies in a given signal. It must be at least ten points for the shortest period. The influence of the change of the sampling period was tested only for one shock. Maximum differences of 15% in the corner frequency and of 30% in the long-period amplitude level were obtained in cases in which the sample lengths were nearly the same (Table IV).

d) The sample length influences the numerical values of both the corner frequency and the long-period spectral amplitude (Table V). The percentual changes of the sample length, the long-period spectral amplitude and the corner frequency are related there to the numerical values of the shortest sample. With increasing sample length the long-period spectral amplitude increases and the corner frequency decreases. Most substantial changes occurr in cases when the longer sample contains a next wave group. If short and long samples contain only one wave group, the changes of the long-period spectral amplitudes and the corner frequency were negligible. The longer the sample length, the smaller is the influence of its changes on the investigated values. Table VI shows the influence of the change of the sample length on the numerical values of the source parameters by the obtained maximum changes of the long-period spectral amplitudes and of the corner frequency.

e) For the computation of the amplitude spectra we use the components EW, NS and Z. The long-period spectral values and the corner frequencies are not the same, as original records differ. A detailed statistical analysis of the numerical results in Table II shows that the ratio of long-period spectral amplitudes is the same in the components EW, NS and Z for the *P*, *S* and surface waves and an inverse relationship is valid for the corner frequencies. The ratio in the components EW, NS and Z probably depends on the orientation of the fault with respect to the direction of the seismic

Table IV

Greece May 23, 1978; $dt1 = 0.151$ s, $dt2 = 0.148\,37$ s for body waves, $dt1 = 0.303$ s, $dt2 = 0.343\,33$ s for surface waves $[\Omega_0] =$ mm s, $[f_0] =$ Hz, SL = sample length in minutes, dt — sampling period, L— surface waves

	$\Omega_0(1)$	$\Omega_0(2)$	$f_0(1)$	$f_0(2)$	SL(1)	SL(2)
P : NS	0.0023	0.0030	0.165	0.141	0.63	0.63
EW	0.0027	0.0030	0.144	0.158	0.53	0.59
Z	0.0030	0.0030	0.161	0.158	0.73	0.71
S : NS	0.008	0.004	0.065	0.089	0.77	0.64
EW	0.011	0.016	0.084	0.089	0.53	0.60
Z	0.004	0.003	0.110	0.106	0.58	0.47
L: NS	0.672	0.697	0.093	0.100	8.20	15.7
EW	0.578	0.612	0.108	0.106	7.41	7.88
Z	0.675	0.523	0.106	0.089	7.56	7.62

Table V

L— surface waves, SL — sample length

P:	ΔSL = 0–180%	maximum $\Delta\Omega_0 = 100\%$	maximum $\Delta f_0 = 50\%$
S:	ΔSL = 0–68%	maximum $\Delta\Omega_0 = 70\%$	maximum $\Delta f_0 = 50\%$
L:	ΔSL = 0–320%	maximum $\Delta\Omega_0 = 38\%$	maximum $\Delta f_0 = 26\%$

Table VI

Dispersion of source parameters

$M_0, r, \Delta\sigma, u, E$ — correspond to Ω_0 and f_0

$M_0, r', \Delta\sigma', u', E'$ — correspond to $\Omega_0 + \Delta\Omega_0$ and $f_0 - \Delta f_0$

maximum $\Delta\Omega_0 = 100\%$, maximum $\Delta f_0 = 50\%$

$M_0' = 2M_0$, $r' = 2r$, $\Delta\sigma' = 0.25\Delta\sigma$, $u' = 0.5u$, $E' = 0.5E$

Relations among the source parameters determined on the basis of the P, S and the surface (L) waves

$\Omega_0(P) < \Omega_0(S) < \Omega_0(L)$, $f_0(P) > f_0(S) > f_0(L)$

$M_0(P) \leqq M_0(S) < M_0(L)$ — maximum difference 1–1.5 order

r — irregular rate, maximum difference $r_{max} = 2r_{min}$

$\Delta\sigma(L) > \Delta\sigma(P) \geqq \Delta\sigma(S)$ — maximum difference 2 orders

$u(L) > u(P) \geqq u(S)$ — maximum difference 2 orders

$E(L) > E(P) \geqq E(S)$ — maximum difference 2 orders

Comparison of seismic energy

$\log E_1 = 4.8 + 1.5M$, $E_2 = \Delta\sigma M_0 : (2\mu)$, $[E] = J$

usually: $E_1 \geqq E_2$, maximum difference $E_1 : E_2 = 100$

Comparison of magnitudes

$M_W = 2$ ($\log M_0$): 3–6.03, $M(M_0) = (\log M_0 - 9.95) : 1.4$

$M(E) = (\log E_2 - 4.8) : 1.5$, M — surface wave magnitude determined in the Seismological Centres;

$[M_0] =$ N m, $[E] = J$

$M \geqq M_W \geqq M(M_0) \geqq M(E)$

$M_W = M(M_0)$ considering the error in the magnitude determination equals to ± 0.3 magnitude unit

$M_L = (\log M_0(\text{surface wave}) - 9.95) : 1.4$

$M_W \geqq M_L \geqq M(M_0)$

station. From a physical point of view it is necessary to consider the whole vector and not the individual components when calculating the source parameters. From a practical point of view the most important question is how to obtain the spectrum of the whole displacement vector from the spectra of the individual components. It follows from the theoretical considerations:

$$\Omega_0=\sqrt{(\Omega_0^{EW})^2+(\Omega_0^{NS})^2+(\Omega_0^{Z})^2}, \qquad f_0=(f_0^{EW}+f_0^{NS}+f_0^{Z}):3\,. \tag{1}$$

Source parameters of selected earthquakes

The numerical results in Table II were obtained on the basis of records of the 3-component broad-band FBV system recording at the seismic station Kašperské Hory; the magnification curve of this seismograph is shown in Fig. 4. The digital input data were obtained from an analog magnetic tape. The sampling period was chosen sufficiently small, at least ten points for the shortest period. The sample length was

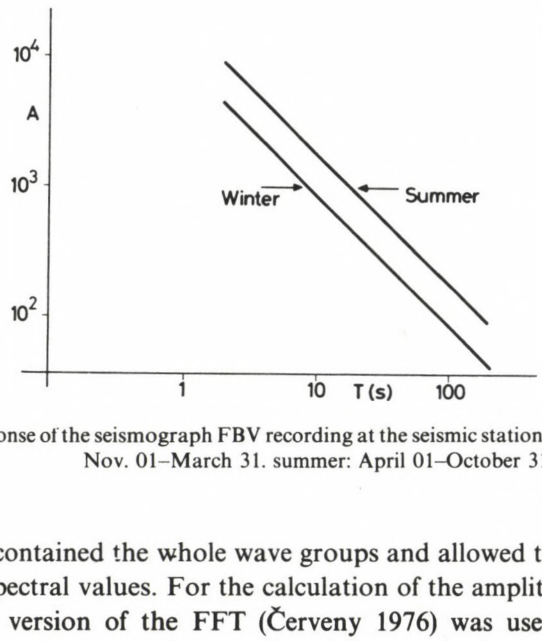

Fig. 4. Amplitude response of the seismograph FBV recording at the seismic station Kašperské Hory: winter: Nov. 01–March 31. summer: April 01–October 31

chosen so that it contained the whole wave groups and allowed the determination of the long-period spectral values. For the calculation of the amplitude spectra, the so-called FCOOLR version of the FFT (Červeny 1976) was used. The long-period spectral values and the corner frequencies of the whole displacement vector were computed from Eq. (1). Before the calculation of the spectrum, input data were corrected to a zero level by substracting the mean amplitude value in order to obtain a stationary series with zero mean value and in order to avoid a distortion of the spectrum and the occurrence of very high spectral values (Anděl 1976).

The source parameters were determined assuming the values $\rho = 2.7$ g/cm^3, $v_P = 6$ km/s, $v_S = 3.5$ km/s, $v_L = 3$ km/s, $\mu = 3 \cdot 10^{10}$ Nm^{-2} and $R_{\vartheta\Phi} = 0.4$. Table VI shows a comparison of the source parameters determined on the basis of the P, S and surface waves. A comparison of the seismic energies determined on the basis of the seismic moment and the stress drop and on the basis of the relationship between the seismic energy and the magnitude ($\log E = 4.8 + 1.5\,M$, $[E] = J$) proves that the seismic energy calculated using the surface wave magnitude is usually greater; the maximum difference amounts to about two orders. The table also compares the magnitude defined by Kanamori ($M_w = 2 \log M_0/3 - 6.03$, $[M_0] = \mathrm{Nm}$), which is determined from the mean values of the seismic moment and of the seismic energy of the P, S and surface waves as well as the magnitude determined by seismological centres.

Figure 5 shows the empiric relationship between the seismic moment M_0 and the surface wave magnitude M. The least squares method yields $\log M_0 = 9.95 + 1.4\,M$; $[M_0] = \mathrm{Nm}$. This formula, especially the coefficient of M is close to that of other investigators. The numerical values of the seismic moment obtained by North (1977) for 72 events in the Mediterranean and Middle East areas during 1963–70 from the Rayleigh wave amplitude agree well with this relationship.

Further empirical relationships between surface wave amplitudes, stress drop, source dimension and average displacement across the fault were found (Procházková 1980). Having a greater number of data on the numerical values of the source parameters, the relationships can change a little.

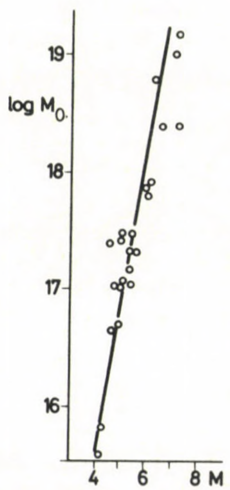

Fig. 5. Seismic moment M_0 vs surface magnitude M. $[M_0] = \mathrm{Nm}$

Conclusions

A study of the methodical questions of the source parameters determination showed that:

a) for the computation of the source parameters it is possible to use in addition to *P* and *S* waves also surface and coda waves. It is necessary to find a relation between the long-period spectral amplitudes of the coda waves and the long-period spectral amplitudes of the *S* waves for the area of Europe;

b) it is necessary to take care of the choice of the input data, of the computing method and of the formulas. Particularly in cases of short epicentral distances, results not only from one seismic station, but from several ones distributed around the fault should be used;

c) for the computation of the source parameters it is necessary to take into account all components, not only one or two.

Numerical values of the source parameters of several earthquakes are given in Chapter 3. and Table II. The main task is now to calculate source parameters and to collect them in order to apply them in the seismological practice and for discovering further regularities of the seismic regime and to improve earthquake prediction.

Acknowledgements

The author thanks Professor A R Ritsema for very helpful discussions and words of encouragement and for reading the manuscript. She also thanks Professor B Bolt and Professor K Aki for discussions.

References

Aki K, Patton H 1978: Determination of seismic moment tensor using surface waves. *Tectonophysics*, 49, p. 213.

Anděl J. 1976: Statistická analýza časových řad. SNTL Praha.

Båth M 1974: Spectral Analysis in Geophysics. Verlag Amsterdam.

Brune J N 1968: Seismic moment, seismicity and rate of slip along major fault zones. *J.G.R.*, 73, p. 777.

Brune J N 1970: Tectonic stress and the spectra of seismic shear waves from earthquakes. *J.G.R.*, 75, p. 4997.

Červený V 1976: Jednoduché procedury pro Fourierovu a Hilbertovu transformaci. Unpublished

Fučík P, Rudájev V 1979: Physical parameters of rockburst sources, *Publ. Inst. Geophys. Pol. Acad. Sc.*, 123, p. 21.

Gutowski P R, Robinson E A, Treitel A 1978: Spectral Estimation: Fact or Fiction. Modern Spectrum Analysis. IEEE Press New York

Hanks T C, Wyss M 1972: The use of body-wave spectra in the determination of seismic source parameters. *B.S.S.A.*, 62, p. 561.

Lander J 1979: Report of Working Group on Earthquake Parameters. IASPEI, Denver, unpublished

North R C 1977: Seismic moment, source dimensions and stresses associated with earthquakes in the Mediterranean and Middle East. *Geoph. J. R. Astr. Soc.*, 48, p. 137.

Procházková D 1982: Source parameters: seismic moment, stress drop, source dimension and average displacement. *Bolletino di Geof., Trieste* (in press)

Rautian T G, Khalturin V I 1978: The use of the coda for determination of the earthquake source spectrum. *B.S.S.A.*, 60, p. 923.

Acta Geodaet., Geophys. et Montanist. Hung. Volume 18 (1—2), pp. 97—106 (1983)

ON THE HYDROMAGNETIC RADIAL OSCILLATIONS IN THE EARTH'S LIQUID .CORE AND THE GEOMAGNETIC SECULAR SHORT-PERIOD VARIATIONS

LE MINH TRIET[1]

Geodetic and Geophysical Research Institute of the Hungarian Academy of Sciences, Sopron

[Manuscript received December 5, 1981]

By comparing the theoretic spectrum of hydromagnetic radial oscillations in the Earth's liquid core with the periods of short-period geomagnetic secular variations it can be shown that the latter occur in consequence of hydromagnetic radial oscillations in the Earth's liquid core. Due to the action of Earth's rotation and the presence of a torodial magnetic field in the core-mantle boundary layer, the periods of the geomagnetic secular variation presumably depend on the latitude. Further, it may be shown that the secular change in the daylength is closely connected with the propagation of hydromagnetic waves in the boundary layer between the Earth's core and mantle.

Keywords: earthquake frequency; Earth's core; geomagnatic secular variation; hydromagnetic oscillation; length of the day

Introduction

It is well known that the geomagnetic field measured at the surface of the Earth undergoes complicated changes with time. Systematic studies on the properties of the geomagnetic field enabled to separate this field into two parts: the main field of internal origin and a small remaining part of external origin. The main field experiences slow, gradual changes, the so-called geomagnetic secular variation. On the basis of results obtained from the analyses of experimental (observatory, archaeomagnetic and palaeomagnetic) data the following periods of the geomagnetic secular variation may be revealed; 22 – 25, 50 – 70, 100 – 120, 180, 300 – 400, 500 – 600, 1000 – 1200, 1500 – 1800 and 7000 – 8000 years (Janovsky 1978, Pushkov et al. 1977). According to the classification by Braginsky (1970a) the geomagnetic secular variations with the above discrete periods may be divided into three classes: variations with periods of about $7.5 \cdot 10^3$ years, variations with periods of the order of 10^3 years, and the short-period variations which have periods less than 100 years.

In spite of advances in the theory of the short-period geomagnetic secular variation, up to now the most characteristic property, the period-spectrum of this variation is still far from being completely explained. Nagata and Rikitake (1963)

[1] Permanent address: Centre of Scientific Researches, 1 Mac Dinh Chi, Ho Chi Minh City, Vietnam

pointed out that the northward shifting of the dipole field is manifested in the geomagnetic secular variation and period of the S_2^0 quadrupole field can be determined by

$$T=\frac{2\pi R}{4.3}\frac{1}{S_1}\sqrt{\frac{7\pi\rho}{3}}, \tag{1}$$

where R is the radius of the Earth's core, ρ the mass density, S_1 a steady poloidal magnetic field in the core. Taking $\rho=10\,\mathrm{gcm}^{-3}$, $R=3.5\cdot10^8$ cm and $S_1=1.8$ Gauss, the period of a simple harmonic oscillation of the S_2^0 field is of about 80 years. In this theoretical model the role of the liquid core is omitted. According to Braginsky (1970b) the period of 60 years in the geomagnetic secular variation and in the secular change of the daylength can be understood as the period of Alfvén type torsional oscillations in the Earth's liquid core,

$$\omega\sim\frac{B_s}{L\sqrt{4\pi\rho}}. \tag{2}$$

Taking the radial component of the magnetic field in the Earth's core $B_s\approx3$ Gauss, $L\sim10^8$ cm, and $\rho=10\,\mathrm{gcm}^{-3}$, we obtain $T\approx60$ years. According to the "free hydromagnetic oscillation theory" proposed by Hide (1965), if the intensity of the magnetic torodial field is 100 Gauss, the periods of the free hydromagnetic oscillations of a rotating spherical shell are fairly well corresponding to the periods of the short-period geomagnetic secular variation. However, in the above mentioned theories the periodicity of the short-period geomagnetic secular variation is incidentally concerned.

In the present paper the spectrum of the short-period geomagnetic secular variation will be investigated on the basis of a new assumption namely that the hydromagnetic radical oscillation in the Earth's liquid core may be responsible for it.

Hydromagnetic radial oscillations in the Earth's liquid core

ıt is generally accepted that the Earth's liquid core may be considered as a medium satisfying the hydromagnetic conditions. Therefore, it is possible to assume that the velocity v of small disturbances in the Earth's liquid core are equal to the Alfvén velocity. It should be further assumed that in the liquid core the main magnetic field is predominantly of radial direction, namely $H_r\gg H_\theta$, H_φ. Besides, we can suppose that the Earth's liquid core satisfies the condition of the thermal equilibrium and consequently there is no global thermal convection there. The time-scale characteristic for changes in the hydromagnetic processes in the Earth's liquid core is indeed long enough to suppose the material of the Earth's liquid core incompressible.

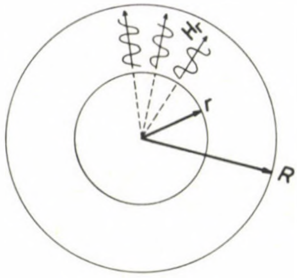

$R = 3.5 \times 10^8$ cm
$r = 1.4 \times 10^8$ cm

Fig. 1.

With these conditions we shall examine small amplitude oscillations in a spherical shell between the inner core and outer core filled with a conducting fluid (Fig. 1).

In the case of radial oscillations the velocity potential A depends only on r and t time. Consequently, the velocity potential A satisfies the following wave equation

$$\frac{\partial^2 A}{\partial t^2} = v^2 \left(\frac{\partial^2 A}{\partial r^2} + \frac{2}{r} \frac{\partial A}{\partial r} \right). \tag{3}$$

In solving Eq. (3) we use the boundary conditions

$$\left. \frac{\partial A}{\partial r} \right|_{r=r} = \left. \frac{\partial A}{\partial r} \right|_{r=R} = 0 . \tag{4}$$

The solution of Eq. (3) can be expressed by

$$A = T(t) U(r) .$$

By substituting this expression into Eq. (3) we obtain

$$\frac{T''(t)}{v^2 T(t)} = \frac{U''(r) + \frac{2}{r} U'(r)}{U(r)} = -\lambda^2 \tag{5}$$

where $-\lambda^2$ denotes the common value of the two sides of Eq. (5). Thus we obtain the following two equations

$$T''(t) + \lambda^2 v^2 T(t) = 0 , \tag{6}$$

$$U''(r) + \frac{2}{r} U'(r) + \lambda^2 U(r) = 0 . \tag{7}$$

The general solution of Eq. (7) is

$$U(r) = C_1 \frac{\sin \lambda r}{r} + C_2 \frac{\cos \lambda r}{r}, \tag{8}$$

where C_1 and C_2 are arbitrary constants which can be determined by the boundary conditions.

By virtue of the spherical symmetry of the problem we can set $C_2 = 0$ and assume $C_1 = 1$ in examining the frequencies of the radial oscillations. Thus, the solution of Eq. (7) becomes

$$U(r) = \frac{\sin \lambda r}{r}. \tag{9}$$

Substituting this solution into the boundary conditions (4) we obtain

$$\tan \lambda(R-r) = \frac{\lambda(R-r)}{1+\lambda^2 Rr}. \tag{10}$$

To find the real roots λ we construct the curves of two functions in the right and left sides of Eq. (10), and the abscissae of the intersection of two curves give the roots (Le Minh Triet 1973a).

In order to give a semiquantitative estimation for the periods of the hydromagnetic radial oscillations in the Earth's liquid core we can consider the approximate value

$$\lambda \approx k \cdot \pi, \tag{11}$$

where k is a positive integer.

Then the general solution of Eq. (6) can be written as

$$T_k = a_k \cos \frac{vk\pi t}{R-r} + b_k \sin \frac{vk\pi t}{R-r}, \tag{12}$$

where a_k and b_k are constants satisfying the initial conditions. From Eq. (12) the periods of the harmonics of the hydrogmagnetic radial oscillation in the Earth's liquid core may be determined by the following simple formula

$$T_k = \frac{2\pi}{\omega} = \frac{2}{kv}(R-r), \tag{13}$$

with $k = 1, 2, 3, \ldots n$.

At present, it is generally supposed that the magnetic field in the Earth's core is essentially radial, and its radial component is of about 3 Gauss. Then, the propagation velocity of hydromagnetic disturbances takes the value $v = H/\sqrt{4\pi\rho} \approx 0.25$ cm sec^{-1}, if $\rho = 10$ gcm^{-3}. Therefore, the period-spectrum of hydromagnetic radial oscillation in the Earth's liquid core may be given by

$$T_k = \frac{2}{k} \frac{(3.5 \cdot 10^8 - 1.4 \cdot 10^8)\,\text{cm}}{0.25\,\text{cm sec}^{-1}} \approx \frac{50}{k}\,\text{years}. \tag{14}$$

The spectrum of the short-period geomagnetic secular variations

Now, we can state the relationship between the short-period geomagnetic secular variations and the hydromagnetic radial oscillation of the Earth's liquid core by comparing the periods of two processes.

With $k = 1$, the fundamental period of the hydromagnetic radial oscillation is in agreement with the period of about 50 years unambiguously determined in many investigations during the three last decades (Barta 1963, Pushkov et al. 1977). Analogously, the period of about 25 years in secular variation corresponds to the second harmonics of the hydromagnetic radial oscillation. Further, the period of about 11 years is presumably connected with the fifth harmonics. The coincidence of the periods of the secular variation with those of the hydromagnetic radial oscillation of the Earth's liquid core, supposing a magnetic radial component of about 3 Gauss, leads to the conclusion that the hydromagnetic radial oscillations are responsible for the short-period geomagnetic secular variation. In other words, the short-period geomagnetic secular variation at the Earth's surface is an observable manifestation of hydromagnetic radial oscillations in the Earth's liquid core.

All the harmonics of the hydromagnetic radial oscillation are present in the liquid core, their periods can be determined by Eq. (14). However, according to investigations by McDonald (1957) and Currie (1967) the amplitudes of magnetic disturbances with periods <4 years are strongly attenuated by the electromagnetic screening of the Earth's surface, only the harmonic components with periods longer than 4 years remain. Thus, the complete spectrum of the short-period geomagnetic secular variations can be determined by Eq. (14) if k varies from 1 to 13.

In connection with the period of about 11 years it should be noted that the period of 11 years is usually attributed to the cycle of the solar activity. On the basis of the above explanation the geomagnetic variation with a period of about 11 years can be divided into internal and external parts. The internal part is obviously connected with the hydromagnetic radial oscillation in the liquid core, the external part can be attributed to the 11 years cycle of solar activity.

It is necessary to remark here that the magnetic observations made in the past are generally inaccurate, so it is difficult to determine exactly the periods possibly corresponding to different harmonics of the hydromagnetic radial oscillation in the Earth' liquid core. Besides, a discrepancy between the theoretically determined periods and those from observations is perhaps related to the different penetration of the various harmonic components of the hydromagnetic radial oscillation from the core into the mantle of the Earth. In spite of these uncertainties the predominant period of about 50 years in the short-period variation can be found in almost all magnetic observatories. However, for a more complete explanation of the spectrum the role of the mantle and crust should be investigated in details in the penetration of magnetic signals originating in the Earth's liquid core.

In this analysis the role of the core-mantle boundary layer and of the toroidal magnetic field are not taken into account, as the toroidal field is mainly concentrated in a thin boundary layer and it does not significantly influence the hydromagnetic radial oscillations. The core-mantle boundary layer is considerably thinner than the dimension of the Earth's liquid core, therefore, the existence of the boundary layer cannot cause a perceptible change in the periods of the hydromagnetic radial oscillations which depend mainly on the hydromagnetic conditions and the dimensions of the Earth's liquid core. However, in connection with the spectrum of the secular variation at the Earth's surface, we have to consider the role of the magnetic toroidal field and the boundary layer between the core and mantle of the Earth.

Propagation of the hydromagnetic waves in the core-mantle boundary layer and its influence on the short-period geomagnetic secular variation

On the basis of the correlation between the hydromagnetic radial oscillation in the Earth's liquid core and the short-period geomagnetic secular variation we can state that this variation observed at the Eath's surface is closely associated with the propagation of hydromagnetic waves in the Earth's liquid core, especially, in the core-mantle boundary layer where a high intensity magnetic toroidal field is concentrated. The propagation of hydromagnetic waves in the Earth's liquid core is influenced by the Earth's rotation. Under its action the hydromagnetic waves propagating in the liquid core become dispersive, and two kinds of hydromagnetic waves can propagate with different phase velocities (Le Minh Triet 1972). These two kinds of waves can be identified in the spectrum of short-period geomagnetic secular variation. The phase velocity of the hydromagnetic waves propagating in the Earth's liquid core can be determined from the following dispersion relation

$$\omega^2 - k^2 H_0^2 \cos^2 \varphi / 4\pi\rho \pm 2\omega\Omega \cos \alpha = 0 \,, \tag{15}$$

where ω is the frequency of the hydromagnetic waves, Ω the angular velocity of the Earth's rotation and k the wave number (Fig. 2).

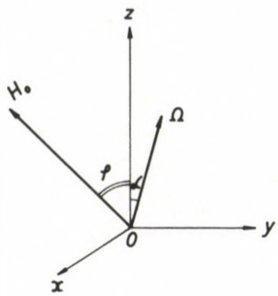

Fig. 2.

From Eq. (15) it follows

$$\omega = \pm\Omega \cos\alpha \{1 \pm \sqrt{1+4R_m^2}\}$$

where R_m denotes the Rossby magnetic number defined by

$$R_m = \frac{kH_0 \cos\varphi}{2\Omega \cos\alpha \sqrt{4\pi\rho}}.$$

In the Earth's liquid core the Rossby magnetic number $R_m \ll 1$ (Hide 1965), consequently, the phase velocity of the hydromagnetic waves propagating in the liquid core can be approximated by (Le Minh Triet 1972)

$$v_f = \frac{\omega}{k} = \frac{H_0 \cos\varphi}{\sqrt{2}\sqrt{4\pi\rho}}. \tag{16}$$

The toroidal magnetic field concentrated in the core-mantle boundary layer is estimated as (Le Minh Triet 1973):

$$H_\varphi = Cr \sin\alpha, \tag{17}$$

where C is a constant to be determined from the boundary conditions.

Substituting this value into Eq. (16) we obtain

$$v_f = \frac{Cr \sin\alpha \cos\varphi}{\sqrt{2}\sqrt{4\pi\rho}}. \tag{18}$$

Taking $\varphi = 0$, i.e., when the hydromagnetic waves are propagating along the toroidal magnetic field in the core-mantle boundary layer, their phase velocity depends on the latitude. Consequently, the spectrum of the short-period geomagnetic secular variation depends also on the latitude.

It is necessary to mention that at the equator the effect of Earth's rotation is not present, therefore, with $\alpha=\pi/2$ the phase velocity of the hydromagnetic waves propagating in the equatorial zone is equal to the ordinary Alfvén velocity, namely

$$v_1=\frac{Cr}{\sqrt{4\pi\rho}}. \tag{19}$$

In latitudes of about 40° (where the centre of the non-dipole field corresponding to the geomagnetic secular variation lies) the phase velocity of hydromagnetic waves has the value

$$v_2=\frac{Cr\sin 50^\circ}{\sqrt{2}\sqrt{4\pi\rho}}. \tag{20}$$

In comparing Eq. (19) with Eq. (20) it is evident that in the equatorial zone the phase velocity, and consequently, the frequency of the hydromagnetic waves reaching the core-mantle boundary is about twice as at the middle latitudes. This is really observed in the spectrum of short-period geomagnetic secular variation at the Earth's surface. Thus the predominant period of about 25 years at low latitudes and in the zones near the equator originates not only from the second harmonics of the hydromagnetic radial oscillation, but also from the fundamental harmonics with a period of 50 years. This conclusion is quite opposite to the explanation proposed by certain authors who suppose that the occurrence of a period of about 22–25 years would be connected to the Abbot cycle, to the circulation of the general magnetic field in the Sun.

As the phase velocity of hydromagnetic waves propagating in the core-mantle boundary layer changes under the action of Earth's rotation, the periods of the short-period geomagnetic secular variation vary as a function of latitude. However, in practice, it is difficult to determine exactly this change from a series of observational data obtained at various magnetic observatories, as the accuracy of the magnetic measurements made in the past is not high enough to deduce a precise value of the periods appearing in the geomagnetic secular variation. In addition, inhomogeneities in the electrical conductivity of the mantle and crust also cause difficulties in the determination of the periods and amplitudes of various components of the geomagnetic secular variation.

Correlation between short-period geomagnetic secular variation, geomagnetic westward drift and secular change in the rate of the Earth's rotation

The possibility of a correlation between geomagnetic secular variation, westward drift of the geomagnetic field and secular change in the rate of Earth's rotation or in the daylength has long been studied. However, the physical nature of this empirical correlation is still a problem to be investigated in details. On the basis of the hydromagnetic radial oscillation and the propagation of hydromagnetic waves in the Earth's liquid core we try to explain the physical nature of this correlation.

In the conditions of the Earth's liquid core hydromagnetic radial oscillations and propagation of hydromagnetic waves are obviously connected with mass displacements, especially with the coupling between the core and mantle of the Earth. Therefore, the periods observed in the secular variation appear also in the geomagnetic westward drift and in the secular change of the Earth's rotation. We can suppose that under the action of hydromagnetic oscillations taking place in the liquid core of the Earth, the magnetic toroidal field in the core-mantle boundary layer varies with the periods of the hydromagnetic waves reaching the core-mantle interface. Consequently, the electromagnetic core-mantle coupling also varies with the periods of the hydromagnetic oscillations. Thus, the periodicity of the secular change in the rate of Earth's rotation and in the geomagnetic westward drift can be considered as consequences of hydromagnetic radial oscillations occurring in the Earth liquid core. We illustrate this conclusion by the curves of the short-period geomagnetic secular variation, the velocity of the geomagnetic westward drift and the secular change in the daylength (Fig. 3) (Vestine and Kahle 1968, Le Minh Triet 1974).

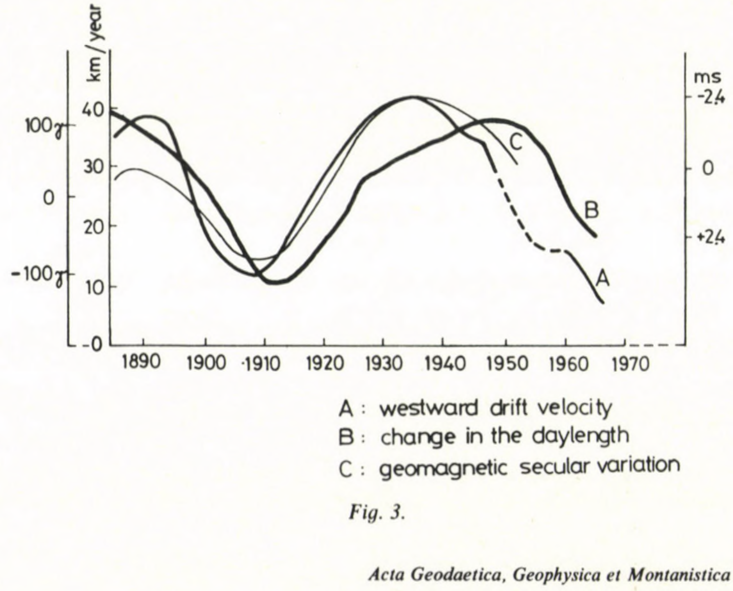

Fig. 3.

From Fig. 3 follows that the period of the secular change in the daylength is similar to that of the geomagnetic secular variation and of the secular variation in the velocity of the geomagnetic westward drift. Consequently, it can be assumed that the geomagnetic secular variation, the geomagnetic westward drift and the secular change in the rate of Earth's rotation have the same origin, namely, hydromagnetic radial oscillations in the Earth's liquid core. However, we found a phase lag of about 6–7 years between the secular change in the daylength and the short-period geomagnetic secular variation, or the secular change in the velocity of the geomagnetic westward drift. According to Kahle et al. (1967) this phase lag can be attributed to the time needed for the magnetic signal to diffuse through the mantle. However, on the basis of the propagation of hydromagnetic waves through the core-mantle boundary layer we can assume that the phase lag of about 6–7 years between the geomagnetic westward drift and the secular change in the daylength can be associated with the dispersion of hydromagnetic waves propagating in the core boundary rotating with the Earth. The dispersion time of the dispersive hydromagnetic waves appears as a phase lag between the secular variation of the geomagnetic westward drift and the secular change in the daylength (Le Minh Triet 1974).

The dispersion time of these waves can be estimated by a well-known formula

$$T=\frac{2\pi}{k(v_g-v_f)}, \tag{21}$$

where k, v_g and v_f are the wave number, group and phase velocities respectively.

In the case of slow hydromagnetic waves with periods comparable with the time scale of the short-period geomagnetic secular variations, the Rossby magnetic number $R_m \ll 1$. Therefore, we have

$$v_f=\frac{\omega}{k}=v_A\{\sqrt{1+4R_m^2}\pm 1\}/2R_m \approx \frac{v_A^2 k}{2\Omega},$$

$$v_g=\frac{\mathrm{d}\omega}{\mathrm{d}k}=2R_m v_A/\sqrt{1+4R_m^2}\approx \frac{v_A^2 k}{\Omega}$$

and consequently, the dispersion time of hydromagnetic waves propagating in the Earth's liquid core is estimated by

$$T=\frac{4\pi\Omega}{k^2 v_A^2} \tag{22}$$

where v_A is the Alfvén velocity.

In the boundary layer between the core and mantle of the Earth the toroidal field H_T is supposed to be 50 Gauss (according to the Bullard's model), the thickness d of the core-mantle boundary layer is 160 km. Then

$$v_A = \frac{H_T}{\sqrt{4\pi\rho}} = 0.05 \text{ m sec}^{-1}, \qquad k = \frac{2\pi}{d} = 3.9 \cdot 10^{-5} \text{m}^{-1},$$

$$\Omega = 7 \cdot 10^{-5} \text{ sec}^{-1}.$$

Therefore, the dispersion time of the hydromagnetic waves responsible for the short-period geomagnetic secular variation is about 6 years ($1.8 \cdot 10^8$ sec). This value coincides with the phase lag between the secular variation, the geomagnetic westward drift and the secular change in the rate of Earth's rotation. Consequently, it can be assumed that the secular change in the rate of Earth's rotation and the geomagnetic westward drift occur in consequence of a core-mantle periodic coupling governed by the hydromagnetic radial oscillations in the Earth's liquid core.

References

Barta Gy 1963: The secular variation in the geomagnetic field and other geophysical phenomena. *Annales Universitatis Scientiarum Budapestiensis de Roland Eötvös Nominate., Sec. Geol.*, 7, 71.

Брагинский С И 1970а: О спектре колебаний гидромагнитного динамо Земли. *Геомаг. и Аэрономия*, 10, 221.

Брагинский С И 1970б: Магнитогидродинамические крутильные колебания в земной ядре и вариации длины суток. *Геомаг. и Аэрономия*, 10, 3.

Currie R G 1967: Magnetic shielding properties of the Earth's mantle. *J. Geophys. Res.*, 62, 2623.

Hide R 1965: Free hydromagnetic oscillations of the Earth's core and the theory of the geomagnetic secular variation. *Phil. Trans. Roy. Soc. London.*, Ser. A 259, 615.

Яновский Б М 1978: Земной магнетизм. Ленинград.

Kahle A B 1969: Prediction of geomagnetic secular change confirmed. *Nature*, 223, n° 5202, 165.

Le Minh Triet 1972: On the role of the Earth's rotation in the occurrence of the geomagnetic secular variation. *Acta Geod., Geoph., Mont. Hung.*, 7, 147–154.

Le Minh Triet 1973a: Sur la périodicité de la variation séculaire du champ magnétique terrestre. *Acta geophysica polonica*, 21, 159.

Le Minh Triet 1973b: On the distribution of magnetic fields in the Earth's core. *Acta Geod., Geoph., Mont. Hung.*, 8, 403–408.

Le Minh Triet 1974: A note on the phase lag between the westward drift of the geomagnetic field and the secular change in the Earth's rotation. *Acta geophysics polonica.*, 22, 21.

McDonald K L 1957: Penetration of the geomagnetic secular field through a mantle with variable conductivity. *J. Geophys. Res.*, 62, 117.

Nagata T, Rikitake T 1963: The northward shifting of the geomagnetic dipole and stability of the axial magnetic quadrupole of the Earth. *J. Geomagn. Geoelect. Japan*, 213.

Пушков А Н, Коломийцева Г И, Чернова Т А 1977: Свойства геомагнитного поля на интервалах различной длительности. «Исследование пространственно-временной структуры геомагнитного поля». Наука, Москва.

Vestine E H, Kahle A B 1968: The westward drift and geomagnetic secular change. Geophys. *J. Roy. Astr. Soc. London.*, 15, 29.

Acta Geodaet., Geophys. et Montanist. Hung. Volume 18 (1—2), pp. 109—117 (1983)

TURBULENCE IN THE LOWER THERMOSPHERE DURING GEOMAGNETIC STORMS DEDUCED FROM IONOSPHERIC SPORADIC *E* PARAMETERS

P BENCZE[1]

Geodetic and Geophysical Research Institute, Hungarian Academy of Sciences, Sopron

[Manuscript received November 15, 1981]

The turbulence in the lower thermosphere during geomagnetic storms has been investigated by means of ionospheric sporadic *E* parameters. Computing the vertical shear of the horizontal wind on the basis of the wind shear theory of mid-latitude sporadic *E* for day-time hours first the gradient Richardson number has been determined. Then, using the relation between the gradient Richardson number and the vertical turbulent wind the turbulent intensity and the vertical turbulent diffusivity have been computed.

It has been found that the vertical turbulent diffusivity above 110 km decreases during geomagnetic storms. This would mean that the height of the turbopause increases. Thus, the results seem to support those studies, which explain the composition changes of the upper atmosphere during geomagnetic storms by the increase of the height of the turbopause.

Keywords: horizontal shear; ionospheric wind; lower thermosphere; geomagnetic storm; sporadic *E*-layer; turbulence

Introduction

Studies of turbulence in gases have shown that a laminar flow becomes turbulent, if the stabilizing influence of the vertical temperature gradient is smaller than the destabilizing effect due to the vertical shear of the horizontal wind component. The state of motion can most suitably be characterized by the ratio of the Vaisala–Brunt frequency and the vertical wind shear squared. This ratio is called the gradient Richardson number. Thus, turbulence develops, if the gradient Richardson number is less than one. Investigations carried out in the free atmosphere have indicated that turbulence sets in, if this number is <0.25 [1]. In earlier papers [2, 3] it has been emphasized that from the quantities, which can be deduced from the vertical sounding of the ionosphere, the sporadic *E* parameters may directly be connected with the dynamical conditions of the upper atmosphere. On the basis of the wind-shear theory of mid-latitude sporadic *E* the vertical shear of the horizontal wind component [4] and thus, one of the quantities determining turbulence can be computed. This is a

[1] H-9401 Sopron, P.O. Box 5, Hungary

possibility, of which we should make use realizing that the state of flow is more sensitive to the change of wind shear than to that of the vertical temperature gradient (we should remember that in the formula of the gradient Richardson number the square of wind shear, but only the first power of the vertical potential temperature gradient, determining the Vaisala–Brunt frequency appears). Thus, reasonable values of the gradient Richardson number may be obtained by calculating the vertical potential temperature gradient from models of the upper atmosphere (e.g. CIRA 1972 [5]) and computing the vertical wind shear on the basis of measured ionospheric sporadic E parameters. Then, following Zimmermann and Murphy [6], the turbulent intensity and vertical diffusivity can be determined.

Calculation of turbulent parameters

As it has been explained above, such formulas are needed for the determination of turbulent parameters from ionospheric data, which relate the former quantities to the wind shear. Such an expression is that of the gradient Richardson number R_i

$$R_i = \frac{g}{\Theta} \frac{\dfrac{\partial \Theta}{\partial z}}{\left(\dfrac{\partial u}{\partial z}\right)^2}$$

where $g\,(\mathrm{ms}^{-2})$ is the gravitational acceleration, Θ (K) and $\partial\Theta/\partial z\,(\mathrm{Km}^{-1})$ are the potential temperature, respectively its vertical gradient and $\partial u/\partial z\,(\mathrm{s}^{-1})$ is the vertical shear of the horizontal wind component. The vertical shear of the horizontal wind component was computed from the parameters of ionospheric sporadic E assuming the validity of mid-latitude wind shear theory [4]. For the determination of the neutral wind shear first the calculation of the ion-convergence is necessary. Assuming that the effective recombination coefficient inside of the layer is equal to that outside of it, the ion-convergence has been computed by means of the equation

$$\frac{\mathrm{d}v_{iz}}{\mathrm{d}z} = -\alpha' N_m \left(\frac{N_0^2}{N_m^2} - 1\right)$$

where v_{iz} is the vertical component of the ion drift velocity in ms^{-1}, α' is the effective recombination coefficient in $\mathrm{m}^3\mathrm{s}^{-1}$, N_m and N_0 are the maximum electron density of the sporadic E layer, respectively the background electron density in m^{-3}. The maximum electron density of the Es layer was calculated from the measured blanketing frequency of the layer, $fbEs$. In order to determine the background electron density as accurately as possible, model ionospheres [7] were used for its computation taking the measured critical frequency of the E layer, foE and the virtual height of the Es layer, $h'Es$. It has been supposed that the actual height of the Es layer does not differ significantly from that given by $h'Es$, if h type Es layers are excluded from the investigation. Thus, neglecting the contribution of the $N-S$ wind component, an effective wind shear could be calculated on the basis of the relation

$$\left(\frac{\mathrm{d}u}{\mathrm{d}z}\right)_{\mathrm{eff}}=-\frac{1+\left(\frac{\nu_{in}}{\omega_i}\right)^2}{\left(\frac{\nu_{in}}{\omega_i}\right)\cos I}\alpha' N_m\left(\frac{N_0^2}{N_m^2}-1\right).$$

Here $u(\mathrm{ms}^{-1})$ is the horizontal component of the neutral wind, $\nu_{in}\,(\mathrm{s}^{-1})$ and $\omega_i\,(\mathrm{s}^{-1})$ are the ion-neutral collision frequency, respectively the ion gyrofrequency, I being the magnetic dip angle.

The potential temperature was calculated according to the equation

$$\Theta=T\left(\frac{10^5}{p}\right)^{0.286},$$

where T is absolute temperature in K, p is pressure in Nm^{-2}. T and p were determined on the basis of formulas used for the deduction of atmospheric models taking into account the level of solar activity by the solar radio flux $F_{10.7}$ and the geomagnetic activity with the three hourly planetary geomagnetic index K_p [5]. The potential temperature was computed for heights corresponding to $h'Es$, as well as greater, respectively less by 1 km than $h'Es$. The difference between the potential temperature corresponding to an altitude greater by 1 km than $h'Es$ and that obtained for $h'Es$, as well as the difference between the latter value and the potential temperature corresponding to an altitude less by 1 km, than $h'Es$ were calculated. The average of the differences has been adopted as the vertical gradient of the potential temperature.

The gravitational acceleration was computed for the height z given by $h'Es$ by means of the formula

$$g=g_0\left(1+\frac{z}{R_E}\right)^{-2}$$

where $g_0=9.80665\ \mathrm{ms}^{-2}$, $R_E=6.356766\cdot 10^6$ m.

On the basis of the above calculations the gradient Richardson number can be determined. Then, the relation

$$w=(-0.15\sqrt{R_i}+0.08)u$$

based on the studies of Deacon [8], Lumley and Panofsky [9] has been used for the computation of the amplitude of the vertical turbulent wind $w\,(\mathrm{ms}^{-1})$ [6]. For the determination of the horizontal wind, which has been supposed to be equal to the W – E component, the thermal wind equation

$$u=-\frac{gz}{fT}\frac{\partial T}{\partial y}$$

was applied, where $f=2\Omega \sin \varphi\,(s^{-1})$ is the Coriolis parameter, Ω being the angular velocity of the Earth's rotation and φ the geographical latitude. Namely, we think that calculating the horizontal wind by means of the thermal wind equation more reliable data can be deduced than those, which were measured at a different time and far from the geographical location in question. The meridional gradient of the temperature $\frac{\partial T}{\partial y}$ was determined on the basis of atmospheric models [5] by calculating the temperature for the point of observation and for places located 1 km to the north, as well as 1 km to the south of the point of observation. Taking the difference between the temperature corresponding to the point located 1 km to the north of the station and that obtained for the station, as well as the difference between the latter value and the temperature corresponding to the point located 1 km to the south of the station, the average of these differences was considered as the meridional gradient of the temperature.

Thus, the amplitude of the vertical turbulent wind and the turbulent intensity $\langle w^2 \rangle$ could be calculated. Following [6] it has been assummed that the vertical turbulent spectrum is inertial and limited to a transition wavenumber towards the buoyant subrange. Thus, the vertical turbulent diffusivity K can be determined by means of the equation

$$K=\frac{\langle w^2\rangle \Theta^{1/2}}{\left(g\frac{\partial \Theta}{\partial z}\right)^{1/2}}.$$

Data and analysis

For the investigation of the turbulence in the lower thermosphere during geomagnetic storms the events reviewed by Prölss [10] on the basis of satellite measurements were selected. Thus, the results could be controlled by comparing the conclusions, which have been drawn from the results, with the indications of the satellite measurements.

The turbulent diffusivity was computed using the above method for the period of twelve geomagnetic disturbances of the year 1973. The computations were performed with the data of the ionospheric stations Békéscsaba, Hungary (46°40′N, 21°10′E) and Juliusruh, GDR (54°38′N, 13°23′E) [11, 12]. We determined the vertical turbulent diffusivity for the day-time hours from 08 to 15 hours LT and the average of these day-time values has been calculated for intervals lasting from three days before to ten days after the start of the geomagnetic storm. The number of diffusivity values, on the basis of which the daily means were calculated, varied between one and eight depending on the availability of ionospheric sporadic E observations. The scattering of the values amounts to the absolute value of the corresponding mean. From the twelve events four cases representing the different seasons are selected and presented here.

In Fig. 1 the variations of the average vertical turbulent diffusivity are shown from three days before to ten days after the geomagnetic disturbance of 20.01. 1973 determined for Békéscsaba and Juliusruh. The diffusivity shows a sharp decrease at both places after the onset of the geomagnetic disturbance, which lasts in Juliusruh more or less continuously till the +9th day. In Békéscsaba the decrease at the beginning of the geomagnetic disturbance is followed by an increase about day +4 and after that a depression appears again. The rise of the diffusivity around day +4 is also indicated by the data of Juliusruh. Thus, it can be pointed out that diffusivity shows at the two places concurrent variations, which consist of a double depression. In the upper part of the figure averages of the three hourly planetary geomagnetic index K_p are also plotted. These were calculated from the three K_p values, referring to the period beginning 6, 7 hours before the interval, for which the turbulent diffusivity has been determined, that is daily from 0 to 9 hours. Thus, the time lag of the atmospheric effect behind the geomagnetic disturbance is also taken into consideration. It might be assumed that the lasting depression of the diffusivity is due also to the increasing level of geomagnetic activity after the geomagnetic disturbance.

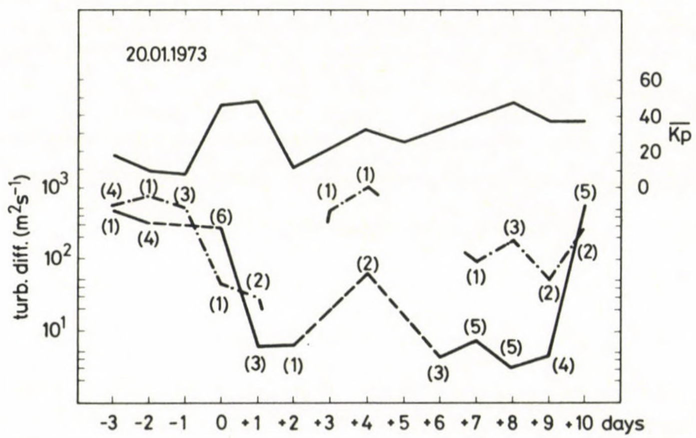

Fig. 1. Variation of the average vertical turbulent diffusivity deduced from ionospheric sporadic E parameters of the stations Békéscsaba (dash- and dot line) and Juliusruh (full line) during the geomagnetic disturbance of January 20, 1973 (below), as well as variation of the three hourly planetary geomagnetic indices averaged daily for the interval 8–15 hours LT (above). Numbers in brackets indicate the number of data used for the calculation of the averages

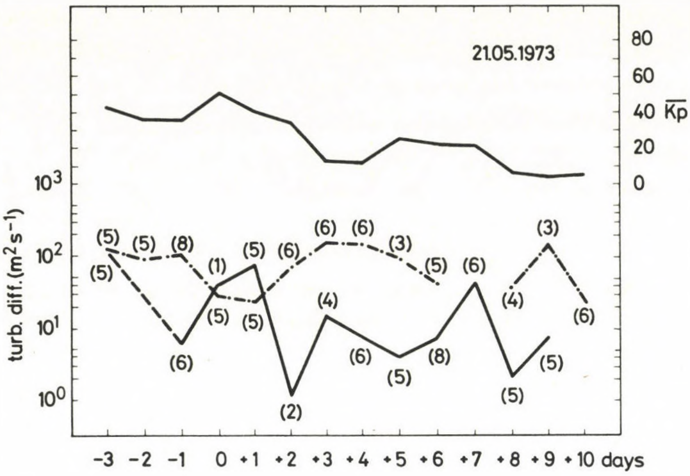

Fig. 2. Variation of the average vertical turbulent diffusivity deduced from ionospheric sporadic *E* parameters of the stations Békéscsaba (dash- and dot line) and Juliusruh (full line) during the geomagnetic disturbance of May 21, 1973 (below), as well as variation of the three hourly planetary geomagnetic indices averaged daily for the interval 8–15 hours LT (above). Numbers in brackets indicate the number of data used for the calculation of the averages

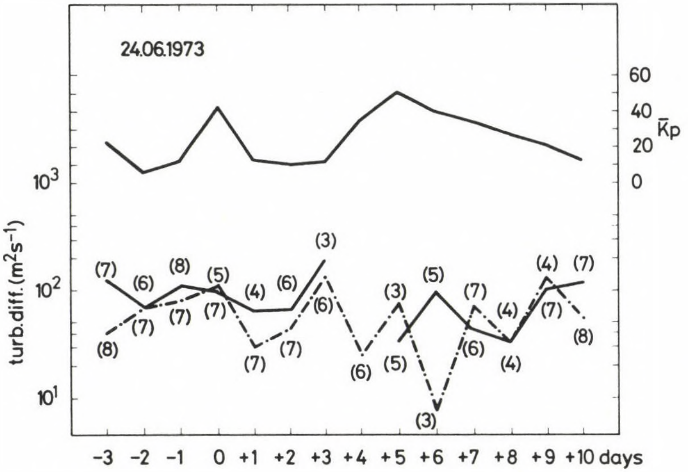

Fig. 3. Variation of the average vertical turbulent diffusivity deduced from ionospheric sporadic *E* parameters of the stations Békéscsaba (dash- and dot line) and Juliusruh (full line) during the geomagnetic disturbance of June 24, 1973 (below), as well as variation of the three hourly planetary geomagnetic indices averaged daily for the interval 8–15 hours LT (above). Numbers in brackets indicate the number of data used for the calculation of the averages

In Fig. 2 the variations of the average vertical turbulent diffusivity determined for Békéscsaba and Juliusruh from three days before to ten days after the geomagnetic disturbance of 21. 05. 1973 are shown. The variation in Juliusruh is rather a single minimum. In Békéscsaba the decrease of the diffusivity at the onset of the geomagnetic disturbance is followed by a second fall about day +7, though the lack of data of this day prevents the judgement of the situation. Thus, the variations at the two places are fairly different. In the upper part of the figure averages of the three hourly planetary geomagnetic index K_p, calculated as described above, are plotted. It can be seen that in this case the geomagnetic disturbance is of fairly small amplitude, which is followed by a second smaller increase on day +5 and appears in a period of steadily declining geomagnetic activity.

The variations of the average vertical turbulent diffusivity after the geomagnetic disturbance of 24. 06. 1973 can be regarded again as a double depression, the first following immediately the onset of the geomagnetic disturbance and the second centered in Békéscsaba on day +6 (Fig. 3). The comparison of the data obtained for Békéscsaba and Juliusruh is hampered by the lack of data in Juliusruh for day +4. Nevertheless, it can be stated that the variation of diffusivity at the two places is similar, even if not as much as in other cases. In the upper part of Fig. 3 the daily averages of the three hourly planetary geomagnetic indices are plotted, which were determined in the same manner as described in connection with Fig. 1. In this case the second minimum of the diffusivity may also be related to the increase of geomagnetic activity on the days +4 and +5.

In Fig. 4 the variations of the average vertical turbulent diffusivity are shown from three days before to ten days after the geomagnetic disturbance of 28. 10. 1973 determined for Békéscsaba and Juliusruh. The shape of the temporal change can hardly be established at both stations due to lack of data. Nevertheless the variation of the diffusivity in Juliusruh suggests a double depression, the first occurring during the increase of geomagnetic activity and the second in the post storm period. The data of Békéscsaba do not contribute to the clearing of the situation because of the fluctuating character of the variation. In the upper part of Fig. 4 the daily averages of the three hourly planetary geomagnetic indices are given. In this case the geomagnetic activity displays a single increase, which lasts four days. After the decline of the event the geomagnetic activity reaches a nearly constant level.

Discussion

The four events, presented in this paper, show in individual cases that in agreement with former investigations [13] the vertical turbulent diffusivity decreases after geomagnetic disturbances. The decrease is larger in winter (20. 01. 1973) than in the other seasons. The variation of the vertical turbulent diffusivity after geomagnetic

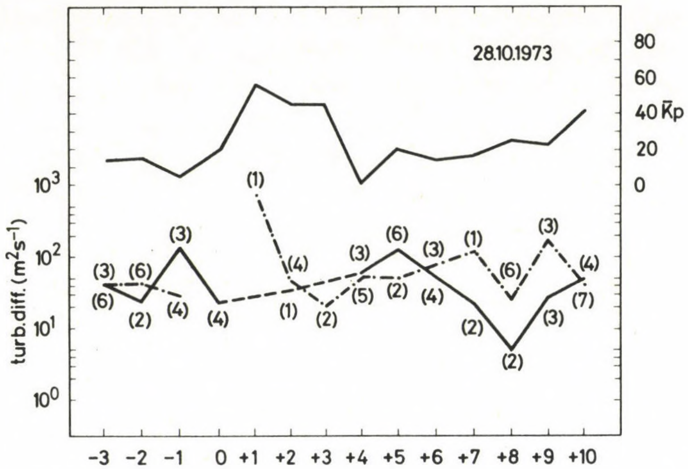

Fig. 4. Variation of the average vertical turbulent diffusivity deduced from ionospheric sporadic *E* parameters of the stations Békéscsaba (dash- and dot line) and Juliusruh (full line) during the geomagnetic disturbance of October 28, 1973 (below), as well as variation of the three hourly planetary geomagnetic indices averaged daily for the interval 8–15 hours LT (above). Numbers in brackets indicate the number of data used for the calculation of the averages

disturbances consists of a double depression, the first of which starts after the beginning of the geomagnetic disturbance, while the second occurs after the decline of the geomagnetic activity during the period of the after effect (20. 01. 1973, 28. 10. 1973). In two cases this cannot be proved, since the double shape of the variation may be attributed to the subsequent increase of the geomagnetic activity (21. 05. 1973, 24. 06. 1973).

It is known that the turbopause is defined as the height, where molecular diffusivity increasing with altitude becomes equal to turbulent diffusivity. Since molecular diffusivity shows only slight changes, the variation of the turbopause is mainly determined by the changes of turbulent diffusivity. It should be noted that the mean values of the vertical turbulent diffusivity are related here generally to heights higher than about 110 km, as the number of data referring to altitudes less than 110 km is less, than that of the data computed for greater heights. This is in agreement with the result of model calculations [14], according to which during geomagnetic storms the turbulent diffusivity decreases above about 110 km and increases below that height.

This would mean that on the basis of the investigation of individual cases after geomagnetic disturbances an increase of the height of the turbopause may be expected. However, rising of the turbopause results in the increase of concentration of the molecular gases, which agrees with the results of satellite measurements. Thus, the method used here enables by the use of ionospheric sporadic *E* parameters the determination of change of the turbopause height in accordance with the indications of satellite measurements.

References

1. Roper R G: Turbulence in the lower thermosphere. In: *The Upper Atmosphere and Magnetosphere*. National Academy of Sciences, Washington, D.C. 1977.
2. Bencze P: Height variation of wind shear deduced from ionospheric sporadic *E* during stratospheric warmings. *Acta Geod. Geoph. Mont. Hung.*, 15 (1980), 247–256.
3. Bencze P—Märcz F: A study of the variation of ionospheric absorption and wind induced ion-convergence after geomagnetic disturbances. *Acta Geod. Geoph. Mont. Hung.*, 16 (1981), 405–414.
4. Reddy C A—Matsushita S: The variations of neutral wind shears in the *E*-region as deduced from blanketing *Es*. *J. atmosph. terr. Phys.*, 30 (1968), 747–762.
5. Cira 1972, Cospar International Reference Atmosphere. Akademie Verlag, Berlin, 1972.
6. Zimmermann S P—Murphy E A: Stratospheric and mesospheric turbulence. In: *Dynamical and Chemical Coupling Between the Neutral and Ionized Atmosphere* (eds B Grandal and J A Holtet). D Reidel Publ. Co., Dordrecht–Holland, 1977.
7. Rawer K—Rama Krishnan S: Tentative Tables of Electron Density and Excess Electron Temperature for Temperate Latitude. Arbeitsgruppe f. Physik. Weltraumforschung, Freiburg, 1972.
8. Deacon E L: The problem of atmospheric diffusion. *Intern. J. Air. Pollution* 2 (1959), 92.
9. Lumley J L—Panofsky H A: The Structure of Atmospheric Turbulence. Interscience Publishers, New York, 1964.
10. Prölss G W: Magnetic storm associated perturbations of the upper atmosphere: Recent results obtained by satellite-born gas analyzers. *Rev. Geophys. Space Phys.*, 18 (1980), 183–202.
11. HHI Geophysical Data, 1973, Akademie der Wissenschaften der DDR, Zentralinstitut für solar-terrestrische Physik (HHI), Berlin.
12. Ionospheric Data Békéscsaba, Hungary, 1973. Central Institute of Meteorology, Budapest.
13. Bencze P: Turbulence at the top of the middle atmosphere deduced from ionospheric sporadic *E*. (manuscript).
14. Sinha A K—Chandra S: Seasonal and magnetic storm related changes in the thermosphere induced by eddy mixing. *J. atmosph. terr. Phys.*, 36 (1974), 2055–2066.

Acta Geodaet., Geophys. et Montanist. Hung. Volume 18 (1—2), pp. 119—128 (1983)

FAULTS AND EARTHQUAKES IN HUNGARIAN TERRITORY EAST OF THE RIVER TISZA

T Zsiros[1]

Geodetic and Geophysical Research Institute of the Hungarian Academy of Sciences Department of Seismology, Budapest

[Manuscript received March 12, 1982]

The seismic activity of the territory east of the river Tisza is presented in the paper. An attempt was made to compare the earthquake data with faults traced by seismic surveys and geodetical and gravitational observations.

Keywords: gravimetric map: isostatic anomalies; Pannonian Basin; recent crustal movement; seismicity; tectonics

Introduction

In Hungary, 320 earthquakes have occurred since 1860 not counting fore- and aftershocks.

The focal depths based on macroseismic observations are determined for 100 events, mainly by Csomor and Kiss (1962). The depths vary between 1 and 21 km and their distribution with depth shows a maximum (40 per cent of the total number of the shocks) between 4 and 7 km (Fig. 1).

Therefore, it seems to be interesting to compare the data of earthquakes to the map of faults exhibited by seismic surveys. By the help of the reflection seismic method, the faults — surpassing some minimum vertical offset — can be traced. The map of these faults may help to construct a new seismic hazard map of Hungary. For this aim we collected the data of faults in the territory east of the river Tisza, where the seismic oil and gas exploration has been going on for more than 20 years. About 70 per cent of this territory has been investigated by seismic surveys in detail.

Faults

The Pre-Austrian basin floor shows big variety in depth in the territory investigated. (From about 1 km to more than 6 km.) On the territory east of the river Tisza, there are Miocene-Quarternary sediments above the Pre-Austrian basin floor. The thickness of these sediments accumulated during the past 20 million years is more

[1] Seismological Observatory of GGRI of Hungarian Academy of Sciences. H-1112 Budapest, Meredek u. 18.

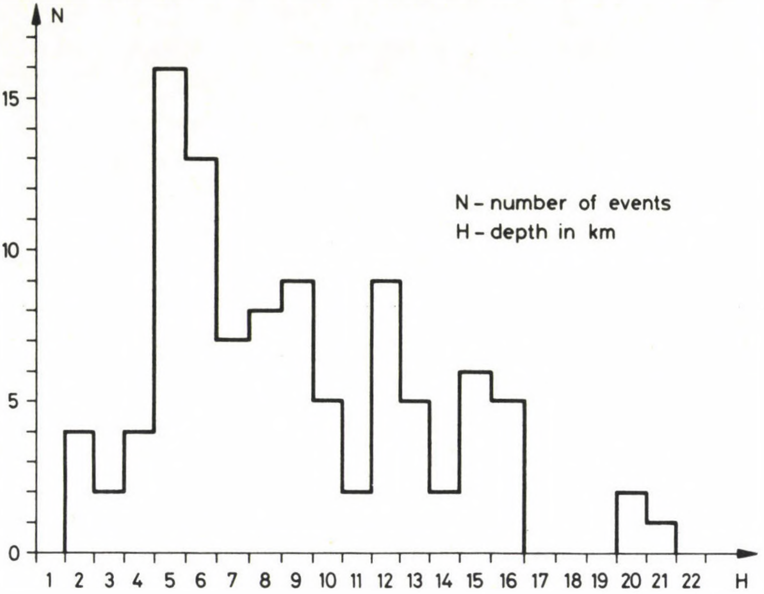

Fig. 1. Distribution of focal depths in Hungary

than 7 km at several places. This is a very short time span in geology so the tectonic evolution of the territory was characterized by very fast subsidences. (Mainly depressions were formed.) (Pogácsás 1980). Figure 2 shows the faults revealed by seismic surveys. The total length of the known faults is nearly 600 km. The large part of them (about 90 per cent of the total length) belongs to the crystalline basement which consists of Paleozoic or older rocks. The younger (Mezozoic or Cenozoic) rocks are influenced only by 10 per cent of the faults (Fig. 2). The youngest fault is determined near Derecske. It spreads from the crystalline basin at about 5 km depth into the upper Pannonian sediments at a depth of about 1.5 km.

In several cases the vertical extent of the faults is very small, only about 50–100 m which can hardly be determined at depths of 4 or 5 km. However, in a few cases the vertical size surpasses 0.5 km or even 1 km (Fig. 2). Allowing for denudation and compaction, the actual values must have been even larger.

Earthquakes

In seismological respect the territory east of the river Tisza shows the smallest seismicity in comparison with the other geographical parts of Hungary (Fig. 3). Between 1860 and 1981 only 28 earthquakes occurred in this territory compared to 320 events in the whole country. If we count every earthquake known in time, the total

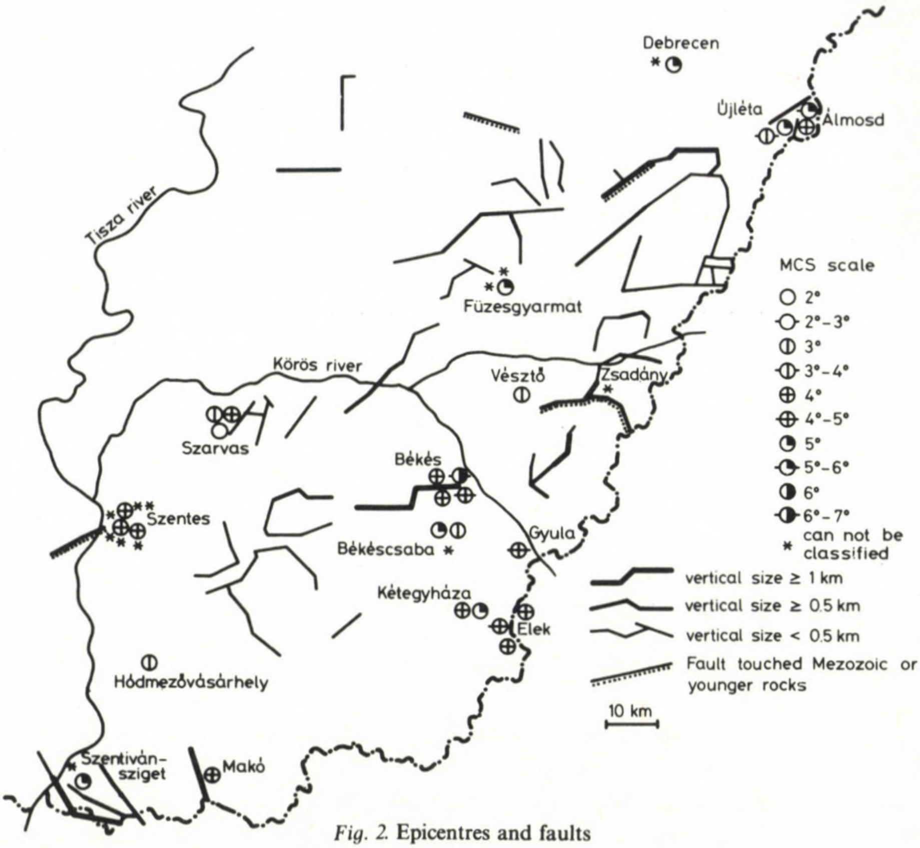

Fig. 2. Epicentres and faults

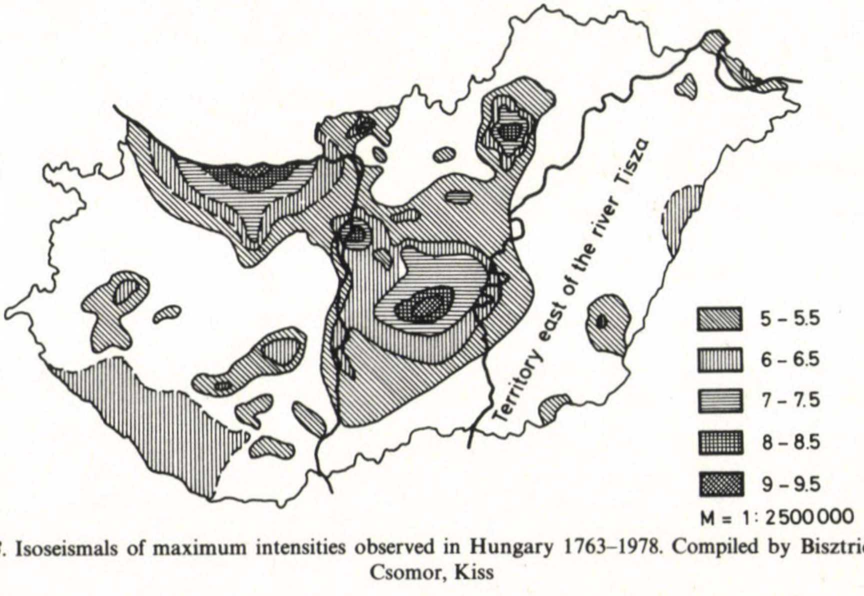

Fig. 3. Isoseismals of maximum intensities observed in Hungary 1763–1978. Compiled by Bisztricsány, Csomor, Kiss

Table I

	Date		Location (Epicenter)	I_0		″(km)
1.		1444	Szeged	?		
2.	March	1631	Debrecen	5°	3.7^+	
3.	Sep. 8	1746	Szentes	?		
4.	Feb. 20	1763	Szentes	?		
5.	Aug. 21	1772	Szentes	?		
6.		1789	Füzesgyarmat	?		
7.	June 8	1794	Szentes	?		
8.	Sep. 6	1794	Szentes	?		
9.	March 3	1795	Debrecen	?		
10.		1819	Füzesgyarmat	?		
11.	June 11	1823	Füzesgyarmat	5°	3.7^+	
12.	Feb. 15	1852	Békéscsaba	5°	3.7^+	
13.	March 16	1866	Békéscsaba	?		
14.	March 28	1869	Kétegyháza	5°	3.7^+	
15.	Feb. 2	1870	Zsadány	?		
16.	Dec. 1	1871	Hódmezővásárhely	3°	2.5^+	
17.	March 3	1878	Makó	4°	3.1^+	
18.	Aug. 31	1879	Szentivánsziget	5°	3	4
19.	Oct. 28	1881	Szarvas	4°	3.1^+	
20.	Oct. 28	1881	Szentes	4°	3.1^+	
21.	July 7	1891	Elek	4.5°	3.7	13
22.	May 7	1899	Szentes	4°	2.9	7
23.	Oct. 26	1903	Vésztő	3°	2.5	
24.	Feb. 8	1905	Elek	4°	3.1^+	
25.	Sep. 4	1905	Szentes	4°	3.1^+	
26.	Jan. 28	1917	Gyula	4.5°	3.4	
27.	May 10	1927	Békéscsaba	3°	2.5^+	
28.	Jan. 28	1929	Szarvas	2°	1.9^+	
29.	Oct. 31	1931	Szarvas	3°	2.5^+	
30.	June 26	1933	Kétegyháza	4°	2.9	7
31.	Aug. 6	1935	Békés	4°	3.1	9.5
32	March 23	1939	Álmosd	5.5°	4.7	21.5
33.	Nov. 1	1939	Elek	4°	3.1^+	
34.	Feb. 5	1940	Álmosd	4°	2.6	5
35.	Dec. 8	1940	Újléta-Vértesléta	5°	3.4	6
36.	May 16	1941	Hajdúnánás	3°	2.5^+	
37.	March 27	1957	Újléta-Vértesléta	3.5°	2.8^+	
38.	June 22	1978	Békés	6.5°	4.5^{++}	20
39.	Oct. 30	1979	Békés	4.5°	3.0^{++}	5
40.	March 15	1980	Békés	4°	2.5^{++}	7

$^+$ Calculated with the average focal depth ($H = 9$ km) using $M = 0.6\, I_0 + 1.8 \log h - 1.0$ (Gutenberg-Richter 1942)

$^{++}$ Determined by instrumental data.

number of shocks is 40 in this part of Hungary. Figure 2 shows their areal distributions. In detail, the following events are known (Table I). It can be seen that not only the frequency of the events is small but the magnitudes of the shocks as well. Two shocks, $I_0=6°–7°$ at Békés and $I_0=5°–6°$ at Álmosd, are relatively important. The annual frequency of occurrence vs. epicentral intensity determined by the help of the least squares method for the whole territory of Hungary is:

$$\log N = 1.43 - 0.37\, I_0 \qquad (S_{(\log N)} = 0.6)$$

it means $$\log N = 3.17 - 0.75\, M$$

using $M = 0.49\, I_0 + 1.74$ (Bisztricsány 1974)

where N— number of earthquakes per year
I_0— epicentral intensity
M— magnitude
S— standard deviation.

This relationship is based on events of epicentral intensities equal or larger than 4° occurred since 1860. It includes 186 shocks altogether.

For the territory east of the river Tisza a similar relationship is of no use because of the very small number of events (16 shocks altogether).

The seismic activity is often characterized by a strain release curve. It is calculated for this territory using 5-year intervals. The result is shown in Fig. 4 and is characterized by relative gaps in the seismic activity between 1910–1930 and 1954–1975.

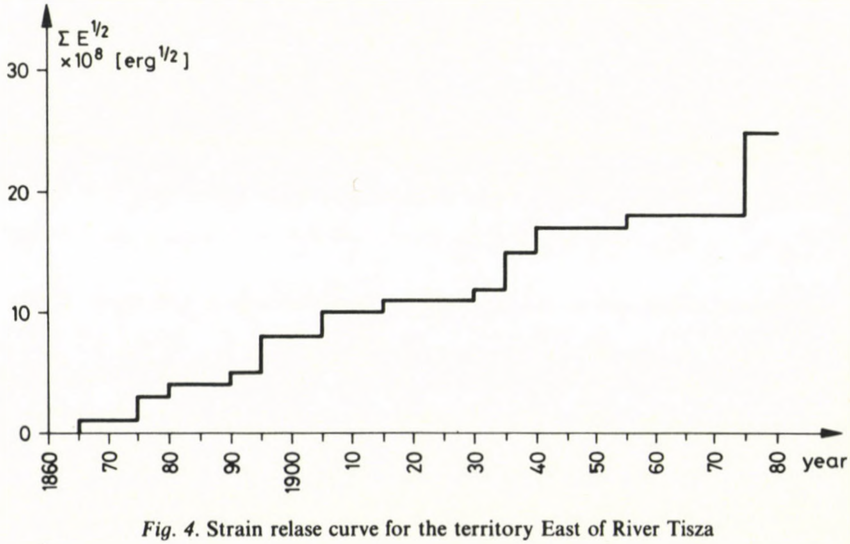

Fig. 4. Strain relase curve for the territory East of River Tisza

Conclusions

The distributions of the epicenters and the faults can be seen in Fig. 2. There are no earthquakes at many faults, but most of the epicenters are at faults. The connections could be clearer if the focal depths were exactly known. However, only 11 focal depths could have been estimated by the help of isoseismal maps. Figure 5 shows some really shallow focal depths such as 4.5 and 6 km but there are deeper ones, too. The 20 km focal depth at Békés and at Álmosd belongs to the deepest ones in Hungary.

In connection with the faults and the earthquakes we examined the geodetical observations and the isostatic anomalies in this territory (Joó 1980, Renner 1959).

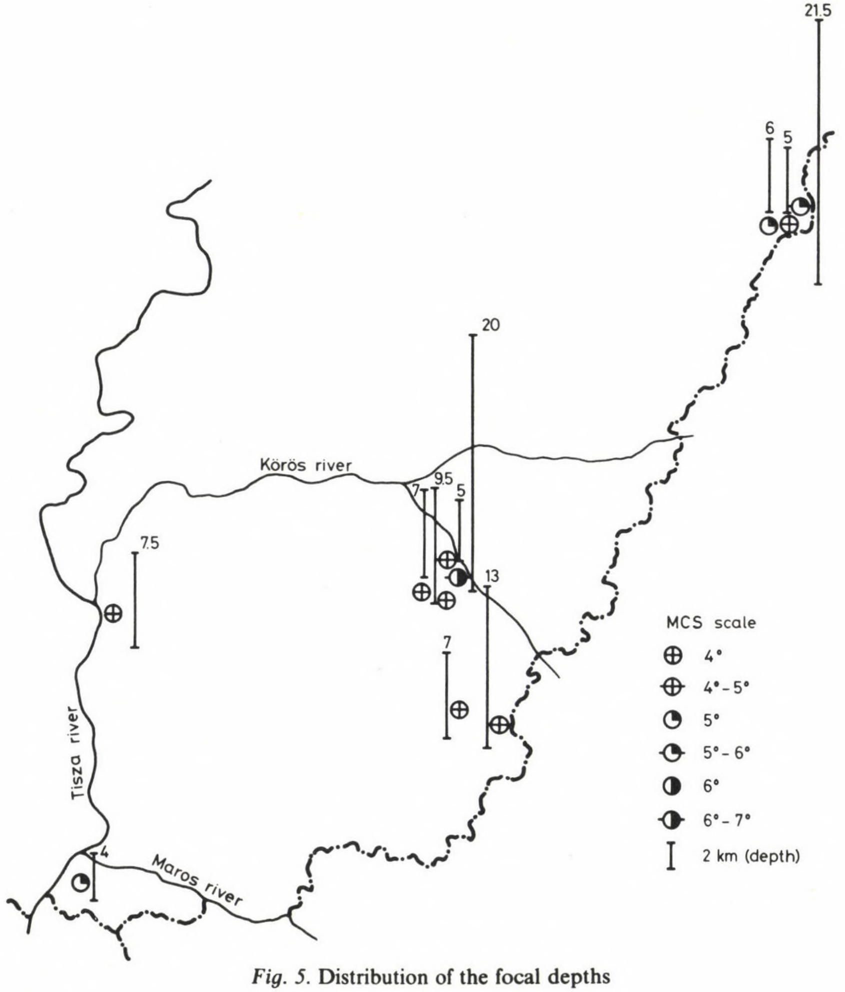

Fig. 5. Distribution of the focal depths

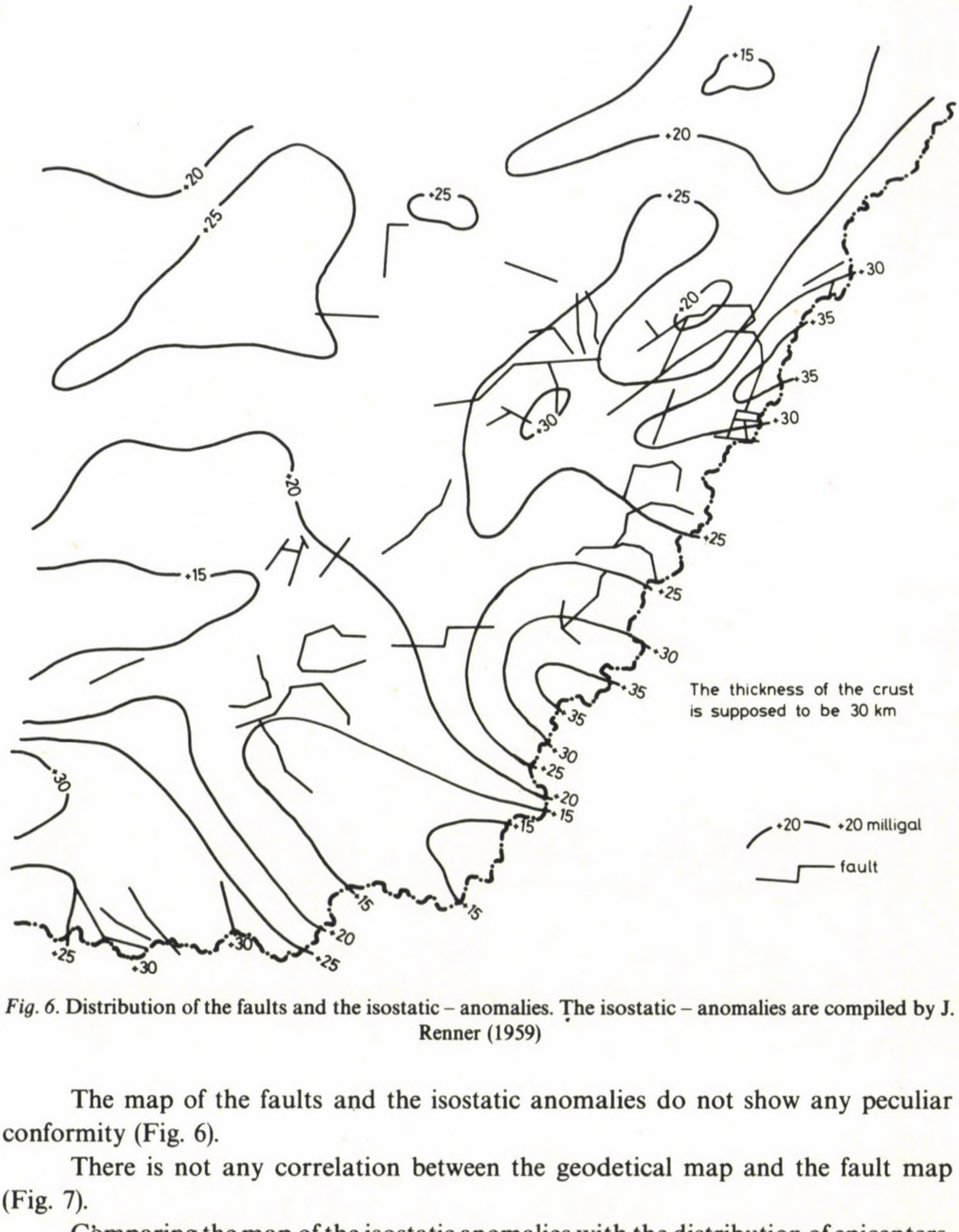

Fig. 6. Distribution of the faults and the isostatic – anomalies. The isostatic – anomalies are compiled by J. Renner (1959)

The map of the faults and the isostatic anomalies do not show any peculiar conformity (Fig. 6).

There is not any correlation between the geodetical map and the fault map (Fig. 7).

Comparing the map of the isostatic anomalies with the distribution of epicenters, it seems that the epicenters have a better fit with isostatic anomalies than the faults, especially in the southern part of the territory (Fig. 8). It is noticeable that this relatively subsiding territory is surrounded by epicenters of several earthquakes (Makó, Hódmezővásárhely, Szentes, Szarvas, Békés, Békéscsaba, Gyula, Kétegyháza, Elek) (Fig. 9).

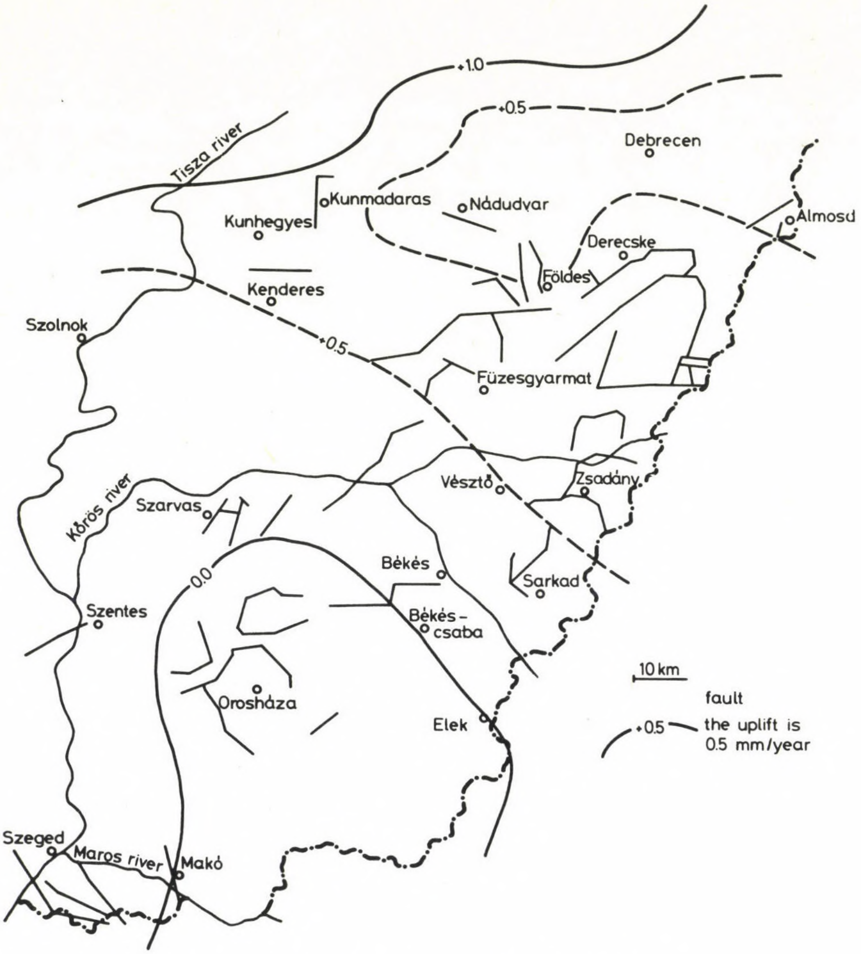

Fig. 7. Faults and the vertical crustal movements

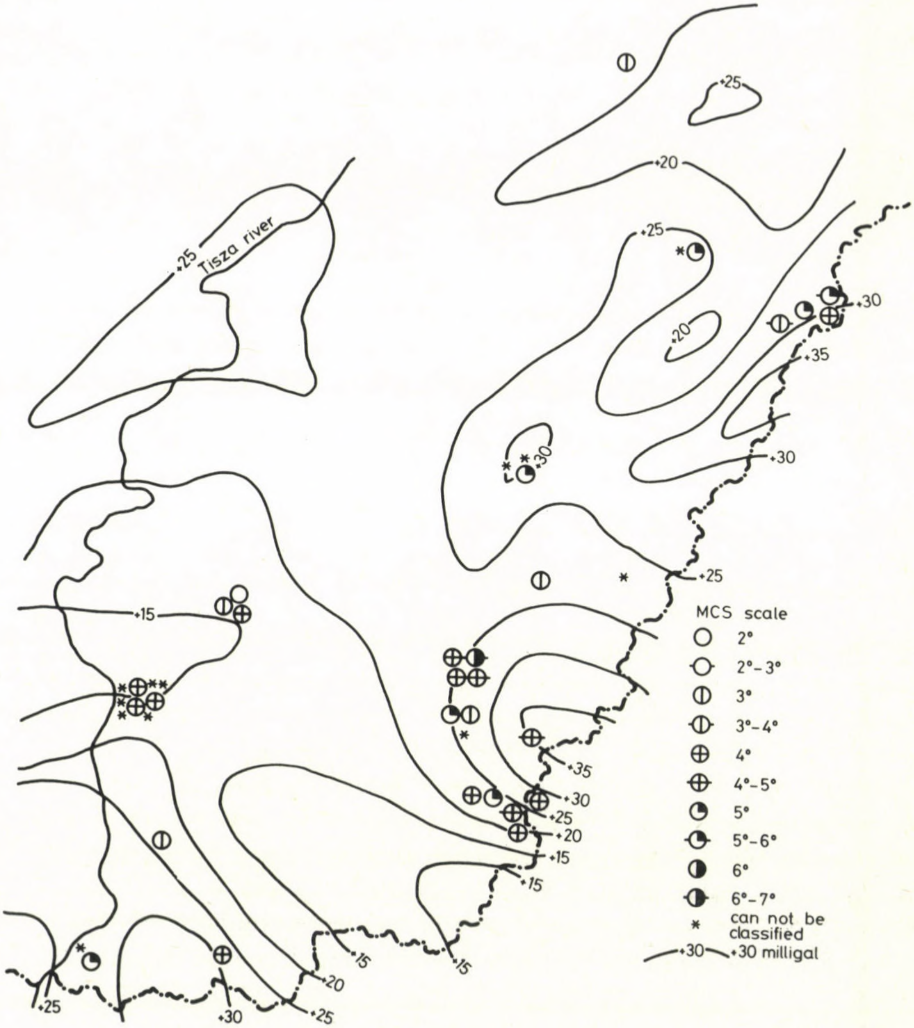

Fig. 8. Distribution of the epicentres and the isostatic – anomalies

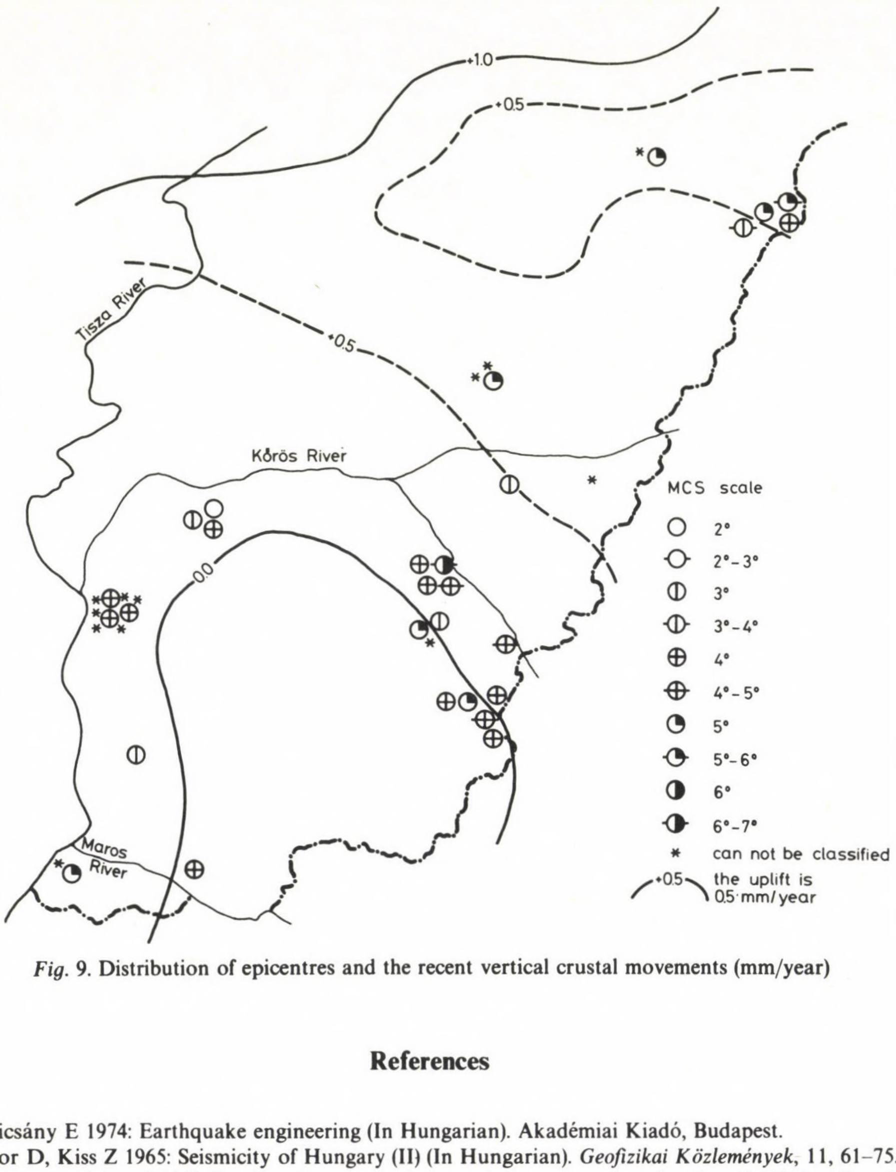

Fig. 9. Distribution of epicentres and the recent vertical crustal movements (mm/year)

References

Bisztricsány E 1974: Earthquake engineering (In Hungarian). Akadémiai Kiadó, Budapest.

Csomor D, Kiss Z 1965: Seismicity of Hungary (II) (In Hungarian). *Geofizikai Közlemények*, 11, 61–75.

Gutenberg B, Richter C 1942: Earthquake magnitude, intensity, energy and acceleration. *Bull Seism. Soc. Am.* 32.

Joó I 1980: Recent vertical crustal movements in the Carpatho-Balkan Region. Seventh annual meeting of European Geophysical Society, Symposium on the recent crustal movements and associated seismicity, Budapest.

Pogácsás Gy 1980: Evaluation of Hungary's neogene depressions in the light of geophysical surface measurements (In Hungarian). *Földtani Közlöny*, 110, 485–497.

Renner J 1959: Final elaboration of the measurements of the national Hungarian network of gravity bases. *Geofizikai Közlemények*, 8, 105–119.

Reports of seismic surveys of Geophysical Exploration Company

Acta Geodaet., Geophys. et Montanist. Hung. Volume 18 (1—2), pp. 129—134 (1983)

THE ÉRMELLÉK EARTHQUAKE OF 1834

T ZSIROS[1]

Geodetic and Geophysical Research Institute of the Hungarian Academy of Sciences
Department of Seismology, Budapest

[Manuscript received March 12, 1982]

Macroseismic observations of the Érmellék earthquake of October 15, 1834 are discussed in the paper. The epicenter intensity of this earthquake reached 9° on MSK scale and it was even felt in Krakow and Lvov.

Keywords: earthquake; Érmellék earthquake; Pannonian Basin; seismicity

It is known that Hungary does not belong to countries of high seismicity since both the recurrence of the earthquakes and the energy released by them are small e.g. compared to Balkan countries in the neighbourhood. However, we know that some large earthquakes occurred in Hungary during the past centuries which certainly have considerable importance concerning the seismicity map of Europe.

One of them is the so-called Érmellék earthquake. It occurred about 40 km east of Debrecen (this territory now belongs to Rumania) between 7^h and 8^h a.m. local time on October 15, 1834.

The maximum intensities were felt at Piskolt (48.6 N, 22.2 E), Dengeleg (47.5 N, 22.4 E), Érendréd (47.5 N, 22.4 E), and Gálospetri (47.5 N, 22.2 E). (Geographic names are given according to the situation at the time of the earthquake; present names be found in Appendix A).

Some descriptions of this earthquake were published by Réthly "The Earthquakes of the Carpathian Basins (455–1918)". In order to classify the intensities induced by this shock at different places we thoroughly studied these descriptions. The epicentral intensity of Érmellék earthquake can be estimated to 9° on the MSK scale.

The territories of the various intensities have the following average radii: $R(I=9°)$ 7 km; $R(I=8°)$ 20 km; $R(I=7°)$ 78 km; $R(I=6°)$ 125 km. The felt area of the event was about 250 000 km^2. From these figures, using Kövesligethy's (1907) formula, a

$$\frac{1}{3}(I_k - I_{k+1}) = \log\frac{R_{k+1}^2 + h^2}{R_k^2 + h^2},$$

where I_k— intensity k

R_k— radius of intensity k (in km)

h— depth of the earthquake (in km)

[1] Seismological Observatory of GGRI of Hungarian Academy of Sciences. H-1112 Budapest, Meredek u. 18.

a focal depth of 30–35 km can be derived. The magnitude of the earthquake can be estimated to 7.0–7.1 using

$$M = 0.6\, I_0 + 1.8 \log h - 1.0$$

relationship of Gutenberg and Richter (1942),

where M magnitude of the earthquake
I_0 epicentral intensity
h depth of the earthquake (in km).

The main shock was followed by many aftershocks which lasted for over 3 years.

Considering the recent seismic activity of the Carpathian Basin the results ($I_0 = 9°$, $h = 30$–35 km) may seem to be overestimated but they are based on the original descriptions. We must note that the buildings, in the last century, were certainly less earthquake-resistant than they are today and this factor isn't taken into account in this paper.

Appendix A contains the locations where the earthquake of October 15, 1834 was felt, with the observations and the intensities estimated on the MSK scale.

Appendices B and C are the intensity maps of the main shock.

References

Gutenberg B, Richter C F 1942: Earthquake magnitude, intensity, energy and acceleration. *Bull. Seism. Soc. Am.*, 32.
Kövesligethy R 1907: Seismischer Stärkegrad und Intensität der Beben. *Gerlands Beitr. Z. Geophysik*, 13.
Réthly A 1952: The Earthquakes of the Carpathian Basins (455–1918). Budapest (in Hungarian)

Appendix A

1. Alsó-Szopor (Supurul de Ios) (47.5N; 22.8 E) 7°
   Several chimneys fell down and most of the houses cracked
2. Arad (Oradea) (46.2 N; 21.3 E) 5°
   Pictures knocked against the wall. Floors and walls cracked. Hanging objects swang considerably.
3. Asszonyvásár (Asonvasar) (47.4 N; 22.2 E) 7°–8°
   The earthquake was not as severe as at Gálospetri (26), Piskolt (64), Érendréd (18), Dengeleg (14), Iriny (34), Érkörtvélyes (20), Mezőpetri (48), and Szaniszló (72).
4. Bártfa (Bardejov) (49.3 N; 21.3 E) 4°
   The earthquake was felt by a few people.
5. Békéscsaba (46.7 N; 21.1 E) 7°
   Large and deep cracks in the walls of a new church.
6. Beregszász (Beregovo) (48.2 N; 22.6 E) 6°
   Some chimneys fell down. A small steeple bell rang.
7. Berkesz (48.1 N; 21.9 E) 6°
   The earthquake caused a lot of damage.

8. Bihardiószeg (Diosag) (48.3 N; 22.0 E) 7°–8°
See Asszonyvásár (3)
9. Budapest (47.5 N; 19.1 E) 4°
It was felt.
10. Bustyaháza (Bustino) (48.1 N; 23.4 E) 6°
Several chimneys fell down and most of the houses cracked.
11. Csanálos (Urziceni) (47.3 N; 22.1 E) 7°–8°
Water levels changed in wells.
12. Csokoly (Ciocaia) (47.3 N; 22.0 E) 7°–8°
See Asszonyvásár (3)
13. Debrecen (47.5 N; 21.6 E) 7°–8°
Many chimneys fell down. Walls cracked at many houses, including the church.
14. Dengeleg (Dindeleag) (47.5 N; 22.4 E) 9°
None of the houses remained intact. The shocks caused gaps in the walls of the churches and the houses. Most of the houses collapsed. Cracks and fissures occurred in the ground and the flat land was overflown of water. One of the fissures in the ground spread over 17 km with a vertical movement. (It is not clear whether the vertical movement happened during the shock or after it. The spread of the vertical displacement is not mentioned.)
15. Déva (Deva) (45.9 N; 22.9 E) 5°–6°
Hanging pictures and other objects knocked against the wall. The small steele bell rang.
16. Éradony (Adoni) (47.4 N; 22.2 E) 7°–8°
See Asszonyvásár (3)
17. Eger (47.9 N; 20.4 E) 6°
It was felt by most of the people. Church was damaged by the shake.
18. Érendréd (Andrid) (47.5 N; 22.4 E) 9°
Only the wooden houses remain intact. Stone walls collapsed. Cracks occurred in the ground. It was impossible for people to remain standing. Water from fissures welled up to 7–8 meter high and overflowed the land. However the water disappeared in two hours. Sand and mud remained on the ground. The church and most of the houses collapsed.
19. Érkeserű (Chesereu) (47.4 N; 22.1 E) 7°–8°
See Asszonyvásár (3)
20. Érkörtvélyes (Curtiuseni) (47.6 N; 22.2 E) 8°
The new and big church collapsed.
21. Eperjes (Presov) (49.0 N; 21.3 E) 4°–5°
The earthquake was felt by many people.
22. Értarcsa (Tarcea) (47.3 N; 22.2 E) 8°
Chimneys fell down. Parts of buildings lost their cohesion. Unloaded carts (wagons) were running in the yards.
23. Érvasad (Vasad) (47.5 N; 22.3 E) 8°
The new church collapsed.
24. Ferenczvölgye (48.0 N; 23.5 E) 6°
Several houses considerably demaged.
25. Füzesgyarmat (47.1 N; 21.2 E) 6°–7°
Bells rang.
26. Gálospetri (Galospetreu) (47.5 N; 22.2 E) 9°
Dry wells refilled. The church partly collapsed. A deep fissure and a lot of cracks occurred in the ground. The land was owerflown by water within a quarter of an hour. After an hour the water disappeared and mud or sand remained on many spots.
27. Gálszécs (Secovce) (48.7 N; 21.7 E) 6°–7°
The shocks caused large cracks in the walls of churches and towers.
28. Gebe (47.9 N; 22.2 E) 6°
Plaster fell down. Walls cracked at many places.
29. Gibárt (48.3 N; 21.2 E) 5°
It was felt by many people.

30. Gyula (46.6 N; 21.3 E) 6°
The earthquake caused cracks in some buildings. The shock was strong.
31. Homonna (Humenne) (48.9 N; 21.9 E) 4°
The earthquake was felt.
32. Huszt (Khust) (48.2 N; 23.3 E) 6°
Bells rang. The tower of the church cracked. Several chimneys fell down.
33. Igló (Spisska Nova Ves) (48.9 N; 20.6 E) 5°–6°
The cross of the church fell down. The small steeple bell rang.
34. Iriny (Irina) (47.6 N; 22.4 E) 8°–9°
Nearly every steeples fell down. The churches partly collapsed. Many houses became uninhabitable. Cracks occurred in the ground. The flat land was overflown of water.
35. Kabolapolyána (Kobilecka Poljana) (48.1 N; 24.1 E) 4°
It was felt.
36. Kaplony (Capleni) (47.7 N; 22.5 E) 7°
The church and the cloister became uninhabitable.
37. Karcag (47.3 N; 20.9 E) 5°–6°
The shock was strong.
38. Kassa (Kosice) (48.7 N; 21.3 E) 7°
Church walls got gaps. Nearly every house in the town cracked. Many people found it difficult to stand. Several chimneys fell down. The bells rang.
39. Kerlés (Chirales) (47.1 N; 24.3 E) 5°
Sleeping people were raised by the shake. Roofs of buildings cracked. Many people lost their balances.
40. Királymező (Corna) (48.3 N; 23.9 E) 3°–4°
The shock was slightly felt.
41. Kiskereki (Cherechiul mic) (47.4 N; 22.1 E) 7°–8°
See Asszonyvásár (3)
42. Kolozsvár (Cluj) (46.8 N; 23.6 E) 6°
Every furniture began to move in rooms. Plaster fell down. Several chimneys and arches collapsed. Some houses cracked.
43. Kőrösmező (Jasina) (48.3 N; 24.4 E) 4°
The earthquake was felt.
44. Krakow (50.0 N; 19.9 E) 3°
It was slightly felt.
45. Lvov (49.9 N; 24.0 E) 3°–4°
It was felt.
46. Máramarossziget (Sighet) (47.9 N; 23.9 E) 4°
It was felt.
47. Meczenzéf (Medzev) (48.7 N; 20.9 E) 4°
It was felt by a few people.
48. Mezőpetri (Petresti) (47.6 N; 22.4 E) 8°–9°
Nearly every house became uninhabitable. Only the wooden houses remained intact. The steeple of the church fell down. Stone walls were destroyed. Many cracks and fissures occurred in the ground. The land was overflown by water. It was impossible for people to remain standing.
49. Miskolc (48.1 N; 20.8 E) 7°
Most people were frightened. Separate parts of the buildings lost their cohesion.
50. Munkács (Mukachevo) (48.5 N; 22.7 E) 6°
Waves were formed on the Latorca River by the shake.
51. Nagybánya (Baia Mare) (47.7 N; 23.6 E) 6°
The walls of several houses were cracked.
52. Nagykágya (Cadea) (47.3 N; 22.1 E) 7°
The earthquake was felt by everybody. It caused considerable damage.
53. Nagykálló (47.9 N; 21.8 E) 7°
The shocks caused considerable cracks in walls and arches. The steeple bell rang. Several chimneys were damaged or totally destroyed.

54. Nagykároly (Carei) (47.7 N; 22.5 E) 7°–8°
Only a few chimneys remained intact in the town. (Altogether 234 chimneys fell down.) Many houses became uninhabitable. People were frightened and ran outdoors. Most of them spent the following nights in tents. The bigger buildings were greatly damaged.
55. Nagykáta (47.4 N; 19.7 E) 5°
The earthquake was felt by everybody.
56. Nagyrév (47.0 N; 20.2 E) 4°
It was felt.
57. Nagyszeben (Sibiu) (45.8 N; 24.2 E) 4°–5°
It was felt by many people.
58. Nagyvárad (Oradea) (47.1 N; 21.9 E) 6°–7°
The walls of the military barrack cracked considerably. Pictures on the wall began to move. Buildings trembled throughout. Many houses cracked. Coffee split from the cup. Parts of chimneys fell down.
59. Napkor (48.0 N; 21.9 E) 6°
Many chimneys fell down.
60. Nyírbéltek (47.7 N; 22.1 E) 7°–8°
The ground was cracked at more than 20 places.
61. Nyíregyháza (48.0 N; 21.7 E) 7°
Buildings trembled throughout. Most chimneys fell down. The strong arch of the Evangelical church and the walls of the Reformed church cracked.
62. Ottomány (Otoman) (47.4 N; 22.2 E) 7°–8°
See Asszonyvásár (3)
63. Palócz (Palovce) (48.6 N; 22.1 E) 5°
Windows cracked. Plaster fell to the ground. The small bell rang.
64. Piskolt (Piskolt) (48.6 N; 22.3 E) 9°
Cats ran to and fro in confusion and cried. People were in great panic. They spent the following nights in tents. All chimneys fell down. Most of the houses including the church collapsed. One part of a sank hill sank into a deeper position. Cracks and fissures occurred in the ground. The land was overflown by water and occasionally by mud.
65. Portelek (Portitu) (47.6 N; 22.4 E) 8°–9°
The damage was nearly the same as at Dengeleg (14)
66. Reszege (Resighea) (48.6 N; 22.3 E) 8°
Steeples fell down. The churches collapsed nearly completely. Many houses became uninhabitable. Cracks occurred in the ground. The land was overflown by water.
67. Rimaszombat (Sobota) (48.4 N; 20.0 E) 4°
The earthquake was felt.
68. Rónaszék (Costinui) (47.9 N; 24.0 E) 5°–6°
The church was damaged by the shake.
69. Sárospatak (48.3 N; 21.6 E) 7°
Several chimneys fell down. Standing objects on the table fell to the ground. Stone walls cracked or collapsed. Many buildings cracked.
70. Sátoraljaújhely (48.4 N; 21.7 E) 7°
A steeple bell rang. Stone walls cracked. Chimneys fell down. Many people found it difficult to stand. People were frightened and ran into the streets.
71. Sugatag (Ocna Sugatag) (48.8 N; 23.9 E) 4°
It was felt.
72. Szaniszló (Sanislau) (47.6 N; 22.3 E) 8°
The Catholic and the Orthodox churches collapsed. Many houses became uninhabitable. Cracks occurred in the ground. The land was overflown by water.
73. Szásznádas (Nadásul-Sasesc) (46.3 N; 24.8 E) 4°
It was felt by a few people.
74. Szatmárnémeti (Satu Mare) (47.8 N; 22.9 E) 6°–7°
The city hall and many private houses cracked.

75. Szeged (46.3 N; 20.2 E) 5°
Objects (in the room) rattled or were shifted.
76. Székelyhíd (Sacuieni) (47.4 N; 22.1 E) 7°–8°
See Asszonyvásár (3)
77. Szentes (46.7 N; 20.3 E) 4°
It was felt.
78. Szlatina (Solotvina) (48.0 N; 23.9 E)
It was felt in the mines, too.
79. Tállya (48.2 N; 21.2 E) 6°
Many chimneys cracked or fell down.
80. Tiszaujlak (Vilok) (48.1 N; 22.9 E) 3°–4°
The earthquake was slightly felt.
81. Torda (Turda) (46.6 N; 23.8 E) 4°
It was felt.
82. Ungvár (Uzhgorod) (48.6 N; 22.3 E) 6°
Buildings were cracked. The cross of the church fell down. Latorca River was turbid by the shake.
83. Visó (Visanl) (47.7 N; 24.4 E) 3°–4°
It was slightly felt.
84. Wieliczka (50.0 N; 20.0 E) 3°
It was slightly felt.

Appendix B

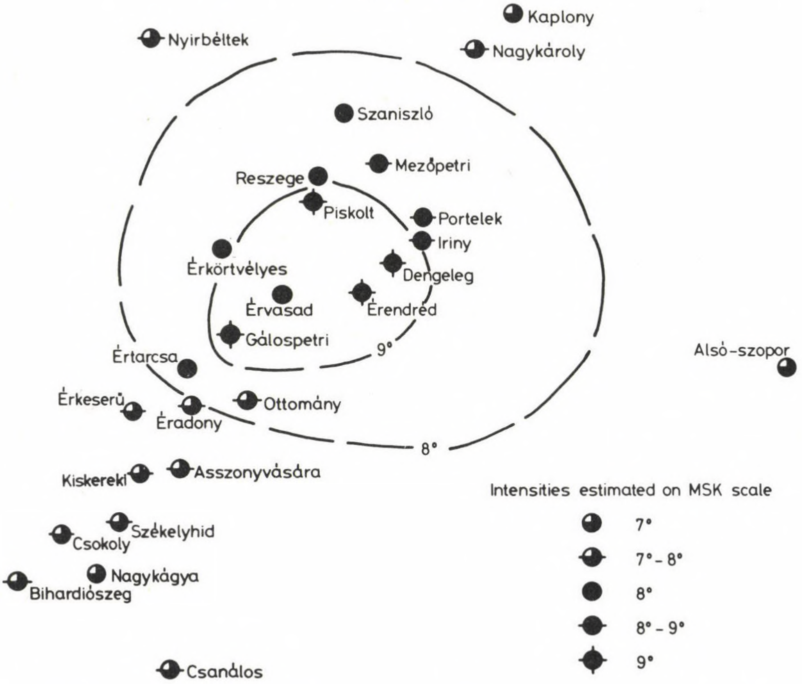

Felt intensities near the epicenter of the Érmellék earthquake of 1834, October 15
M = 1 : 600 000

Appendix C

DISTRIBUTION OF FELT INENSITY FOR THE ÉRMELLÉK EARTHUAQE OF OCTOBER 15, 1834

M = 1: 750000

(Compiled by Tibor Zsiros; Seismological Observatory, Budapest 1982)

Acta Geodaet., Geophys. et Montanist. Hung. Volume 18 (1—2), pp. 135—140 (1983)

LIMIT DISTRIBUTION OF THE MOST FREQUENT VALUES OF SAMPLES FROM SYMMETRICAL DISTRIBUTIONS

L CSERNYÁK[1]

College of Finance and Accountancy, Budapest

F STEINER[2]

Technical University for Heavy Industry, Miskolc

[Manuscript received March, 1982]

The most frequent value introduced by Steiner (1973) has for samples from symmetrical distributions with large number of elements, N, a Gaussian distribution whose scatter is the value $\varepsilon/\sqrt{N \cdot n(\varepsilon)}$ to be determined from the density function. Here ε denotes a scale factor, the so-called "reciprocal cohesion" or "dihesion" which is obtained simultaneously with the most frequent value, and $n(\varepsilon)$ is the number of data effectively taken into account, in relation to the total number of data. The estimation with the most frequent value can be used generally, without any premisses, as the ratio $\varepsilon/\sqrt{n(\varepsilon)}$ has for all probability distributions a finite value.

Keywords: cohesion; most frequent value; probability theory; symmetrical distribution

For sake of simplicity (without limiting the generality of the subsequent discussions) let us suppose that the symmetry point of the distribution characterized by its density function $f(x)$ is in the origin. For any positive $\bar{\varepsilon}$ we define the following quantity:

$$n(\bar{\varepsilon}) \equiv \int_{-\infty}^{\infty} \frac{\bar{\varepsilon}^2 \cdot f(x)}{\bar{\varepsilon}^2 + x^2} \, dx. \tag{1}$$

Let ε be the greatest of the maxima of the function

$$\bar{F}(\bar{\varepsilon}) = \frac{n^2(\bar{\varepsilon})}{\bar{\varepsilon}} \tag{2}$$

(see also Steiner 1973). At least one such a maximum does exist as shown by Csernyák (1983). The quantity ε is the reciprocal of another quantity κ which characterizes the cohesion of the majority of the data, therefore it can be called reciprocal cohesion or

[1] H-1149 Budapest, Buzogány u. 10–12.
[2] H-3515 Miskolc-Egyetemváros

dihesion; this quantity plays a similar role as the scatter, yielding a scale factor (the scatter, however, does not exist for a number of distributions).

A possible estimation of the symmetry point is if one determines *the most frequent value* of the sample (its definition both for discrete and continuous distributions is given by Steiner (1973)). An upper limit for the error of this estimation is also given by Steiner (1980) in $1.5\,\varepsilon/\sqrt{N\cdot n(\varepsilon)}$, where $n(\varepsilon)$ is the value of function (1) at the place ε; $n(\varepsilon)$ can be else considered as the ratio of the data number playing a role in the determination of the most frequent value to the total number of data. For the reality of this estimation Steiner (1980) published results of simple investigations using the Monte-Carlo method.

Monte-Carlo investigations are quite expensive in case of high N values, therefore only rather limited accuracies can be reached by this way. As it has been shown by Landy et al. (1982), however, in case of an U-distribution exact results can be obtained. The distribution of the occurrence frequencies of the most frequent values was shown there for the U-distribution to approximate a Gaussian distribution with a width *exactly* twice as wide as the distribution of the averages. The scatter for this distribution is exactly 1, that of $\varepsilon/\sqrt{n(\varepsilon)}$ is exactly 2. Thus the idea emerged that the most frequent values from samples with N elements from symmetrical distributions have a distribution with a scatter of $\varepsilon/\sqrt{N\cdot n(\varepsilon)}$. It is to be added that it has already been shown by Csernyák, Hajagos and Steiner (1981) that for increasing N-s the frequency curves approximate a Gaussian distribution.

In a next step, ε, $n(\varepsilon)$ and $\varepsilon/\sqrt{n(\varepsilon)}$ have been determined for distributions of very different types (see Table I). Distributions 1–8 are from Csernyák and Steiner (1982), 9–12 from Csernyák, Hajagos and Steiner (1981), 13–16 are often cited in the probability theory (Gaussian, uniform, Laplace- and U-distributions). The last two are special distributions: 17, where K_0 is a modified Bessel-function, has in the origin an infinite value of the probability, and distribution 18 has an infinite number of maximum places. All these distributions are given in its most simple form. A k-times stretching can be obtained by substituting x through x/k, and dividing the new $f(x)$ by k. By the stretching, ε gets also k-times greater, $n(\varepsilon)$ remains, however, unchanged:

$$n^{(k)}(\varepsilon)=\int_{-\infty}^{\infty}\frac{k^2\varepsilon^2}{k^2\varepsilon^2+x^2}\frac{1}{k}f\left(\frac{x}{k}\right)\mathrm{d}x=\int_{-\infty}^{\infty}\frac{\varepsilon^2}{\varepsilon^2+\left(\frac{x}{k}\right)^2}\frac{1}{k}f\left(\frac{x}{k}\right)\mathrm{d}x=$$

$$=\int_{-\infty}^{\infty}\frac{\varepsilon^2}{\varepsilon^2+y^2}f(y)\mathrm{d}y=n(\varepsilon).$$

Therefore a k-times stretching increases $\varepsilon/\sqrt{n(\varepsilon)}$ also k-times.

Table I

	$f(x)$	ε	$n(\varepsilon)$	$\varepsilon/\sqrt{n(\varepsilon)}$
1.	$\dfrac{1}{6.2691\cdot(\sqrt{x^2+1})^{1.4}}$	1.500	0.356	2.513
2.	$\dfrac{1}{4.5545\cdot(\sqrt{x^2+1})^{1.6}}$	1.272	0.426	1.949
3.	$\dfrac{1}{3.6791\cdot(\sqrt{x^2+1})^{1.8}}$	1.112	0.469	1.623
4.	$\dfrac{1}{\pi(x^2+1)}$	1.000	0.500	1.414
5.	$\dfrac{1}{2.5056\cdot(\sqrt{x^2+1})^{2.4}}$	0.840	0.537	1.146
6.	$\dfrac{1}{2.1348\cdot(\sqrt{x^2+1})^{2.8}}$	0.735	0.558	0.984
7.	$\dfrac{1}{1.8873\cdot(\sqrt{x^2+1})^{3.2}}$	0.662	0.573	0.875
8.	$\dfrac{2}{\pi(x^2+1)^2}$	0.562	0.590	0.732
9.	$\dfrac{3\cdot\sqrt{3}}{4\pi}\cdot\dfrac{1}{\|x\|^3+1}$	0.832	0.596	1.078
10.	$\dfrac{3\cdot\sqrt{3}}{8\pi}\cdot\dfrac{1}{\|x\|^{3/2}+1}$	1.299	0.373	2.128
11.	$\dfrac{1}{2(\|x\|+1)^2}$	0.683	0.419	1.055
12.	$\begin{cases}\dfrac{1}{4}, & \text{if } \|x\|\leqq 1\\ \dfrac{1}{4x^2}, & \text{if } \|x\|>1\end{cases}$	1.240	0.561	1.655
13.	$\dfrac{1}{\sqrt{2\pi}}e^{-\frac{x^2}{2}}$	0.925	0.631	1.165
14.	$\begin{cases}\dfrac{1}{2}, & \text{if } \|x\|\leqq 1\\ 0, & \text{if } \|x\|>1\end{cases}$	0.719	0.681	0.871
15.	$\dfrac{1}{2}e^{-\|x\|}$	0.807	0.562	1.076
16.	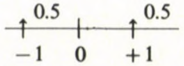	1.732	0.750	2.000
17.	$\dfrac{2\cdot K_0^2(x)}{\pi^2}$	0.0447	0.364	0.0741
18.	$\dfrac{1}{\pi}\left(\dfrac{\sin x}{x}\right)^2$	1.075	0.589	1.401

The Monte-Carlo investigations with other goals confirmed our supposition for all distributions in the Table: the semi-interquartile ranges were within the accuracy of our computations, i.e. within 10% identical with the 0.6745-times of $\varepsilon/\sqrt{n(\varepsilon)}$ (as it is known, if Φ is the distribution function of a Gaussian distribution, then $\Phi(0.6745) = 0.75$)).

Our idea can be proven exactly using the influence curve (IC) of the theory of robust estimations, or by the known connection of this function with the asymptotic scatters (see e.g. Andrews et al. 1972).

As

$$\varepsilon^2 = \frac{\int\limits_{-\infty}^{\infty} \frac{3x^2 f(x)}{(x^2+\varepsilon^2)^2}\,\mathrm{d}x}{\int\limits_{-\infty}^{\infty} \frac{f(x)}{(x^2+\varepsilon^2)^2}\,\mathrm{d}x} \tag{3a}$$

(Csernyák 1983, Hajagos 1980), after some rearrangement one gets

$$\int\limits_{-\infty}^{\infty} \frac{x^2 f(x)\mathrm{d}x}{(x^2+\varepsilon^2)^2} = \frac{1}{3}\varepsilon^2 \int\limits_{-\infty}^{\infty} \frac{f(x)\mathrm{d}x}{(x^2+\varepsilon^2)^2}\,. \tag{3}$$

As it is known, the equation of the influence curve (F is the distribution function belonging to f) is:

$$IC(x; F; M) = \frac{1}{\int\limits_{-\infty}^{\infty} \frac{\varepsilon^2 - y^2}{(\varepsilon^2+y^2)^2} f(y)\mathrm{d}y} \frac{x}{\varepsilon^2 + x^2} \tag{4}$$

thus M is the square of the asymptotic scatter of the most frequent value:

$$A^2(F) = \int\limits_{-\infty}^{\infty} [IC(x; F; M)]^2 f(x)\mathrm{d}x =$$

$$= \frac{1}{\left[\int\limits_{-\infty}^{\infty} \frac{\varepsilon^2}{(\varepsilon^2+y^2)^2} f(y)\mathrm{d}y - \int\limits_{-\infty}^{\infty} \frac{y^2}{(\varepsilon^2+y^2)^2} f(y)\mathrm{d}y\right]^2} \times$$

$$\times \int\limits_{-\infty}^{\infty} \frac{x^2}{(\varepsilon^2+x^2)^2} f(x)\mathrm{d}x. \tag{5a}$$

Using Eq. (3) several times one gets:

$$A^2(F)=\frac{1}{\left[\int\limits_{-\infty}^{\infty}\frac{\varepsilon^2}{(\varepsilon^2+y^2)^2}f(y)\mathrm{d}y-\frac{1}{3}\int\limits_{-\infty}^{\infty}\frac{\varepsilon^2}{(\varepsilon^2+y^2)^2}f(y)\mathrm{d}y\right]^2}\times$$

$$\times\frac{1}{3}\int\limits_{-\infty}^{\infty}\frac{\varepsilon^2}{(\varepsilon^2+x^2)^2}f(x)\mathrm{d}x=\frac{1}{\int\limits_{-\infty}^{\infty}\frac{\frac{4}{3}\varepsilon^2}{(\varepsilon^2+y^2)^2}f(y)\mathrm{d}y}=$$

$$=\frac{1}{\int\limits_{-\infty}^{\infty}\left[\frac{\varepsilon^2}{(\varepsilon^2+y^2)^2}+\frac{\frac{1}{3}\varepsilon^2}{(\varepsilon^2+y^2)^2}\right]f(y)\mathrm{d}y}=$$

$$=\frac{1}{\int\limits_{-\infty}^{\infty}\left[\frac{\varepsilon^2}{(\varepsilon^2+y^2)^2}+\frac{y^2}{(\varepsilon^2+y^2)^2}\right]f(y)\mathrm{d}y}=\frac{1}{\int\limits_{-\infty}^{\infty}\frac{f(y)}{\varepsilon^2+y^2}\mathrm{d}y}=\frac{\varepsilon^2}{n(\varepsilon)}. \qquad (5)$$

The practical use of this now established statement is promoted by the Table where the values of $\varepsilon/\sqrt{n(\varepsilon)}$ are given numerically for many cases.

It is known that the scatter asymptotically characterizing the accuracy of the averages (i.e. for great N values) is infinite for many different type of distributions. The problem is if there are distributions for which $\varepsilon/\sqrt{n(\varepsilon)}$ is infinite, too?

In case of a finite ε, $\varepsilon/\sqrt{n(\varepsilon)}$ cannot be infinite, as in such a case $n(\varepsilon)$ would be zero what is impossible, as ε is the greatest maximum place of function (2). On the other hand, ε cannot be infinite according to Csernyák's (1982) investigations.

A density function $f(x)$ can be artificially produced, e.g. as limiting value, for which $\varepsilon=0$. In such cases, however, the function $\bar{F}$ in Eq. (2) is a monotonously decreasing one (else there would be a maximum, and ε would be finite). The reciprocal value of $\bar{F}$ multiplied by $\bar{\varepsilon}^5$, is a monotonously increasing function starting in the origin, thus its fourth root, $\bar{\varepsilon}/\sqrt{n(\bar{\varepsilon})}$ is also a monotonously increasing function. If $\bar{\varepsilon}$ converges to zero, the value of $\bar{\varepsilon}/\sqrt{n(\bar{\varepsilon})}$ converges to zero, too. This "absolute accuracy" however, cannot be realized in the practice, at best a very high accuracy can be reached, but even that only in case of very high N-s.

The results of the present paper are further proofs of the statements by Csernyák et al. (1981) and Csernyák and Steiner (1982) i.e. that the law of the large numbers is valid for the most frequent value, without any limitation of the form of the distribution function, and the rate of increase in the accuracy of the law of large numbers is always $1/\sqrt{N}$.

A last comment in connection with the introductory remark: if one uses the multiplicator 1.5, as proposed by Steiner (1980), a value will be obtained which is in 87% of the cases greater than the actual error ($\Phi(1.5)=0.9332$).

References

Andrews D F, Bickel P J, Hampel F R, Huber P J, Rogers W N, Tukey J W 1972: Robust Estimates of Location. Princeton University Press. Princeton, N. J. 1972.

Csernyák L: Investigation on the existence of the most frequent value and of the reciprocal cohesion (in press)

Csernyák L, Hajagos B, Steiner F 1981: General validity of the law of large numbers in case of adjustments according to the most frequent value. *Acta Geod., Geoph., Mont. Hung.*, 16, 73–90.

Csernyák L, Steiner F 1982: Untersuchungen über das Erfüllungstempo des Gesetzes der großen Zahlen. Publications of the Technical University for Heavy Industry, Series A Mining 37 No. 1

Hajagos B 1980: Method for the rapid calculation of the most frequent value and M-fitting problems. *Acta Geod., Geoph., Mont. Hung.*, 15, 75–85.

Landy I, Lantos M, Steiner F 1982: Untersuchungen von *U*-Verteilungen. Publications of the Technical University for Heavy Industry, Series A Mining 37 No. 1.

Steiner F 1980: Estimated error of the most frequent value. *Acta Geod., Geoph., Mont. Hung.*, 15, 87–96.

Steiner F 1973: Most frequent value and cohesion of probability distributions. *Acta Geod., Geoph., Mont. Hung.*, 8, 381–395.

Acta Geodaet., Geophys. et Montanist. Hung. Volume 18 (1—2), pp. 141—156 (1983)

RELATION BETWEEN TWO ESTIMATES OF LOCATION: THE MOST FREQUENT VALUE AND THE ARITHMETIC MEAN

L CSERNYÁK[1]

College of Finance and Accountancy, Budapest

F STEINER[2]

Technical University for Heavy Industry, Miskolc

[Manuscript received March 31, 1982]

The evaluation of estimates is from the point of view of engineers unambiguous: the estimate of the location for a given type of distribution is the better the less data are necessary to reach a given accuracy (e.g. in case of geophysical problems: less field measurements are necessary to obtain the same geological information). According to the present results, if the flanks of the distribution have ordinary widths, the use of the most frequent value is more advantageous, but if the distributions are nearer to the sterile Gaussian distribution, then the use of the averages is more advantageous (i.e. using the least squares principle). If a marginal case is to be evaluated — when the distribution can be approximated by some mixture of two different Gaussian distributions — the authors propose to use a system of isolines N_E/N_M (here the ratio N_E/N_M is the ratio of the data needed for a similarly accurate estimate using the averages and the most frequent values, respectively); the estimate by the most frequent value uses at worst by 36% more data for an estimate of the same accuracy (in case of the sterile Gaussian distribution), while the averages (the principle of the least squares) yield ratios N_E/N_M without any upper limit (thus the surplus expenses have no upper limit, either). For the symmetrical distributions with finite scatter, which are not treated in this paper, the value N_E/N_M can be obtained from Eq. (5).

Keywords: arithmetic mean; estimation of location; Gaussian distribution; most frequent value

One has to strive at economy in geophysics, too: the geophysicist has to produce the necessary geological information with the possible lowest expenses. This requirement includes the necessity to apply the most powerful methods of estimation, as the quantity of data to be collected for an information on the layer depth with an accuracy of 2–3% can reach values of 10^4–10^5 and very expensive instruments are used for obtaining them (Landy 1982).

The choice of the best estimate is easy if the distribution of the data is known. Let us suppose that the data have uniform distribution. If the symmetry point is estimated by the arithmetic mean of the highest and lowest value in the sample, the scatter of the

[1] H-1149 Budapest, Buzogány u. 10–12.
[2] H-3515 Miskolc-Egyetemváros

estimate is (see e.g. Prékopa 1962):

$$\sqrt{\frac{2}{(N+1)(N+2)}}$$

that means that the accuracy of the estimate increases for N not with $\sqrt{N}$ (as usual for the average in case of finite scatters), but much quicker, with N, i.e. the accuracy increases in proportion with the number of the data used. Thus this estimate is very advantageous for the estimation of the symmetry point if the data have uniform distribution. But the uniform distribution is too much sterile in our opinion and such distributions do not occur even exceptionally in actual data systems.

The uniform distribution is really an extremely sterile one and nobody would really consider its use in the data evaluation neither in geophysical, nor in the general measurement praxis. An other sterile distribution, the Gaussian one, is, however, very often considered as a common one in the measurement praxis. Authors, however, who treated in fact great amounts of data very carefully, have a very different opinion. Some citations should illustrate this from Tukey's book: "... the Gaussian is a reference standard, *not* an example of what in fact is ..." (p. 645); "When the underlying distribution, as always, is non Gaussian ..." (p. 661); "...we have introduced the Gaussian distribution, and we have been careful to avoid thinking of real data as in any sense 'exactly Gaussian'." (p. 644).

Practical engineers were well aware of these facts for a rather long time. Morsteller and Tukey (1977) write citing Student's (W S Gosset) paper from 1927 (p. 7): "Student himself always remembered that observations and measurements were never distributed in magic bell-shaped curves, even when they were chemical determinations of commercial importance made under his own supervision." "The history of statistics and data analysis is a messy mixture of healthy skepticism and naive optimism about the exact shapes of the distributions of observations. Such optimism has often been inflated by the wonderful properties of a single family of distributions, the 'normal' distributions ..." "Some misinterpret the word 'normal' to mean 'the ordinarily occurring'— but, so far as we know, distributions that exactly fit this formula never occur in practice ..."

Kerékfy (1978) cites Hampel's statement that long geodetic and astronomical measurements have distributions with more stretched flanks than those following from a Gaussian type distribution.* The Gaussian distribution is exactly from this point of view a sterile distribution.

* Compare also Romanowski M, Green E 1965: Practical applications of the modified normal distribution, *Bull. Géodésique*, 76, 1–20 and Bessel F W 1818: Fundamenta Astronomiae, Königsberg: Nicolovius

In a maximum likelihood-sense the best estimate belonging to a Gaussian distribution is the average. It is, however, useful to express the connection between the Gaussian distribution and the estimate from the sample average more exactly following Rényi (1954): "the function $\prod_{i=1}^{N} f(x_i - x)$ has then and only then a maximum for all values of the variables $x_1, \ldots, x_n$ at the place $\frac{1}{N}\prod_{i=1}^{N} x_i$, if $f(x) = \frac{1}{\sigma \cdot \sqrt{2\pi}} e^{-\frac{x^2}{2^2}}$." That means that for Gaussian distributions the symmetry point can be estimated most advantageously with the average; if the estimation would be carried out e.g. using medians, then the data quantity necessary to reach the same accuracy would be $\pi/2$ times higher (see e.g. Claerbout and Muir 1973). At the same time there is no other type of distribution then the Gaussian one for which the averaging would be the most powerful estimation.

Let us cite only one example from the literature how small deviations of $f(x)$ from the Gaussian distribution result already in the fact that estimates differing from the average yield better results. Let us define the following family of distributions for $\sigma_c > 1$:

$$f(p; \sigma_c; x) = (1-p) \cdot f_G(1; x) + p \cdot f_G(\sigma_c; x), \tag{1}$$

where

$$f_G(\sigma; x) = \frac{1}{\sigma \cdot \sqrt{2\pi}} e^{-\frac{x^2}{2\sigma^2}} \tag{1a}$$

is the density function of the Gaussian distribution. Kerékfy (1978) cites Tukey who found for $\sigma_c = 3$ that already for $p = 0.0018$ the method using the minimum of the averages (instead of the least squares principle i.e. averaging) yields better results, in spite of the fact that in case of small p's, $f(p; \sigma_c; x)$ hardly differs from the Gaussian distribution, as shown by Eq. (1).

Distributions defined by Eq. (1) can also be considered as standard Gaussian distributions contaminated in the ratio p with Gaussian distributions having a scatter σ_c. The rate of the contamination, or even its presence cannot be surely determined by the usual method of quick information got from the illustration of the distribution in a Gaussian grid-system. (If the number of data is increased infinitely, then the contamination can be naturally exactly determined, but actually one has always a given number of data). In case of $\sigma_c = 10$ and increasing p by more than a full magnitude to 0.02 (2%), the theoretical values of the cumulative frequencies can be seen in Fig. 1 denoted by small circles (if the distribution function of Eq. (1a) is denoted by Φ, then the figure shows some values of the distribution function $[1-0.02]\Phi(x) + 0.02\Phi[x/10]$). Supposing $N = 100$, the scatter in the central point, in the median can be given ($= 0.125$), the error of other points is greater. Thus the fact that all represented points lie within the range of twice the scatter of the median shows, that the contaminated character of the distribution could remain undetected.

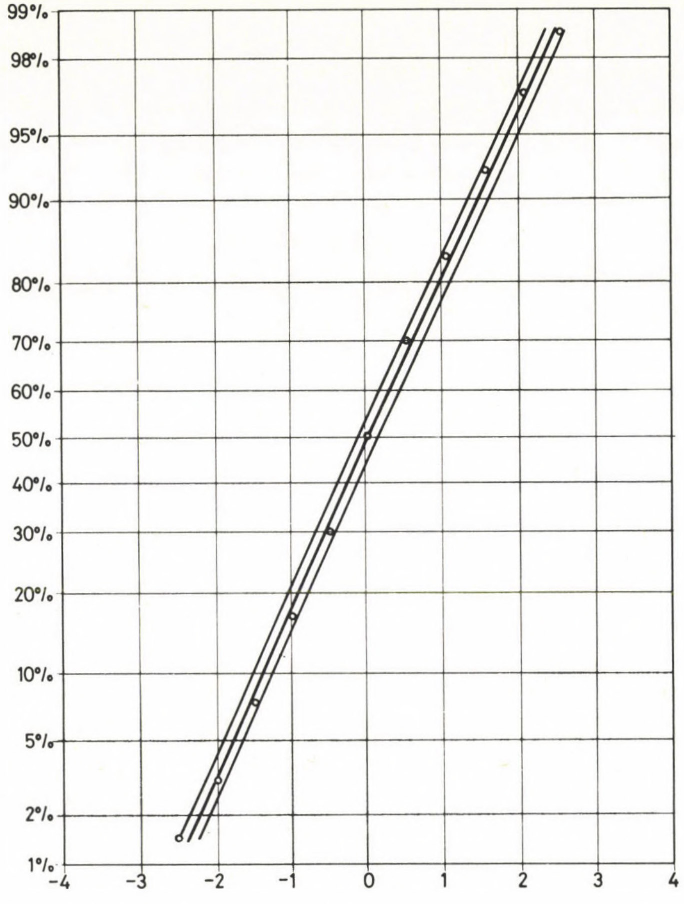

Fig. 1. A standard Gaussian distribution is contaminated in a ratio of 2% by a Gaussian distribution with a ten times greater scatter. The cumulative frequencies are represented in a Gaussian grid. In case of $N = 100$ the presence of contamination cannot be determined

In geophysics, however, it is hardly possible to analyze distributions when carrying out routine work, and even less possible to increase the data quantity of the measurements for increasing the accuracy of the analyses. Moreover, even if the distribution of the data were known from every measurement series, it would be impossible to use for each case a different type of interpretation program package. Two, casually three variations can be yet dealt with, more never, therefore some generally applicable system should be striven at.

The mathematical statistical principle behind the present interpretation programs is the least squares principle. The cause for this is surely not that practical engineers are convinced about the Gaussian distribution of their data but the relative (and hardly increaseable) simplicity of these computations which is the most important factor not only in geophysics, but also in other branches of science. At present, however, when the computational costs for one operation are rather low and they will further decrease, the methodological question must be raised whether the least squares method should remain the basis for future interpretation methods as the most economical one (in respect of the costs of field measurements and computer times together).

As the costs of computer time are continually decreasing and the quantity of computations means therefore a decreasing factor, the disadvantageous characteristics of the averaging should be clearly evaluated and then a choice should be taken from among methods without these disadvantageous properties. There are a number of disadvantageous properties of the averaging, as it has already been stated by Andrews et al. (1972) based on 68 different types of estimates for 14 types of distributions (p. 240) that "The arithmetic mean, in its strict mathematical sense, is 'out'."

Let us consider distributions of the type Eq. (1). Their scatter is evidently

$$\sigma=\sqrt{(1-p)+p\cdot\sigma_c^2}\,. \tag{2}$$

The occurrence of very crude errors called "blunders" in earlier papers means very high values of σ_c; in the manual evaluation, such far-off values have been simply omitted, now, in the time of the automatized evaluation, they can occur unobservedly. In case of $\sigma_c \gg 1$, $\sigma=\sigma_c\sqrt{p}$, that means that the curious case occurs when the contamination — being very small, possibly of some permille part of the sample, but with a very high scatter — determines the inaccuracy of the average of samples with a very high number of elements. The density function of the averages of samples with N elements is in this case

$$f_N(x)=N[f(Nx)]^{N*} \tag{3}$$

and it is connected only by the very thin channel of the scatter with the original density function $f(x)$ (the exponent means the N-times convolution of $f(x)$ with itself, the result is reduced N-times by writing in the argument Nx). For other, in the engineering practice sometimes more important quantities, as e.g. the semi-interquartile range there is no general connection between the values characterizing $f(x)$ and $f_N(x)$, and no conclusion can be drawn on the basis of one of them about the other (it can happen that even the orders of magnitude cannot be estimated).

Equation 3 is valid independently of the type of the distribution for the distribution of the averages from samples with N elements and it expresses that the long flanks of the density function $f(x)$ play an amplified role in the determination of the averages. It is known that in case of an $f(x)$ with finite scatter σ, the scatter $\sigma/\sqrt{N}$ has for high values of N a Gaussian distribution, but it can be significantly, even several times wider than that without contamination (estimates with averages can be then less accurate by one or two orders of magnitude). But according to Hampel, a contamination of 5–10% is more the law, then the exception.

To trace the actual situation (using the form $\exp[-0.5(\sigma t)^2]$ for the characteristic function of the Gaussian distribution), the density function $f_N(p; \sigma_c; x)$ of the averages from samples with N elements from distributions having the form of Eq. (1) can be expressed explicitly:

$$f_N(p, \sigma_c; x) = \sum_{K=0}^{N} \binom{N}{K} (1-p)^{N-K} \cdot p^K \cdot f_G(\sqrt{(N-K)+K \cdot \sigma_c^2}; x) \tag{4}$$

(for the definition of f_G see Eq. 1a).

The value of p can be chosen up to $p=0.4$, as according to Landy et al. (1982) the most frequent value as an estimate of location (see Steiner 1973) yields even in case of such high contamination values practically depending only on the parameters of the basic distribution. Let us choice at first $p=0.08$ *and* $\sigma_c=10$.

Using Eq. (4) for the numerical determination of the quartiles, the semi-interquartile range can be studied for different values of N (similarly to Eq. 4), in function of $1/\sqrt{N}$. In case of a sterile Gaussian distribution, the Q_N semi-interquartile range of the averages from samples with N elements divided by the semi-interquartile range Q_1 of the original sample correspond to points along a straight line with a direction angle of 45°, if the abscissae represent $1/\sqrt{N}$ and the other axis has the same scale. The values of Q_N/Q_1 from uniform and U-type distributions which cut off the flanks even more sterilely than the Gaussian distribution, would tend asymptotically to straight lines having direction angles smaller than this value (for high values of N, Q_N tends to $0.6745\sigma/\sqrt{N}$). For the distribution of the type Eq. (1) and for the values of the parameters given above the curve represented in Fig. 2 by small circles is obtained. For the tangent of the direction angle 2.74 was obtained as product of $\sigma=2.987$ (from Eq. 2) by 0.6745 and divided by $Q_1=0.735$. — For small values of N the semi-interquartile range does not decrease even approximately in accordance with $1/\sqrt{N}$: the value of Q_1 corresponding to $N=1$, and the values of Q_N belonging to small values of N (where the effect of the flanks is not strongly amplified according to Eq. 3) promises more advantageous errors (as compared to $1/\sqrt{N}$) than what is asymptotically realized.

The disadvantageous effects of the flanks are even more clear, if $p=0.25$, $\sigma_c=150$. The results for this pair of parameters can be represented only if the ordinates are contracted 1:10 (see Fig. 3). The curve starts in direction of the previously described straight line (but in this system of coordinates with a different direction angle) corresponding to the sterile Gaussian distribution, but for increasing N-s one gets at first increasing Q_N-s (till $N=6$) (the maximum value of Q_N/Q_1 is nearly 17), but then the curve continues along a straight line with a tangent 52.7, crossing the origin (as according to Eq. (2), $\sigma=75.005$ and $Q_1=0.96$). Figure 3 represents a very significant example for the surprises of the estimation of locations by averages: if the error is measured by the interquartile range, one single measured value can be by an order of

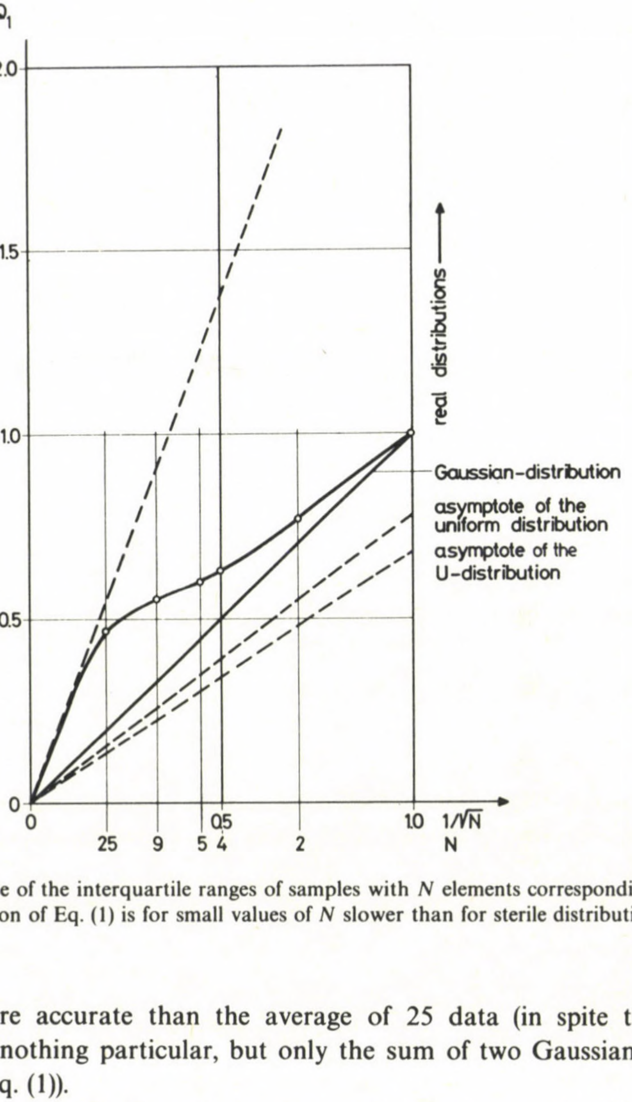

Fig. 2. The decrease of the interquartile ranges of samples with N elements corresponding to the density function of Eq. (1) is for small values of N slower than for sterile distributions

magnitude more accurate than the average of 25 data (in spite that the basic distribution is nothing particular, but only the sum of two Gaussian distributions according to Eq. (1)).

In the present paper the authors compare the simple averaging (the least squares principle) with the estimation of location by the most frequent value after Steiner (1973). This has been made possible as they and their co-workers carried out numerous computations with these methods which automatically excludes the effect of blunders. These studies involved theoretical, practical and Monte-Carlo methods. Some unexpected results of these studies were: 1. from the point of view of the information theory, the computational algorithm of the most frequent value can be deduced analogously to the averaging (Hajagos 1982); 2. the law of large numbers is always fulfilled for any distribution, if the most frequent values are computed from samples

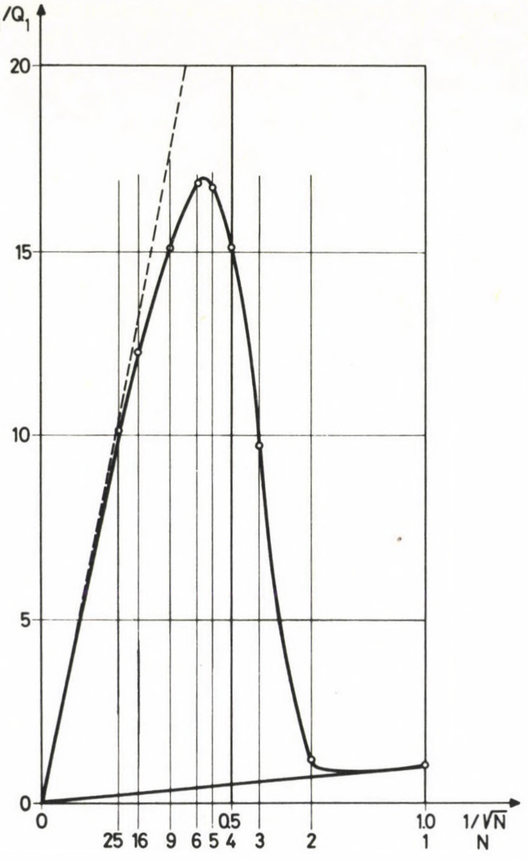

Fig. 3. For a certain pair of the parameters (p, σ_c), the increase of N causes a transitional increase of the interquartile ranges instead of the expected decrease

with N elements (Csernyák et al. 1981); 3. the interquartile range of the most frequent values decreases as $1/\sqrt{N}$ — this has been shown in a good approximation with Monte-Carlo methods (Csernyák and Steiner 1982); 4. according to recent results, the scatter of the most frequent values from samples with N elements approximates asymptotically $\varepsilon/\sqrt{n(\varepsilon)}$; here $\varepsilon/\sqrt{n(\varepsilon)}$ is always a finite value (Csernyák and Steiner 1983). (The limit distribution is always a normal distribution, as it has been already shown by Csernyák et al. (1981).)

Csernyák and Steiner (1983) published the data $\varepsilon/\sqrt{n(\varepsilon)}$ characterizing the asymptotic property; by these values a possibility is given to compare the averaging with the estimation by the most frequent values. In case of a high number of elements, the accuracy of the average is equal with the accuracy of the most frequent value for symmetrical distributions with finite scatter, if the number of elements N_E in the averaging and the number of elements N_M in the computation of the most frequent value are in the following relation:

$$\frac{\varepsilon}{\sqrt{N_M \cdot n(\varepsilon)}} = \frac{\sigma}{\sqrt{N_E}}. \tag{5a}$$

The ratio of the two extents of the necessary samples for the averaging and for the most frequent value (being the ratio of the necessary field works) is evidently computable as

$$N_E/N_M = \frac{\sigma^2 \cdot n(\varepsilon)}{\varepsilon^2}. \tag{5}$$

In case of finite scatters Eq. (5) enables some orientation: if $N_E/N_M > 1$, the most frequent value can be used more economically as an estimate of location. If the scatter is infinite then the economy of the averages cannot be discussed, even in cases when the law of large numbers is fulfilled for the actual distribution.

The infinite scatter can be accompanied not only with the invalidity of the law of large numbers, but even its reverse can be true: the error increases monotonously with the number of elements, N, in the sample (not only for a limited interval, as in case of Fig. 3). Therefore it is advantageous to separate in the Table of this paper the distributions, for which the value of N_E/N_M is asymptotically infinite, into groups for which the law of large numbers is fulfilled or for which it is not fulfilled.

Table I

		$f(x)$	$\frac{\varepsilon}{\sqrt{n(\varepsilon)}}$	σ	Is the law of great numbers fulfilled for averages?	Asymptotic value of N_E/N_M
1	1	$\frac{1}{6.2691 \cdot (\sqrt{x^2+1})^{1.4}}$	2.513	∞	no its reverse is true	∞
	2	$\frac{1}{4.5545 \cdot (\sqrt{x^2+1})^{1.6}}$	1.949	∞	no its reverse is true	∞
	3	$\frac{1}{3.6791 \cdot (\sqrt{x^2+1})^{1.8}}$	1.623	∞	no its reverse is true	∞
	4	$\frac{3 \cdot \sqrt{3}}{8\pi} \frac{1}{\lvert x\rvert^{3/2}+1}$	2.128	∞	no its reverse is true	∞

Table I. (cont.)

	5	$\frac{1}{\pi(x^2+1)}$	1.414	∞	no	∞
	6	$\frac{1}{2(\lvert x\rvert+1)^2}$	1.055	∞	no	∞
2	7	$\frac{1}{4}$, if $\lvert x\rvert \leqq 1$ $\frac{1}{4x^2}$, if $\lvert x\rvert > 1$	1.655	∞	no	∞
	8	$\frac{1}{\pi}\left(\frac{\sin x}{x}\right)^2$	1.401	∞	no	∞
	9	$\frac{1}{2.5056 \cdot (\sqrt{x^2+1})^{2.4}}$	1.146	∞	yes	∞
3	10	$\frac{1}{2.1348 \cdot (\sqrt{x^2+1})^{2.8}}$	0.984	∞	yes	∞
	11	$\frac{3 \cdot \sqrt{3}}{4\pi} \frac{1}{\lvert x\rvert^3+1}$	1.078	∞	yes	∞
	12	$\frac{1}{1.8873 \cdot (\sqrt{x^2+1})^{3.2}}$	0.875	2.236	yes	6.530
	13	$\frac{1}{\sqrt{2\pi}} e^{-\frac{x^2}{2}}$	1.165	1.000	yes	0.737
	14	$\frac{1}{2}$, if $\lvert x\rvert \leqq 10$, if $\lvert x\rvert > 1$	0.871	0.577	yes	0.439
	15	$\frac{1}{2} e^{-\lvert x\rvert}$	1.076	1.414	yes	1.726
	16	$\frac{2 \cdot K_0^2(x)}{\pi^2}$	0.0741	0.35	yes	22
4	17	$\underset{-1}{\overset{0.5}{\uparrow}} \quad \underset{0}{+} \quad \underset{+1}{\overset{0.5}{\uparrow}}$	2.000	1.000	yes	0.250
	18	$\frac{2}{\pi(x^2+1)^2}$	0.732	1.000	yes	1.866
	19	$(1-p) f_G(1;x) + p \cdot f_G(\sigma_c;x)$: $p=0.08$; $\sigma_c=10$	1.21	2.987	yes	6.1
	20	$p=0.25$; $\sigma_c=150$	1.342	75.005	yes	3 124
	21	$p=0.001$; $\sigma_c=10000$	1.165	316.229	yes	73 680

The distributions 1, 2, 3, 5, 9, 10, 12 and 18 are members of a family of distributions which has been defined by Csernyák and Steiner (1982) as

$$f_a(x) = \frac{1}{c(a) \cdot (\sqrt{x^2+1})^a} \tag{6}$$

($a > 1$; the norming factor which depends on a is to be computed from

$$c(a) = \frac{\sqrt{\pi} \cdot \Gamma\left(\frac{a-1}{2}\right)}{\Gamma\left(\frac{a}{2}\right)}). \tag{6a}$$

The distributions of this type have evidently a finite scatter only if $a > 3$, and then

$$\sigma = \sqrt{\frac{1}{a-3}}. \tag{7}$$

If $2 < a \leq 3$, then the law of large numbers is fulfilled, but for these distributions a computation of the errors of the averages similarly to Figs 2 and 3 would yield curves with infinite derivates in the origin, therefore in such cases one has already asymptotically $N_E/N_M = \infty$. If $a = 2$, the Cauchy-distribution is obtained for which the law of large numbers is no more fulfilled, but the error of the averages does not increase with the increase of N; the latter which can be called the reverse law of large number, is valid in the domain $1 < a < 2$ (see also Csernyák and Steiner 1982). As it follows from the general laws, independently from the different dependences of the averages, the accuracy of the most frequent values (which is always increasing with $\sqrt{N}$) is always finite, as the value $\varepsilon/\sqrt{n(\varepsilon)}$ determining its scatter is similarly finite (see Table I).

In group 4 of the distributions in the Table I i.e. among the distributions with finite scatter, there are three distributions for which N_E/N_M is less than 1: they are the Gaussian, the uniform and the U-distributions. From the point of view of the flanks, all the three distributions can be specified as sterile ones; in the practice they will be never met with.

As on one hand even in case of the sterile Gaussian distribution only by 36% more data are necessary for the estimation using the most frequent values in comparison to the estimation by averaging, — on the other the averaging leads often to infinite N_E/N_M values, the "robustness of efficiency" discussed by Mosteller and Tukey (1977) speaks unambiguously in favour of the most frequent value (p. 206, "We want to have high efficiency in a variety of situations, rather than in any one situation.").

We do not exclude, however, the possibility that for certain measurement series the contamination of the distributions of the type (1) is so slight that for them $N_E/N_M < 1$. For a quick orientation in such cases, in the interval p 0.02–0.33 (i.e. for 2–33%) further in the interval $1<\sigma_c<15$ the values of σ, ε, $n(\varepsilon)$ and $\varepsilon/\sqrt{n(\varepsilon)}$ have been determined (see Figs 4–7) as well as from them the values of N_E/N_M according to Eq. (5) (see Fig. 8). In Fig. 8, the area to the left from the thick isoline $N_E/N_M=1$ has values (p, σ_c) for which the averaging is the more advantageous estimate of location, while for the area to the right of this line it becames ever more economical to use the estimation with the most frequent values. (Figures 4–7 representing the data for the calculation of the isoline system N_E/N_M are in themselves interesting: Fig. 5 shows e.g. that for an identical modification of ε, the smallest p is necessary around $\sigma_c=3$).

For great values of σ_c, the value ε can be left nearly unchanged, and in the computation of $n(\varepsilon)$ the following approximation is allowed:

$$n(\varepsilon)\equiv\int\limits_{-\infty}^{\infty}\frac{\varepsilon^2 f(x)}{\varepsilon^2+x^2}\,dx\approx 0.631\cdot(1-p)+p\cdot f_G(\sigma_c;0)\cdot\int\limits_{-\infty}^{\infty}\frac{\varepsilon^2}{\varepsilon^2+x^2}\,dx=$$

$$=0.631\cdot(1-p)+p\cdot\frac{0.925}{\sigma_c}\cdot\sqrt{\frac{\pi}{2}}=1.159\frac{p}{\sigma_c}+0.631\cdot(1-p)$$

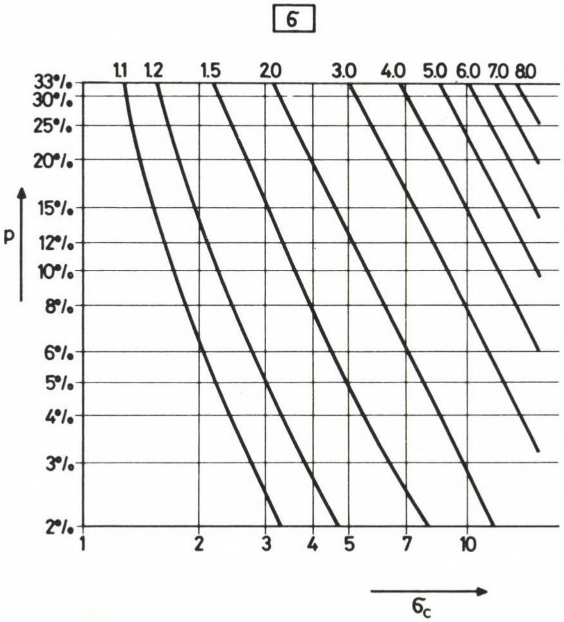

Fig. 4. The scatter of the distributions of Eq. (1) in function of p and σ_c

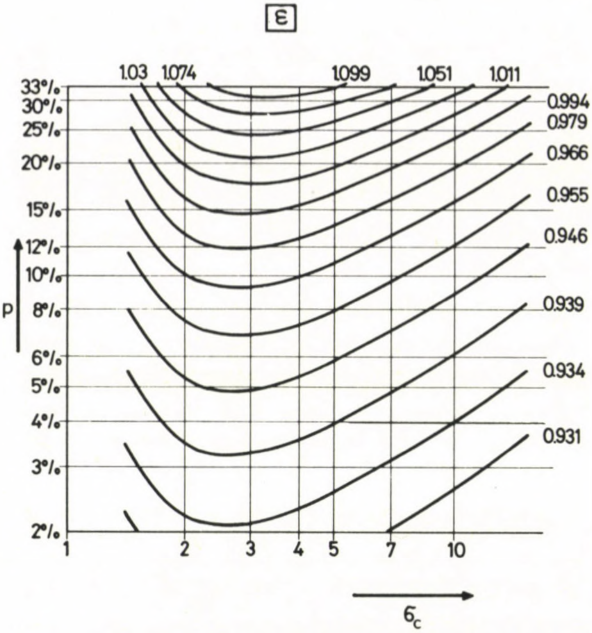

Fig. 5. The values of ε for the distributions of the type Eq. (1) in function of p and σ_c

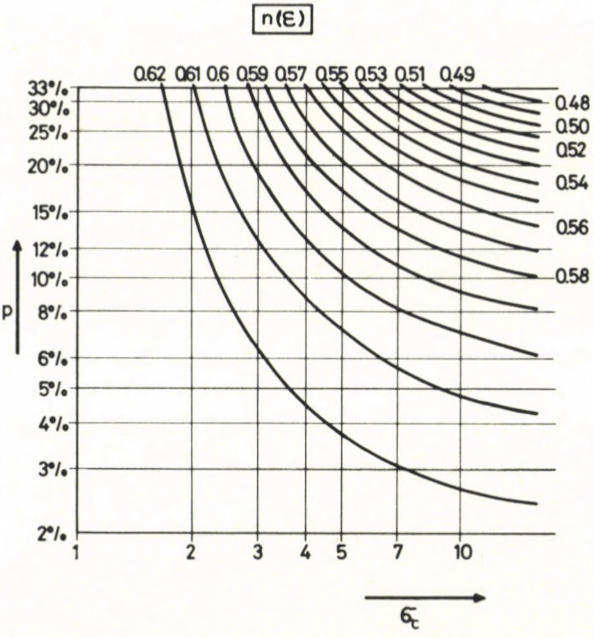

Fig. 6. The values of $n(\varepsilon)$ for the distributions of the type Eq. (1) in function of p and σ_c

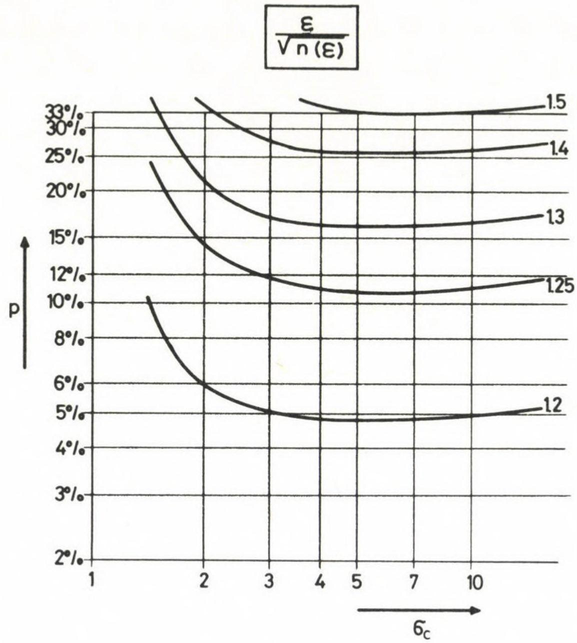

Fig. 7. The values of $\varepsilon/\sqrt{n(\varepsilon)}$ for the distributions of the type Eq. (1) in function of p and σ_c

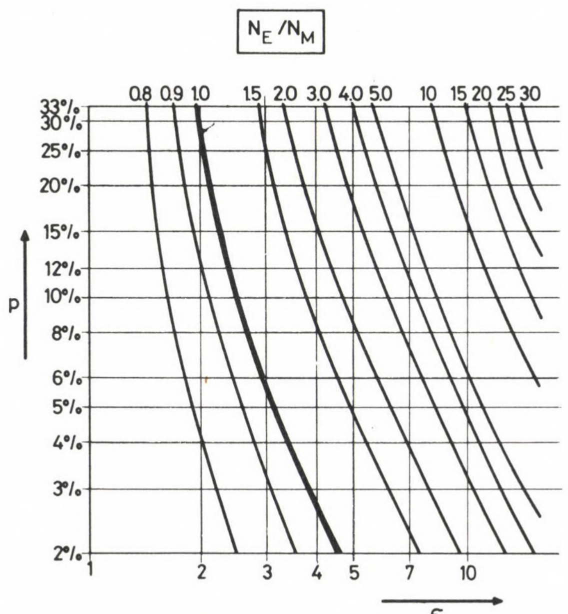

Fig. 8. The values of N_E/N_M for the distributions of the type Eq. (1) in function of p and σ_c. The ratio N_E/N_M indicates the ratio of the number of data necessary for estimations of location of the same accuracy given by averages and by most frequent values, respectively

(0.631 is the value of $n(\varepsilon)$ belonging to a sterile Gaussian distribution). If the symmetrical distribution with finite scatter of a data set does not correspond to any $f(p, \sigma_c; x)$ and no distribution appearing in the Table would be a reasonable approximation of the actual distribution, the efficiency of the two kinds of estimations can be evaluated with a calculation according to Eq. (5).

At last a statement of theoretical importance should be made which has general validity: N_E/N_M has no upper limit, and its lower limit is 1/4. For its proof let us suppose without loss of generality that the symmetry point is in the origin, and using the following equations to be found at Hajagos (1982):

$$\int_{-\infty}^{\infty} \frac{\varepsilon^2 f(x)}{(\varepsilon^2+x^2)^2} \mathrm{d}x = 3 \int_{-\infty}^{\infty} \frac{x^2 f(x)}{(\varepsilon^2+x^2)^2} \mathrm{d}x, \tag{8}$$

and

$$n(\varepsilon) \equiv \int_{-\infty}^{\infty} \frac{\varepsilon^2 f(x)}{\varepsilon^2+x^2} \mathrm{d}x \leqq 3/4. \tag{8}$$

$$\begin{aligned} N_E/N_M = \left(\frac{\sigma}{\varepsilon/\sqrt{n(\varepsilon)}}\right)^2 &= \int_{-\infty}^{\infty} x^2 f(x)\mathrm{d}x \cdot \int_{-\infty}^{\infty} \frac{1}{\varepsilon^2+x^2} f(x)\mathrm{d}x = \\ &= \int_{-\infty}^{\infty} x^2 f(x)\mathrm{d}x \cdot \int_{-\infty}^{\infty} \frac{x^2+\varepsilon^2}{(x^2+\varepsilon^2)^2} f(x)\mathrm{d}x = \\ &= \int_{-\infty}^{\infty} x^2 f(x)\mathrm{d}x \cdot \int_{-\infty}^{\infty} \frac{4x^2}{(x^2+\varepsilon^2)^2} f(x)\mathrm{d}x \geqq \\ &\geqq 4 \cdot \left[\int_{-\infty}^{\infty} \frac{x^2}{x^2+\varepsilon^2} f(x)\mathrm{d}x\right]^2 \end{aligned} \tag{9}$$

(in the last step the Schwarz-inequality is used). As it is evidently

$$n(\varepsilon) + \int_{-\infty}^{\infty} \frac{x^2}{x^2+\varepsilon^2} f(x)\mathrm{d}x \equiv 1$$

it follows from Eqs (8) and (9) that

$$N_E/N_M \geqq 1/4.$$

The lower limit is exact, see distribution 17 in Table I.

References

Andrews D F, Bickel P J, Hampel F R, Huber P J, Rogers W, Tukey J W 1972: Robust Estimates of Location. Princeton University Press, Princeton N J.

Claerbout J F, Muir F 1973: Robust modeling with erratic data. *Geophysics*, 38, 826–844.

Csernyák L, Hajagos B, Steiner F 1981: General validity of the law of large numbers in case of adjustments according to the most frequent value. *Acta Geod., Geoph. Mont. Hung.*, 16, 73–90.

Csernyák L, Steiner F 1982: Untersuchungen über das Erfüllungstempo des Gesetzes der grossen Zahlen. Publications of the Technical University for Heavy Industry, Series A Mining, 37, No. 1

Csernyák L, Steiner F 1983: Limit distribution of the most frequent values of samples from symmetrical distributions. *Acta Geod., Geoph. Mont. Hung.* (present issue)

Hajagos B 1982: Der häufigste Wert, als eine Abschätzung von minimalen Informationsverlust, und zugleich als die beste "maximum likelihood" Abschätzung. Publications of the Technical University for Heavy Industry, Series A Mining, 37, No. 1

Kerékfy P 1978: A robusztus becslésekről (On robust estimations). *Alkalmazott Matematikai Lapok*, 4, 327–357.

Landy I 1982: Praktische Beispiele zur Erfüllung des Gesetzes der großen Zahlen. Publications of the Technical University for Heavy Industry, Series A Mining, 37, No 1

Landy I, Lantos M, Steiner F 1982: Untersuchung von *U*-Verteilungen. Publications of the Technical University for Heavy Industry, Series A Mining, 37, No. 1

Mosteller F, Tukey J W 1977: Data Analysis and Regression. Addison-Wesley, Reading, Mass.

Prékopa A 1962: Valószínűségelmélet (Probability theory). Műszaki Könyvkiadó, Budapest

Rényi A 1954: Valószínűségszámítás (Probability calculus). Tankönyvkiadó, Budapest

Steiner F 1973: Most frequent value and cohesion of probability distributions. *Acta Geod., Geoph. Mont. Hung.*, 8, 381–395.

Tukey J W 1977: Exploratory Data Analysis. Addison-Wesley, Reading, Mass.

Acta Geodaet., Geophys. et Montanist. Hung. Volume 18 (1—2), pp. 157—164 (1983)

GEOMAGNETIC AFTER-EFFECT IN ATMOSPHERIC RADIO NOISE AND ITS RELATION TO PC 1-TYPE PULSATIONS

F. MÄRCZ[1]

Geodetic and Geophysical Research Institute, Hungarian Academy of Sciences
Sopron, Hungary

[Manuscript received April 2, 1982]

Connections have been studied between atmospheric radio noises (ARN) measured at two middle latitude stations (Panská Ves, Czechoslovakia and Kühlungsborn, GDR) and the occurrence of Pc 1-type pulsations (in Irkutsk) following selected geomagnetic disturbances of the interval 1969–1975. An increase in the ARN-level lasting about a fortnight was found at both stations after disturbances associated with a clear after-effect in Pc 1-type pulsations. Whistler activity indices of the interval 1969–1970 were also taken into account. On this basis a possible relationship between whistler activity and the ARN after-effect is discussed, too.

Keywords: atmospheric radio noise; geomagnetic after-effect; Pc1-type pulsations; whistlers

1. Introduction

An enhancement of the absorption of radio waves reflected from the lower ionosphere can be observed at middle latitudes after certain geomagnetic disturbances. The causes of the phenomenon have thoroughly been studied in last years [1, 2, 3, 4]. Investigations have also shown that geomagnetic activity may influence the level of atmospheric radio noise (ARN), too [5, 6]. In addition, other results hinted at a relationship between the ARN-level and Forbush-decreases occurring in galactic cosmic rays [7].

The absorption enhancement is principally attributed to an increased ionization in the lower ionosphere due to electrons (with energies >40 keV) precipitating from the radiation belts of the magnetosphere. The precipitation originates from an interaction between ELF-waves and trapped electrons [4]. Increased geomagnetic activity can also be followed by an increased activity of Pc 1-type pulsations. Both Pc 1 pulsations recorded at ground-based stations and ELF-waves observed in space hint at some kind of plasma turbulence generated near the plasmapause, or within the plasmasphere. There are few observations of ELF-waves in space, Pc 1-type pulsations are, however, continuously recorded at several stations. As a nearly simultaneous occurrence of the

[1] H-9401 Sopron, P.O. Box 5, Hungary

two phenomena can be assumed, the appearence of plasmaspheric ELF-waves might be inferred from the enhanced Pc 1 activity observed at the Earth's surface. Consequently, Pc 1-type pulsations could also give some information about the after-effect in ionospheric absorption.

Previous investigations revealed on this basis a close association of the after-effect in ionospheric absorption with Pc 1-type pulsations [8, 9]. The increase of ionospheric absorption was generally well pronounced if the enhanced geomagnetic activity was followed by a clear after-effect in Pc 1-type pulsations. On the contrary, the after-effect in absorption was lacking or weaker when a distinct Pc 1 after-effect was missing.

2. Investigations and results

These considerations were valid in case of the after-effect occurring in absorption of MF- and LF-waves. The results [8, 9] were deduced from a number of data and for different frequencies (1178, 272, 245 and 127 kHz). The present study tries to answer the question whether a similar relation may be found between the after-effect in the ARN (VLF-waves) and the occurrence of Pc 1-type pulsations.

The ARN-levels measured at two middle latitude stations (Panská Ves: $\varphi_{\text{geogr.}} = 50°32'$ N and Kühlungsborn: $\varphi_{\text{geogr.}} = 54°07'$ N) have been analysed after selected geomagnetic disturbances of the period 1969–1975, together with the occurrence of Pc 1-type pulsations (in Irkutsk: $\varphi_{\text{geogr.}} = 52°16'$ N). The selection of disturbances was carried out on the basis of the daily sum of K_p-indices (ΣK_p). Days with $\Sigma K_p \geqq 30$ were chosen as key days for superposed epoch analyses, with an additional criterion. Namely it was required that on two days out of three preceding the key day the daily sum of K_p should not surpass the mean value of ΣK_p determined for the corresponding year. In this way a rather quiet period was assured before the individual disturbances.

For the Panská Ves station [10] Fig. 1 shows the mean departures of the ARN-level (determined for the interval between 16 00 and 20 00 UT) from a reference value on and after the selected key days. The ARN-data measured on three days preceding the key day (i.e. in a calm period) were averaged and applied as reference value. In Fig. 1, top, the changes of ARN-departures given in percentages are quite small. Here the total number of disturbances (n), selected according to the mentioned criteria, was 94 in the interval between 1969 and 1975. In Fig. 1, bottom, two independent superposed epoch analyses are presented according to the presence, or lack of a clear after-effect in Pc 1-type pulsations.

Similarly to [8], the Pc 1 after-effect was accepted as a clear one when an appropriate ratio surpassed the value of 1. (The ratio of Pc 1 duration averages between days +2 and +7 to the Pc 1 duration averages of days −3, −2, +8, +9 and +10 was calculated for each selected geomagnetic disturbance). There were 55 disturbances with a real Pc 1 after-effect and 39 without it. (Fig. 1, bottom). In case of the former the ARN-

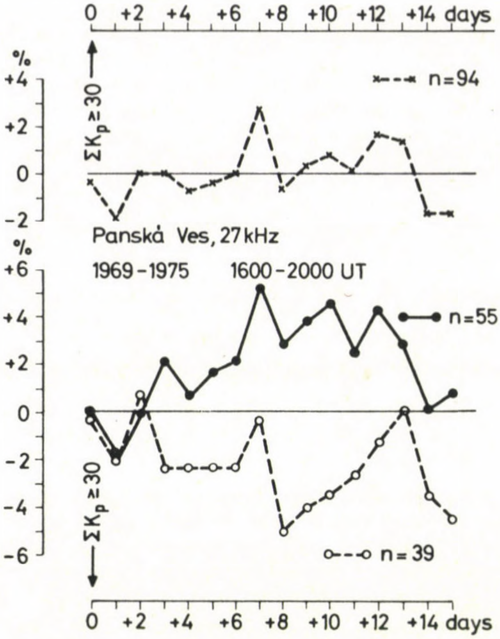

Fig. 1. Top: ARN-departures from a reference value at Panská Ves following geomagnetic disturbances (1969–1975). Bottom: ARN-departures in dependence of an after-effect in Pc 1-type pulsations, (full line: clear Pc 1 after-effect, dotted line: no Pc 1 after-effect)

departures (full line) beginning from day + 3 are positive for a rather long time, ceasing only after about a fortnight. The opposite is true in case of the remaining part of the selected disturbances. The ARN-departures (dotted line) remain below the reference level, when the disturbances are not followed by an after-effect in Pc 1-type pulsations.

For comparison, ARN-data determined during the period 1969–1975 at the Kühlungsborn station [11] were analysed in the same way as in case of Panská Ves. Samples were taken from the interval between 16 00 and 20 00 LT. (LT at Kühlungsborn = UT + 1 hour). The presentation of results corresponds to that applied in Fig. 1. The ARN-departures are again clearly positive following the disturbances associated with a real after-effect in pearl-type pulsations (indicated by full line in Fig. 2, bottom). The enhancement in the ARN-level lasts for about a fortnight like in case of Panská Ves. When the after-effect in Pc 1-type pulsations is missing no durable increase appears in the ARN-level (dotted line in Fig. 2, bottom).

Figure 3 shows the changes of the summarized duration of Pc 1-type pulsations observed in Irkutsk [12, 13, 14] in the interval from 1969 to 1975 around geomagnetic disturbances associated with a clear after-effect. The total duration of pearl-type pulsations (Pc 1) expressed in hours is presented for each day. The horizontal line indicates a normal level of Pc 1 occurrences. (It is the averaged duration for the days

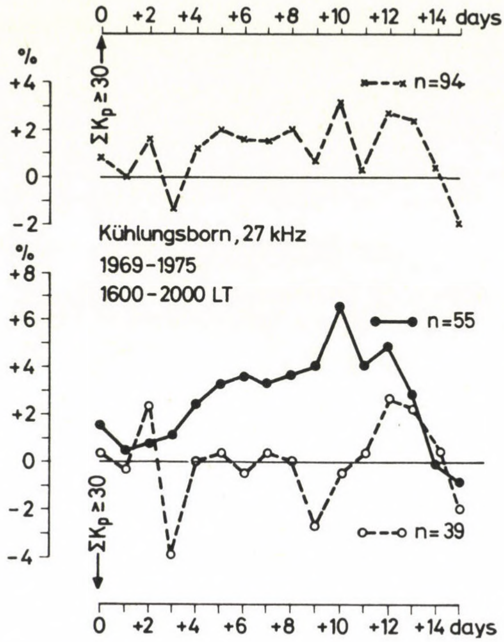

Fig. 2. The same as in Fig. 1, but for the Kühlungsborn station

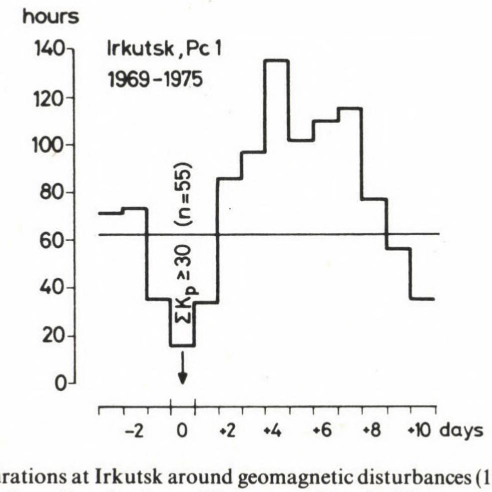

Fig. 3. Changes in Pc 1 durations at Irkutsk around geomagnetic disturbances (1969–1975) associated with a clear after-effect (horizontal line: normal level of Pc 1 occurrences)

-3, -2, $+8$, $+9$ and $+10$). In addition to a clear after-effect, rather low Pc 1-activity can be seen on the day of disturbance (0) and on the two days (-1 and $+1$) surrounding it. These results are in accordance with earlier ones obtained from a shorter interval [8, 9].

3. Discussion

The presented results show the after-effect in ARN related to the occurrence of Pc 1-type pulsations. Following geomagnetic disturbances associated with a clear after-effect in pearl-type pulsations, not only the ionospheric absorption of MF- and LF-radio waves is influenced effectively [8, 9], but a distinct enhancement is developing in the ARN-level measured at two stations. Consequently, there are certain connections between the after-effect in ARN and in Pc 1-type pulsations at middle latitudes.

It is known that the source of atmospheric radio noise is lightning discharges which radiate electromagnetic waves in the VLF-range propagating in the earth-ionosphere wave guide. If the upper wall of this wave guide (i.e. the ionosphere) is affected by the particle precipitation following certain geomagnetic disturbances, then the propagation conditions for VLF-waves change as a consequence of the ionospheric effect. Actually, the results presented in the previous section have shown this change by an increase of the ARN-level.

A further VLF radio noise phenomenon the whistlers also have their source in the electromagnetic energy radiated by lightning discharges in the atmosphere. Whistlers, however, propagate along geomagnetic field lines through the magnetosphere and their energy can be reflected back and forth between hemispheres. Along this path the whistlers may interact with trapped electrons. Thus together with plasmaspheric ELF-waves, whistlers can also alter the pitch-angle distribution of a population of trapped particles, some of which move into the loss cone and precipitate into the lower ionosphere.

In the foregoing the occurrence of plasmaspheric ELF-waves was inferred from the appearance of Pc 1-type pulsations. Like these pulsations, whistlers can be observed at ground-based stations. At Neustrelitz ($\varphi_{\text{geogr.}} = 53°17'$ N) the number of whistlers was counted within 2 minutes between the 50th and 52th minute of each hour (UT) of the day. Based on this sampling a mean daily whistler activity index (W) was published [11] using a scale between 0 and 9. These indices were available for the years 1969 and 1970, i.e. in years when the occurrence of pearl-type pulsations was also known at Irkutsk. The number of selected geomagnetic disturbances was 17 during 1969 and 1970. In 8 cases there was a real after-effect in Pc 1-type pulsations, in the remaining 9 cases no effect could be observed.

In Fig. 4, top, the full line shows the varying duration sums of Pc 1 pulsations around geomagnetic disturbances followed by a clear after-effect. Pearl-type pulsations

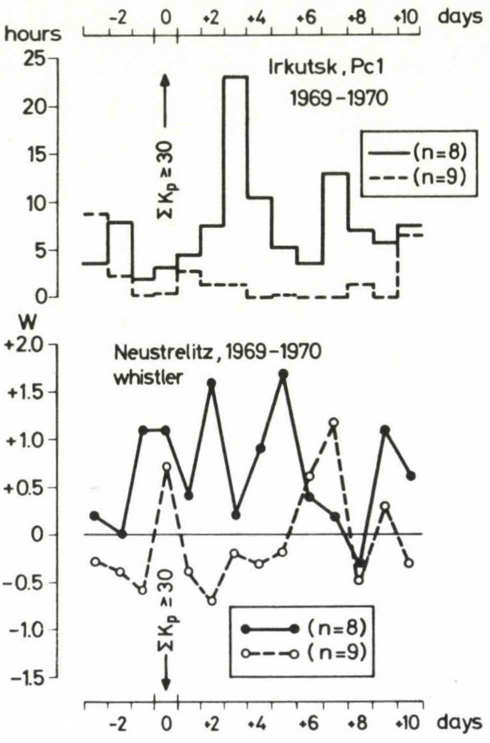

Fig. 4. Top: Changes in Pc 1 durations at Irkutsk around selected geomagnetic disturbances (1969–1970) (full line: disturbances with an after-effect, dotted line: disturbances without an after-effect). Bottom: Departures of whistler activity indices (W) from a reference value at Neustrelitz, in dependence of an after-effect in Pc 1-type pulsations, (full line: clear Pc 1 after-effect, dotted line: no Pc 1 after-effect)

were rather rare around the remaining disturbances, thus an after-effect did not appear (dotted line). Figure 4, bottom, presents the whistler activity in cases of both kinds of disturbances. Mean departures of activity indices (W) from the appropriate monthly average value are shown. Notwithstanding the fluctuations in the departures, the whistler activity was for a longer time above the average level when an after-effect could be observed in Pc 1 pulsations (full line) and mostly below the normal, when Pc 1 activity was missing (dotted line).

The sources of Pc 1 pulsations and plasmaspheric ELF-waves are quite different from that of whistlers. However, during the simultaneous occurrence of these phenomena after certain geomagnetic disturbances the increase in the ARN-level is well pronounced. This can be seen in Fig. 5, which shows the mean departures of the ARN-level measured at Kühlungsborn (between 16 00 and 20 00 LT) from a reference value determined in the same way as in the previous section. When the geomagnetic disturbances are associated with a clear after-effect in Pc1 pulsations and

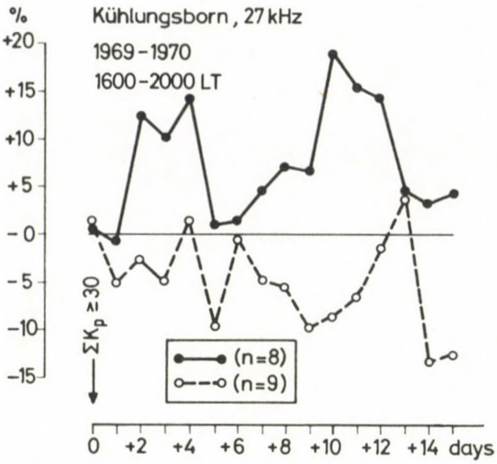

Fig. 5. ARN-departures from a reference value at Kühlungsborn following selected geomagnetic disturbances (1969–1970) (full line: clear Pc 1 after-effect and increased whistler activity, dotted line: no Pc 1 after-effect and decreased whistler activity)

simultaneously the whistler activity is also increased, then a rather distinct and long-lasting enhancement appears in the ARN-level (full line in Fig. 5). No positive effect can be seen in case of disturbances without the associated phenomena (dotted line).

In Fig. 5 the maximum increase of the ARN-level is about three times higher than that shown in the appropiate part of Fig. 2 for the same station, but for a longer period. Unfortunately the whistler indices were not available for the interval between 1971 and 1975. In addition the number of events is smaller in Fig. 5, therefore a detailed comparison of the results is restricted.

In both cases, i.e. for the shorter (1969–70) and the longer (1969–75) period it was known that Pc 1 activity was enhanced following a group of geomagnetic disturbances. In such cases the enhancement of plasmaspheric ELF-waves as well as an effective particle precipitation can also be supposed. Thus first of all, an increased ionization in the lower ionosphere could be responsible for the enhanced ARN-level. Either this common cause was more effective in the years 1969 and 1970 than in the whole period 1969–1975, or another cause had also contributed to the stronger enhancement of the ARN-level. The increased whistler activity should hint at more lightning sources, due to which a natural enhancement of the atmospheric radio noise may also be expected, because ARN similarly originates from lightning discharges. In any case, the real chances may fall short of these expectations due to the following facts.

Firstly, whistlers are generated not only by lightnings occurring at the same hemisphere where the observation site is situated. They are also radiated from remote sources at the opposite hemisphere and will travel from there along geomagnetic field lines in dependence of the actual propagation conditions. If these conditions are advantageous, the counting rates of whistlers will increase within an appropriate area around the observation site. Further, the influence of distant sources on the ARN-level is rather different, it depends on time and season. Consequently, an increase of the whistler activity can really be associated with a certain enhancement in the ARN-level, however, the degree of correlation may be variable for the mentioned causes.

References

1. Lauter E A, Knuth R: Precipitation of high energy particles into the upper atmosphere at medium latitudes after magnetic storms. *J. Atm. Terr. Phys.*, 29 (1967), 411–417.
2. Märcz F: Ionospheric absorption and geomagnetic activity. *Acta Geod. Geoph. Mont. Hung.*, 6 (1971), 83–93.
3. Märcz F: Further studies on ionospheric absorption and geomagnetic activity. *Acta Geod. Geoph. Mont. Hung.*, 8 (1973), 297–311.
4. Spjeldvik W N, Thorne R M: The cause of storm after effect in the middle latitude D-region. *J. Atm. Terr. Phys.*, 37 (1975), 777–795.
5. Lauter E A, Shäning B: Ergebnisse und Aspekte von Messungen des atmosphärischen Funkstörpegels im Längstwellenbereich in verschiedenen Breiten. NKGG DAW Veröff. Nr. II/3. (1966), 95–130. Berlin.
6. Bencze P, Szemerédy P: Variation of the level of atmospheric radio noise after geomagnetic disturbances I. *Acta Geod. Geoph. Mont. Hung.*, 8 (1973), 251–257.
7. Sátori G: Recent results concerning the investigation of the relation between the level of atmospheric radio noise and Forbush-decrease. *Acta Geod. Geoph. Mont. Hung.*, 16 (1981), 91–96.
8. Märcz F, Verő J: Ionospheric absorption and Pc1-type micropulsations following enhanced geomagnetic activity. *J. Atm. Terr. Phys.*, 39 (1977), 295–302.
9. Märcz F: Geomágneses utóhatás a rádióhullámok ionoszférikus abszorpciójában. Légköri és extraterresztrikus kapcsolatok. Kandidátusi értekezés, 1980 (Geomagnetic after-effect in ionospheric absorption of radio waves. Atmospheric and extraterrestrial relations. Cand. Dissertation, 1980. Sopron, 1–185).
10. Ionospheric data. Observatories Průhonice and Panská Ves. 1969–1975.
11. HHI Geophysikalische Beobachtungsergebnisse. 1969–1975.
12. Vinogradova V N: Pc 1 pulsations catalogue. Issledovanija po geomagnetismu, aeronomii i fizike solnca. Vüpusk 24. 1972. Irkutsk, 272–295.
13. Vinogradova V N: Pc 1 pulsations catalogue. Issledovanija po geomagnetizmu, aeronomii i fizike solnca. Vüpusk 34. 1974. Irkutsk, 110–123.
14. Vinogradova V N: Pc 1 pulsations catalogue. Issledovanija po geomagnetizmu, aeronomii i fizike solnca. Vüpusk 39. 1976. Irkutsk, 234–254.

Acta Geodaet., Geophys. et Montanist. Hung. Volume 18 (1—2), pp. 165—171 (1983)

FORMALIZED 2D INTERPRETATION OF THE INDUCTION ANOMALY IN THE SOVIET CARPATHIANS

M S ZHDANOV—IV M VARENTSOV

Institute of Terrestrial Magnetism, Ionosphere and Radio Wave Propagation USSR Academy of Sciences (IZMIRAN), Troitsk, Moscow Region, USSR

A I BILINSKY

Institute of Applied Problems of Mechanics and Mathematics Ukrainien SSR Academy of Sciences, Lvov, USSR

[Manuscript received April 16, 1982]

Results of the interpretation of electromagnetic data measured synchronously along International DSS profile III are presented. The observed geomagnetic fields have been separated into normal and anomalous, surface and deep parts respectively. The deep anomaly has been inverted by means of the analytical continuation technique and formalized trial procedure (tightening surfaces method).

Keywords: Carpathians; geoelectric anomaly; geomagnetic sounding; inverse problem

The Carpathian geomagnetic anomaly is one of the largest and most perfectly investigated regional anomalies. It is traced practically over the whole extension of the Carpathian folded system. It is studied most comprehensively in the Soviet Carpathians, where synchronous measurements of the electromagnetic fields have been made along several profiles (Bondarenko et al. 1972, Bondarenko and Bilinsky 1976)[1] and numerous MTS point observations were carried out (Rokityansky et al. 1976, Rokityansky 1975).

The results of the interpretations made by Bondarenko and Bilinsky (1976), Rokityansky et al. (1976), Ádám (1980), Berdichevsky and Zhdanov (1981) indicate the existence of a considerable anomaly of the electrical conductivity in the Earth's crust in the sharp transition zone between the Folded Carpathians and the Transcarpathian trough (Carpathian basin) (Fig. 1). The depth to the upper edge of the geoelectric inhomogeneity formally estimated from longitudinal MTS curves obtained in the region of the anomaly axis is in the range from 12 to 21 km (Rokityansky et al. 1976, Rokityansky 1975). The inversion of the magnetovariation profiling (in the class of

[1] It should be noted that synchronous geomagnetic measurements have also been made in large scale in the northern Carpathians (Jankowski et al. 1975, Jankowski et al. 1977, Jankowski et al. 1979, Ádám et al. 1975). The most detailed 2D geoelectric model corresponding to these data is given by Červ and Pek (1981).

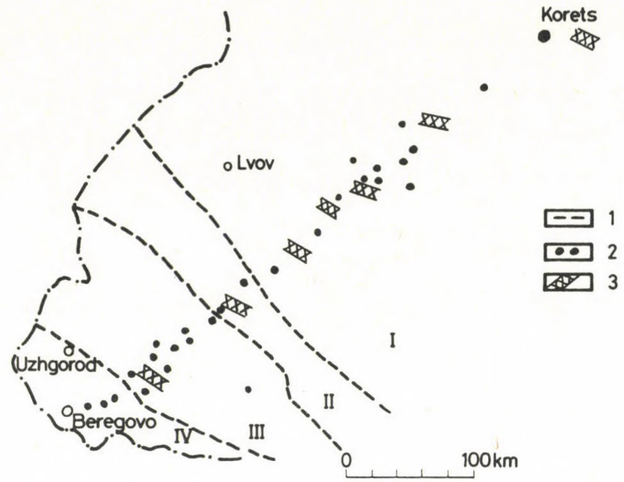

Fig. 1. Geomagnetic observations along the International DSS profile III. 1 — tectonic boundaries, 2 — observation points, 3 — fault zones, I — Russian Platform, II — Forecarpathian trough, III — Folded Carpathians, IV — Transcarpathian trough

simple models) points to the presence of a well-conducting body with an integral conductivity $\Sigma_i = (2-3) \cdot 10^8\ \mathrm{S} \cdot \mathrm{m}^2$ at a depth of 15 – 30 km. Available geothermal data and modern petrophysical ideas enable to suppose that at a depth of 10 – 20 km the electrical conductivity may raise up to 1 S/m (Rokityansky et al. 1976, Ádám 1980). This effect is attributed to a partial melting of rocks in the presence of some water (1 – 2%) in the amphibole facies of metamorphism. Together with deep geoelectrical inhomogeneities the Carpathian anomaly results from variations of the near surface conductivity — especially from the sharp increase of the thickness of the conductive sedimentary cover in the adjoining troughs. Thus the geoelectric structure in this region is rather complicated and quantitative results can be obtained only applying the modern methods of separation and interpretation of electromagnetic anomalies (Berdichevsky and Zhdanov 1981). These methods have been realized in the computerized SYSPAIN system specially intended for the analysis and interpretation of the magnetovariation profiling (Varentsov 1981).

MVP observations, obtained in the Beregovo–Korets interval along International DSS profile III (Fig. 1) (Bondarenko et al. 1972, Bondarenko and Bilinsky 1976) have been used for the interpretation with the SYSPAIN system.

In the first stage of the interpretation anomaly is separated into different parts. Synchronous values of the three components (H_x, H_z, E_y) of an E-polarized electromagnetic field with a period of one hour were considered in an even grid with

[2] $\Sigma_i = \iint_Q \sigma_i \mathrm{d}Q$, where Q is the region of the inhomogeneity and σ_i its conductivity.

the interval of 10 km. In the region left from the line $x = 60$ km (Fig. 2) — in the territory of Hungary, where observations have not been carried out field values have been extrapolated. The amplitudes $H_{x,z}$ of the observed magnetic field are shown in Fig. 2a. All amplitudes are normalized to the value of the horizontal magnetic field in Korets (Fig. 1).

The simplest model of the normal geoelectric section — a homogeneous halfspace with an electrical conductivity $\sigma_n = 10^{-3}$ S/m—was studied as it has been shown (Berdichevsky and Zhdanov 1981, Ádám and Tátrallyay 1979) that the addition of deep well-conducting layers do not change significantly the geomagnetic anomaly for a one hour period. In the model mentioned the observed geomagnetic fields were separated into normal and anomalous parts (Berdichevsky and Zhdanov 1981). The normal field was found to be rather close to the plane wave model and the anomalous field is plotted in Fig. 2b. Next a model of a horizontally inhomogeneous subsurface layer with a thickness of 10 km and variable conductivity $\sigma_s(x)$ was considered. The conductivity distribution $\sigma_s(x)$ was determined by Bilinsky and Shilova by a complex analysis of available geological and geophysical data. Using the observed surface electric field and applying the approximate boundary conditions on the both sides of the layer (Berdichevsky and Zhdanov 1981), the surface geomagnetic anomalies $H^S_{x,z}$ (Fig. 2c) were obtained. These fields are four times less than the total anomaly indicating again the deep nature of the Carpathian geomagnetic anomaly. Subtracting the surface anomaly $H^S_{x,z}$ from the total anomaly $H^a_{x,z}$ we get the deep anomaly $H^D_{x,z}$ (Fig. 2d) free of subsurface distortions. The shape of this anomaly is quite symmetrical and it is rather typical for the anomalies originated from local deep conducting objects.

In the following stage the deep anomaly was investigated by different 2D inverse methods. The simplest model of an infinite line current in a homogeneous space with a conductivity 10^{-3} *S/m* was used to detect the approximate location of the center of deep anomalous currents (Jankowski et al. 1977, Summers 1981). The depth to the effective line current was found from the H^D_z/H^D_x ratio to be about 12 km.

In a next step the analytical continuation technique was used (Berdichevsky and Zhdanov 1981, Varentsov 1981). Figure 2e shows a map of the analytically continued magnetic field H^D_z and Fig. 2f a map of the continuation of the flux function of the magnetic field (being proportional to the electric field). The well conducting inhomogeneity appears rather clearly on both maps. An analysis of the continued fields shows that the depth to the upper edge of inhomogeneity is 10 – 13 km, and its width does not exceed 10 – 20 km.

The interpretation was completed by the formalized inversion using the tightening surfaces method (Berdichevsky and Zhdanov 1981, Varentsov 1981, Zhdanov and Varentsov 1980, Zhdanov and Varentsov 1982). The model of a deep inhomogeneity constructed from the results of analytical continuation was checked with different initial approximations of the shape of the conductive body, laying at a depth of 20 – 30 km, (dotted contours in Fig. 3a). In all cases the location of

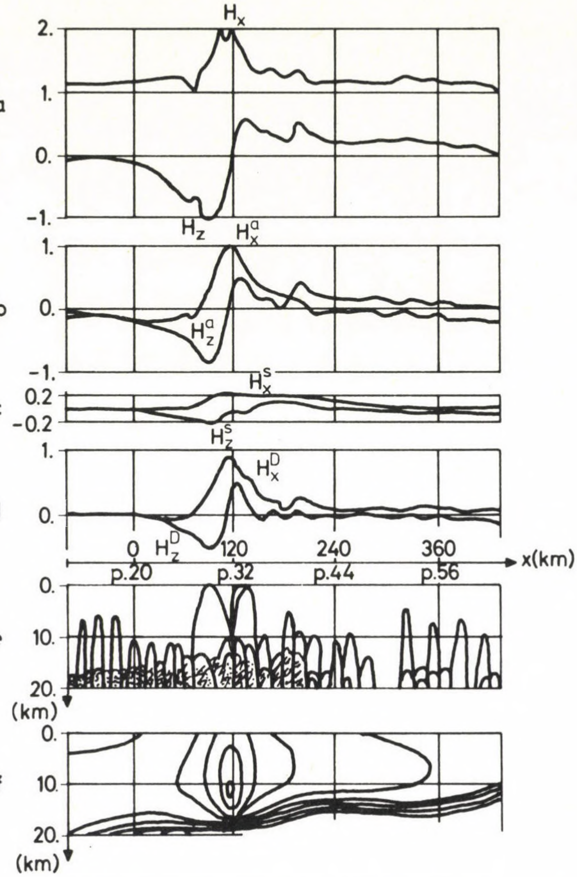

Fig. 2. Separation and analytical continuation of geomagnetic fields: a — observed fields, *b* — anomalous fields, *c* — surface part of the anomaly, *d* — deep part of the anomaly, *e* — analytical continuation of the H_z^D field, *f* — analytical continuation of the magnetic field flux function

the selected models is in a good agreement with the results of the analytical continuation. The trial error was reduced to 20 – 30%, being in agreement with the errors of the initial data.

A more accurate inhomogeneity model (a circular cylinder with a diameter of 10 km, its center at a depth of 15 km, electrical conductivity $\sigma_i = 1.0\ S/m$ — dotted contours, Fig. 3b) has been used as a new initial approximation for the tightening surfaces method. Figure 3b shows very similar trial results obtained in this case for the different components of the deep magnetic anomaly. A comparison between deep geomagnetic anomalies separated from the observed field and calculated theoretically for the last inversion results is given in Fig. 4. The areas of all inhomogeneity regions, constructed in the trial process are practically equal (about 70 km^2), i.e. their integral

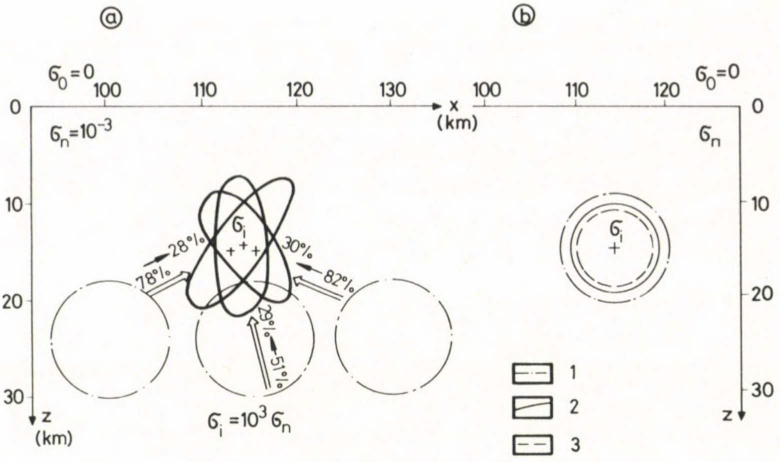

Fig. 3. Inverse problem solution using the tightening surfaces method: a — localization of inhomogeneity, *b* — further determination of its shape, 1 — initial approximations of the conductive inhomogeneity, 2 — models selected by the H_z^D field, 3 — model selected by H_x^D field

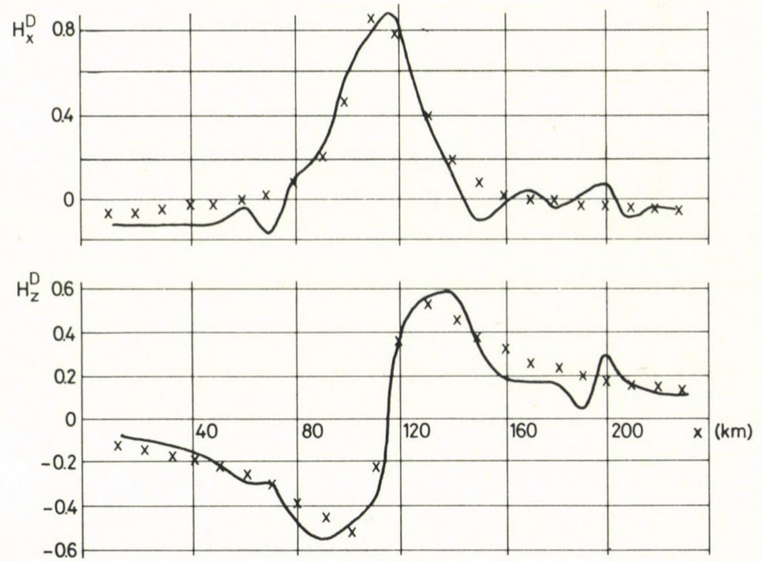

Fig. 4. Deep magnetic anomalies, calculated for the models in Fig. 3b (crosses), and separated from the observed field (solid lines)

conductivity Σ_i is approximately $0.7 \cdot 10^8$ S · m^2. This value is very close to those by Červ and Pek (1981) for the geoelectric model along International DSS profile V in the northern Carpathians. However, it is worth noting that the shape of the inhomogeneity can be determined rather crudely mainly because of substantial errors in the initial data (especially in the phases of the electromagnetic fields).

The results of this interpretation correlate fairly well with the latest generalized estimations made by Ádám (1980). At the same time it should be emphasized that the conductive inhomogeneity, defined by the deep geomagnetic anomaly appeared to be closer to the Earth's surface (at a depth of 10 – 20 km), than from a simple interpretation of the observed anomaly (Rokityansky et al. 1976, Rokityansky 1975).

In the separation of the deep anomaly, normal and surface components with comparatively low spatial frequencies (Fig. 2) were subtracted from the observed field. Thus, the high frequency part of the resulting spatial spectrum becomes relatively more intensive than in the observed anomaly. This explains the decrease of the depth to the upper edge of inhomogeneity and of the value of the integral conductivity in the constructed model.

Acknowledgements

In conclusion the authors express their thanks to Mrs. A M Shilova, who prepared the geoelectrical model of subsurface inhomogeneous layer, and Mrs. N Baglaenko, who took part in the interpretation of the anomaly by the tightening surfaces method.

References

Ádám A 1980: The change of electrical structure between an orogenic and ancient tectonic area (Carpathians and Russian Platform). *Geomagnetism and Geoelectricity*, 32, 1–46.

Ádám A, Tátrallyay M 1979: Numerical electromagnetic modelling of the asthenosphere in the deep structures of the Carpathians. *Gerlands Beitr. Geophysik*, 88, 240–248.

Ádám A, Holló L, Verő J, Wallner Á 1975: New data about the Carpathian conductivity anomaly. In: *To the 75th birthday of Prof. A. Tárczy-Hornoch: Communications of the Geod. Geophys. Res. Inst. Sopron*, 220–239.

Berdichevsky M N, Zhdanov M S 1981: Interpretation of the anomalies of the variable electromagnetic field of the Earth. Nedra, Moscow (in Russian).

Bondarenko A P, Bilinsky A I 1976: Anomaly of geomagnetic bays in the East Carpathians. In: *Geoelectric and geothermal studies*, Ed. A Ádám, Akadémiai Kiadó, Budapest, 589–599.

Bondarenko A P, Bilinsky A I, Sedova F I 1972: Geoelectromagnetic variations in the Soviet Carpathians. Naukova dumka, Kiev (in Russian).

Červ V, Pek J 1981: Numerical solution of the two-dimensional inverse geomagnetic induction problem. *Studia geoph. et geod.*, 25, 69–80.

Jankowski J, Szymanski A, Pěčova J, Praus O, Petr V 1975: Electromagnetic induction study on DSS profile No V (Carpathians). *Studia geoph. et geod.*, 19, 95–102.

Jankowski J, Szymanski A, Peč K, Červ V, Petr V, Pěčova J, Praus O 1977: Anomalous induction in the Carpathians. *Studia geoph. et geod.*, 21, 35–57.

Jankowski J, Petr V, Pěčova J, Praus O 1979: Induction vector estimates in the Polish–Czechoslovak part of the Carpathians. *Studia geoph. et geod.*, 23, 89–93.

Rokityansky I 1975: Investigation of electric conductivity anomalies by the method of magnetovariational profiling. Naukova dumka, Kiev (in Russian).

Rokityansky I I, Amirov V K, Kulik S N, Logvinov I M, Shuman V N 1976: The electric conductivity anomaly in the Carpathians. In: *Geoelectric and geothermal studies*, Ed. A Ádám, Akadémiai Kiadó, Budapest, 604–612.

Summers D M 1981: Interpreting the magnetic fields associated with two-dimensional induction anomalies. *Geophys. J. R. astr. Soc.*, 65, 535–552.

Varentsov Iv M 1981: Development of the methods for magnetovariational profiling data interpretation in the class of two-dimensional heterogeneous models. Cand. dissertation, IZMIRAN SSSR, Moscow (in Russian).

Zhdanov M S, Varentsov Iv M 1980: Interpretation of local geomagnetic anomalies by tightening surfaces method. AN SSSR Geologiya i Geofizika, N 12, 106–117 (in Russian).

Zhdanov M S, Varentsov Iv M 1982: Interpretation of the deep local electromagnetic anomalies by the formalized trial procedure. *Geophys J. R. astr. Soc.* (in press).

Acta Geodaet., Geophys. et Montanist. Hung. Volume 18 (1—2), pp. 173—186 (1983)

DERIVATION OF COEFFICIENTS REDUCING MAGNETIC ANOMALIES TO THE MAGNETIC POLE AND TO THE MAGNETIC EQUATOR

K. KIS[1]

Department of Geophysics, Eötvös Loránd University, Budapest

[Manuscript received May 5, 1982]

Reduction of vertical and total magnetic anomalies to the magnetic pole as well as reduction of horizontal magnetic anomalies to the magnetic equator are effective tools for the interpretation of corresponding anomalies. The coefficients (the digital weight function) have not been derived directly from the theoretical system functions by their inverse Fourier transform. The inverse Fourier transformation can be carried out with the application of a suitable truncating function. The actual system function of the derived coefficients is a good approximation to the theoretical system function. The effectivity of the suggested method is illustrated by the reduction of synthetic anomalies.

Keywords: inverse Fourier transform; reduction to magnetic equator; reduction to magnetic pole; magnetic anomaly

Introduction

The positions of the maxima and minima of the magnetic anomalies are the functions of the magnetic declination and inclination as well. This fact makes difficult the interpretation of the magnetic anomalies and their comparison with other geological and geophysical data.

In order to get rid of this unwanted effect an appropriate transformation, i.e. the so-called reduction of the magnetic anomalies to the pole was suggested by several authors. The studies took Poisson's relation

$$W = \frac{J}{4\pi\mu_0 G\rho} \frac{\partial}{\partial s} V \tag{1}$$

as starting point where W is the magnetic potential, J the magnetic polarization, μ_0 the permeability of vacuum, G the universal gravitational constant, ρ the density, s the direction of the magnetic polarization and V the gravity potential (Telford et al. 1976). Baranov (1957, 1975), Baranov and Naudy (1969) presented a method and coefficients

[1] H-1083 Budapest, Kun Béla tér 2., Hungary

in hexagonal grid reducing the magnetic anomalies to the magnetic pole. Bhattacharyya (1965), Kanasewich and Agarwal (1970) suggested an other approach carrying out the reduction in the frequency domain. Seiberl (1979) also offered coefficients for the reduction of the magnetic anomalies.

Theoretical system function

A fixed-parameter linear system may be represented in a frequency domain by its system function (transfer function). The theoretical system function of the reduction to the magnetic pole as well as to the magnetic equator can be obtained without using Poisson's relation (Kis 1981). The theoretical system function of the reduction to the magnetic pole of the vertical magnetic anomalies is expressed as:

$$S_Z(f_x, f_y) = \frac{(f_x^2 + f_y^2)^{1/2}}{N(f_x^2 + f_y^2)^{1/2} + j(Lf_x + Mf_y)} \tag{2}$$

where f_x and f_y are the spatial frequencies in the x and y directions, respectively. The directional cosines are defined by

$$\begin{aligned} L &= \cos\alpha\cos\beta \\ M &= \cos\alpha\sin\beta \\ N &= \sin\alpha, \end{aligned} \tag{3}$$

where α and β denote the inclination and declination of the magnetic polarization. The theoretical system function of the reduction to the magnetic equator of the horizontal anomalies may be given in the form:

$$S_H(f_x, f_y) = -\frac{f_x\cos D + f_y\sin D}{Lf_x + Mf_y - jN(f_x^2 + f_y^2)^{1/2}} \tag{4}$$

where D denotes the magnetic declination. Equation (4) differs in a negative sign from the form given in a previous paper of the same author (Kis 1981). The negative sign involves a phase-shift which equals to π, i.e. the horizontal anomaly reduced to the magnetic equator appears in a maximum form instead of a minimum one. The theoretical system function of reduction to the magnetic pole of the total magnetic anomalies may be obtained in the form of the following equation:

$$S_T(f_x, f_y) = \frac{f_x^2 + f_y^2}{(N(f_x^2 + f_y^2)^{1/2} + j(Lf_x + Mf_y))\,(n(f_x^2 + f_y^2)^{1/2} + j(lf_x + mf_y))} \tag{5}$$

where the directional cosines are

$$l = \cos I \cos D$$
$$m = \cos I \sin D \tag{6}$$
$$n = \sin I.$$

I and D denote the magnetic inclination and declination, respectively.

The complex system function can be characterized by its amplitude density spectrum $A(f_x, f_y)$ and by its phase density spectrum $P(f_x, f_y)$. For them we can write:

$$A(f_x, f_y) = (\mathrm{Re}^2[S(f_x, f_y)] + \mathrm{Im}^2[S(f_x, f_y)])^{1/2} \tag{7}$$

and

$$P(f_x, f_y) = \tan^{-1} \frac{\mathrm{Im}[S(f_x, f_y)]}{\mathrm{Re}[S(f_x, f_y)]} \tag{8}$$

where $S(f_x, f_y)$ denotes whichever of the $S_Z(f_x, f_y)$, $S_H(f_x, f_y)$ and $S_T(f_x, f_y)$ system functions. In the upper part of the Figs 1–3 the contours of the amplitude and phase density spectra are depicted for the parameters $\alpha = 60°$, $\beta = 0°$, $I = 60°$, $D = 0°$. These values are approximately equal to the inclination and declination in the territory of Hungary. In these figures the spatial frequencies are given in dimensionless units. The dimensionless or relative frequencies are defined by $f'_x = \tau f_x$ and $f'_y = \tau f_y$, where τ is the sampling unit.

It can be seen that the system functions $S_Z(f_x, f_y)$, $S_H(f_x, f_y)$ and $S_T(f_x, f_y)$ depend only on the direction of the magnetic polarization and the magnetic direction. They are independent of the other parameters of the magnetic source as well.

Derivation of the coefficients

A fixed-parameter linear system can be characterized in a space domain by its weight function (unit impulse response). The result of the reductional operation $G_{out}(x, y)$ is given in a space domain by the

$$G_{out}(x, y) = \int_{-\infty}^{+\infty} \int_{-\infty}^{+\infty} G_{in}(u, v) S(x-u, y-v) \mathrm{d}u \mathrm{d}v \tag{9}$$

convolution integral of the input anomaly $G_{in}(x, y)$ and the weight function $S(x, y)$ or its digitized version. In Eq. (9) $G_{in}(x, y)$ denotes either the vertical magnetic anomaly $Z(x, y)$ or the total magnetic anomaly $T(x, y)$ or the horizontal magnetic anomaly $H(x, y)$ which have to be reduced; $S(x, y)$ the weight function $S_Z(x, y)$ or $S_T(x, y)$ of the reduction to the magnetic pole or the weight function $S_H(x, y)$ of the reduction to the

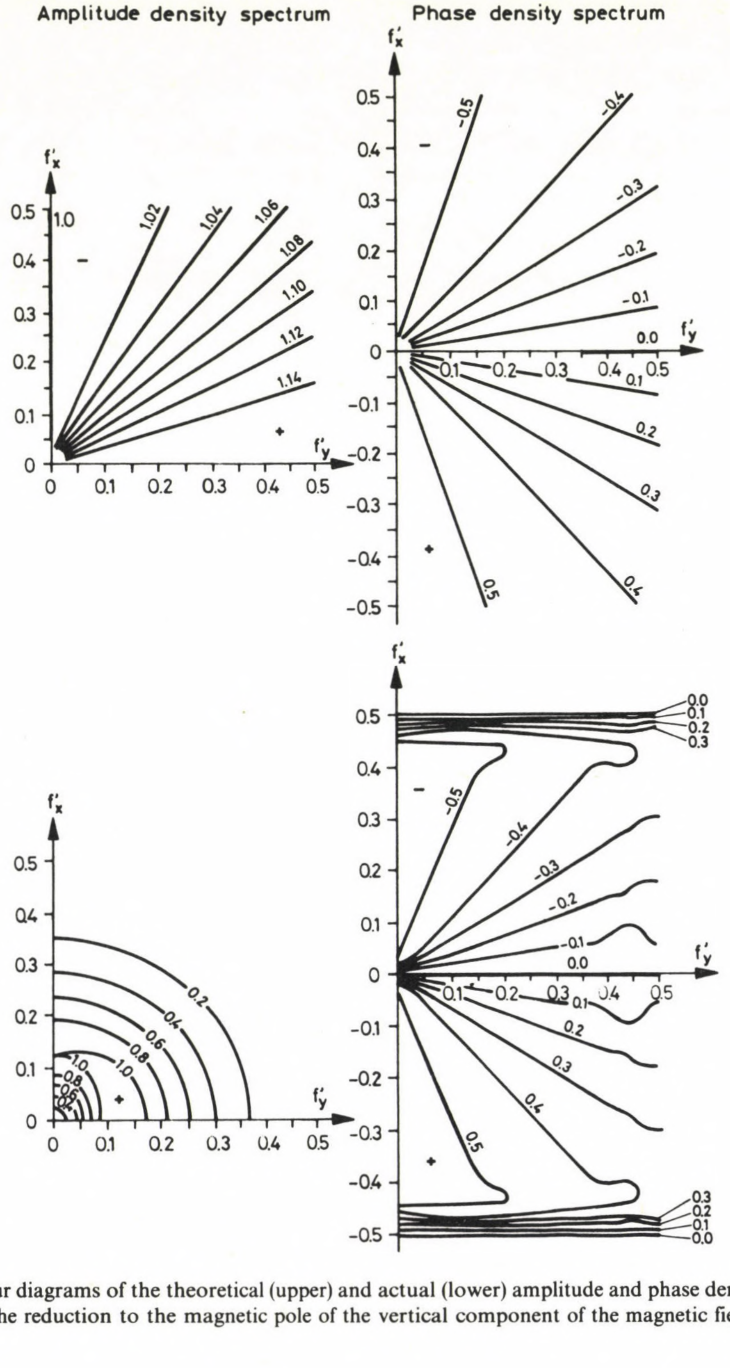

Fig. 1. Contour diagrams of the theoretical (upper) and actual (lower) amplitude and phase density spectra for the reduction to the magnetic pole of the vertical component of the magnetic field

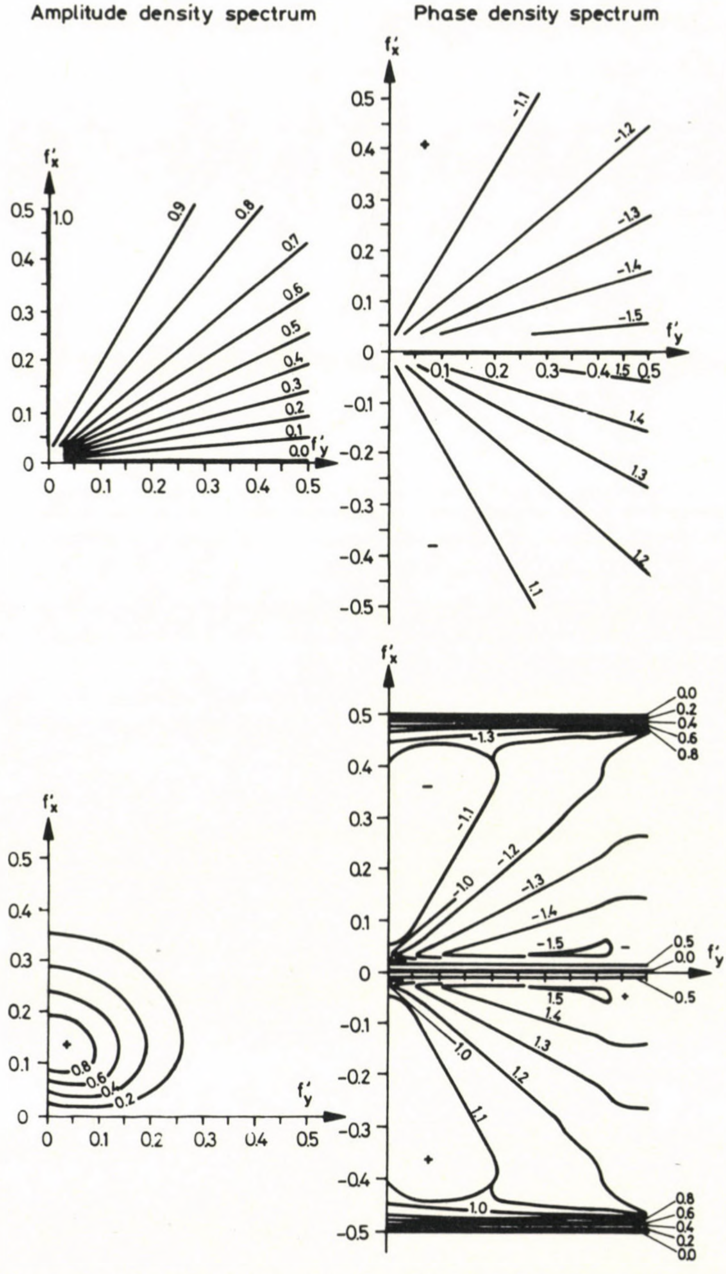

Fig. 2. Contour diagrams of the theoretical (upper) and actual (lower) amplitude and phase density spectra for the reduction to the magnetic equator of the horizontal component of the magnetic field

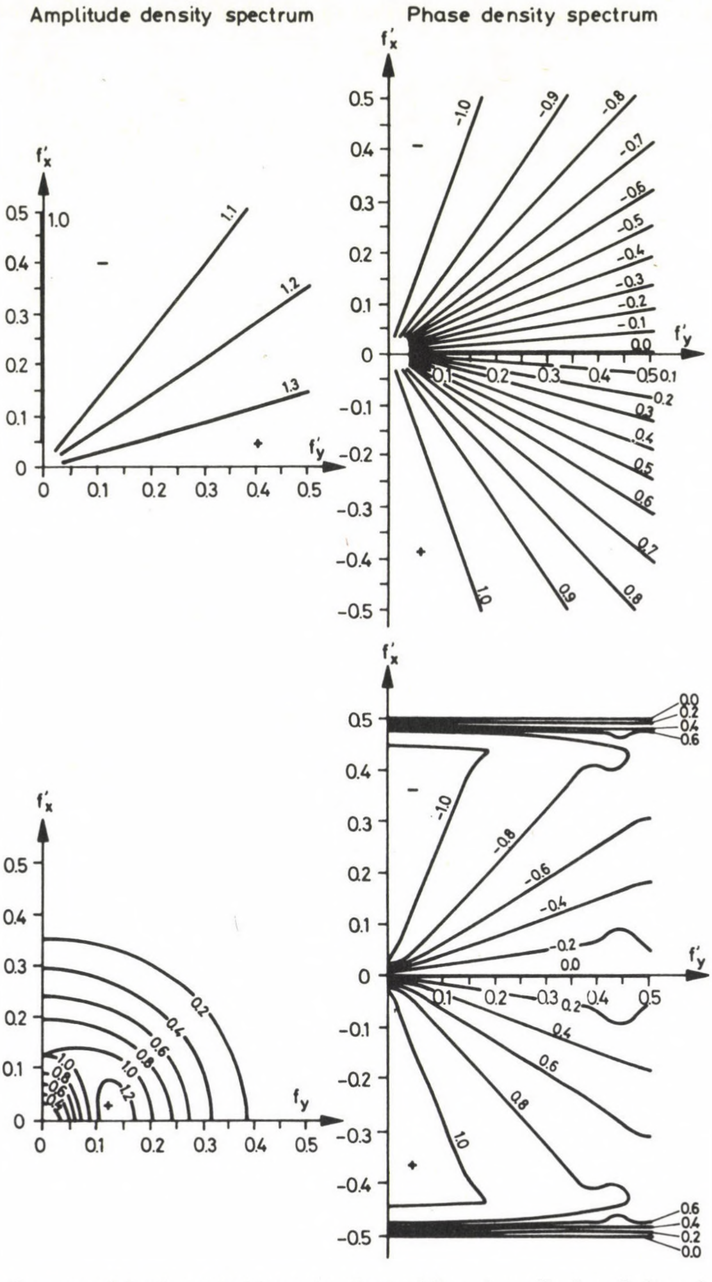

Fig. 3. Contour diagrams of the theoretical (upper) and actual (lower) amplitude and phase density spectra for the reduction to the magnetic pole of the total magnetic field

magnetic equator. $G_{out}(x, y)$ means the reduced vertical, total or horizontal anomalies. The weight functions $S_Z(x, y)$, $S_H(x, y)$ and $S_T(x, y)$ are the inverse Fourier transforms of the system functions $S_Z(f_x, f_y)$, $S_H(f_x, f_y)$ and $S_T(f_x, f_y)$ which are needed for the evaluation of the convolutional integrals.

Let us denote whichever of the system functions $S_Z(f_x, f_y)$, $S_H(f_x, f_y)$, $S_T(f_x, f_y)$ by $S(f_x, f_y)$, and $S(x, y)$ whereby one of the weight functions corresponds to the system function. The weight function is given by the inverse Fourier transform

$$S(x, y) = \int_{-\infty}^{+\infty} \int_{-\infty}^{+\infty} \cdot S(f_x, f_y) e^{j2\pi(f_x x + f_y x)} \mathrm{d} f_x \mathrm{d} f_y \tag{10}$$

if the $S(f_x, f_y)$ function exists. The (2), (4), (5) system functions have a finite discontinuity at $f_x = f_y = 0$.

For the calculation of the inverse Fourier transform a suitable truncating function has been applied. The aim of the application of the truncating function is two-fold. It eliminates the discontinuity at the origin and removes the disadvantageous enhancement of the system functions in the higher frequency domain. The maintenance of the phaseshift properties of the system functions is also required. Thus, the application of a truncating function should be the band-pass filter proposed by Meskó (1969), which meets the demands mentioned above. The system function of the suggested band-pass filter is

$$S_{BP}(f_x, f_y) = C\left(e^{-\frac{36^2(f_x^2 + f_y^2)^{1/2}}{m_1^2}} - e^{-\frac{36^2(f_x^2 + f_y^2)^{1/2}}{m_2^2}}\right) \tag{11}$$

the normalization factor C equals to:

$$C = \frac{1}{e^{-\frac{36^2 f_{r\max}^2}{m_1^2}} - e^{-\frac{36^2 f_{r\max}^2}{m_2^2}}} \tag{12}$$

where

$$f_{r\max} = \frac{m_1 m_2}{36} \left(\frac{2}{m_1^2 - m_2^2} \log \frac{m_1}{m_2} \right)^{1/2} \tag{13}$$

and the $m_1 > m_2$ relation is valid for the parameters of the band-pass filter.

The system function $S^*(f_x, f_y)$ truncated by a band-pass filter can be expressed in the form:

$$S^*(f_x, f_y) = (\mathrm{Re}[S(f_x, f_y)] + j\,\mathrm{Im}[S(f_x, f_y)]) S_{BP}(f_x, f_y). \tag{14}$$

This kind of system function has no discontinuity because the value of the band-pass filter at the origin is zero which fulfils the conditions mentioned above.

The coefficients, the digitized weight function $S(x, y)$ can be obtained by the inverse Fourier transform of the system function truncated by a band-pass filter:

$$S(x, y) = \frac{1}{M^2} \sum_{p=-\frac{M}{2}}^{\frac{M}{2}} \sum_{r=-\frac{M}{2}}^{\frac{M}{2}} S^*\left(\frac{p}{M}, \frac{r}{M}\right) e^{j\frac{2\pi}{M}(xp+yr)} \tag{15}$$

where x and y are the discrete space variables

$$\begin{aligned} x &= -\frac{N}{2}, -\frac{N}{2}+1, \dots, 0, \dots, \frac{N}{2} \\ y &= -\frac{N}{2}, -\frac{N}{2}+1, \dots, 0, \dots, \frac{N}{2} \end{aligned} \tag{16}$$

(the sampling unit is regarded one unit), p and r are the discrete spatial frequency variables

$$\begin{aligned} p &= -\frac{M}{2}, -\frac{M}{2}+1, \dots, 0, \dots, \frac{M}{2} \\ r &= -\frac{M}{2}, -\frac{M}{2}+1, \dots, 0, \dots, \frac{M}{2}. \end{aligned} \tag{17}$$

In this way three sets of coefficients, i.e. the digitized weight functions $S_Z(x, y)$, $S_H(x, y)$, $S_T(x, y)$ can be determined. The numerical calculations have been carried out for the parameters $m_1 = 9$, $m_2 = 3$, $M = 32$, $N = 14$. Tables I–III contain the coefficients for reducing the vertical, horizontal and total magnetic anomalies, respectively. Utilizing the symmetry the tables contain one half of the sets of the coefficients (the first column is the vertical symmetry axis).

Table I

Coefficients reducing the vertical magnetic anomalies to the magnetic pole for the parameters $\beta = 0°$, $\alpha = 60°$

−0.0013	−0.0013	−0.0013	−0.0012	−0.0009	−0.0007	−0.0005	−0.0003
−0.0028	−0.0027	−0.0026	−0.0023	−0.0017	−0.0012	−0.0008	−0.0005
−0.0040	−0.0043	−0.0045	−0.0041	−0.0031	−0.0020	−0.0012	−0.0006
−0.0051	−0.0060	−0.0072	−0.0068	−0.0051	−0.0032	−0.0018	−0.0009
0.0028	−0.0026	−0.0096	−0.0104	−0.0077	−0.0046	−0.0024	−0.0011
0.0494	0.0211	−0.0102	−0.0147	−0.0105	−0.0060	−0.0030	−0.0014
0.2016	0.0979	−0.0064	−0.0190	−0.0129	−0.0070	−0.0032	−0.0015
0.2563	0.1188	−0.0117	−0.0219	−0.0135	−0.0070	−0.0031	−0.0015
0.0691	0.0165	−0.0263	−0.0208	−0.0118	−0.0059	−0.0026	−0.0011
−0.0270	−0.0286	−0.0243	−0.0154	−0.0086	−0.0043	−0.0018	−0.0007
−0.0212	−0.0192	−0.0144	−0.0093	−0.0053	−0.0026	−0.0010	−0.0003
−0.0100	−0.0092	−0.0072	−0.0047	−0.0027	−0.0012	−0.0005	−0.0001
−0.0046	−0.0041	−0.0031	−0.0020	−0.0011	−0.0004	−0.0001	0.0000
−0.0011	−0.0011	−0.0010	−0.0006	−0.0003	−0.0001	0.0000	0.0001
−0.0006	−0.0004	−0.0002	0.0000	0.0000	0.0001	0.0001	0.0001

Table II

Coefficients reducing the horizontal magnetic anomalies to the magnetic equator for the parameters $\beta=0°$, $\alpha=60°$, $D=0°$

0.0004	0.0001	−0.0004	−0.0007	−0.0007	−0.0007	−0.0005	−0.0004
0.0006	0.0004	−0.0002	−0.0008	−0.0011	−0.0010	−0.0007	−0.0005
0.0049	0.0036	0.0012	−0.0006	−0.0013	−0.0013	−0.0009	−0.0006
0.0130	0.0100	0.0042	0.0000	−0.0015	−0.0015	−0.0011	−0.0006
0.0370	0.0265	0.0098	0.0010	−0.0015	−0.0016	−0.0011	−0.0006
0.0869	0.0564	0.0158	0.0010	−0.0017	−0.0015	−0.0009	−0.0005
0.0952	0.0549	0.0088	−0.0018	−0.0019	−0.0010	−0.0005	−0.0002
−0.0687	−0.0483	−0.0190	−0.0058	−0.0015	−0.0003	0.0001	0.0002
−0.1342	−0.0862	−0.0256	−0.0049	−0.0001	0.0008	0.0007	0.0005
−0.0455	−0.0297	−0.0086	−0.0003	0.0017	0.0016	0.0011	0.0007
−0.0050	−0.0021	0.0014	0.0028	0.0027	0.0020	0.0013	0.0008
0.0047	0.0045	0.0041	0.0036	0.0027	0.0019	0.0012	0.0007
0.0039	0.0039	0.0037	0.0030	0.0022	0.0015	0.0009	0.0006
0.0035	0.0032	0.0026	0.0021	0.0015	0.0010	0.0007	0.0004
0.0016	0.0017	0.0016	0.0013	0.0009	0.0007	0.0005	0.0003

Table III

Coefficients reducing the total magnetic anomalies to the magnetic pole for the parameters $\beta=0°$, $\alpha=60°$, $D=0°$, $I=60°$

0.0003	−0.0001	−0.0009	−0.0014	−0.0016	−0.0014	−0.0010	−0.0007
0.0000	−0.0006	−0.0018	−0.0027	−0.0028	−0.0022	−0.0015	−0.0010
0.0027	0.0007	−0.0029	−0.0048	−0.0047	−0.0035	−0.0022	−0.0012
0.0088	0.0041	−0.0042	−0.0081	−0.0074	−0.0050	−0.0029	−0.0015
0.0339	0.0177	−0.0052	−0.0128	−0.0109	−0.0068	−0.0036	−0.0017
0.1105	0.0559	−0.0072	−0.0195	−0.0145	−0.0082	−0.0040	−0.0017
0.2593	0.1226	−0.0132	−0.0266	−0.0168	−0.0086	−0.0038	−0.0016
0.2220	0.0866	−0.0316	−0.0296	−0.0162	−0.0076	−0.0030	−0.0013
0.0089	−0.0247	−0.0411	−0.0245	−0.0123	−0.0055	−0.0020	−0.0006
−0.0420	−0.0383	−0.0267	−0.0149	−0.0074	−0.0032	−0.0010	−0.0001
−0.0200	−0.0175	−0.0121	−0.0071	−0.0035	−0.0012	−0.0002	0.0002
−0.0064	−0.0059	−0.0043	−0.0025	−0.0010	−0.0001	0.0003	0.0004
−0.0022	−0.0017	−0.0009	−0.0003	0.0002	0.0004	0.0005	0.0004
0.0007	0.0005	0.0004	0.0005	0.0006	0.0005	0.0004	0.0003
0.0002	0.0004	0.0006	0.0006	0.0005	0.0004	0.0003	0.0003

The actual system function, i.e. the numerical Fourier transform of the derived coefficients were calculated. The lower part of the Figs 1–3 depict the amplitude density spectra and the phase density spectra of the actual system functions. The digitized weight function makes its spectrum periodical. This phenomenon can be seen in the actual spectra. The actual system functions are in good agreement with the theoretical ones.

Synthetic examples

The operations in the space domain are illustrated by the reduction of the vertical and horizontal components of the magnetic field as well as of the total magnetic field due to a dipole.

The vertical component of the magnetic field due to a dipole can be seen in the left side of Fig. 4. The dipole is placed at the point $(0, 0, d)$ where $d=5$ (in sampling units) and m_d, i.e. its magnetic moment is equal to $4\pi 10^{-4}$ Vms. The vertical component of the magnetic field due to the dipole is given by

$$Z(x, y, 0)= -\frac{m_d}{4\pi}\left(\frac{3Lxd}{r^5}+\frac{3Myd}{r^5}-\frac{3Nd^2}{r^5}+\frac{N}{r^3}\right) \tag{18}$$

where

$$r=(x^2+y^2+d^2)^{1/2}. \tag{19}$$

For the directional cosines given by Eq. (3) the values $\alpha=60°$, $\beta=0°$ have been substituted. The middle part of Fig. 4 shows the result when band-pass filtering was applied without reduction to the pole. This kind of band-pass filter causes changes only in the amplitude of the anomaly and cannot cause any phaseshift at all. The field reduced to the magnetic pole can be seen on the right side of this figure. Reduction to the pole was computed by the coefficients of Table I.

The same procedures are illustrated in Fig. 5 for the horizontal component of the same dipole given by the formula

$$\begin{aligned} H(x, y, 0) &= \frac{m_d}{4\pi}\cos D\left(\frac{3Lx^2}{r^5}+\frac{3Mxy}{r^5}-\frac{3Nxd}{r^5}-\frac{L}{r^3}\right)+ \\ &+\frac{m_d}{4\pi}\sin D\left(\frac{3Lxy}{r^5}+\frac{3My^2}{r^5}-\frac{3Nyd}{r^5}-\frac{M}{r^3}\right). \end{aligned} \tag{20}$$

The original anomaly, its band-pass filtered version and the anomaly reduced to the magnetic equator are shown (from left to right). The reduction to the magnetic equator was computed by the coefficients of Table II.

Figure 6 depicts the total magnetic field of the same dipole presented by the formula

$$\begin{aligned} T(x, y, 0) &= \frac{m_d}{4\pi}l\left(\frac{3Lx^2}{r^5}+\frac{3Mxy}{r^5}-\frac{3Nxd}{r^5}-\frac{L}{r^3}\right)+ \\ &+\frac{m_d}{4\pi}m\left(\frac{3Lxy}{r^5}+\frac{3My^2}{r^5}-\frac{3Nyd}{r^5}-\frac{M}{r^3}\right)+ \\ &+\frac{m_d}{4\pi}n\left(\frac{3Lxd}{r^5}-\frac{3Myd}{r^5}+\frac{3Nd^2}{r^5}-\frac{N}{r^3}\right), \end{aligned} \tag{21}$$

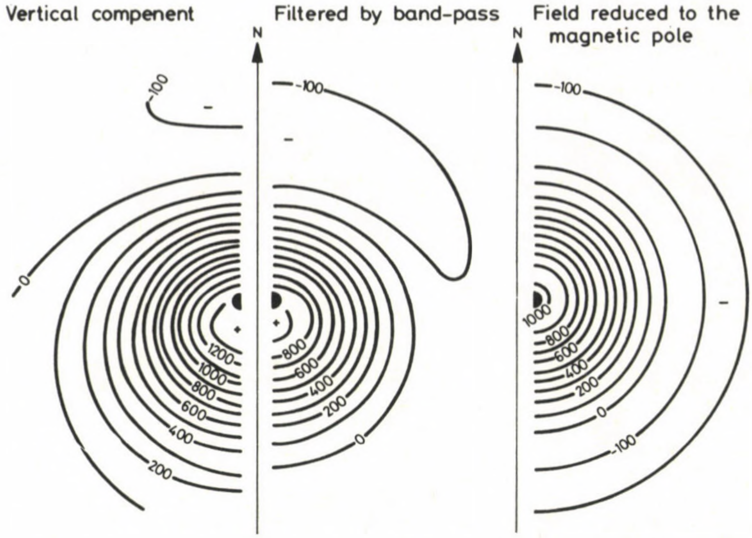

Fig. 4. Vertical component of the magnetic field due to a dipole (left), its band-pass filtered field (middle), its field reduced to the pole (right). Contours are given in nanoteslas

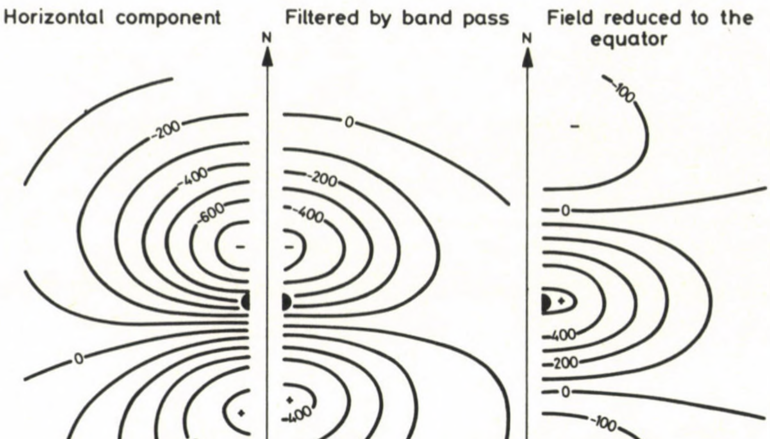

Fig. 5. Horizontal component of the magnetic field due to a dipole (left), its band-pass filtered field (middle), its field reduced to magnetic equator (right). Contours are given in nanoteslas

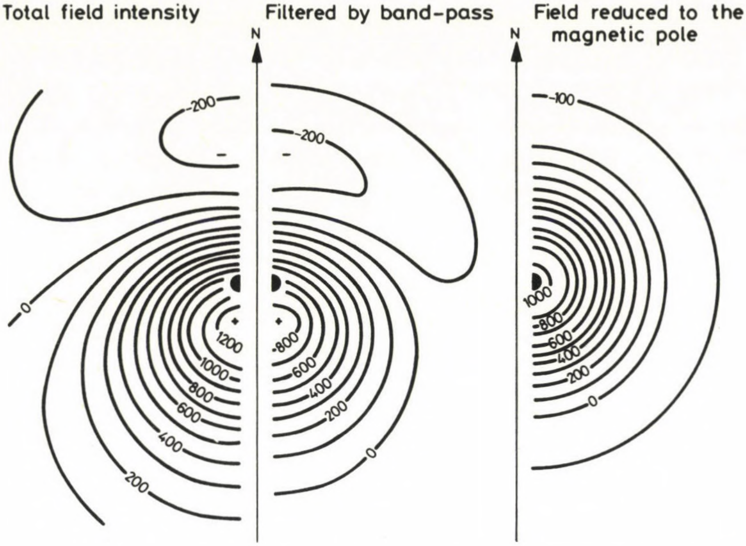

Fig. 6. Total magnetic field due to a dipole (left), its band-pass filtered field (middle), its field reduced to the magnetic pole (right). Contours are given in nanoteslas

its band-pass filtered anomaly and its field reduced to the magnetic pole. For the directional cosines given by Eqs (3) and (6) the values $\alpha=60°, \beta=0°, I=60°, D=0°$ have been substituted. The reduction to the magnetic pole was computed by the coefficients of Table III.

In Figs 7–9 the investigations of the effect of random noise are illustrated. The random noise was generated by random numbers with Gaussian distribution, their expected value equalled to 0, their variance was $(10\ nT)^2$. In the case of these investigations dipole field plus random noise was used as a synthetic magnetic anomaly. The magnetic moment of the dipole was $4\pi 10^{-5}$ Vms, its position and direction were the same as in the former case. It was found that the random noise did not disturb the effectivity of this method.

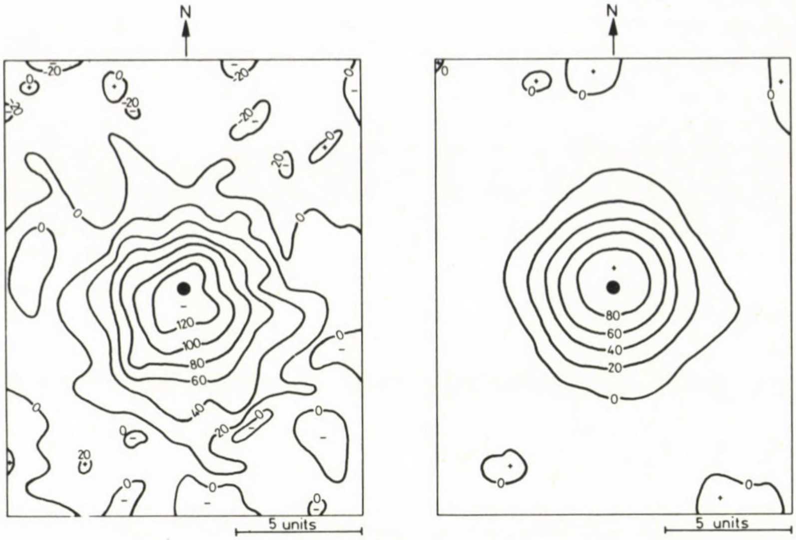

Fig. 7. Vertical component of the magnetic field due to a dipole plus random noise (left), the field reduced to the magnetic pole (right). Contours are given in nanoteslas

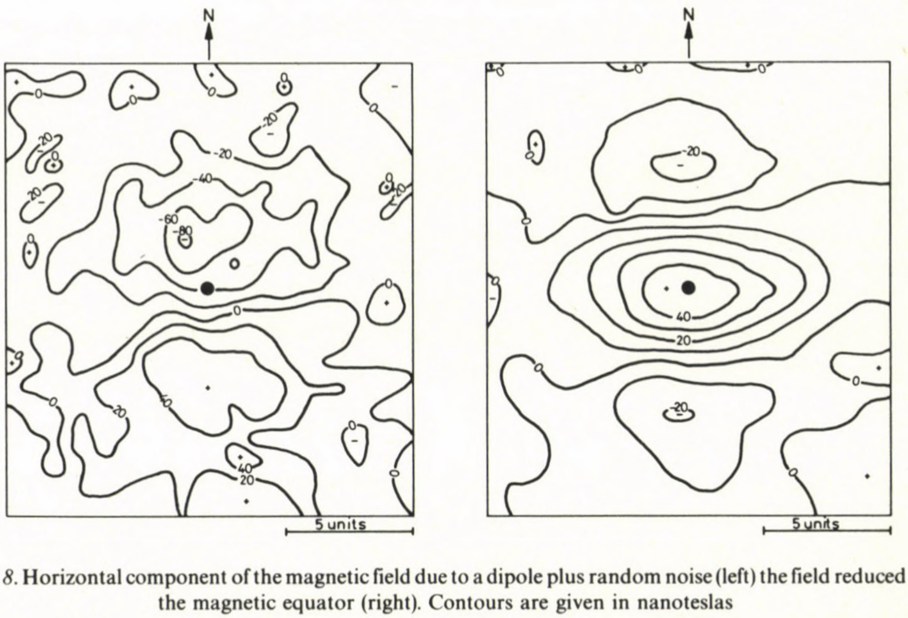

Fig. 8. Horizontal component of the magnetic field due to a dipole plus random noise (left) the field reduced to the magnetic equator (right). Contours are given in nanoteslas

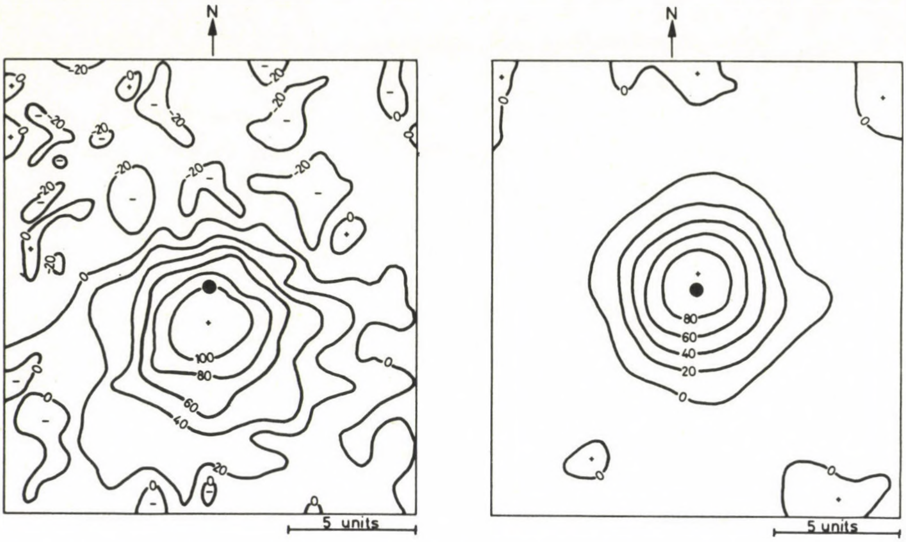

Fig. 9. Total magnetic field due to a dipole plus random noise (left) the field reduced to the magnetic pole (right). Contours are given in nanoteslas

Acknowledgements

The author is indebted to Prof. A Meskó for his help in the method of investigation. Computations were done by the computer CDC-3300 of the Research Institute for Computing Methods and Automation of the Hungarian Academy of Sciences. The permission for using the computing facilities is being highly acknowledged.

References

Baranov V 1957: A new method for interpretation of aeromagnetic maps: pseudo-gravimetric anomalies. *Geophysics*, 22, 359–383.

Baranov V 1975: Potential fields and their transformations in applied geophysics. Gebrüder Borntrager, Berlin–Stuttgart

Baranov V, Naudy H 1964: Numerical calculation of the formula of reduction to the magnetic pole. *Geophysics*, 29, 67–79.

Bhattacharyya B K 1965: Two-dimensional harmonic analysis as a tool for magnetic interpretation. *Geophysics*, 30, 829–857.

Kanasewich R G, Agarwal E R 1970: Analysis of combined gravity and magnetic fields in wave number domain. *Journal of Geophysical Research*, 29, 5702–5712.

Kis K 1981: Transfer properties of reduction of the magnetic anomalies to the magnetic pole and to the magnetic equator. *Annales Univ. Sci. Budapestiensis, Sectio Geologica*, 23, 75–88.

Meskó A 1970: Gravity interpretation and filter theory design and application of low-pass, high-pass and band-pass filters. *Annales Univ. Sci. Budapestiensis. Sectio Geologica*, 13, 67–80.

Seiberl W 1979: Die Transformationen des Schwere- und Magnetfelds im Bereich der Ostalpen. Die Sitzingsberichte der Österreichischen Akademie der Wissenschaften Mathem.-naturw. Klasse. Abteilung II., 187, Heft 1–3.

Telford W M et al. 1976: Applied Geophysics. Cambridge University Press. Cambridge–London–New York–Melbourne

Acta Geodaet., Geophys. et Montanist. Hung. Volume 18 (1—2), pp. 187—200 (1983)

REGIONAL BOUGUER GRAVITY MAPS OF HUNGARY

A MESKÓ[1]

Department of Geophysics, Eötvös Loránd University

[Manuscript received May 5, 1982]

A set of regional Bouguer gravity maps have been derived by two-dimensional Gaussian low-pass filters of form $\exp[-(kf_r)^2]$. The two-dimensional smoothed power spectrum of the gravity field indicates that the cut-off frequency should be somewhere between 0.01/km and 0.02/km or the cut-off wavelength between 50 km and 100 km. Three examples from the set of the regional maps are shown. The filter with cut-off wavelength $\lambda_c = 20$ km hardly provides for more than a smoothing, the filter with cut-off wavelength $\lambda_c = 45$ km presents an intermediate stage and the filter with cut-off wavelength $\lambda_c = 60$ km is considered to yield acceptable regional field.

In the Appendices it is proven that the Gaussian low-pass is the best possible filter in the sense that it combines direction-independent zero-phase transfer with separability and optimum concentration of energy both in the space and in the spatial frequency domain.

Keywords: Bouguer map, Hungary; cut-off frequency; filters in gravimetry; regional gravity

Introduction

It has long been known that the long wavelength components of the Bouguer gravity anomalies are in close connection with the depth of the Mohorovičić discontinuity. Jordan (1978) in a paper inferred from a worldwide statistical analysis of gravity, topography and density constrasts in the Earth that "about 97% of the energy in Bouguer gravity anomalies is caused by Moho relief", which, in turn, is caused by isostatic compensation of terrain.

The regional Bouguer gravity fields have been computed as aids for the investigation of the structure of the lithosphere on the territory of Hungary. It is also hoped that these maps might contribute to the building of a consistent tectonic model and thus to a better understanding of the formation and evolution of the Pannonian Basin.

The present paper describes the method of the computation, which is the application of linear two-dimensional filters, and gives three regional Bouguer gravity anomaly maps as representative examples from the set of the computed maps. A statistical analysis of these maps as well as their comparison with other geological and geophysical data will be given in a separate paper.

[1] H-1083 Budapest, Kún Béla tér 2, Hungary

Method

The regional residual separation can not be solved by any pre-set method. Linear filtering, however, is a generally accepted method for providing reasonable estimates of the regional field. The regional component as well as the residual component possess spectra which may vary significantly from one area to the other. Moreover the spectra overlap each other. In order to obtain geologically meaningful regionals the spectral properties of the components should be established and the transfer properties of the filters should be changed accordingly. Careful analysis of input data combined with *a priori* informations (if such are available) are the preliminaries for constructing filters.

The central part of the smoothed power spectrum of the Bouguer gravity field is shown in Fig. 1. Data over an area of 320×320 km^2 have been used in the computation. The power spectrum has been obtained as the squared magnitude of the Fourier spectra of the data. The latter has been determined by the FFT algorithm. A slight smoothing with a Gaussian window provided the results given in Fig. 1. The energy is

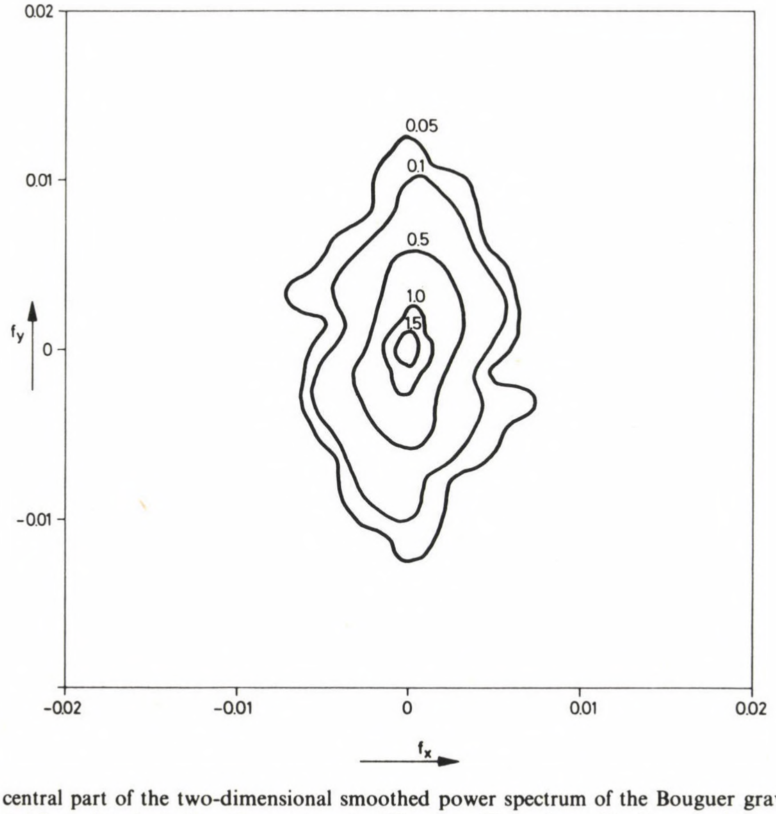

Fig. 1. The central part of the two-dimensional smoothed power spectrum of the Bouguer gravity field, computed from data including the most part of Hungary. The values of isolines are indicated

concentrated around the origin, the spectral power beyond the radial frequency $f_r \geqq 0.02\,(1/\text{km})$ is down by at least two orders of magnitude.

In spite of the obvious ambiguity of the regional residual separation there are certain requirements what the regional filters should fulfill. By taking into consideration the requirements we can derive a set of low-pass filters. Filters belonging to the set have transfer functions of the same form. The transfer function has a free parameter and each filter of the set corresponds to one particular value of this parameter. The range of the parameter is determined by certain considerations, involving digital implementation and reasonable size, which are discussed in Appendix 1. The range of the parameter, however, is large enough to allow the user to seek out a value which is best suited for each particular task. The performance of the filters may be very close to that of the optimum filters.

The requirements which unambiguously determine the shape of the transfer function of the filters are as follows:

1. Direction independent zero-phase transfer,
2. The shortest possible weight function.

The first requirement is met when the transfer function is circularly symmetric

$$S(f_x, f_y) = S(f_r)\,; \qquad f_r^2 = f_x^2 + f_y^2\,, \tag{1}$$

and positive for all radial frequencies

$$S(f_r) \geqq 0\,. \tag{2}$$

The second requirement is more difficult to formulate in mathematical terms. It is heuristically obvious that the implementation of a separable two-dimensional filter involves less computational efforts than the implementation of a non-separable filter. In the latter case two one-dimensional convolution should be computed instead of one two-dimensional convolution. It is not obvious that a separable filter has a short weight function. It turns out, however, that the separable filter necessarily has a Gaussian form and the Gaussian pulse attains the theoretically best concentration of information both in space and in spatial frequency domain.

The derivation of the transfer function of the filter from the requirements is given in Appendix 1. The optimum property of the Gaussian pulse concerning the pulse size spectral bandwidth product is shown in Appendix 2.

The low-pass filter is

$$S(f_r) = e^{-(kf_r)^2} \tag{3}$$

with the weight function

$$s(r) = \frac{\pi}{k^2}\, e^{-\left(\frac{\pi r}{k}\right)^2}, \tag{4}$$

which can be separated as

$$s(r)=s(x)s(y)=\frac{\sqrt{\pi}}{k}e^{-\left(\frac{\pi x}{k}\right)^2}\frac{\sqrt{\pi}}{k}e^{-\left(\frac{\pi y}{k}\right)^2}.$$

(The free parameter is k.)

The digital weight function, to be used in both one-dimensional convolution is

$$s_l=\frac{\sqrt{\pi}}{k}e^{-\left(\frac{\pi ld}{k}\right)^2} \tag{5}$$

$$(l=-n,\,-n+1,\,\ldots,\,-1,0,1,\,\ldots,n)$$

where d is the grid interval (in both directions), and n is the size of the filter.

The application of these filters has been first suggested by the present author (Meskó 1966, 1968). For the sake of completeness it may be mentioned that in the last 15 years the filters have mainly been used for the computation of residual fields in such a way that the regionals have been subtracted from the original data.

The cut-off frequency of the filter can be considered

$$(f_r)_c=\frac{1}{k}, \tag{6}$$

which corresponds to

$$S(f_r=(f_r)_c)=\frac{1}{e}.$$

The cut-off wavelength is

$$\lambda_c=k. \tag{7}$$

Results

The results of the applications of three filters have been chosen to illustrate the obtained regional Bouguer gravity maps. The central parts of the filters are shown in Fig. 2, together with the radial power spectrum of the gravity field. The latter is obtained from the two-dimensional smoothed power spectrum by averaging over circles, i.e.

$$G(f_r)=\frac{1}{2\pi}\int_0^{2\pi}G(f_r\cos\varphi,\,f_r\sin\varphi)\,\mathrm{d}\varphi. \tag{7}$$

The integral has been approximated by finite sums of $G(f_r\cos\varphi_i,\,f_r\sin\varphi_i)$ values, obtained by interpolation.

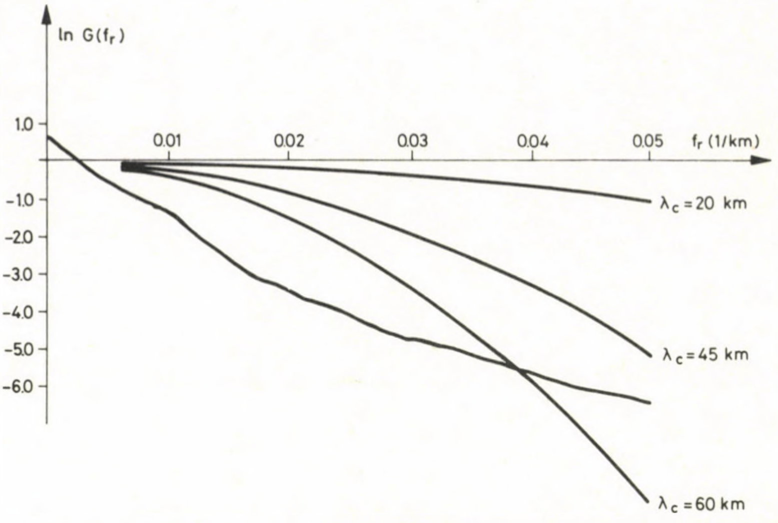

Fig. 2. The central part of the radial power-spectrum of the Bouguer gravity field and the transfer functions of three low-pass filters with cut-off wavelengths 20 km, 45 km and 60 km, respectively. The vertical scale is logarithmic

The cut-off wavelengths of the three filters are 20 km, 45 km and 60 km, respectively. It can be seen that the first filter $\lambda_c = 20$ km hardly provides for more than a slight smoothing. Its output is shown in Fig. 4. The obtained field obviously contains significant contributions from local density inhomogeneities, and it is presented to appreciate the performance of the third filter $\lambda_c = 60$ km in removing local features.

The regional fields obtained by the second and third filter $\lambda_c = 45$ km and $\lambda_c = 60$ km are shown in Figs 5 and 6. Both the comparison of the transfer functions to the radial power spectrum as well as the gravity maps indicate that the regional obtained by the cut-off wavelength $\lambda_c = 60$ km is the less influenced by local features. The main characteristics of the regional Bouguer gravity anomaly field in Hungary are the long positive anomaly through the Transdanubian Middle Range with an approximately SSW–NNE strike, the positive anomaly over the Mecsek and Villány Mountains, a negative anomaly in the little Hungarian Plain and mainly, though not exclusively, small negative anomalies over the Great Hungarian Plane.

Elevated terrain, in general, corresponds to positive Bouguer anomalies, in contrast with expectations. The most controversial part is the Transdanubian Middle Range. Moho depths of 31km – 37 km have been obtained from recent seismic investigations (Posgay et al. 1981) while the average Moho depth is about 27 km in the Pannonian Basin. Instead of the negative Bouguer anomaly which should correspond to the Moho depression the largest positive anomaly of the whole area is found here. The explanation might be sought in the anomalous low density of the mantle material (Ádám 1977, Horváth et al. 1979).

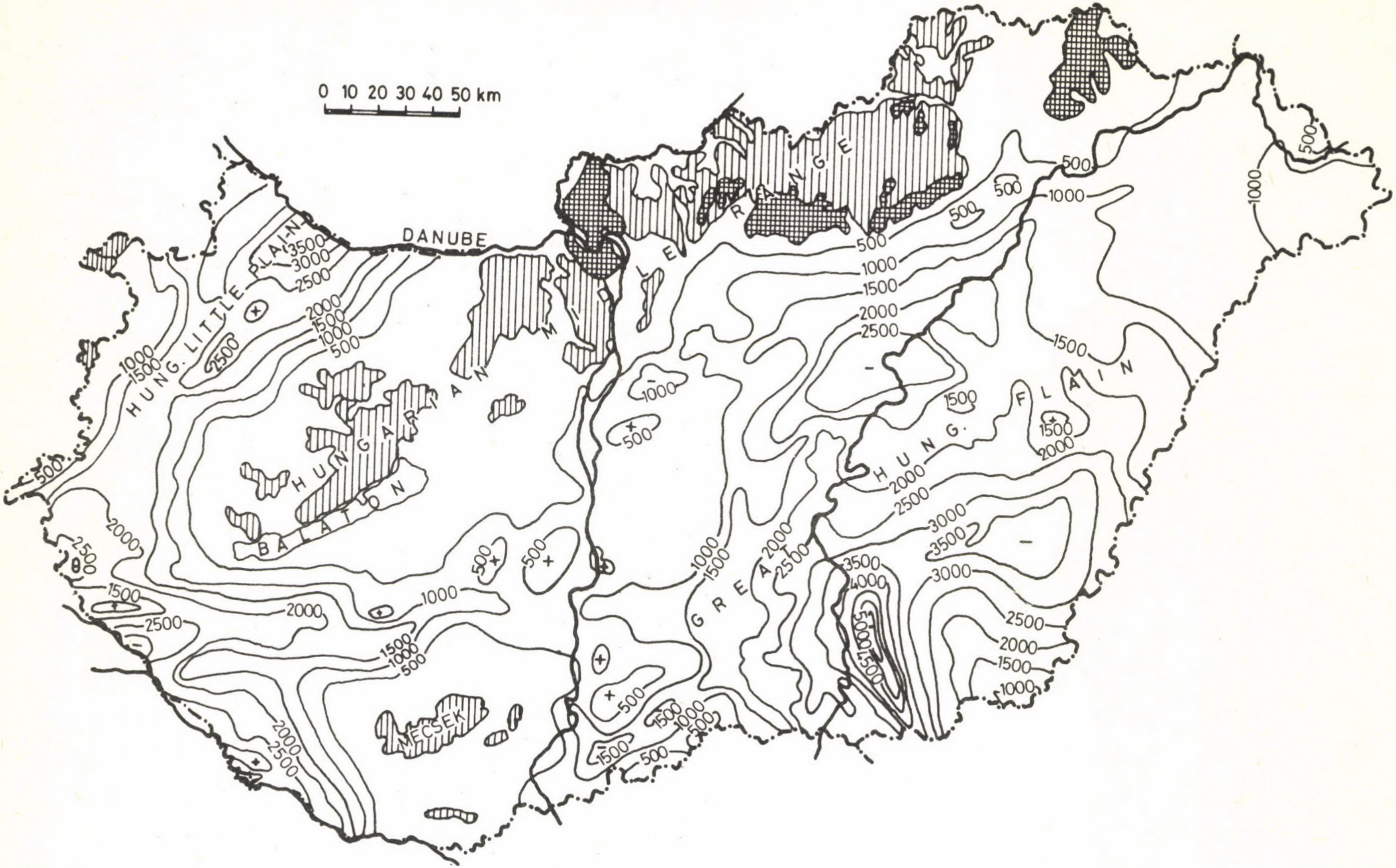

Fig. 3. Geological sketch of the Pannonian Basin. (Modified after Horváth et. al., 1979) Isolines show the bottom of the Pliocene sediments (in metres), hachured areas denote outcrops of pre-Pliocene rocks, cross-ruling denotes Miocene volcanites

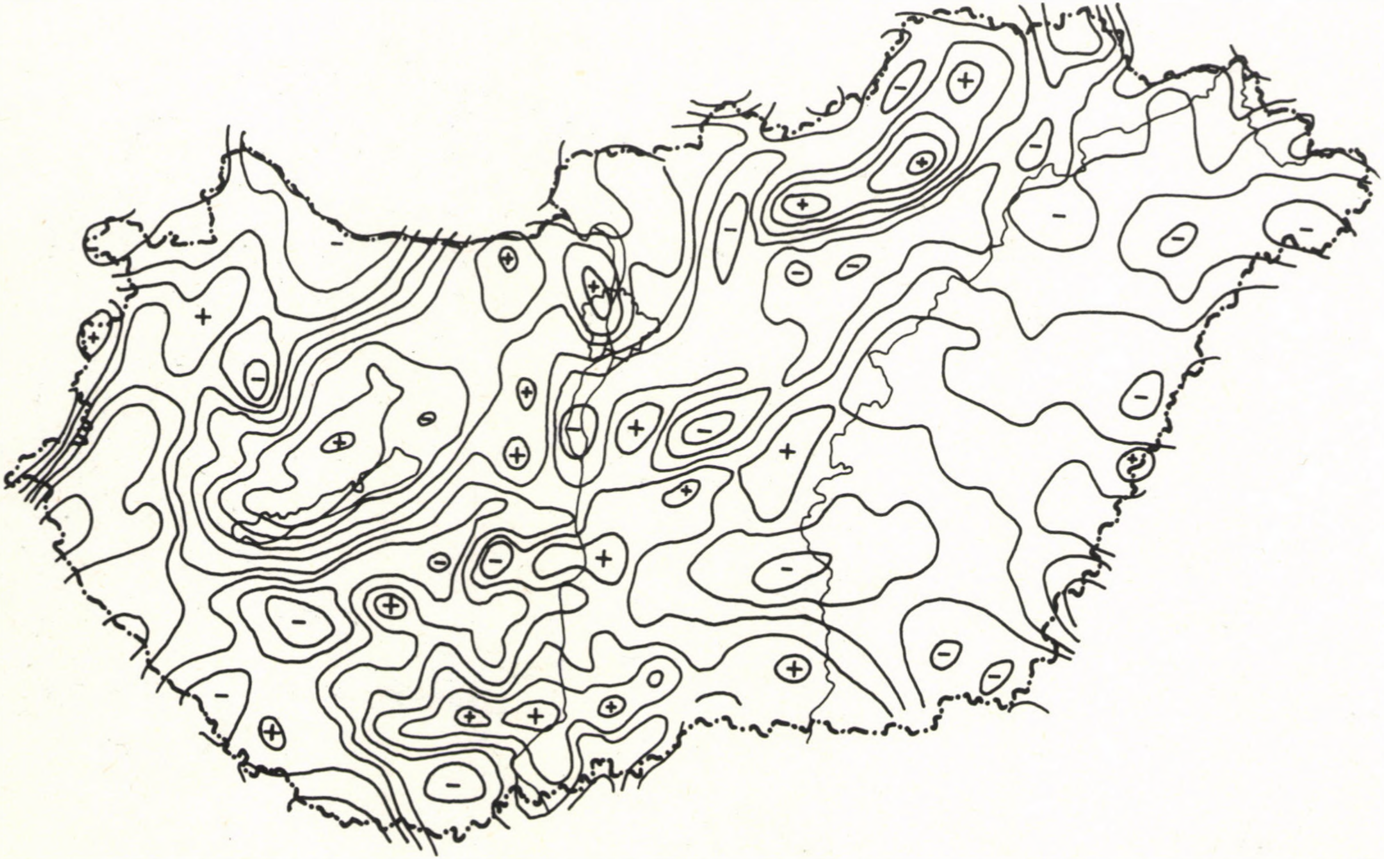

Fig. 4. Regional Bouguer anomaly map of Hungary obtained by the low-pass filter with cut-off frequency of 20 km. The isolines are 5 mgals apart

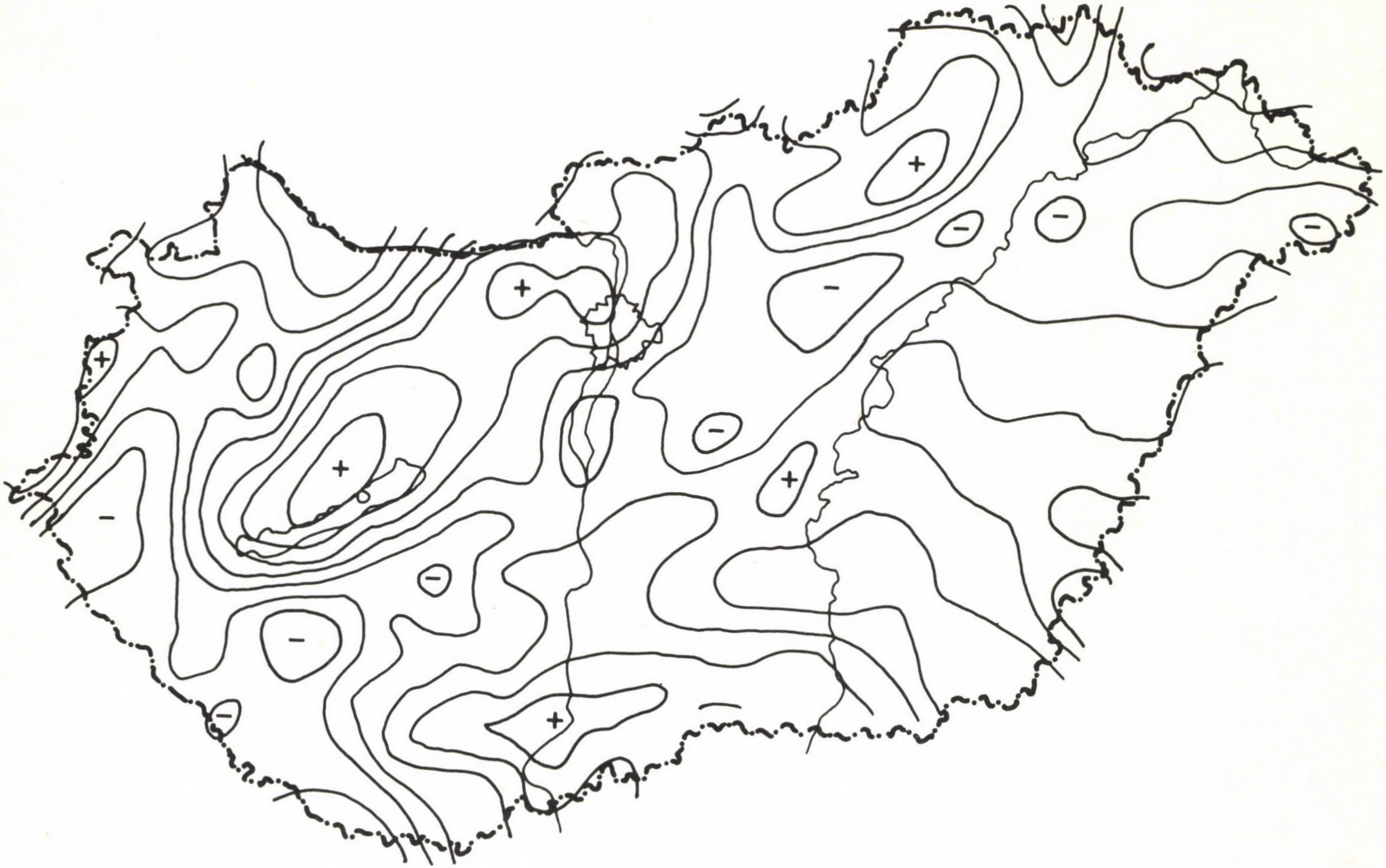

Fig. 5. Regional Bouguer anomaly map of Hungary obtained by the low-pass filter with cut-off frequency of 45 km. The isolines are 5 mgals apart

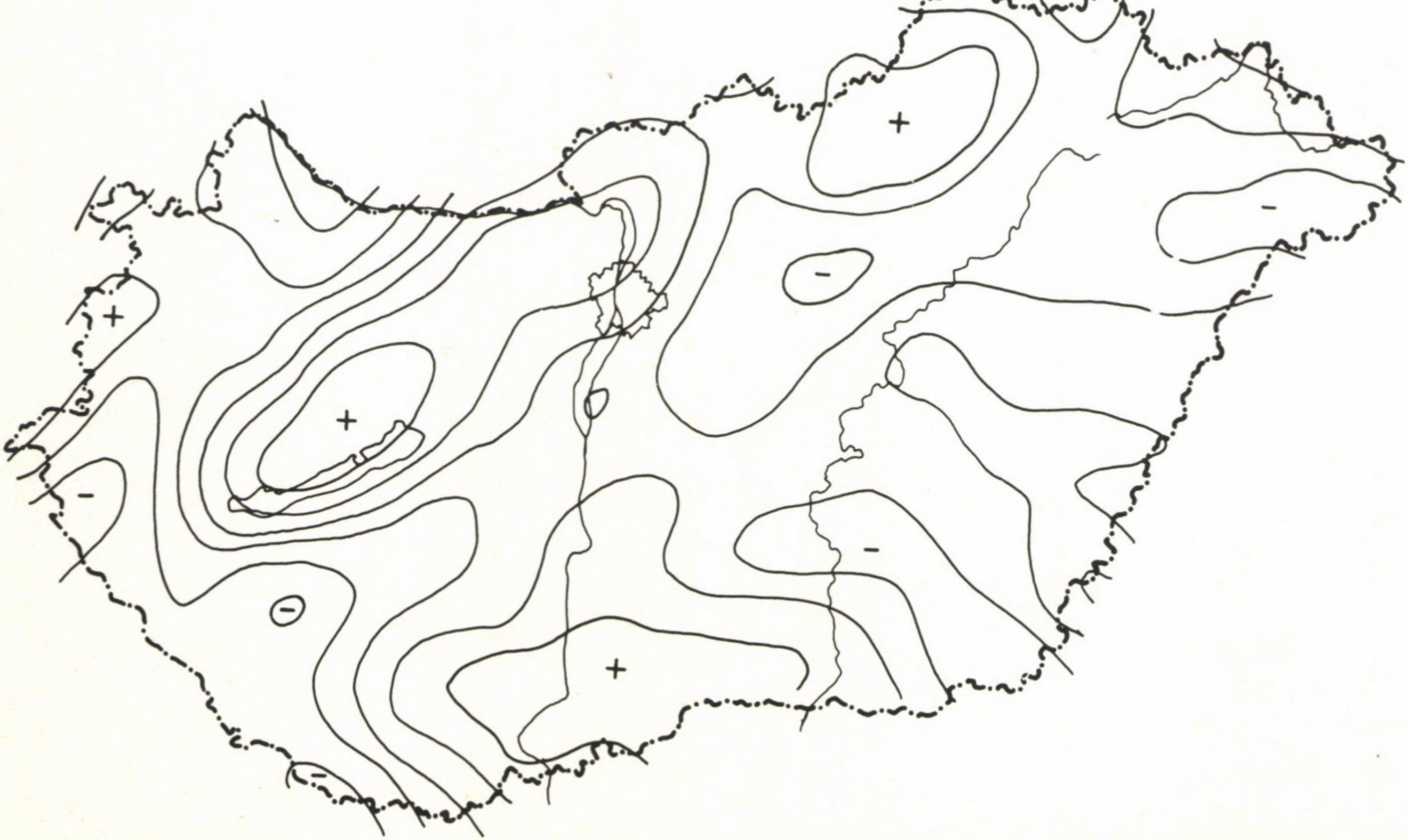

Fig. 6. Regional Bouguer anomaly map of Hungary obtained by the filter with cut-off frequency of 60 km. Isolines are 5 mgals apart

Acknowledgements

The isolines of the gravity maps are computer drawn. The corresponding program, based on bicubic spline interpolation between grid data, has been written by Mr. J. Závoti. My sincere thanks are due to Mr. J Závoti for the preparation of the maps, shown in Figs 4–6 as well as to the Computing Centre of the Hungarian Academy of Sciences, Budapest and the Geodetic and Geophysical Research Institute of the Hungarian Academy of Sciences, Sopron for providing computational facilities.

Appendix 1

Circularly symmetric, separable low-pass filters

For the sake of simplicity let us consider first continuous weight functions and transfer functions. If the transfer function is circularly symmetric, i.e.

$$S(f_x, f_y)=S(f_r) \tag{A–1}$$

and its inverse Fourier transform exists, the weight function is necessarily also circularly symmetric

$$s(x, y)=\int\limits_{-\infty}^{\infty}\int\limits_{-\infty}^{\infty} S(f_x, f_y)e^{j2\pi(f_x x+f_y y)}\,\mathrm{d}f_x\,\mathrm{d}f_y$$

$$=\int\limits_{0}^{\infty} S(f_r)J_0(f_r r)f_r\,\mathrm{d}f_r=s(r)\,. \tag{A–2}$$

A two-dimensional filter is called separable when

$$s(x, y)=s_1(x)s_2(y)\,. \tag{A–3}$$

From (A–1) follows that the functions s_1 and s_2 have to be identical and therefore we obtain

$$s(r)=s_1(x)s_1(y)\,. \tag{A–4}$$

Introducing the polar coordinates r, φ and taking the logarithm of both sides Equation (A–4) yields

$$\ln s(r)=\ln s_1(r\cos\varphi)+\ln s_1(r\sin\varphi)\,.$$

Differentiation with respect to φ gives

$$0=-r\sin\varphi\frac{s_1'(r\cos\varphi)}{s_1(r\cos\varphi)}+r\cos\varphi\frac{s_1'(r\sin\varphi)}{s_1(r\sin\varphi)}=-y\frac{s_1'(x)}{s_1(x)}+x\frac{s_1'(y)}{s_1(y)}\,.$$

After a rearrangement of terms we obtain

$$\frac{s_1'(x)}{xs_1(x)}=\frac{s_1'(y)}{ys_1(y)}\,.$$

Since x and y are completely independent both sides of the equation have to be equal to a common constant

$$\frac{s_1'(x)}{xs_1(x)}=n=\frac{s_1'(y)}{ys_1(y)}\,.$$

Thus we obtain for $s_1(x)$ the differential equation

$$\frac{s_1'(x)}{s_1(x)} = nx .$$

The solution is

$$\ln s_1(x) = \frac{1}{2} nx^2 + C_1 ,$$

where C_1 is a constant. The solution corresponds to the (one-dimensional) weight function

$$s_1(x) = C_1 e^{\frac{1}{2}nx^2}.$$

In order to obtain a stable filter the constant in the exponent should be negative. Therefore we write $\frac{1}{2} n = -m^2$ where m may be an arbitrary real number. The one-dimensional weight function becomes

$$s_1(x) = C_1 e^{-m^2x^2},$$

which gives

$$s(r) = C_1 e^{-m^2x^2} C_1 e^{-m^2y^2} = Ce^{-m^2r^2} \tag{A-5}$$

for the separable and circularly symmetric weight function of the two-dimensional filter.

The corresponding transfer function can be obtained by taking the Hankel transform of (A–5), which gives

$$S(f_r) = \frac{C\pi}{m^2} e^{-\left(\frac{\pi f_r}{m}\right)^2}. \tag{A-6}$$

The transfer function shows that the filter is a low-pass. A natural requirement is

$$S(f_r = 0) = 1 ,$$

which gives for the constant C

$$C = \frac{m^2}{\pi}.$$

Introducing k for π/m we obtain the weight function as well as the transfer function in the form used in the main text

$$S(f_r) = e^{-(kf_r)^2}, \tag{A-7}$$

and

$$s(r) = \frac{\pi}{k^2} e^{-\left(\frac{\pi}{k}r\right)^2}, \tag{A-8}$$

respectively. The weight function in separated form reads as

$$s(r) = \frac{\sqrt{\pi}}{k} e^{-\left(\frac{\pi}{k}x\right)^2} \frac{\sqrt{\pi}}{k} e^{-\left(\frac{\pi}{2}y\right)^2}. \tag{A-9}$$

The transfer function is real and positive for all f_r thus the transfer is zero-phase.

Samples taken from the continuous weight functions (A–9) yield the coefficients of the digital low-pass filters. When we use a regular square grid with grid interval d the coefficients become

$$c_{il} = s_1(id)s_1(ld) . \tag{A-10}$$

Sampling and the necessary truncation of the continuous and theoretically (in both directions) infinite weight function may influence the circular symmetry. Transfer functions of the digital weight functions can be used to check the goodness of the approximations. The actual transfer function is obtained by

$$S_{\text{digital}}(f'_x, f'_y)=\left[s_1(0)+2\sum_{i=1}^{n} s_1(i)\cos 2\pi i f'_x\right]\cdot\left[s_1(0)+2\sum_{l=1}^{n} s_1(l)\cos 2\pi l f'_y\right]. \tag{A–11}$$

By comparing $S_{\text{digital}}(f'_x, f'_y)$ to the theoretical $S(f_r)$, given in (A–7) the significance of distortions due to sampling and truncation can be determined. By passing it should be mentioned that such comparison is meaningful only in the Nyquist interval, defined by

$$|f'_x|\leqq 0.5, \qquad |f'_y|\leqq 0.5$$

or

$$|f_x|\leqq \frac{1}{2d}, \qquad |f_y|\leqq \frac{1}{2d},$$

where the dimensionless spatial frequencies are $f'_x=f_x d$, $f'_y=f_y d$. Digital weight functions have periodic transfer functions and therefore 'good approximation' is understood as proportionality to a high degree between $S(f_r d)$ and $S_{\text{digital}}(f'_x, f'_y)$ in the Nyquist interval.

Computations showed that the deviation from the theoretical transfer is less than 2 percent for the range of the parameter $4d\leqq k\leqq 36d$ and filter sizes used in routine processing. The size also depends on the parameter and usually $n=k/2d$ is used. When the parameter k is small the approximation to the theoretical circularly symmetric transfer functions can be made very good even with relatively small sets of coefficients.

The parameter k can not be arbitrarily small or large. When k is too small $S(f_r)$ does not decrease rapidly and aliasing distorts the transfer function of the digital weight function. When k is too large, on the other hand, though $S(f_r)$ decreases rapidly and aliasing becomes negligible, the weight function becomes too large to be practical.

Let us estimate, at last, what is gained by the application of separable filters. Each output value is obtained by $2(2n+1)$ multiplications and additions, instead of $(2n+1)^2$ multiplications and additions what the application of non-separable two-dimensional filter with the same size would require. The saving is $(2n+1)/2\approx n$ i.e. about one order of magnitude for filters of practical interest.

Appendix 2

The lower limit of the signal duration spectral bandwidth product (uncertainty relation)

It has long been known that the signal duration spectral bandwidth product can not be arbitrarily small. The product for the Gaussian pulse is equal to the theoretically possible lower limit (see e.g. Bracewell 1965, Robinson 1967 etc.). Therefore Gaussian transfer functions possess the shortest weight functions for any given bandwidth. For the sake of completeness this remarkable property is shown in this Appendix.

In the case of spatial filtering the space variable x substitutes time and frequency is understood as the spatial frequency f_x. The physical meaning of the variables has no bearing on the fact that a transfer function of Gaussian shape gives the best concentration around the origin both in space as well as in the spatial frequency domain.

Let us confine the discussion to real, even pulses.

The energy of a pulse $g(x)$ is defined by

$$E=\int_{-\infty}^{\infty} g^2(x)\,\mathrm{d}x\,. \tag{A–12}$$

The same energy is contained in the spectrum of the pulse, i.e.

$$E=\int_{-\infty}^{\infty} G^2(f_x)\,\mathrm{d}f_x=\int_{-\infty}^{\infty} g^2(x)\,\mathrm{d}x\,. \tag{A–13}$$

(A–13) is a special case of the Bessel's equality for real, even pulses.

The pulse size is defined by the normalized second moment as follows

$$(\Delta x)^2=\frac{1}{E}\int_{-\infty}^{\infty} x^2 g^2(x)\,\mathrm{d}x\,, \tag{A–14}$$

and the spectral bandwidth by

$$(\Delta f_x)^2=\frac{1}{E}\int_{-\infty}^{\infty} f_x^2 G^2(f_x)\,\mathrm{d}f_x\,. \tag{A–15}$$

Due to the derivative theorem of the Fourier transform (A–15) can be written as

$$(\Delta f_x)^2=\frac{1}{4\pi^2 E}\int_{-\infty}^{\infty} [g'(x)]^2\,\mathrm{d}x\,. \tag{A–16}$$

The signal size spectral bandwidth product then becomes

$$(\Delta x\Delta f_x)^2=\frac{1}{4\pi^2 E^2}\int_{-\infty}^{\infty} [xg(x)]^2\,\mathrm{d}x\int_{-\infty}^{\infty} [g'(x)]^2\,\mathrm{d}x\,. \tag{A–17}$$

Due to Schwarz's inequality it is valid for the products of the integrals

$$\int_{-\infty}^{\infty} [xg(x)]^2\,\mathrm{d}x\int_{-\infty}^{\infty} [g'(x)]^2\,\mathrm{d}x\geqq\left[\int_{-\infty}^{\infty} xg(x)g'(x)\,\mathrm{d}x\right]^2=$$

$$=\left[\frac{1}{2}\int_{-\infty}^{\infty} x\frac{\mathrm{d}}{\mathrm{d}x}g^2(x)\,\mathrm{d}x\right]^2. \tag{A–18}$$

Integration by parts gives

$$\int_{-\infty}^{\infty} x\frac{\mathrm{d}}{\mathrm{d}x}g^2(x)\,\mathrm{d}x=[xg^2(x)]_{-\infty}^{\infty}-\int_{-\infty}^{\infty} g^2(x)\,\mathrm{d}x=-E\,,$$

since $g^2(x)$ vanishes at both limits. Thus (A–18) can also be written as

$$\int_{-\infty}^{\infty} [xg(x)]^2\,\mathrm{d}x\int_{-\infty}^{\infty} [g'(x)]^2\,\mathrm{d}x\geqq\frac{1}{4}E^2$$

and (A–17) simplifies to

$$(\Delta x \Delta f_x)^2 \geqq \frac{1}{4\pi^2 E^2} \cdot \frac{1}{4} E^2 = \left(\frac{1}{4\pi}\right)^2.$$

Thus we obtain for the signal size spectral bandwidth product the inequality

$$\Delta x \Delta f_x \geqq \frac{1}{4\pi}. \tag{A–19}$$

Let us consider now the Gaussian transfer function

$$S(f_x) = e^{-(kf_x)^2}.$$

Its spectral bandwidth according to the definitions (A–15) and (A–13) becomes

$$\Delta f_x = \frac{1}{2k}. \tag{A–20}$$

The corresponding weight function is

$$s(x) = \frac{\sqrt{\pi}}{k} e^{-\left(\frac{\pi x}{k}\right)^2} \tag{A–21}$$

with size

$$\Delta x = \frac{k}{2\pi}. \tag{A–22}$$

The signal size spectral bandwidth product for the Gaussian pulse is

$$\Delta x \Delta f_x = \frac{k}{2\pi} \cdot \frac{1}{2k} = \frac{1}{4\pi},$$

i.e. the pulse actually attains the theoretically possible lowest bound.

References

Ádám O 1977: Major tectonics of the Transdanubian Central Mountains and their foreland in light of geophysical measurements. (in Hungarian) Magyar Állami Földtani Intézet 1977. évi jelentése, 269–287.

Bracewell R 1965: The Fourier Transform and its Applications. Mc Graw Hill, New York

Horváth F, Bodri L, Ottlik P 1979: Geothermics of Hungary and the Tectonophysics of the Pannonian Basin "Red Spot". In: Terrestrial Heat Flow in Europe. (Edited by V. Čermák and L. Rybăch) Springer Verlag, Berlin–Heidelberg–New York

Jordan S K 1978: Statistical model for gravity, topography and density contrasts in the Earth. *Journ. of Geophys. Res.*, 83, 1816–1824.

Meskó A 1966: Linear transformations of gravity fields as linear two-dimensional filters. C. Sc. Thesis, in Hungarian.

Meskó A. 1968: Koeffizientenreihen zur linearen Transformation von Schwerekarten. *Geophysik* (Berlin), 13, 57–60.

Posgay K, Albu I, Bodoky T, Kaszás M, Kovács B, Ráner G 1981: Seismic methodological and instrumental research. Magyar Állami Eötvös Loránd Geofizikai Intézet 1980. évi jelentése: 61–72 (in Hungarian with Figures) and 151–156 (in English)

Robinson E 1967: Statistical Communication and Detection. Griffin, London

Acta Geodaet., Geophys. et Montanist. Hung. Volume 18 (1—2), pp. 201—208 (1983)

EQUATORIAL ELECTRIC FIELDS GENERATED BY THE QUIET-DAY DYNAMO AND BY SOLAR DISTURBANCES

A K AGARWAL[1], R G RASTOGI[1], B P SINGH[1]

Indian Institute of Geomagnetism, Colaba, Bombay

[Manuscript received July 5, 1982]

The latitudinal profile of equatorial electric fields associated with the ionospheric dynamo and with the geomagnetic disturbances of solar origin has been investigated by means of the changes in the horizontal component (H) of the geomagnetic field. Data were taken from a close chain of magnetic observatories lying within $\pm 5°$ of the dip-equator in the Ethiopian region. It is noticed that the maxima in H during storm-time variations lie very close to the dip-equator whereas for both Sq and solar flares, there appears a shift of about 1° south of the dip-equator. The results suggest that the structure of the equatorial electric field associated with storm-time disturbances differ from that of Sq and solar flares. The coincidence of maximum enhancement for solar flares with electrojet ranges indicates that there are no major changes in the distribution of dynamo generated Sq electric field for the flares considered here.

Keywords: equatorial electric fields; geomagnetic activity; equatorial enhancement; solar flare effect; Sq; quiet-day geomagnetic variation

Introduction

The two main sources of electric field in the ionosphere are: the motion of neutral atmosphere across the Earth's magnetic dipole field lines and the interaction of solar wind with the Earth's magnetic field. The former is known as the dynamo generated electric field which is found to be responsible for the behaviour of the solar quiet-day (Sq) variations of magnetic field components. The changes in the latter type of electric field also affect the nature of the geomagnetic variations observed at all latitudes. Possible correlations between geomagnetic variations observed at high-latitudes and low-latitudes were studied by various authors (Akasofu and Chapman 1963, Onwumechilli et al. 1973 and others) and it was noticed that mostly the variations of different latitudes are closely correlated in time. For determining the behaviour of geomagnetic variations, Alfven (1976) stressed the importance of thinking in terms of currents driven by the interplanetary electric field ($\vec{E} = -\vec{V} \times \vec{B}$). This electric field is considered to be mapped onto the high-latitude ionosphere (Mozer et al. 1974). Further Kikuchi et al (1978) suggest that the electric field can propagate instantaneously from

[1] Colaba, Bombay 400005, India

pole to equator. Some recent studies indicate the presence of these electric fields in the low-latitude ionosphere, too (Rastogi and Patel 1975, Patel 1978, Fejer et al. 1979).

It is important to note that the low-latitude region, in particular the equatorial region, is more convenient to study the effect of such an electric field than the high-latitude region because it is free from particle precipitation. Another important advantage is the very little if any movement of the equatorial electrojet with the changes in the magnetic activity compared with the movements of the auroral electrojet (Akasofu 1977). The region close to the dip-equator is also very sensitive to the changes in the electric field because of the high electric conductivity of the medium as a result of the special configuration of the magnetic and electric fields above the equator. Thus, one would expect that the equatorial electrojet will show the effect of the electric field mapping in a more pronounced way.

Many of the earlier studies (Kane 1978, Rastogi 1963, Rastogi et al. 1964, Mason 1963, Raja Rao and Rao 1963, Sugiura 1953, Forbush and Vestine 1955, Matsushita 1960 and others) reported an equatorial enhancement of the geomagnetic variations during day-time by studying the horizontal component (H) during short-period fluctuations, such as storm sudden commencements (SSCs), sudden impulses (SIs), solar flares, etc. Some of them also investigated the nature of electric fields associated with these variations. The enhancement of long period variations, such as quiet-day variations (Sq) and storm time variations (Dst), were studied by Rastogi (1962), Mason (1963), Sastri and Jayakar (1970), Ogbuehi and Onwumechilli (1964) and others. Their results, however, are of limited value since the spacing of the stations was too large to identify the detailed features of the equatorial enhancement. Porath et al. (1973) and Kane and Rastogi (1977) used the data from the close network in the Ethiopian region to study the equatorial enhancement for Sq-daily variations and storm-time variations. It would be of interest to compare the enhancement of short-period variations observed during the period of magnetic storms with electrojet ranges and solar flares in order to distinguish the nature of the equatorial electric fields associated with them. Recently, we also examined the equatorial enhancement of the short-period variations and its dependence on the north-south (Bz) component of the IMF by using the above close chain of magnetic stations (Agarwal et al. 1979). The geographic and dip-latitudes of the observatories used for the present analysis are listed in Table I.

Data analysis

The data of the magnetic array in the Ethiopian region has been used here. This array study was carried out in Eastern Ethiopia by the late Porath during the period from November 1970 to May 1971. The stations were mainly situated along the western edge of the Afar depression and the main Ethiopian rift with a further line of stations across the centre of the Afar depression. A part of the array data con-

Table I
The geographic coordinates and dip-latitudes of the observatories used in the present study

S. No.	Station Name	Geographic coordinates Lat.	Long lat.	Dip-lat.	Station used for Sq	Solar flare	Storm
1.	6 ADI	14.27	39.47	4.87	N	Y	N
2.	1 MAK	13.50	39.48	4.10	Y	N	Y
3.	19 ASS	12.97	42.70	3.57	N	Y	N
4.	20 BUR	12.62	42.28	3.22	Y	Y	N
5.	3 ALA	12.40	39.55	3.00	Y	Y	Y
6.	9 ELI	12.23	42.08	2.83	Y	Y	N
7.	21 WOL	11.82	39.58	2.42	Y	Y	N
8.	22 DUB	11.73	41.03	2.33	Y	Y	N
9.	16 AIS	11.55	41.45	2.50	N	Y	N
10.	15 ELO	11.27	40.33	1.87	Y	Y	N
11.	8 BOM	11.22	39.63	1.82	Y	Y	N
12.	18 BAT	11.20	40.02	1.80	Y	Y	N
13.	17 DEG	11.12	39.88	1.72	Y	Y	N
14.	14 MAJ	10.55	39.83	1.15	Y	Y	Y
15.	22 HAR	9.93	41.98	0.53	N	N	Y
16.	24 DBH	9.67	39.50	0.27	N	Y	Y
17.	16 DIR	9.60	41.87	0.20	N	N	Y
18.	18 ALE	9.38	42.02	−0.02	N	N	Y
19.	26 MUF	9.33	38.17	−0.07	Y	Y	N
20.	15 BIS	9.17	43.55	−0.23	N	N	Y
21.	27 DBZ	8.75	38.92	−0.65	Y	N	Y
22.	25 WON	8.47	39.22	−0.93	N	Y	N
23.	29 ASE	7.97	39.12	1.43	Y	N	N
24.	28 LAN	7.63	38.70	−1.77	Y	Y	N
25.	4 KOL	7.33	38.03	−2.07	Y	N	N
26.	30 DOU	7.17	37.77	−2.23	N	Y	N
27.	11 GUR	7.12	39.80	−2.28	Y	Y	N
28.	2 COF	7.08	38.77	−2.32	N	Y	N
29.	23 AWA	7.05	38.47	−2.35	Y	N	Y
30.	13 DOD	6.95	39.17	−2.45	N	Y	N
31.	12 LAP	6.57	37.87	−2.83	Y	Y	Y
32.	20 ABM	6.08	37.65	−3.32	N	Y	N
33.	5 YAV	4.90	38.12	−4.50	Y	N	Y

Y = YES
N = NO

taining various geomagnetic events was available in digitised form on magnetic tape at Dallas and has been acquired by Rastogi. Using these values on tape, at first we analysed the storm-time variations of 9th April 1971. The analysis is very much similar to that one adopted in our earlier papers (Agarwal et al. 1979, 1978). Amplitude variations corresponding to peaks at 70 min and 21 min are isolated for all the Ethiopian stations by using a filter of a weight function with 141 points designed after the procedure of Behannon and Ness (1966). For studying the latitudinal dependence of enhancement, peak to peak amplitudes are measured at all stations arount 0900 UT and 0950 UT. Figure 1 shows the latitudinal dependence of the enhancement for the two selected periods. The values are normalized to the amplitude at 5 YAV (dip-lat. $\simeq 4.50$) which is fairly outside the equatorial electrojet. The smooth curve is obtained by the best-visual fit.

For the enhancement in electrojet ranges, we have chosen two ordinary days, the 1st and 2nd March, 1971. The ranges for both days and for all stations were calculated by taking the difference between the maximum hourly mean H-value and the local midnight value. In Fig. 1 the variation of the enhancement of the Sq range with the dip-latitude is also shown. The enhancements are again normalized to 5 YAV and the smooth curve is obtained by the best-visual fit.

The latitudinal dependence of solar flare enhancement was studied by analysing the two solar flares occurred on the 11th and 12th December, 1970 at 1027 UT and 0903 UT, respectively. For both flares, the maximum change in amplitude of H was measured at all the stations of the Ethiopian array. The values so obtained were normalized to the corresponding change at 6 ADI (dip-lat. $\simeq 4.87$). Unfortunately, the corresponding data for the solar flares at 5 YAV were missing and this forced us to normalize with respect to 6 ADI. However, 6 ADI is also fairly outside of the equatorial electrojet. Figure 2 shows the latitudinal dependence of the enhancement for the two solar flares and both curves were again obtained by best-visual fit. For the sake of comparison the variation of the enhancement for the Sq range is also included in Fig. 2.

Results and discussion

It is clearly seen from Fig. 1 that shorter periods are more enhanced than longer ones. A similar result was already reported by Mason (1963). Sometimes the large scatter in the data points has been attributed to perturbations in the flow of internal currents near these stations, which arise due to the anomalies in the electrical conductivity distribution beneath the Afar depression (a tectonically active zone). It is also noticed that the peak in the enhancement of short-time disturbances does not coincide with the peak position of the electrojet ranges or solar flares (Figs 1, 2). For storm-time disturbances it is very close to the dip-equator whereas for both the electrojet and the solar flares this shows a shift of about 1° towards south of the dip-equator (i.e. between the geographic and the dip-equator). This characteristic difference can be explained if we assume that the changes in the horizontal component (ΔH) at the ground stations are proportional to changes in currents in the E-region of the ionosphere. The changes in currents depend on the conductivity of the ionosphere (σ) and on the electric field variations associated with geomagnetic disturbances. Remembering that the conductivity (σ) is a function of the electron number density (Ne), we can write:

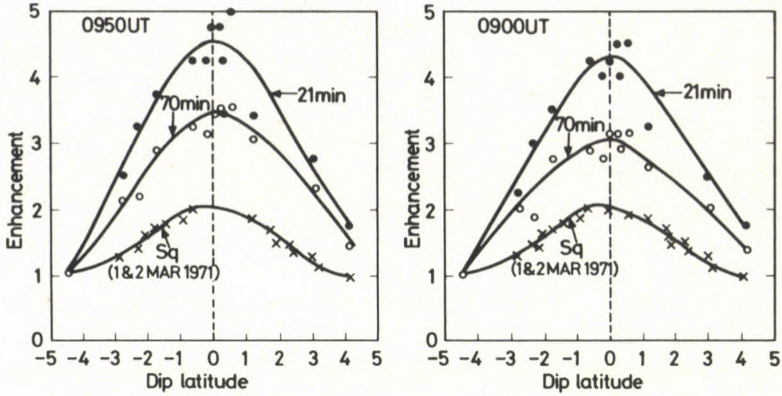

Fig. 1. The variation of the enhancement of horizontal component with dip-latitudes for the periods of 70 min and 21 min at two different times 0950 UT and 0900 UT and for the average Sq-ranges of March 1 and 2, 1971 in the Ethiopian region. The enhancement values are obtained by normalising to the corresponding variations at 5 YAV

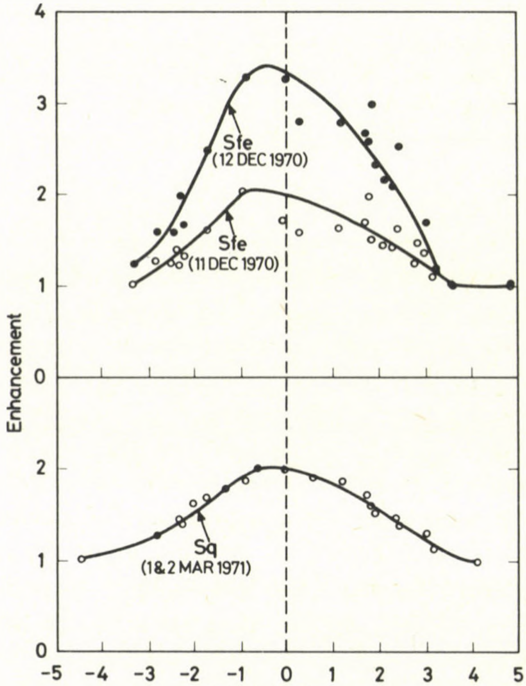

Fig. 2. The variation of the enhancement of horizontal component with dip-latitudes for two solar flares recorded on the 11th and 12th December, 1970. The enhancement values are obtained by normalising to corresponding variations at 6 ADI. In this figure, the variation of the enhancement for Sq-ranges is also included

$$\Delta H \alpha \Delta i \text{ at ionosphere } (E\text{-region})$$

$$\alpha \Delta(\sigma E)$$

$$\alpha \Delta[Ne(Esq \pm Esw)]$$

where Esq – Electric field due to dynamo action,
Esw – Electric field due to solar wind

During storm-time disturbances, the currents are affected by changes in the convective electric field ($\Delta Ey = -V \times \Delta Bz$), and since the conductivity is maximum near the dip-equator, the enhancement of variations is expected to be maximum there. On the other hand, the position of maximum enhancement for electrojet ranges can be explained from the currents produced by the dynamo generated Sq-electric field. These currents will critically depend on (i) the ionospheric conductivity which is controlled by the dip equator and (ii) on the atmospheric tides, which are controlled by the geographic equator. Thus, the position of the maximum enhancement in this case will be a resultant effect of the two equators as emphasized by Onwumechilli (1967). Since the positions of maximum enhancement do not coincide for the Sq variations and the sub-storm events, and the latitudinal profile of the conductivity variation is likely to be the same for both, it is suggested that the structure of the electric fields in the equatorial ionosphere produced by the dynamo and by storm-time disturbances differ from each other.

Another interesting result noticed is that the centres of electrojets for both the electrojet ranges and the solar flares almost coincide with each other (Fig. 2). This is true for both events of solar flares. Though solar flare is a short-period phenomenon, the coincidence of its latitude of maximum enhancement with that of the electrojet ranges suggests that the solar flare current system is an augmentation of the electrojet current system. This augmentation is the consequence of the fact that ultraviolet radiations emitted during solar flares immediately produce the increase of the conductivity of the ionosphere (σ) through an enhanced electron number density (Ne) in the dynamo region. Since the electrojet is a part of the normal Sq current system, it is suggested that the solar flare current system is nothing else than an augmentation of the normal Sq-current system as observed by Raja Rao and Rao (1963). It is also concluded that there are no major changes in the equatorial electric field distribution during both types of disturbances, otherwise the current system would not have been the same as observed from the peak of the maximum enhancement.

Conclusions

(i) As the centre of the maximum enhancement for storm-time variations does not coincide with that of solar flares and electrojet ranges, it is suggested that the structures of the equatorial electric field associated with them differ from each other.

(ii) Data from a close chain of records indicate that there are no major changes in the distribution of the Sq-electric field and the solar flares considered here.

Acknowledgements

We would like to thank Dr. R Rajaram for many useful discussions. We are also thankful to Prof. Mark Landisman and Dr. B R Lienert of the Institute for Geosciences, the University of Texas at Dallas for making the data from the Ethiopian chain available to us.

References

Agarwal A K, Rastogi R G, Nityananda N, Singh B P 1978: IMF effects on short-period fluctuations at low-latitudes. *Nature*, 272, 517.

Agarwal A K, Singh B P, Rastogi R G, Nityananda N 1979: Fluctuations of *H* at equatorial stations and interplanetary magnetic field. COSPAR Symp. Series. Ed. A. P. Mitra, Pergamon Press, 8, 43.

Akasofu S I 1977: Physics of Magnetospheric Sub-Storms. D. Reidel, Dordrecht

Akasofu S I, Chapman S 1963: The enhancement of the equatorial electrojet during polar magnetic substorms. *J. Geophys. Res.*, 68, 2375.

Alfven H 1976: On frozen-in lines and field-line reconnection. *J. Geophys. Res.*, 81, 4019.

Behannon K W, Ness N F 1966: The design of numerical filters for geomagnetic data analysis. NASA Technical Note No. D 3341.

Fejer B G, Gonzales C A, Farley D T, Kelley M C 1979: Equatorial electric fields during magnetically disturbed conditions–1. The effect of the interplanetary magnetic field. *J. Geophys. Res.*, 84, 5797.

Forbush S E, Vestine E H, 1955: Day-time enhancement of size of sudden commencements and initial phase of magnetic storms at Huancayo. *J. Geophys. Res.*, 60, 299.

Kane R P 1978: Equatorial enhancement of SSC magnitudes. *J. Geomag. Geoelectr.*, 30, 631.

Kane R P, Rastogi R G 1977: Some characteristics of the equatorial electrojet in Ethiopia (East Africa). *Ind. J. Radio and Sp. Phys.*, 6, 85.

Kikuchi T, Araki T, Maeda H, Maekawa K 1978: Transmission of ionospheric electric fields to the equator. *Nature*, 273, 650.

Mason R G 1963: Equatorial electrojet in central pacific. Scripps. Inst. Oceanogr. No. 63–13, 1.

Matsushita S 1960: Studies of sudden commencements of geomagnetic storms using IGY data from United States stations. *J. Geophys. Res.*, 65, 1423.

Mozer F S, Gonzales W D, Bogott F, Kelley M C, Schutz S 1974: High-latitude electric fields and the three dimensional interaction between the interplanetary and terrestrial magnetic fields. *J. Geophys. Res.*, 79, 56.

Ogbuehi P O, Onwumechilli A 1964: Daily and seasonal changes in the equatorial electrojet in Nigeria. *J. Atmos, Terr. Phys.*, 26, 889.

Onwumechilli C A 1967: Geomagnetic variations in the equatorial zone. In: *Physics of Geomagnetic Phenomena*, Vol. I. 425–507. eds S Matsushita and W H Campbell, Academic Press, New York and London

Onwumechilli A, Kawasaki K, Akasofu S I 1973: Relationships between the equatorial electrojet and polar magnetic variations. Planet. Space Sci., 21, 1.

Patel V L 1978: Interplanetary magnetic field variations and the electromagnetic state of the equatorial ionosphere. *J. Geophys. Res.*, 83, 2137.

Porath H, Dziewonski A, Gouin P, Bennett D J 1973: Ground observations of the magnetic field of the electrojet with a large array of magnetometers. Paper presented at the first Lloyd V. Berkner Symposium on Irregularities in the Equatorial Ionosphere. University of Texas at Dallas, Texas, May 14–17, 1973.

Raja Rao K S, Rao M P 1963: On the location of the ionosphere current system causing geomagnetic solar flare effects. *J. atmos. terr. sci.*, 29, 498.

Rastogi R G 1962: Longitudinal variation in the equatorial electrojet. *J. atmos. terr. phys.*, 24, 1031.

Rastogi R G 1963: Longitudinal inequalities in the lunar tide and in sudden commencement in *H* near the magnetic equator. *J. atmos. terr. phys.*, 25, 393.

Rastogi R G, Patel V L 1975: Effect of interplanetary magnetic field on ionosphere over the magnetic equator. Proc. Ind. Acad. Sci., 82A. 121.

Rastogi R G, Trivedi N B, Kaushika N D 1964: Some relations between the sudden commencement in *H* and the equatorial electrojet. *J. atmos. terr. phys.*, 26, 771.

Sastri N S, Jayakar R W 1970: Equatorial enhancement of geomagnetic field in the Indian region. *Ind. J. Met. Geophys.* 21, 279.

Sugiura M 1953: The solar diurnal variation in the amplitude of sudden commencements of magnetic storms at the geomagnetic equator. *J. Geophys. Res.*, 58, 558.

BOOK REVIEWS

C C TSCHERNING ed.: *Proceedings of the International Symposium Management of Geodetic Data.* København 24–26. August 1981 Geodaetisk Institut, Meddelelse No 55

The report no. 55 of the Danish Geodetic Institute contains the lectures presented at the International Symposium "Management of Geodetic Data" which took place in Copenhagen 1981.

The topics of the meeting were as follows:

Session 1: Geodetic Data Bases
Session 2: Entry and Validation of Geodetic Data
Session 3: Data Handling in Support of Geodetic Operations or Major Computational Processes
Session 4: Data Availability
Session 5: Meeting of SSG 4.66

The management of data is a very important task also in geodesy. The lectures held on this field have given a good overwiev about the problems and solutions. The book printed in offset consisting of 448 pages is nice to look at. It has a considerable desert: the short time of printing. So a half year after the symposium it was already issued.

J Somogyi

J Y CHEN: *Geodetic Datum and Doppler Positioning.* Dissertation. Mitteilungen der Geodätischen Institute der Technischen Universität Graz. Folge 39, Graz, 1982. p. 255.

The modern development in science and technology makes possible the updating and improvement of existing geodetic networks all the over the world.

Chen's dissertation investigates the updating techniques which are adequate to the needs of the geodetic network established twenty years ago in China.

Chapter One gives the theoretical bases of relationships between different coordinate systems related to geodetic datum and investigates the choice of ellipsoidal parameters and coordinate systems. Computational formulae are derived for the changes of different geodetic elements caused by the redefinition of the geodetic datum. Some possible schemes for the redefinition in China are investigates and evaluated.

In Chapter Two the accuracy of Doppler positioning and especially of the translocation technique is carefully studied. The author recommends some ways to reduce the systematic and random errors in Doppler point positioning when the broadcast ephemerides (BE) are used.

The Simplified Short Arc Method (SSAM) is proposed for China where a large scale geodetic network exists and only BE are available.

The four orbital corrections: the semi-major axis, the inclination, the longitude of the ascending node and the eccentric anomaly, introduced in SSAM are particularly significant in regions distant from OPNET. The adjustment of a large scale Doppler network is divided into two steps.

In the first step phased adjustment is used in the groups considered as blocks of the network.

In the second step the blocks are adjusted where the overlapping stations between groups are used as the joint parameters between the blocks.

The combination of a terrestrial network with the Doppler one resulting from SSAM is suggested in the Chapter Three both for a three-dimensional and a two-dimensional adjustment. The author demonstrates that the separation of Doppler stations — the shortest and the most effective distance wich can improve the terrestrial network — is different in case of different networks and equals the distance whose accuracy is equal both in the Doppler network and in the terrestrial one.

In Chapter Four a method using gravimetric height anomalies and deflections of the vertical for an independent test of the accuracy of Doppler positioning is discussed in details.

In conclusion this book is very useful not only for the necessary and urgent updating and improvement of the geodetic network in China, but for all those who deal with similar problems or are interested in Doppler geodesy.

L Bányai

G Buntebarth: *Geothermie. Eine Einführung in die allgemeine und angewandte Wärmelehre des Erdkörpers.* Hochschultext. Springer Verlag, Berlin–Heidelberg–New York, 1980. 64 Abb., 11 Tab. IX, 156 Seiten Dm 24.–, US $ 14.20

Das Buch enthält eine überaus gründliche Besprechung der unmittelbar mit der Geothermie zusammenhängenden Fragen. Die theoretischen Erörterungen sind reichlich mit praktischen Beispielen illustriert, so daß auch jene, die nur oberflächliche Kenntnisse über dieses Sachgebiet besitzen, sich leicht orientieren können. Es ist besonders hervorzuheben, daß der Verfasser viele Randgebiete mit einbezogen hat, wodurch an zahlreiche Zusammenhänge hingewiesen werden konnte.

Die sechs Kapitel des Buches erörtern zuerst kurz die physikalischen Grundlagen zur Wärmeleitung, dann die thermischen Eigenschaften von Gesteinen (Wärmeleitfähigkeit, spezifische Wärme, radiogene Wärmeproduktion). Die mathematische Beschreibung von konduktiven Temperaturausgleichsvorgängen ist mit besonders vielen, die Verhältnisse gut illustrierenden Beispielen begleitet.

Kapitel 4 enthält zuerst Angaben über thermische Vorgänge in der oberflächennahen Erdkruste mit der Erörterung der Störeffekte (meteorologische Temperaturschwankungen, Topographie, Wasserbewegung, geologische Strukturen); dann folgt eine Zusammenfassung unserer Kenntnisse über den thermischen Zustand im tieferen Erdinncren. Kapitel 5 ist den geophysikalischen Methoden der Temperaturerfassung gewidmet, wobei den Geothermometern und den direkten und indirekten Temperaturmessungen (gravimetrische, geoelektrische, seismische Methoden) etwa gleicher Raum gewidmet wurde.

Kapitel 6 befaßt sich mit der Nutzung der geothermischen Energie an Hand mehrerer Beispiele aus verschiedenen Ländern (z.B. Japan, Ungarn, Italien usw.). Ein reichhaltiges Literaturverzeichnis hilft jenen, die sich eingehender mit den einzelnen Problemen beschäftigen wollen.

Das rasche Erscheinen ermöglichte dem Verfasser, daß auch ganz neue Ergebnisse einbezogen werden konnten. Dementsprechend ist das Buch sämtlichen Studenten der Geothermie und der Geophysik im allgemeinen ein sehr guter Wegweiser zu weiteren Studien.

J Verő

S K Saxena ed. in chief: *Thermodynamics of Minerals and Melts.* Advances in Physical Geochemistry. Editors: *R C Newton—A Navrotsky—B J Wood.* Volume 1. Springer-Verlag, Berlin–Heidelberg–New York, 1981, 304 pages, 66 figs, Cloth DM 78,– approx. US $ 35.50

This book is the first volume of a new series which deals with the elucidation of physicochemical principles and their application in geosciences.

The volume gives a cross-section of the current activity in several areas of thermodynamical geochemistry on the basis of a lecture series on thermodynamics of mineral systems held in the Department of the Geophysical Sciences at the University of Chicago in 1979.

The first paper is a commentary by George Tunell on the basic equation of chemical equilibrium by J Willard Gibbs, which underlies all of chemical thermodynamics. The other papers are grouped into "minerals" or "melts" and, within each group, they generally proceed from the general problem through special ones to the application (according to the Preface).

The most interesting topics are: recent work on energy properties of melts, volatile interactions in magmas, modeling of melt-mineral systems, mineral system thermodynamics, and geothermometry-geobarometry.

Since many different symbols have been used in the papers, a table of notation is given.

This overview will be very useful to research scientists, advanced students of mineralogy, petrology, geochemistry and thermodynamics. Some parts of the book are also recommended to the attention of geophysicists dealing with the investigation of the earth's physical parameters under high pressure and temperature and the structure of the Earth's interior.

A Ádám

J B Gill: *Orogenic Andesites and Plate Tectonics.* Minerals and Rocks 16. Editor in Chief: *P J Wyllie.* Editors: *A El Goresy, W von Engelhardt, T Hahn.* Springer-Verlag, Berlin–Heidelberg–New York, 1981, 390 pages, 97 figs.

The book summarizes the entire field of andesite genesis. More emphasis is given to relevant data than to hypothetic models. The author annotates the over 1100 references cited.

The book is written for graduate students and professional earth scientists.

The subject of this book is called by the author "orogenic andesite" which forms a subset of hypersthene-normative volcanic rocks with 53% to 63% SiO_2. This can be distinguished chemically from other subsets by assuming that members of it have $K_2O < (0.145 \times SiO_2 - 5.135)$ and $TiO_2 < 1.75\%$.

Andesites are associated mainly with convergent plate boundary. Their bulk compositions are similar to estimates of the composition of terrestrial crust. Andesitic volcanism is studied because eruption prediction has great social importance as well as it seems to be related to the formation of many ore deposits.

The author summarizes selected geologic, physical, chemical and mineralogic characteristics of orogenic andesites in Chapters 2 to 6, and discusses the spatial and temporal variations of these characteristics in Chapter 7. Evaluations of genetic hypotheses are included into Chapters 8 to 11 where the characteristics are organized pro and contra and tested against several hypotheses. Chapter 12 presents a synthesis, and proposals for future researches (Citation from the Overview 1.4). The author's conclusion is that the differentiation of basalt by crystal fractionation of anhydrous minerals at low pressure is the most frequent and most fundamental process of orogenic andesite genesis, supplemented to an unknown extent by crystal fractionation of hornblende, selective crustal interaction, magma mixing, and vapor fractionation.

The book is very clearly written, its system analysis is outstanding and its argumentation is very convincing, therefore it is warmly recommended to the attention of earth scientists.

A Ádám

C MONTY ed.: *Phanerozoic Stromatolites.* Case Histories Springer-Verlag, Berlin. 1981, pp. I–X, 1–249; 121 figs, 10 pls.

Stromatolites are calcareous, dolomitic, or siliceous biosedimentary structures resulting from the life processes and rock-building activity of primitive algal (Cyanophyta) communities.

Blue-green algae, being most ancient and resistant forms of the organic world, played very important role as stromatolitic reef-builders through several milliard years in the Precambrian. Within the Phanerozoic, i.e. in the last 570 million years, their importance somewhat diminished, however, as it is proved by this book, their geologic significance remained essential.

This book contains the majority of the papers presented on the 2nd International Symposium on Fossil Algae in Paris, 1979. The 17 papers give a comprehensive approach to the morphology and the circumstances of formation of stromatolites. 6 papers describe Paleozoic, 4 Mesozoic and 5 Cenozoic material, respectively. The introductory paper of the Editor deals with the generally interesting problems of the classification of blue-green algal structures. J Kazmierczak suggests a cyanophytic origin for the extinct stromatoporoids — this paper will undoubtedly arise wide controversy.

The book is valuable primarily for researchers interested in the ecology, environment or complex lithification history of stromatolites. Especially interesting are the results of studies on stromatolites and cryptalgal laminites associated with Messinian gypsum of Cyprus and on sub-Recent manganese-bearing stromatolites along shorelines of the Dead-Sea.

The presentation of this book so important for sedimentologists is high-standard, and its content would be stimulating for similar studies in Hungary.

B Géczy

Erosion and Sediment Transport Measurement. Proceedings of the Florence Symposium, 22–26 June, 1981. Published by the International Association of Hydrological Sciences as IAHS Publication No. 1113 in June 1981, pp. XII + 527, 54 US $

There is an increasing need for detailed and reliable data on erosion and sediment transport in order to evaluate problems such as soil loss, land degradation, reservoir sedimentation, debris transport and deposition; to permit the design of effective hydraulic structures and channel management strategies; and to provide information on the transfer of material from the land surface to the oceans. The aim of the symposium was to provide a forum for the review of recent developments in the measurement of erosion and sediment transport, for the exchange of ideas and experiences, and for the definition of outstanding problems and research needs.

The 55 papers report developments and experiences from 19 countries with a wide spectrum of measuring techniques in a great variety of environments ranging from tropical Nigeria to the Negev Desert in Israel and the Yellow River region of China; the papers were grouped under the following topics:

1. Measurement of sediment transport (36 papers)
1.1 Measurement of bed load transport (6 papers)
1.2 Techniques for continuous monitoring of suspended sediment concentrations (5 papers)
1.3 Suspended sediment sampling apparatus (4 papers)
1.4 Suspended sediment sampling (4 papers)
1.5 The reliability of sediment load data (5 papers)
1.6 Laboratory experimentation and the measurement of debris flows and mass movement (6 papers)
1.7 Design of data collection programmes (6 papers)
2. Measurement of erosion (19 papers)
2.1 Measurement of rainfall erosivity and splash erosion (5 papers)
2.2 Rainfall simulators and laboratory experiments (4 papers)
2.3 Erosion plot studies (5 papers)
2.4 Field measurement of erosion (5 papers)

As a general conclusion it may be summarized that it is very little understood so far about the transport of solid material by water. To extend knowledge and information both laboratory and field measurements are essential. This volume informs both about the recent results of development achieved concerning measuring techniques and apparatus of sediment transported and about measurement of characteristics of erosion processes. So this volume can serve as a "state-of-art" report, too.

The book is available from either the Office of the Treasurer, IAHS (2000 Florida Avenue NW, Washington, DC 20009, USA), or the IUGG Publications Office (39 ter Rue Gay Lussac, 757005 Paris, France).

K Stelczer

I M Varentsov and Gy Grasselly eds: *Geology and Geochemistry of Manganese*. Publication of the 2. International Conference on Geology and Geochemistry of Manganese (Sydney, August 17–24, 1976). Vol. I–III, Akadémiai Kiadó, Budapest, 1980. 463, 513, 357 pages.

The three-volume publication contains the complete material of the Second International Symposium on Manganese (all papers in full length), and it covers nearly all fields of the element manganese and its natural compounds (mineralogy, petrology, geology, material investigation, geochemistry, economic geology) with special attention to genetic problems. It is characterized by both advantages and disadvantages of multi-author works coordinated only by the common object of investigations: in the different special fields the leading experts discuss their ideas, thus the reader gets up-to-date treatments of the problems from the "first hand", without any misinterpretation; but at the same time an uneven level of the papers is nearly inavoidable, and certain areas are discussed twice or even more times (being not always a disadvantage), while others are not included at all.

The natural compounds of manganese (mainly oxides and hydroxides) have in recent times an increasing use, and together with other raw materials, this resulted in increasing efforts for the discovery of their deposits, for a survey of their characteristics and application. Therefore a general summarization of the results from time to time has great importance. In case of manganese, the first great world-wide conference was held 1956 in Mexico City, this was followed by a second in 1976 in Sydney. A comparison of the material of the two conferences reflects clearly the immense development in these 20 years both in ideas and results.

The Hungarian publishers are to be praised that they overtook the responsibility for the publication of the symposium material, and by this they made not only a service to the scientific community, but at the same time they draw the attention of the scientific world to the internationally highly ranking efficiency of our publications. And though the outer appearance of the three volumes is worthy of the inner content, it is regrettable that the changing paper quality deteriorates this qualification.

The first volume includes papers on mineralogy, geochemistry and investigation methods. The grouping into narrower disciplines, however, does not always cover the content of the different papers. This somewhat artificial distribution re-appears again and again in the grouping of the subjects in the volumes, very likely to be traced back to a subsequent grouping of certain papers. Namely the greatest part of the papers covers wider fields, and it would be most adequately to describe them as belonging to economic geology.

Only one of the 7 papers under the heading Mineralogy deals really with minerology, all others belong only partly here. This one (written by G Frenzel) lists the most important parameters and data of the 30 manganese minerals occurring most frequently in the nature (mostly oxides and hydroxides, no carbonates are included), and therefore it is an indispensable data bank for anybody dealing with manganese exploration. From among the other papers, two deal with manganese nodules from the deep sea (this topic is dealt with in more details in Volume 3), one describes sedimentary iron oxideminerals, one the manganese oxides in soils, one is concerned with the progressive metamorphism of manganese carbonates and cherts, and the last one is devoted to manganese minerals in gold-silver deposits.

The 5 papers under the heading Geochemistry correspond much better to the point of view of the grouping. Two of them discuss the general geochemical character of manganese, one deals with the geochemistry and generation of the manganese dioxide. The last two are also quite concrete papers on the geochemical description of the manganese and some other metals appearing often in its deposits in marine environment.

"Methods" are represented by two papers. The first one deals with the statistical treatment of a many-variable system on the example of the evaluation of ocean-bottom manganese nodules, the other presents a combined analysis with X-ray fluorescence and emission spectrography for manganese ores and products, giving the computation method for about 50 elements in wide concentration limits.

The second volume has the subtitle: continental manganese deposits. This topic covers the traditional economic geology with the deficiencies in completeness, as already mentioned. It includes a general (genetic) part and a systematic (regional) part. The latter is the less complete one, the description of several important deposits cannot be found here, and this lack cannot be substituted by an enumeration in the introduction of the volume. On the other hand, the description of other deposits is detailed, in some cases even too many details are given. All these are the natural consequences of the scope of similar works.

The general (genetic) part includes 5 papers, from which the most detailed one is the second, written by H Borchert, who summarizes the genetic types of manganese deposits. These are the following:

I. Enrichments of manganese ores of gondites in connection with lateritic weathering;

II. Deposits developed in connection with the reducing facies of the carbon dioxide zone in marine and limited basin environments (Nikopol-Chiatura type);

III. Manganese nodules on deep sea bottom;

IV. Manganese ore deposits in shale-chert — spilite formation;

V. Deposits in probable connection with initial basaltic volcanism;

VI. Manganese enrichments as lateritic weathering products of ultrabasic rocks;

VII. Manganese enrichments in connection with sialic-palingenic magmatism;

VIII. Deposits due to very specific interaction processes between two ground-water masses with oxidizing and reducing character (Lindener Mark-type);

IX. Deposits of similar origin with additional epimetamorphic effects (Postmasburg-type);

X. Lake and bog ores of the terrestrial tundra facies.

From the other two genetic papers the first deals with the sedimentary manganese formations, and it tries to find a connection between products and processes in recent and ancient manganese deposits. The other discusses the origins of Precambrian biogenic-sedimentary manganese deposits.

The systematic (regional) geology of manganese is further subdivided according to continents and countries. Africa is represented by a single paper (Gabon), South-America also by one (Brasil), Australia by two, New Zealand by one, Europe by two (Hungary), Asia by four (including three on India and one on South Korea), and the Soviet Union, representing a special part of Eurasia, by nine papers. This can be easily explained by the overwhelming role of the Soviet Union in the manganese production of the Earth.

Hungary is not very important from the point of view of the world production, but its manganese deposits (Úrkút and Eplény) are exploited and represented in this book by two papers. The first gives a geologic-stratigraphic description of the deposits, the other deals in more details with the origin of the oxidic manganese ores of the Úrkút Basin. The main point of the theory is that they were originally sedimentary manganese carbonates, and later certain parts of the deposit became oxidized due to the sulphuric acid from the pyrite weathering, at the end they were partly eroded and newly deposited.

The third volume deals with the manganese nodules of some Recent basins, where the development of manganese deposits is recently active. Their importance is partly due to the fact that the genesis of these manganese deposits can be immediately observed, on the other hand these deposits on the bottom of some oceanic basins represent a high potential value. In the description of them a general (genetic) and a systematic (regional) part can be separated.

The genetic part includes four papers. The first two discuss the genetics of the manganese accumulated in ocean bottom nodules, favouring a terrestrial origin in one, and a cosmic (meteoric) origin in the other paper. The other two describe in more details the processes of the development of these deposits: the first is based on the investigation of natural materials, while the second uses artificial experimental material and processes for the simulation of the natural ones.

In the regional part, basins are separated according to their geographic situations. Two papers present nodular manganese deposits on the Pacific ocean floor, as explored by expeditions, similar deposits in the Atlantic and Indian Oceans are represented by one paper each. Three following papers deal with manganese deposits in shallow water basins: the first discusses generally the genesis of ferromanganese concretions in Recent basins, the second gives a more concrete example for this from the Baltic Sea. The third paper deals with the freshwater ferromanganese-deposits in North America.

The volume is concluded by three papers on general (genetic) problems which concern microbiological aspects. It is not clear why these papers appear at this place, as they were more logical at the beginning of this volume, or in one of the earlier volumes.

The last paper gives a survey on the problems of the mining of polymetallic manganese nodules from the ocean floor. The final conclusion is that in spite of all difficulties the problems of their mining will be solved in a short time, as the technical problems of the oil production from the sea bottom were solved in a relatively short space of time.

P Kisházi

V GONSER ed.: *Topics in Current Physics — Mössbauer Spectroscopy II.* The Exotic Side of the Method Founded by H K V Lotsch, Vol. 25 Springer–Verlag, Berlin–Heidelberg–New York, 1981, 196 pp. 67 figs DM 62, US $ 28.20

Since its discovery in 1957, Mössbauer effect has run an exceptional course. It is used as one of the standard spectroscopies in many fields of solid state physics, chemistry, mineralogy and biology as described in the first volume of the present work (Mössbauer Spectroscopy, Topics in Applied Physics, Vol. 5). On the other hand, these investigations have not exhausted the field, novel possibilities are discovered even after a rather long period of time. Some of these more sophisticated and exotic applications of the effect are reviewed in the present volume including the phase problem in the structure determination of biological molecules, resonance γ-ray polarimetry and ion implantation studied by conversion-electron Mössbauer spectroscopy. It is suggested that further unexpected applications will be found in physics as well as in interdisciplinary research areas.

L Takács

D J SOUTHWOOD ed.: *ULF Pulsations in the Magnetosphere.* Advances in earth and planetary sciences, 11 Center for Académic Publications. Tokyo and D. Reidel, Dortrecht–Boston–London

The volume contains the review papers presented at the IAGA Symposium on pulsations held during the 17th General Assemply of UGGI in Canberra, December 1979. The 9 papers cover practically all the fields of recent pulsations research. A special advantage is that as several authors discuss related topics, a more complete picture can be obtained by comparing the different views on the same phenomenon.

The reviews were written at a moment, when the discussions on the origin of the ULF pulsations (this name is proposed in the book instead of geomagnetic pulsations, as it seems to the authors that geomagnetic is a too narrow adjective for the phenomenon) resulted in a consensus that pulsations are either excited in, or are strongly influenced by the extramagnetospheric space. The solar wind, the direction and magnitude of the interplanetary magnetic field all influence certain parameters of the pulsations, and as soon as some secondary influences can be expressed numerically, pulsations may be used as an efficient tool for the determination of certain interplanetary parameters. The papers discuss both the excitation and the modification of the hydromagnetic waves responsible for the pulsations. Most papers are accompanied by a short account on the history of the topic. It is really admirable how many impetus in this field is due to Dungey's ideas: nearly all papers begin with his name.

Rostoker, Samson and Olson discuss longitudinal and latitudinal variations of Pc 4, 5 pulsations with the result that a great part of the characteristics are consistent with a Kelvin–Helmholtz source, but for certain events an inner magnetospheric source cannot be excluded.

Kokubun reports on satellite-ground correlation of Pc pulsations. He summarizes the types which occur in space and lists also the ground occurrences. He summarizes the causes for the differences. Most of his paper is also concentrated on Pc 4, 5.

Hughes gives an account on multi-satellite observations of pulsations. This new possibility is very effective in pulsations research. Among others, the idea of shell resonances has been confirmed by it, and the width of the resonant shells could also be determined to be less than 1 R_E. There is a great difference between morning and afternoon Pc 4 waves which hint at different physical origins.

A possible mechanism responsible for the afternoon Pc 4 activity has been elucidated by Southwood in a following paper. The excitation would be due to energetic particles. He compares theoretical results with observations and finds an acceptable agreement, including the lack of this type of activity at ground.

McPherron describes substorm-associated pulsations at synchronous orbits. He can distinguish a number of different types of activity, for which he enumerates the main characteristics and possible excitation mechanisms.

Greenstadt, McPherron and Takahashi describe the solar wind control of daytime pulsations. They give a review of previous results, select sure results and propose a model which can explain most of the observed characteristics. In this model, a part of the waves are generated in the quasi-parallel bow shock in the forenoon sector by local cyclotron instability, while at the flanks of the magnetosphere the Kelvin–Helmholtz instability is active.

Walker and Greenwald describe the auroral radar pulsations which add an important aspect to other existing methods. In the Pc 5 range, the results confirm several results obtained by conventional methods, e.g. the rotation of the magnetic field in the ionosphere, and can already be used for the determination of the equatorial plasma density and height integrated ionospheric conductivity.

Knox and Allen, as well as Andrews, Lanzerotti and Maclennan deal with the ionospheric modification of pulsation waves. The first paper discusses damping and coupling of the waves in the ionosphere, and their consequences, the second one describes a new method, the Doppler shift on whistler mode signals from VLF transmitters which could be used for the verification of the rotation of the magnetic field in the ionosphere.

Most papers summarize some future tasks which the authors consider to be necessary to solve in the next years. Thus the book can be qualified as state of art on the pulsations research, as well as an agenda on experimental and theoretical fields. In any way, this is a very important and also interesting work for all pulsation people and even for those who are interested in related topics.

J Verő

H Swinney and J P Gollub eds: *Hydrodynamic Instabilities and the Transition to Turbulence.* Haverford, PA, USA Springer–Verlag, Berlin–Heidelberg–New York 1981. 81 figures, 8 tables, 292 pages

In the classical physics there are most unsolved problems in hydrodynamics, within it chiefly in the subject of instabilities and turbulence, therefore it has been very timely to publish this book.

After an introduction the book consists of eight papers, seperated, nevertheless connected with each other, creating an organic unity. The first three papers are of theoretical character, describing the processes of the hydrodynamic stability, the transition to turbulence, the bifurcation and the chaotic behavior of the fluids in several kinds of flow. The following three chapters deal with some special cases (the transition to turbulence in Rayleigh–Bénard convection, the instabilities in flow between concentric rotating cylinders, the shear flow instabilities and vortexes etc.). It is a recommendable model in these papers that following the deduction of the basic equations the authors lead the readers beginning from the discussion of the linear and nonlinear theories, with presentation of results obtained by numerical and analitical approximation methods and where it is possible, with the comparison of results with the experimental observation through all the steps of the given problem.

For geoscientists the eighth chapter is of much more interest, where practical questions as the instabilites in a stratified fluid, the shear processes, the baroclinic instability, the multidiffusive instabilites etc. are discussed. Though because of the wide range of the discussed problems and the concise treatment some parts are more difficult to understand (this refers to some parts of the theoretical papers, too) the abundant references help readers in full understanding. The ninth chapter deals with the instabilities and chaos in nonhydrodynamical systems studying such examples (the Rikitake dynamo model for the Earth's magnetic field, the Belousov–Zhabotinskii chemical reaction, population dynamics, the van der Pol equation applicable in a lot of fields of physics etc.). That interests a wide range of readers from geophysicists through engineers till economists, alike.

This book is filling a gap in every respect, and gives useful knowledge both to inexperienced and well versed readers in some problem.

M Varga

G Kovács: *Seepage Hydraulics.* Jointly published by Akadémiai Kiadó, Budapest and Elsevier Scientific Publishing Company, Amsterdam, 1981, 730 pages, 480 Ft

The 730 page book has been written in five parts and is containing altogether nineteen chapters; it is a revised and up-dated version of Author's book with a similar title published in Hungarian in 1972. In *Part 1* a review is given of the fundamentals of the investigation of seepage (general characteristics, physical and mineralogical parameters influencing permeability, dynamics of soil moisture, balance of the ground-water space). *Part 2* deals with the dynamic interpretation and determination of hydraulic conductivity in homogeneous loose clastic sediments (dynamic analysis of seepage, hydraulic conductivity of saturated layers, seepage through unsaturated layers). *Part 3* discusses the permeability of natural layers and processes influencing its change in time (hydraulic conductivity of loose clastic sediments, motion of grains in cohesionless loose clastic sediments, investigation of clogging, hydraulic conductivity and intrinsic permeability of fissured and fractured rocks). *Part 4* gives a kinematic characterization of seepage (kinematic relationships for laminar seepage, boundary and initial conditions of potential flow through porous media, kinematic characterization of non-laminar seepage). Finally, *Part 5* presents the solution of movement equations describing seepage (characterization of two-dimensional potential seepage, combined application of various mapping functions, horizontal unconfined steady seepage, investigation of horizontal unsteady seepage, model laws for sand box models).

The Author's intention was to give in this book a summary of the results attained recently in seepage hydraulics covering the bordering fields of earth sciences, technical sciences and physics. A better understanding of the processes which govern the movement of water through porous media has resulted in recent years from improved experimental methods and from the availability of computers in carrying out intricate investigations. His aim was to establish an integrated system that comprises all fields of seepage hydraulics, by starting with the dynamic analysis of the process, then determining both theoretically and in practical ways the parameters characterizing water movement and storage in porous media, and to give kinematic descriptions of the phenomena. Theoretical and practical, physical and mathematical approaches were considered together with scientific aspects of hydraulics, hydrology, geology and soil science.

A remarkable new feature of the book is to characterize porous media on the basis of a continuum approach where the random change of the internal structure is considered by the application of statistical models both for granular and for fractured media. Dynamic principles are used to determine the capacities of transport and of storage of water of loose clastic sediments and of fractured rocks, resulting in the introduction of simple relationships for characterizing both saturated and unsaturated conditions.

From a practical engineering aspect it should be appreciated that Author has compared through numerous examples the soulution of kinematic equations with precise theoretical methods and with simplified approximations used in practice, and has proved the applicability of the latter.

The book should primarily be considered as a manual which helps in solving practical problems concerning water movement in porous media and will thus be useful for those working in mining, civil engineering and agricultural engineering. Further, as it contains an extensive amount of field- as well as experimental data, it can also serve as a basis for researches interested in the same fields.

P Major

T Rikitake ed.: *Current Research in Earthquake Prediction I.* (Developments in Earth and Planetary Sciences 02) Center for Academic Publications Japan, Reidel, Dordrecht, 1981, 383 pl.

The increasing interest in and success of earthquake prediction is reflected by the increasing number of books published on this topic. Quite recently another publication dealt with the general trends of earthquake occurrence, e.g. with seismic gaps; now this one summarizes more the immediate precursors, as height changes, precursory seismological events, anomalous behaviour of animals, magnetic and electric phenomena. Most data of this book are from Japan, but appropriate attention is paid to results achieved in the United States, Soviet Union and China, too. A common feature of the discussion of the precursors is that a clear selection of precursors and the determination of the precursor

— seismic event time difference is always striven at. This helps the readers to differentiate between vague and too early, may be often dubious precursors, and such ones which precede shortly the main shock and can be immediately identified as precursory events. This is already clear in Professor Rikitake's introductory review, where two different kinds of precursors are separated. The first one has a precursor time depending on the magnitude of the quake, reaching a value of several years for a really great shock (magnitude of about 8.0). The second kind has a precursor time of some hours, independently of the magnitude. There is perhaps a third type with a delay of several days.

Rikitake follows with a detailed survey of the precursors of the Izu-Oshima earthquake (1978, magnitude 7.0), when a successful prediction has been issued two hours before the main shock. It was based on a sudden decrease of the earthquake activity. In addition to this, there were many other observations including vertical movements, radon content, magnetic and electric variations, etc. The anomalous animal behaviour for this shock is described in a separate paper, including nearly as many observations as were previously known for all other events.

M Wyss deals with earthquake prediction in the US: The methods include there measurements of seismic velocity, seismicity, crustal deformations (including the most famous one, the Palmsdale Bulge), stress measurements, magnetic field data and a number of other possibilities. The gradation of predictions leads over already to the next paper, on the public reaction on earthquake prediction (J R Hutton, J H Sorensen, D S Mileti). The real danger of false prediction could be seen just a few years ago in Hungary, in a country with not too many dangerous earthquakes, when uncontrollable sources predicted a strong earthquake just in the capital, in Budapest and there was general alarm, nearly panic in spite of denials from all official seismological sources. It is clear that damages due to earthquakes must be compared with expenses due to false alarms.

In the second part of the book, surveys of the most promising methods are given, mainly based on Japanese data, but reporting also successful Chinese and Soviet pridictions. T Dambara reviews geodetic methods, level changes, prediction of the rupture zones, occurrence times, tidal observations, horizontal movements. This is the most comprehensive paper of the book, and its data are very useful for the planning of geodetic surveys for prediction purposes. K Hamada summarizes prediction-oriented seismology, where different aspects of this possibility are presented with great care to avoid uncontrollable statements. Y Honkura reviews two of the most promising methods, those of magnetic and electric variations. It seems that in spite of accuracy problems, electric field and resistivity changes will prove as one of the most powerful tools to predict earthquakes.

In the last years, the first successful predictions of earthquakes were issued. Greatest interest was arosen by the prediction of some Chinese quakes. It seems that a warning is possible in the near future, in spite of many setbacks and human problems which are sure to happen.

J Verő

A BEN-MENAHEM and S J SINGH: *Seismic Waves and Sources.* Springer Verlag, Berlin–Heidelberg–New York, 1981, XXI + 1108 pages, with 307 Figs

The authors' aim has been to give a comprehensive account on the generation of elastic waves by realistic earthquake sources and their propagation through realistic earth. They also claim to fill a wide gap between the level of existing textbooks on seismology and the level of advanced papers appearing in research journals.

The field to be covered is vast and the authors should necessarily be selective. As they state in the preface they had been forced to concentrate on the topics that belong to the mainstream of contemporary seismology, and exclude e.g. the discussion of scattering and diffraction of seismic waves or the theory of leaking modes.

Chapter 1 gives a brief summary of classical continuum dynamics. Besides the fundamental concepts of stress, strain, deformations and the derivation of field equations it includes the Lagrangian formulation which is then used in Chapters 5 and 10.

Chapter 2 deals with the solution of the wave equation for infinite space. The plane wave solution in Cartesian, circular cylinder and spherical coordinates are given and their interrelation is pointed out.

Chapter 3 is devoted to the interaction of plane waves with planar discontinuities, including reflection and refraction at a single interface, reflection at a free surface, surface waves, spectral response of a multilayered crust as derived with the aid of the matrix propagator algorithm. The utilization of dispersion curves of seismic surface waves in estimation of crustal and upper mantle structure is briefly discussed here.

Chapter 4 deals with seismic sources and the application of elasticity theory of dislocations. The fundamental Stokes-Love solution of the inhomogeneous Navier equation is the starting point and from it the theory of dipolar point sources is developed and used for describing displacement dislocations. The theory of earthquake sources, fault-plane geometry, theoretical seismograms in an infinite medium, displacements in the near and for fields, radiations from spherical cavities, finite moving sources are discussed in detail.

Chapter 5 is devoted to the surface-wave amplitude theory. The amplitudes of surface waves are related to the kinematic parameters (fault length and rupture velocity) of the sources. Several examples illustrate the application of this new field of seismology, justly called "terrestrial interferometry".

Chapter 6 deals with the free oscillations of the Earth, including basic theory of free oscillations, numerical methods for the calculation of the eigenfrequencies and spectral amplitudes for realistic models. The splitting effects due to the rotation of the earth and the effects of source finiteness and motion are also discussed.

Chapter 7 concerns geometric elastodynamics, rays and generalized rays. It starts from the equation of motion and after the asymptotic body wave theory it develops the amplitude theory of body waves in a radially inhomogeneous earth. The concept of a generalized ray is introduced here and ground motion is determined by the generalized ray method.

The connection of normal modes and rays is explained in Chapter 8, which discusses the asymptotic theory of earth's normal-mode situations in great detail.

Chapter 9 is devoted to atmospheric and water waves excited by earthquakes or nuclear explosions, such as tsunamis, seiches, air waves, pressure-induced surface waves, coupled air-sea waves as well as Rayleigh waves and acoustic-gravity waves.

Chapter 10 deals with the propagation of waves in viscoelastic solids. The attenuation of body waves and dispersion of attenuated surface waves are discussed.

The book is well illustrated with numerous figures, tables and solved examples. The material is indexed and a list of references is given at the end of each chapter. An addition several appendices describe the mathematical tools employed in the book.

Functional both as a textbook and a handbook this work may be useful to university students and research workers alike and it is a welcome addition to the literature.

A Meskó

PRINTED IN HUNGARY

Akadémia Nyomda, Budapest

— treble underlining: bold-face italics
— red underlining: Greek letters
— green underlining: script letters.

Rules for mathematical-physical notations:

— trigonometric, logarithmic, analytic symbols, symbols for units and functions are in roman type (not underlined)
— letter symbols in mathematical and physical formulas, scalars, and subscripts of algebraic and physical quantities are in italics (underlined)
— vectors, matrices, operators in probability theory are in bold-face roman type (double underlining)
— tensors, operators and some special functions are in script letters (green underlining). These cannot be bold.
— Greek letters (red underlining) cannot be bold or extra bold type (thus they cannot be used for vectors or tensors)
— void upper lines e.g. for vectors
— avoid possible confusion between o (letter) and 0 (zero), l (letter) and 1 (one), ν (Greek nu) and v, u (letters) etc.
— explain ambiguous or uncommon symbols by making marginal notes in pencil
— be careful about superscripts and subscripts
— formulae must be numbered consecutively with the number in parentheses to the right of the formula. References in text to the equations may then usually be made by the number in parenthesis. When the word equation is used with a number, it is to be abbreviated, Eq. or Eqs in the plural
— the International System of Units (SI) should be used.

Authors are liable for the cost of alteration in the *proofs*. It is, therefore, the responsibility of the author to check the text for errors of facts before submitting the paper for publication.

3. *References* are accepted only in the Harvard system. Citations in the text should be as:

. . . (Bomford 1971) . . . or Bomford (1971)

. . . (Brosche and Sündermann 1976) . . .

. . . (Gibbs et al. 1976b) . . .

The list of references should contain names and initials of all authors (the abbreviation et al. is not accepted here); for *journal articles* year of publication, the title of the paper, title of the journal abbreviated, volume number, first and last page.

For *books* or *chapters in books*, the title is followed by the publisher and place of publication.

All items must appear both in the text and references.

Examples:

Bomford G 1971: Geodesy. Clarendon Press, Oxford

Brosche P, Sündermann J 1976: Effects of oceanic tides on the rotation of the earth. Manuscript. Univ. of Bonn

Buntebarth G 1976: Temperature calculations on the Hungarian seismic profile-section NP-2. In: *Geoelectric and Geothermal Studies (East-Central Europe, Soviet Asia), KAPG Geophysical Monograph*. Akadémiai Kiadó, Budapest, 561–566.

Gibbs N E, Poole W G, Stockmeyer P K 1976a: An algorithm for reducing the bandwidth and profile of a sparse matrix. *SIAM J. Number. Anal.*, 13, 236–250.

Gibbs N E, Poole W. G, Stockmeyer P K 1976b: A comparison of several bandwidth and profile reduction algorithms. *ACM Trans. on Math. Software*, 2, 322–330.

Szarka, L., 1980: Potenciáltérképezés analóg modellezéssel (Analogue modeling of potential mapping). *Magyar Geofizika*, 21, 193–200.

4. *Footnotes* should be typed on separate sheets.

5. *Legends* should be short and clear. The place of the tables and figures should be indicated in the text, on the margin.

6. *Tables* should be numbered serially with Roman numerals. Vertical lines are not used.

All the illustrations should contain the figure number and author's name in pencil on the reverse.

Figures will be redrawn. Therefore the most important point is clearness of the figures, even pencil-drawings are accepted (with a duplicate).

Photographs and *half-tone* illustrations should be sharp and well contrasted.

If a specific reduction or enlargement is required, please indicate this in blue pencil on the figure.

The editors will send information to the first author about the *arrival* and acceptance of the papers. A galley proof is also sent to the first author for *correction*. Hundred *offprints* are supplied free of charge.

Index: 26.031

FORMERLY ACTA GEODAETICA, GEOPHYSICA ET MONTANISTICA ACADEMIAE SCIENTIARUM HUNGARICAE

Acta Geodaetica, Geophysica et Montanistica Hungarica

VOLUME 18, NUMBER 3, 1983

1828

Akadémiai Kiadó, Budapest

AGGM 18 (3) 219-336 (1983) HU ISSN 0374-1842

ACTA GEODAETICA, GEOPHYSICA et MONTANISTICA HUNGARICA
A Quarterly Journal of the Hungarian Academy of Sciences

Acta Geodaetica, Geophysica et Montanistica (AGGM) publishes original reports on geodesy, geophysics and minings in English.

AGGM is published in yearly volumes of four numbers by

AKADÉMIAI KIADÓ

Publishing House of the Hungarian Academy of Sciences

H-1054 Budapest, Alkotmány u. 21.

Manuscripts and editorial correspondence should be addressed to

AGGM Editorial Office

H-9401 Sopron P.O. Box 5

Subscription information

Orders should be addressed to

KULTURA Foreign Trading Company

H-1389 Budapest P.O. Box 149

INSTRUCTIONS TO AUTHORS

Manuscripts should be sent to the editors (MTA Geodéziai és Geofizikai Kutató Intézete, AGGM Editorial Office, H-9401 Sopron, P.O.Box 5, HUNGARY). Only articles not submitted for publication elsewhere are accepted.

Manuscripts should be typewritten in duplicate, double-spaced, 25 lines with 50 letters each. The papers generally include the following components, which should be presented in the order listed.

1. Title, name of author(s), affiliation, dateline, abstract, keywords
2. Text, acknowledgements
3. References
4. Footnotes
5. Legends
6. Tables and illustrations

1. The *affiliation* should be as concise as possible and should include the complete mailing address of the authors. The *date of receipt* of the manuscript will be supplied by the editors. The abstract should not exceed 250 words and should clearly and simply summarize the most important methods and results. 5–10 significant expressions describing the content are used as *keywords*. Authors may recommend these keywords.

2. The *text* should be generally in English and as short and clear as possible. From Hungarian authors papers are also accepted in Hungarian.

The section heading should *not* be underlined or in capitals.

Please note that underlining denotes special types:

— single underlining: italics

— double underlining: bold-face roman

Acta Geodaet., Geophys. et Montanist. Hung. Volume 18 (3), pp. 219—234 (1983)

PROZESS-ANALYSE EINES FLOTATIONSWERKES MIT HILFE EINES COMPUTER-PROGRAMMES

SZ PETHŐ[1]

[Eingegangen am 6. Januar 1981]

Der Trennungsprozeß in Flotationswerken und die dafür geltenden Beziehungen und Funktionen werden in allen Einzelheiten einer Analyse unterzogen. Für ein Flotationswerk zur Anreicherung von Chalkopyrit wird ein Computer-Programm aufgeschrieben, mit dessen Hilfe alle jene Änderungen erfaßt und verfolgt werden können, die sich aus der systematischen Veränderung der Kopplung der Flotationszellen für die Hauptparameter, wie: Massenausbringen, Mineralgehalt, Mineralausbringen und Trennwirkungsgrad ergeben. Auf Grund der erzielten Ergebnisse werden bezüglich des Flotationsbetriebes auf Chalkopyrit wichtige Gesetzmäßigkeiten erkannt und festgestellt. Die wichtigsten von diesen können verallgemeinert werden.

Keywords: chalkopyrite; computer programs; effectivity of flotation; flotation plant; process-analysis

Die Trennungs-Funktionen des Flotationswerkes im Falle einer Zurückführung des Zwischenproduktes

Wie bekannt, ergibt sich bei einem Zellenkopplungssystem nach Abb. 1 das Massenausbringen an Schaum m_h und an abgehendem Bergematerial m_m (Pethő 1977a, Pethő 1978) aus den Beziehungen

$$m_h = \sum_{i=1}^{n} \sum_{j=1}^{r} m_{ij} \frac{1 - \prod\limits_{\nu=N_1+1}^{N_1+N_2} q_{ij\nu} + \prod\limits_{\nu=N_1+1}^{N} q_{ij\nu} - \prod\limits_{\nu=1}^{N} q_{ij\nu}}{1 - \prod\limits_{\nu=N_1+1}^{N_1+N_2} q_{ij\nu} + \prod\limits_{\nu=N_1+1}^{N} q_{ij\nu}} \tag{1}$$

und

$$m_m = \sum_{i=1}^{n} \sum_{j=1}^{r} m_{ij} \frac{\prod\limits_{\nu=1}^{N} q_{ij\nu}}{1 - \prod\limits_{\nu=N_1+1}^{N_1+N_2} q_{ij\nu} + \prod\limits_{\nu=N_1+1}^{N} q_{ij\nu}} \tag{2}$$

[1] Technical University for Heavy Industry, Chair for Ore Processing H-3515 Miskolc, Hungary

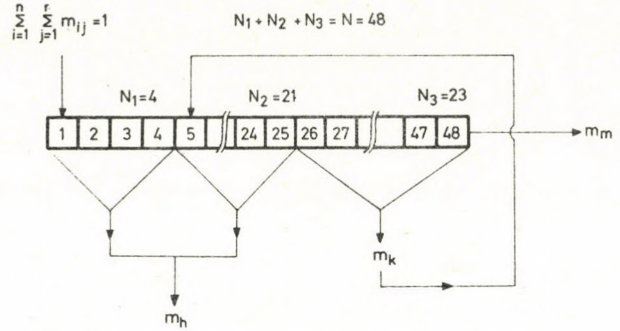

Abb. 1. Schema der Zellenkopplung ın einem Flotationswerk

Der Massenanteil des zurückgeführten Zwischenproduktes m_k aber ist:

$$m_k = \sum_{i=1}^{n} \sum_{j=1}^{r} m_{ij} \frac{\prod_{v=1}^{N_1+N_2} q_{ijv} \left(1 - \prod_{v=N_1+N_2+1}^{N} q_{ijv}\right)}{1 - \prod_{v=N_1+1}^{N_1+N_2} q_{ijv} + \prod_{v=N_1+1}^{N} q_{ijv}}. \tag{3}$$

Nach Abb. 1 ist die Gesamtanzahl der Zellen N (48). Der Schaum der ersten Zelle $N_1 + N_2(4+21=25)$ ist das Konzentrat, während von den letzten Zellen N_3 (23) das Zwischenprodukt auf die Zelle $(N+1)$ rezirkuliert. Zwischen den Zellenzahlen besteht folgende Beziehung:

$$N = N_1 + N_2 + N_3. \tag{4}$$

Das Aufgabegut von Masseneinheit besteht aus n Mineralien. Das Mineral i von Massenquote m_i kann je nach seiner Flotierbarkeit in r Teile geschieden werden (Pethő 1977a, Pethő 1977b, Pethő 1978). Für das Ausbringen k_{ij} jedes dieser Massenanteile m_{ij} als Funktion der Zeit t gilt die Gleichung

$$k_{ij} = 1 - \exp(-\lambda_{ij} t); \qquad i = 1, 2, \ldots, n \quad \text{und} \quad j = 1, 2, \ldots, r. \tag{5}$$

In dieser Gleichung bedeutet λ_{ij} die Neigung zum Flotiertwerden. Die Kennzeichnung des der Zellenreihe aufgegebenen Materials lautet demnach:

$$\sum_{i=1}^{n} \sum_{j=1}^{r} m_{ij} = \sum_{i=1}^{n} m_i = 1. \tag{6}$$

q_{ijv} ist in dem aus der Zelle $v(v=1, 2 \ldots, N)$ abfließenden Produkt das Ausbringen j an Mineral i, dessen Abhängigkeit von der Neigung zum Flotiertwerden λ_{ij} und der Aufenthaltszeit T_v aus folgender Beziehung hervorgeht:

$$q_{ijv} = \exp(-\lambda_{ij} T_v). \tag{7}$$

Der Mineralgehalt b_i und c_i des Schaumes und des abfließenden Produktes beträgt

$$b_i = \frac{1}{m_h} \sum_{j=1}^{r} m_{ij} \frac{1 - \prod_{v=N_1+1}^{N_1+N_2} q_{ijv} + \prod_{v=N_1+1}^{N} q_{ijv} - \prod_{v=1}^{N} q_{ijv}}{1 - \prod_{v=N_1+1}^{N_1+N_2} q_{ijv} + \prod_{v=N_1+1}^{N} q_{ijv}} \tag{8}$$

$$c_i = \frac{1}{m_m} \sum_{j=1}^{r} m_{ij} \frac{\prod_{v=1}^{N} q_{ijv}}{1 - \prod_{v=N_1+1}^{N_1+N_2} q_{ijv} + \prod_{v=N_1+1}^{N} q_{ijv}} . \tag{9}$$

Die Mineralausbringen k_i und K_i betragen in den beiden Trennprodukten:

$$k_i = \frac{1}{m_i} \sum_{j=1}^{r} m_{ij} \frac{1 - \prod_{v=N_1+1}^{N_1+N_2} q_{ijv} + \prod_{v=N_1+1}^{N} q_{ijv} - \prod_{v=1}^{N} q_{ijv}}{1 - \prod_{v=N_1+1}^{N_1+N_2} q_{ijv} + \prod_{v=N_1+1}^{N} q_{ijv}} \tag{10}$$

und

$$K_i = \frac{1}{m_i} \sum_{j=1}^{r} m_{ij} \frac{\prod_{v=1}^{N} q_{ijv}}{1 - \prod_{v=N_1+1}^{N_1+N_2} q_{ijv} + \prod_{v=N_1+1}^{N} q_{ijv}} . \tag{11}$$

Die Summe von k_i und K_i ist $= 1$.

Analyse der Trennungsfunktionen

Oft kommt es vor, daß das Mittelprodukt auf die erste Zelle rezirkuliert wird. In diesem Falle ist $N_1 = 0$ und $N_2 + N_3 = N$. Dementsprechend ist laut (1) das Massenausbringen an Konzentrat

$$m_h = \sum_{i=1}^{n} \sum_{j=1}^{r} m_{ij} \frac{1 - \prod_{v=1}^{N} q_{ijv}}{1 - \prod_{v=1}^{N_2} q_{ijv} + \prod_{v=1}^{N} q_{ijv}} . \tag{12}$$

Das Massenausbringen des abfließenden Produktes, der Mineralgehalt und die Mineralausbringen der Produkte können entsprechend dem bisherigen, in diesem Spezialfall gleichfalls berechnet werden.

Das Massenausbringen des Schaumproduktes nach (1) kann auch in folgender Form aufgeschrieben werden

$$m_h = 1 - \sum_{i=1}^{n} \sum_{j=1}^{r} m_{ij} \frac{\prod_{\nu=1}^{N} q_{ij\nu}}{1 - \prod_{\nu=N_1+1}^{N_1+N_2} q_{ij\nu} + \prod_{\nu=N_1+1}^{N} q_{ij\nu}}. \tag{13}$$

Das Massenausbringen hat ein Maximum, wenn der Nenner den Maximalwert 1 annimmt:

$$\left(1 - \prod_{\nu=N_1+1}^{N_1+N_2} q_{ij\nu} + \prod_{\nu=N_1+1}^{N} q_{ij\nu}\right)_{\max} = 1.$$

Die Gleichheit wird nur in den Fällen $N_2 = N_3 = 0$, und $N_1 = N$ erfüllt. Deswegen ist das Massenausbringen im Falle des Inreiheschaltens einer Anzahl N an Zellen maximal, d. h.:

$$m_{h\,\max} = 1 - \sum_{i=1}^{n} \sum_{j=1}^{r} m_{ij} \prod_{\nu=1}^{N} q_{ij\nu} \quad \text{bei } \nu = 1. \tag{14}$$

In diesem Falle ist das Massenausbringen des abfließenden Bergeproduktes minimal.

Wenn der Nenner (13) minimal ist, dann hat auch das Massenausbringen ein Minimum. Dies aber erfolgt nur dann, wenn das 2. Glied mit negativem Vorzeichen den möglichst größten, das 3. Glied mit positivem Vorzeichen aber den möglichst kleinsten Wert annimmt. Die beiden Bedingungen werden in den Fällen $N_2 = 0$ und $N_1 = 0$ erfüllt. Hierbei erfolgt die Ableitung des Schaumes nur von der ersten Zelle, während der Schaum der übrigen $N+1$ Zellen auf die Zelle 1 rezirkuliert wird.

Das Schaumprodukt von minimalen Massenausbringen beträgt dann:

$$m_{h\,\min} = 1 - \sum_{i=1}^{n} \sum_{j=1}^{r} m_{ij} \frac{\prod_{\nu=1}^{N} q_{ij\nu}}{1 - q_{ij1} + \prod_{\nu=1}^{N} q_{ij\nu}}. \tag{15}$$

Das in (3) angegebene rückgeführte Produkt hat in diesem Falle ein Maximum

$$m_{k\,\max} = \sum_{i=1}^{n} \sum_{j=1}^{r} m_{ij} \frac{q_{ij1}\left(1 - \prod_{\nu=2}^{N} q_{ij\nu}\right)}{1 - q_{ij1} + \prod_{\nu=1}^{N} q_{ij\nu}}. \tag{16}$$

Somit beträgt die Gesamtaufgabe der Zelle 1: $1 + m_{k\,\max}$. Dabei hat auch das abfließende Bergeprodukt ein Maximum.

Praktische Anwendung und Computer-Programm

In Tabelle I sind die Ergebnisse der mit einem chalkopyritisch-pyritischen Erz durchgeführten Flotationsversuche angegeben. Die Produkte wurden auf Cu und Fe analysiert (Spalte 4 und 5); aus diesen wurden die Gehalte an Chalkopyrit, Pyrit und Bergen bestimmt. Mit den Mineralgehalten (Spalte 6, 7, 8) können die Ausbringen (Spalte 9, 10, 11) errechnet werden. In Abb. 2 wurde die Ausbringungsfunktion des Chalkopyrit dargestellt. Mit dem in der Abbildung dargestellten Entwurf (Pethő 1977a, Pethő 1978) kann nach Flotierbarkeit der Chalkopyrit in drei Fraktionen getrennt werden ($0{,}5819 \cdot 0{,}0166 = 0{,}009\,66 \ldots$). Die sich daraus ergebenden Massenquotienten (m_{ij}), und ihre Flotationsneigung (λ_{ij}) können aus Tabelle II entnommen werden.

Der Zellenrauminhalt v beträgt 16 m^3, das aufgegebene Arbeitstrübevolumen $V = \frac{5}{6} 10^3$ m^3/h; $T_1 = 1{,}152$ min. Mit den Kennwerten für Flotationsneigung λ_{ij} und der Flotationszeit T_1 können dann die Zellenausbringen q_{ij1} direkt berechnet werden (Tabelle II).

In den Tabellen III und IV sind die Trennungsergebnisse (Massenausbringen, Mineralgehalte, Mineralausbringen und Flotationszeit) bei der Kopplung von zwei Zellenreihen zu finden. Die Gesamtzahl der Zellen (N) beträgt in beiden Fällen 48. In Tabelle III sind die Trennergebnisse der Reihenschaltung zu sehen. Bei der Kopplung nach Tabelle IV wird der Schaum der letzten 16 Zellen auf die 17. Zelle zurückgeleitet; somit ist $N_1 = N_2 = N_3 = 16$. Die Trennergebnisse der beiden Kopplungsarten weichen von einander ab. Bei der Rezirkulation des Schaumes ist das Massenausbringen an Schaumprodukt kleiner, doch bessert sich die Qualität der Produkte. Das Ausbringen an Chalkopyrit verschlechtert sich etwas, zugleich aber bessert sich das Bergeausbringen.

Tabelle I. Auswertung der Ergebnisse der Flotationsversuche

Produkt	Massen-ausbrin-gen	Flo-tier-zeit	Metallgehalt		Mineralgehalt			Mineralausbringen		
			Cu	Fe	Chal-kopyrit	Pyrit	Berge	Chalko-pyrit	Pyrit	Berge
1	2	3	4	5	6	7	8	9	10	11
$K_1 + K_2$	0,1038	10	0,0420	0,1212	0,1212	0,1810	0,6978	0,758	0,210	0,081
$K_3 + K_4$	0,1518	20	0,0130	0,1846	0,0376	0,3714	0,5910	0,867	0,408	0,113
$K_5 + K_6$	0,1870	20	0,0058	0,1029	0,0167	0,2096	0,7737	0,902	0,491	0,143
M	1,0000	–	0,00070	0,0268	0,00202	0,0562	0,9418	1,000	1,000	1,000
Insgesamt, Mittelwert		50	0,00574	0,0468	0,0166	0,0897	0,8937			

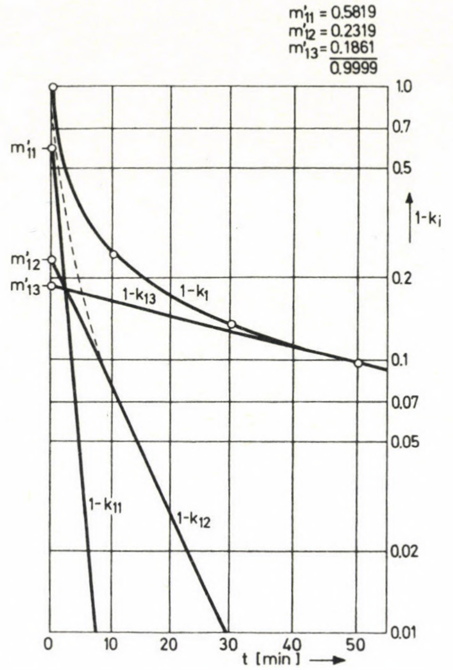

Abb. 2. Ausbringungs-Funktionen für ein chalkopyritisches Erz, das aus Anteilen von verschiedener Flotationsneigung besteht

Mit Anwendung der bisherigen Daten haben wir für den Fall der Zellenanzahl $N=48$ und jede mögliche Kopplung die Trennergebnisse mit dem Computer (ODRA) berechnet. Mit Berücksichtigung von Abb. 1 beträgt die Anzahl sämtlicher möglicher Kopplungen:

$$\sum_{\nu=1}^{N-1} (N-\nu)+1\,.$$

Mit dem Computer ließen wir das Massenausbringen des Schaumproduktes, ferner den Chalkopyrit-, Pyrit- und Bergegehalt aller beider Produkte, wie auch die auf beide Produkte der gleichen Mineralien bezüglichen Ausbringen ausschreiben. Von diesen Ergebnissen ist — mit Ausnahme der auf Pyrit bezüglichen Trennergebnisse — ein Teil ($N_1=9$, $N_2=1, 2 \ldots, 38$; $N_1=10$, $N_2=1, 2, \ldots, 37$) in Tabelle V enthalten. Diese Tabelle enthält außerdem noch die Differenzen zwischen der mit η_1 bezeichneten Differenz k_1-m_h (Differenz des Chalkopyrit-Ausbringens und des Massenausbringens an abfließendem Produkt) und der Größe H_3, wobei $H_3=K_3-m_m$ ist. Diese sind proportional mit den entsprechenden Wirkungsgraden.

Tabelle II. Durch Versuche ermittelte Parameter: Massenanteile m_{ij}, Flotationsneigung λ_{ij} und Zellenausbringen q_{ij1}

	Chalkopyrit	
Massenanteil	Flotationsneigung	Zellenausbringen
1	2	3
$m_{11}=0{,}009\,66$	$\lambda_{11}=0{,}5640$	$q_{111}=0{,}5222$
$m_{12}=0{,}003\,85$	$\lambda_{12}=0{,}1077$	$q_{121}=0{,}8833$
$m_{13}=0{,}003\,09$	$\lambda_{13}=0{,}0128$	$q_{131}=0{,}9854$
$m_1\;=0{,}016\,60$		

	Pyrit	
Massenanteil	Flotationsneigung	Zellenausbringen
4	5	6
$m_{21}=0{,}0296$	$\lambda_{21}=0{,}081\,40$	$q_{211}=0{,}9105$
$m_{22}=0{,}0601$	$\lambda_{22}=0{,}005\,85$	$q_{221}=0{,}9933$
$m_2\;=0{,}0897$		

	Berge	
Massenanteil	Flotationsneigung	Zellenausbringen
7	8	9
$m_{31}=0{,}0554$	$\lambda_{31}=0{,}304\,00$	$q_{311}=0{,}7045$
$m_{32}=0{,}8383$	$\lambda_{32}=0{,}001\,88$	$q_{321}=0{,}9978$
$m_3\;=0{,}8937$		

Tabelle III. Trennparameter des Flotierwerkes für Chalkopyrit ($N=48$, $T=64{,}846$ min)

Trennparameter		Aufgabe	Konzentrat	Berge
1		2	3	4
Massenausbringen		1,–	0,2153	0,7847
Mineralogische Zusammensetzung	Chalkopyrit	0,0166	0,0708	0,0017
	Pyrit	0,0897	0,2249	0,0526
	Berge	0,8937	0,7043	0,9457
	Zusammen	1,0000	1,0000	1,0000
Mineralausbringen	Chalkopyrit	1,–	0,9186	0,0814
	Pyrit	1,–	0,5398	0,4602
	Berge	1,–	0,1696	0,8304

Tabelle IV. Trennergebnisse des Flotierwerkes für Chalkopyrit, wenn $N_1 = N_2 = N_3 = 16$, N aber $= 48$ ist

Trennparameter		Aufgabe	Konzentrat	Berge
1		2	3	4
Massenausbringen		1,–	0,1542	0,8458
	Chalkopyrit	0,0166	0,0967	0,0020
Mineralogische	Pyrit	0,0897	0,2795	0,0551
Zusammensetzung	Berge	0,8937	0,6238	0,9429
	Zusammen	1,–	1,0000	1,0000
	Chalkopyrit	1,–	0,9092	0,0908
Mineralausbringen	Pyrit	1,–	0,5104	0,4896
	Berge	1,–	0,1190	0,8810

Detaillierte Prozeßanalyse der Chalkopyrit-Flotation

Um ihre Gesetzmäßigkeiten klarer erkennen zu können, haben wir die Änderungen der Trennergebnisse auch in Diagrammen dargestellt. In Abb. 3 sind — für den Fall, daß N_1 konstant ($N_1 = 23$) ist — in Abhängigkeit von $N_2(N_2 = 1, 2, \ldots, 24;\ N_3 = 25 - N_2)$ — die Änderungen des Massenausbringens m_h, des Chalkopyrit-Gehaltes b_1, des Chalkopyrit-Ausbringens K_1 und der Differenzen $\eta = k_1 - m_h$ zu sehen. In Abb. 4 aber sind — wie vorher — in Abhängigkeit von N_2 die Änderungen des Massenausbringens an Bergen m_m, des Ausbringens K_3 und der Differenz $H_3 = K_3 - m_m$ dargestellt. In den nächsten zwei Abbildungen ist N_2 konstant ($N_2 = 22$) und N_1 ist die unabhängig variable Größe ($N_1 = 1, 2, \ldots, 25$, $N_3 = 26 - N_1$). Dementsprechend kann man in Abb. 5 die Veränderungen der Größen m_h, b_1, k_1 und η, in Abb. 6 aber die der Größen m_m, K_3 und H_3 verfolgen.

Auf Grund der Werte in Tabelle V, bzw. der Funktionen der vorherigen vier Abbildungen können bezüglich der Änderungen der Trennparameter gewisse Gesetzmäßigkeiten festgestellt werden. Jene Zahlenwerte, welche diese Gesetzmäßigkeiten ausdrücken, sind in den Tabellen VI und VII zusammengefaßt.

Die Gestaltung der Trennergebnisse, wenn N_1 konstant ist

Ist N_1 konstant, dann wächst m_h mit steigendem $N_2(N_2 = 1, 2, \ldots, N - N_1 - 1)$, bzw. mit sinkendem N_3. Diese Zunahme aber verläuft nicht gleichmäßig: Wenn z. B. bei $N_1 = 23$ (Abb. 3) N_2 von 1 auf 2 zunimmt, dann wird das Massenausbringen um 0,00222 größer. Wenn sich aber N_2 von 23 auf 24 ändert, dann ändert sich m_h um den Betrag 0, 00156. — Es ist sehr wichtig hervorzuheben, daß unabhängig von dem Wert N_1 die durchschnittliche Zunahme des Massenausbringens Δm_h (Tabelle VI) prak-

Tabelle V. Detail aus dem Computer-Program

N_2	$N_1=9,\ N_3=39-N_2$						$N_1=10,\ N_3=38-N_2$					
	m_h	b_1	k_1	η_1	K_3	H_3	m_h	b_1	k_1	η_1	K_3	H_3
1	0,114 06	0,122 47	0,841 48	0,727 42	0,924 29	0,038 35	0,115 80	0,120 99	0,843 98	0,728 18	0,922 89	0,038 69
2	0,116 70	0,120 48	0,846 97	0,730 27	0,922 80	0,039 50	0,118 41	0,119 07	0,849 33	0,730 92	0,921 39	0,039 80
3	0,118 88	0,118 91	0,851 56	0,732 68	0,921 31	0,040 19	0,120 58	0,117 54	0,853 81	0,733 23	0,919 90	0,040 48
4	0,120 93	0,117 47	0,855 72	0,734 79	0,919 82	0,040 75	0,122 62	0,116 14	0,857 86	0,735 24	0,918 41	0,041 03
5	0,122 91	0,116 09	0,859 56	0,736 65	0,918 34	0,041 25	0,124 59	0,114 80	0,861 60	0,737 01	0,916 93	0,041 52
6	0,124 84	0,114 77	0,863 13	0,738 29	0,916 85	0,041 69	0,126 52	0,113 50	0,865 08	0,738 56	0,915 45	0,041 97
7	0,126 75	0,113 48	0,866 47	0,739 72	0,915 37	0,042 12	0,128 41	0,112 25	0,868 33	0,739 92	0,913 97	0,042 34
8	0,128 62	0,112 23	0,869 60	0,740 98	0,913 90	0,042 52	0,130 28	0,111 03	0,871 38	0,741 10	0,912 49	0,042 77
9	0,130 48	0,111 01	0,872 54	0,742 06	0,912 42	0,042 90	0,132 13	0,109 83	0,874 25	0,742 12	0,911 02	0,043 15
10	0,132 31	0,109 82	0,875 31	0,743 00	0,910 95	0,043 26	0,133 96	0,108 67	0,876 95	0,742 99	0,909 55	0,043 51
11	0,134 13	0,108 65	0,877 92	0,743 79	0,909 48	0,043 61	0,135 77	0,107 54	0,879 50	0,743 73	0,908 08	0,043 85
12	0,135 93	0,107 52	0,880 39	0,744 46	0,908 02	0,043 95	0,137 56	0,106 43	0,881 91	0,744 35	0,906 62	0,044 18
13	0,137 71	0,106 41	0,882 73	0,745 02	0,906 56	0,044 27	0,139 33	0,105 34	0,884 19	0,744 86	0,905 16	0,044 49
14	0,139 47	0,105 33	0,884 94	0,745 47	0,905 10	0,044 57	0,141 09	0,104 29	0,886 35	0,745 26	0,903 70	0,044 79
15	0,141 22	0,104 27	0,887 04	0,745 82	0,903 65	0,044 87	0,142 83	0,103 25	0,888 41	0,745 58	0,902 25	0,045 08
16	0,142 96	0,103 23	0,889 04	0,746 08	0,902 19	0,045 15	0,144 56	0,102 24	0,890 36	0,745 80	0,900 80	0,045 36
17	0,144 68	0,102 22	0,890 93	0,746 25	0,900 75	0,045 43	0,146 27	0,101 25	0,892 21	0,745 94	0,899 35	0,045 62
18	0,146 38	0,101 24	0,892 74	0,746 36	0,899 30	0,045 68	0,147 97	0,100 29	0,893 98	*0,746 01*	0,897 91	0,045 88
19	0,148 08	0,100 27	0,894 46	*0,746 38*	0,897 86	0,045 94	0,149 66	0,099 34	0,895 66	0,746 00	0,896 47	0,046 13
20	0,149 76	0,099 33	0,896 10	0,746 34	0,896 43	0,046 19	0,151 34	0,098 42	0,897 27	0,745 93	0,895 04	0,046 38
21	0,151 43	0,098 41	0,897 67	0,746 24	0,895 00	0,946 43	0,153 00	0,097 52	0,898 81	0,745 81	0,893 61	0,046 61
22	0,153 08	0,097 51	0,899 17	0,746 09	0,893 57	0,046 65	0,154 65	0,096 64	0,900 28	0,745 63	0,892 18	0,046 83
23	0,154 72	0,096 62	0,900 61	0,745 89	0,892 14	0,046 86	0,156 29	0,095 77	0,901 68	0,745 39	0,890 76	0,047,05
24	0,156 36	0,095 76	0,901 98	0,745 62	0,890 72	0,047 08	0,157 91	0,094 93	0,903 03	0,745 12	0,889 34	0,047 25
25	0,157 98	0,094 92	0,903 29	0,745 31	0,889 31	0,047 29	0,159 53	0,094 10	0,904 31	0,744 78	0,887 92	0,047 45
26	0,159 59	0,094 09	0,904 55	0,744 96	0,887 89	0,047 48	0,161 13	0,093 29	0,905 55	0,744 42	0,886 51	0,047 64
27	0,161 19	0,093 28	0,905 76	0,744 57	0,886 48	0,047 67	0,162 72	0,092 50	0,906 74	0,744 02	0,885 10	0,047 82
28	0,162 77	0,092 49	0,908 93	0,744 16	0,885 08	0,047 85	0,164 31	0,091 72	0,907 87	0,743 56	0,883 70	0,048 01
29	0,164 35	0,091 71	0,908 04	0,743 69	0,883 68	0,048 03	0,165 88	0,090 96	0,908 97	0,743 09	0,882 30	0,048 18
30	0,165 92	0,090 96	0,909 12	0,743 20	0,882 28	0,048 20	0,167 44	0,090 22	0,910 02	0,742 58	0,880 90	0,048 34
31	0,167 48	0,090 21	0,910 15	0,742 67	0,880 88	0,048 36	0,168 99	0,089 49	0,911 03	0,742 04	0,879 51	0,048 50
32	0,169 02	0,089 48	0,911 14	0,742 12	0,879 49	0,048 51	0,170 54	0,088 77	0,912 01	0,741 47	0,878 12	0,048 66
33	0,170 56	0,088 77	0,912 10	0,741 54	0,878 11	0,048 67	0,172 07	0,088 07	0,912 95	0,740 88	0,876 73	0,048 80
34	0,172 09	0,088 07	0,913 02	0,740 93	0,876 72	0,048 81	0,173 60	0,087 39	0,913 85	0,740 25	0,875 35	0,048 95
35	0,173 61	0,087 38	0,913 91	0,740 30	0,875 34	0,048 95	0,175 11	0,086 71	0,914 72	0,739 61	0,873 98	0,049 09
36	0,175 12	0,086 71	0,914 76	0,739 64	0,873 97	0,049 09	0,176 62	0,086 05	0,915 56	0,738 94	0,872 60	0,049 22
37	0,176 62	0,086 05	0,915 59	0,738 97	0,872 60	0,049 22	0,178 11	0,085 41	0,916 38	0,738 27	0,871 23	0,049 34
38	0,178 12	0,085 40	0,916 39	0,738 27	0,871 23	0,049 35						

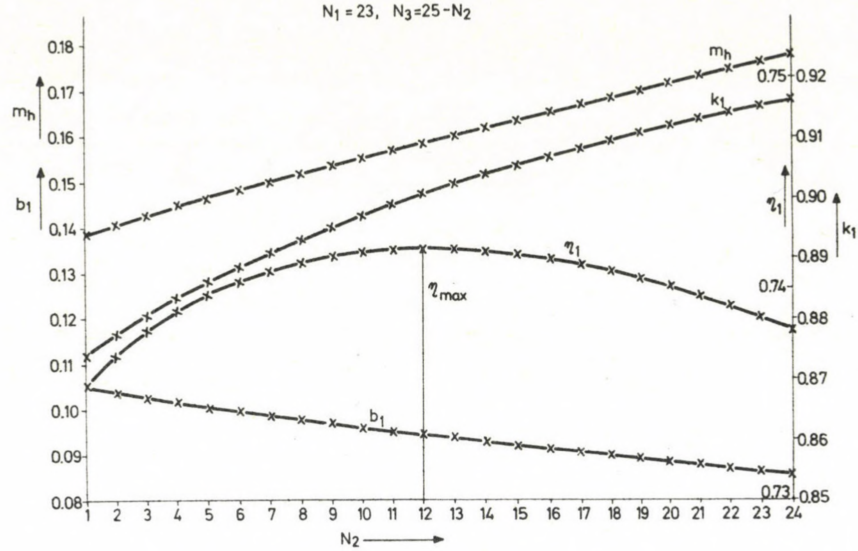

Abb. 3. Die Änderungen der Größen m_h, b_1, k_1 und η_1 als Funktionen von N_2

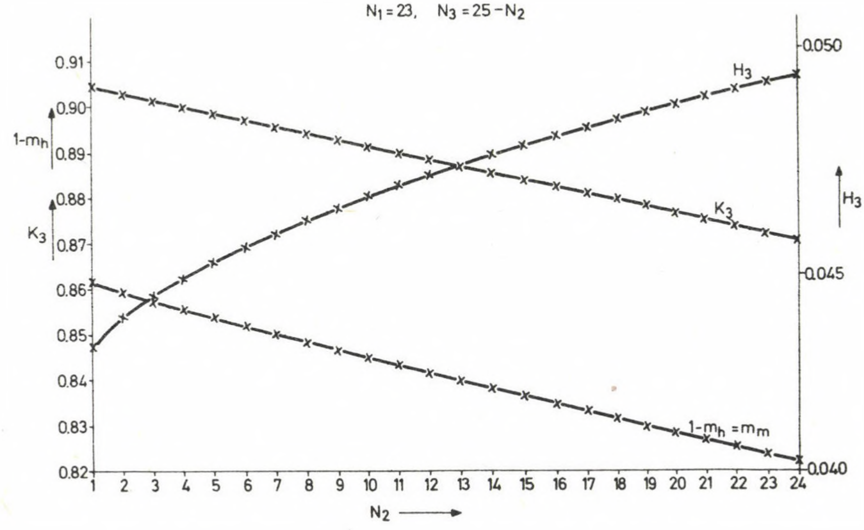

Abb. 4. Die Änderungen der Größen m_m, K_3 und H_3 als Funktionen von N_2

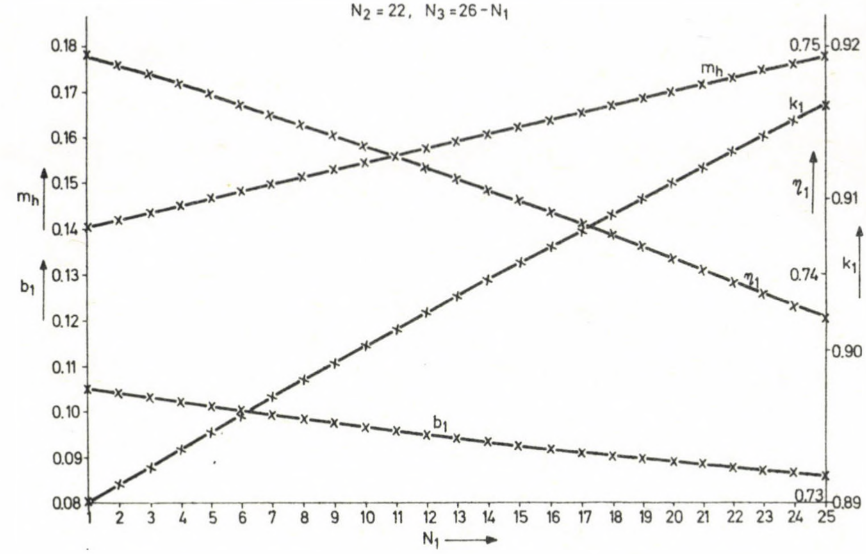

Abb. 5. Die Änderungen der Größen m_h, b_1, k_1 und η_1 als Funktionen von N_1

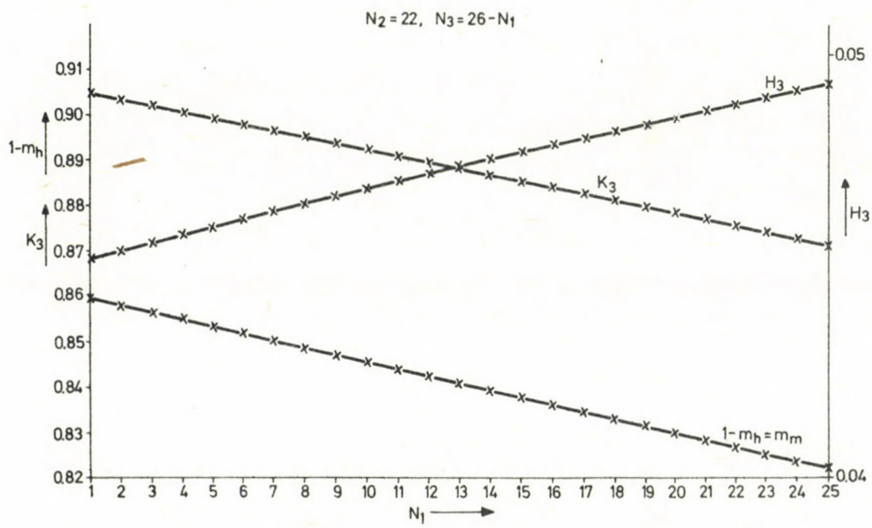

Abb. 6. Die Änderungen der Größen m_m, K_3 und H_3 als Funktionen von N_1

Tabelle VI. Die Änderung der Mittelwerte der Trennparameter, wenn N_1 und N_2 konstant sind

Zellenkopplung	$m_{h\,max}$	$m_{h\,min}$	Δm_h	$b_{1\,max}$	$b_{1\,min}$	Δb_1	$k_{1\,max}$	$k_{1\,min}$	Δk_1	$K_{3\,max}$	$K_{3\,min}$	ΔK_3
$N_1 = 9$, $N_3 = 39 - N_2$	0,178 12	0,114 06	0,001 73	0,122 47	0,085 40	0,001 00	0,916 39	0,841 48	0,002 02	0,924 29	0,871 23	0,001 43
$N_1 = 10$, $N_3 = 38 - N_2$	0,178 11	0,115 80	0,001 73	0,120 99	0,085 41	0,000 99	0,916 38	0,843 98	0,002 01	0,922 89	0,871 23	0,001 44
$N_1 = 23$, $N_3 = 25 - N_2$	0,178 06	0,138 45	0,001 72	0,104 77	0,085 41	0,000 84	0,916 18	0,873 79	0,001 84	0,904 42	0,871 26	0,001 44
$N_2 = 9$, $N_3 = 39 - N_1$	0,177 98	0,117 22	0,001 64	0,121 52	0,085 42	0,000 98	0,915 88	0,858 10	0,001 56	0,923 62	0,871 29	0,001 41
$N_2 = 10$, $N_3 = 38 - N_1$	0,177 99	0,119 11	0,001 64	0,120 06	0,085 42	0,000 96	0,915 90	0,861 47	0,001 51	0,922 14	0,871 29	0,001 41
$N_2 = 23$, $N_3 = 25 - N_1$	0,178 05	0,142 19	0,001 56	0,104 10	0,085 41	0,000 81	0,916 17	0,891 74	0,001 06	0,903 24	0,871 26	0,001 39

Tabelle VII. Änderung der Trennergebnisse, wenn N_3 konstant ist

Zellenkopplung	m_h	b_1	k_1	η_1	m_m	c_1	K_3	H_3
$N_1 = 23$, $N_2 = 4$	0,144 56	0,101 45	0,883 44	0,738 88	0,855 44	0,002 26	0,899 97	0,044 53
$N_1 = 18$, $N_2 = 9$	0,145 32	0,101 36	0,887 33	0,742 01	0,854 68	0,002 19	0,899 73	0,045 05
$N_1 = 9$, $N_2 = 18$	0,146 38	0,101 24	0,892 74	0,746 36	0,853 62	0,002 09	0,899 30	0,045 68
$N_1 = 4$, $N_2 = 23$	0,146 91	0,101 15	0,895 14	0,748 23	0,853 09	0,002 04	0,899 08	0,045 99

tisch identisch ist. So ist z. B. bei dem vorherigen N_1 zwischen $N_2=1$ und $N_2=24$ dieser mittlere Zuwachs 0,00173 und der gleiche Wert ergibt sich auch bei $N_1=9$ und $N_1=10$, wenn N_2 von 1 auf 38 bzw. von $N_2=1$ auf 37 zunimmt. (Bei $N_1=44$ ist der durchschnittliche Zuwachs des Massenausbringens „nur" 0,001 69, doch bei $N_1=1$ ebenfalls 0,001 73.)

Wenn N_1 konstant bleibt und N_2 sich ändert ($N_2=1, 2, \ldots, N-N_1-1$), dann sinkt der Chalkopyritgehalt des Konzentrates zunächst in stärkerem, später dann in geringerem Maße (Abb. 3). Bei $N_1=23$ beträgt diese Verminderung zwischen $N_2=1$ und $N_2=2$ 0,001 22, zwischen $N_2=23$ und $N_2=24$ aber 0,000 66. Die durchschnittliche Verminderung des Chalkopyritgehaltes nimmt mit ansteigendem N_1 ab: Bei $N_1=9$, $N_1=10$, bzw. $N_1=23$ wird mit dem Verändern der Zellenanzahl von N_2 die durchschnittliche Verminderung 0,001 00, bzw. 0,000 99, bzw. 0,000 84 betragen (Tabelle VI).

Da der absolute Wert der Veränderung von m_h größer als der von b_1 ist, wird bei einer Veränderung von N_2 die Veränderung des Chalkopyritausbringens im Schaumprodukt sich ähnlich dem Massenausbringen gestalten. Ebenso wird, wenn bei $N_1=23$ die Größe N_2 von 1 auf 2 zunimmt, k_1 um 0,003 72, wenn sie aber von 23 auf 24 zunimmt nur um 0,001 01 wachsen (Abb. 3). Die durchschnittliche Änderung des Ausbringens (die Größe N_2 steigt von 1 auf 24) beträgt 0,001 84. Bei einem höher festgelegten N_1 nimmt diese durchschnittliche Änderung (Δk_1) ab; bei $N_1=9$ bzw. 10 beträgt sie 0,002 02 bzw. 0,002 01; (Tabelle VI); im Falle $N_1=23$ aber ist $\Delta k_1=0{,}001\ 84$.

Mit der Änderung von N_2 hat der Ausdruck $\eta_1=m_h-k_1$ ein Maximum (Abb. 3). Nach der detaillierten Analyse der Ergebnisse des Computer-Programmes wird — bei unpaarig festgelegtem N_1 — der Trennungswirkungsgrad von Chalkopyrit bei $N_2=N_3-1$; wenn N_1 aber als paarige Zahl festgelegt wurde, wird er bei $N_2=N_3$ ein Maximum haben. Ändert sich N_1, dann ändert sich auch der Maximalwert von η_1. So ist z. B. bei $N_1=1$ ($N_2=23$, $N_3=24$) $\eta_1=0{,}749\ 55$. Im Falle $N_1=9$ ($N_2=19$, $N_3=20$) erhält man 0,746 38 und bei $N_1=23$ ($N_2=12$, $N_3=13$) erhält man 0,741 86. Auch aus diesen Werten folgt, daß mit steigendem N_1 das relative Maximum des Wirkungsgrades sinkt. Nach den Ergebnissen des Programmes tritt der Höchstwert bei $N_1=0$, $N_2=24$ und $N_3=24$ auf.

Nach Abb. 4 nimmt das Bergeausbringen K_3 als Funktion der Zellenanzahl N_2 fast gleichmäßig ab. Bei $N_1=23$ beträgt nach Tabelle VI der Mittelwert ΔK dieser Verminderung 0,001 44 (ihr Höchstwert ist 0,001 49, der Mindestwert 0,001 40). Beachtenswert ist ferner, daß der Mittelwert der Verminderung praktisch unabhängig vom Wert N_1 ist. Er beträgt bei $N_1=9$ 0,001 43; im Falle $N_2=10$ aber 0,001 44 (nach Tabelle VI).

Die dem Wirkungsgrad proportionale Differenz $H_3=K_3-(1-m_h)$ hat in Abhängigkeit von N_2 eine monoton steigende Tendenz (Abb. 4). Da das Ausbringen K_3 nahezu linear abnimmt, stimmt die Änderung von H_3 praktisch mit dem Massenausbringen überein. Die durchschnittliche Änderungen von K_3 und m_h sind nach dem Vorhergesagten unabhängig von N_1. Deswegen bezieht sich dasselbe auch auf die durchschnittliche Änderung von H_3. Die Größe der durchschnittlichen Zunahme von ΔH_3 beträgt (0,001 73 – 0,001 44 =) 0,000 29.

Die Gestaltung der Trennergebnisse bei konstantem N_2

Auf Grund von Abb. 5 und 6, sowie Tabelle VI kann man — wenn die Anzahl der Zellen N_2 konstant ist ($N_1 = 1, 2, \ldots, N - N_2 - 1$) — über die Änderungen in Abhängigkeit von den bisher untersuchten Parametern N_1 (bzw. N_3) folgendes feststellen.

Das Massenausbringen m_h nimmt mit Erhöhung der Zellenanzahl N_1 fast linear zu (Abb. 5). Bei $N_2 = 23$ beträgt der mittlere Zuwachs (Tabelle VI) 0,001 56 (Zwischen $N_1 = 1$ und $N_2 = 2$ 0,001 58; mit Änderung von $N_1 = 24$ auf $N_1 = 25$ beträgt der Zuwachs 0,001 55). Bei einer kleineren Zellenanzahl N_2 ist der Zuwachs des mittleren Massenausbringens etwas größer: beträgt bei $N_2 = 9$ und $N_2 = 10$ gleichermaßen 0,001 64 (Tabelle VI).

Ändert sich die Zellenanzahl N_1, so sinkt der Chalkopyritgehalt des Konzentrates. Bei $N_2 = 23$ sinkt b_1 um 0,001 00 bzw. 0,000 68; wenn sich aber $N_1 = 1$ in $N_1 = 2$, bzw. $N_1 = 23$ in $N_1 = 24$ verändert, dann beträgt die durchschnittliche Verminderung im letzten Fall nach Tabelle VI 0,000 81. Im Falle von $N_2 = 9$ und $N_2 = 10$ sind sie aber 0,000 98 bzw. 0,000 96; nimmt also mit dem Wachsen der als konstant betrachteten Zellenanzahl N_2 etwas ab (Tabelle VI).

Während der fast linearen Veränderung von m_h und der von Linearität etwas abweichenden Veränderung der Größe b_1, weicht in geringem Maße auch die Zunahme des Ausbringens k_1 von der linearen Tendenz ab. Zwischen $N_1 = 1$ und $N_1 = 2$ ändert sich dieser Zuwachs um 0,001 15, bei einer Änderung der Größe $N_1 = 23$ auf $N_1 = 24$ aber ändert sich das Ausbringen um 0,001 00. Wenn N_2 abnimmt, wird die Veränderung des durchschnittlichen Chalkopyrit-Ausbringens größer: Bei $N_2 = 9$ beträgt sie 0,001 56; bei $N_2 = 10$ aber 0,001 51 (Tabelle VI).

Die dem Wirkungsgrad proportionale Größe η_1 nimmt im Sinne von Abb. 5 als Funktion von N_1 fast linear ab. Betreffs der sich bei verschiedenen Zellenzahlen meldenden mittleren Veränderungen können auf Grund des Durchschnittwertes der Änderungen von k_1 und m_h Schlußfolgerungen gezogen werden.

Die Änderung von K_3 als Funktion der Zellenanzahl N_1 ist laut Abb. 6 linear, und der Mittelwert der Änderungen ΔK_3 ist im Sinne von Tabelle VI praktisch unabhängig von N_2. Im Falle $N_2 = 9$ bzw. $= 10$ und $= 23$ beträgt das durchschnittliche Sinken von K_3 : 0,001 41, 0,001 41 und 0,001 39 (Tabelle VI).

Bezüglich der Veränderungsmittelwerte können auf Grund der Ergebnisse in Tabelle VI bzw. der bisherigen Ergebnisse noch die folgenden wichtigen Feststellungen gemacht werden: Der mittlere Zuwachs Δm_h des Massenausbringens ist als Funktion von N_2 größer als bei einer von N_1 abhängigen Änderung. Die durchschnittliche

Verminderung des Chalkopyritgehaltes Δb_1 ist in Abhängigkeit sowohl von N_1 wie auch von N_2 die gleiche. Deswegen ist die durchschnittliche Zunahme des Chalkopyrit-Ausbringens Δk_1 bei Erhöhung der Zellenanzahl N_2 größer. Die Verminderung des Bergeausbringens ΔK_3 ist immer die gleiche, unabhängig von der als konstant betrachteten Anzahl der Zellen N_1 und N_2. Bei den untersuchten Zellenkopplungen schwanken die Werte für ΔK_3 zwischen 0,001 39 und 0,001 44.

Gestaltung der Trennergebnisse bei konstantem N_3

Für den Fall, daß N_3 konstant ist, wird jene Wirkung, welche durch die Änderungen der Größen N_2 bzw. N_1 ($N_2 = 1, 2, \ldots, N - N_3 - 1$) auf das Trennergebnis ausgeübt wird, in Tabelle VII zusammengefaßt. In dieser können für die Kopplungsschemen $N_1 = 23$, $N_2 = 4$; $N_1 = 18$, $N_2 = 9$; $N_1 = 9$, $N_2 = 18$; $N_1 = 4$, $N_2 = 23$; (wobei N_3 in allen Fällen $N_3 = 21$ ist) die Werte für m_h, b_1, k_1, m_m, c_1, K_3 und H_3 gefunden werden. Mit Erhöhung der Zellenanzahl N_2 nimmt das Massenausbringen an Schaumprodukt zu; der Chalkopyritgehalt sinkt nur in ganz geringem Maße; deswegen ist die Besserung des Chalkopyritausbringens bedeutender. Ist $N_1 = 23$, $N_2 = 4$, dann ist $m_h = 0{,}144\,56$, $k_1 = 0{,}883\,34$ und $K_3 = 0{,}899\,97$. Bei den anderen drei Kopplungsschemen nimmt das Massenausbringen um 0,000 76, 0,001 82 und 0,002 35, das Chalkopyritausbringen aber um 0,003 89, 0,009 30 und 0,011 70 zu, während das Bergeausbringen um 0,000 24, 0,000 67 und 0,000 89 abnimmt. Das Zuwachsverhältnis des Ausbringens an Chalkopyrit zum Massenausbringen beträgt (z. B. 0,001 170/0,002 35 =)5. Hingegen ist das Zuwachsverhältnis des Berge-Ausbringens zu dem Berge-Massenausbringen nur (z. B. 0,000 89/0,002 35 =)0,4.

Einige Ergebnisse, die verallgemeinert werden können

Im Sinne der bisherigen Ergebnisse kann bei der Kopplung von Flotationszellen nach Abb. 1 die verhältnismäßig gute Qualität der Produkte und ein entsprechendes Konzentrat bzw. Bergeausbringen gesichert werden, wenn

— N_1 eine möglichst kleine Zellenanzahl besagt

— N_2 zu Lasten der Zellenanzahl N_1 groß ist

— die Zellenanzahlen N_2 und N_3 etwa miteinander übereinstimmen.

Eine andere Wahl der Zellenkopplung — z. B. nach wirtschaftlichen Gesichtspunkten — ist auf Grund der Ergebnisse des Computer-Programmes eindeutig möglich.

Danksagen

Das Computer-Program wurde von Herrn Universitäts-Assistentem Raisz ausgearbeitet, dem dafür auch hier mein Dank gesagt sei.

Schrifttum

Pethő Sz 1977a: A flotáló művek folyamatelemzése (Prozeß-Analyse für Flotationswerke). *Bányászati és Kohászati Lapok (BKL), Bányászat*, 110, 763—769.

Pethő Sz 1977b: The functions of flotation plant design and process control. *Acta Techn. Sci. Hung.*, 85, 455—463.

Pethő Sz 1978: Die Funktionen der Planung und der Prozeßsteuerung in Flotationsanlagen. *Freiberger Forschungshefte*, A 594, 149—159.

Acta Geodaet., Geophys. et Montanist. Hung. Volume 18 (3), pp. 235—240 (1983)

CALCULATING THE TERMINAL SETTLING VELOCITY IN THE TRANSITION ZONE

SZ PETHŐ[1]

[Manuscript received February 18, 1981]

There are various graphical methods available for calculating the terminal settling velocity of solid particles at Reynolds numbers 0.6 to 1000.

The paper presents a new computational method, suitable for programming.

Keywords: computer programs; motion of solid particles; settling velocity; terminal settling velocity

Symbols

A = Archimedes constant; Ar = Archimedes number; c = drag coefficient; g = gravitational acceleration; Lj = Lyashchenko number; Re = Reynolds number; v_0 = terminal settling velocity; x = particle size or diameter; γ = density of the medium; δ = density of the solid; η = viscosity of the medium

Summary of the state of the art

There are numerous methods available for calculating the terminal settling velocity of particles settling in stationary media at Reynolds numbers 0.6 to 1000. Some of the best known procedures can be summed up as follows.

a) The Archimedes number Ar is first calculated from the data of the particle and the medium (Schubert 1975):

$$Ar = \frac{3}{4} Re^2 \quad c = \frac{x^3 g}{\eta^2} (\delta - \gamma)\gamma \tag{1}$$

In this relationship Re denotes the Reynolds number, c the drag coefficient, x the particle size, g the gravitational acceleration, δ and γ are densities of the particle and the medium, respectively, and η is the viscosity of the medium. The Lyashchenko number Lj is plotted as a function of Ar and can be read from the diagram. The Lyashchenko number

$$Lj = \frac{v_0^2}{\eta g} \frac{\gamma^2}{\delta - \gamma} \tag{2}$$

[1] Technical University for Heavy Industry, Chair for Ore Processing, H-3515 Miskolc, Hungary

also depends on the terminal settling velocity v_0, that is v_0 can be calculated if Lj is known.

b) In an other graphical method (Tarján 1954) we draw a straight line of slope -2 to the function $\lg c$ plotted against the logarithm of the Reynolds number. The coordinates of the point of intersection are $\lg c$ and $\lg Re$, from there we can calculate the terminal settling velocity either by the relationship

$$v_0 = \sqrt{\frac{4g}{3c}} \sqrt{\frac{x(\delta-\gamma)}{\gamma}} \tag{3}$$

or by

$$Re = \frac{v_0 x \gamma}{\eta} \tag{4}$$

c) In case of the iterational method (Tarján 1954) we calculate first the terminal settling velocity by means of the Newton—Rittinger or the Stokes formula. Next, the Reynolds number is calculated from the v_0. If the value of the Reynolds number is incorrect, this shows that not the proper formula had been used for the terminal settling velocity. Using this Reynolds number the terminal settling velocity is recalculated using the c value obtained from function $\lg c - \lg Re$ or by the suitable formula, or if required by the general relationship (3). The calculation has to be repeated until c and Re correspond to each other. To find the correct value of c the use of diagrams cannot be omitted in this method either.

Numerical method

In the numerical method no diagram has to be constructed or evaluated. The terminal settling velocity can be numerically determined with algebraic or transcendental functions.

In the transition zone, for Reynolds numbers 0.6 to 1000, numerous functions have been proposed for the drag coefficient (Schubert 1975, Tarján 1954, Kürten et al. 1966). The best known and most accurate ones will be briefly analyzed. In the Allen zone, i.e. for Reynolds numbers 30 to 300 the function

$$c = \frac{10}{Re^{1/2}} \tag{5}$$

is valid. — For Reynolds numbers 0.1 to 1000 we have (Kürten et al. 1966):

$$c = \frac{24}{Re} + \frac{4}{Re^{1/3}} \tag{6}$$

while between 0.1 to 4000 the expression

$$c=\frac{21}{Re}+\frac{6}{Re^{1/2}}+0.28 \tag{7}$$

is used. The maximum relative error of function (6) is +7 and −10% while that of function (7) is ±4%. The function

$$c=\frac{24}{Re}(1+0.15Re^{0.687}) \tag{8}$$

is also regarded as exact (Schubert 1975).

Let us now express v_0 from Eq. (4) of the Reynolds number

$$v_0=Re\frac{\eta}{x\gamma} \tag{9}$$

then substitute it into Eq. (3). Taking the square of both sides and after some rearranging we obtain

$$cRe^2=\frac{4}{3}g\frac{x^3(\delta-\gamma)\gamma}{\eta^2}=A. \tag{10}$$

Expression cRe^2 is directly proportional to the Archimedes number, it is constant for a given particle and medium, therefore it will be denoted by A.

The functional forms (5), (6), (7) and (8) for the drag coefficient contain two unknown quantities, *viz.* c and Re. The same unknowns figure in the expression (10) of the Archimedes number. These quantities can be expressed from the respective equations and the terminal settling velocity can be calculated by either Eq. (3) or Eq. (9),

Equation (5) for the Allen zone and Eq. (10) of the Archimedes number enable us to give a closed solution. Substituting the drag coefficient c from Eq. (10) into (5) we have

$$Re=\left(\frac{A}{10}\right)^{2/3} \tag{11}$$

and

$$c=\frac{10^{4/3}}{A^{1/3}}. \tag{12}$$

The terminal settling velocity can be calculated from (9) and (3) as

$$v_0=\left(\frac{A}{10}\right)^{2/3}\frac{\eta}{x\gamma} \tag{13}$$

or

$$v_0=\sqrt{\frac{4A^{1/3}g}{3\ 10^{4/3}}}\sqrt{\frac{x(\delta-\gamma)}{\gamma}}. \tag{14}$$

On re-substituting A into these equations, we obtain Allen's formula of the terminal settling velocity:

$$v_0=\left(\frac{2}{15}\right)^{2/3} x \frac{[g(\delta-\gamma)]^{2/3}}{(\gamma\eta)^{1/3}}. \tag{15}$$

The substitution of c into Eqs (6), (7) or (8) leads to a set of transcendental equations, these, however, can be solved by appropriate calculation techniques, without any diagrams. Computer programs can also be written to solve the problem.

From Eqs (6) and (10) we have

$$Re=\frac{\frac{1}{4}A}{Re^{2/3}+6}. \tag{16}$$

Equation (16) leads to the algorithm

$$Re_{n+1}=\frac{\frac{1}{4}A}{Re_n^{2/3}+6}; \qquad n=1, 2, 3, \ldots \tag{17}$$

define a convergent iteration. To solve Eq. (17) we have to have a first guess of the value of Re_1. Substituting Re_1 into the denominator, Re_2 is calculated; then Re_2 is substituted and Re_3 is obtained, etc. Using this procedure a sequence of approximate values are obtained that gradually approach from above and from below the root of Eq. (17). Given the Reynolds number, c can be calculated from Eq. (6).

On the other hand, from Eqs (7) and (10) we have

$$Re=\frac{A}{0.28Re+6\sqrt{Re}+21} \tag{18}$$

and

$$Re_{n+1}=\frac{A}{0.28Re_n+6\sqrt{Re_n}+21}; \qquad n=1, 2, 3, \ldots \tag{19}$$

From Eq. (17) the Reynolds number can be calculated same way as from Eq. (17).

Finally, from Eqs (8) and (10), the Reynolds number is calculated as

$$Re_{n+1}=\frac{\frac{1}{24}A}{1+0.15\exp(0.687\ln Re_n)}; \qquad n=1, 2, 3, \ldots \tag{20}$$

A practical example*

Let the diameter of the particle be $x=0.1$ cm, its density $\delta=2.65$ g/cm^3; the medium is water of 20 °C, i.e. $\gamma=0.998$ g/cm^3 and $\eta=1.000\,62\cdot10^{-2}$ g/cm s. Using these data we obtain 21555.26 for the Archimedes constant A according to Eq. (10). It is suitable to use in the first step the formulae giving exact solutions: from Eqs (11) and (12) we have $Re=166.87$ and $c=0.7741$. This value of Re will be used as an approximation in the *transcendental* equations. The calculation procedure is illustrated for the case of Eq. (19) (very likely the most accurate from among the equations), see Table I. The Table shows that with a SR-51A calculator using 10 valuable digits the accuracy cannot be increased anymore after 38 steps ($n=38$). Generally, 6—8 steps provide sufficiently accurate results.

Table II contains the values of Re, c and v_0 calculated from the different equations. The terminal settling velocity was calculated from Eqs (3) and (9). Using Eqs (19) and (20) the same results are obtained while those calculated from Eq. (18) only slightly differ.

Table I. Iterative calculation using Eq. (19)

n	Re
1	167
2	148.353 03
3	158.939 843 8
.	.
.	.
.	.
37	154.976 603 7
38	154.976 603 8

Table II. Re, c and v_0 calculated from the different equations

Number of equation	Re	c	v_0 cm/s
11	166.87	0.774 13	16.72
18	154.75	0.900 14	15.52
19	154.977	0.897 47	15.54
20	154.979	0.897 45	15.54

* The computations were carried out by Assistant Professor Raisz

References

Kürten H, Raasch I, Rumpf H 1966: Beschleunigung eines kugelförmigen Feststoffteilchens im Strömungsfeld konstanter Geschwindigkeit. *Chemie Ing. Techn.*,38, 941—948.

Schubert H 1975: Aufbereitung fester mineralischer Rohstoffe. VEB Deutscher Verlag für Grundstoffindustrie, Leipzig

Tarján G 1954: Ore Processing. University text-book, Budapest (In Hungarian)

Acta Geodaet., Geophys. et Montanist. Hung. Volume 18 (3), pp. 241—245 (1983)

LAWS OF MOTION OF SOLID PARTICLES IN STATIONARY MEDIA FOR ALLEN'S DRAG FORMULA

SZ PETHŐ[1]

[Manuscript received February 18, 1981]

The study analyses the displacement-time, velocity-time and acceleration-time functions for solid spheres settling in stationary media for $30 \leqq Re \leqq 300$. The use of these functions are illustrated by a numerical example.

Keywords: acceleration; Allen's drag formula; motion of solid particle; settling displacement; settling in stationary media; velocity

Symbols

a = acceleration; B = constant in Eq. (8); c = drag coefficient; F = force; g = acceleration due to gravity; g_0 = Finkey's constant: initial acceleration of the particle in the medium; J = constant in Eq. (7); j = quotient of the mass moving with the particle and the volume of the particle; Re = Reynolds number; t = time; v_0 = terminal settling velocity; x = diameter of the solid sphere; z = variable, defined in Eq. (9); δ = density of the solid; γ = density of the medium; η = viscosity of the medium

Subscripts

A = buoyancy; F = due to gravity; i = transport force of the medium; T = transport force of the solid particle

As well-known, the drag coefficient c of a solid sphere moving in a stationary fluid or gaseous media can be expressed, according to Allen, for Reynolds numbers from 30 to 300 as

$$c = \frac{10}{\sqrt{Re}}. \tag{1}$$

Since the terminal settling velocity v_0 of a solid sphere of density δ and diameter x in a medium of density γ is given by

$$v_0 = \sqrt{\frac{4g}{3c}} \sqrt{\frac{x(\delta-\gamma)}{\gamma}} \tag{2}$$

[1] Technical University for Heavy Industry, Chair for Ore Processing H-3515 Miskolc, Hungary

in the Allen zone this expression becomes (Tarján 1954, Schubert 1975)

$$v_0 = \left(\frac{2}{15}\right)^{2/3} x \frac{[g(\delta-\gamma)]^{2/3}}{(\eta^{\gamma})^{1/3}}. \tag{3}$$

In these equations g is the acceleration due to gravity, η is the viscosity of the medium in g/cm s.

A solid particle starting its motion at the time-instant $t=0$ with velocity $v=0$, accelerates until it reaches the terminal velocity. The forces acting on the particle satisfy:

$$\vec{F}_F + \vec{F}_A + \vec{F}_T + \vec{F}_i = 0 \tag{4}$$

where F_F is the force due to gravity, F_A the bouyancy, F_T is the transport force of the solid particle and F_i that of the medium moving together with the solid particle. The forces acting on the particle are parallel, their directions are different and their sum gives zero (Schubert 1975).

The differential equation of motion for the solid particle can be expressed from Eq. (4) in scalar form as

$$\frac{\mathrm{d}v}{\mathrm{d}t} = \frac{g_0}{J}\left[1 - \left(\frac{v}{v_0}\right)^{3/2}\right] \tag{5}$$

where g_0 is Finkey's constant (Finkey 1924), giving the initial acceleration of the solid particle in a medium

$$g_0 = g\frac{\delta-\gamma}{\delta} \tag{6}$$

is a further constant, defined as (Schubert 1975):

$$J = 1 + j\frac{\gamma}{\delta} \tag{7}$$

where j denotes the quotient of the volumes of the mass moving with the particle and the volume of the particle. It will be convenient to combine the two constants as

$$B = \frac{g_0}{J}. \tag{8}$$

To solve the differential equation (5) in a closed form we introduce a new variable

$$v = v_0 z^2; \quad z = z(t) \qquad \text{and} \qquad 0 \leqq z \leqq 1. \tag{9}$$

After a few rearrangements we have

$$\frac{2v_0}{B}\int\limits_{z=0}^{z=z}\frac{z}{1-z^3}\,\mathrm{d}z=\int\limits_{t=0}^{t=t}\mathrm{d}t=t \tag{10}$$

which is a differential equation that can be directly solved as

$$t=\frac{2v_0}{B}\left[\frac{1}{6}\ln\frac{z^2+z+1}{(z-1)^2}-\frac{\sqrt{3}}{3}\operatorname{arctg}\frac{2z+1}{\sqrt{3}}+\frac{\sqrt{3}}{3}\frac{\pi}{6}\right]. \tag{11}$$

For $z=0$, $t=0$ since

$$\operatorname{arctg}\frac{1}{\sqrt{3}}=\frac{\pi}{6}$$

For $z=1$, $t=\infty$.

Acceleration a becomes

$$a=B(1-z^3). \tag{12}$$

According to this equation the initial acceleration (at $t=0$) is $a=B$, or in the case $J\approx 1$ it is $a=g_0$; while for $z=1$ we have $a=0$.

Finally, the displacement s can be written as

$$s=\frac{v_0^2}{3B}\ln\frac{z^2+z+1}{(z-1)^2}-\frac{2v_0^2}{B}z+\frac{2\sqrt{3}}{3}\frac{v_0^2}{B}\operatorname{arctg}\frac{2z+1}{\sqrt{3}}-\frac{2\sqrt{3}}{3}\frac{v_0^2}{B}\frac{\pi}{6} \tag{13}$$

The displacement-time, velocity-time and acceleration-time functions can be used as follows. We choose distinct values continuously increasing from 0 to 1 for the parameter z. From Eq. (11) the time t, from Eq. (9) the instantaneous velocity v, from Eq. (12) the acceleration a and, finally, from Eq. (13) the displacement s are calculated.

Table I displays the values of the displacement-time, velocity-time and acceleration-time functions for identical particle sizes, terminal settling velocities and densities. The particle sizes and densities are as follows: $x=0.1$ cm, $\delta=7.5$ g/cm^3; $x=0.1$ cm, $\delta=2.65$ g/cm^3; $x=0.04009$ cm, $\delta=7.5$ g/cm^3 (the terminal settling velocities are equal for the two latter particles) and $x=0.04009$ cm, $\delta=2.65$ g/cm^3. The medium is water of 10 °C temperature, therefore $\gamma=1$ g/cm^3 and $\eta=0.013$ g/cm s. The value of $\dot{J}$ has been chosen for 1. Figure 1 illustrates the displacement-time, velocity-time and acceleration-time curves of a particle of diameter $x=0.1$ cm and density $\delta=2.65$ g/cm^3.

The first column of the Table contains the values of parameter $z^2=v/v_0$, but various time values t correspond to them for the various particles. The time required to reach 99% of the terminal settling velocity for the four particles is 0.148; 0.083; 0.059 and 0.033 s, and the displacements are 4.30; 0.96; 0.69 and 0.15 cm. Thus, these values

Table I. Displacement-time, velocity-time and acceleration-time functions for particles of equal size, density and terminal settling velocity

z^2	$x=0.1$ cm, $\delta=7.5$ g/cm^3				$x=0.1$ cm, $\delta=2.65$ g/cm^3			
	t	v	a	s	t	v	a	s
0	0	0	$g_0=850.2$	0	0	0	$g_0=610.81$	0
0.1	0.004 58	3.8168	823.31	0.008 73	0.002 54	1.5302	591.50	0.001 95
0.2	0.009 32	7.6336	774.16	0.036 1	0.005 20	3.0604	556.18	0.008 09
0.4	0.020 1	15.267	635.11	0.161 3	0.011 2	6.1208	456.29	0.036 1
0.6	0.034 2	22.901	455.06	0.432 5	0.019 1	9.1812	326.93	0.096 8
0.8	0.056 6	30.534	241.85	1.042	0.031 6	12.242	173.75	0.233 0
0.9	0.078 2	34.351	124.29	1.745	0.043 6	13.772	89.29	0.390 4
0.99	0.147 8	37.786	12.72	4.297	0.082 5	15.149	9.139	0.961 4
0.999	0.216 8	38.130	1.275	6.92	0.121 0	15.287	0.916 0	1.548
0.9999	0.285 7	38.164	0.127 5	9.55	0.159 4	152.300	0.091 6	2.136
1.–		$v_0=38.168$	0			$v_0=15.302$	0	

z^2	$x=0.040\,09$ cm, $\delta=7.5$ g/cm^3				$x=0.040\,09$ cm, $\delta=2.65$ g/cm^3			
	t	v	a	s	t	v	a	s
0	0	0	$g_0=850.2$	0	0	0	$g_0=610.81$	0
0.1	0.001 82	1.530 2	823.31	0.001 40	0.001 02	0.613 5	591.50	0.000 31
0.2	0.003 74	3.060 4	774.16	0.005 81	0.002 08	1.226 9	556.18	0.001 30
0.4	0.008 07	6.120 8	635.11	0.025 9	0.004 50	2.453 9	456.29	0.005 80
0.6	0.013 7	9.181 2	455.06	0.069 5	0.007 65	3.680 8	326.93	0.015 6
0.8	0.022 7	12.242	241.85	0.167 4	0.012 7	4.907 8	173.75	0.037 5
0.9	0.031 3	13.772	124.29	0.280 5	0.017 5	5.521 2	89.29	0.062 8
0.99	0.059 3	15.149	12.72	0.690 7	0.033 1	6.073 4	9.139	0.154 5
0.999	0.086 9	15.287	1.275	1.112	0.048 5	6.128 6	0.916 0	0.248 8
0.9999	0.114 5	15.300	0.127 6	1.535	0.063 9	62.134 1	0.091 6	0.343 4
1.—		$v_0=15.302$	0			$v_0=6.134\,1$	0	

cannot be neglected in case of particles of greater diameter and density. From among particles of equal terminal settling velocities those of greater density run ahead because of the greater initial acceleration g_0(or B). The *greater* particle makes 0.96 cm displacement in 0.083 s, while the particle of *greater density* makes a $0.69+(0.083-0.059)\cdot 15.302=1.06$ cm path during the same time. The difference is 1 mm which is maintained during the further motion because of the equal terminal settling velocities of the particles.

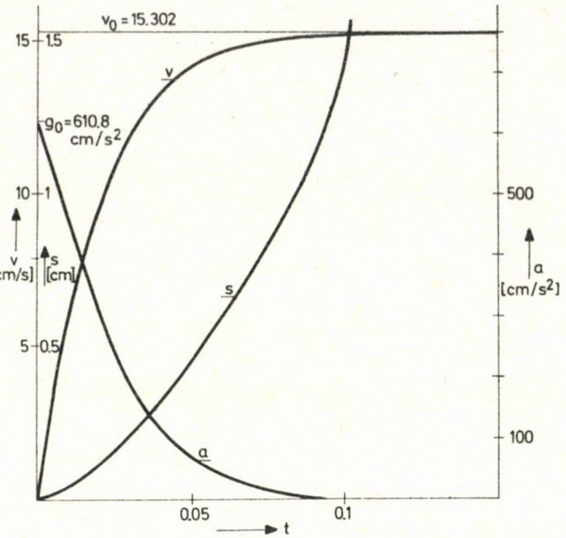

Fig. 1. Displacement-time, velocity-time and acceleration-time curves for Allen's drag formula

Acknowledgement

The help of Reader I Raisz in solving the differential equation and carrying out the calculations is gratefully acknowledged.

References

Finkey J 1924: Die wissenschaftlichen Grundlagen der nassen Erzaufbereitung. Julius Springer Verlag, Berlin

Schubert H 1975: Aufbereitung fester mineralischer Rohstoffe. VEB Deutscher Verlag für Grundstoffindustrie, Leipzig

Tarján G 1964: Ore Dressing. Tankönyvkiadó, Budapest (In Hungarian)

PHYSICAL REASONS FOR THE SIZE-EFFECT IN ROCK-MECHANICAL LABORATORY ANALYSES

Zs Somosvári[1]

[Manuscript received June 22, 1981]

Mechanical properties of rocks are mostly investigated in laboratories using uniaxial and triaxial compression tests. Both uniaxial and triaxial compression tests show an observable influence on the measured values of the uniaxial or triaxial strength of the rock caused by the size of the test piece. This phenomenon is called size-effect in the respective literature. In the following we shall discuss the size-effect in a more wide sense, we are also pointing out its influence on the determination of Poisson's ratio and on the modulus of elasticity. After having analysed the reasons of the phenomenon we are giving a measuring method for the determination of the rock-parameters.

Keywords: modulus of elasticity; Poisson's ratio; rock mechanics; size-effect; triaxial compression; uniaxial compression

Symbols

σ'_D = measured uniaxial compression strength; σ_D = uniaxial compression strength as rock-parameter (CSRP); Φ = angle of the internal friction of the rock; σ'_{Dt} = measured triaxial compression strength; σ_{Dt} = triaxial compr. strength as rock-parameter; $\bar{\sigma}_D, \sigma\bar{\bar{\sigma}}_D$ = asymptotes of the measured compression strengths; σ_z = axial stress; σ_1 = the largest principal stress; σ_3 = the smallest principal stress; σ_r = the mantle pressure, radial stress; σ'_r = mantle pressure substituting the friction of the end plates; σ_φ = hoop stress; τ = shear stress; ε_r = radial strain; ε_φ = tangential strain; ε_1 = axial strain; l = the length of the test piece; D = the diameter of the test piece; d = the width of the test piece; m = Poisson's ratio; m' = measured Poisson's ratio; E = Young's modulus; E' = measured Young's modulus; a, b, f, k, n, q, B = constants; μ = friction's coefficient

In the respective literature (Bieniewski 1968, Denkhaus and Bieniewski 1970, Dreyer and Borchert 1962a, 1962b, Dreyer 1967, 1974, Mikeska et al. 1970, Protodjakonov and Kojfman 1964, Salustowicz 1965, Voropinov and Kittrich 1966, Vutukuri et al. 1974) authors content themselves with analysing the contribution of the size-effect to the compression strength only giving the experienced functions of the variables without investigating the real sense and the deep reasons of the phenomenon. A great part of the articles takes the size-effect for being one of the rock properties, an idea that can not be accepted. Should the size-effect be one of the rock properties, one could not speak about compression strength and other rock properties characterizing the rock materials, one could not speak about mechanical-material properties of rocks.

[1] University for Heavy Industry, Faculty for Mining, H-3515 Miskolc, Hungary

Size-effect in the determination of the uniaxial compression strength

It is well known that the breakdown (damaging) load depends on the diameter (D) and length (l) and also on the ratio of l/D (slenderness) of the cylinder shape specimen if uniaxial compression tests of the same rock material are carried out. The best way to show the phenomenon is to present a set of measurement results. Table I shows laboratory compression test results of the failure stress (σ'_D) investigating the same quality rock-salt, prismatic (length: l, width: d) test pieces at quasi-static loading

Table I

l [cm]	d [cm] 5	10	15	20
	σ'_D [MPa]			
5	26.6	44.3	60.3	66.0
10	16.3	29.8	48.0	50.9
15	15.9	26.5	37.4	41.5
20	15.3	22.8	23.7	39.6

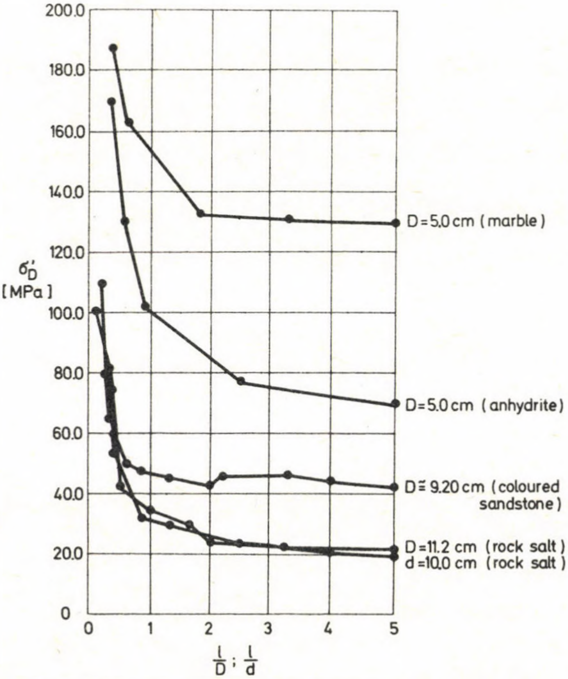

Fig. 1. **The measured compression strength against slenderness of the test piece**

(Salustowicz 1965). Any of the data in the table represents an average of at least three measurings.

Overlooking the table the practical question arises: which one of the results varying from 15.3 MPa to 66 MPa should be taken for the compression strength of the investigated rock body. Our study aims at answering this question.

The measured compression strength is

$$\sigma'_D = f(l, D),$$

or rather

$$\sigma'_D = f(l, l/D), \qquad \text{or} \qquad \sigma'_D = f(D, l/D).$$

Figures 1–4 show the shapes of the above functions. In the case of Fig. 1, the width of the specimen is constant and the compression strength is shown as a function of the slenderness at marble, anhydrite, rock salt, coloured sandstone (Dreyer and Borchert 1962a). The same test results are presented on Fig. 2 as a function of the reciprocal value of the slenderness. Figure 3 gives the changing of the measured compression strengths at different rock types with the same slenderness but changing values of the diameter (Protodjakonov and Kojfmann 1964). Figure 4 gives own measurement (Somosvári 1980a) results for clay slate, anhydrite, gypsum, serpentine at constant slenderness.

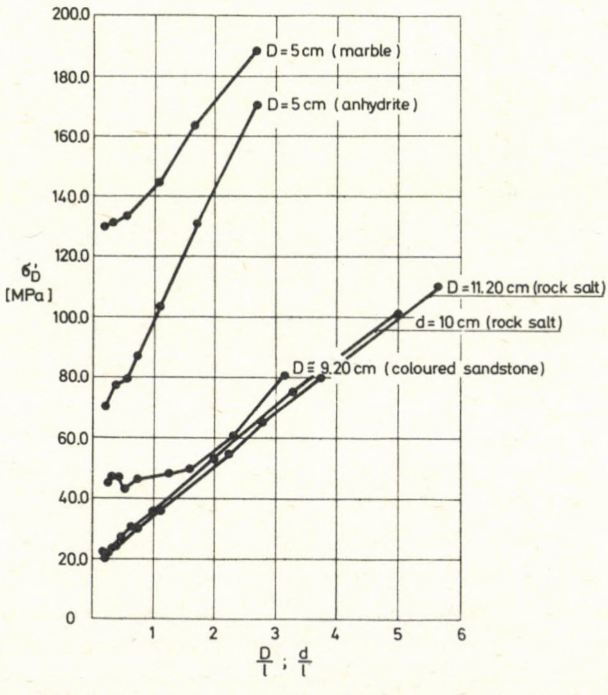

Fig. 2. The measured compression strength against inverse slenderness of the test piece

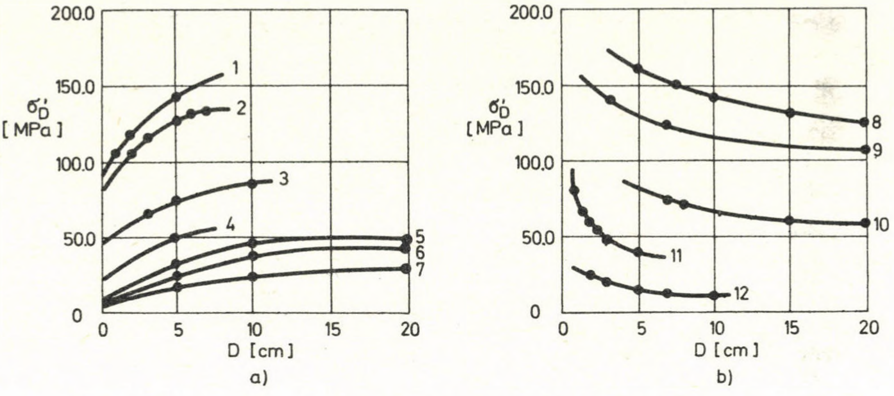

Fig. 3. The measured compression strength against diameter of the test piece

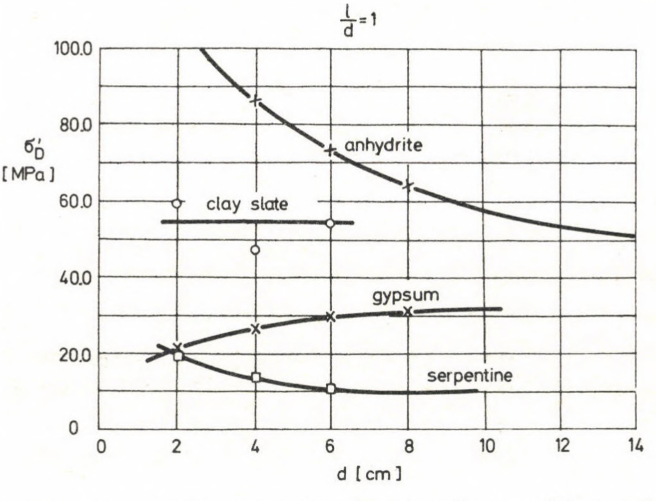

Fig. 4. The measured compression strength against diameter of the test piece

As slenderness grows (at constant diameter) the measured compression strength will definitely drop following a hyperbolic function. With the growth of the inverse slenderness compression strength increases almost linearly. At constant slenderness and changing diameter the behaviour of the compression strength is ambiguous, that is, there are groups of rocks, where it grows, decreases or remains almost constant as the diameter increases.

There are several empirical functions describing the measurement results from which the most generally known is the Dreyer–Borchert function:

$$\sigma'_D = a + b\left(\frac{D}{l}\right)^k; \qquad D = \text{const.}$$

where a, b, k, are rock parameters. Considering $l/D = \text{const.}$ Protodjakonov has given the following empirical functions for describing the phenomenon:

for the first group of rocks

$$\sigma'_D = \bar{\bar{\sigma}}_{D_1} \frac{D + n_1 b_1}{D + b_1}, \qquad n_1 < 1$$

$$\text{if} \quad D = 0, \qquad \sigma'_D = n_1 \bar{\bar{\sigma}}_D,$$

$$\text{if} \quad D = \infty, \quad \sigma'_{D_1} = \bar{\bar{\sigma}}_{D_1};$$

for the second group of rocks

$$\sigma'_{D_2} = \bar{\bar{\sigma}}_{D_2} \frac{D + n_2 b_2}{D + b_2}, \qquad n_2 > 1$$

$$\text{if} \quad D = 0, \quad \sigma'_{D_2} = n_2 \bar{\bar{\sigma}}_{D_2},$$

$$\text{if} \quad D = \infty, \quad \sigma'_{D_2} = \bar{\bar{\sigma}}_{D_2};$$

for the third group of rocks

$$\sigma'_{D_3} = \bar{\bar{\sigma}}_{D_3} \frac{D + n_1 b_1}{D + b_1} \cdot \frac{D + n_2 b_2}{D + b_2}; \qquad n_1 < 1, \quad n_2 > 1$$

$$\text{if} \quad D = 0, \quad \sigma'_{D_3} = n_1 n_2 \bar{\bar{\sigma}}_{D_3},$$

$$\text{if} \quad D = \infty, \quad \sigma'_{D_3} = \bar{\bar{\sigma}}_{D_3}.$$

In the above functions $\bar{\bar{\sigma}}_D$ represents the value of the asymptote, n and b are constants.

In the following we make an attempt to explain the essence of the observed phenomenon.

The role of the slenderness in measuring the compression strength

It is known from experience that under uniaxial compression loading the cylinder shape stubby specimen deform into a stave shape. This shows that on the end plates of the specimen the friction is large enough to prohibit the movement into side-directions. Besides normal stresses, shear stresses also appear on the end plates, thus, the uniform distribution of normal stresses will be distorted (see Fig. 5). We have to realize that there is no constant and uniaxial stress distribution inside the specimen during the measurements as one would imagine it.

The complex state of stresses inside compressed specimen of rocks has been studied by several authors (Mikeska et al. 1970, Balla 1953). The stresses were investigated by both photoelastic and theoretical methods. These studies analyse the stresses on the elastic strain field, thus, one could not use them when investigating the

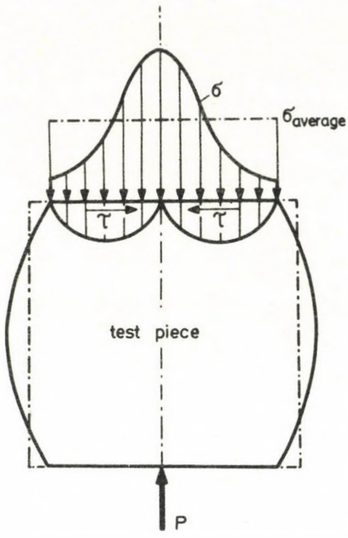

Fig. 5. Distribution of stresses on the end plates of the test piece

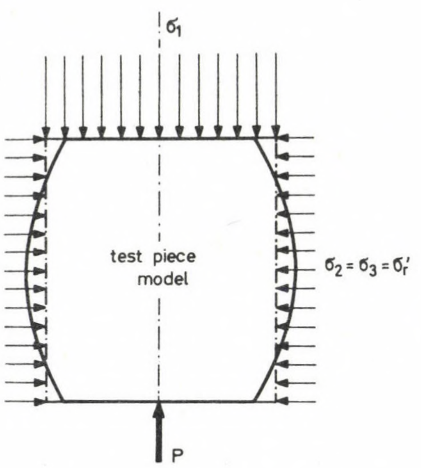

Fig. 6. Loading model of the test piece

fracture field, as the elastic state is followed by a plastic state before reaching the breakdown (fracture) phase. To avoid this problem we shall construct models which reflect the important elements of the phenomenon.

Let us see first the failure stress as a function of l/D if $D=\text{const}$. Normal stresses on the end plate will be substituted by $\sigma_z=\text{const}$. stress, whilst shear stresses will be represented by $\sigma_r=\text{const}$. stress acting on the mantle of the cylinder (Fig. 6). At the breakdown phase (Somosvári 1975, Somosvári 1980a):

$$\sigma_z = \sigma'_D$$

$$\sigma'_r = \frac{\sigma'_D}{m-1} \cdot \frac{1}{\frac{1}{f} + \frac{b}{\mu}\frac{l}{D}}$$

where:

μ: friction-coefficient on the end plates

m: Poisson's ratio of the rock

f, b: constants.

Accepting Mohr's hypothesis on failure and a linear envelope curve, the condition of the failure is

$$\sigma'_1 = \bar{\sigma}_D + B\,\sigma_3; \qquad B = \tan^2\left(45 + \frac{\Phi}{2}\right)$$

where:

$\bar{\sigma}_D$: real compression strength

Φ: angle of the internal friction of the rock.

It is to be remarked that the linear failure curve is not valid in the pulled region and also in the compressed region it has only a limited validity. In qualitative investigations, however, as in the present case, one can still use it. By the substitution $\sigma_1 = \sigma'_D$, $\sigma_3 = \sigma'_r$ the measured compression strength is

$$\sigma'_D = \bar{\sigma}_D(m-1)\frac{\frac{1}{f}\frac{D}{l} + \frac{b}{\mu}}{\left(\frac{m-1}{f} - B\right)\frac{D}{l} + \frac{b(m-1)}{\mu}}.$$

if $B = \dfrac{m-1}{f}$, then

$$\sigma'_D = \bar{\sigma}_D\left[1 + \frac{B}{(m-1)b}\frac{D}{l}\right],$$

that is, we have formulated a linear function between measured compression and inverse slenderness determined earlier by the measuring tests. The larger the friction coefficient, the higher is the size-effect; the larger is Poisson's ratio (i.e. the less is side-strain of the test piece), the smaller the size-effect; and finally the steeper the failure envelope curve of the rock, the larger the internal friction angle is, the higher size-effect will occur as it is seen from the above function.

The cause for the size-effect on the measured compression strength is that the side deviation is prohibited because of the end plate friction inducing an effect similar to triaxial conditions (Somosvári 1980a, Somosvári 1975, Martos 1961, Somosvári

1980b). The more stubby the test piece is (the less is the value of l/D), effect will be more triaxial-like, and the larger compression strength will be measured. Figure 7 gives an opportunity to follow this mechanism.

If one accepts a linear failure envelope curve, the measured compression strength will be σ'_D instead of $\bar{\sigma}_D$, because $\sigma'_r \neq 0$.

Experiments prove that by reducing μ, that is, if the end plates are smoother, the measured compression strength will be smaller. The measured value of μ varies generally between 0.2 and 0.3 (Martos 1961).

In the following we shall analyse the influence of the test piece's diameter, considering $l/D = \text{const.}$

The influence of the diameter on the measured compression strength

The friction on the end plates distorts the uniform distribution of the normal compression stresses (see Fig. 5), the normal stress will be much higher in the centreline of the cylinder-shaped test piece than on the periphery. Inside the specimen there are not only axial, but also radial (σ_r) and hoop (σ_φ) stresses acting.

Because of the symmetrity, $\tau_{r,\varphi} = \tau_{\varphi,r} = 0$ and on the mantle ($r = R$) of the specimen (free surface) $\tau_{z,r} = \tau_{r,z} = 0$, $\sigma_r = 0$.

Considering the concentration of the axial normal stresses the cylinder-shaped specimen can theoretically be divided into two parts (see Fig. 8), that is, into an inside cylinder and an outside ring. When compression in an axial direction the inside cylinder stretches the outside ring, thus, stresses will occur in the ring that are similar to the thick-wall tube loadings whereas the worst load will appear on the outside mantle of the ring ($r = R$).

At failure the axial stress on the mantle ($r = R$) will be

$$\sigma_z = q\sigma'_D; \qquad 0 \leqq q \leqq 1; \qquad q(\mu, m).$$

$$\text{if} \quad \mu = 0, \quad \text{then} \quad q = 1 \quad \text{and} \quad \sigma_z = \sigma'_D;$$

$$\text{if} \quad m = \infty, \quad \text{then} \quad q = 1 \quad \text{and} \quad \sigma_z = \bar{\sigma}_D.$$

Temporarily supposing an elastic state until the failure phase, the tangential stress on the mantle will be (Somosvári 1980b):

$$\sigma_\varphi = E\varepsilon_\varphi + \frac{q\sigma'_D}{m},$$

where

E: modulus of elasticity,

ε_φ: tangential strain.

For $\varepsilon_\varphi = \varepsilon_r$ (symmetricity) and $m = -\varepsilon_z/\varepsilon_r$, $E = \sigma'_D/\varepsilon_z$, the tangential stress is

$$\sigma_\varphi = -\frac{\sigma'_D}{m}(1 - q).$$

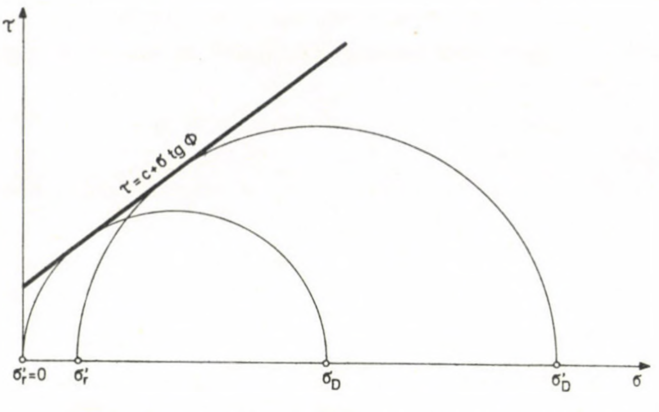

Fig. 7. The measured compression strength on Mohr's plain

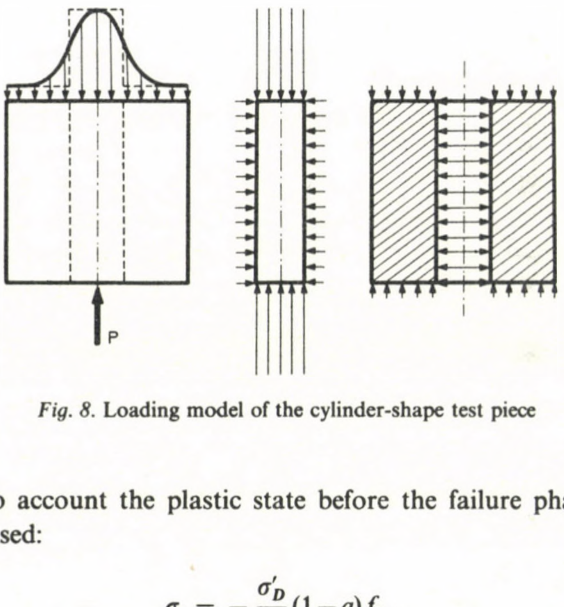

Fig. 8. Loading model of the cylinder-shape test piece

Taking into account the plastic state before the failure phase the following function can be used:

$$\sigma_\varphi = -\frac{\sigma'_D}{m}(1-q)f_1,$$

where $f_1 = \text{const.}$

The stress distribution on the mantle at the failure phase is characterized by

$$\sigma_1 = \sigma_z = q\sigma'_D$$

$$\sigma_z = \sigma_r = 0$$

$$\sigma_3 = \sigma_\varphi = \frac{\sigma'_D}{m}(1-q)f_1 \quad \text{(pulling stress).}$$

On the other hand, the tangential stress on the mantle as a stress of the thick-wall will follow the function below (Ponomarjov 1963):

$$\sigma_\varphi = \frac{\sigma'_D}{m} \frac{f_1}{f_2 D^2 + 1} \, .$$

Thus,

$$1 - q = \frac{1}{f_2 D^2 + 1}$$

and

$$q = \frac{f_2 D^2 - 1}{f_2 D^2 + 1} \, .$$

For $q(\mu, m)$, f_2 has to be $f_2(\mu, m)$ and if $\mu = 0$ or $m = \infty$, $f_2 = \infty$ in both cases. Thus, the formula of f_2 is

$$f_2 = f_3 \frac{m}{\mu} \, .$$

The largest and smallest principal stresses are

$$\sigma_1 = \sigma_D \frac{f_2 D^2 - 1}{f_2 D^2 + 1} \, ,$$

$$\sigma_3 = -\frac{\sigma'_D}{m} \frac{f_1}{f_2 D^2 + 1} \, .$$

Substituting into the breakdown condition

$$\sigma_1 \geqq \bar{\bar{\sigma}}_D + B\sigma_3 \, ,$$

the measured compression strength is:

$$\sigma'_D = \bar{\bar{\sigma}}_D \frac{f_3 \frac{m}{\mu} D^2 + 1}{f_3 \frac{m}{\mu} D^2 + f_1 \frac{B}{m} - 1} \, .$$

$$\text{if} \quad D = \infty, \quad \text{then} \quad \sigma'_D = \bar{\bar{\sigma}}_D \, ,$$

$$\text{if} \quad D = 0, \quad \text{then} \quad \sigma'_D = \bar{\bar{\sigma}}_D \frac{1}{f_1 \frac{B}{m} - 1} \, .$$

Furthermore:

a) $$\text{if} \quad f_1 \frac{B}{m} > 2, \quad \text{then} \quad \sigma'_D < \bar{\bar{\sigma}}_D$$

b) if $f_1\frac{B}{m}<2$, then $\sigma'_D>\bar{\bar{\sigma}}_D$

c) if $f_1\frac{B}{m}=2$, then $\sigma'_D=\bar{\bar{\sigma}}_D$.

The above function describes the tendencies of the characteristic differences of the compression strengths as a function of the diameter, if $l/D=\text{const}$. The measured compression strength increases in case *a*, decreases in case *b*, and there is no change in case *c*. As it was seen above the character of the change will be essentially determined by Poisson's ratio and by the angle of the inside friction of the rock.

Reflecting the experience the above function gives larger size-effect if the inside friction factor grows and less size-effect if Poisson's ratio increases.

The reason why the measured compression strength changes if the specimen's diameter also changes is that the friction on the end plates of the test piece distorts the distribution of the normal stresses. The value of the normal stresses will be higher in the centreline of the piece as in the mantle region.

The test piece can be divided into a central, cylinder-shaped core and an outside thick-wall ring. If compressed, the inside core will stretch the outside ring in radial direction, so the mantle has tangential pulling stresses depending on Poisson's ratio of the core and also on the diameter of the test piece.

The failure depends on the angle of inside friction, thus, the character of the size-effect is determined by Poisson's ratio and the angle of inside friction, whilst the *volume* of the size-effect is determined by Poisson's ratio and the friction-coefficient.

Determination of the compression strength as a rock-parameter (CSRP)

As slenderness and diameter work together and at the same time, $\bar{\sigma}_D$ and $\bar{\bar{\sigma}}_D$ could not give real material properties (parameters) of the rock unless one of them does not induce any effect. Considering both of the influences the measured compression strength will be:

$$\sigma'_D=\sigma_D\left(1+\frac{\mu_B}{b}\frac{D}{l}\right)\frac{f_3\frac{m}{\mu}+1}{f_3\frac{m}{\mu}f_1\frac{B}{m}-1}=\sigma_D f(D, l/D),$$

where

σ_D: compression strength as rock-parameter (CSRP)

If $D/l\to 0$ and $D\to\infty$, then $\sigma'_D=\sigma_D$.

Furthermore

$$\bar{\sigma}_D=\sigma_D\frac{f_3\frac{m}{\mu}D^2+1}{f_3\frac{m}{\mu}D^2+f\frac{B}{m}-1},$$

and

$$\bar{\bar{\sigma}}_D=\sigma_D\left(1-\frac{\mu_B}{b}\frac{D}{l}\right).$$

If $\mu=0$, then $\bar{\sigma}_D=\sigma_D$, $\bar{\bar{\sigma}}_D=\sigma_D$.

There are two possible ways to determine CSRP (σ_D). One of these is to use specimens of a slenderness and a diameter the measured value of which is practically equivalent to CSRP.

As test results have shown, test pieces of $l/D=2.5-4$, and $D=100-150$ mm would meet this condition. The International Bureau of Rock Mechanics (IBRM) recommends to use test pieces of $D=42$ mm, and $l/D=1$ [18]. To meet the above condition one should use pieces of 2000–10 000 cm^3 volume instead of the 58 cm^3 pieces recommended by the IBRM. That is, 30–170 times more rock-material would be required for the preparation of the specimens. The requested size and volume will hardly be producible from the drilled cores or slot-samples, CSRP will rarely be determined by using the required large-size test pieces.

Another way to solve the problem would be to use normal size test pieces in the compression tests. Two series of trials will be sufficient to determine CSRP. The purpose of the first series is to determine the function

$$\sigma'_D=f(l/D), \qquad \text{if } D=D_0=\text{const.},$$

the second one serves the elaboration of

$$\sigma'_D=f(D), \qquad \text{if } l/D=(l/D)_0=\text{const.}$$

After having the results of the series, CSRP will be calculated by

$$\sigma_D=\frac{\bar{\sigma}_D\bar{\bar{\sigma}}_D}{\sigma_D^*} \qquad \text{(See Fig. 9)}$$

Returning to the rock-salt's compression strength tabulated in Table I, the real compression strength is

$$\sigma_D=27\ \text{MPa},$$

the measured strength is

$$\sigma'_D=27\frac{d^2+20}{d^2+60}\left(1+0.5\frac{d}{l}\right),\ \text{MPa}\ d\ [\text{cm}].$$

If determining CSRP one has to use sufficiently large pieces and make measurements for — at least — three values of D and l/D to provide a good surface for the function:

$$\sigma'_D=\sigma_D f(D,\ l/D).$$

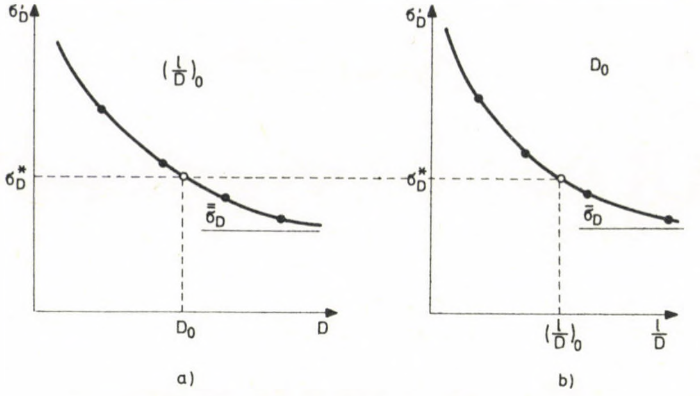

Fig. 9. Determination of CSRP

The size-effect in triaxial compression tests

As a consequence of the above statements, the size-effect also appears in the triaxial tests. Figure 10 shows triaxial compression test-results at different slendernesses, using test pieces of $D=3.0$ cm. The mantle pressure (σ_3) was 3 MPa (Кунтыш 1973). The characteristics of the deviations are very similar to the results drawn from the uniaxial tests. Comparing the also available results of the uniaxial compression tests for limestone, it can be seen that the uniaxial compression strength at $l/D=0.4$ is equal to the triaxial compression strength at $l/D=4$, if $\sigma_3=3$ MPa. If the test is uniaxial and the slenderness $l/D=0.4$, the effect of the end plate friction prohibiting the side-deformation corresponds to a mantle-pressure of $\sigma_r=3$ MPa.

The triaxial CSRP will be

$$\sigma_{Dt}=\sigma_D+B\sigma_3,$$

if one accepts a linear failure curve and uses quasistatic loading.

The measured triaxial compression strength:

$$\sigma'_{Dt}=\sigma_{Dt}f(l/D, D)=\sigma_D f(l/D, D)+B\sigma_3=\sigma'_D+B\sigma_3.$$

The result differs from the uniaxial strength function only by a constant ($B\sigma_3$). Figure 10 shows this in case of limestone.

The determination of the triaxial CSRP at a given mantle pressure could be carried out in a way similar to the test series as it was arranged in the uniaxial case. However, a triaxial test of a piece takes definitely more time as the time required for the uniaxial test. So, in triaxial tests, there is no real possibility to use the same method as in the uniaxial tests. In case of larger diameters the lack of the capacity of the compression-testing machine would also prohibit the determination of the triaxial compression strengths. The only way to solve the problem is to make uniaxial test-series for the determination of the size-effect, thus, converting the results obtained from the triaxial tests and determining the triaxial CSRP. The conversion is shown in the following example.

Let us take specimens of $D=3$ cm, $l/D=1$, where the measured compression strengths were as follows:

$$\text{at} \quad \sigma_3=0 \text{ MPa}, \qquad \sigma'_{Dt}=40 \text{ MPa}=\sigma'_D$$

$$\text{at} \quad \sigma_3=2 \text{ MPa}, \qquad \sigma'_{Dt}=60 \text{ MPa},$$

$$\text{at} \quad \sigma_3=6 \text{ MPa}, \qquad \sigma'_{Dt}=100 \text{ MPa}.$$

Let the uniaxial CSRP be $\sigma_D=20$ MPa, the triaxial CSRP will be calculated by the following function:

$$\sigma_{Dt}=\sigma_D+\sigma_{Dt}-\sigma'_D.$$

Thus,

$$\text{at} \quad \sigma_3=0 \text{ MPa}, \qquad \sigma_{Dt}=20 \text{ MPa}=\sigma_D \qquad \sigma'_{Dt}/\sigma_{Dt}=2.$$

$$\text{at} \quad \sigma_3=2 \text{ MPa}, \qquad \sigma_{Dt}=40 \text{ MPa}, \qquad \sigma'_{Dt}/\sigma_{Dt}=1.5$$

$$\text{at} \quad \sigma_3=6 \text{ MPa}, \qquad \sigma_{Dt}=80 \text{ MPa}, \qquad \sigma'_{Dt}/\sigma_{Dt}=1.25.$$

As it is to be seen, if confining pressure increases, the ratio of the measured triaxial strength and the triaxial CSRP decreases, as the role of the friction is smaller and smaller as confining pressure grows.

As explained above the uniaxial compression test cannot be avoided, the results of the triaxial measurements will be of value if the size-effect is also determined by uniaxial tests carried out parallelly.

The size-effect in determining Poisson's ratio

Derived from Hooke's law, Poisson's ratio will be determined from the corresponding values of ε_1, ε_r, elastic strains:

$$m= -\frac{\varepsilon_1}{\varepsilon_r}, \qquad \varepsilon_1>0, \qquad \varepsilon_r<0;$$

where

ε_1 is the axial strain,

ε_r is the radial strain.

Because of the end-plate frictions the load is not uniaxial, side-deviation is prohibited, the measured Poisson's ratio (m') will be larger than the real value of it if the piece is stubble. Using Hooke's law and the equation $\sigma'_r = \sigma'_\varphi$:

$$m' = \frac{m\sigma_1 - 2\sigma'_r}{\sigma_1 - \sigma'_r(m-1)}.$$

If the stress is unidirectional, that is, $\sigma'_r = \sigma'_\varphi = 0$, then $m' = m$.

The friction's effect prohibiting the side-deviation has been taken into account by the following:

$$\sigma'_r = \frac{\sigma_1}{\dfrac{m-1}{f} + \dfrac{b}{\mu}\dfrac{l}{D}}.$$

Thus,

$$m' = \frac{m\left(\dfrac{m-1}{f}\dfrac{b'}{\mu}\dfrac{l}{D}\right) - 2}{\dfrac{m-1}{f'} + \dfrac{b'}{\mu}\dfrac{l}{D} - (m-1)}$$

if $f' = 1$, then

$$m' = m + \frac{\mu}{b'}[m(m-1)-2]\frac{D}{l} = \frac{m\dfrac{l}{D} + \dfrac{\mu}{b'}[m(m-1)-2]}{\dfrac{l}{D}}.$$

There are no available results in the technical literature for the function $m'(l/D)$, thus, we have to rely on our own measurements. We prepared specimens of the same quality and $D = 4$ cm from cement, for a large number of tests. First we investigated the compression strength at the slendernesses of $l/D = 0.5$; 0.66; 1.0; 1.5; 2.0; 3.0; 6.0 four times at the same slenderness, that is, all together in 28 tests.

Figures 11 and 12 show the correlation between the compression strength and the slenderness and inverse slenderness, respectively. By the help of regression analysis:

$$\sigma'_D = 20.5\left(1 + 0.52\frac{D}{l}\right)\text{MPa},$$

where the correlation index (r) is equal to 0.945. Specimens of cement show tendencies of compression strength similar to those of rocks, thus, they have to show similar changes as far as Poisson's ration is concerned.

Measurements have been carried out for the determination of the Poisson's ratio at constant slenderness equal to those used for the determination of the compression strength. Figures 13 and 14 show the measured Poisson's ratios against slenderness and inverse slenderness, respectively. It can be seen thát stubby specimens give large Poisson's ratios.

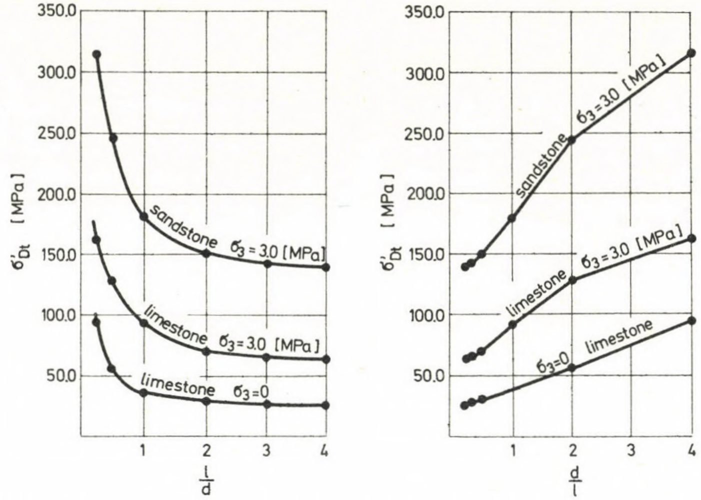

Fig. 10. The measured triaxial compression strength against slenderness and inverse slenderness of the test piece

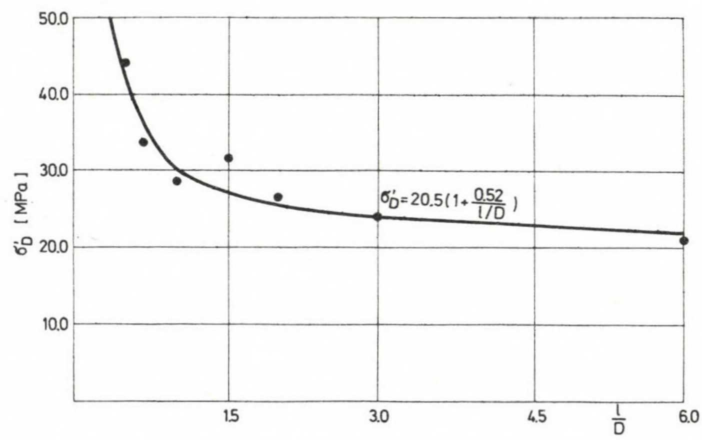

Fig. 11. Measured compression strengths against slenderness of the test piece

By a regression analysis:

$$m' = 2.1\left(1 + 7.5\frac{D}{l}\right),$$

where the correlation index is 0.99. Poisson's ratio as a rock-parameter: $m = 2.1$.

The measured Poisson's ratio is more sensitive to slenderness than compression strength is. This is rather natural for the friction's effect prohibiting the side deviation

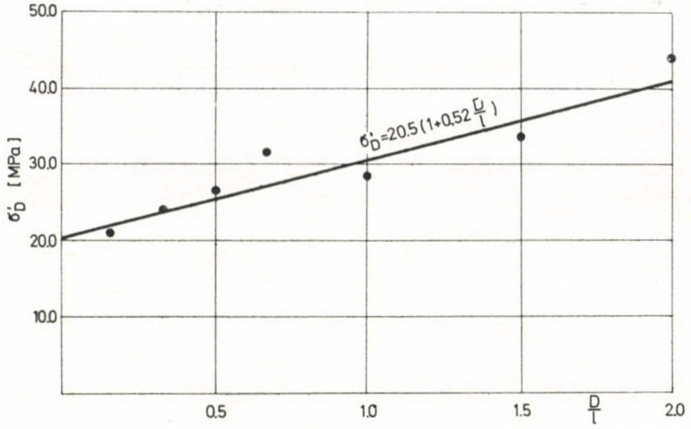

Fig. 12. Measured compression strengths against inverse slenderness of the test piece

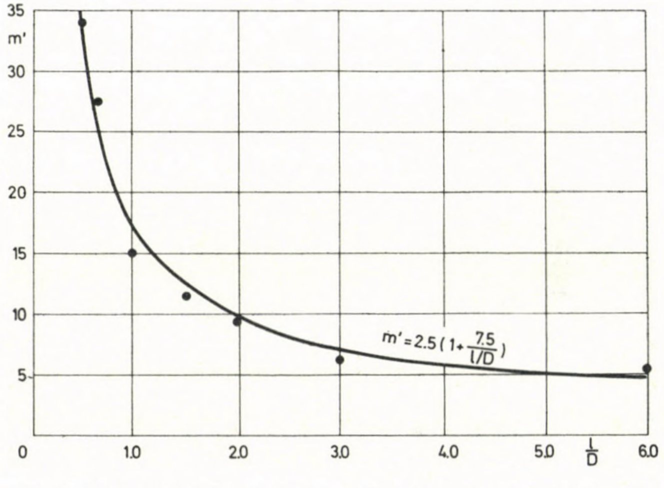

Fig. 13. Measured Poisson's ratios against slenderness of the test piece

works directly when determining Poisson's ratios, whilst it works indirectly when examining compression strength.

From the above statements follows that when determining Poisson's ratio as a rock-parameter one has to do the same as when analysing CSRP. What differs is that one does not have to deal with the changes in diameter if slenderness is constant. It also follows that publish Poisson's ratios determined by using normal ($l/D = 1-2$) test specimens are larger than their real value. Publications give even $m = 15-25$ values for

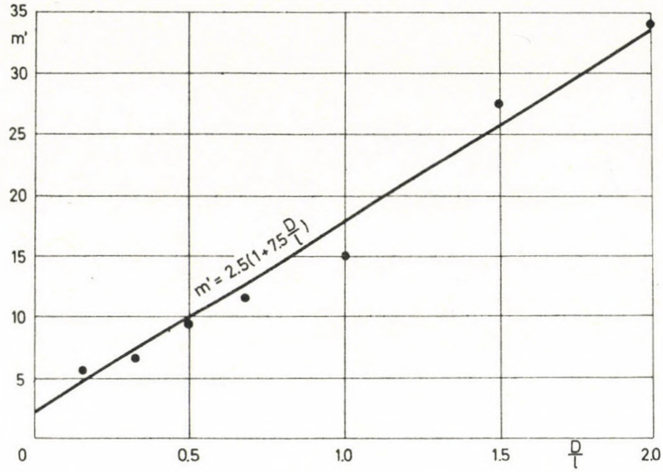

Fig. 14. Measured Poisson's ratios against inverse slenderness of the test piece

that ratio which has to be considered as a consequence of the size-effect. Poisson's ratios of rocks vary between 2 and 6.

Poisson's ratio can also be determined by triaxial tests. Deriving from Hooke's law (Somosvári 1976):

$$m = \frac{\frac{\sigma_r}{\sigma_1}\left(2 - \frac{\varepsilon_1}{\varepsilon_r}\right) - \frac{\varepsilon_1}{\varepsilon_r}}{1 - \frac{\varepsilon_1}{\varepsilon_r}\frac{\sigma_r}{\sigma_1}}$$

where

σ_1 is the axial stress,

σ_r is the mantle pressure.

In case of stubby specimens we reckon with less σ_r and measure less ε_r than the real value of them because of the friction on the end plates. Thus, the determined Poisson's ratio (m') will be larger than the real one.

Figure 15 shows both the uniaxial and triaxial compression test-results of the same rock. It can be seen that the confining pressure has been kept constant at $\sigma_3 = 3$ MPa.

Poisson's ratio calculated on the base of the uniaxial test will be

$$m = 5.2,$$

when the values taken into account are:

$$\sigma_1 = 75 \text{ MPa}, \qquad \varepsilon_1 = 2.1‰, \qquad \varepsilon_r = -0.4‰.$$

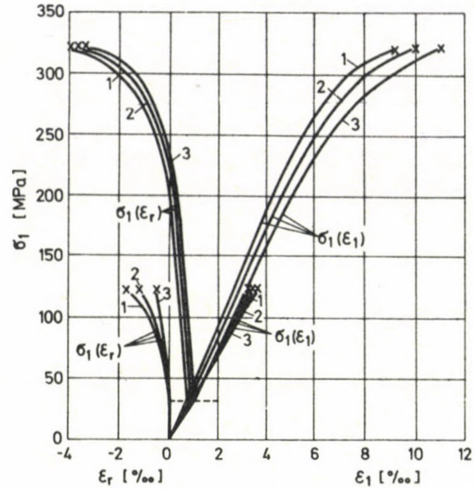

Fig. 15. Charts of the triaxial compression tests

On the base of the triaxial test the Poisson's ratio is

$$m' = 3.7,$$

whilst

$$\sigma_1 = 150 \text{ MPa}, \qquad \varepsilon_1 = 3.5‰, \qquad \varepsilon_r = -0.5‰.$$

Poisson's ratio obtained from the triaxial test is less than that obtained from the uniaxial test because the effect of the friction prohibiting the side-deviation is less if $\sigma_r > 0$. When using $l/D = 2$ specimens in the triaxial tests one can reach a close-to-real value of Poisson's ratio as a rock-parameter.

Size-effect in determining Young's modulus

As it is well known, following Hooke's law, Young's modulus will be calculated from the coherent values of σ_1 and ε_1 obtained from the compression tests:

$$E = \frac{\sigma_1}{\varepsilon_1}.$$

Since the load is not uniaxial because of the friction on the end-plate, the measured Young's modulus will be:

$$E' = \frac{1}{\varepsilon_1}\left(\sigma_1 - \frac{2\sigma_r'}{m}\right); \qquad \sigma_r' > 0.$$

Young's modulus as rock-parameter appears when $\sigma'_r=\sigma'_\varphi=0$, thus,

$$E'=E\left(1-\frac{2\sigma'_r}{m\sigma_1}\right),$$

that is, Young's modulus determined by stubby test pieces will be smaller than Young's modulus as a real rock-parameter. Considering σ'_r which corresponds to the friction's effect:

$$E'=E\left[1-\frac{2}{m}\frac{1}{\frac{m-1}{f''}+\frac{b''}{\mu}\frac{l}{D}}\right]$$

or

$$E'=E\left[1-\frac{2}{m}\frac{\frac{D}{l}}{\frac{m-1}{f''}\frac{D}{l}\frac{b''}{\mu}}\right].$$

If $\dfrac{m-1}{f''}=0$, then

$$E'=E\left[1-\frac{2}{m}\frac{\mu}{b''}\frac{D}{l}\right].$$

There are no published results concerning the function $E'(l/D)$, thus, we have to rely on our measurements. Using the cement test pieces mentioned before, we measured Young's modulus with four pieces at each slenderness. Figures 16 and 17 show the measured Young's modulus against slenderness and inverse slenderness, respectively. Using regression analysis, we get:

$$E'=7386\left(1-0.40\frac{D}{l}\right);\quad \text{MPa},$$

whereby the correlation index is equal to — 0.95. Young's modulus as rock-parameter is:

$$E=7386 \text{ MPa}.$$

The measured Young's modulus is less sensitive to the slenderness than the compression strength.

When determining Young's modulus as a rock-parameter we have to work in a way similar to what we have done at Poisson's ratio.

Young's modulus can also be determined by the help of triaxial tests. Referring Hooke's law (Somosvári 1976):

$$E=\frac{\sigma_1}{\varepsilon_1}\frac{2}{m}\frac{\sigma_r}{\varepsilon_1}.$$

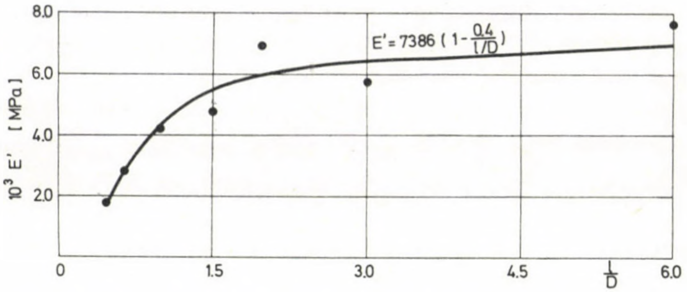

Fig. 16. Measured Young's modulus against slenderness of the test piece

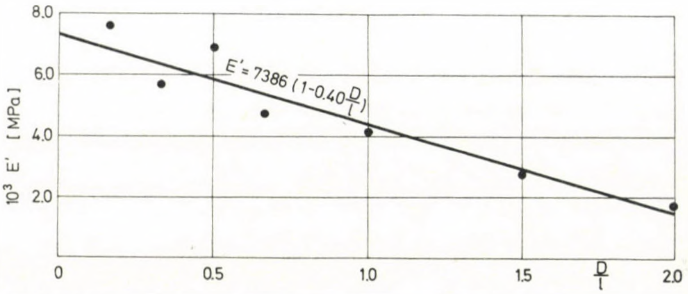

Fig. 17. Measured Young's modulus against inverse slenderness of the test piece

Because of the friction on the end plates the effect prohibiting side-deviation is larger than σ_r, the determined Young's modulus is smaller than the real value of it.

As it can be seen in Fig. 15, according to the uniaxial test, Young's modulus is: $E = 38\,000$ MPa. Parallelly, taking the following data from the triaxial test:

$$\sigma_1 = 200 \text{ MPa}$$

$$\varepsilon_1 = 46‰,$$

$$\sigma_r = 30 \text{ MPa}$$

$$m = 3.5 \text{ (estimated)}$$

Young's modulus will be:

$$E' = 39{,}750 \text{ MPa}.$$

The triaxial Young's modulus is larger because the friction's effect is smaller, if $\sigma_r > 0$.

Good results are obtained for Young's modulus as a rock parameter if using $l/D = 2$ slenderness in triaxial testing.

We have to remark that in the uniaxial compression tests the first part of the $\sigma-\varepsilon$ function will not be completely linear, thus, the determination of Young's modulus is still problematic and requires a special settling.

Test results presented in this study are related to a few kinds of rocks. The listed references contain results that are similar to the tendencies analysed by us and are based on such a wide range of rocks as from the magmatic to the metamorphic deposits. Therefore, the validity of our statements is not restricted to certain groups of rocks, the more so, since they are based on theoretical analysis.

Summary

The size-effect observed in compression tests was analysed in a wide sense and demonstrated in the determination of Poisson's ratio and Young's modulus. The reasons of the size-effect were also analysed and a proof was given for the size-effect not being a material property but rather an effect caused by the friction on the end plates of the test pieces. It was also shown that size-effect appears in triaxial tests as well, thus, triaxial test can be valuable if they are combined with uniaxial test series enabling the determination of the compression strength as a real rock-parameter. The study has given a method for eliminating the size-effect in the determination of rock-parameters (uniaxial and triaxial compression strengths, Poisson's ratio, Young's modulus).

References

Balla A 1953: Problems of Compression. *Acta Technica*, 6, 445—477.

Bieniewski Z T 1968: Eine Studie des Bruchmechanismus von Kohle in situ. 9. Ländertreff. Internat. Gebirgsmech., Leipzig, 1967. Akademie Verlag, Berlin.

Denkhaus H G, Bieniewski Z T 1970: Festigkeit von Gestein und Gebirge. 10. Ländertreff. Internat. Gebirgsmechn. Leipzig, 1968. Akademie-Verlag, Berlin.

Dreyer W 1967: Die Festigkeitseigenschaften natürlicher Gesteine insbesondere der Salz und Karbongesteine. Claustahler Hefte zur Lagerstättenkunde und Geochemie der mineralischen Rohstoffe. H. 5.

Dreyer W 1974: Gebirgsmechanik im Salz. Ferdinand Enke Verlag, Stuttgart.

Dreyer W, Borchert H 1962a: Kritische Betrachtung zur Prüfkörperformel von Gestein. *Bergbautechnik*, 12, 265—272.

Dreyer W, Borchert H 1962b: Ein Beitrag zur Gesteinsphysik und Gebirgsdruckforschung. *Bergbauwissenschaften*, 9, 356—361.

Кунтыш М Ф 1973: О влиянии размера образцов горных пород на их прочность в условиях объемного сжатия. *Горныи Журнал*, 149, No. 5, 63—65.

Martos F 1961: Kőzetek egytengelyű nyomószilárdságát befolyásoló tényezők, különös tekintettel a nyomott felületeken fellépő súrlódásra (Factors influencing uniaxial compressive strength of rocks, with special attention to friction on the pressed surfaces). *BKI Közleményei*, 6, 104—113.

Martos F 1964: Irányelvek néhány kőzetmechanikai vizsgálat végrehajtásának egységesítéséhez (Instructions for the unification of the realization of some test measurements in rock mechanics). *BKI Közleményei*, 9, 105—112.

Mikeska J, Riman A, Vavro M 1970: Mechanika hornin II. Prague.

Ponomarjov Sz D 1963: Szilárdsági számítások a gépészetben (Static computations in mechanics). Műszaki Könyvkiadó, Budapest.

Protodjakonov M M, Kojfmann M I 1964: Über den Meßstabseffekt bei Untersuchung von Gestein und Kohle. 5. Ländertreff. Internat. Gebirgsmech. Leipzig. 1963. Akademie-Verlag, Berlin.

Salustowicz A 1965: Mechanika Górotworu. Stalingród.

Somosvári Zs 1975: Kőzetek anyagjellemzőként számba vehető nyomószilárdságának meghatározása (Determination of compressive strength as the material characteristic of rocks (Part I). *Tatabányai Szénbányák Műszaki-Gazdasági Közleményei*, 15, 80—87.

Somosvári Zs 1976: Determination of elastic characteristics of cohesive soils. 5th Conf. Soil Mech. and Found. Eng. Akadémiai Kiadó.

Somosvári Zs 1980a: Kőzetek nyomószilárdságának értékeléséről (An evaluation of the compressive strength of rocks (Part I)). *BKL. Bányászat*, 113, 96—104.

Somosvári Zs 1980b: Kőzetek nyomószilárdságának értékeléséről (An evaluation of the compressive strength of rocks (Part II)). *BKL. Bányászat*, 113, 161—169.

Voropinov J, Kittrich R 1966: Mechanika hornin I. Prague.

Vutukuri V S, Lama R D, Saluja S S 1974: Handbook on mechanical properties of rock I. Trans. techn. publications.

Acta Geodaet., Geophys. et Montanist. Hung. Volume 18 (3), pp. 271—280 (1983)

CAPACITY OF COAL-BASED ENERGY GENERATING COMPLEXES

F KOVÁCS[1]

[Manuscript received October 9, 1981]

A method is presented to calculate the optimum capacity and life of mine-power station complexes. The specific cost of electric energy is determined by taking account the dependence of the fuel costs on the parameters of the mine. According to the method the optimum parameters can be calculated without iterations.

The optimum parameters (capacity, life, specific costs) are analysed as functions of the quantity and heat value of the mineral resources. The effects of specific heat consumption and capacity utilization are also determined.

It is shown that the parameters W_0 and c of the mineral resources and the operational parameters c_0 and t_0 of the power station have a much stronger effect on the specific cost of electric energy than the capacity of the power station.

Keywords: capacity of mines; coal-based energy; life of mines; optimum capacity; specific cost of energy

*Symbols**

a = coefficient (constant) of the investment cost function of mining, Ft $a^{\mu}t^{-\mu}$, b = coefficient (constant) of the operational cost function of mining, Ft $a^{\nu-1}$ t^{ν}, c = heat value of mineable coal, kJ/kg, c_0 = amount of heat required to generate a unit electric energy in the power station, kJ/kWh, d = coefficient (constant) of the investment cost function of the power station, Ft $MW^{-\alpha}kJ^{-\omega}kg^{\omega}$, e = coefficient (constant) of the operational cost function of the power station, Ft a^{-1} $MW^{-\beta}$, k_a = specific cost of electric energy using simple amortization, k_{ar} = specific cost of electric energy using interest-based amortization, Ft/kWh, k_{Ap} = specific investment cost of power station construction, Ft/kWh, k_{Bp} = specific operational cost of the power station, Ft/kWh, k_c = specific cost of coal mining without capitalization, Ft/t, K_{Ap} = investment cost of the power station, 10^6 Ft, K_{Bp} = annual operational cost of the power station, 10^6 Ft/a, k_i = specific investment cost, k_0 = specific operational cost, m = intercalar time, year, n = life of the mine-power station complex, year, p = interest factor, q = production capacity (annual output) of the mine, 10^6 t/a, q_0 = optimum mine capacity, 10^6 t/a, Q = mineable amount of coal in the mine, 10^6 t, t_0 = average annual time of operation of the power station at nominal capacity, h/a, T = nominal power output of the power station, MW, T_0 = optimum power station capacity, MW, W_0 = energy content of mineable coal reserves of the mine, 10^6 kWh, W_{0u} = amount of electric energy generated during unit time, MWh/a, α = exponent of the capacity term in the investment cost function of the power station, β = exponent of the operational cost function of the power station, μ = exponent of the investment cost function of the mine, ν = exponent of the operational cost function of the mine, ω = exponent of the heat value term in the investment cost function of the power station.

[1] Department of Mining Engineering of the Technical University for Heavy Industry, H-3515 Miskolc-Egyetemváros, Hungary

* Ft denotes the Hungarian currency, Forint.

The sharp rise in oil prices has made it clear that the electric energy generation cannot be further increased by constructing new hydrocarbon burning power stations. Studies analyzing the long-term problems of energy generation claim to find the solution in coal and nuclear energy. The raw material requirements of coal-based energy generation can be largely met by open-pit lignite mines. Therefore, it is reasonable that the economic problems of establishing mine-power station complexes should be analyzed and their optimum parameters determined.

The problem had been earlier investigated by academician Zambó (1974) in great detail. The investment cost function of power stations had been determined as a function of capacity and coal quality, and the investment costs were compared with those of hydrocarbon burning and nuclear power stations. Attention has been drawn to the distorting effect of the interest rate in the determination of the optimum capacity and in problems connected with interest. It was also suggested that in the analysis of specific problems the specific fuel cost should be determined as a function of the parameters of the mine.

Earlier analyses provided different results for the optimum parameters (capacity, life) of the open-pit mine and of the power station, respectively, if they were determined separately. The problem that usually occurred was that the calculations concerning the power station had furnished rather high optimum or economical capacities. Although, technically the corresponding mine capacity can be established, the total investment costs of mine construction, however, can only be met in exceptional cases. To obtain more realistic results one must determine the optimum capacity and life for the whole complex as an undivided entity instead of calculating the optimum parameters of the mine and of the power station separately (Németh 1979).

One of the possible solutions to jointly determine the optimum parameters of the mine-power station complex is to treat the specific coal cost as a capacity-depending parameter in determining the fuel costs of the power station with the help of cost functions. The problem will be investigated in what follows using this method.

The specific cost of coal mining can be written in the general form

$$k_c = \frac{a \cdot q^{\mu}}{Q} + bq^{\nu-1}, \ Ft/t \tag{1}$$

if no capitalization is applied. In Eq. (1):

Q mineable coal reserves of the mine, 10^6 t

q annual output of the (open-pit) mine, 10^6 t/a

a constant of the investment cost function of mining, Ft a^{μ} $t^{-\mu}$

b constant of the operational cost function of mining, Ft $a^{\nu-1}$ t^{ν}

μ, ν exponents of the cost functions of the mine to be determined by regression analysis.

If the specific cost of the electric energy referred to the final product is used in the investigation, the total energy content W_0 [10^6 kWh] of the lignite reserves seems more convenient than Q. The relationship between Q and W_0 can be written as

$$W_0 = 10^3 Q \frac{c}{c_0},\ 10^6\ \mathrm{kWh} \qquad Q = \frac{W_0}{10^3} \frac{c_0}{c},\ 10^6\ \mathrm{t} \tag{2}$$

with c heat value of the mineable coal, kJ/kg
c_0 amount of heat required to generate a unit electric energy in the power station, kJ/kWh.

If fuel is supplied to the power station by a single mine, the relationship between the capacities of the open-pit mine and the power station can be determined as:

$$q = 10^{-6}\, T\, t_0 \frac{c_0}{c},\ 10^6\ \mathrm{t\ a^{-1}}$$
$$T = 10^6\, q \frac{c}{t_0\, c_0},\ \mathrm{MW} \tag{3}$$

with T nominal power output of the power station, MW
t_0 average annual time of operation of the power station at nominal capacity, h/a.

By dividing the Ft/t coal mining costs by $10^3 c/c_0$ one arrives at Ft/kWh specific values representing specific fuel costs within the total costs of electric energy generation:

$$k_c = \frac{a}{W_0}\left(10^{-6}\, t_0 \frac{c_0}{c} T\right)^{\mu} + \frac{b}{10^3}\left(\frac{c_0}{c}\right)^{\nu} (10^{-6}\, t_0\, T)^{\nu-1},\quad \mathrm{Ft/kWh}. \tag{4}$$

Equations 1 to 4 do not express the interrelationships between the parameters c, c_0 and q, and the specific cost k_c in multi-seam coal fields exploited by selective mining techniques. If selectivity increases, i.e. a purer product is obtained, certain positive effects improving economy can be found in the increase of c and a simultaneous decrease of c_0 with a resulting increase in the total amount of heat W_0. Economic efficiency is, however, decreased at the same time due to the lower productivity of the machinery which results in higher specific fuel costs in the power station. This latter effect may cause a change in the coefficient b.

A change of c, on the other hand, can modify the specific investment costs given by Eq. (5) and—through relationship $c_0 = f(c)$ — the parameters characterizing the operation of the power station (e.g. t_0) and costs (e.g. the constant e) as well.

The investment cost of the power station can be written, using the cost function introduced by Zambó (1974) as

$$K_{A_p} = d T^{\alpha} c^{\omega}\ 10^6\ \mathrm{Ft}$$

where d is a constant to be determined by regression analysis, Ft, $\mathrm{MW}^{-\alpha}\ \mathrm{kJ}^{-\omega}\ \mathrm{kg}^{\omega}$,
α and ω are exponents to be determined by regression analysis.

If the lifes of the power station and the open-pit mine are equal and coinciding, and we assure that the total energy content W_0 of the coal reserves is utilized, the specific investment cost of power station construction can be expressed as

$$k_{Ap} \frac{d\,T^{\alpha}\,c^{\omega}}{W_0}, \text{ Ft/kWh.} \tag{5}$$

The operational cost for unit time without fuel costs becomes

$$K_{Bp} = e\,T^{\beta}\,10^6 \text{ Ft/a.}$$

The electric energy generated during unit time (year) is

$$W_{0u} = t_0\,T \text{ MWh/a}$$

while the specific operational cost can be given by

$$k_{Bp} = \frac{e\,T^{\beta}}{t_0\,T} = 10^3 \frac{e}{t_0\,T^{1-\beta}}, \quad \text{Ft/kWh} \tag{6}$$

where e is a constant to be determined by regression analysis, Ft a^{-1} $MW^{-\beta}$
β an exponent to be determined by regression analysis.

Applying simple amortization, the total cost of electric energy generation can be written on the basis of Eqs (4), (5) and (6) as

$$k_a = \frac{d\,T^{\alpha} c^{\omega}}{W_0} + \frac{a}{W_0}\left(10^{-6} t_0 \frac{c_0}{c}\,T\right)^{\mu} + 10^3 \frac{e}{t_0\,T^{1-\beta}} +$$

$$+ \frac{b}{10^3}\left(\frac{c_0}{c}\right)^{\nu} (10^{-6}\,t_0\,T)^{\nu-1}\,. \tag{7}$$

When analysing the economics of investment or comparing the efficiency of various projects one also has to consider the time factor of the expenditure, i.e. the capitalized investment costs should be taken into account. For the mine-power station complex an equal life is assumed:

$$n = 10^3 \frac{W_0}{t_0\,T}, \text{ year.}$$

The effect of the time factor is expressed by the factor f (Zambó 1974):

$$f = p^m n (p-1) \frac{p^n}{p^n - 1} \tag{8}$$

where p is the interest factor,
m the intercalar time, i.e. the time span between the main point of the investment period and the starting year of production (clearing investment credits)
n the number of years of production or the time of writing off fixed assets (clearing credits).

Using interest-based amortization for the investment costs, the specific cost of the generated electric energy becomes

$$k_{ar}=\frac{10^3 p^m(p-1)}{t_0}\frac{p^{\frac{10^3 W_0}{t_0 T}}}{p^{\frac{10^3 W_0}{t_0 T}}-1}\left[dc^{\omega}T^{\alpha-1}+a\left(10^{-6}t_0\frac{c_0}{c}\right)^{\mu}T^{\mu-1}\right]+$$
$$+10^3\frac{e}{t_0}T^{\beta-1}+\frac{b}{10^3}\left(\frac{c_0}{c}\right)^{\nu}(10^{-6}t_0)^{\nu-1}T^{\nu-1}. \tag{9}$$

The total specific cost, as usual, can be divided into an investment cost k_i and an operational cost k_o. In case of capitalization, k_i will be replaced by k_{i_r}. The sum of the capitalized specific investment costs of the power station and of the open-pit mine is given by the first term of Eq. (9) while the operational costs appear as the sum of the second and third terms.

The parameters of the cost functions have been determined on the basis of Zambó's (1974) and Németh's (1979) results as well as from the data of the Thorez open-pit mine and the Gagarin power station for the years 1980 and 1981 (Research Report, 1981a). The following parameters were used in the calculations:

$\mu=0.75$ $a=3700$ $\nu=0.70$ $b=325$

$\alpha=0.84$ $\omega=-0.14$ $d=400$ $\beta=0.90$ $e=1.90$

$W_0=250\,000$ $c=6255$ $c_0=12\,510$ $t_0=5200.$

The optimum capacity was determined by the principle of minimum cost, using a numerical method on a desk top calculator. Interest rates used in the investigation were 0 to 12 percent.

The specific costs obtained without capitalization (i.e. $p=1.00$) are illustrated in Fig. 1. The optimum power station capacity is 610 MW and the specific cost becomes 0.74 Ft/kWh.

Figure 2 shows the specific costs as a function of the capacity for 10 percent interest rate i.e. $p=1.10$. The optimum capacity becomes

$$T_0=2010\text{ MW (for } p=1.05 \text{ we have } T_0=1230\text{ MW)}.$$

The mine capacity corresponding to T_0 can be calculated as

$$q_0=10^{-6}\,T_0 t_0\frac{c_0}{c}=10^{-6}\cdot 2010\cdot 5200\cdot\frac{12\,510}{6255}=20.9\cdot 10^6\text{ t/a}.$$

The life of the mine-power station complex will be

$$n_0=10^3\frac{W_0}{t_0 T_0}=10^3\frac{250\,000}{5200\cdot 2010}=23.9\approx 24\text{ years}.$$

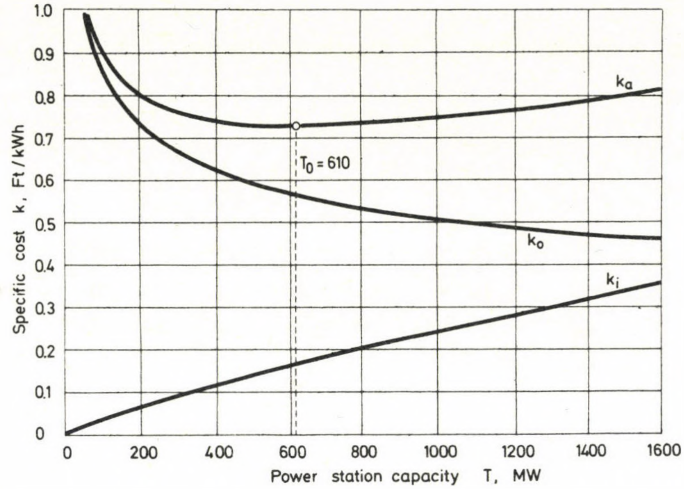

Fig. 1. Specific costs as functions of capacity (p = 1.00)

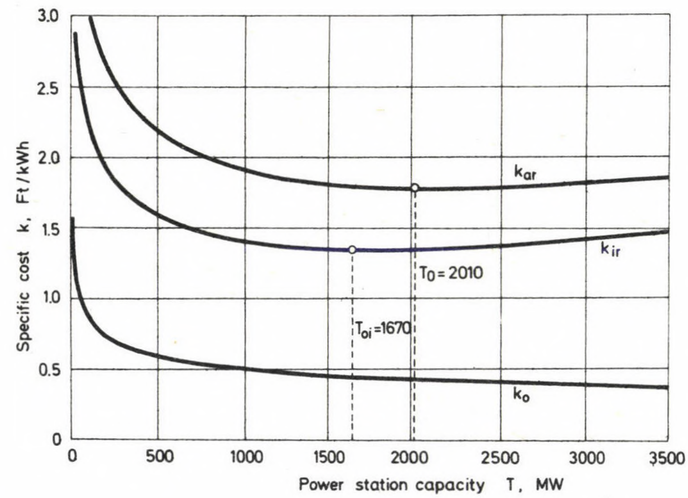

Fig. 2. Specific costs as functions of capacity (p = 1.10)

The basic parameters of the mine-power station complex (capacity, life and specific cost of current) are determined using the natural properties of the deposit and the main technological characteristics of the mine and of the power station. The capacity of the power station is primarily determined by the total amount of mineable energy W_0, being composed of the amount Q of the minerals and the heat value c. The specific cost could be considerably modified by the properties of the mine and of the power station. A detailed analysis of the effect of the main parameters was reported in the Research Report (1981b).

The increase of the total mineable amount of heat W_0 brings about a proportional increase in optimum capacity with a decreasing tendency of the specific cost. The life is not significantly modified by the value of W_0, the optimum operating time of the complex mainly depends on the interest rate. Using simple amortization, the life becomes roughly 80 years, for 1.05 40 years, and for $p=1.10$ 24 years. The mineable area of the mine and the mineable amount of heat can considerably change the specific costs. The exploitability of twice as large an amount from a deposit results in a 13—15 percent saving in the specific cost if other parameters are kept at optimum.

Analyzing the optimum capacity of the power station one finds that it is not significantly affected by the heat value of the coal, it rather depends on the interest factor. The optimum capacity of the open-pit mine, however, considerably decreases with the increase of the heat value of the coal because smaller amounts of better quality coal can ensure the heat requirement of the power station. As a result of a reduction in the amount of mined coal and because of the use of better quality coal, the specific cost of electric energy decreases.

The results obtained by analyzing the effect of parameters W_0 and c indicate the importance of a thorough investigation of the economics of selective production. An increase of selectivity increases the mineable amount of heat, thus improving quality. At the same time, however, the reduction of the exploitation of capacity increases the cost of mining i.e. that of fuel. Widening the scope of the analysis and taking into account the counteracting effects, one can decide whether the reduction of energy costs would compensate for the cost of equipment and labour intended to improve quality.

The effects of the parameters c_0 and t_0 characterizing the electric energy generation have also been investigated. The optimum power station capacity T_0 is practically independent of c_0 while the capacity of the open-pit q_0 significantly increases. An unchanged power station capacity at a higher specific heat consumption but steady heat value of fuel requires that the mine production should be increased. The specific cost of electric energy increases as a function of c_0.

The upper limit of the capacity exploitation of the power station is more or less determined by its character, technology and technical standards. Within these frames there is a rather great freedom to decide about the exploitation of capacity on the grounds of load and economics. As in other branches of industry, a higher exploitation of capacity provides, as a rule, better economic results. According to the results of the investigations, the increase of t_0 significantly reduces the optimum (built-in) capacity of the power station. Increasing the capacity exploitation by 25 percent (e.g. from 4000 h/a to 5000 h/a), 16—18 percent savings can be achieved in power station construction. A 50 percent increase of t_0 yields about 30 percent saving in power station investment. An increase of the exploitation of capacity requires a smaller increase in the mine capacity. Increasing the capacity exploitation, the cost of electric energy generation is considerably reduced, due partly to savings in investment, partly to the reduction of specific operating costs. According to the calculations a one percent increase in the exploitation of capacity reduces the specific costs by 0.3—0.5 percent.

The analysis of the effect of t_0 has also been extended to the case when T_0 does not change with the increase of t_0 that is to the analysis of the utilization of an established (constructed) capacity. The result was practically the same as in the previous case.

It has also been shown that the capitalized investment cost has a minimum at capacity T_{0i}. This investment "optimum" also determines somewhat smaller optimum capacities than those corresponding to the place of minimum of the total specific costs. Figure 4 shows parameter values determined by the minima $k_{ir,\,\min}$ and $k_{ar,\,\min}$ as functions of the interest factor. Though there is a considerable difference between capacity values T_{0i} and T_0 (at $p=1.05$ we have $T_{0i}=870$ MW and $T_0=1230$ MW and at $p=1.10$ $T_{0i}=1670$ MW and $T_0=2010$ MW), the total specific costs k_{ar} at T_{0i} and T_0 do not differ significantly. In the example illustrated by Fig. 3 ($p=1.10$) the minimum total cost at T_0 equals 1.9385 Ft/kWh while that at $T_{0i}=1670$ MW gives 1.9467 Ft/kWh, a mere 0.4 percent increase.

The optimum capacity and life values can be found within the interest factor limits of $p=1.06$—1.10. In the case illustrated in Fig. 4 the capacity of the power station lies between 1400 and 2000 MW, the annual output of the open-pit mine can be 14—21 Mt/a and its life 25—35 years. At a higher interest rate (10 percent) the capacity lies on the upper limit, the life on the lower one. With lower interest rate (6 percent) the situation is the opposite.

The effect of the chosen power station capacity on the specific costs of electric energy has already been analyzed by Zambó (1974) in great detail for a given seam and for seams of various extension. It has been found by the author that the capacity may be varied in a wide range in the vicinity of the optimum capacity without considerably increasing the specific costs. Figure 3 of the present study shows practically the same results. In case of a capacity 50 percent lower than the optimal $T_0=2000$ MW (i.e. in case of $T=1000$ MW) the specific cost increases by 6.6 percent only. To one percent capacity reduction (which does not mean any reduction in exploiting the already established capacity) there belongs a 0.13 percent cost increase in this case. At capacities greater than the optimum, say, by 50 percent (i.e. at $T=3000$ MW), the increase is only 2.99 percent which means that a one percent change of the capacity brings about 0.06 percent rise in costs.

Because of the parabolic character of the cost function the cost-increasing effect of any change in the capacity is, of course, much more moderate if the capacity is not too far from the optimum. With the parameters of Fig. 3 a 10 percent reduction of the established capacity (1800 MW instead of 2000 MW) results in a 0.14 percent cost for each percent of capacity reduction. A 20 percent reduction ($T=1600$ MW) brings about 0.72 percent increase in the specific cost resulting in a 0.036 percent cost increase

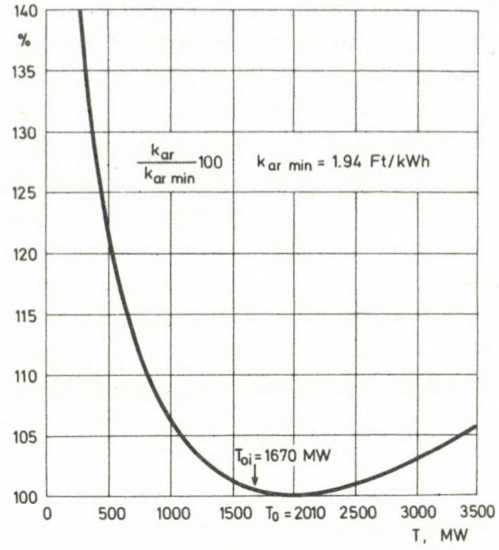

Fig. 3. Specific cost as a function of capacity (p = 1.10)

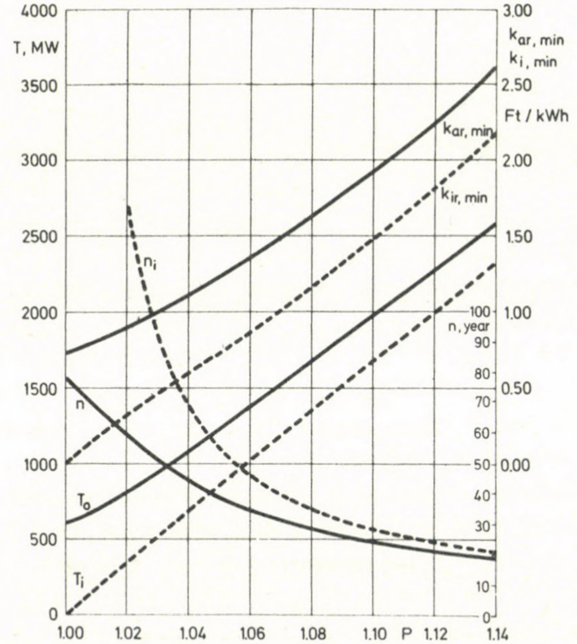

Fig. 4. The optimum capacity, life and specific cost as functions of the interest factor

for each percent of capacity reduction. In the range of capacities beyond 2000 MW the cost increase is almost negligible.

As for the effect of the other parameters, it can be shown that a 1 percent change of the natural parameters W_0, c and of the technical parameters c_0, t_0 may cause a 0.2—0.5 percent specific cost reduction. The positive influence of a joint effect of the investigated parameters — taking into account their connections and the cost of their change — is certainly greater than the result of the capacity change. Under favourable conditions the cost-decreasing effect of improving the investigated parameters by 1 percent may exceed the effect of the capacity selection by even one order of magnitude. A more precise comparison can be carried out by analyzing the joint effect of W_0, c, c_0 and t_0.

The results of the present analysis show that the power station capacity of a mine-power station complex can be selected within rather wide limits in the planning stage without considerably impairing the economical parameters. On the other hand, the importance of technology selection in the planning stage and the quality of work during operation should be strongly emphasized. The engineering work can significantly contribute to the increase of W_0 and c, and to the improvement of c_0, while the parameter t_0 is influenced by external effects as well.

References

Department of Mining Engineering of the Technical University for Heavy Industry 1981a: Basic relationships of establishing new mines and power stations and connecting mine fields. (In Hungarian) Research Report

Department of Mining Engineering of the Technical University for Heavy Industry 1981b: Investigation of the basic parameters of open pit-power station complexes. (In Hungarian) Research Report

Kovács F 1966: Determination of the basic parameters of open-pit mines. (In Hungarian). Ph. D. Thesis. Miskolc

Kovács F 1978: Analytical investigations on the planned lignite open-pit mines in Hungary. (In Hungarian) Paper delivered at the Lignite Seminar. Gyöngyös

Németh I 1979: Analysis of the economy of coal-based energy generating complexes using systems models. (In Hungarian) *Tatabányai Szénbányák Műszaki-Közgazdasági Közleményei* (Technical Economical Publications of the Tatabánya Coal Mines), 19, 18—23.

Zambó J 1974: On coal-burning power stations. (In Hungarian) *BKL Bányászat*, (Mining). 107, 611—615.

Acta Geodaet., Geophys. et Montanist. Hung. Volume 18 (3), pp. 281—290 (1983)

ON A GENERALIZED POYNTING—THOMSON MODEL

M DOBRÓKA[1]

[Manuscript received January 3, 1982]

A possible modification of the equation governing to the spherical stress- and strain tensors of the Poynting—Thomson model is proposed. The generalized state equations are solved in the case of uniaxial tension.

Keywords: Poynting—Thomson model; state equations; strain tensor; stress tensor; uniaxial tension.

As it is well known, a large number of laboratory and in-situ measurements show that rheological properties of rock continua can be treated with sufficient accuracy by the Poynting—Thomson model. In its framework the relationship between the stress- and deformation deviators $\boldsymbol{T}$ and $\boldsymbol{E}$ is given as a differential equation in the form:

$$\boldsymbol{T}=2G\boldsymbol{E}+2\eta\dot{\boldsymbol{E}}-\tau\dot{\boldsymbol{T}} \tag{1}$$

where G is the shear modulus, η is the coefficient of viscosity, τ is the relaxation time and the dot denotes differentiation with respect to time. On the other hand the isotropic parts of the stress- and strain tensors ($\boldsymbol{T}_0$, $\boldsymbol{E}_0$) satisfy a linear equation

$$\boldsymbol{T}_0=3K\boldsymbol{E}_0, \tag{2}$$

where K is the modulus of compression being independent of the stress, strain, rate of stress and rate of strain.

From a practical point of view Eqs (1) and (2) give a good approximation to describe the majority of rock mechanical motions. At the same time it is clear that Eq. (2) cannot be an exact equation. In the present form it means that due to a lack of $\dot{\boldsymbol{E}}_0$ and (or) $\dot{\boldsymbol{T}}_0$ energy dissipation cannot be realized in pure volume changes regardless of their velocity (or frequency). In slowly varying processes this can be a good approximation, but in more rapid rock motions (explosions, seismic waves) this assumption is incorrect.

There is an analogous problem in the case of viscous fluids. The isotropic part of the stress tensor can be written as

$$\boldsymbol{T}_0=3K\boldsymbol{E}_0+3\zeta_V\dot{\boldsymbol{E}}_0,$$

[1] Technical University for Heavy Industry, Department of Geophysics, H-3515 Miskolc, Hungary

ζ_V being the volume viscosity. The study of the absorption of ultrasonic waves shows that $\zeta_V > 0$. On the other hand in certain flow problems it can be assumed in a good approximation that $\zeta_V = 0$ (Navier—Stokes fluid).

Rock mechanical measurements show that the coefficient of viscosity (η) of rocks can be extremely large (Asszonyi and Kapolyi 1972) in comparison with fluids so we can expect that the volume viscosity ζ_V of rocks can also be large, enough to play a significant role in real rock motions.

In the following we propose a modification of Eq. (2) making it suitable to describe (relaxational-retardational) dissipative processes, too.

The generalized state equations

A possible way of the generalization is shown by the original Poynting—Thomson model itself. As it is well known this model contains one Hookean and one Maxwellian body, in parallel coupling (Fig. 1).

The stress tensor of the Hookean body can be written as

$$\boldsymbol{F}_H = 2G\boldsymbol{D}_H + \left(K - \frac{2}{3}G\right)\Theta_H \boldsymbol{I}, \tag{3}$$

where $\boldsymbol{D}_H$ is the deformation tensor of the Hookean body, Θ_H its trace and $\boldsymbol{I}$ is a unit tensor.

The Maxwellian body consists of a Hookean body and a Newtonian liquid coupled in series. The stress tensors of the Hookean and the Newtonian bodies are

$$\boldsymbol{F}_{H'} = 2G'\boldsymbol{D}_1 + \left(K' - \frac{2}{3}G'\right)\Theta_1 \boldsymbol{I}$$

$$\boldsymbol{F}_N = 2\eta'\dot{\boldsymbol{D}}_2 + \left(\zeta'_V - \frac{2}{3}\eta'\right)\dot{\Theta}_2 \boldsymbol{I}.$$

$\boldsymbol{D}_1$ and $\boldsymbol{D}_2$ are the deformation tensors in the constituent bodies, Θ_1 and $\dot{\Theta}_2$ are their traces, G' and K' are the shear- and compression moduli of the Hookean body, η' and ζ'_V are the coefficients of viscosity and the volume viscosity of the Newtonian liquid. In present we assume $\zeta'_V \neq 0$.

Because of the series coupling one has to require for all components

$$\boldsymbol{F}_{H'} = \boldsymbol{F}_N = \boldsymbol{F}_M$$

$$\boldsymbol{D}_M = \boldsymbol{D}_1 + \boldsymbol{D}_2,$$

where $\boldsymbol{F}_M$ and $\boldsymbol{D}_M$ are the stress- and deformation tensors of the Maxwellian body.

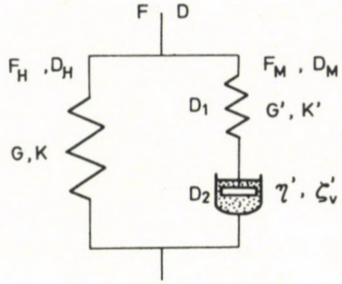

Fig. 1. Model for Poynting—Thomson body

Similarly in the parallel coupling of the Hookean and Maxwellian bodies one requires

$$\boldsymbol{D}_H=\boldsymbol{D}_M=\boldsymbol{D}$$

$$\boldsymbol{F}=\boldsymbol{F}_H+\boldsymbol{F}_M$$

where $\boldsymbol{F}$ and $\boldsymbol{D}$ are the stress- and deformation tensors of the complex body.

Taking the above requirements into account one has for the Maxwellian body

$$\boldsymbol{F}_M=2\eta'\dot{\boldsymbol{D}}+\left(\zeta'_V-\frac{2}{3}\eta'\right)\dot{\Theta}\boldsymbol{I}-\frac{\eta'}{G'}\dot{\boldsymbol{F}}_M+$$

$$+\frac{1}{3K'}\left[\frac{\eta'}{G'}\left(K'-\frac{2}{3}G'\right)-\left(\zeta'_V-\frac{2}{3}\eta'\right)\right]\dot{S}_M\boldsymbol{I}, \tag{4}$$

where $S_M=\text{Trace }\boldsymbol{F}_M=\text{Spur }\boldsymbol{F}_M$.

Adding Eqs (3) and (4), the rheological equation of the generalized Poynting—Thomson body is obtained:

$$\boldsymbol{F}=2G\boldsymbol{D}+\left(K-\frac{2}{3}G\right)\Theta\boldsymbol{I}+2\eta'\dot{\boldsymbol{D}}+\left(\zeta'_V-\frac{2}{3}\eta'\right)\dot{\Theta}\boldsymbol{I}-\frac{\eta'}{G'}\dot{\boldsymbol{F}}+$$

$$+\frac{\eta'}{G'}\left[2G\dot{\boldsymbol{D}}+\left(K-\frac{2}{3}G\right)\dot{\Theta}\boldsymbol{I}\right]+$$

$$+\frac{1}{3K'}\left[\frac{\eta'}{G'}\left(K'-\frac{2}{3}G'\right)-\left(\zeta'_V-\frac{2}{3}\eta'\right)\right](\dot{S}-3K\dot{\Theta})\boldsymbol{I}, \tag{5}$$

where $S=\text{Trace }\boldsymbol{F}$.

This equation can be split into two parts. The deviatoric equation

$$\boldsymbol{T}=2G\boldsymbol{E}+2\eta'\left(1+\frac{G}{G'}\right)\dot{\boldsymbol{E}}-\frac{\eta'}{G'}\dot{\boldsymbol{T}} \tag{6}$$

can be written completely in the form of Eq. (1) with the substitution

$$\eta=\eta'\left(1+\frac{G}{G'}\right), \qquad \tau=\frac{\eta'}{G'}.$$

The equation of the spherical tensors $\boldsymbol{T}_0$ and $\boldsymbol{E}_0$ by means of Eq. (5) gives the form

$$\boldsymbol{T}_0=3K\boldsymbol{E}_0+3\zeta'_V\left(1+\frac{K}{K'}\right)\dot{\boldsymbol{E}}_0-\frac{\zeta'_V}{K'}\dot{\boldsymbol{T}}_0, \tag{7}$$

which can be considered as a generalization of Eq. (2). In (in time) slowly varying rock mechanical motions the second and third terms on the right hand side of Eq. (7) can be neglected in comparison with the first one. In these cases Eq. (7) yields Eq. (2). It is to be noted that the result is similar if the volume viscosity equals zero, or in other words in the model we use a Navier—Stokes fluid instead of the Newtonian body.

Introducing the notations

$$\tau=\frac{\eta'}{G'}, \qquad \vartheta=\frac{\eta'}{G'}\left(1+\frac{G'}{G}\right)$$

$$\tau_0=\frac{\zeta'_V}{K'}, \qquad \vartheta_0=\frac{\zeta'_V}{K'}\left(1+\frac{K'}{K}\right)$$

Eqs (6) and (7) take the form

$$\left\{1+\tau\frac{\partial}{\partial t}\right\}\boldsymbol{T}=\left\{1+\vartheta\frac{\partial}{\partial t}\right\}2G\boldsymbol{E}, \tag{8}$$

$$\left\{1+\tau_0\frac{\partial}{\partial t}\right\}\boldsymbol{T}_0=\left\{1+\vartheta_0\frac{\partial}{\partial t}\right\}3K\boldsymbol{E}_0. \tag{9}$$

The quantities τ and ϑ are the deviatoric relaxation time and the deviatoric retardation time, while τ_0 and ϑ_0 are the volume relaxation and volume retardation time. It can be seen that in the model the relations

$$\vartheta\geqq\tau, \qquad \vartheta_0\geqq\tau_0$$

are fulfilled.

Approximate forms of the state equations

In special cases Eqs (8) and (9) can be substituted by simpler (approximate) equations. Let T denote the time interval characteristic of the rock motion.

If all the field quantities vary slowly in time so that

$$\vartheta\ll T, \qquad \vartheta_0\ll T$$

Equations (8) and (9) can be written as

$$\boldsymbol{T}=2G\boldsymbol{E} \qquad T_0=3K E_0$$

resulting in a Hookean body with the elastic parameters G and K.

In a case when

$$\vartheta_0 \ll T, \qquad \vartheta \approx T$$

Eqs (8) and (9) give the equations

$$\left\{1+\tau\frac{\partial}{\partial t}\right\}\boldsymbol{T}=\left\{1+\vartheta\frac{\partial}{\partial t}\right\}2G\boldsymbol{E}$$

$$T_0=3K E_0$$

applied to the description of relatively slow rock motion in practice (Asszonyi 1972). In the approximation when

$$\vartheta_0 \ll T \ll \tau$$

one has an approximate Hookean body

$$\boldsymbol{T}=2\frac{\vartheta}{\tau}G\boldsymbol{E}, \qquad T_0=3K E_0$$

with the elastic parameters $\frac{\vartheta}{\tau}G=G+G'$ and K.

With decreasing characteristic time (more rapid rock motions) the relations

$$T \approx \vartheta_0 \ll \tau,$$

are valid, when Eqs (8) and (9) can be approximated with the equations

$$\boldsymbol{T}=2(G+G')\boldsymbol{E}$$

$$\left\{1+\tau_0\frac{\partial}{\partial t}\right\}T_0=\left\{1+\vartheta_0\frac{\partial}{\partial t}\right\}3K E_0 .$$

For rapid rock motions, when

$$T \ll \vartheta_0 \ll \tau$$

we find an approximate Hookean body

$$\boldsymbol{T}=2(G+G')\boldsymbol{E}$$

$$T_0=3\frac{\vartheta_0}{\tau_0}K E_0$$

with the elastic parameters

$$G+G', \quad \frac{\vartheta_0}{\tau_0}K=K+K'.$$

Uniaxial tension

In order to show the model properties under uniaxial tension Eqs (8) and (9) are to be solved for deformations. Equation (8) can be written as an inhomogeneous linear differential equation

$$\dot{\boldsymbol{T}}-2G\dot{\boldsymbol{E}}+\frac{1}{\vartheta}\left(\boldsymbol{T}-2G\boldsymbol{E}\right)=\left(1-\frac{\tau}{\vartheta}\right)\dot{\boldsymbol{T}} \quad .$$

solvable with the method varying the constant. Looking for a solution in the form

$$\boldsymbol{T}-2G\boldsymbol{E}=\boldsymbol{C}(t)e^{-\frac{t}{\vartheta}}$$

we find

$$\boldsymbol{C}(t)=\left(1-\frac{\tau}{\vartheta}\right)\int_0^t \dot{\boldsymbol{T}}e^{\frac{t'}{\vartheta}}\mathrm{d}t'+\boldsymbol{A},$$

where the quantities $\boldsymbol{A}$ are constant, and so

$$\boldsymbol{T}-2G\boldsymbol{E}=e^{-\frac{t}{\vartheta}}\left\{\boldsymbol{A}+\left(1-\frac{\tau}{\vartheta}\right)\int_0^t e^{\frac{t'}{\vartheta}}\dot{\boldsymbol{T}}\mathrm{d}t'\right\}.$$

The solution of Eq. (8) can be written in the form

$$\boldsymbol{E}=\frac{1}{2G}\left\{\boldsymbol{T}-e^{-\frac{t}{\vartheta}}\left[\boldsymbol{A}+\left(1-\frac{\tau}{\vartheta}\right)\int_0^t e^{\frac{t'}{\vartheta}}\dot{\boldsymbol{T}}\mathrm{d}t'\right]\right\} \tag{10}$$

and similarly

$$\boldsymbol{E}_0=\frac{1}{3K}\left\{\boldsymbol{T}_0-e^{-\frac{t}{\vartheta_0}}\left[\boldsymbol{B}+\left(1-\frac{\tau_0}{\vartheta_0}\right)\int_0^t e^{\frac{t'}{\vartheta_0}}\dot{\boldsymbol{T}}_0\mathrm{d}t'\right]\right\}, \tag{11}$$

where the quantities $\boldsymbol{B}$ are constants determined by the initial conditions. By means of Eqs (10) and (11) the deformation tensor can be written as

$$\boldsymbol{D}=\frac{1}{2G}\boldsymbol{T}+\frac{1}{3K}\boldsymbol{T}_0-\frac{1}{2G}e^{-\frac{t}{\vartheta}}\left\{\boldsymbol{A}+\left(1-\frac{\tau}{\vartheta}\right)\int_0^t e^{\frac{t'}{\vartheta}}\dot{\boldsymbol{T}}\mathrm{d}t'\right\}-$$

$$-\frac{1}{3K}e^{-\frac{t}{\vartheta_0}}\left\{\boldsymbol{B}+\left(1-\frac{\tau_0}{\vartheta_0}\right)\int_0^t e^{\frac{t'}{\vartheta_0}}\dot{\boldsymbol{T}}\mathrm{d}t'\right\}. \tag{12}$$

In the case of uniaxial tension, the stress- and deformation tensors, the stress- and strain deviator- and spherical tensors take the form

$$\boldsymbol{F}=\begin{Vmatrix} \sigma & 0 & 0 \\ 0 & 0 & 0 \\ 0 & 0 & 0 \end{Vmatrix} \qquad \boldsymbol{D}=\begin{Vmatrix} \varepsilon & 0 & 0 \\ 0 & \varepsilon' & 0 \\ 0 & 0 & \varepsilon' \end{Vmatrix}$$

$$\boldsymbol{T}=\begin{Vmatrix} \frac{2}{3}\sigma & 0 & 0 \\ 0 & -\frac{1}{3}\sigma & 0 \\ 0 & 0 & -\frac{1}{3}\sigma \end{Vmatrix} \qquad \boldsymbol{E}=\begin{Vmatrix} \frac{2}{3}(\varepsilon-\varepsilon') & 0 & 0 \\ 0 & -\frac{1}{3}(\varepsilon-\varepsilon') & 0 \\ 0 & 0 & -\frac{1}{3}(\varepsilon-\varepsilon') \end{Vmatrix}$$

$$\boldsymbol{T}_0=\begin{Vmatrix} \frac{1}{3}\sigma & 0 & 0 \\ 0 & \frac{1}{3}\sigma & 0 \\ 0 & 0 & \frac{1}{3}\sigma \end{Vmatrix} \qquad \boldsymbol{E}_0=\begin{Vmatrix} \frac{1}{3}(\varepsilon+2\varepsilon') & 0 & 0 \\ 0 & \frac{1}{3}(\varepsilon+2\varepsilon') & 0 \\ 0 & 0 & \frac{1}{3}(\varepsilon+2\varepsilon') \end{Vmatrix}$$

where σ is the only existing stress, ε and ε' are the relative changes of length along with and perpendicular to the axis of the tension. In the following solutions of Eqs (10) and (12) in two special cases are given when the rate of change of the stress is constant and when the stress is constant.

In the first case $\dot{\sigma}=\dot{\sigma}_a=$constant. The solutions of the Eqs (10) and (11) are

$$\varepsilon-\varepsilon' = \frac{1}{2G}\left\{\sigma-e^{-\frac{t}{\vartheta}}\left[A+(\vartheta-\tau)\dot{\sigma}_a(e^{\frac{t}{\vartheta}}-1)\right]\right\}, \tag{13}$$

$$\varepsilon+2\varepsilon' = \frac{1}{3K}\left\{\sigma-e^{-\frac{t}{\vartheta_0}}\left[B+(\vartheta_0-\tau_0)\dot{\sigma}_a(e^{\frac{t}{\vartheta_0}}-1)\right]\right\}. \tag{14}$$

Let us assume that at the beginning of the tension the stress and all the deformations in the specimen are zero, so the constant in Eqs (13) and (14) must be $A=0$ and $B=0$. Taking this into account one has

$$\varepsilon-\varepsilon' = \frac{1}{2G}\{\sigma-\dot{\sigma}_a(\vartheta-\tau)(1-e^{-\frac{t}{\vartheta}})\} \tag{15}$$

$$\varepsilon+2\varepsilon' = \frac{1}{3K}\{\sigma-\dot{\sigma}_a(\vartheta_0-\tau_0)(1-e^{-\frac{t}{\vartheta_0}})\} \tag{16}$$

and by means of Eq. (12) we can write

$$\varepsilon = \frac{3K+G}{9KG}\sigma - \frac{1}{3G}(\vartheta-\tau)\dot{\sigma}_a(1-e^{-\frac{t}{\vartheta}}) - \frac{1}{9K}(\vartheta_0-\tau_0)\dot{\sigma}_a(1-e^{-\frac{t}{\vartheta_0}}) \tag{17}$$

$$\varepsilon' = \frac{3K-2G}{18KG}\sigma + \frac{1}{6G}(\vartheta-\tau)\dot{\sigma}_a(1-e^{-\frac{t}{\vartheta}}), - \frac{1}{9K}(\vartheta_0-\tau_0)\dot{\sigma}_a(1-e^{-\frac{t}{\vartheta_0}}). \tag{18}$$

In other special case, when in a given moment of time, $t=t_1$ the stress is fixed at a value $\sigma=\sigma_1$, then by means of Eqs (10) and (11) we can write

$$\varepsilon-\varepsilon' = \frac{1}{2G}(\sigma_1-Ae^{-\frac{t}{\vartheta}})$$

$$\varepsilon+2\varepsilon' = \frac{1}{3K}(\sigma_1-Be^{-\frac{t}{\vartheta_0}}).$$

Supposing the deformations at $t=t_1$ to be $\varepsilon=\varepsilon_1$, $\varepsilon'=\varepsilon_1'$ the constants are

$$A=\sigma_1-2G(\varepsilon_1-\varepsilon_1')$$

$$B=\sigma_1-3K(\varepsilon_1+2\varepsilon_1')$$

and the solution of Eqs (10) and (11) can be written as

$$\varepsilon-\varepsilon' = \frac{1}{2G}\{\sigma_1-[\sigma_1-2G(\varepsilon_1-\varepsilon_1')]e^{-\frac{t-t_1}{\vartheta}}\}, \tag{19}$$

$$\varepsilon+2\varepsilon' = \frac{1}{3K}\{\sigma_1-[\sigma_1-3K(\varepsilon_1+2\varepsilon_1')]e^{-\frac{t-t_1}{\vartheta_0}}\}. \tag{20}$$

Similarly, by means of Eq. (12) we find

$$\varepsilon = \frac{3K+G}{9KG}\sigma_1 - \frac{1}{3G}[\sigma_1-2G(\varepsilon_1-\varepsilon_1')]e^{-\frac{t-t_1}{\vartheta}} -$$

$$-\frac{1}{9K}[\sigma_1-3K(\varepsilon_1+2\varepsilon_1')]e^{-\frac{t-t_1}{\vartheta_0}}, \tag{21}$$

$$\varepsilon' = \frac{3K-2G}{18KG}\sigma_1 - \frac{1}{9K}[\sigma_1-3K(\varepsilon_1+2\varepsilon_1')]e^{-\frac{t-t_1}{\vartheta_0}} +$$

$$+\frac{1}{6G}[\sigma_1-2G(\varepsilon_1-\varepsilon_1')]e^{-\frac{t-t_1}{\vartheta}}. \tag{22}$$

On the base of Eqs (15)—(22) the elastic parameters G, K and the rheological time parameters ϑ, τ, ϑ_0, τ_0 can be determined.

It is well known that because of the friction between the specimen and the plates in a real measurement the stress state will not be uniaxial. The result of the friction appears mainly in a decrease of ε'. From this point of view the most useful formula is Eq. (17), because it contains only ε_i, measured at different times t_i. All the other equations (at least at $t=t_1$) contain ε_i', too.

The effect of the friction is highly dependent upon the $\frac{D}{l}$ (diameter to length) ratio of the specimen and can be negligible at small $\frac{D}{l}$. On the other hand in uniaxial compression measurements $\frac{D}{l} = 1, \ldots 0.5$, and so the measured ε_i' deformations must be corrected.

This correction in the framework of the linearly elastic model has been obtained in (Somosvári 1983). By means of theoretical investigations and laboratory experiments the Poisson number must be corrected as

$$m_{\text{measured}} = m_{\text{real}}\left(1 + c\frac{D}{l}\right),$$

where the constant c is dependent upon the coefficient of friction μ between the specimen and the plate. So the correction of deformation takes the form

$$\varepsilon'_{\text{real}} = \varepsilon'_{\text{measured}}\left(1 + c\frac{D}{l}\right).$$

In a Poynting—Thomson body the parameter c besides the coefficient of friction, depends on the time and the circumstances of measurements: $c=c(\mu, \dot{\sigma}_a, t)$ or $c=c(\mu, \sigma_1, t)$. The calculation of these factors should be made in future investigations.

The proposed generalization of the Poynting—Thomson model results in the fact that the equation determining the time development of the spherical tensors is similar to that of the deviators. The new rheological time parameters — the volume relaxation and retardation times — are probably much smaller than the deviatoric ones. So significant corrections can be expected in rapid rock motions, in transient and wave features of the rock continua. In a following work we derive the equation of motion and dispersion relations for a generalized Poynting—Thomson continuum.

Acknowledgements

The author thanks to Cs Asszonyi and to Zs Somosvári for helpful discussions and encouragement.

References

Asszonyi Cs 1972: On the rheological field around mineopenings of circular section. I. Drifts in a primary hydrostatic field. *Acta Geod. Geoph. Mont. Hung.*, 7, 441—472.

Asszonyi Cs—Kapolyi L 1972: Rheological basic relations of rock mechanics. *Acta Geod. Geoph. Mont. Hung.*, 7, 3—34.

Filcek H 1962: The influence of the time parameter on the stress and deformation state in the neighbourhood of underground openings (in Polish). Komitet Gornitzwa PAN 1.

Somosvári Zs 1983: Physical reasons for the size-effect in rock-mechanical laboratory analyses. *Acta Geod. Geoph. Mont. Hung.*, 18 (in press)

Acta Geodaet., Geophys. et Montanist. Hung. Volume 18 (3), pp. 291—303 (1983)

RAISING OF SOLID MINERALS TO THE SURFACE THROUGH VERTICAL PIPES IN HYDRAULIC MINERALS MINING SYSTEMS

L BALLA[1]

[Manuscript received January 5, 1982]

One of the most important subsystems in a hydraulic minerals mining system is the raising of solid-fluid mixtures through pipes. The transport subsystem can be designed and optimized on the basis of the pressure loss in the pipe.

Two transport systems, *viz.* those with jet pump and air lift, are spreading in practice. Transport calculations applied so far are critically analysed with the help of a unified view in the paper.

Keywords: air lift; hydraulic mining; jet pump; raising of minerals; solid-fluid mixtures; transport by pipes

Symbols

A = pipe cross-section, C = drag coefficient, d = grain size, D = pipe diameter, f = function, F = drag surface, g = acceleration due to gravity, G = gravity force, K = constant, l = distance along the pipe, L = length, m = mass, n = constant, p = pressure, Q = flow rate, r = radial distance, S = frictional force, v = velocity, W = drag force, α = coefficient, ε = in situ volumetric ratio, ρ = density, τ = shear stress, λ = friction factor, η = efficiency

Subscripts

a = feeding, f = fluid, g = air, m = mixture, o = normal state, R = pipe wall, T = transport, s = solid

One of the mining systems with the highest perspective in future is the borehole hydraulic minerals mining system, illustrated in Fig. 1. The vertical pipe transport system in the borehole separated from the whole mining system is investigated in the paper. This separation is justifiable since the costs of the system depend to a great extent on pipe diameter and borehole diameter (latter parameter being in close connection with pipe diameter). The separation is further justified by the fact that the subsystems are in interaction at the connection points thus the actions can be regarded as boundary conditions in the model of the subsystem. In the analysis of the whole system it has to be taken into consideration, of course, that the boundary conditions which have to agree in each connection point for all subsystems, can be determined from the operation of the subsystems and the connection graphs of the subsystems.

[1] Chemical Research Laboratory for Mining of the Hungarian Academy of Sciences Miskolc

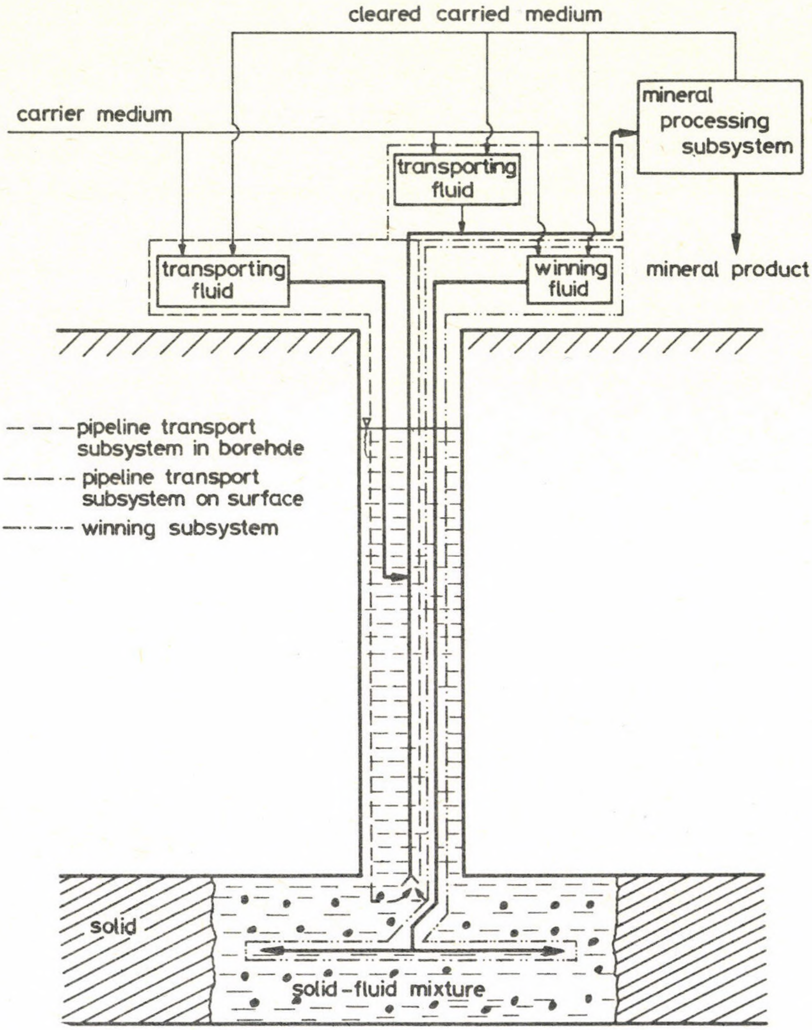

Fig. 1. Borehole hydraulic minerals mining system

Because of the characteristics of the borehole mining system (comparatively small borehole diameter, bottom pressure around hydrostatic, depths considerably exceeding 10 m and solids density greater than that of the transport medium (Fly 1970)), two forms of the vertical transport system are spreading in practice (Arens 1975, Pols 1980): those with jet pump and air lift.

In the systems applying jet pump, high-pressure water is pumped from the surface through a jet pump into the pipe transporting the solid material. In the jet pump

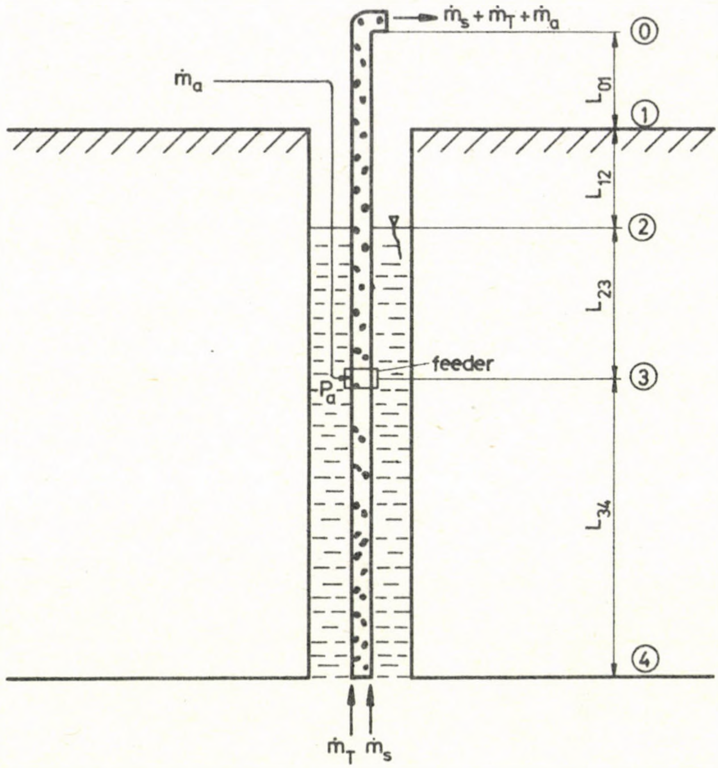

Fig. 2. Pipeline transport subsystem in borehole

kinetic energy is converted into pressure energy and, combined with hydrostatic pressure, it lifts the solid-liquid mixture to the surface.

In systems with air lift, air is compressed from the surface through an air feeder into the pipe transporting the solid material where the air, due to its density smaller than that of the transporting fluid, decreases bottom pressure resulting from the weight of the flowing fluid in the pipe. Thus hydrostatic pressure is sufficient to raising the solid-fluid-air mixture to the surface.

The structures of the two systems are similar; they differ, however, from the fluid flow point of view, because the state of the fluid injected to the pipe is different. The main characteristics of the two systems can be seen in Fig. 2.

From the flow regime point of view, taking the number of the flowing phases into account, the system applying jet pump is a two-phase system while that with air lift is a three-phase one. Four steady flow regimes (Weber 1974) can be distinguished for both systems (Fig. 3) taking into account the concentration of the solid, the distribution of the solid, the settling velocity of the particles in flowing and stationary media and the

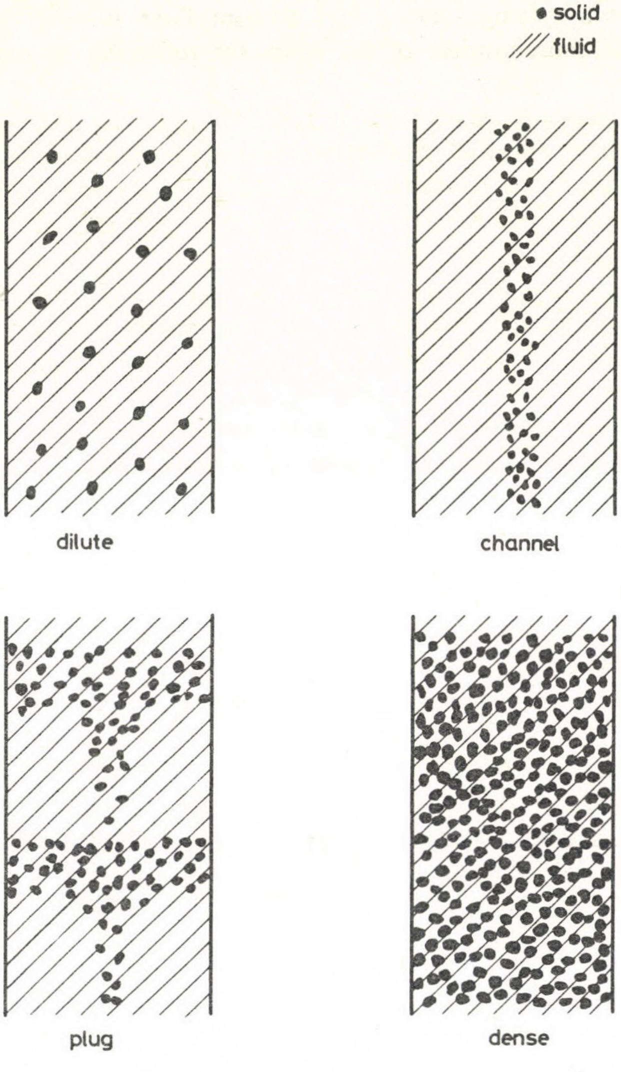

Fig. 3. Solid-fluid flow regimes

velocity of the transport fluid. A general definition to distinguish the regimes does not exist.

The hydraulic solid minerals mining system being one of the most general mining systems (Patvaros 1979) uses water as a basic transport medium ensuring the combination of winning, haulage and processing into a unified chain even taking the aspects of environment protection into account. The Newtonian character of the water can be, however, changed by the fine particles of the solid or additives (e.g. polymers) mixed to the water thus producing a non-Newtonian transport medium.

Within both systems, taking into account fluid velocity, size and shape distribution and concentration of the solid, the following four groups can be distinguished:

— *homogeneous, Newtonian flow:* only non-settling solid particles are present in the fluid but only to that extent that the fluid does not change its Newtonian character;
— *homogeneous, non-Newtonian flow:* only non-settling particles can be found in the fluid but to an extent that they give a non-Newtonian character to it;
— *heterogeneous, Newtonian flow:* the fluid contains practically settling (coarse) solid particles only that do not change the Newtonian character of the fluid;
— *heterogeneous, non-Newtonian flow:* the fluid contains besides a great quantity of settling (coarse) solid particles also non-settling (fine) solid particles to that extent that they give a non-Newtonian character to the fluid.

The effect of the additives can be interpreted in a similar way.

General vertical flow equations

Practical experience and the lack of boundaries of general validity among various flow regimes suggest to assume for the analysis of the flow in the pipe that the solids distribution is homogeneous in the fluid, and the flow is one-dimensional, steady and isothermal. Any deviation from this model is taken into account by various slip, form and friction parameters. The forces acting on the element of volume are shown in Fig. 4 (Weber 1974).

The equations are according to Weber (1974) and Palarski (1981) as follows.
Momentum equations:

$$v_s \frac{\mathrm{d}(m_s v_s)}{\mathrm{d}l} = -G_s - \varepsilon_s A \,\mathrm{d}p - S_{Rs} + W_s[v_f - v_s]$$

$$v_g \frac{\mathrm{d}(m_g v_g)}{\mathrm{d}l} = -G_g - \varepsilon_g A \,\mathrm{d}p - S_{Rg} + W_g[v_f - v_g]$$

$$v_f \frac{\mathrm{d}(m_f v_f)}{\mathrm{d}l} = -G_f - \varepsilon_f A \,\mathrm{d}p - S_{Rf} - W_s - W_g .$$

Continuity equation:

$$\operatorname{div} \rho_s \varepsilon_s \mathrm{v}_s = 0$$

$$\operatorname{div} \rho_g \varepsilon_g \mathrm{v}_g = 0$$

$$\operatorname{div} \rho_f \varepsilon_f \mathrm{v}_f = 0.$$

Packing density:

$$\varepsilon_s + \varepsilon_g + \varepsilon_f = 1$$

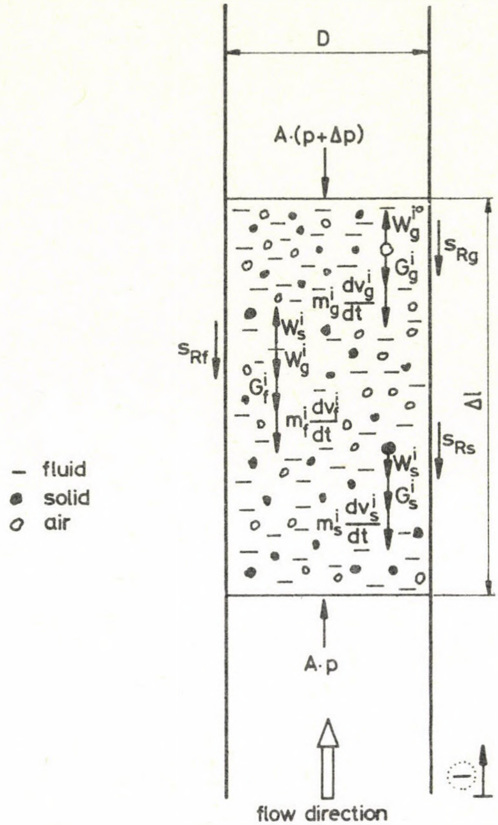

Fig. 4. Force components on a volume element

with

$$m_i = \rho_i \varepsilon_i A \, \mathrm{d}l$$

$$G_i = m_i g \qquad i = s, g, f$$

and the equations of state for densities ρ_i are known.

The number of the equations characterizing the system is seven while there are twelve unknowns, *viz.* $\varepsilon_s, \varepsilon_g, \varepsilon_f, v_s, v_g, v_f, p, S_{Rs}, S_{Rg}, S_{Rf}, W_s$ and W_g. In order to provide the sufficient number of equations for determining all unknowns, 5 more independent equations are needed in case of three phases and 3 additional equations for two-phase flow. There is no settled opinion as to which equations should be used for this purpose. Most equations are based on statistical analysis of measurement data therefore calculated results are reliable in the investigated regions only.

In designing hydraulic transport systems, the knowledge of the pressure gradient in the pipe is of principal importance. For two- and three-phase flows it has to be calculated in different ways.

Two-phase flow

Homogeneous, Newtonian flow

This case may be considered as the one-phase flow of the carrier medium with modified density and velocity. The velocities of the solid and the carrier medium are the same, i.e. $v_f = v_s$ from which $W_s = 0$ follows. The value of $S_{Rf} + S_{Rs}$ is known with a comparatively high accuracy (Govier and Aziz 1972). Thus, as the 3 additional equations are known, the pressure gradient can be determined.

This kind of flow regime is rather rare in practice. Critical point is the determination of the diameter of the particles that just do not settle in the fluid. This diameter depends also on the fluid velocity and usually lies below 1 mm.

Homogeneous, non-Newtonian flow

The flow can be regarded as a one-phase flow of the carrier medium with modified density, velocity and rheological properties. For this case $v_f = v_s$ and $W_s = 0$ also hold. For the equation of $S_{Rf} + S_{Rs}$ Hanks' (1978) theory is most generally accepted because of its validity for both laminar and turbulent flow of fluids with rheological equation:

$$\tau = \tau_0 + K\left(-\frac{\mathrm{d}v}{\mathrm{d}r}\right)^n .$$

This flow regime is also rather rare in practice but its role in the heterogeneous flow is important. It is also a critical point in the analysis of this type of flow the determination of the diameter of the just-non-settling particles.

Heterogeneous, Newtonian flow

This flow regime is the two-phase flow of the carrier medium and settling particles, thus $v_f \neq v_s$. Two theories are known to calculate the pressure gradient but no comparison is available between them. The additional equations according to Newitt et al. (Clauss 1970) are as follows:

$$S_{Rf} = \lambda_f \frac{\rho_f v_f^2}{2D} \varepsilon_f A \,\mathrm{d}l$$

$$S_{Rs} = f_s(\alpha S_{Rf})$$

$$v_f - v_s = f_v(\varepsilon_s, W_s)$$

where λ_f can be determined from the Colebrook formula (Govier and Aziz 1972) and f_s and f_v are obtained from measurements.

The additional equations are according to Weber (1974)

$$S_{Rf} = \lambda_f \frac{\rho_f v_f^2}{2D} \varepsilon_f A \, dl$$

$$S_{Rs} = \lambda_s \frac{\rho_s v_s^2}{2D} \varepsilon_s A \, dl$$

$$W_s = C_s \frac{\rho_f}{2} (v_f - v_s) |v_f - v_s| F_s$$

where λ_f is determined from the Colebrook formula, λ_s and C_s from measurements.

This is the most common flow regime in practice. Critical point is the determination of slip velocities, the additional friction force due to the solid and the degradation of certain solids (e.g. coal) in some kinds of flow regimes. The problem has been so far investigated for horizontal pipes since it is assumed to be more important there (Shook et al. 1979).

Heterogeneous, non-Newtonian flow

This flow regime can be characterized by the two-phase flow of the carrier medium with modified density, velocity and rheological properties and of settling particles.

Little attention has been paid to it so far because of its complicated character. Prettin and Gaessler (1976) established their theory from which the additional equations required to calculate the pressure gradient, are

$$S_{Rf} = \lambda_f^* \rho_f^* \frac{v_f^2}{2D} \varepsilon_f^* A \, dl$$

$$S_{Rs} = \lambda_s \rho_s \frac{v_f^2}{2D} \varepsilon_s^* A \, dl$$

$$v_s = f(\varepsilon_s^*, W_s)$$

whereas λ_f^* is determined from the Colebrook formula as a function of Reynolds number with the modified viscosity while λ_s and f from measurements. The sign * indicates modified parameters.

This flow regime is also common in practice but, as shown, the determination of the pressure gradient is rather empirical and the non-Newtonian character of the fluid is not clearly reflected.

Critical is the prediction of the solids amount that modifies the carrier medium and that of the modified viscosity. Shook et al's (1979) capillary viscosimeter in vertical position seems to be acceptable over a wide range. Viscosimeters applying coaxial cylinders can only be used in certain flow regimes because of the sedimentation. In further investigations of the flow regime, the latest results of Masuyama et al. (1978) and Sakamoto et al. (1978) about horizontal flow should be taken into account.

Three-phase flow

Homogeneous, Newtonian flow

This is the two-phase flow of the carrier medium with modified density and velocity and of air. The additional 5 equations are

$$v_s = v_f,\ W_s = 0 \quad \text{and those for} \quad S_{Rf} + S_{Rs}, S_{Rg} \quad \text{and} \quad v_f - v_g.$$

Equations of sufficient accuracy are known for the latter three (Weber 1974, Szilas 1975, Govier and Aziz 1972).

This flow regime is very rare in practice. Critical is the determination of the diameter of the just-non-settling particle and the slip of air.

Homogeneous, non-Newtonian flow

This case can be considered as the two-phase flow of the carrier medium with modified density, velocity and rheological properties and of air.
The additional 5 equations are

$$v_s = v_f,\ W_s = 0 \quad \text{and those for} \quad S_{Rf} + S_{Rs}, S_{Rg} \quad \text{and} \quad v_f - v_g.$$

As regards the latter three, only the theoretical analysis of Heywood and Charles (1978) is known which is valid for pseudoplastic, laminar, plug-like flow.

This type of flow is also rare in practice.

The determination of the diameter of the just-non-settling particle and of the slip of air is also critical.

Heterogeneous, Newtonian flow

The carrier medium, the settling particles and the air are lifted in a three-phase flow.

One of the first analyses in this field was that of Lévárdi (1969) who regarded the solid and liquid phases as those with modified properties. He neglected the slip velocity in the determination of the pressure gradient. His theoretical results can only be used in the general sense for orientation but it is suitable for designing gravel transport.

The energy approach of Husain (1975) is new but it is not suitable for the calculation of the pressure gradient. The equation of Kato et al. (1975) ensures the calculation of the pressure gradient for the transport of manganese nodules of certain size only since his constants are determined for a given case. The method largely relies on empirical equations, its application for a general case is rather difficult to imagine.

One of the most applicable theories is that of Weber (1976) with the following 5 additional equations:

$$S_{Rs}=\lambda\frac{\rho_s v_s^2}{2D}\varepsilon_s A\,\mathrm{d}l$$

$$S_{Rg}=\lambda\frac{\rho_g v_g^2}{2D}\varepsilon_g A\,\mathrm{d}l$$

$$S_{Rf}=\lambda\frac{\rho_f v_f^2}{2D}\varepsilon_f A\,\mathrm{d}l$$

$$v_f-v_s=\left[\frac{4}{3}\frac{dg}{C_s}\frac{\rho_s-\rho_f}{\rho_f}\varepsilon_f\right]^{1/2}$$

$$v_g-v_f=f(Q_g).$$

Friction factor λ is determined from the Colebrook formula, C_s and f from measurements. Critical is the determination of function f which depends on depth or pressure (Weber et al. 1978).

The theory of Palarski (1981) also seems acceptable with the following 5 additional equations:

$$S_{Ri}=\lambda_i\frac{\rho_i v_i^2}{2D}\varepsilon_i A\,\mathrm{d}l \qquad i=s, g, f$$

$$W_g=C_g\frac{\rho_f}{2}(v_f-v_g)|v_f-v_g|F_g$$

$$W_s=C_s\frac{\rho_f}{2}(v_f-v_s)|v_f-v_s|F_s$$

whereas λ_i, C_g and C_s are determined from measurements. No comparison is known concerning the two methods.

This kind of flow is one of the most frequent in practice if air lift is applied. Slip phenomena due to the various densities of the three phases and the excess friction forces are critical to determine.

Heterogeneous, non-Newtonian flow

This flow regime contains the three-phase flow of the carrier liquid with modified density, velocity and rheological properties due to the non-settling particles, of settling particles and air.

There is no study concerning this flow regime available so far. This may also be a common type of flow if air lift system is applied.

Slip phenomena due to the various densities of the three phases, excess friction forces and the modified rheological properties are critical points in the analysis of this type of flow.

Designing vertical transport systems

In knowledge of the pressure gradient the vertical transport system can be designed and optimized.

The condition of operation of the transport system can be expressed as

$$p_0+\Delta p_{03}+\Delta p_a+\Delta p_{34}\leqq\rho_f g L_{24}-\frac{1}{2}\rho_m v_m^2 .$$

Pressure difference Δp_{03} can be determined from the equations discussed at the two- and three-phase flows. For two-phase flow $\dot{m}_f=\dot{m}_T+\dot{m}_a$ holds while for three-phase flow $\dot{m}_f=\dot{m}_T$ and $\dot{m}_g=\dot{m}_a$.

Change of pressure Δp_a is negative if jet-pump feeding equipment is applied while it is positive for air-lift feeding equipment. The calculation of pressure difference Δp_a depends on the construction of the equipment. Δp_{34} can be determined from the equation discussed at two-phase flow, $\dot{m}_f=\dot{m}_T$. Kinetic energy $\frac{1}{2}\rho_m v_m^2$ of the entering solid-fluid mixture can be calculated from the densities, mass flow rates and pipe diameter.

The efficiency of the transport system calculated for the solid is

$$\eta_s=\frac{Q_s g[(\rho_s-\rho_f)L_{24}+\rho_s L_{02}]}{f(Q_a, p_a)}$$

whereas

$$f(Q_a, p_a)=\begin{cases} Q_{a0}p_0\ln\dfrac{p_a}{p_0} & \text{for air-lift system} \\ Q_a p_a & \text{for jet-pump system.}\end{cases}$$

The overall efficiency of the transport system can be obtained by multiplying compressor efficiency or pump efficiency with η_s:

$$\eta = \eta_s \eta_T.$$

The choice between the two systems can be made with the aid of $\eta \to \max$ whereas the operational condition forms the sub-condition. Weber et al. (1978) compares the two transport systems on a theoretical basis. It can be stated that the maximum efficiency is around or below 40 percent. The optimum of the two transport systems can be selected for a general case only by carrying out the necessary calculations.

The optimization ensures the optimum efficiency of the transport system only, it does not necessarily mean the optimum of the overall costs. As regards the particle size distribution, finer particles are benefitial from the transport point of view while they are disadvantageous concerning winning and mineral dressing. These equations have already been analyzed for horizontal flow (Asszonyi et al. 1970, Asszonyi et al. 1972, Wiedenroth and Kischner 1972). Similar equations should be established also for vertical flow.

Summing up, it can be stated that the transport of solid in vertical pipe is practically feasible but the economical transport is not ensured in every case because the flow regimes are not distinguished clearly from each other. The effect of the size and shape distribution of the solid is generally not known, the majority of the calculations is therefore empirical, thus ensuring satisfactory accuracy in the investigated region only.

Theoretical research has to be enwidened, the results should be checked by reliable experiments. More general equations have to be established and the optimum conditions more accurately determined.

References

Arens V Zh 1975: Geotechnological methods of minerals mining. Nedra, Moscow (In Russian).

Asszonyi Cs, Kapolyi L, Meggyes T 1970: Optimization of Particle Size in Hydraulic Pipelining of Solids. *Hydrotransport*, 1, K2.

Asszonyi Cs, Kapolyi L, Kántás Cs, Meggyes T 1972: An Experimental Method to Produce a Size Distribution Ensuring Maximum Pipeline Capacity. *Hydrotransport*, 2, D3.

Clauss G 1970: Hydrodynamic Optimisation of Hydraulic Lifting of Fluid-Solid Mixtures. *Hydrotransport*, 1, B2.

Fly A B 1970: Subsurface Hydraulic Mining Through Small Diameter Boreholes. *Hydrotransport*, 1, B1.

Govier G W, Aziz K 1972: The Flow of Complex Mixtures in Pipes. Van Nostrand Reinhold Company, New York.

Hanks R W 1978: Low Reynolds Number Turbulent Pipeline Flow of Pseudohomogeneous Slurries. *Hydrotransport*, 5, C2.

Heywood N I, Charles M E 1978: The Pumping of Pseudo-Homogeneous, Shear-Thinning Suspensions Using the Air-Lift Principle. *Hydrotransport*, 5, F5.

Husian L A 1975: On the Gas-Lift Pump: A New Approach. 2nd Symposium on Jet Pumps and Ejectors and Gas Lift. *Techniques*, G2.

Kato H, Tamiga S, Miyazawa T 1975: A Study of Air-Lift Pump for Solid Particles and its Application to Marine Engineering. 2nd Symposium on Jet Pumps and Ejectors and Gas-Lift. *Techniques*, G3.

Lévárdi F 1969: Prospecting and production of sub-water deposits and fluid mechanical investigation of three-phase mixtures. Doctor's Thesis. (In Hungarian).

Masuyama T, Kawashima T, Noda K 1978: Pressure Loss of Pseudo-Plastic Fluid Flow Containing Coarse Particle in a Pipe. *Hydrotransport*, 5, D1.

Palarski J 1981: Ein Beitrag zur Theorie der Hydropneumatischen Förderung von Schüttgütern. *Hydromechanisation*, 2, B1.

Patvaros J 1979: Hydromechanische Gewinnung mineralischer Rohstoffe — das am breitesten verwendbare technologische System im Bergbau. (In German and in Hungarian.) *Hydromechanisation*, 1, D1.

Pols A C 1980: Hydraulic Mining through Boreholes. Meded. Rijks Geol. Dienst., 41—56.

Prettin W, Gaessler H 1976: Bases of Calculation and Planning for the Hydraulic Transport of Run-of-Mine Coal in Pipelines According to the Results of the Hydraulic Plants of the Ruhrkohle AG. *Hydrotransport*, 4, E2.

Sakamoto M, Mase M, Nagawa Y, Uchida K, Kamino Y 1978: A Hydraulic Transport Study of Coarse Materials Including Fine Particles with Hydrohoist. *Hydrotransport*, 5, D6.

Shook C A, Haas D B, Husband W H W, Richards A D 1979: A Vertical Tube Viscometer for Suspensions Containing Coarse Particles. *Hydrotransport*, 4, F4.

Szilas A P 1975: Production and Transport of Oil and Gas. Akadémiai Kiadó, Budapest

Weber M 1974: Strömungs-Fördertechnik. Krausskopf-Verlag, Mainz

Weber M 1976: Transport of Solids According to the Air-Lift Principle. *Hydrotransport*, 4, H1.

Weber M, Dedegil Y, Feldle G 1978: New Experimental Results Regarding Extreme Operating Conditions in Air Lifting and Vertical Hydraulic Transport of Solids According to the Jet Lift Principle and its Applicability to Deep-Sea Mining. *Hydrotransport*, 5, F7.

Wiedenroth W, Kischner M 1972: A Summary and Comparison of Known Calculations of Critical Velocity of Solid-Water Mixtures and Some Aspects of the Optimisation of Pipelines. *Hydrotransport*, 2, E1.

Acta Geodaet., Geophys. et Montanist. Hung. Volume 18 (3), pp. 305—332 (1983)

CHARACTERISTICS OF GAS RELEASE IN LONGWALL WORKINGS OF MINES WITH HIGH GAS OUTPUT

F KOVÁCS[1]

[Manuscript received August 11, 1982]

By means of gas concentration values measured in 21 longwall workings of Mecsek coalmines the characteristics of gas release are investigated.

Analysing gas release as a function of time it has been found that the gas output is hardly affected by the daily and weekly rhythm of the working production. It is due to the high ratio of secondary gas output deriving from the seams. The thorough investigation into the whole life of workings has given a relationship concerning working speed, periodical roof failure and extremely high gas output values.

The effect of geological characteristics of the deposit and that of the technical parameters of workings the changeability factor i is examined. General statements are deduced, comparisons are made with the data in the literature.

Analysing the relationship between the seam thickness and the specific gas release a correlation between the two parameters is pointed out. On the basis of analysing statistical data it is stated that the specific gas output in the workings of the first slice of thick seams is 2 to 5 times as high as in workings of the further slices.

Mathematical statistical examinations resulted in the following conclusion: the mean and maximum methane concentration values of the working return air current and the changeability factor's values of the gas release can be characterized by lognormal distribution.

Keywords: gas output of mines; gas release; longwall workings; Mecsek Coalmines; methane concentration; specific gas release

Symbols

M = seam thickness (m), m_f = face height (m), α = seam dipping (degree), L = length of working face (m), v = rate of advance (m/d), Q = return air current in the working (m^3/min), c_a = methane concentration of the return air current (percent), c_s = specific gas release in the working (m^3/t), i = changeability factor of gas release, i_d = daily changeability factor of gas release, i_w = weekly changeability factor of gas release, i_l = changeability factor for the total life of working, η = ratio of productive time at the workings (quotient of workdays and calendar days), v_0 = average rate of advance on calendar interval (m/d), l_0 = distance between the gas output maxima (roof failures) (m), N = number of measurement data, $F_n(x)$ = empirical distribution function, $F(x)$ = theoretical distribution function, δ = standard deviation of the theoretical distribution function, m = expected value of the theoretical distribution function

[1] Department of Mining Engineering of the Technical University for Heavy Industry, H-3515 Miskolc, Hungary

Firedamp is one of the most considerable dangers among the forces jeopardizing directly mine activities. Firedamp explosions commonly cause mass accidents. In the Ruhr region, for example, firedamp explosions in 1940—50s demanded 15 tolls on an average.

Statistics of the last 100 years about firedamp explosions in Hungary show that there were 29 firedamp explosions demanding deaths; altogether 340 people died with 12 deaths at an explosion on the average. In the decade between 1969 and 1978 among the 10 mass accidents there occurred also 2 firedamp explosions with 29 people falling victim to the accidents, i.e. 41 percent of the aggregate deaths.

Gas danger arises, first of all, on the spot of working. Because of the large open surface, the free coal face and the presence of the cut coal a great quantity of gas is released, the intensity of the thorough ventilation cannot be freely increased, fire causes with high temperature appear relatively often, accidental firedamp explosions jeopardize more people. As a consequence it is of paramount importance to analyse the regularity of gas release at the workings.

When the ventilation is planned it is essential to know also gas release as a function of time in addition to the expected values of the mean gas output. The gas release also depends on the natural characteristics of the worked deposit and the technical parameters of the mining. Thus it is indispensable that besides data already published in course of analysing the gas release as a function of time we should also take into consideration the results of the measurements carried out in mines of the region in question.

The issues of gas release in workings are investigated on the basis of French, German and Soviet data (Otto 1962, Osipoff 1964, Schmidt-Krehl 1967, Bruyet 1970, Kaffanke 1980). The authors define the specific gas output values, investigate the rhythm of methane release in detail, the changeability in the gas release, the distribution of the irregularity factor. These are the questions dealt with in this paper on the basis of the data gained at the longwall workings in the Mecsek Coalmines.

During the investigation the data of gas concentration measured in altogether 21 longwall workings have been analysed. The measurements were carried out in the period between October 1978 and Februar 1980. The denomination data, the natural and technical characteristics of the workings are shown in Tables I and II. The gas release as a function of time, the irregularity of methane concentration in the return air current in the workings, the relationship between the gas output and seam thickness, the efficiency of gas drainage, the relationship of the irregularity factor and of gas concentration distribution have been investigated.

Table I. Identifying of the workings investigated

N°	Denomination number	Mine, level, crosscut field, direction of advance, method of mining and support, number of seam
1.	Pb 1	Pécsbánya mine level V. Westward of the western crosscut 3, retreating, hand winning, timber support, working in seam 3
2.	Pb 2	Pécsbánya mine level V. Westward of the western crosscut 3, advancing, hand winning, timber support, working in seam 6/II.
3.	Pb 3	Pécsbánya mine level V. Eastward of the western crosscut 4 (Eastward from the chute westward of the 3rd western crosscut), retreating, hand winning, timber support, working in seam 6/I.
4.	Pb 4	Pécsbánya mine level V. Eastward of the western crosscut 3, retreating, hand winning, timber support, working in seam 6/III.
5.	Pb 5	Pécsbánya mine level V. Westward of the western crosscut 3, advancing, hand winning, timber support, working in seam 7
6.	Pb 6	Pécsbánya mine level V. Westward of the western crosscut 3, advancing, hand winning, timber support, working in seam 7
7.	Pb 7	Pécsbánya mine level V. Eastward of the western crosscut 3, retreating, hand winning, timber support, working in seam 7 (western face)
8.	Pb 8	Pécsbánya mine level V. Eastward of the western crosscut 3, retreating, hand winning, timber support, working in seam 7 (eastern face)
9.	Pb 9	Pécsbánya mine level V. Eastward of the eastern crosscut 2, advancing, hand winning, SOW support, working in seam 11/I.
10.	Pb 10	Pécsbánya mine level IV. Westward of the western crosscut 1, advancing, hand winning, timber support, working in seam 23
11.	K 1	Kossuth mine level VIII—IX. field "B" concentration 3/10, retreating, hand winning, SOW-40 support, working in seam 8
12.	K 2	Kossuth mine level VI—VIII. field "B" western concentration 3/9, retreating, hand winning, SOW-50 support, working in seam 10/1
13.	K 3	Kossuth mine level VIII—X. field "A" S pillar, retreating, hand winning, individual hydraulic prop, working in seam 14/2
14.	K 4	Kossuth mine level VIII—X. field "A" fault concentration E/6, retreating, hand winning, individual hydraulic prop, working in seam 16/1
15.	K 5	Kossuth mine level IX—X. field "A" southern concentration E/6, retreating, mechanical winning (2 K-52), SOW-50 support, working in seam 16/1
16.	K 6/1	Kossuth mine level IX—X. field "A" fault concentration E/6, retreating, hand winning, individual hydraulic prop, single unit working 16/2
17.	K 6/2	Kossuth mine level IX—X. field "A" fault concentration E/6, retreating, hand winning, individual hydraulic prop, double unit working 16/2
18.	Z 1	Zobák mine level II. Southern crosscut 4, retreating, hand winning, timber support, working 601 in the third slice, seam 10
19.	Z 2	Zobák mine level II. Southern crosscut 2, retreating, hand winning, SOW support, working 604 in the first slice, seam 10
20.	Z 3	Zobák mine level II. Southern crosscut 2, advancing, hand winning, individual hydraulic prop, working 603 in the first slice, seam 12
21.	Z 4	Zobák mine level II. Southern crosscut 4, advancing, hand winning, timber support, working 602 in the first slice, seam 16

Table II. Natural and technical characteristics of workings, values of gas output

N°	Denomination number	Seam number	Whole seam thickness M [m]	Slice number	Height of working m_f [m]	Seam dipping α [°]	Length of face L [m]	Rate of advance v [m]	Working air current Q [m^3/min]	Gas concentration c_a percent	Specific gas release c_f[m^3/t]	Time (day)
1.	Pb 1	3	2.00	1	2.06	48	70	1.28	562	0.34	7.75	213
2.	Pb 2	6	2.15	1	2.15	45	74	1.33	499	0.71	13.32	122
3.	Pb 3	6	2.31	1	2.31	45	80	1.13	394	0.33	4.86	61
4.	Pb 4	6	2.23	1	2.23	45	74	1.39	458	0.61	9.51	110
5.	Pb 5	7	2.31	1	2.31	45	61	1.43	311	0.36	4.22	84
6.	Pb 6	7	3.08	1	3.08	42	80	1.05	397	0.29	3.56	67
7.	Pb 7	7	2.92	1	2.92	48	58	1.00	261	0.23	2.57	67
8.	Pb 8	7	3.16	1	3.16	48	60	0.92	320	0.45	5.99	38
9.	Pb 9	11	9.00	1	3.30	39	80	1.01	890	0.91	18.24	172
10.	Pb 10	23	2.00	1	2.41	40	84	0.72	391	0.57	9.11	110
11.	K 1	8	2.70	1	2.67	30	125	0.96	582	0.50	12.01	119
12.	K 2	10	3.00	1	2.16	45	113	0.50	704	0.36	17.86	138
13.	K 3	14	5.33	2	2.40	10	122	1.00	496	0.13	1.19	94
14.	K 4	16	7.00	1	2.43	20	157	1.46	796	0.38	13.41	179
15.	K 5	16	6.00	1	2.40	10	71	2.00	761	0.21	4.39	168
16.	K 6/1	16	6.30	2	2.40	15	132	0.92	730	0.35	3.05	106
17.	K 6/2	16	6.30	2	2.40	16	65	0.92	1107	0.21	2.73	253
18.	Z 1	10	6.80	3	2.50	46	66	1.30	420	0.40	7.14	29
19.	Z 2	10	6.00	1	2.85	7	127	1.70	1010	0.64	10.38	58
20.	Z 3	12	9.00	1	3.38	9	82	0.90	510	0.89	14.13	84
21.	Z 4	16	5.50	1	2.50	52	63	1.27	520	0.90	14.72	99

Gas release as a function of time

The rhythm of gas release was previously examined by Otto and Kaffanke (Otto 1962, Kaffanke 1980). In their diagrams the effect of the production activities in the workings definitely appears. In the productive shifts the gas release and the methane concentration of the return air current in the workings firmly increase, the cyclic character in production and winning results a regular *daily rhythm* in the gas release. At the workings investigated the primary gas output amounted to 50—55 percent, the secondary gas output deriving from the adjacent deposits and partition rocks to 45—50 percent of the total gas release.

Analysing in detail the data of 21 workings investigated in the Mecsek region it has been found that the change of the maximum methane concentration measured in the return air current in the workings does not show a regular period, the change in the gas output is not connected with the daily cycle of the production. There is no considerable difference between the gas outputs on workdays and those of standstill periods. This refers to the fact that only a minor part of the total gas output gets released from the worked deposit during the winning, the major part of the methane gets into the return air current from the coal seam sequence. The daily change of the gas release cannot be characterized by the parameters of the working cycle.

The data of the investigated 21 workings show fundamentally identical trends, so only some characteristic examples are illustrated in the diagrams.

Figure 1 shows the maximum methane concentration in the return air current of working Pb 1 based on hourly data. In the periods of non-workdays dotted lines mark the change in the methane concentration. The diagram shows the change in the surface air pressure as well. Figure 2 shows the data of working Z 1.

A characteristic diagram is published by Kaffanke (1980) on the basis of the weekly rhythm of the gas release. In diagram 1 of the paper of Kaffanke a considerable difference can be observed among the days of the week on the basis of the values of the working return methane content. From Monday on the gas output increases, by Thursday—Friday a "saturation" level sets in, and finally on Saturday—Sunday, i.e. on standstill days, there is a sudden decrease.

Relying on the data of the mines referring to the days of the week the daily mean and maximum concentrations c_{max}, c_{mean} were examined. Within the weekly cycle the quotient of the weekly absolute maximum and the weekly average of the maximum values and the quotient of the highest mean concentration and the weekly average of the mean concentration were calculated as parameters characterizing the irregularity of gas release. These parameters were compared with values i_w (Kovács 1981). The comparison answered the question whether the changeability in the working gas release is affected rather by the weekly rhythm of the mining activity or by other outside factors.

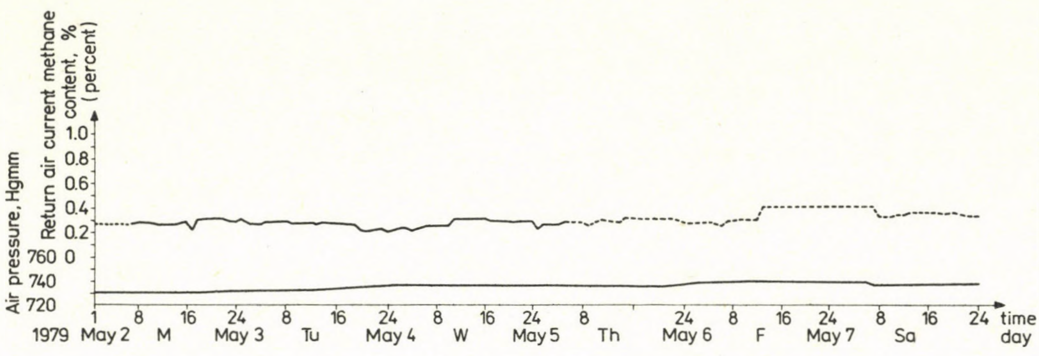

Fig. 1. Hourly data of methane concentration values of the return air current in working Pb 1. Change of air pressure

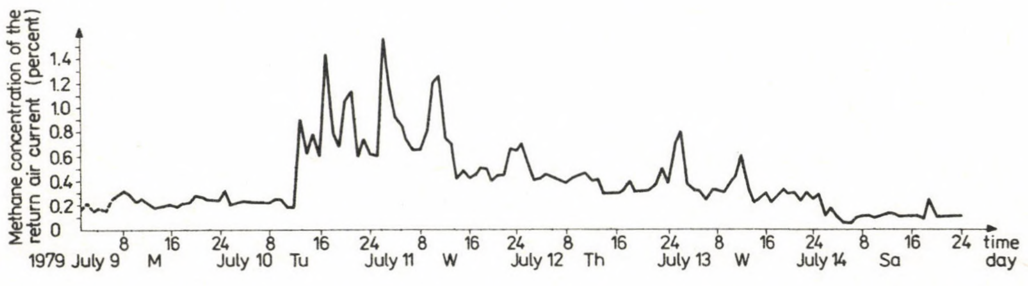

Fig. 2. Hourly data of methane concentration values of the return air current in working Z 1

Of the data of Pécsbánya mine the diagram of working Pb 1 is presented in Fig. 3 and the summarized (mean) data of the 10 workings are also shown in Fig. 4. The ratio of the maxima and means within the weekly cycle is 1.05 and 1.04. The average of values i_w determined for the same 10 workings is 1.68. This means that the weekly rhythm of the production results in 13 to 17 times less difference between the daily maximum and the weekly average than that caused by other effects between the weekly mean and weekly maximum gas concentration.

Gas concentration values measured on the days of the week can also be characterized as numbers of order. Based on data of the workings the days of the week were classified according to the mean and maximum concentration values. The smallest number of order, i.e. 1 was assigned to the day with the highest concentration. Summing the numbers of order of each working we obtain data that show on which day of the week it is more common (more probable) that the highest concentration occurs. The smaller the sum of the numbers of order, the more common the highest gas release.

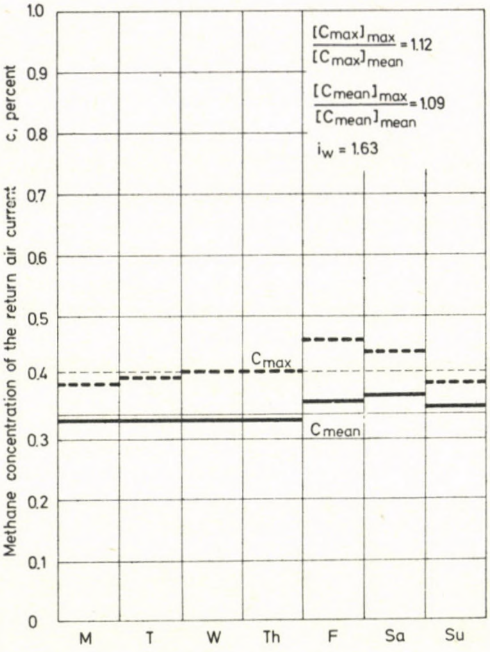

Fig. 3. **Mean and maximum methane concentration data of the working return air current for the days of the week (Pb 1)**

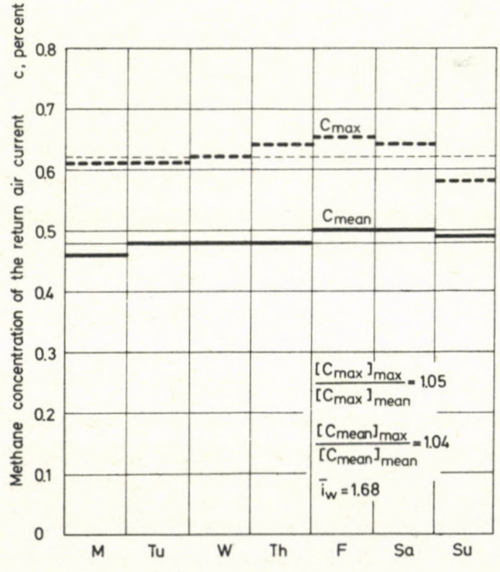

Fig. 4. **Mean and maximum methane concentration data of the working return air current for the days of the week (Pécsbánya summarized data)**

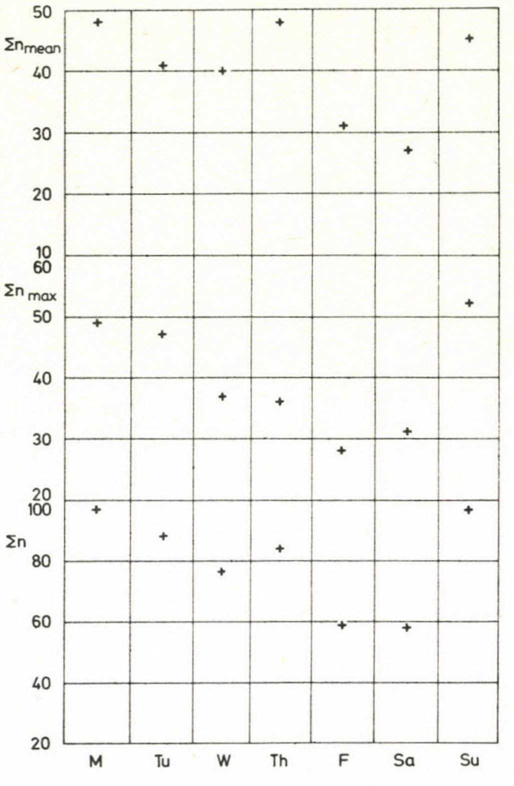

Fig. 5. Numbers of order according to gas concentration based on data in Pécsbánya workings

Characteristics determined on the basis of data in Pécsbánya workings are shown in Fig. 5.

Data of workings in Kossuth and Zobák mines gave similar results. The diagrams plotted on the basis of the aggregate data of 21 workings in the 3 mines are shown in Figs 6—9. The averages of the maximum and mean concentrations in the return air current show maxima on Fridays alike. On the basis of the numbers of order it is on Friday when the maximum concentration occurs most frequently. Based on the aggregate numbers of order the danger on Fridays is the greatest, then come Thursday, Saturday, Wednesday with nearly the same degree of danger. The danger is considerably less on Tuesday succeeded by Monday and finally Sunday.

To judge the determined order of danger realistically it is also necessary to note that the maximum and mean concentration values of the days of the week do not differ considerably. The greatest difference between the maximum concentration values (Sunday and Friday) is 0.55—0.64, i.e. 0.09 percent CH_4 concentration, the difference between the mean values (Monday and Friday) is 0.45—0.49, i.e. 0.04 percent methane

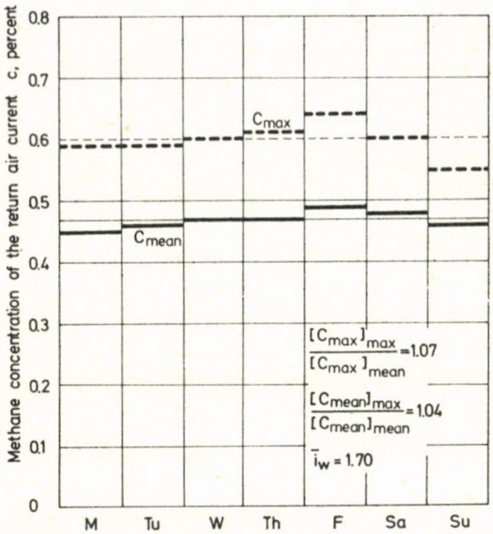

Fig. 6. **Mean and maximum methane concentration data of the working return air current for the days of the week (Summarized data of three mines)**

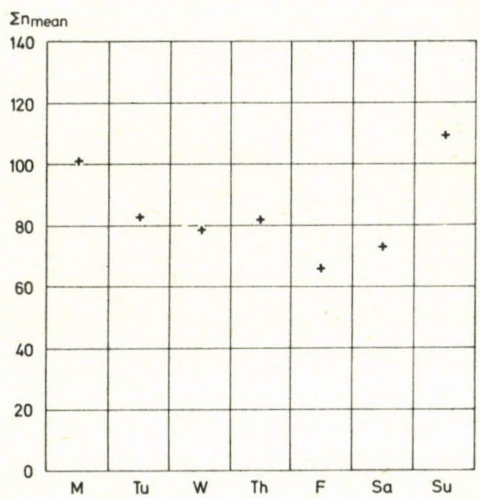

Fig. 7. **Numbers ot order according to gas concentration based on summarized data of 21 workings**

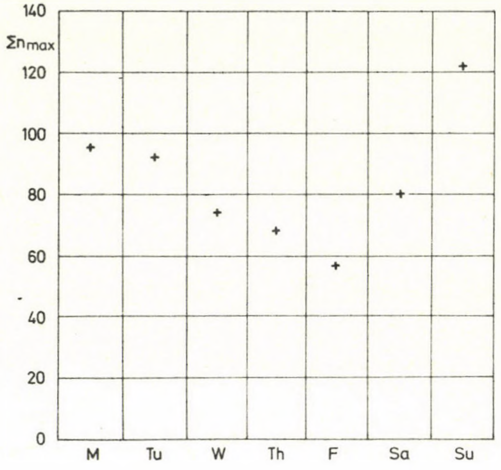

Fig. 8. Numbers of order according to gas concentration based on summarized data of 21 workings

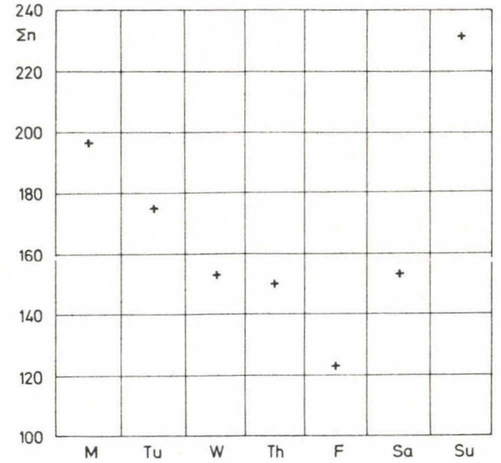

Fig. 9. Numbers of order according to gas concentration based on summarized data of 21 workings

concentration. This difference, concerning the actual degree of danger, is not considerable; consequently, the potential degree of firedamp danger on each day of the week is practically the same. Thus the weekly change of the production cycle does not considerably affect the degree of potential gas danger. The actual degree of danger, naturally, depends also on the fact that on workdays the high-temperature spots are obviously more common to appear.

The fact that the methane concentration in the working return air current depends only to a small extent on the weekly cycle of the production primarily results from the following: the majority of methane in the working return air current is of secondary nature at the workings investigated, it is not released from the cut coal.

The change in gas release has also been investigated through analysing the total life of the workings (measurements).

On the basis of Figs 9 and 10 by Otto (1962) and Fig. 5 by Kaffanke (1980) it can be stated that the methane concentration of the return air current (its time data freed from the daily and weekly rhythm) shows a sudden rise returning periodically. The maximum and mean concentration values of the return air current in 21 Mecsek workings have been analysed as functions of face advance. Based on the analysis it has been found that the maximum and mean methane concentrations as functions of time follow each other, the gas output of the working shows a periodical sudden rise at the same time. The interval between the occurrence of the maximum values is different at each working, they may appear every 3 to 8 weeks.

Of the data investigated the diagrams of workings Pb 1, Pb 9, K 2 and K 5 are shown in Figs 10—13. In the figures the change of the outer air pressure is also illustrated; the beginning of the sudden concentration rise is marked by an arrow. The extraordinary cause had an effect of long duration (7—14 days) on the rise of the gas output.

Taking into account the mechanism of gas release, the general laws and experience concerning gas release in the workings, it can be assumed that the phenomenon which returns periodically, lasts for a long time and results in a considerable rise in the gas output, is in causative connection with the failure of the roof sequence and with the loosening of the underlying layers. Based on the diagrams and other data of the workings (rate of advance) the intervals between the gas output maxima have been determined also for calendar- and workdays; on the basis of these two data the ratio η of productive time has been calculated. By means of the rate of advance the mean rate of advance v_0 has been determined on calendar intervals.

Figures 14 and 15 illustrate the data of workings Pb 1 and Pb 9, Figs 16 and 17 those of K 2, K 4 and K 5. Figure 18 shows the data of Pécsbánya and Kossuth mines together. It can be ascertained that the interval l_0 between roof failures (gas output maxima) increases with increasing ratio of productive time and average rate of advance. In Fig. 17 the data of working K 6 worked in the second slice are also illustrated. On the basis of Figs 14—18 it can be stated that parallelly with the increase of η and v_0 the time interval between gas output maxima gradually increases, the roof failures become "less frequent". At the workings in the second slice the interval of roof failures is twice of that in the first slice (with identical v_0). Regression function in Figs 17 and 18 shows that value l_0 with an advance below $v_0 = 0.2$ m/d decreases to zero indicating that workings with such a low rate of advance cannot be sustained any more or only at the expense of great difficulties.

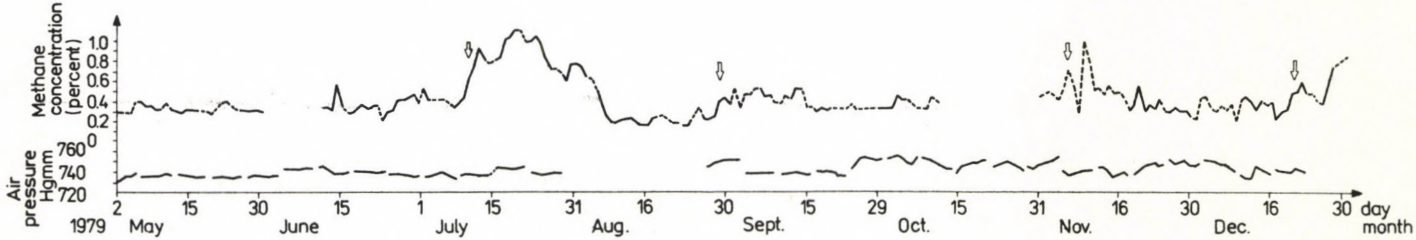

Fig. 10. **Maximum methane concentration of the working return air current and the exterior air pressure (Pb 1)**

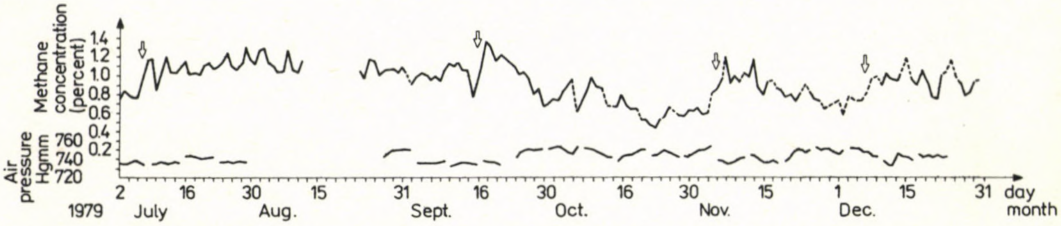

Fig. 11. Maximum methane concentration of the working return air current and the surface air pressure (Pb 9)

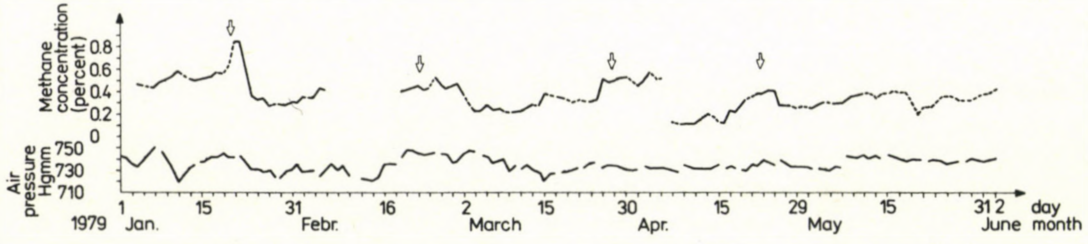

Fig. 12. Mean methane concentration of the working return air current and the surface air pressure (K 2)

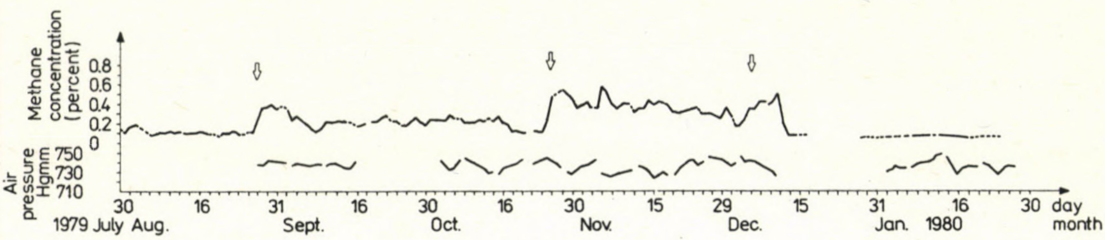

Fig. 13. Mean methane concentration of the working return air current and the surface air pressure (K 5)

The spasmodic gas output rises last 5 to 15 days, the intensity of gas inflow comes to 50—300 percent of the mean values of the previous interval. The period of 5—15 days is 15—25 percent of the complete 20—100-day-cycle, which means that the decrease in the intervals of roof failures, resulting from a slowdown in the rate of advance, increases considerably the gas burden summed on the total life in the return air current of the workings. *The slowdown of the mean rate of advance v_0 increases,*

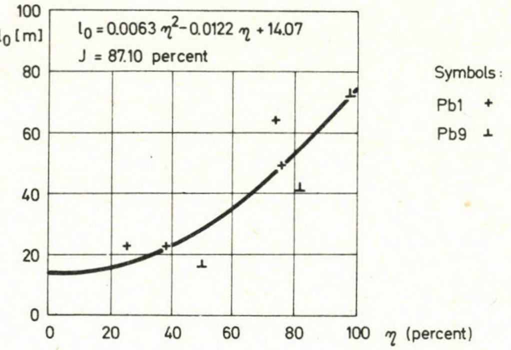

Fig. 14. Relationship between the interval of appearance of gas output maxima and the ratio of productive time

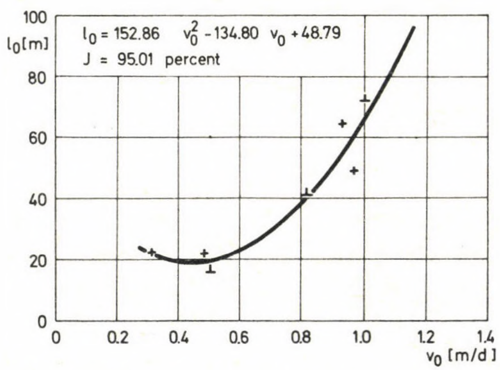

Fig. 15. Relationship between the interval of appearance of gas output maxima and the mean rate of advance (Pb 1, 9)

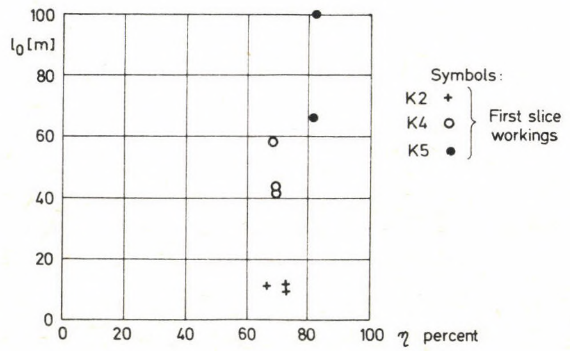

Fig. 16. Relationship between the interval of appearance of gas output maxima and the ratio of productive time (K 2, 4, 5)

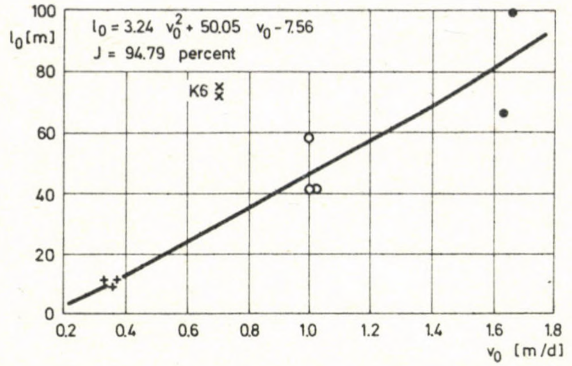

Fig. 17. Relationship between the interval of gas output maxima and the rate of advance (K 2, 4, 5)

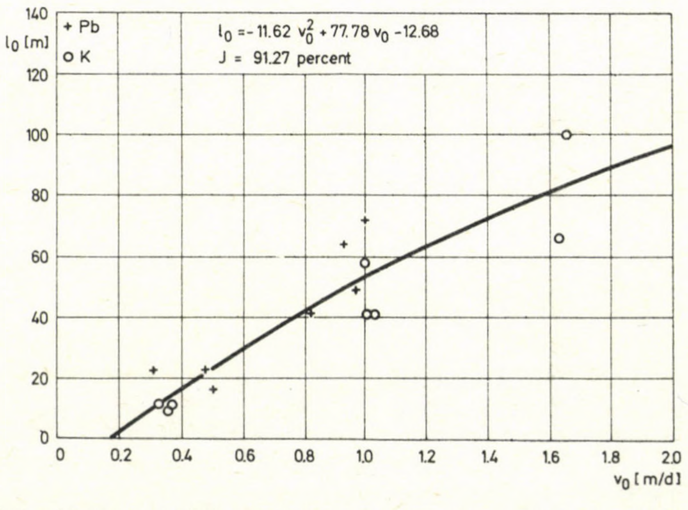

Fig. 18. Relationship between the interval of gas output maxima and the rate of advance (Pb, K)

according to the $l_0 = f(v_0)$ relationship, the frequency of roof failures and that of spasmodic gas inflows due to failures, the gas burden in the working return air current deriving from the very high ratio of the secondary gas output and *the mean specific gas output to a considerable extent*. The sudden (unexpected) rise of the methane concentration increases the degree of firedamp danger and presents a potential source of danger.

By analysing the relationship between the air pressure change and the gas concentration at the workings in Kossuth mine it has been obtained that an 1 Hgmm air pressure change resulted in a repeatedly recurrent round 0.01 percent of methane concentration fluctuation. In course of further investigations the gas output increasing effect of the air pressure should be determined at different gas release values based on planned observations and data collections controlled in accordance with the aim to enhance the reliability of the ventilation. Namely, during the actual operation one should also learn the quantitative relationship in addition to the tendency of the air pressure—gas release connection.

The present investigations have pointed out that under Mecsek conditions, as a consequence of the great thickness of the coal seam sequence storing gas, the ratio of the secondary gas output is very high, the gas inflow due to roof failures from the adjacent rocks is very intensive. Therefore from the viewpoint of ventilation as well it is of high priority to analyse the issues of periodical roof movements in detail. Besides examining the mechanics of this question the operation observations also gain an important role. While the workings advance, the time and place of movements also affecting the higher roof can be registered with geophysical, working and drift convergence measurements. The gas concentration in the return air current of the workings must be observed parallelly with these measurements. Comparing the change in the roof movement as a function of time and space to that of gas release the relationship between the parameters of roof failures and the gas output can be determined. With this knowledge, on one hand, the number of objective data concerning the planning of ventilation is increased and, on the other, a more precise knowledge about the roof movement is instrumental in improving roof control.

Changeability of methane release as a function of natural and technical parameters

Experience discloses that in workings gas release considerably changes in time. The maximum and minimum values can notably differ from the mean gas output values. In the workings the irregularity of gas release is of varying degree depending on geological and mining conditions, on the character and timing of work processes, but it is an almost always occurring factor. Even if the extraordinary effects are not counted in, the maximum gas output repeatedly reaches 1.5—2.0 times that of the mean value at workings of normal operation. Having extraordinary values (gas release of 3 to 5 times) we are bound to cut production from time to time to maintain security.

Real values describing the irregularity of methane outflow refer to longwall workings almost without exception. The irregularity parameter i of gas release concerning one given place of working is the ratio of the maximum and mean methane content (percent) in the mine air. To determine value i the weekly mean and maximum gas content values of the same period are considered as a rule. It infers from the definition of the irregularity parameter of gas release that $i \geqq 1$. The more regular the methane release and the change in the methane content in the air of the working, the smaller the value *i*.

Conclusions that can be drawn on the basis of examining the data by Otto (1962), Osipov (1964), Bruyet (1970), Tarasov and Kolmakov (1978) concerning irregularity parameters are as follows:

The effect of *seam thickness* can be regarded as a factor which increases unambiguously and positively the irregularity of gas release. The increase of seam thickness is undoubtedly unfavourable in this respect.

The effect of *seam dipping* is analysed by Tarasov and Kolmakov (1978) only; relying on the basic data the irregularity factor increases in case of steep seams.

The effect of the *length of face* based on French data can be characterized as follows: the longer the face is — particularly in the Nord-Pas-de-Calais basin with varying seam conditions — the higher the value of the irregularity factor becomes. On the other hand Osipov (1964) (though based on data of two workings only) ascribes a favourable effect to a longer face in this respect.

It can be considered as a general experience that, with identical technology, an increase in the *advance* of the working face considerably decreases the irregularity of gas release. In the Ruhr region experience displays that ploughing increased value *i* to 1.5—2.0 whereas working by hand had a value *i* of 1.0—1.5. Osipov (1964) also discloses that although ploughing increases irregularity in gas release the degree of the increase, however, is considerably smaller than the increase in the output resulting from the ploughing introduced.

French experience points to the fact that intensifying the *working air current* increases ventilation stability and decreases the irregularity factor.

On the basis of Tarasov and Kolmakov's (1978) paper value *i* tends to be smaller in the case of higher *gas output*. This is in contradiction to the following French conclusion: when applying preventive gas drainage the irregularity factor becomes smaller since in this case the methane deriving from the worked seam has a smaller proportion in the ventilation where the methane content tends to be a function of the indispensable discontinuity of the working.

It has also been found that the more *time* observing the irregularity of gas release takes, the higher the irregularity factor will be.

The quantity and irregularity of gas release can be determined precisely only on the basis of actual data. By means of the data of a great number of measurements it can also be detected how natural and mining parameters affect the irregularity of gas release. The characteristics of gas release have been determined by means of data measured by AMT instruments recording methane content. Of the basic data referring to the 21 workings the changeability parameters of working Z 1 denoted by 18 are less reliable because of the short observation time.

The changeability parameters of gas release have been determined on days and weeks and also on the total life of the workings. The natural and technical

Table III. Changeability data of gas release parameters of 21 longwall workings in the Mecsek Coal Mines

N°	Denomination number	Average of daily values $\bar{i}_d$	Average of weekly values $\bar{i}_w$	Values for the whole observation period i_t
1.	*Pb* 1	1.26	1.63	3.21
2.	Pb 2	1.25	1.63	2.18
3.	Pb 3	1.17	1.28	2.88
4.	Pb 4	1.56	2.09	3.93
5.	Pb 5	1.26	1.65	2.92
6.	Pb 6	1.20	1.53	2.52
7.	Pb 7	1.49	2.05	5.21
8.	Pb 8	1.41	1.76	2.44
9.	Pb 9	1.30	1.67	2.75
10.	Pb 10	1.16	1.46	2.32
11.	K 1	1.12	1.37	2.00
12.	K 2	1.12	1.36	2.56
13.	K 3	1.28	2.12	4.23
14.	K 4	1.22	1.60	4.34
15.	K 5	1.26	1.66	3.57
16.	K 6/1	1.10	1.24	1.49
17.	K 6/2	1.14	1.36	4.28
18.	Z 1	1.85	3.53	4.47
19.	Z 2	1.28	1.44	2.03
20.	Z 3	1.24	1.29	2.81
21.	Z 4	1.34	1.90	2.47

characteristics of the workings are given in Table II, the irregularity (changeability) factors i_d, i_w, i_t, in Table III. The relationship between the changeability of gas release and the natural and technical parameters of the workings have been analysed with methods of mathematical statistics. It has also been investigated whether the changeability (methane concentration) of gas release on workdays differ from that in the intervals of standstill. The effect of the advance course of the workings has also been examined.

Comparing changeability factors for days i_d, weeks i_w and for the total life of workings i_t the conclusion can be drawn that the longer the *observation* (evaluation) *time is the higher the changeability factor becomes.* In the workings of the Mecsek region the interval of the changeability factor of gas release is 1.10—1.56 (1.85) based on daily data, 1.24—2.12 (3.53) based on weekly data and 1.49—5.21 based on data for the total life of workings. Using weekly data i_w the general conclusion can be drawn that the methane concentration value in the working return air current is repeatedly 1.5 to 2.0 times as high as the mean value. Values $i = 1.49$—5.21 relating to the total life of workings indicate with great probability to what extent the periodical roof failures in the progress of workings increase the gas inflow compared to the mean gas output.

It was also possible to compare values i_d and i_w of the workdays and those of the days in standstill. Based on data of 10 workings in Pécsbánya (Table III serial number 1—10) the mean changeability factor of workdays is $\bar{i}_{dwo}=1.38$, the same on days in standstill is $\bar{i}_{ds}=1.22$. The average of values i for the whole life is $\bar{i}_{lwo}=2.88$ in case of workdays and $\bar{i}_{ls}=2.78$ for days in standstill. According to the relating data of 7 workings (11—17) in Kossuth mine $\bar{i}_{dwo}=1.19$, $\bar{i}_{ds}=1.14$. The average of values i for the total life are $\bar{i}_{lwo}=2.95$ and $\bar{i}_{ls}=3.28$. Based on data of 3 workings in Zobák mine (19—21) the same values are

$$\bar{i}_{dwo}=1{,}47, \quad \bar{i}_{ds}=1.31, \quad \bar{i}_{lwo}=2.83, \quad \bar{i}_{ls}=2.47.$$

Comparing the data it can be stated that the changeability factor is higher on workdays than on days in standstill. The difference, however, is not considerable.

The effect of *the advance course of the working* has also been investigated. In Pécsbánya five workings were retreating and five advancing. Lifting out the weekly values of the changeability factor the mean value of i_w is 1.76 for retreating workings and 1.59 for the advancing ones. In Kossuth mine each working was advancing, the average of i_w is 1.53. In Zobák mine for the advancing workings $i_w=1.44$, the average of i_w in the two advancing workings is 1.59.

The average of values i_w in the 13 retreating workings is 1.60, the same mean value for the 7 advancing workings is 1.59. The changeability parameter of the retreating and advancing workings *do not differ* considerably.

The relationship between the natural and technical parameters and that of the changeability factor of gas release has been examined by determining one- or more-variable regression functions, too (Department of the Technical University of Heavy Industry 1981). Of the natural parameters seam thickness M [m] and seam dipping α^0, of the technical parameters of the workings the length of the face H [m], the daily mean advance v [m/d], the quantity of air flowing through the working face Q [m^3/min] and the specific gas output of the working air current q [m^3/t] were included. The significant results of the analysis are as follows:

The thicker the seam, the higher the changeability factor of gas release. This statement concurs with the experience in other countries On the basis of the examined data it is also to be established, however, that value i does not rise considerably as a function of M, mean values i for thin and thick seams do not differ considerably.

An ascent in the dipping of the seam increases the irregularity factor of gas release. This justifies the Soviet results published.

Our examinations prove that the longer the working face is, the smaller the changeability factor becomes. The one-variable linear functions show a definitely decreasing tendency in each case, the exponent of L in the more-variable functions was only in one case a positive value around zero. This result concurs with that of (Osipov 1964) but contradicts experiences gained in the Nord-Pas-de-Calais basin.

Enhancing *the rate of advance increases* the irregularity of gas release following a definite tendency. Of the investigated 21 workings, winning was carried out by hand in 20 cases. This result contradicts data published so far. Research workers in other countries state, scil., that enhancing the rate of advance incurs the reduction of changeability factor.

The increase of *air current* flowing through the working face *decreases* the irregularity of gas release. This concurs with French experiences. A greater air quantity makes the ventilation more stable, assures a greater safeguard against firedamp.

With an increase in the *specific gas output* of the working air current the value of the changeability factor *decreases* in a majority of regression functions. This coincides with the data obtained in the Kuznetsk basin.

A special emphasis has been put on analysing the relationship between the specific gas output and the changeability factor. This issue is of extraordinary importance as the specific gas output and the gas concentration of the working air current and its change have a primary role in evolving firedamp danger. It has been investigated in what direction the changeability of gas release changes with an increase in the gas output. The gas output change has been characterized by the average methane concentration c_a (percent) of the working return air current.

Based on the results of the regression analysis it can be ascertained that the daily values of the changeability factor i_d are practically independent of values c_a, factor i_d does not change as a function of methane concentration. There was no definite tendency as to the change of the weekly values of the changeability factor either. Value i_w seems to be also independent of the gas content in the return air current. Data of statistic examinations show that the average of values i_d is between 1.2 and 1.3 independently of the values c_a; the average of values i_w is round 1.6.

Figure 19 illustrates values i_l relating to the total life of workings. With an increase in the methane content of the return air current the changeability factor presents a definitely decreasing tendency. At smaller concentration values (0.2—0.3 percent of CH_4) the irregularity of gas release is considerably bigger ($i_l = 3-5$); in case of a higher gas release ($c_a = 0.6-1.0$ percent) the irregularity factor does not change significantly, it is 2—3 as a rule.

Calculating ventilation it is advisable to take into consideration parameters characterizing the changeability of gas release. Besides the mean absolute value of the gas output released on the working face the degree of firedamp danger is also influenced to a great extent by the gas release as a function of time. In developing planning and control methods of ventilation it is expedient to examine, with security and economic aspects also taken into account, which of the parameters i_d, i_w and i_l has to be considered as primary for the determination of the air current of workings.

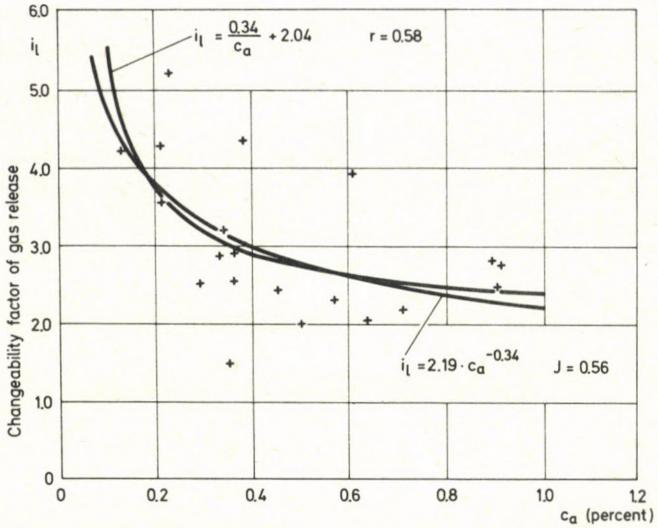

Fig. 19. Mean methane concentration of the return air current changeability factor of gas release

Gas release and seam thickness

Using data of the workings in three Mecsek mines (Fig. 2) the mean methane concentration c_a (percent CH_4) of the return air current, the specific gas output [m^3/t] in the light of air quantity Q [m^3/min] and the production t/d and the specific gas release in the working c_s [m^3/t] with the help of the gas content of the working intake air current, have been determined. In our statistic investigations the characteristics of gas release have been determined for workdays and intervals of standstill. Analysing data of the gas release the effect of the preventive gas drainage has been examined, a particular attention has been paid to the role of seam thickness.

Data of the workings in Pécsbánya showed a 0.44 percent methane concentration on an average for *workdays*, 0.41 percent for days of *standstill*. The specific methane content of the return air current is 7.29 m^3/t for workdays and 6.70 m^3/t for days of standstill. In short the gas concentration of the return air current, the gas output on days of standstill are hardly lower than those on workdays. The gas output on workdays is only by 8—9 percent higher.

In the seven workings of Kossuth mine the mean methane concentration of the return air current is 0.32 percent on workdays, 0.27 percent on days of standstill. The mean specific methane content of the return air current is 9.18 m^3/t and 8.07 m^3/t. Production on the face increased the gas concentration of the return air current by 18 percent on an average and the specific gas content by 14 percent.

According to data from Zobák mine the mean methane concentration of the return air current is 0.69 percent on workdays and 0.72 percent on days of standstill. The specific gas content of the return air current is 13.98 m^3/t and 14.92 m^3/t. These mean values were gained in the following way: in two workings the gas release was, according to expectations higher on workdays, in two other workings, however, the gas content of the return air current was greater on days of standstill. On days of standstill a greater gas content might be caused by caving activity or by a less intensive ventilation.

Data of the three mines give information about primary and secondary gas release and the ratio of these two factors. The data seem to indicate that the majority of the released gas output is secondary, coal production does not considerably increase gas release. The gas content of the return air current is practically independent of the work carried out on the working face. Detailed data of the workings give practically the same picture.

It has been analysed in detail what relationship exists between the *specific gas output* and the *seam thickness.*

Nine of the workings in Pécsbánya mine worked thin seams (3, 6, 7 and 23), one of them worked in the first slice of thick seam 11. Workings in thin seams that can be mined in one slice, produced an average specific gas release of 6.76 m^3/t, in the first slice of thick seam 11 the gas output amounted to 18.24 m^3/t at the same time. Experiences in Pécsbánya mine have also shown an increased gas release in the first slice of thick seams. In 1200 m^3/min return air current the methane concentration was namely 1.0 to 1.2 percent which means 12—14 m^3/min CH_4 gas output. In the workings of the second and third slices, with the same coal output, in 600 m^3/min return air current the gas content was 0.5—1.0 percent which yielded a 3—6 m^3/min CH_4 gas output. Consequently, gas release in the first slice was 2—5 times higher than that in the further slices.

In Kossuth mine the methane output was 9.80 m^3/t in the first slice workings of the thick seams 14 and 16 and 2.32 m^3/t in workings of the second slices at the same time. In Zobák mine the specific gas output was 13.07 m^3/t in the first slice workings of thick seams 10, 12 and 16, in a working of the third slice it was, however, 7.14 m^3/t. Data obtained in Kossuth and Zobák mines prove a round *2—4 times higher* specific gas output *in the first slice* than in workings of the further slices.

Calculating the average of all three mines the mean specific gas release is 9.77 m^3/t for first slice workings whereas it is 3.53 m^3/t in workings of the second and third slices. In first slice workings (including workings of seams that can be worked in one slice) the specific gas output is 2.76 times higher than that in workings of the second and third slices.

A detailed statistical analysis of the set of data showed that with an increase in seam thickness the specific gas output is intensified nearly twice as sharply in the first slice workings as the average gas release (concerning the whole production).

Based on the data the relationship between specific gas release and seam thickness can be characterized by the regression function

$$c_s = 5.64 \cdot M^{0.39} \quad [m^3/t].$$

Exponent 0.39 indicates that the specific gas output depends on the increase of seam thickness according to a nearly square-root character. This tendency apparently bears a relation to the fact that with an increase in seam thickness the height of roof failure and the secondary gas output due to that, also are on the increase.

It has also been investigated whether the changeability factor of gas release is different in workings of thin and thick seams. In 11 workings of thin seams the average of i_w is 1.62 and 1.78 in 10 workings of thick seams. Neglecting data of short life working Z 1 in Zobák mine the average i_w of thick seam workings is 1.59. Thus the result coincides with the conclusion drawn already before, *viz.* the changeability factor of the gas release does not considerably change with the increase of seam thickness.

Comparing data of workings in the first slice and those of the second and third slices of thick seams the following results were obtained: the average i_w is 1.59 in the first slice workings whereas it is 2.06 in workings of the second and third slices. The reason for this finding can be as follows: in workings of the second and third slices the specific gas output is 2—6 times less than that in first slice workings and the changeability factor is reciprocally proportional to the specific gas output (Fig. 19). And in workings of the second and third slices a more intensive gas inflow may occur from the debris of the first slice in the course of caving.

The relationship between seam thickness and specific gas output, the ratio of the gas output in the workings of the first slice and that in the workings of the further slices, the characteristics of the gas release changeability can be utilized when the ventilation of longwall workings is planned and when the parameters of the working concentration is determined.

Probability parameters of the return air current concentration and the changeability factor of gas release

Authors investigating also gas release as a function of time establish the frequency function of gas concentration and that of the gas output per unit of time based on measurements in mines. Otto gives the relative frequency of concentration relying on data obtained in the return air current of a Ruhr region, no data are given, however, about the character of distribution (Otto 1962). Osipov (1964) publishes the frequency function of the return air current concentration in the above mentioned working of the Ruhr region and that of the Don basin. The character of distribution is regarded as normal, no reference is made, however, to adjustment investigation. Bruyet (1970) also deals with the distribution of the maximum gas concentration in the return air current. In the diagram illustrating the definition of the changeability factor the distribution of the gas concentration is characterized by a frequency function of normal distribution.

The question has been examined on the basis of gas concentration data gained in 21 longwall workings of the Mecsek Coal Mines by ranging the maximum and mean gas concentration values of the return air current and the changeability factor values calculated as their quotient. From this analysis the conclusion has been drawn that the minimum values have little frequency; then the frequency of higher values suddenly increases and later it gradually decreases. This result gave reason for examining the hypothesis of a lognormal distribution.

The relevance of our hypothesis concerning a lognormal distribution of data (concentration, changeability factor) has been checked by Kolmogorov's theory (Rényi 1954). On sets of data of each working the empirical distribution function $F_n(x)$ and the parameters σ and m of the theoretical distribution function $F(x)$ have been determined.

At the selected 99 percent probability level the hypothesis can be considered acceptable if inequality

$$\frac{1.63}{\sqrt{N}} > \Delta F_{\max} = \sup_{-\infty < x < \infty} [F_n(x) - F(x)]$$

holds, where N is the number of data (measured values).

The investigation has been carried out on 126 sets of data altogether based on 21 workings. Adjustment investigations have been made separately on daily and weekly data. Doing so the distribution of the maximum and mean gas concentrations and the values of changeability factor i interpreted as their quotient have been analysed. Out of 126 cases the condition was not met in 4 cases, i.e. in 3.1 percent of all cases the value of $\Delta F_{\max}$ exceeded that of $1.63/\sqrt{N}$. The four extreme cases: maximum and mean values of daily methane concentration in working Pb 1 and the daily maximum methane concentration values of Pb 9 and K 6/2. For the changeability factor the hypothesis of lognormal distribution has been justified in each case.

The detailed data of the calculations and the determined distribution frequency functions are contained in a research report (Department of Mining of the Technical University of Heavy Industry 1982b). Of the determined functions only the diagram of working K 2 is now published. Figure 20 illustrates the empirical function $F_n(x)$ and theoretical frequency function $F(x)$ of the daily mean values and Fig. 21 that of the maximum methane concentration values. Figure 22 shows the empirical and theoretical frequency function of the daily changeability factor i_d, Fig. 23 displays the empirical and theoretical frequency function of the daily mean values and Fig. 24 that of the maximum gas concentration values. Figure 25 shows the frequency function of the changeability factor of gas release i_w.

The diagrams clearly display our finding proved also by the result of the adjustment investigation, *viz.* $\Delta F_{\max} \ll 1.63/\sqrt{N}$: the distribution of the maximum and

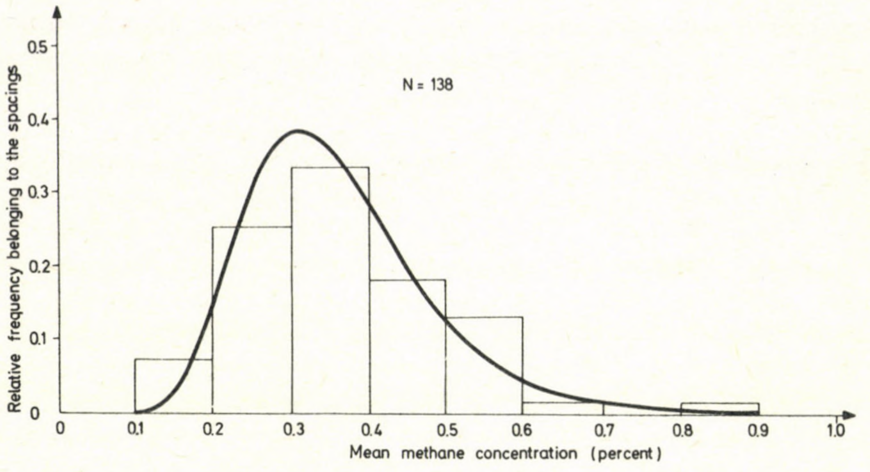

Fig. 20. Empirical and theoretical frequency function of the daily mean concentration values of return air current in working K 2

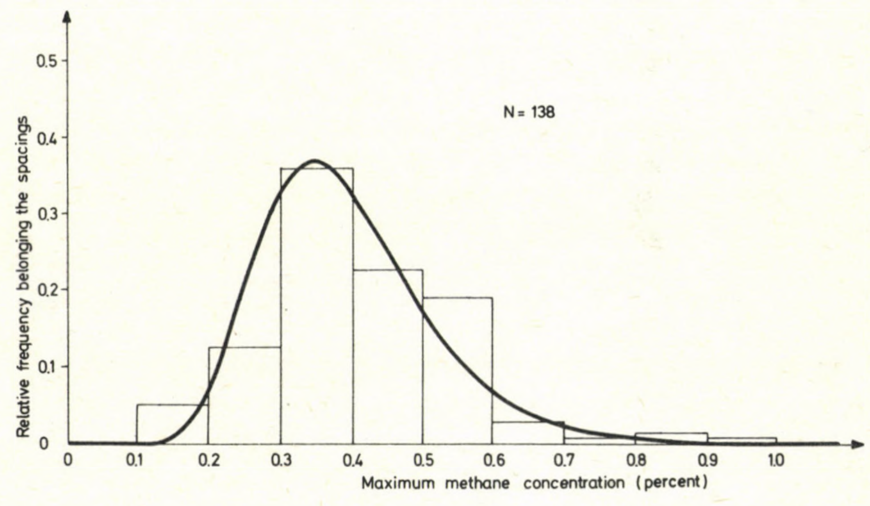

Fig. 21. Empirical and theoretical frequency function of the daily maximum concentration values of return air current in working K 2

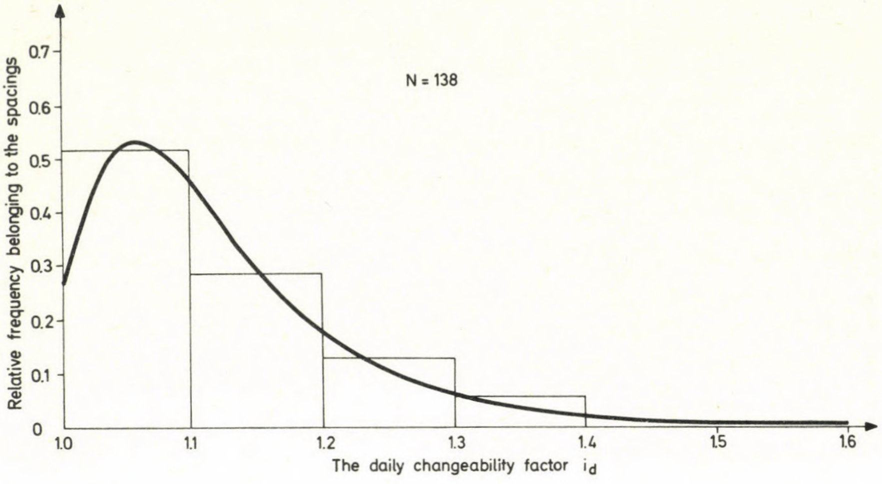

Fig. 22. Empirical and theoretical frequency function of daily values i_d of the changeability factor using data of working K 2

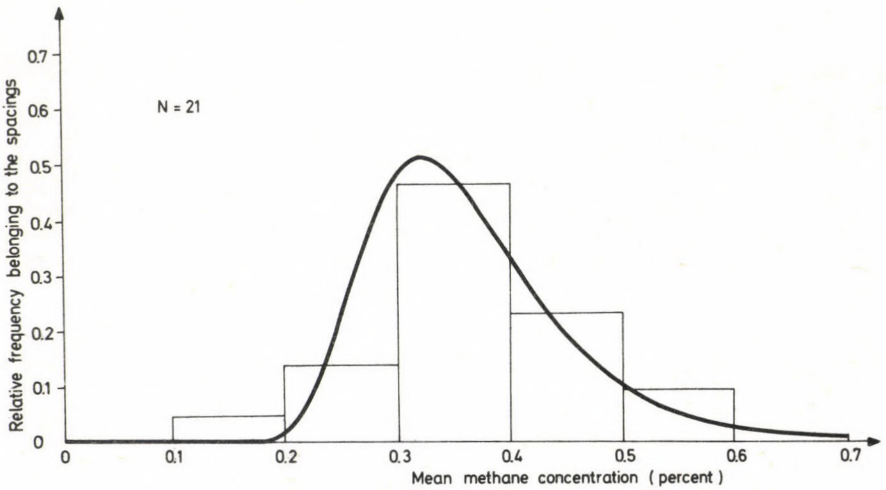

Fig. 23. Empirical and theoretical frequency function of the weekly mean concentration values of return air current in working K 2

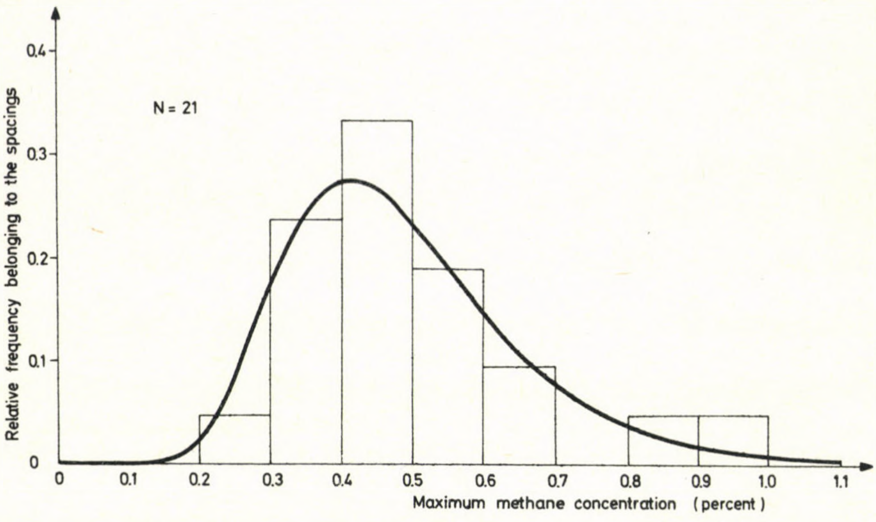

Fig. 24. Empirical and theoretical frequency function of the weekly maximum concentration values of return air current in working K 2

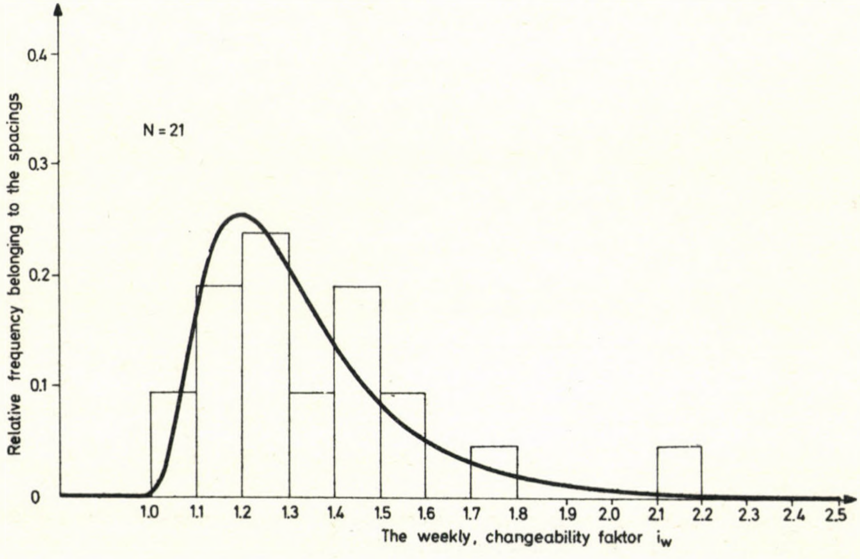

Fig. 25. Empirical and theoretical frequency function of weekly values i_w of the changeability factor using data of working K 2

mean methane concentration in the return air current obeys a lognormal distribution. On the basis of data of the investigation it can also be definitely claimed that the distribution of the daily and weekly values of the changeability factor of gas release is lognormal as well. From the data of ventilation measurements the probability parameters, the expected value m and its standard deviation σ of the methane concentration values in the return air current and those of the changeability factor of gas release can be determined. These parameters can be used for determining the characteristics of gas release and for calculating the parameters of the ventilation.

References

Bruyet B 1970: L'irregularité du degagement de grison et sa mesure: definition, utilisation et valeurs du coefficient d'irregularité. Revue de l'Industrie Minerale No. 4.

Department of Mining of the Technical University of Heavy Industry 1981: Relationship between the specific gas output and changeability of gas release and the natural and technical parameters in longwall workings of the Mecsek Coal Mines. (In Hungarian) Research report for the Mecsek Coal Mines

Department of Mining of the Technical University of Heavy Industry 1982a: Distribution parameters of the change in gas concentration of the return air current in longwall workings of mines with high gas output. (In Hungarian) Research report for the Ministry of Industry

Department of Mining of the Technical University of Heavy Industry 1982b: Distribution parameters of the change in gas concentration of the return air current in longwall workings of mines with high gas output. (In Hungarian) Research report for the Ministry of Industry

Kaffanke H 1980: Mittelfristige Vorhersage des Methangehaltes im Ausziehwetterstrom von Abbaubetrieben. Grubengas, Grubenklima und Wetterführung im Steinkohlenbergbau der Europäischen Gemeinschaften. Luxemburg. Verlag Glückauf GmbH.

Kovács F 1981: Relationship between changeability factor of gas release and the natural and technical parameters. (In Hungarian) *Bányászati és Kohászati Lapok, Bányászat*, 114, 289—300.

Osipov S M 1964: Methane separation at coal plough workings in layers with high gas output. (In Russian) *Ugol'Ukraini*, No. 5, 47—48.

Otto G 1962: Ergebnisse der Überwachung zweiter Abbaubetriebe mit hoher Ausgasung. *Glückauf* 89, 1286—1298.

Rényi A 1954: Theory of Probability. Tankönyvkiadó, Budapest

Schmidt-Krehl W 1967: La maitrise du grison dans les mines de charbon. Tache de recherche et d'exploitation. Annales des Mines de Belgique No. 2.

Tarasov B G, Kolmakov V A 1978: Gas barriers in coal mines. (In Russian) Nedra. Moskva

Acta Geodaet., Geophys. et Montanist. Hung. Volume 18 (3), pp. 333—335 (1983)

BOOK REVIEWS

E C Dahlberg: *Applied Hydrodynamics in Petroleum Exploration.* Springer-Verlag, New York—Heidelberg—Berlin, 1982. 161 p. 48 DM

In the preface the author clearly declares that his intention is to fulfil a real need having existed since long for a concise handbook on practical hydrodynamics for representatives of both geologists and petroleum engineers active in hydrocarbon exploration. Really, this goal can be verified by the fact that while some fields of theoretical and practical hydrodynamics have been well developed and summarized (e.g. hydrocarbon traps and reservoirs), a detailed analysis of the source and the fluid system, even more a book treating the system as an integral whole lacked until now. The book consists of eight chapters which comprehend all aspects of applied hydrodynamics in petroleum exploration.

Chapter 1 "Fluids in the Subsurface Environments" (15 pages, 8 figures) gives a general characterization on the nature of fluids and fluid environments, the concept of potential energy in subsurface system and terminology of force fields, flow lines, gradients, formation of traps and source of formation pressure data.

Chapter 2 "Hydrogeological conditions" (18 pages, 12 figures) deals with the hydrostatic and hydrodynamic environments and the role of hydrocarbon-water interfaces in forming a reservoir is discussed.

In Chapter 3 "Hydrodynamics Exploration Analysis" (3 pages, 1 figure) the different evaluation procedures are shortly listed.

Chapter 4 "The potentiometric surface" (12 pages, 12 figures) is devoted to the analysis of potentiometric surfaces and to the inferences drawn from subsurface flow patterns.

Chapter 5 "Pressure-Depth Gradients" (22 pages, 20 figures) is focussed on the geological interpretation of pressure-depth gradient diagrams, and on its subsurface hydrological correlations with the aim to estimate water/oil contact and hydrocarbon pay thickness.

Chapter 6 "Hydrocarbon Entrapment Potential Constructions" (8 pages, 6 figures) summarizes the relationships between oil and water potentiometric surfaces, the mapping principles of relative fluid potential energy levels and finally the predicting methods of hydrocarbon migration and accumulation by U, V and Z mapping.

Chapter 7 "Entrapment Potential Cross-Section" (30 pages, 31 figures) illustrates different structural traps and their models in detail and some documented cases are shown for tilted oil and gas pools.

Chapter 8 "Hydrodynamic Mapping" (20 pages, 15 figures); data and methods are demonstrated here for mapping structural and non-structural hydrodynamic traps by using natural formations.

The chapters are completed with two appendices comprising the symbols and abbreviations appearing in the text and in Hubbert's Proof and Exercise Answers, respectively. Fundamental works are included into the references and some suggested readings are also listed. Unfortunately the index is limited.

The author succeeded in his intention rather to tell than to write the story of hydrodynamics in petroleum exploration in the book; it can be recommended to everyone from graduate students to scientists.

I Lakatos

G J Borradaile, M B Bayly, C A McPowell eds: *Atlas of Deformational and Metamorphic Rock Fabrics.* Springer Verlag, Berlin—Heidelberg—New York 1982, 649 figures, XIII + 551 pages

I studied with great interest this book on Deformational and Metamorphic Rock Fabrics. Scientists deal in recent years more and more with rock fabrics and many useful results of these studies are reflected in this book, too. The difficulties in a new field of science start with nomenclature even if the authors speak the same language. Problems of the nomenclature get even more difficult if authors use different languages or if authors speaking different languages write in the same language. The edition of the book was motivated by the necessity of a common nomenclature, and the present book aims to reach this goal in English.

The book gives a summary on rocks, as on anisotropic and heterogeneous materials, and processes of cleavage and cracking in them. (The nomenclature should be worked out in Hungarian and supposedly also in other languages, too, as e.g. the term cleavage generally used in this book refers in Hungarian only to minerals).

The book summarizes in three chapters theoretical and observational principles being unavoidable for an understanding of the followings.

Chapter I gives a definition of cleavage and several expressions connected with it, and these expressions are used thereafter uniformly and homogeneously in the book.

Chapter II reviews processes leading to cleavage and gives a survey on its differently developed forms and on the process of cleavage itself.

Chapter III presents connections between observational facts and past or present processes. Appendix I belonging to this Chapter contains the gist of the book: it lists the possibilities for conclusions from observational facts to processes in the rocks.

Chapter IV presents plates illustrating unambiguously the processes described in the previous Chapters. As the uniformization of the nomenclature is based on the uniform observation of the facts, the publishers tried to use all possibilities of modern technics to illustrate rock fabrics, thus in addition to normal photos optical micrographs and scanning electronmicrographs also presented. The production of the photographs is excellent, all details can be seen in spite of the black-and-white technics and thus they can be well interpreted. An understanding of the plates is promoted by the scales on them and by the corresponding petrological explanation.

More than 600 plates enable to cover all processes involved in this group of rocks. The *first main group* summarizes continuous cleavage, discussing in sub-sections processes due to stretched mineral particles, cleavages in rocks composed by phyllosilicates or other minerals.

The second main group reviews phenomena connected with spaced cleavage presenting pictures in 11 sub-sections. They include cracking, splitting phenomena at the boundary of mineral granules, "flame-like" smelting phenomena of schists and phenomena due only to granular differentiation, to list only the most important items.

In the framework of the system, but independently of it some more photos are presented on topics like non-planar differentiation and blastesis deformation and schistosy etc.

The book is useful both for the classification and presentation of processes and for the development of a uniform nomenclature. The concise text is accompanied by excellent figures emphasizing the essence and enabling a quick survey. The book can be recommended to all dealing with rock fabrics.

P Kertész

K O THIELHEIM ed.: *Primary Energy — Present Status and Future Perspectives.* Springer Verlag, Berlin—Heidelberg—New York 1982, 224 figs, 371 pages, DM 71

From Lancret's gay swing to the complicated economic and population problems in the Third World to be expected in the near future, a wide range of topics are connected with Primary Energy. Increasing energy production necessitates more raw materials or other sources of energy, it means increasing pollution of the atmosphere and surface, increasing hazards for nuclear disasters, or even noise problems, as in case of the exploitation of the wind energy or the destruction of estuaries by tidal power plants. Earth sciences play an important role in the discovery of the possible energy sources, e.g. as exploration methods for raw materials, as data bases, e.g. for solar or wind plants, or even in the determination of certain risk factors, e.g. by earthquakes for nuclear plants or waste deposits. Thus the present book is a most interesting lecture both from a technical and a personal point of view, offering a wide vista on problems and possibilities in energy supply from primary sources.

An introductory chapter of the physical concept of energy by the editor is followed by reviews on resources of fossil and nuclear fuels, on synthetic fuels and on the carbon dioxide problem. Then about 40% of the book deals with different kinds of nuclear energy production, with the perspectives and risks of the present and future methods, including deposition of radioactive waste. The next part of the book deals with other primary energy sources, hydroelectricity, solar energy, wind and tidal plants and geothermal energy. In the last chapters, the expected future energy demands and their resources, as well as the energy strategies are evaluated.

The picture resulting from the book is neither very optimistic, nor too pessimistic. It seems that without nuclear energy, energy demands cannot be met, other sources can cover only fractions of the demand, and even the biggest efforts cannot reduce the energy demand of the next 50 years below a level which could be covered by fossil fuel and other sources of energy.

Most chapters are written by German specialists, a few by leading experts from other countries (France, Switzerland, Austria), and the examples are also mostly taken from the corresponding countries, what does not mean that developments in other countries are neglected. A possibly world-wide picture is striven at.

The high level of the book is somewhat disturbed in certain places (e.g. p. 320) by low-quality, hardly legible figures. The book can be recommended to all earth scientists interested in the future of world economy and energy supply.

J Verő

CONTENTS

PRINTED IN HUNGARY
Akadémiai Kiadó és Nyomda, Budapest

— treble underlining: bold-face italics
— red underlining: Greek letters
— green underlining: script letters.

Rules for mathematical-physical notations:

— trigonometric, logarithmic, analytic symbols, symbols for units and functions are in roman type (not underlined)
— letter symbols in mathematical and physical formulas, scalars, and subscripts of algebraic and physical quantities are in italics (underlined)
— vectors, matrices, operators in probability theory are in bold-face roman type (double underlining)
— tensors, operators and some special functions are in script letters (green underlining). These cannot be bold.
— Greek letters (red underlining) cannot be bold or extra bold type (thus they cannot be used for vectors or tensors)
— void upper lines e.g. for vectors
— avoid possible confusion between o (letter) and 0 (zero), l (letter) and 1 (one), ν (Greek nu) and v, u (letters) etc.
— explain ambiguous or uncommon symbols by making marginal notes in pencil
— be careful about superscripts and subscripts
— formulae must be numbered consecutively with the number in parentheses to the right of the formula. References in text to the equations may then usually be made by the number in parenthesis. When the word equation is used with a number, it is to be abbreviated, Eq. or Eqs in the plural
— the International System of Units (SI) should be used.

Authors are liable for the cost of alteration in the *proofs*. It is, therefore, the responsibility of the author to check the text for errors of facts before submitting the paper for publication.

3. *References* are accepted only in the Harvard system. Citations in the text should be as:

. . . (Bomford 1971) . . . or Bomford (1971)

. . . (Brosche and Sündermann 1976) . . .

. . . (Gibbs et al. 1976b) . . .

The list of references should contain names and initials of all authors (the abbreviation et al. is not accepted here); for *journal articles* year of publication, the title of the paper, title of the journal abbreviated, volume number, first and last page.

For *books* or *chapters in books*, the title is followed by the publisher and place of publication.

All items must appear both in the text and references.

Examples:

Bomford G 1971: Geodesy. Clarendon Press, Oxford

Brosche P, Sündermann J 1976: Effects of oceanic tides on the rotation of the earth. Manuscript. Univ. of Bonn

Buntebarth G 1976: Temperature calculations on the Hungarian seismic profile-section NP-2. In: *Geoelectric and Geothermal Studies (East-Central Europe, Soviet Asia), KAPG Geophysical Monograph.* Akadémiai Kiadó, Budapest, 561–566.

Gibbs N E, Poole W G, Stockmeyer P K 1976a: An algorithm for reducing the bandwidth and profile of a sparse matrix. *SIAM J. Number. Anal.*, 13, 236–250.

Gibbs N E, Poole W G, Stockmeyer P K 1976b: A comparison of several bandwidth and profile reduction algorithms. *ACM Trans. on Math. Software,* 2, 322–330.

Szarka L 1980: Potenciáltérképezés analóg modellezéssel (Analogue modeling of potential mapping). *Magyar Geofizika,* 21, 193–200.

4. *Footnotes* should be typed on separate sheets.

5. *Legends* should be short and clear. The place of the tables and figures should be indicated in the text, on the margin.

6. *Tables* should be numbered serially with Roman numerals. Vertical lines are not used.

All the illustrations should contain the figure number and author's name in pencil on the reverse.

Figures will be redrawn. Therefore the most important point is clearness of the figures, even pencil-drawings are accepted (with a duplicate).

Photographs and *half-tone* illustrations should be sharp and well contrasted.

If a specific reduction or enlargement is required, please indicate this in blue pencil on the figure.

The editors will send information to the first author about the *arrival* and acceptance of the papers. A galley proof is also sent to the first author for *correction*. Hundred *offprints* are supplied free of charge.

Periodicals of the Hungarian Academy of Sciences are obtainable at the following addresses:

AUSTRALIA
C.B.D. LIBRARY AND SUBSCRIPTION SERVICE
Box 4886, G.P.O., *Sydney N.S.W. 2001*
COSMOS BOOKSHOP, 145 Ackland Street
St. Kilda (Melbourne), Victoria 3182

AUSTRIA
GLOBUS, Höchstädtplatz 3, *1206 Wien XX*

BELGIUM
OFFICE INTERNATIONAL DE LIBRAIRIE
30 Avenue Marnix, *1050 Bruxelles*
LIBRAIRIE DU MONDE ENTIER
162 rue du Midi, *1000 Bruxelles*

BULGARIA
HEMUS, Bulvar Ruszki 6, *Sofia*

CANADA
PANNONIA BOOKS, P.O. Box 1017
Postal Station "**B**", *Toronto, Ontario M5T 2T8*

CHINA
CNPICOR, Periodical Department, P.O. Box 50
Peking

CZECHOSLOVAKIA
MAD'ARSKÁ KULTURA, Národní třida 22
115 66 Praha
PNS DOVOZ TISKU, Vinohradská 46, *Praha 2*
PNS DOVOZ TLAČE, *Bratislava 2*

DENMARK
EJNAR MUNKSGAARD, Norregade 6
1165 Copenhagen K

FEDERAL REPUBLIC OF GERMANY
KUNST UND WISSEN ERICH BIEBER
Postfach 46, *7000 Stuttgart 1*

FINLAND
AKATEEMINEN KIRJAKAUPPA, P.O. Box 128 *SF- 00101 Helsinki 10*

FRANCE
DAWSON-FRANCE S. A., B. P. 40, *91121 Palaiseau*
EUROPÉRIODIQUES S. A., 31 Avenue de Versailles, *78170 La Celle St. Cloud*
OFFICE INTERNATIONAL DE DOCUMENTATION ET LIBRAIRIE, 48 rue Gay-Lussac
75240 Paris Cedex 05

GERMAN DEMOCRATIC REPUBLIC
HAUS DER UNGARISCHEN KULTUR
Karl Liebknecht-Straße 9, *DDR-102 Berlin*
DEUTSCHE POST ZEITUNGSVERTRIEBSAMT Straße der Pariser Kommüne 3–4, *DDR-104 Berlin*

GREAT BRITAIN
BLACKWELL'S PERIODICALS DIVISION
Hythe Bridge Street, *Oxford OXI 2ET*
BUMPUS, HALDANE AND MAXWELL LTD.
Cowper Works, *Olney, Bucks MK46 4BN*
COLLET'S HOLDINGS LTD., Denington Estate *Wellingborough, Northants NN8 2QT*
WM. DAWSON AND SONS LTD., Cannon House *Folkstone, Kent CT19 5EE*
H. K. LEWIS AND CO., 136 Gower Street
London WCIE 6BS

GREECE
KOSTARAKIS BROTHERS INTERNATIONAL BOOKSELLERS, 2 Hippokratous Street, *Athens-143*

HOLLAND
MEULENHOFF-BRUNA B. V., Beulingstraat 2, *Amsterdam*
MARTINUS NIJHOFF B.V.
Lange Voorhout 9–11, *Den Haag*
SWETS SUBSCRIPTION SERVICE
347b Heereweg, *Lisse*

INDIA
ALLIED PUBLISHING PRIVATE LTD., 13/14
Asaf Ali Road, *New Delhi 110001*
150 B-6 Mount Road, *Madras 600002*
INTERNATIONAL BOOK HOUSE PVT. LTD.
Madame Cama Road, *Bombay 400039*
THE STATE TRADING CORPORATION OF INDIA LTD., Books Import Division, Chandralok 36 Janpath, *New Delhi 110001*

ITALY
INTERSCIENTIA, Via Mazzé 28, *10149 Torino*
LIBRERIA COMMISSIONARIA SANSONI, Via Lamarmora 45, *50121 Firenze*
SANTO VANASIA, Via M. Macchi 58
20124 Milano
D. E. A., Via Lima 28, *00198 Roma*

JAPAN
KINOKUNIYA BOOK-STORE CO. LTD.
17-7 Shinjuku 3 chome, Shinjuku-ku, *Tokyo 160-91*
MARUZEN COMPANY LTD., Book Department, P.O. Box 5050 Tokyo International, *Tokyo 100-31*
NAUKA LTD. IMPORT DEPARTMENT
2-30-19 Minami Ikebukuro, Toshima-ku, *Tokyo 171*

KOREA
CHULPANMUL, *Phenjan*

NORWAY
TANUM-TIDSKRIFT-SENTRALEN A.S., Karl Johansgatan 41–43, *1000 Oslo*

POLAND
WĘGIERSKI INSTYTUT KULTURY, Marszalkowska 80, *00-517 Warszawa*
CKP-I W, ul. Towarowa 28, *00-958 Warszawa*

ROUMANIA
D. E. P., *Bucuresti*
ILEXIM, Calea Grivitei 64–66, *Bucuresti*

SOVIET UNION
SOJUZPECHAT — IMPORT, *Moscow*
and the post offices in each town
MEZHDUNARODNAYA KNIGA, *Moscow G-200*

SPAIN
DIAZ DE SANTOS, Lagasca 95, *Madrid 6*

SWEDEN
GUMPERTS UNIVERSITETSBOKHANDEL AB
Box 346, *401 25 Göteborg 1*

SWITZERLAND
KARGER LIBRI AG, Petersgraben 31, *4011 Basel*

USA
EBSCO SUBSCRIPTION SERVICES
P.O. Box 1943, *Birmingham, Alabama 35201*
F. W. FAXON COMPANY, INC.
15 Southwest Park, *Westwood Mass. 02090*
READ-MORE PUBLICATIONS, INC.
140 Cedar Street, *New York, N. Y. 10006*

YUGOSLAVIA
JUGOSLOVENSKA KNJIGA, Terazije 27, *Beograd*
FORUM, Vojvode Mišića 1, *21000 Novi Sad*

Index: 26.031

FORMERLY ACTA GEODAETICA, GEOPHYSICA ET MONTANISTICA ACADEMIAE SCIENTIARUM HUNGARICAE

Acta Geodaetica, Geophysica et Montanistica Hungarica

VOLUME 18, NUMBER 4, 1983

1828

Akadémiai Kiadó, Budapest

AGGM 18 (4) 337-516 (1983) HU ISSN 0374-1842

ACTA GEODAETICA, GEOPHYSICA et MONTANISTICA HUNGARICA
A Quarterly Journal of the Hungarian Academy of Sciences

Acta Geodaetica, Geophysica et Montanistica (AGGM) publishes original reports on geodesy, geophysics and minings in English.

AGGM is published in yearly volumes of four numbers by

AKADÉMIAI KIADÓ
Publishing House of the Hungarian Academy of Sciences
H-1054 Budapest, Alkotmány u. 21.

Manuscripts and editorial correspondence should be addressed to

AGGM Editorial Office
H-9401 Sopron P.O. Box 5

Subscription information

Orders should be addressed to

KULTURA Foreign Trading Company
H-1389 Budapest P.O. Box 149

INSTRUCTIONS TO AUTHORS

Manuscripts should be sent to the editors (MTA Geodéziai és Geofizikai Kutató Intézete, AGGM Editorial Office, H-9401 Sopron, P.O.Box 5, HUNGARY). Only articles not submitted for publication elsewhere are accepted.

Manuscripts should be typewritten in duplicate, double-spaced, 25 lines with 50 letters each. The papers generally include the following components, which should be presented in the order listed.
1. Title, name of author(s), affiliation, dateline, abstract, keywords
2. Text, acknowledgements
3. References
4. Footnotes
5. Legends
6. Tables and illustrations

1. The *affiliation* should be as concise as possible and should include the complete mailing address of the authors. The *date of receipt* of the manuscript will be supplied by the editors. The abstract should not exceed 250 words and should clearly and simply summarize the most important methods and results. 5–10 significant expressions describing the content are used as *keywords*. Authors may recommend these keywords.

2. The *text* should be generally in English and as short and clear as possible. From Hungarian authors papers are also accepted in Hungarian.

The section heading should *not* be underlined or in capitals.

Please note that underlining denotes special types:
— single underlining: italics
— double underlining: bold-face roman

CONTENTS

Book reviews

Acta Geodaet., Geophys. et Montanist. Hung. Volume 18 (4), pp. 337—347 (1983)

ADJUSTMENT OF LONG EXTENDED TRAVERSE NETS COMBINED WITH ORIENTATION MEASUREMENTS BY GYROTHEODOLITES

H ABDELHAMID KAMAL[1]

[Manuscript received September 20, 1981]

The paper presents a compact solution of a network of traverses combined with the calibration of, and azimuth measurements by a gyrotheodolite used for the orientation purposes. The proposed adjustment model is rigorous, based on the least squares principle incorporating the measurements and the instrument constant of the gyrotheodolite as well as the available control points in the surveyed area.

The described method provides a simple solution for the problem of horizontal control densification by using rapid orientation by gyrotheodolites and combining its measurements with the traverse network in one adjustment model. The technique of the method requires to establish a system of elementary traverse chains, linked to each other by junction points (nodal points), and at the same time, the elementary traverses are also joined to the existing control points (fixed coordinates).

The coordinates of the nodal points of the elementary traverses are calculated in advance from the measurements as approximate coordinates, their variations as well as the corrections for the measurements are then calculated using the adjustment model, thus new control points (the nodal points) are obtained. In this method the volume of adjusting calculations is reduced in a great extent, because the coordinates of the intermediate points of the elementary traverses are not included in the adjustment model. Finally, the coordinates of these intermediate points are to be calculated from the adjusted measurements using the obtained new control points and the original ones.

Keywords: adjustment of traverse nets; gyrotheodolite orientation; long traverse nets; nodal points

Introduction

The paper presents a least squares adjustment for traverse networks combined with gyrotheodolite calibration and azimuth measurement. The gyrotheodolite is used here to provide azimuths for the intermediate orientation of some of the traverse sides. The calibration results obtained from the control stations (the instrument constant) are included in the model. The gyro-azimuth data of the oriented lines are also included in the adjustment model: namely the gyro-north values N and the geodetic sighting to the oriented line I (read on the horizontal circle limb of the theodolite).

The proposed adjustment is applicable when surveying long extended areas as e.g. the area along the Nile valley in Egypt. The solution of the adjustment yields coordinates for new points (nodal points of the net) which can later be used as a basic

[1] Banha University, Faculty of Engineering, Shobra, Shobra Street, 108, Cairo, Egypt

points to establish the main skeleton of lower order traverses for cadastral or agricultural mapping. The specifications to be followed in such traverse nets are given by Mueller and Ramsayer (1979).

In the adjustment, the traverse network is regarded as a system of elementary traverses which are linked together with common points (nodal points), the elementary traverses are also connected to the control points present in the surveyed area. The adjustment and solution of the network are carried out in two main steps, the first is calculating approximate values for the coordinates of the nodal points, then their variations as well as corrections for the traverse and orientation measurements (lengths of the traverse sides, subtended angles, gyro-orientation measurements and the instrument constant) are calculated after solving the proposed adjustment model, thus we obtain the adjusted observations and the coordinates of the nodal points with their covariances. The second step is to use the results of the first step and the coordinates of the original controls to calculate the coordinates of the intermediate points of the elementary traverses.

The proposed solution is rigorous in the treatment of the traverse measurements, the gyro-orientation observations as well as the coordinates of the fixed higher order control points, at the same time, it is a flexible mathematical model; it can easily accommodate triangulation and trilateration observation nets which form in most cases an organic part of the network.

The proposed method reduces the volume of the preliminary manual calculations as well as the adjusting calculations themselves because the coordinates of the intermediate points of the elementary traverses are not included in the model.

In the adjustment model, there are three condition equations for each elementary traverse, one angle condition and two coordinate conditions. The start and the end points of the whole traverse network are preferably fixed points (controls). In such a case when composing the coordinate conditions for the chain in which they occur, the corresponding variations will be zero and a variation will be taken into account only for the nodal point.

The computational procedures can be programmed easily. The program section which calculates the preliminary values of the coordinates of the nodal points can also be used (after the adjustment) in the calculation of the adjusted coordinates of the intermediate points of the elementary traverses.

Observations and measurements

Figure 1 shows an elementary traverse of a traverse network. It consists of n points, the first, point 1 is fixed (control point) having the coordinates (X_1, Y_1) while the last one, point n is a nodal point by which the first traverse chain is jointed to the other chains. Point n may also be a control point as the first point; in the proposed adjusting model it is not necessary for each elementary traverse to begin and to end with control points, but the first and end points of the whole network are preferably control points.

Each elementary traverse consists of $n-1$ measured distances, $n-1$ measured interior angles, and $n-2$ intermediate points whose coordinates are required. At both

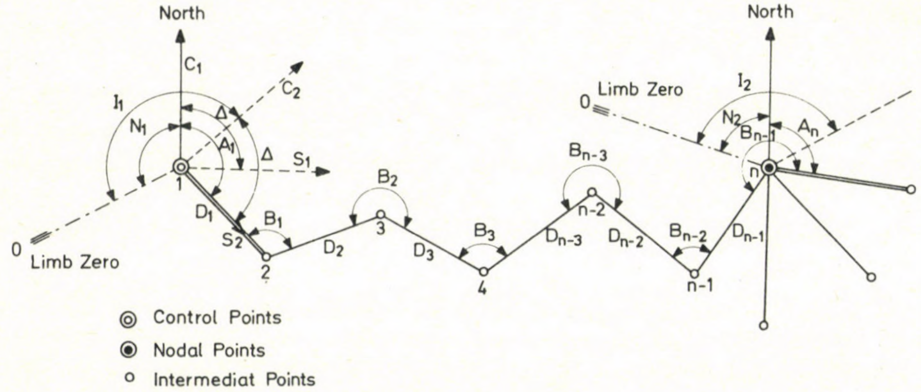

Fig. 1

nodal points, gyrotheodolite observations are made for the determination of the azimuth of the first leg of each elementary traverse, the angles at the nodal points (connecting the elementary traverses) are also measured. In this case each elementary traverse is considered to be oriented at both ends. The gyrotheodolite orientations made at the nodal points and the control points include the determination of the gyro-north N and the geodetic sights I. As shown in Fig. 1, during the gyro-measurements at point 1 and other nodal and control points, the direction of the autocollimator axis is denoted by $C1$, i.e., to the north as it is customary in gyrotheodolite observations, while the direction of the line of sight is $S1$. In this position the gyro-north $N1$ is determined after applying the torsion corrections, then the telescope is turned towards point 2, the new direction of the sight line will be $S2$ and that of the autocollimator axis will be $C2$ preserving the angle (the instrument constant) between them. The horizontal circle reading I_1 is then recorded. The instrument constant can be obtained from the calibration measurements made using more calibration (control) directions which are present in the surveyed area (lines joining the control points). The azimuths of these directions are calculated from the fixed coordinates of the control points after correcting them for the meridian convergence. For the determination of the meridian convergence at any measuring station in Egypt, a simple method is described by Abdelhamid and Szádeczky (1982) being suitable for the rapid determination of the meridian convergence exact to the nearest 0.1″ in field in a few minutes using small a pocket calculator.

The mathematical model of the elementary traverse

The model of the elementary traverse involving all the measured quantities is expressed by two coordinate and one angle condition equations as follows:

$$\left(A_1 + \sum_{i=1}^{n-1} B_i - (n-2)\pi - A_n\right) - K(2\pi) = 0 \tag{1}$$

$$X_1 + \sum_{i=1}^{n-1} D_i \cos A_i - X_n = 0 \tag{2}$$

$$Y_1 + \sum_{i=1}^{n-1} D_i \sin A_i - Y_n = 0 \tag{3}$$

where

X_1, Y_1 = coordinates of the first (control) point,
X_n, Y_n = coordinates of the last (nodal) point,
$D_1, D_2, \ldots D_{n-1}$ = measured lengths of the traverse legs,
$B_1, B_2, \ldots B_{n-1}$ = observed interior angles,
A_i = calculated azimuths of the intermediate traverse legs,
A_1, A_n = gyro-azimuths observed at the terminal stations,
$K = 1$, if the term in brackets (Eq. 3) is more than 2π, and
$K = 0$ if it is less than 2π.

The gyro-azimuths used in Eq. (1) and azimuths of the intermediate lines are calculated as follows:

$$A_1 = I_1 - N_1 + \Delta \qquad \text{(gyro-azimuth)} \tag{4}$$

$$A_n = I_2 - N_2 + \Delta \qquad \text{(gyro-azimuth)} \tag{5}$$

$$A_i = I_1 - N_1 + \Delta + \sum_{j=1}^{i-1} B_j - (i-1)\pi \tag{6}$$

where $i = (2, 3, \ldots n-1)$.

The coordinates to the intermediate points (2 to $n-1$) are not included in the mathematical model, what in turn reduces the size of the matrices involved in the adjustment and the volume of computations.

In order to proceed with linearization of the model we divide the involved quantities in Eqs (1–3) into measured and unknown quantities as follows:

$$(\mathbf{L})^{\mathrm{T}} = (N_1 I_1 B_1 B_2 \ldots B_{n-1} D_1 D_2 \ldots D_{n-1} N_2 I_2),$$

(measurements), and

$$(\mathbf{X}_0)^{\mathrm{T}} = (X_1 Y_1 X_n Y_n) \quad \text{(unknowns)}.$$

The three scalar equations (1–3) of the model can be written in a matrix form as follows:

$$\mathrm{F}(\mathbf{U}, \mathbf{X}) = 0\,. \tag{7}$$

The two sets are related through the respective corrections as follows:

$$\mathbf{U}=\mathbf{L}+\mathbf{V}, \tag{8}$$

$$\mathbf{X}=\mathbf{X}_0+\mathbf{x} \tag{9}$$

where $\mathbf{U}$ and $\mathbf{X}$ represent the adjusted values of the observations and the unknowns respectively, $\mathbf{V}$ = the vector of the residuals or corrections and $\mathbf{x}$ = the vector of the variations of the unknowns, $\mathbf{x}^{\mathrm{T}}=(x_1 y_1 x_n y_n)$.

Linearization of the mathematical model

The linearization of the model was carried out with the assumption that vectors of the residuals and of the variations ($\mathbf{V}$ and $\mathbf{x}$) are composed of small quantities, therefore the linearized form of the mathematical model is as follows:

$$V_{I_1}-V_{N_1}-V_{I_2}+V_{N_2}+V_{B_1}+V_{B_2}\ldots+V_{B_{n-1}}+w_1=0 \tag{10}$$

$$\begin{aligned}
&\cos A_1 V_{D_1}+\cos A_2 V_{D_2}+\ldots+\cos A_{n-1} V_{D_{n-1}}-\\
&-\frac{1}{\rho}\sum_{i=1}^{n-1} D_i \sin A_i V\Delta-\frac{1}{\rho}\sum_{i=1}^{n-1} D_i \sin A_i V_{N_1}-\\
&-\frac{1}{\rho}\sum_{i=1}^{n-1} D_i \sin A_i V_{I_1}-\frac{1}{\rho}\sum_{i=2}^{n-1} D_i \sin A_i V_{B_1}-\\
&-\frac{1}{\rho}\sum_{i=3}^{n-1} D_i \sin A_i V_{B_2}\ldots-\frac{1}{\rho} D_{n-1}\sin A_{n-1} V_{B_{n-2}}-\\
&-x_n+w_2=0.
\end{aligned} \tag{11}$$

$$\begin{aligned}
&\sin A_1 V_{D_1}+\sin A_2 V_{D_2}+\ldots+\sin A_{n-1} V_{D_{n-1}}+\\
&+\frac{1}{\rho}\sum_{i=1}^{n-1} D_i \cos A_i V\Delta-\frac{1}{\rho}\sum_{i=1}^{n-1} D_i \cos A_i V_{N_1}+\\
&+\frac{1}{\rho}\sum_{i=1}^{n-1} D_i \cos A_i V_{I_1}+\frac{1}{\rho}\sum_{i=2}^{n-1} D_i \cos A_i V_{B_1}+\\
&+\frac{1}{\rho}\sum_{i=3}^{n-1} D_i \cos A_i V_{B_2}\ldots+\frac{1}{\rho} D_{n-1}\cos A_{n-1} V_{B_{n-2}}-\\
&-y_n+w_3=0
\end{aligned} \tag{12}$$

where the misclosures w_1, w_2, w_3 are:

$$w_1=I_1-N_1-I_2+N_2+\sum_{i=1}^{n-1} B_i-(n-1)\pi-K(2\pi), \tag{13}$$

$$w_2 = \sum_{i=1}^{n-1} D_i \cos A_i + X_1 - X_n \tag{14}$$

$$w_3 = \sum_{i=1}^{n-1} D_i \sin A_i + Y_1 - Y_n. \tag{15}$$

From Eqs (10–12) the matrix form of the linearized model is

$$\underset{(r,m)}{\mathbf{B}^{\mathrm{T}}} \underset{(m,1)}{\mathbf{V}} + \underset{(r,g)}{\mathbf{C}^{\mathrm{T}}} \underset{(g,1)}{\mathbf{x}} + \underset{(r,1)}{\mathbf{W}} = 0 \tag{16}$$

where

$\mathbf{C}^{\mathrm{T}}$ = coefficient matrix of the variations,
$\mathbf{B}^{\mathrm{T}}$ = coefficient matrix of the residuals,
$\mathbf{W}$ = vector of misclosures (absolute terms),
r = number of the conditions,
m = number of the observations, and
g = number of the unknowns.

Matrices **C** and **B** can be written in the following schemes from Eqs (10–12):

$$\begin{array}{cc} x_n & y_n \end{array}$$
$$\mathbf{C}^{\mathrm{T}} = \begin{pmatrix} 0 & 0 \\ -1 & 0 \\ 0 & -1 \end{pmatrix} \tag{17}$$

In this case no corrections are applied to X_1, Y_1 as they are fixed, but if both the terminal points of the elementary traverse are nodal points (and not controls), then their approximate coordinates will have variations (x_1, y_1) and (x_n, y_n) therefore matrix **C** will be:

$$\begin{array}{cccc} x_1 & y_1 & x_n & y_n \end{array}$$
$$\mathbf{C}^{\mathrm{T}} = \begin{pmatrix} 0 & 0 & 0 & 0 \\ 1 & 0 & -1 & 0 \\ 0 & 1 & 0 & -1 \end{pmatrix}. \tag{18}$$

At the last chain of the elementary traverses, if the first terminal point is a nodal point and the last one is a control point, then matrix **C** will be:

$$\begin{array}{cc} x_1 & y_1 \end{array}$$
$$\mathbf{C}^{\mathrm{T}} = \begin{pmatrix} 0 & 0 \\ 1 & 0 \\ 0 & 1 \end{pmatrix}. \tag{19}$$

And matrix **B** is in Eq. (20):

$$
\mathbf{B}_T=\begin{array}{c}
\begin{matrix} N_1 & I_1 & B_1 & B_2 \ldots & \ldots B_{n-2} & B_{n-1} & D_1 & D_2 \ldots & D_{n-1} & N_2 & I_2 & \Delta \end{matrix}\\
\begin{pmatrix}
-1 & 1 & 1 & 1 & 1 & 1 & 0 & 0 & 0 & 1 & -1 & 0\\
-\frac{1}{\rho}\sum_{i=1}^{n-1} D_i \sin A_i & -\frac{1}{\rho}\sum_{i=1}^{n-1} D_i \sin A_i & -\frac{1}{\rho}\sum_{i=2}^{n-1} D_i \sin A_i & -\frac{1}{\rho}\sum_{i=3}^{n-1} D_i \sin A_i & -\frac{1}{\rho} D_{n-1} \sin A_{n-1} & 0 & \cos A_1 & \cos A_2 & \cos A_{n-1} & 0 & 0 & -\frac{1}{\rho}\sum_{i=1}^{n-1} D_i \sin A_i\\
\frac{1}{\rho}\sum_{i=1}^{n-1} D_i \cos A_i & \frac{1}{\rho}\sum_{i=1}^{n-1} D_i \cos A_i & \frac{1}{\rho}\sum_{i=2}^{n-1} D_i \cos A_i & \frac{1}{\rho}\sum_{i=3}^{n-1} D_i \cos A_i & \frac{1}{\rho} D_{n-1} \cos A_{n-1} & 0 & \sin A_1 & \sin A_2 & \sin A_{n-1} & 0 & 0 & \frac{1}{\rho}\sum_{i=1}^{n-1} D_i \cos A_i
\end{pmatrix}
\end{array}
\qquad (20)
$$

The elements of the vector of the misclosures are found in Eqs (13–15).

The matrices **C**, **B** and the vector **W** are to be formed for each elementary traverse of the entire network including the observations and the approximate values of the unknowns in the same manner as described before. The connection of the linearized models of the elementary traverses, composing the entire network, is achieved through the common unknowns. It should be noted that the higher order control points existing in the network are treated as fixed points what provides constraints in the mathematical model. Finally the complete set of the linearized mathematical models is organized as a superposition, taking care to place the terms of the matrices **C** into the appropriate columns to get an overlap due to the common unknowns.

The above mentioned connection is also achieved through the gyrotheodolite constant which appears as a common value in all gyro-azimuths of the whole network, and increases the accuracy of azimuth results, where the instrument can be calibrated several times alternatively with azimuth measurements making use of azimuths of the control directions present in the surveyed area.

Solution of the traverse network system

Having integrated the linearized mathematical models of the elementary traverses of the entire network, a complete set of the linearized models is obtained. For simplicity, the same notations as described in Eq. (16) will be used for the integrated mathematical model. According to the least squares principles, this is solved considering it as a combination of two simple types of adjustment; an adjustment of indirect measurements with independent unknowns, and an adjustment of direct measurements with conditions. Therefore the method of the Lagrange multiplicator is used as follows:

$$\mathbf{V}^{\mathrm{T}}\mathbf{P}\mathbf{V}-2\mathbf{K}^{\mathrm{T}}(\mathbf{B}^{\mathrm{T}}\mathbf{V}+\mathbf{C}^{\mathrm{T}}\mathbf{x}+\mathbf{W})=\min \tag{21}$$

where

$\mathbf{K}^{\mathrm{T}}$ is the vector of unknown correlates and

$\mathbf{P}$ is the weight matrix of the observations.

The solution of Eq. (21) (Detrekői 1977) yields the vector of residuals **V** and a system of normal equations as follows:

$$\mathbf{V}=\mathbf{P}^{-1}\mathbf{B}\mathbf{K} \tag{22}$$

and

$$\begin{bmatrix} \underset{(r,r)}{(\mathbf{B}^{\mathrm{T}}\mathbf{P}^{-1}\mathbf{B})} & \underset{(r,g)}{\mathbf{C}^{\mathrm{T}}} \\ \underset{(g,r)}{\mathbf{C}} & 0 \end{bmatrix} \begin{bmatrix} \underset{(r,1)}{\mathbf{K}} \\ \underset{(g,1)}{\mathbf{x}} \end{bmatrix} + \begin{bmatrix} \underset{(r,1)}{\mathbf{W}} \\ 0 \end{bmatrix} = 0. \tag{23}$$

Solving this system of normal equations we get the vectors of the correlates and the variations, **K** and **x**. Then substituting for **K** in Eq. (22), we obtain the vector of the residuals (corrections for the observed quantities). Thus the adjusted values of the measurements and the unknowns are calculated according to Eqs (8–9).

The calculations are then checked, first, by substituting the obtained results of **U** and **X** in the original conditions which must to be fulfilled, secondly, by calculating $\mathbf{V}^T\mathbf{P}\mathbf{V}$ and $\mathbf{K}^T\mathbf{W}$ which must fulfil the following

$$\mathbf{V}^T\mathbf{P}\mathbf{V} = -\mathbf{K}^T\mathbf{W}. \tag{24}$$

The mean square error of the unit weight of the adjusted unknowns is calculated as follows:

$$\mu_0^2 = \frac{\mathbf{V}^T\mathbf{P}\mathbf{V}}{f} \tag{25}$$

where $f = r - g$ = number of the redundant observations. To calculate the mean square error for the adjusted values of the unknowns, first we calculate the weight coefficient matrix of the adjusted unknowns, $\mathbf{Q}_{(x)}$,

$$\mathbf{Q}_{(x)} = (\mathbf{C}\mathbf{N}^{-1}\mathbf{C}^T)^{-1} \tag{26}$$

where

$$\mathbf{N}^{-1} = (\mathbf{B}^T\mathbf{P}^{-1}\mathbf{B})^{-1}.$$

Finally, the mean square errors matrix **M** of the unknowns is as follows:

$$\mathbf{M} = \mu_0^2\mathbf{Q}_{(x)}. \tag{27}$$

Solution of the individual elementary traverses

The coordinates of the intermediate points of elementary traverses are then calculated from the coordinates of the nodal points (which are held fixed after the first adjustment) using the adjusted distances, angles, and gyro-azimuths as follows:

i. Azimuths calculations

a) The adjusted gyro-azimuths at the nodal points are calculated according to Eqs (4–5) using the adjusted values of I, N and Δ. As I, N and Δ are independent quantities, therefore the mean square error of the gyro-azimuth is:

$$\mu_{A_i}^2 = \mu_{I_i}^2 + \mu_{N_i}^2 + \mu^2\Delta, \qquad i = 1, n \tag{28}$$

b) Azimuths of the intermediate lines:

These azimuths are calculated as in Eq. (6) using the adjusted gyro-azimuths and angles, and their mean square error is,

$$\mu_{A_i}^2 = \mu_{A_1}^2 + (i-1)\mu_B^2. \tag{29}$$

ii. The coordinates of the intermediate points: using the adjusted azimuths and distances, the coordinates of the intermediate points are,

$$X_i = X_1 + \sum_{j=1}^{i-1} \Delta X_j \tag{30}$$

$$Y_i = Y_1 + \sum_{j=1}^{i-1} \Delta Y_j \tag{31}$$

where

ΔX_j, $\Delta Y_j = X$ and Y components of the traverse legs calculated as follows:

$$\Delta X_j = D_j \cos A_j$$

$$\Delta Y_j = D_j \sin A_j$$

X_1, Y_1 = coordinates of the start point (nodal or control).

The mean square errors of the calculated coordinates are as follows:

$$\mu^2_{X_i} = \mu^2_{X_1} + \sum_{j=1}^{i-1} \left(\frac{\Delta X_j}{D_j}\right)^2 \mu^2 D_j + \sum_{j=1}^{i-1} \left(\frac{\Delta Y_j}{\rho}\right)^2 \mu^2 A_j \tag{32}$$

$$\mu^2_{Y_i} = \mu^2_{Y_1} + \sum_{j=1}^{i-1} \left(\frac{\Delta Y_j}{D_j}\right)^2 \mu^2_{D_j} + \sum_{j=1}^{i-1} \left(\frac{\Delta X_j}{\rho}\right)^2 \mu^2_{A_j} \tag{33}$$

where

D_j = adjusted lengths of the traverse sides,
A_j = calculated azimuths using the adjusted angles,
$i = (2, 3, \ldots n-1)$, and
n = number of points of the elementary traverse.

Conclusion

The development of high accuracy gyrotheodolites and of electro-optical distance measuring instruments and the availability of digital computers made it possible to use traverses in the establishment of geodetic control of various degrees of accuracy especially for narrow, extended areas, as the Nile valley in Egypt. The paper presents a method for the adjustment of such traverse networks oriented with the help of gyrotheodolites. The combination of the gyrotheodolite observations and calibration data in one adjusting model, as described in the paper, enables to survey large areas in shorter time where the orientation of the network can be achieved quickly with high accuracy at all the nodal points of the elementary traverses constituting the whole network, independently from the weather conditions. Furthermore, as only the coordinates of the nodal points are present in the model and the coordinates of all other points of the net are absent more control points are enabled whose coordinates can be used later in the calculation of the coordinates of intermediate points in the network. This is useful for providing a solution for the densification problem of horizontal controls and for the establishment of the main skeletons for extended traverses used for the cadastral or agricultural mapping purposes. In the proposed solution, the calibration of the instrument can be repeated several times making use of the original control directions present in the surveyed area (lines joining the original fixed control points) what enables a periodical control for the gyrotheodolite and provides a reliable value for the instrument constant which in turn affects greatly the results of the gyro-azimuths.

References

Abdelhamid Kamal H, Szádeczky-Kardoss Gy 1983: Simple determination of the convergence of the meridians for the area of Egypt. *Acta Geod. Geoph. Mont. Hung.* 18, 59–66.

Bomford G 1971: Geodesy (3rd ed.). Clarendon Press, Oxford.

Detrekői Á 1977: Adjusting calculations (in Hungarian). Tankönyvkiadó, Budapest.

Hazay L 1976: Adjustment calculation in surveying. Akadémiai Kiadó, Budapest.

Hirvonen R A 1971: Adjustment by least squares in geodesy and photogrammetry. New York.

Mikhail E M 1976: Observations and least squares. IEP-A Dun-Donnelley publisher, New York.

Mueller I I, Ramsayer K H 1979: Introduction to Surveying. Frederick Ungar Publishing Co., New York.

Acta Geodaet., Geophys. et Montanist. Hung. Volume 18 (4), pp. 349—357 (1983)

ADJUSTMENT OF THE CALIBRATION MEASUREMENTS OF GYROTHEODOLITES

H ABDELHAMID KAMAL[1]

[Manuscript received January 5, 1982]

The paper presents a simple formula for calculating the gyrotheodolite constant from the calibration measurements made in control stations. The formula is derived by applying the principles of least squares adjustment. The mathematical model used in the adjustment consists of two simple adjustment types, which contain measured and unknown quantities. The proposed formula is valid for an arbitrary number of independent calibration measurements by gyrotheodolites or by gyro-attachements.

Keywords: adjustment of calibration; adjustment of gyrotheodolite, calibration of gyro-theodolites; gyrotheodolites

Introduction

In the calibration of gyrotheodolites or gyroattachements, the basic parameter to be determined is the instrument constant, being considered as a main term in the basic formula when calculating gyro-azimuths determined with gyrotheodolites or gyroattachements, therefore a reliable value for the instrument constant is required in order to obtain reliable gyro-azimuths. At calibration stations it is costumary to run more measurements with independent starts, the lowest allowable number of these measurements being 2. For higher order geodetic works, more calibration measurements are needed to get a value for the instrument constant accurate enough for these works; the number of the independent measurements in these cases may reach 6 or 8.

Similarly in case of newly manufactured instruments, several calibration measuring sets are made. The sets may also be repeated several days in order to determine the value of the instrument constant to be included into the description of the new instrument.

In the present paper a simple formula is derived for calculating an adjusted value for the instrument constant from the calibration measurements. The formula is valid for any number of independent measurements, and for any category of gyro-orientation instruments (gyrotheodolites or gyroattachements). The mathematical model used in the adjustment is rigorous, based on the principle of least squares in treating both the measurements and the unknown quantities; it is a combination of two simple adjustment types (adjustment of indirect measurements with independent

[1] Banha University, Faculty of Engineering, Shobra, Shobra Street, 108, Cairo, Egypt

unknowns, and adjustment of direct measurements with conditions), where the model contains measurements and unknowns. The limb reading of the horizontal circle of the theodolite when sighting the control direction and the torsion-free gyro-north are the measured quantities in the model, while the instrument constant is the unknown quantity. An approximate value for this unknown was used in the model, this value is 90° or 00° depending on the type of the instrument to be calibrated, e.g. for gyrotheodolites of the types MOM Gi-B1 or Gi-B2, the approximate value for the constant is 90°, while for gyroattachements type WILD, ARK1 and GAK1 or type MOM Gi-C and Gi-D, the value used is 00°.

The calculated variation for the approximate value of the constant obtained from the adjustment is independent from the weights of the measurements. The corrections for the measurements are also calculated in the same model with simple formulae.

The mathematical model used in the adjustment

The general formula of calculating the gyro-azimuth (Halmos 1977) is

$$A=I-N+\Delta \tag{1}$$

where

A = the required azimuth of the sighted reference object,

I = the horizontal circle reading corresponding to the geodetic sighting to the reference object,

N = the torsion-free gyro-north, and

Δ = the instrument constant.

From Eq. (1) the instrument constant Δ can be calculated as follows:

$$\Delta=A-I+N. \tag{2}$$

A is in Eq. (2) the astronomical azimuth of the control direction sighted from the calibration station, being considered as a fixed value in the adjustment.

In the calibration I and N are the measured quantities; several values are obtained both for I and N depending on the number of independent measurements made at the calibration station.

For the instrument constant, an approximate value Δ' is used (Δ' can be 90° or 00°, as mentioned, depending on the type of the gyrotheodolite). In the adjustment, a correction (d) for this approximate value (its variation) is calculated.

According to the number of the calibration measurements, a set of observation equations can be written according to Eq. (2) as follows:

$$\begin{aligned} &I_1 - N_1 + \Delta - A = 0 \\ &I_2 - N_2 + \Delta - A = 0 \\ &\dots\dots\dots\dots\dots\dots\dots \\ &\dots\dots\dots\dots\dots\dots\dots \\ &I_n - N_n + \Delta - A = 0 \end{aligned} \tag{3}$$

where n is the number of the independent calibration measurements.

The quantities involved in the model (3) are subdivided into measurements and unknowns as follows:

$$(\mathbf{L})^{\mathrm{T}} = (I'_1 N'_1 I'_2 N'_2 \ \dots \ I'_n N'_n) \text{ (measurements), and}$$

$$(X_0) = (\Delta') \text{ (unknowns).}$$

The above scalar equations (3) of the model can be written in the following form:

$$F(\mathbf{U}, \mathbf{X}) = 0. \tag{4}$$

The two sets **U** and **X** are related through the respective corrections as follows:

$$\mathbf{U} = \mathbf{L} + \mathbf{V} \tag{5}$$

$$\mathbf{X} = \mathbf{X}_0 + \mathbf{x} \tag{6}$$

where **U** and **X** represent the vectors of the adjusted values of the measurements and the unknowns respectively, while **V** and **x** represent the vectors of the residuals and variations, respectively, thus,

$$\begin{aligned} &\mathbf{U}^{\mathrm{T}} = (I_1 N_1 I_2 N_2 \ \dots \ I_n N_n), \\ &\mathbf{X} = (\Delta) \\ &\mathbf{V}^{\mathrm{T}} = (V_{I_1} V_{N_1} V_{I_2} V_{N_2} \ \dots \ V_{I_n} V_{N_n}), \text{ and} \\ &\mathbf{x} = (d). \end{aligned}$$

An approximation of the model is possible with the assumption that the vectors of the residuals and the variations (**V** and **x**) are composed of small quantities, thus, the form of the mathematical model will be,

$$\begin{array}{l} V_{I_1}-V_{N_1}+d+w_1=0 \\ V_{I_2}-V_{N_2}+d+w_2=0 \\ \dots\dots\dots\dots\dots\dots \\ \dots\dots\dots\dots\dots\dots \\ V_{I_n}-V_{N_n}+d+w_n=0 \end{array} \tag{7}$$

where $w_1, w_2 \dots w_n$ are the misclosures. Their values are calculated depending upon the type of the gyrotheodolite as follows:

$$w_i=I_i'N_i'+90^\circ-A \quad \text{or} \tag{8}$$

$$w_i=I_i'-N_i'-A. \tag{9}$$

Equation (8) is used when the instrument to be calibrated is a gyrotheodolite, while Eq. (9) is used in the case of a gyroattachement.

Equation (7) can be written in the following matrix form

$$\begin{pmatrix} 1 & -1 & 0 & 0 & 0 & 0 & 0 & 0 & 0 & 0 \\ 0 & 0 & 1 & -1 & 0 & 0 & 0 & 0 & 0 & 0 \\ \cdot & \cdot & \cdot & \cdot & \cdot & \cdot & \cdot & \cdot & \cdot & \cdot \\ \cdot & \cdot & \cdot & \cdot & \cdot & \cdot & \cdot & \cdot & \cdot & \cdot \\ \cdot & \cdot & \cdot & \cdot & \cdot & \cdot & \cdot & \cdot & \cdot & \cdot \\ 0 & 0 & 0 & 0 & 0 & 0 & 0 & 0 & 1 & -1 \end{pmatrix} \left| \begin{array}{c} V_{I_1} \\ V_{N_1} \\ V_{I_2} \\ V_{N_2} \\ \cdot \\ \cdot \\ \cdot \\ \cdot \\ \cdot \\ \cdot \\ V_{I_n} \\ V_{N_n} \end{array} \right| + \begin{pmatrix} 1 \\ 1 \\ \cdot \\ \cdot \\ \cdot \\ 1 \end{pmatrix}^{(d)} + \begin{pmatrix} w_1 \\ w_2 \\ \cdot \\ \cdot \\ \cdot \\ w_n \end{pmatrix} = 0$$

or

$$\underset{(n,m)}{\mathbf{B}^{\mathrm{T}}} \cdot \underset{(m,1)}{\mathbf{V}} + \underset{(n,g)}{\mathbf{C}^{\mathrm{T}}} \cdot \underset{(g,1)}{\mathbf{x}} + \underset{(n,1)}{\mathbf{W}} = 0 \tag{10}$$

where

$\mathbf{C}^{\mathrm{T}}$ = coefficient vector of the variation,
$\mathbf{B}^{\mathrm{T}}$ = coefficient matrix of the residuals,

$\mathbf{W}$ = vector of the misclosures,

n = number of observation equations (number of the independent calibration measurements),

m = number of the calibration observations, and

g = number of the unknowns (in this case $g = 1$).

According to the least squares principles, the above mathematical model (10) can be solved by considering it as a combination of two simple adjustment types; of an adjustment of indirect measurements with independent unknowns, and an adjustment of direct measurements with conditions. The method of the Lagrange multipliers is applied (Detrekői 1977), and the solution is

$$\mathbf{V} = \mathbf{P}^{-1}\mathbf{B}\mathbf{K} \tag{11}$$

and

$$\begin{bmatrix} \underset{(n,n)}{(\mathbf{B}^T\mathbf{P}^{-1}\mathbf{B})} & \underset{(n,g)}{\mathbf{C}^T} \\ \underset{(g,n)}{\mathbf{C}} & 0 \end{bmatrix} \begin{bmatrix} \underset{(n,1)}{\mathbf{K}} \\ \underset{(g,1)}{\mathbf{x}} \end{bmatrix} + \begin{bmatrix} \underset{(n,1)}{\mathbf{W}} \\ 0 \end{bmatrix} = 0 \tag{12}$$

the diagonal elements of the weight matrix $\mathbf{P}$ are as follows:

$$P_{I_1} P_{N_1} P_{I_2} P_{N_2} \ldots P_{I_n} P_{N_n}. \tag{13}$$

With the assumption that all geodetic sights, Is are observed with the same accuracy (the same theodolite), and all gyro-north values Ns are also observed with the same accuracy (the same gyrotheodolite), therefore,

$$P_{I_1} = P_{I_2} = \ldots = P_{I_n} = P_I, \quad \text{and}$$

$$P_{N_1} = P_{N_2} = \ldots = P_{N_n} = P_N.$$

Solving the system of normal equations (12) we get the vectors $\mathbf{K}$ and $\mathbf{x}$

$$\mathbf{x} = \frac{1}{n}(w_1 + w_2 + w_3 + \ldots w_n) \qquad \text{or} \qquad d = \frac{1}{n}\sum_{i=1}^{n} w_i. \tag{14}$$

It should be noted that (14) gives the value of d independently from the weights of the measurements (P_I and P_N), i.e. they do not affect the calculation of the instrument constant.

The adjusted value of the instrument constant is then calculated according to Eq. (6) as follows:

$$\Delta = \Delta' + \frac{1}{n}\sum_{i=1}^{n} w_i \tag{15}$$

the correlate vector obtained from the solution is:

$$\begin{pmatrix} K_1 \\ K_2 \\ \cdot \\ \cdot \\ K_n \end{pmatrix} = \begin{pmatrix} \frac{P_I P_N}{n(P_I+P_N)}[(n-1)w_1+w_2+\ \ldots\ +w_n] \\ \frac{P_I P_N}{n(P_I+P_N)}[w_1+(n-1)w_2+\ \ldots\ +w_n] \\ \cdots\cdots\cdots\cdots\cdots\cdots \\ \cdots\cdots\cdots\cdots\cdots\cdots \\ \frac{P_I P_N}{n(P_I+P_N)}[w_1+w_2+\ \ldots\ +(n-1)w_n] \end{pmatrix}. \tag{16}$$

According to Eq. (11), the vector of residuals **V** can be obtained using the correlate vector (16). The general formulae for the calculation of the residuals are

$$V_{I_i} = \frac{P_N}{P_I+P_N}[w_0 - w_{(\frac{j+1}{2})}], \qquad (j=1,3,5,\ \ldots\ 2n-1) \tag{17}$$

$$V_{N_i} = \frac{P_I}{P_I+P_N}[w_0 - w_{(\frac{j}{2})}], \qquad (j=2,4,6,\ \ldots\ 2n) \tag{18}$$

where

$$w_0 = \frac{1}{n}\sum_{i=1}^{n} w_i .$$

From Eqs (17), (18) it is clear that the difference $(w_0 - w_i)$ is distributed among V_{I_i} and V_{N_i} according to the ratio P_N/P_I, or

$$\frac{V_{I_i}}{V_{N_i}} = \frac{P_N}{P_I}. \tag{19}$$

This means that depending the weights given to I and N, the correction will be distributed in the same ratio between V_{I_i} and V_{N_i}.

The adjusted values of I and N are then calculated according to Eq. (5).

To calculate the mean square error of the adjusted value of Δ, the value of $[VV]$ is calculated first from Eqs (17) and (18), the mean square error of the unit weight is then as follows:

$$\mu_0^2 = \frac{\mathbf{V}^{\mathrm{T}}\mathbf{P}\mathbf{V}}{f} \tag{20}$$

where $f=n-g$ (number of the redundant observations). The weight coefficient matrix of the adjusted unknown is calculated as follows:

$$\mathbf{Q}_{(x)}=(\mathbf{C}\mathbf{N}^{-1}\mathbf{C}^{\mathrm{T}})^{-1} \tag{21}$$

where $\mathbf{N}=\mathbf{B}^{\mathrm{T}}\mathbf{P}^{-1}\mathbf{B}$.

$\mathbf{Q}_{(x)}$ in this problem is a single value which is as follows:

$$Q_{(x)}=\frac{1}{n}\left(\frac{P_i+P_N}{P_I P_N}\right). \tag{22}$$

Finally μ_Δ is calculated as follows:

$$\mu_\Delta^2=\mu_0^2\cdot Q_{(x)} \qquad \text{or}$$

$$\mu_\Delta=\pm\mu_0\sqrt{\frac{P_I+P_N}{n(P_I P_N)}}. \tag{23}$$

Numerical example

The following example is the calibration results of a MOM Gi-B2 gyrotheodolite. The calibration station is the Bánfalva observatory in Sopron, latitude, $\varphi=47°\ 40'\ 55.56''$; the calibration of the instrument lasted three days. This example shows the calculations of one day calibration measurements.

The calibration data

Astronomical azimuth of the control direction,

$$A=116°\ 34'\ 31.00''.$$

Number of independent measurements, $n=6$.

Measurements when sighting the calibration direction, Is,

$$I'_1=182°\ 19'\ 16.16'', \qquad I'_2=182°\ 19'\ 16.88'',$$

$$I'_3=182°\ 19'\ 15.99'', \qquad I'_4=182°\ 19'\ 16.79'',$$

$$I'_5=182°19'\ 18.30'', \qquad I'_6=182°\ 19'\ 17.26''.$$

The accuracy of geodetic sight $\mu_I=\pm 1''$.

Gyro-north observations, Ns,

$$\mathrm{N}'_1=154°\ 33'\ 48.83'', \qquad N'_2=154°\ 33'\ 52.12'',$$

$$N'_3=154°\ 33'\ 49.82'', \qquad N'_4=154°\ 33'\ 52.97'',$$

$$N'_5=154°\ 33'\ 56.73'', \qquad N'_6=154°\ 33'\ 53.46''.$$

The accuracy of observing N is $\mu_N=\pm 3''$.

For this type of gyrotheodolite, an approximate value for the constant is $\Delta' = 90°$.

Applying Eq. (8) using the measurements Is' and Ns' and the approximate value of the constant, the misclosures were calculated and found to be:

$$w_1 = -1° \, 10' \, 56.33'', \qquad w_2 = -1° \, 10' \, 56.33'',$$

$$w_3 = -1° \, 10' \, 55.17'', \qquad w_4 = -1° \, 10' \, 52.82'',$$

$$w_5 = -1° \, 10' \, 50.57'', \qquad w_6 = -1° \, 10' \, 52.80''.$$

According to Eq. (14), the variation d is calculated as follows:

$$d = \frac{1}{n} \sum_{i=1}^{n} w_i = -1° \, 10' \, 53.575''.$$

The adjusted value of the instrument constant will be:

$$\Delta = \Delta' + d = 90° - 1° \, 10' \, 53.575'' = 88° \, 49' \, 06.425''.$$

The corrections for the measurements were calculated applying Eqs (17) and (18) and found to be:

$$V_{I_1} = 0.2755'', \qquad V_{I_2} = 0.0185'', \qquad V_{I_3} = 0.1595'',$$

$$V_{I_4} = -0.0755, \qquad V_{I_5} = -0.3005, \qquad V_{I_6} = -0.0755,$$

and

$$V_{N_1} = 2.4795'', \qquad V_{N_2} = 0.1665'', \qquad V_{N_3} = 1.4355'',$$

$$V_{N_4} = -0.6795, \qquad V_{N_5} = -2.7045, \qquad V_{N_6} = -0.6975.$$

The mean square error of the unit weight for the adjusted value of Δ (Eq. 20) is:

$$\mu_0 = \pm \sqrt{\frac{[PVV]}{f}} = \pm 1.91'',$$

and for Δ, the mean square error (23) is:

$$\mu_\Delta = \pm \mu_0 \sqrt{\frac{P_I + P_N}{n(P_I P_N)}} = \pm 0.82''.$$

Having calculated the adjusted values of the measurements, they were used with the adjusted value of the constant in a backward calculation for the azimuth (A) of the control direction, the mean of the obtained 6 values was found to be 116° 34′ 31.00″, i.e. the same as the value used before, which is the azimuth of the control direction.

Conclusion

In the presented paper an adjusted value is calculated for the gyrotheodolite constant using a simple formula. This formula contains the correction to be applied to the approximate value of the instrument constant (90° or 0° depending on the category of the instrument) independently from the weights of the measurements.

The formula is valid for both gyrotheodolites and gyroattachements; it is also simple and applicable in the field where it requires short calculating time and can be used with repeated calibration measurements depending on the extension of the surveyed area and to the availability of the control directions. It is also useful for factory calibrations where many calibration measuring sets are made. In the given numerical example, the obtained accuracy for the adjusted value of the instrument constant is less than 1″.

References

Abdelhamid K 1981: Results of evaluation and methods of azimuth determination with old and new gyrotheodolites. Invited paper at the XVI Congress of the International Federation of Surveyors (FIG), Committee 6E, Montreux, Switzerland.

Detrekői Á 1972: Adjustment calculations (in Hungarian). Tankönyvkiadó, Budapest.

Gregerson L F 1970: An investigation of the MOM's Gi-B2 gyrotheodolite. *The Canadian Surveyor*, 24, 117–135.

Halmos F 1967: Determination and reliability of the constant of gyrotheodolites. *Acta Geod. Geoph. Mont. Hung.*, 2, 293–316.

Halmos F 1971: Instrumentelle und methodische zeitgemässen Kreiseltheodoliten. *Allgemeine Vermessungsnachrichten*, Karlsruhe, 105–111.

Halmos F 1972: Systematic and random errors of direction measurements with gyrotheodolites. *MOM Review* 4, 24–32.

Halmos F 1977: Theoretical and practical problems of the use of gyrotheodolites in Geodesy. MTA GGKI Publication, No. 6.

Hazay I 1976: Adjustment calculations in surveying. Akadémiai Kiadó, Budapest.

Hirvonen R A 1976: Adjustment by least squares in geodesy and photogrammetry. New York.

Acta Geodaet., Geophys. et Montanist. Hung. Volume 18 (4), pp. 359—368 (1983)

CAPACITIVE TRANSDUCERS FOR HORIZONTAL PENDULUMS AND GRAVIMETERS

GY MENTES[1]

[Manuscript received October 9, 1982]

The paper deals with the construction principles of capacitive transducers which are applicable for horizontal pendulums and gravimeters. It describes advantages and disadvantages of various kinds of transducers and transducer circuits.

Keywords: capacitive transducer; gravimeter; horizontal pendulum

Introduction

The general progress of measuring technics necessitates an updating of old gravimeters and horizontal pendulums, too. For this purpose capacitive transducers are most suitable. The construction and working principle of capacitive transducers used in practice are very diversified. Various kinds of capacitive transducers can be used for horizontal pendulums and gravimeters depending on the construction of the instrument and the method of the recording (analog, digital, or both simultaneously). In this paper these transducers are discussed and measuring methods on the basis of own experiences presented.

Principle of the capacitive transducers

To understand the working principle of a capacitive transducer, let us see the single plate-condenser (Fig. 1) whose capacity is:

$$C=\varepsilon_0 \varepsilon_r \frac{A}{d} \tag{1}$$

where

C = the capacity of the condenser

ε_0 = the dielectric constant of the vacuum

ε_r = the relative dielectric constant of the dielectric between the plates

A = the surface of the opposite-standing plates

d = the distance between the plates.

[1] Geodetic and Geophysical Research Institute of the Hungarian Academy of Sciences, H-9401 Sopron, P.O.B. 5, Hungary

From Eq. (1) it can be seen that there are three ways to build a capacitive transducer, i.e. to get a change of capacity from a mechanical displacement.

a) The mechanical displacement causes a change in the position of the dielectric (Fig. 2).

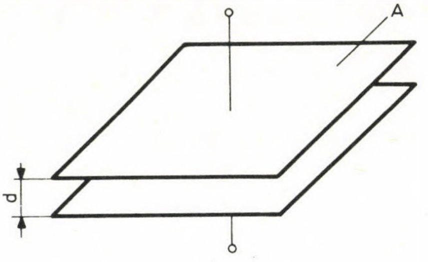

Fig. 1

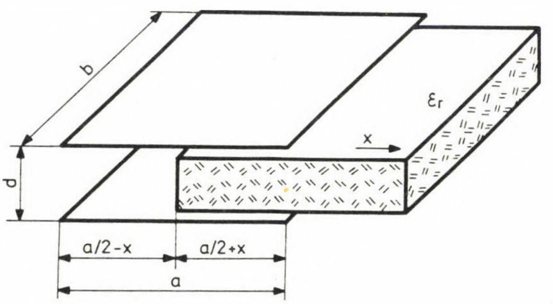

Fig. 2

In this case the capacity is in function of the displacement:

$$C(x)=\varepsilon_0 \frac{b}{d}\left[\frac{a}{2}(\varepsilon_r+1)+x(\varepsilon_r-1)\right] \tag{2}$$

where

a, b, d the mechanical sizes of the transducer

x = the displacement of the dielectric.

b) The mechanical displacement causes a change of the surface of the opposite-standing plates (Fig. 3).

The capacity is in this case:

$$C(x)=\varepsilon_0 \frac{b}{d}\left(\frac{a}{2}+x\right). \tag{3}$$

c) The mechanical displacement changes the distance of the condenser plates (Fig. 4):

$$C(x)=\varepsilon_0 \frac{A}{d+x}. \tag{4}$$

To use this single condenser as transducer is not the most suitable solution, because its output signal is not zero without any displacement and Eq. (4) is non-linear. For this reason in the measuring technics differential condensers and different compensation methods are used which have linear characteristics and do not give any output signal without a mechanical displacement.

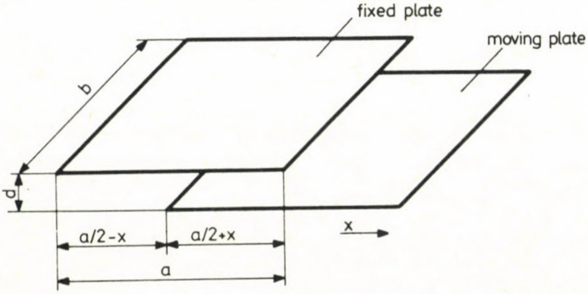

Fig. 3

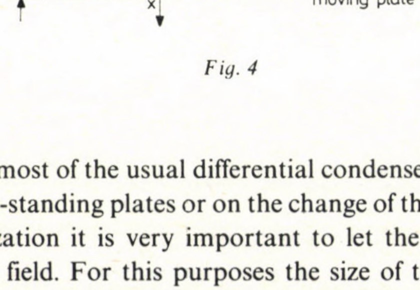

Fig. 4

Figure 5 shows most of the usual differential condensers based on the change of the surface of opposite-standing plates or on the change of the distance between plates. In the practical realization it is very important to let the moving plate work in a homogeneous electric field. For this purposes the size of the moving plate must be smaller than those of the outside plates, and the fixed plates must be as near to the moving plate as only possible.

On Fig. 5a there are fixed plates on both sides of the moving plate which are metallically jointed together, so the capacitances of the opposite sides of the moving plate are in parallel connection. Both solutions in Fig. 5 ensure that the moving plate moves in a homogeneous electrostatic field. For example on Fig. 6 a schematic sketch and dimensions in mm of a differential condenser are shown designed to a horizontal pendulum. The transducer is made of incorrodible steel. On Fig. 7 a differential

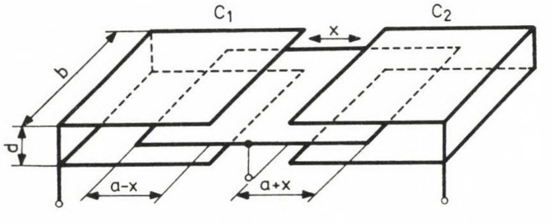

Fig. 5a

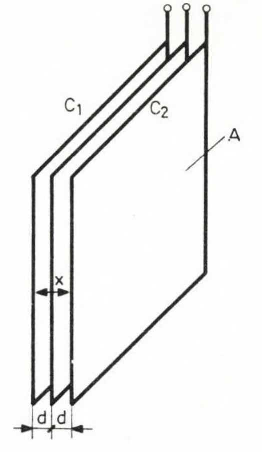

Fig. 5b

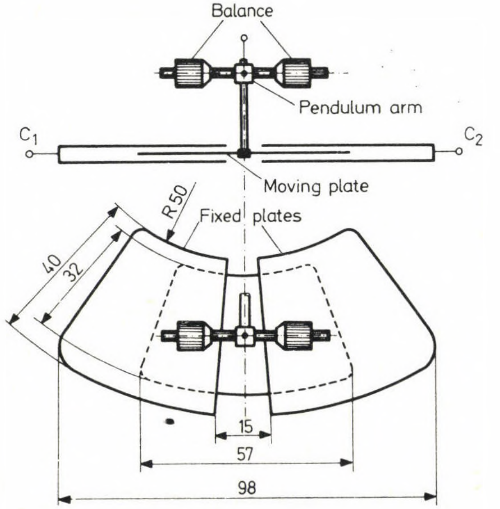

Fig. 6

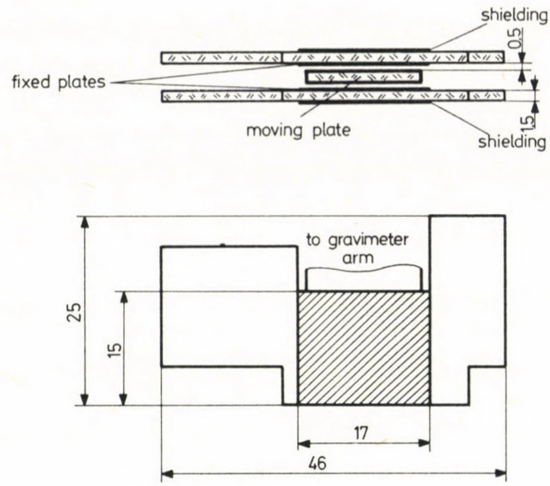

Fig. 7

condenser to a GS-11 gravimeter is presented. As material of the transducer a printed-circuit plate is used with a double-sided gilded copper layer. This material has high mechanical strength. Insulation and shielding problems can be solved so easily and hereby the dimensions of the transducer can be hold sufficiently small.

Electric measuring methods

Differential condensers are used in most cases in unbalanced bridge-circuits as shown in Fig. 8. The output voltage of the bridge-circuits is:

$$U_0 = \frac{U}{2} \frac{C_2 - C_1}{C_2 + C_1} \tag{5}$$

where U is the supply voltage of the bridge.

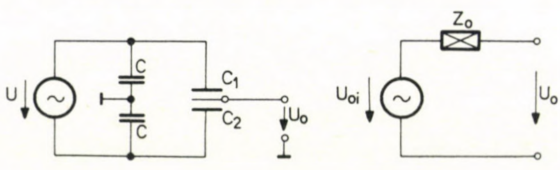

Fig. 8

Substituting the values of C_2 and C_1 on the basis of Fig. 5 into Eq. (5) we get the output voltage of the bridge U_0 as the function of the displacement x.

For the differential condenser in Fig. 5a we get:

$$C_1 = 2\varepsilon_0 \frac{b(a-x)}{d}, \qquad C_2 = 2\varepsilon_0 \frac{b(a+x)}{d}$$

and (6)

$$U_0 = \frac{U}{2}\frac{x}{a}$$

for the differential condenser in Fig. 5b:

$$C_1 = \varepsilon_0 \frac{A}{d+x}, \qquad C_2 = \varepsilon_0 \frac{A}{d-x}$$

and (7)

$$U_0 = \frac{U}{2}\frac{x}{d}.$$

From Eqs (6) and (7) it can be seen that the characteristics of the differential condenser is linear and the output voltage of the bridge is zero when the displacement of the moving plate of the transducer from the midpoint is zero ($x=0$). The bridge must be supplied with a voltage of high stability, because the output voltage of the bridge is according to Eqs (6) and (7) directly proportional to the supply voltage and therefore the fluctuations of the supply voltage would cause errors in the measurements. The supply voltage can be both DC and AC, but the application of the latter is more advantageous, as the amplification of low DC voltages is problematic because of the drift of DC amplifiers. It is evident that the sensitivity of the bridge can be increased by the increase of the supply voltage and by the decrease of the parameters a or d. Of course, the sensitivity cannot be increased beyond all bounds since a very high voltage causes a relatively great reactive force to the arm of the pendulum or to that of the gravimeter. In addition a high voltage can cause damages in other parts of the electronics, e.g. in the preamplifier.

The values of a and d cannot be made as small as we should like to do as the capacitance of rest ($x=0$) must be at least 1–10 pF.

For the planning of the preamplifier it is very important to know the output impedance of the bridge-circuit, which is according to Fig. 8:

$$Z_0 = \frac{1}{\omega}\left[\frac{1}{C_1+C_2} + \frac{1}{2C}\right] \tag{8}$$

where

ω = the angular frequency of the supply voltage of the bridge.

As it can be seen from Eq. (8), the output impedance is decreasing with increasing frequency of the supply voltage. This is another reason for applying an AC voltage as supply voltage of the bridge.

According to the above mentioned considerations, the usual value of the supply voltage of the bridge is about 20 V and its frequency is about 10–15 kHz. In this case the output impedance of the bridge is a few kΩ (Mentes 1979, 1981).

Because of spurious capacitances it is important which point of the bridge circuit should be connected to the ground. The two possible versions can be seen in Figs 9a and 9b. In the first case (Fig. 9a) the point B is connected to the ground, hereby the

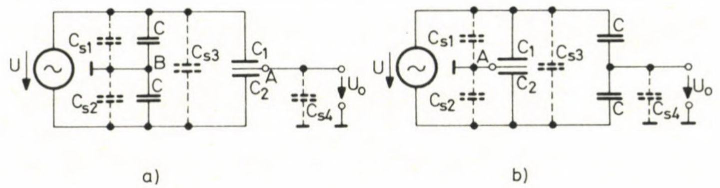

Fig. 9

spurious capacitances C_{s1} and C_{s2} which have values of some pF-s are connected parallel to the fixed capacitances C. The value of the capacitance of C is between 100 pF and 1 nF. For this reason any changes in the capacities C_{s1} and C_{s2} cannot cause as great unbalances of the bridge as in the second case (Fig. 9b). In this case the values of C_{s1}, C_{s2} and C_1, C_2 are in the same order of magnitude, therefore changes of C_{s1} and C_{s2} result in great unbalances of the bridge. The practical balancing of the bridge is a very hard task to solve and in most cases no solution is possible. This is why the transducer point A of the bridge cannot be connected to the ground. This practical view-point is the cause of most problems in reconstruction of old pendulums and gravimeters. In both cases C_{s3} loads the generator supplying the bridge. C_{s4} is the capacity of the shielded wire connected to the output of the bridge and it loads the output signal of the bridge. Its value must be low.

In the practice the moving plate of the differential condenser is fixed to the pendulum arm or to the arm of the gravimeter. In quartz pendulums the moving plate cannot be connected directly to the preamplifier input because the suspension wires are made of quartz and this material is non-conductive. Therefore they cannot be used as leading-out wires of the bridge. At gravimeters the situation is just the opposite, the moving plate of the differential condenser must be insulated from the pendulum arm because this cannot be separated from the gravimeter body which is used as electric ground. For this reason an extra leading-out wire must be added which has then a reactive torque to the gravimeter arm, and causes errors in the measurement.

This problem can be eliminated with a special differential condenser (Ruymbeke 1975) its schematic construction and substitution scheme can be seen in Fig. 10. In principle it is a duplicated differential condenser, but on one side both standing plates are connected electrically. So this side forms a coupling condenser whose capacity does not depend on the displacement of the moving plate. It has the advantage that no leading-out wire is needed to the moving plate of the differential condenser. Its disadvantage is that the coupling condenser is connected serially to the output capacitance of the bridge so the resulting output impedance will be greater. Therefore the preamplifier must have a high input resistance and a very low input capacitance. An

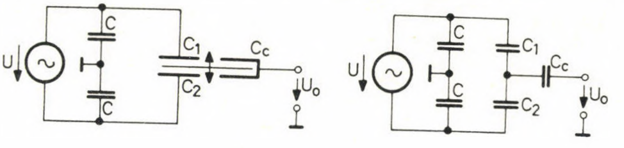

Fig. 10

operational amplifier with JFET input complies with this requirements, but the stray capacitances of the preamplifier built with such a high performance operational amplifier can be in the same order as the capacity of the coupling condenser. In this case the output signal of the bridge will be attenuated according to the ratio of the coupling and loading capacitances. The other disadvantage is that the preamplifier will pick up more disturbances because of the great impedances and therefore the signal-to-noise ratio will be worse. For this reason the differential condenser and the preamplifier must be mounted very carefully.

If the moving plate cannot be insulated from the gravimeter or pendulum arm and hereby from the instrument ground without an extra leading-out wire then a measuring method must be applied where the moving plate is connected to the ground. Such methods can be seen in Figs 11 and 13. In the first case the frequencies of the two oscillators change oppositely because of the movement of the moving plate is connected to the ground. The differential frequency produced by mixing the signals of the two oscillators is proportional to the displacement of the moving plate. The usual oscillator circuit is shown in Fig. 11. It is the most stable type of LC oscillators, its frequency stability can reach a value of 10^{-4}–10^{-5}. The oscillators can be mounted directly on the fixed plates of the differential condenser. The usual frequency of the oscillators is about 1 MHz.

We have made such a transducer for a GS-11 gravimeter. The condenser plates were made of a PC-plate and the two oscillators were built up on the external sides of the plates, with internal copper layers as fixed plates of the differential condenser. The moving plate was made of brass and it was connected directly to the gravimeter arm. For the transducer, only very limited space was available in the gravimeter. For this reason we have built the oscillators from chip-transistors, chip-capacitors and chip-resistors. The construction of the transducer together with the oscillators can be seen in Fig. 12.

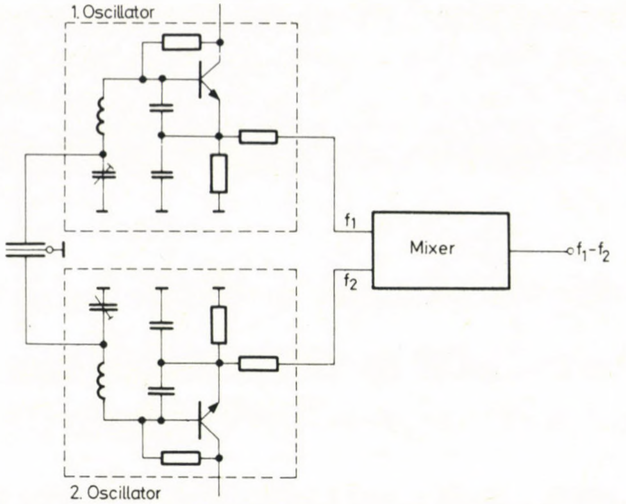

Fig. 11

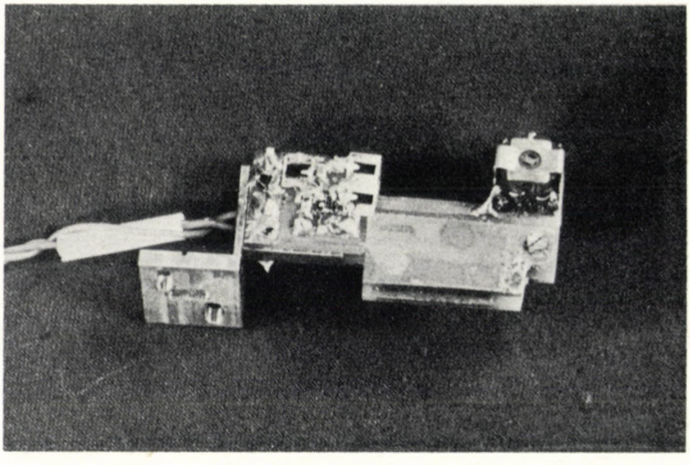

Fig. 12

The frequency stability problems can be eliminated with an another method, which can be seen on Fig. 13. In this case a comparator circuit makes a comparison between the measuring and the reference condensers. The reference condenser can be a constant capacitance or one side of a differential condenser. In both cases the measuring characteristics are linear.

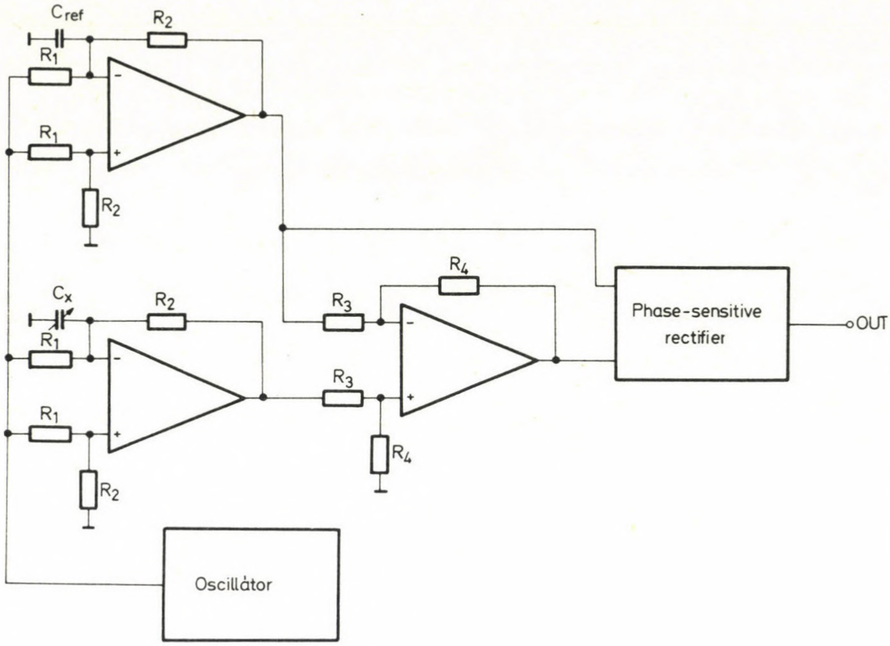

Fig. 13

Conclusion

In addition to the above mentioned methods there are many other methods, too, which are known in the measuring technics and which perhaps can be used to pendulums and gravimeters. The mechanical construction of different capacitive transducers is depending on the range of the quantity to be measured, the place of building-in, etc. E.g. capacitive transducers are to be shielded very carefully because this type of transducers is very sensitive to stray-fields. Besides the change of the humidity of the air can cause great disturbances in the work of the transducer. All these points of view determine the construction of a capacitive transducer. This our aim was only to give a general summary about capacitive transducers and possibilities of their applications in horizontal pendulums and gravimeters.

References

Mentes Gy 1979: Development of horizontal pendulum recordings. *Acta Geod. Geoph. Mont. Hung.*, 14, 101–109.

Mentes Gy 1981: Horizontal pendulum with capacitive transducer. *Acta Geod. Geoph. Mont. Hung.*, 16, 269–280.

Ruymbeke M 1975: Sur un pendule horizontal équipé d'un capteur de déplacement à capacité variable. XVI. Assemblée Générale de L'UGGI, Grenoble.

Acta Geodaet., Geophys. et Montanist. Hung. Volume 18 (4), pp. 369—382 (1983)

RELATIVE MOTION OF A FREE MASS-POINT IN A SPACECRAFT REVOLVING AROUND THE EARTH

L FIAŁOVSZKY[1]

[Manuscript received October 24, 1982]

The relative motion of a free mass-point in a spacecraft in relation to the centre of the spacecraft is investigated, whereby the spacecraft revolves stabilized around the Earth. It will be shown that in a plane with a slight pitch to the plane of revolution the free mass-point will in general hover slowly away from the mass-centre on a spiral path around the mass-centre and the path will be the steeper, the greater is the initial distance of the free mass-point from the mass-centre.

The relative position of the hovering free mass-point can be determined by the formulas deduced for any moment or for any revolution angle. This relative motion is important if an experiment should be planned or made, where the data of the experimental object are to be determined from the observed motion elements of a free mass-point (small body) put in or outside of the spacecraft, or if the free mass-point or mass-points affect the process of the phenomenon investigated.

Keywords: free motion; inertial motion; motion in a spacecraft; spacecraft

Several technical and biological experiments were made in spacecrafts during the last decade; one of their aims was to observe the process of the phenomena investigated under the condition of weightlessness. In connection with these experiments the problem has arisen whether the body (mass-point) in the spacecraft remains quiet with respect to the spacecraft, or will occur a relative motion and of what kind it will be. The answer to this question has a special importance in the planning of experiments to be done in a spacecraft whereby an exact measurement of the motions of one ore more small bodies put into the spacecraft due to the action of the power being the object of the experiment is necessary. Such a case is the Barta and Hajósy's proposal (1980) about a more exact determination of the universal gravity constant.

Two cases will be discussed: in the first the spacecraft is stabilized in a way that its direction in the world-space remains unchanged; in the second it is stabilized in a way that one of its axes (or one of its straights) always shows toward the Earth's centre and the spacecraft does not revolve around this straight line.

[1] H-1118 Budapest, Villányi út 103, Hungary

The spacecraft is stabilized with respect to a constant space direction

Let us suppose that the fastening of the mass-point A will be ceased in its A_0 positions at the initial moment t_0 when the mass-centre C of the spacecraft will reach the lowest point C_0 of its revolution path (Fig. 1). Let be this smallest distance of the point C from the Earth's centre O, $OC_0=r_1$ and let us denote the greatest distance by r_2, further the difference of the initial position A_0 of the mass-point A in an arbitrary direction from the initial position C_0 of the mass-centre C by δ_0. Let us denote the radial component of latter in the direction $OC_0=r_1$ by δ_{0r}, the tangential component in the plane of revolution and perpendicular to δ_{0r} by δ_{0s} and the component perpendicular to the revolution plane by δ_{0q}. The inertial motion of the mass-point A (released at the moment t_0) with respect to the reference point C will be separately investigated as consequence of the three initial difference-components.

The effect of the radial difference component

Let us determine at first the polar distance r_c from the Earth's centre at which the position C_α of the mass-centre C will be at a later moment t, when the mass-centre made a revolution of the angle α with respect to its initial position. It can be written on the basis of Kepler's second law:

$$v_c r_c \cos\varphi_c = v_0 r_1 \tag{1}$$

where v_0 is the tangential velocity (in direction perpendicular to OC_0) of the mass-centre C at the point C_0, v_c the velocity of the mass-centre in point C_α and φ_c the angle between the velocity direction and the direction perpendicular to OC_α. By substituting

$$\cos\varphi_c = \frac{r_c\,d\alpha}{ds_c} \qquad \text{and} \qquad v_c = \frac{ds_c}{dt}$$

one gets from Eq. (1):

$$\frac{r_c^2\,d\alpha}{dt} = v_0 r_1 . \tag{2}$$

The gravitational acceleration in the point C_α will be:

$$g_\alpha = g\frac{R^2}{r_c^2} \tag{3}$$

where g is the gravitational acceleration at the surface of the Earth with radius R, the Earth considered as a sphere and as having a concentric density distribution. The acceleration of point C in the point C_α will be by taking Eq. (3) into account:

$$\frac{dv_c}{dt} = -g_\alpha \sin\varphi_c = -g\frac{R^2}{r_c^2}\cdot\frac{dr_c}{ds_c}, \tag{4}$$

from here:

$$\frac{\mathrm{d}s_c}{\mathrm{d}t} = v_c = -g\frac{R^2}{r_c^2}\cdot\frac{\mathrm{d}r_c}{\mathrm{d}v_c}.$$

Further:

$$v_c \mathrm{d}v_c = -gR^2\frac{\mathrm{d}r_c}{r_c^2} \tag{5}$$

and with integration:

$$v_c^2 = v_0^2 - \frac{2gR^2}{r_1} + \frac{2gR^2}{r_c}. \tag{6}$$

On the basis of Fig. 1 it can be written:

$$(\mathrm{d}s_c)^2 = (\mathrm{d}r_c)^2 + (r_c \mathrm{d}\alpha)^2$$

or

$$\left(\frac{\mathrm{d}s_c}{\mathrm{d}t}\right)^2 = v_c^2 = \left(\frac{\mathrm{d}r_c}{\mathrm{d}t}\right)^2 + r_c^2\left(\frac{\mathrm{d}\alpha}{\mathrm{d}t}\right)^2 =$$

$$= \left(\frac{\mathrm{d}r_c}{\mathrm{d}\alpha}\right)^2\left(\frac{\mathrm{d}\alpha}{\mathrm{d}t}\right)^2 + r_c^2\left(\frac{\mathrm{d}\alpha}{\mathrm{d}t}\right)^2. \tag{7}$$

From Eq. (2)

$$\frac{\mathrm{d}\alpha}{\mathrm{d}t} = v_0\frac{r_1}{r_c^2}$$

substituting this into Eq. (7) we get:

$$v_c^2 = \left(\frac{\mathrm{d}r_c}{\mathrm{d}\alpha}\right)^2\frac{r_1^2 v_0^2}{r_c^4} + \frac{r_1^2 v_0^2}{r_c^2}. \tag{8}$$

From Eqs (6) and (8) follows:

$$v_0^2 - 2gR^2\left(\frac{1}{r_1} - \frac{1}{r_c}\right) = \left(\frac{\mathrm{d}r_c}{\mathrm{d}\alpha}\right)^2\cdot\frac{r_1^2 v_0^2}{r_c^4} + \frac{r_1^2 v_0^2}{r_c^2}$$

and from here:

$$\mathrm{d}\alpha = \frac{r_1 v_0 \mathrm{d}r_c}{r_c\sqrt{\left(v_0^2 - \frac{2gR^2}{r_1}\right)r_c^2 + 2gR^2 r_c - r_1^2 v_0^2}}$$

and by integration:

$$\alpha = \arccos\frac{\frac{r_1 v_0}{r_c} - \frac{gR^2}{r_1 v_0}}{v_0 - \frac{gR^2}{r_1 v_0}} = \arccos\frac{r_1^2 v_0^2 - r_c g R^2}{r_1 v_0^2 r_c - r_c g R^2}.$$

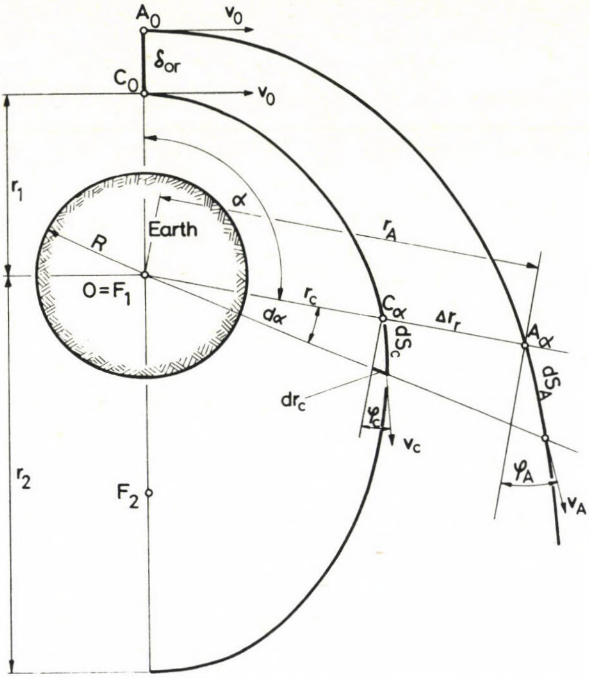

Fig. 1. The effect of the initial radial deviation component $\delta_{0r}=C_0A_0$ of the free mass-point A being in a spacecraft revolving on an elliptical orbit and stabilized to a space direction. The Earth's centre O is also the focus F_1 of the elliptical orbit, while the other focus F_2 is much more nearer to F_1, than shown in the figure

From here:

$$r_c=\frac{r_1^2v_0^2}{gR^2+(r_1v_0^2-gR^2)\cos\alpha}. \tag{9}$$

Let us express the initial velocity v_0 with the distance r_1 between the lowest point of the orbit of the spacecraft and the Earth's centre and with the distance r_2 between the highest point of the orbit and the Earth's centre. For this we use Eq. (9) with the substitutions: $\alpha=\pi$ and $r_c=r_2$:

$$r_2=\frac{r_1^2v_0^2}{2gR^2-r_1v_0^2},$$

from where:

$$v_0^2=\frac{2gR^2r_2}{r_1(r_1+r_2)}. \tag{10}$$

Substituting Eq. (10) into Eq. (9), we get after some rearrangement:

$$r_c = \frac{2r_1 r_2}{r_1 + r_2 + (r_2 - r_1)\cos\alpha}. \tag{11}$$

Equation (11) is substantially the same as the polar equation of the ellipse:

$$r_c = \frac{p}{1 + e\cos\alpha} = \frac{\dfrac{2r_1 r_2}{r_1 + r_2}}{1 + \dfrac{r_2 - r_1}{r_1 + r_2}\cos\alpha}.$$

Let us determine now at which distance $r_A = OA_\alpha$ will be the mass-point A from the Earth's centre O after revolving by an angle α. Since mass-point A was fixed to the spacecraft till the initial moment t_0, the released mass-point A will start with the same tangential velocity v_0, as the mass-centre C. Hence, using Kepler's second law for the motion of the point A in the point A_α it can be written on the analogy of Eq. (1):

$$v_A r_A \cos\varphi_A = v_0(r_1 + \delta_{0r}), \tag{12}$$

where v_A is the velocity of the free mass-point A in the point A_α and φ_A the angle between the velocity direction and the direction perpendicular to OA_α. For the polar distance r_A of the point A_α we get from Eq. (12) — by means of the deduction used at the determination of distance r_c — the expression:

$$r_A = \frac{(r_1 + \delta_{0r})^2 v_0^2}{gR^2 + [(r_1 + \delta_{0r})v_0^2 - gR^2]\cos\alpha} \tag{13}$$

which is analogous to Eq. (9). Substituting Eq. (10) into Eq. (13) and neglecting the higher powers of δ_{0r} and after some rearrangements we get:

$$r_A = \frac{2r_1 r_2}{r_1 + r_2 + (r_2 - r_1)\cos\alpha} + \left(\frac{4r_2}{r_1 + r_2 + (r_2 - r_1)\cos\alpha} - \right.$$
$$\left. - \frac{4r_2^2\cos\alpha}{[r_1 + r_2 + (r_2 - r_1)\cos\alpha]^2}\right)\delta_{0r}. \tag{14}$$

The radial distance of the point A_α from the mass-centre C_α is the difference between Eq. (14) and Eq. (11):

$$\Delta r_r = r_A - r_c = \frac{4r_2}{r_1 + r_2 + (r_2 - r_1)\cos\alpha}\left\{1 - \frac{r_2\cos\alpha}{r_1 + r_2 + (r_2 - r_1)\cos\alpha}\right\}\delta_{0r}. \tag{15}$$

Equation (15) can be suitably expressed by the quotient $\rho = r_1/r_2$ as parameter:

$$\Delta r_r = \frac{4}{1+\rho+(1-\rho)\cos\alpha}\left\{1 - \frac{\cos\alpha}{1+\rho+(1-\rho)\cos\alpha}\right\}\delta_{0r}. \tag{16}$$

From Eq. (16) it can be seen that the inertial moving after α revolution of the free mass-point A with a given initial deviation will only depend on parameter ρ and will be independent of the orbital height of the spacecraft.

If the orbit is a circle than from Eq. (15) by substituting $r_1 = r_2$, or from Eq. (16) by substituting $\rho = 1$:

$$\Delta r_r = (2-\cos\alpha)\delta_{0r}. \tag{17}$$

Now let us calculate the tangential motion ΔS_r of the mass-point A with initial deviation δ_{0r} at the moment t_c, when the mass-centre C made a revolution of the angle α and reached the point C_α. For this purpose we have to determine the moment t_c as well as the moment t_A, when A comes into the position A_α. From Eq. (2) we get:

$$\mathrm{d}t = \frac{r_c^2}{v_0 r_1}\,\mathrm{d}\alpha \tag{18}$$

or by the substitution of Eq. (11):

$$\mathrm{d}t = \frac{4r_1 r_2^2}{[r_1+r_2+(r_2-r_1)\cos\alpha]^2 v_0}\,\mathrm{d}\alpha.$$

From here after integration:

$$t_c - t_0 = \frac{1}{v_0}\left\{-\frac{r_2(r_2-r_1)\sin\alpha}{r_1+r_2+(r_2-r_1)\cos\alpha} + \right.$$

$$\left. + (r_1+r_2)\sqrt{\frac{r_2}{r_1}}\,\mathrm{arc\,tan}\left(\sqrt{\frac{r_1}{r_2}}\tan\frac{\alpha}{2}\right)\right\}. \tag{19}$$

For determining the moment t_A we can write on the basis of Eq. (12) the expression analogous to Eq. (18):

$$\mathrm{d}t = \frac{r_A^2}{v_0(r_1+\delta_{0r})}\,\mathrm{d}\alpha,$$

where now Eq. (14) must be substituted for r_A:

$$\mathrm{d}t = \frac{4r_1 r_2^2}{v_0(r_1+\delta_{0r})}\left\{\frac{r_1+4\delta_{0r}}{[r_1+r_2+(r_2-r_1)\cos\alpha]^2} - \right.$$

$$\left. - \frac{4r_2\cos\alpha}{[r_1+r_2+(r_2-r_1)\cos\alpha]^3}\,\delta_{0r}\right\}\mathrm{d}\alpha. \tag{20}$$

The small second order terms in Eq. (20) were neglected. Integrating Eq. (20), after some transformation and by using the temporary notations

$$
\begin{aligned}
a&=r_1+r_2\\
b&=r_2-r_1\\
c&=r_1+r_2+(r_2-r_1)\cos\alpha\\
d&=(r_1+r_2)\sqrt{\frac{r_2}{r_1}}\arctan\left(\sqrt{\frac{r_1}{r_2}}\tan\frac{\alpha}{2}\right)
\end{aligned}
\tag{21}
$$

we get the following equation:

$$
\begin{aligned}
t_A-t_0=\frac{1}{v_0}\Bigg\{&-\frac{r_2 b\sin\alpha}{c}+d+\Bigg[-\frac{4r_2 b\sin\alpha}{r_1 c}+\frac{4}{r_1}d-\\
&-\frac{2r_2^2 a\sin\alpha}{r_1 c^2}-\frac{r_2(a^2+2b^2)\sin\alpha}{2r_1^2 c}+\\
&+\frac{3bd}{2r_1^2}+\frac{r_2 b\sin\alpha}{r_1 c}-\frac{d}{r_1}\Bigg]\delta_{0r}\Bigg\}.
\end{aligned}
\tag{22}
$$

Therefore, the free mass-point A reaches the revolution angle α by the time

$$\Delta t=t_A-t_c \tag{23}$$

later than the mass-centre C, and consequently the deviation (delay) of the free mass-point in tangential direction will be

$$\Delta S_r=\Delta t v_c \tag{24}$$

where v_c is the velocity of the mass-centre in the point C_α, i.e. on the basis of Eq. (1) it is:

$$v_c=\frac{v_0 r_1}{r_c\cos\varphi_c}, \tag{25}$$

but because the quotient $\frac{r_2-r_1}{r_1+r_2}$ is small it is easy to prove that $\cos\varphi_c\cong 1$, and therefore:

$$v_c\cong\frac{v_0 r_1}{r_c}. \tag{26}$$

For the expressed form of Eq. (24) we get by using Eqs (21), (22), (23), (19) and (26), after some transformation, and by the introduction of the rate of heights $\rho=r_1/r_2$ as parameter:

$$
\begin{aligned}
\Delta S_r=\Bigg\{&\left[\frac{3(\rho^3+3\rho^2+3\rho+1)-3(\rho^3+\rho^2-\rho-1)\cos\alpha}{4\rho^2}\right]\cdot\\
&\cdot\sqrt{\frac{1}{\rho}}\arctan\left(\sqrt{\rho}\tan\frac{\alpha}{2}\right)-\left[\frac{\rho+3}{4\rho^3}+\frac{\rho+1}{\rho^2+\rho+(\rho-\rho^2)\cos\alpha}\right]\sin\alpha\Bigg\}\delta_{0r}
\end{aligned}
\tag{27}
$$

or, if $0.99<\rho<1.01$, than

$$\Delta S_r=\left\{\frac{9\rho-3-3(\rho-1)\cos\alpha}{2\rho-1}\cdot\frac{3-\rho}{2}\operatorname{arc\,tan}\left(\frac{1+\rho}{2}\tan\frac{\alpha}{2}\right)-\right.$$
$$\left.-\left[\frac{\rho+3}{12\rho-8}+\frac{\rho+1}{3\rho-1+(1-\rho)\cos\alpha}\right]\sin\alpha\right\}\delta_{0r}. \tag{28}$$

It can be seen from Eqs (27) and (28) that the tangential motion ΔS_r of the free mass-point with unit radial initial deviation — which motion arose after the spacecraft's revolving by an angle α — also depends on the parameter ρ and is independent of the actual revolution height.

In case of a spherical orbit $\rho=1$ can be used and one gets from Eq. (27) or Eq. (28):

$$\Delta S_r=(3\alpha-2\sin\alpha)\delta_{0r}. \tag{29}$$

On the basis of Eqs (15) and (16), respectively, further on the basis of Eqs (27), (28) and (29), respectively the radial motion Δr_r and the tangential motion ΔS_r of the free mass-point A, occurring due to the effect of the initial radial deviation component δ_{0r} are given in Table I for elliptical ($\rho=0.990$ and 0.995) and spherical ($\rho=1.000$) orbits. The resultant of the Δr_r radial and ΔS_r tangential motions as function of α are illustrated in Fig. 2.

The free mass-point will not move in transversal direction due to the effect of the initial deviation component δ_{0r}:

$$\Delta q_r=0. \tag{30}$$

Table I. The Δr_r radial and ΔS_r tangential motion in δ_{0r} units, caused by the initial radial deviation component δ_{0r} of the free mass-point in a spacecraft stabilized to a space direction (the motion measured from the mass-centre) at the moment reaching the revolving angle α in the case of elliptical orbit ($\rho=0.990$, 0.995) and circular orbit ($\rho=1.000$)

α	Δr_r			ΔS_r		
	in case of			in case of		
	$\rho=0.990$	$=0.995$	$=1.000$	$\rho=0.990$	$=0.995$	$=1.000$
0	1.000	1.000	1.000	0	0	0
$\pi/2$	2.010	2.005	2.000	2.706	2.710	2.712
π	3.040	3.020	3.000	9.472	9.448	9.425
$3\pi/2$	2.010	2.005	2.000	16.334	16.235	16.137
2π	1.000	1.000	1.000	19.137	18.992	18.850
$5\pi/2$	2.010	2.005	2.000	21.747	21.654	21.562

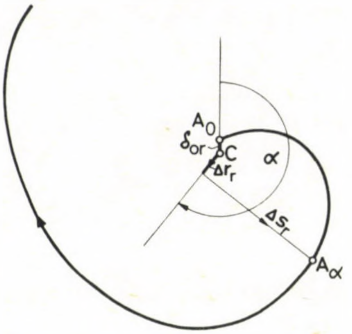

Fig. 2. The path of the free mass-point A referred to the mass-centre C with δ_{0r} initial radial deviation as resultant of the Δr_r radial and ΔS_r tangential motion

The inertial effect of the initial tangential deviation component

The free mass-point A will move after its release on the orbit of the mass-centre C of the spacecraft due to the effect of its initial tangential deviation δ_{0s}, but it will precede the point C everywhere by the distance δ_{0s}. Thus, the free mass-point A will come in the position A_α after a revolution of the mass-centre C by the angle α (Fig. 3). The projection of the motion $C_\alpha A_\alpha = \delta_{0s}$ in the direction OC_0 will be:

$$\Delta r_s = \delta_{0s} \cos(90° - \alpha + \varphi_c) \tag{31}$$

where φ_c is the angle between the $e-e$ tangent belonging to the point C_α of the elliptical orbit and the $i-i$ direction, which is perpendicular to the direction $OC_\alpha = r_c$. This will be according to Fig. 3:

$$\varphi_c = \frac{\varepsilon}{2} = \frac{1}{2} \operatorname{arc\,cos} \left\{ \frac{r_c^2 + (r_1 + r_2 - r_c)^2 - (r_2 - r_1)^2}{2r_c(r_1 + r_2 - r_c)} \right\} \tag{32}$$

where Eq. (11) must be substituted for r_c. The tangential projection of the motion $C_\alpha A_\alpha$ is:

$$\Delta S_s = \delta_{0s} \sin(90° - \alpha + \varphi_c). \tag{33}$$

In case of a spherical orbit $r_2 = r_1 = r_c$; $\varphi_c = 0$ and so one gets from Eq. (31) and (33), respectively:

$$\Delta r_s = \delta_{0s} \sin \alpha \tag{34}$$

$$\Delta S_s = \delta_{0s} \cos \alpha \tag{35}$$

i.e. the free mass-point revolves in the orbital plane of the mass-centre C around the point C on a circle with radius δ_{0s} (it makes a circle during a total revolution).

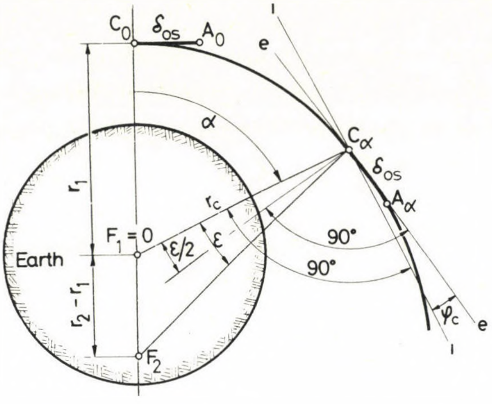

Fig. 3. The effect of the initial tangential deviation component $\delta_{0s} = C_0 A_0$ of the free mass-point A

Effect of the initial deviation component perpendicular to the orbital plane

Due to the effect of the initial deviation component δ_{0q} perpendicular to the orbital plane, the free mass-point A will revolve after its release on an orbit which has the same form as that of the mass-centre C, but it will not revolve in the orbital plane of the point C, but in a plane determined by the straight line going through the point A_0 with initial deviation δ_{0q} and being parallel to the direction of the initial velocity v_0 and the O centre of the Earth. Hence, the free mass-point A will not move in radial and tangential direction during its revolution due to the effect of δ_{0q}:

$$\Delta r_q = 0; \qquad \Delta S_q = 0. \tag{36}$$

The transversal motion will be

$$\Delta q_q = \delta_{0q} \frac{r_c \cos \alpha}{r_1} \tag{37}$$

where Eq. (11) must be substituted for r_c. During a total revolution the motion Δq_q will move from $+\delta_{0q}$ through the O deviation till $-\delta_{0q} r_2 / r_1$, and back through O deviation till $+\delta_{0q}$.

In case of circular orbit ($r_c = r_1$):

$$\Delta q_q = \delta_{0q} \cos \alpha. \tag{38}$$

The δ_{0r} radial, δ_{0s} tangential and δ_{0q} transversal deviation components affect separately the mass-point A having a δ_0 initial deviation in arbitrary direction and due to the joint effect of them, the free mass-point will slowly hover on a spiral path in a plane oblique to the revolving plane around the mass-centre C.

The spacecraft is stabilized toward the centre of the Earth

This investigation is restricted to the case when the spacecraft revolves on a circular orbit. Here again the δ_{0r} radial, δ_{0s} tangential and δ_{0q} transversal components of the initial deviation δ_0 of the mass-point A released in the spacecraft must be separately investigated.

Effect of the radial deviation component

The mass-point A having a δ_{0r} radial initial deviation in the moment t_0, when the mass-point is released from its fixing to the spacecraft, will not revolve with the revolving speed of the mass-centre C:

$$v_0 = R\sqrt{\frac{g}{r_0}} \tag{39}$$

(in Eq. (39) r_0 means the constant distance of the point C from the Earth's centre), but with the initial velocity:

$$v_{A0} = \frac{r_0 + \delta_{0r}}{r_0} v_0 \tag{40}$$

(Fig. 4). Applying Kepler's second law to the position A_α of the point A after revolving by the angle α, it can be written on the analogy of Eq. (2):

$$r_A^2 \frac{\mathrm{d}\alpha}{\mathrm{d}t} = v_{A0}(r_0 + \delta_{0r}). \tag{41}$$

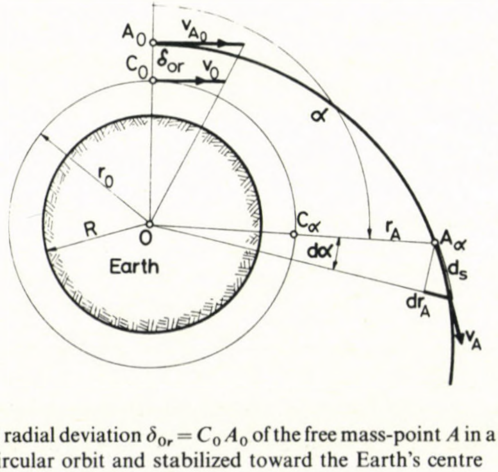

Fig. 4. The effect of the initial radial deviation $\delta_{0r} = C_0 A_0$ of the free mass-point A in a spacecraft revolving on a circular orbit and stabilized toward the Earth's centre

Further, it holds on the analogy of Eq. (5):

$$v_A \mathrm{d}v_A = -gR^2 \frac{\mathrm{d}r_A}{r_A^2} \tag{42}$$

from where we get by integration:

$$v_A^2 = v_{A0}^2 - \frac{2gR^2}{r_0+\delta_{0r}} + 2g\frac{R^2}{r_A}. \tag{43}$$

On the analogy of Eq. (7) it can also be written:

$$v_A^2 = \left(\frac{\mathrm{d}r_A}{\mathrm{d}t}\right)^2 \left(\frac{\mathrm{d}\alpha}{\mathrm{d}t}\right)^2 + r_A^2 \left(\frac{\mathrm{d}\alpha}{\mathrm{d}t}\right)^2$$

from where by the substitution from Eq. (41):

$$\frac{\mathrm{d}\alpha}{\mathrm{d}t} = \frac{v_{A0}(r_0+\delta_{0r})}{r_A^2}$$

we get

$$v_A^2 = \left(\frac{\mathrm{d}r_A}{\mathrm{d}\alpha}\right)^2 \frac{v_{A0}^2(r_0+\delta_{0r})^2}{r_A^4} + \frac{v_{A0}^2(r_0+\delta_{0r})^2}{r_A^2}. \tag{44}$$

From Eqs (43) and (44) one can write:

$$v_{A0}^2 - \frac{2gR^2}{r_0+\delta_{0r}} + \frac{2gR^2}{r_A} = \left(\frac{\mathrm{d}r_A}{\mathrm{d}\alpha}\right)^2 \frac{(r_0+\delta_{0r})^2}{r_A^4} v_{A0}^2 + \frac{(r_0+\delta_{0r})^2}{r_A^2} v_{A0}^2$$

from where:

$$\mathrm{d}\alpha = \frac{(r_0+\delta_{0r})v_{A0}\,\mathrm{d}r_A}{r_A\sqrt{\left(v_{A0}^2 - \dfrac{2gR^2}{r_0+\delta_{0r}}\right)r_A^2 + 2gR^2 r_A - (r_0+\delta_{0r})^2 v_{A0}^2}}$$

and then:

$$\alpha = \arccos\left\{\frac{(r_0+\delta_{0r})^2 v_{A0}^2 - r_A g R^2}{r_A(r_0+\delta_{0r})v_{A0}^2 - gR^2 r_A}\right\}$$

from where we get by taking Eqs (40) and (39) into account:

$$r_A = \frac{(r_0+\delta_{0r})^4}{r_0^3\left\{1 + \left[\left(\dfrac{r_0+\delta_{0r}}{r_0}\right)^3 - 1\right]\cos\alpha\right\}}.$$

After reduction and neglecting the small terms of second and third order it will be:

$$r_A = r_0 + (4 - 3\cos\alpha)\delta_{0r}. \tag{45}$$

The radial distance of the point A from the mass-centre C of the spacecraft will be:

$$\Delta r_r = r_A - r_0 = (4 - 3\cos\alpha)\delta_{0r}. \tag{46}$$

For determining the tangential motion ΔS_r of point A, let us express the differential time dt from Eq. (41):

$$\mathrm{d}t = \frac{r_A^2}{v_{A0}(r_0 + \delta_{0r})}\,\mathrm{d}\alpha$$

or, by substituting Eq. (45):

$$\mathrm{d}t = \frac{\{r_0 + (4 - 3\cos\alpha)\delta_{0r}\}^2}{v_{A0}(r_0 + \delta_{0r})}\,\mathrm{d}\alpha \cong$$

$$\cong \frac{r_0^2 + 8r_0\delta_{0r} - 6r_0\delta_{0r}\cos\alpha}{v_{A0}(r_0 + \delta_{0r})}\,\mathrm{d}\alpha.$$

From here we get by integration and substitution of Eq. (40):

$$t_A - t_0 \cong \frac{1}{v_0}[r_0\alpha + 6\delta_{0r}(\alpha - \sin\alpha)].$$

The mass-centre C comes into the position α during the time:

$$t_c - t_0 = \frac{\alpha r_0}{v_0}$$

thus, the revolving time-surplus of the free mass-point A will be until it reaches the revolving angle α:

$$\Delta t = t_A - t_c = \frac{6\delta_{0r}(\alpha - \sin\alpha)}{v_0}$$

and the tangential moving (delay) will be

$$\Delta S_r = \Delta t v_0 = 6(\alpha - \sin\alpha)\delta_{0r}. \tag{47}$$

Due to the radial initial deviation component δ_{0r}, there will be no motion of the free mass-point in a direction perpendicular to the plane of orbit,

$$\Delta q_r = 0. \tag{48}$$

Effect of the tangential initial deviation component

The free-mass-point with δ_{0s} initial tangential deviation will move during the revolution on the circular orbit of the mass-centre C, but preceding the point C by the distance δ_{0s}, thus the three deviation components will be:

$$\Delta r_s = 0, \qquad \Delta S_s = \delta_{0s}, \qquad \Delta q_s = 0. \tag{49}$$

Effect of the initial deviation component perpendicular to the orbital plane

As consequence of the initial deviation δ_{0q} perpendicular to the revolution plane, the free mass-point will move in the direction of the initial deviation component identically to the case discussed in 1.3, thus the formulas (36) and (38) are still valid.

The free mass-point with initial deviation δ_0 in arbitrary direction will again move on a spiral path being in a plane oblique to the orbital plane of the mass-centre with the angle δ_{0q}/r_0 around the point, but somewhat steeper.

Additional remarks

I. The inertial motion of the free mass-point in the spacecraft referred to the mass-centre of the spacecraft can be affected in a small degree by *a)* the gravitational effect of the body of spacecraft to the free mass-point, if the mass-distribution of the spacecraft body is not concentric, *b)* by the pressure of the solar wind on the spacecraft and *c)* by the resistance of the cosmic medium against the rotation of the spacecraft.

II. The formulas deduced for the inertial motion of the free mass-point valid for the free mass-points outside of the spacecraft, too.

III. On the basis of the statement in II. the formulas deduced for the motion of the free mass-point can be applied in the planning of experiments, in course of which the data being the object of the experiment, must be determined from the deviations of free masses placed outside of and near to the spacecraft (space station) being by several orders of magnitude less than the mass of the spacecraft, from the calculated orbit of the inertial motion. Such an experiment can be the actual determination of the solar wind pressure and the resistance coefficient of the cosmic medium. A free body of very small mass placed outside of a spacecraft will be affected by the following five forces: 1. the effect of inertia discussed here, 2. the unavoidable initial relative velocity of the small body that occurs at its release, 3. the gravitational force of the spacecraft body affecting the small free body, 4. the effect of solar wind on the free small body and 5. the resistance of the cosmic medium on the free small body. Factors 4 and 5 have namely a slackening effect on the very small free bodies with small specific cross-cut load, which is by orders of magnitude more than the effect on the spacecraft body with a great specific cross-cut load. Effects 3, 4 and 5 must be determined from the continuously measured motion elements of the very small free mass placed outside of the spacecraft, but near to it — after correcting with the inertial motion calculated with the method discussed and with the gravitational effect of the spacecraft that can be calculated, too. The solution of this problem needs, however, further intensive and detailed research activity.

Reference

Barta Gy, Hajósy A 1980: Movement of a material point in the gravity field of homogeneous ring. Cospar 23. Plenar Meeting, Magyar Tudományos Akadémia, Budapest

Acta Geodaet., Geophys. et Montanist. Hung. Volume 18 (4), pp. 383—401 (1983)

FUNDAMENTAL EQUATIONS WITH GENERAL VALIDITY OF REAL PROJECTIONS

V VINCZE[1]

[Manuscript received February 1, 1983]

The paper presents the generally valid equations of real, i.e. by realistic projection produceable projections on the basis of the idea that all real projections can be thought as made in two phases. In the first phase the base surface — either a rotational ellipsoid or a sphere — are evolved slip-free around the rotation axis on the picture plane, then in the second phase all points of the tangent meridian are projected from a projection centre in the meridian plane to the picture plane (Fig. 1).

Equation 11 is the generally valid basic equation — with corresponding substitutions — of all real projections (perspective, stereographic, orthographic, equal angle or area conic, cylindric, or plane projections) be the base surface a rotational ellipsoid or a sphere.

Keywords: geographic projections; projections of the ellipsoid; projections of the sphere; real projections; systematization of projections

All real projections of the sphere created by effective projecting were presented by Vincze (1968). The method of deduction described there enabled a uniform treatment of real projections integrated into one system and the introduction of fundamental base surface.

By the development of this method of deduction it was possible to extend it to the case of rotation-ellipsoidal base surfaces and that meant the additional advantage that all real projections could be integrated now into one system irrespective whether the base surface spherical or ellipsoidical.

The main point of this method of deduction is that the creation of real projections — i.e. projections created by effective projecting — can always be divided into two well separable phases. One phase is the proper projecting, the other the slip-free rolling of the base surface on the plane of projection.

It is a fundamental case, when the sphere — and here the chosen ellipsoid, respectively — representing the Earth is placed so on the plane of projection that the straight connecting the poles, i.e. the rotation axis meets the plane of projection in the finite and this intersection remains fixed during the slip-free rolling of the base surface. The projecting is always done in the meridional plane which is just tangential to the plane fitting to the meridional plane from a projecting centre having theoretically an arbitrary position.

[1] Budapest, II. Mártírok útja 56, H-1027

The intersection of the rotation axis can, however, be in the infinite and then the rotation axis remains during the rolling in all position parallel to itself. Another extreme position is, when the intersection is identical — on the pole — with the tangential point and all its meridional points will be separately projected from the projecting centre also being in its plane.

Naturally, the character of projecting also depends in this case on the position of the rotation axis, i.e. if conical, cylindrical or azimuthal plane projection of normal position is in question.

The distortion characteristics of the projection depend on the position of the projecting centre. This point can lie in the finite or in the infinite, it can be fixed or varying in dependence on the geographical latitude. By prescribing suitably the position of the projecting centre, equal-angle, equal-area projections or those of other characteristics can be created.

Considering that the Earth ellipsoid — as a rotation ellipsoid — can be regarded as the general case of the sphere, it is possible to extend the deduction to the Earth ellipsoid thus extending the unity of the projections to all the real projections.

Before discussing the problem let us sum up the notations used here in general on the basis of Hazay's publications (1954, 1964), further some new notations and concepts for sake of a more simple treatment (Fig. 1):

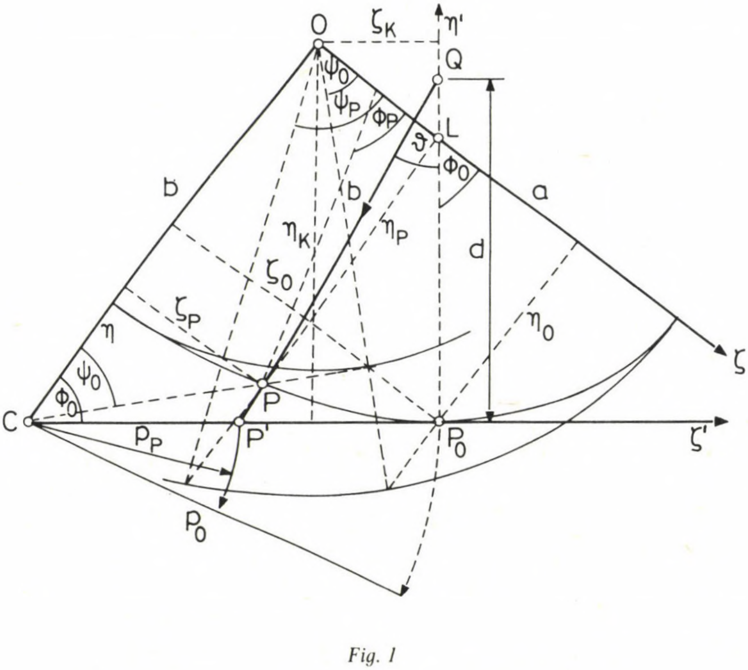

Fig. 1

Ellipsoidal half major axis: a
Ellipsoidal half minor axis: b
Ellipsoidal geographical latitude: Φ
Ellipsoidal geographical longitude: Λ
Reduced geographical latitude: ψ
Geocentral geographical latitude: ψ'
Spherical geographical latitude: φ
Spherical geographical longitude: λ
Radius of the Earth's sphere: R
Oblateness factors

$$\frac{a}{b}=\kappa \quad \text{and} \quad \frac{b}{a}=\kappa', \text{ resp.} \tag{1}$$

Coordinates of the meridional points

$$\begin{aligned} \eta_p &= b \sin \psi_p \\ \xi_p &= a \cos \psi_p . \end{aligned} \tag{2}$$

Linear modules along the meridian or along a parallel circle:

l_m and l_p, respectively.

Arc elements of the meridian:

$$\mathrm{d}m=\sqrt{d\xi^2+\mathrm{d}\eta^2}$$

where

$$\mathrm{d}\xi=-a \sin \psi \mathrm{d}\psi \quad \text{and} \quad \mathrm{d}\eta=b \cos \psi \mathrm{d}\psi$$

i.e.

$$\frac{\mathrm{d}m}{\mathrm{d}\psi}=\sqrt{a^2 \sin^2 \psi+b^2 \cos^2 \psi} \tag{3}$$

in other form

$$\frac{\mathrm{d}m}{\mathrm{d}\psi}=b\sqrt{\kappa^2 \sin^2 \psi+\cos^2 \psi}=bE_\psi \tag{4}$$

or

$$\frac{\mathrm{d}m'}{\mathrm{d}\psi}=a\sqrt{\sin^2 \psi+\kappa'^2 \cos^2 \psi}=aE'_\psi$$

finally

$$\tan \Phi=\kappa \tan \psi=\kappa^2 \tan \psi'. \tag{5}$$

The fundamental equation of each real projection

It is well known that a conical projection will be created when the angle Φ_0 between the rotation axis connecting the poles and the fundamental plane is greater than 0°, but less than 90°. In the co-ordinate system as noted in Fig. 1 the co-ordinates of the tangential points are:

$$\xi_0 = a \cos \psi_0 \qquad \text{and} \qquad \eta_0 = b \sin \psi_0 . \tag{6}$$

In order to establish the projection equation let us introduce the co-ordinate system ξ', η' one axis of which is the tangent in the figure and the other the normal at the tangential point. The co-ordinates of the centre O of the ellipsoid in this system will be:

$$\begin{aligned} \xi'_o &= \xi_0 \sin \Phi_0 - \eta_0 \cos \Phi_0 \\ \eta'_o &= \xi_0 \cos \Phi_0 + \eta_0 \sin \Phi_0 \end{aligned} \tag{7}$$

while the co-ordinates of a point of the meridian will be:

$$\begin{aligned} \xi'_P &= \xi'_o - \xi_P \sin \Phi_0 + \eta_P \cos \Phi_0 \\ \eta'_P &= \eta'_o - \xi_P \cos \Phi_0 - \eta_P \sin \Phi_0 \end{aligned} \tag{8}$$

and after substituting the corresponding co-ordinates:

$$\begin{aligned} \xi'_P &= a(\cos \psi_0 \sin \Phi_0 - \cos \psi_P \sin \Phi_0) + \\ &\quad + b(\sin \psi_P \cos \Phi_0 - \sin \psi_0 \cos \Phi_0) \\ \eta'_P &= a(\cos \psi_0 \cos \Phi_0 - \cos \psi_P \cos \Phi_0) + \\ &\quad + b(\sin \psi_0 \sin \Phi_0 - \sin \psi_P \sin \Phi_0). \end{aligned} \tag{9}$$

Let us suppose that the projecting centre Q lies on the normal through the tangential point in a distance of

$$d = c \frac{\eta_0}{\sin \Phi_0} = c\overline{FP}_0 = cf \tag{10}$$

from it, where the variable depending on the geographical latitude or the arbitrary constant independent from this — latter denoted by k — is a real number.

On the basis of that explained above, the projecting radius-equation of point P belonging to the latitude Φ_P and the reduced latitude ψ_P, respectively, can be written as follows (Fig. 1):

$$p_P = p_0 - q_P = \frac{\xi_0}{\sin \Phi_0} - c \frac{\eta_0}{\sin \Phi_0} \cdot \frac{\xi'_P}{cf - \eta'_P} . \tag{11}$$

This is the equation of all the real conical projections of the ellipsoid, but in the meantime also the equation of all the real projections, because it is valid for all real cylindrical and azimuthal plane projections due to the introduction of the proper parameters characteristical to the projection in question — naturally in case of a normal position.

This equation is, however, valid for all real spherical projections, too, because in this case

$$a=b=R$$

and

$$\Phi_0=\psi_0=\varphi_0$$

$$\Phi=\psi=\varphi \tag{12}$$

further $\kappa=1$.

Substituting these values into Eq. (9) we receive that:

$$\xi'_P=-R(\cos\varphi_P\sin\varphi_0-\sin\varphi_P\cos\varphi_0)=-R\sin(\varphi_P-\varphi_0)$$

and

$$\eta'_P=R-R\cos(\varphi_P-\varphi_0).$$

Thus the projecting radius-equation (Eq. 11) will take in case of a spherical base surface the following form:

$$p_P=R\cot\varphi_0-Rc\frac{R\sin(\varphi_P-\varphi_0)}{Rc-R+R\cos(\varphi_P-\varphi_0)}$$

$$p_P=R\cot\varphi_0-cR\frac{\sin(\varphi_P-\varphi_0)}{c-1+\cos(\varphi_P-\varphi_0)}.$$

This projecting radius-equation can be regarded as the special case of radius-equation (11) referring to the ellipsoid and is by normal position valid for each real spherical projection.

In the followings some projections belonging to the mentioned group of projections will be discussed.

Conical projections

Gnomonic conical projection

The projecting centre is the centre of the base surface (Fig. 2), i.e. the projecting centre does not lie in this case on the normal to the tangential point. On the basis of the figure it can be written:

$$\overline{CT}=b\frac{\cos\Phi_0}{\sin\psi_0}\qquad\text{and}\qquad\overline{OT}=b\frac{\sin\Phi_0}{\sin\psi_0}$$

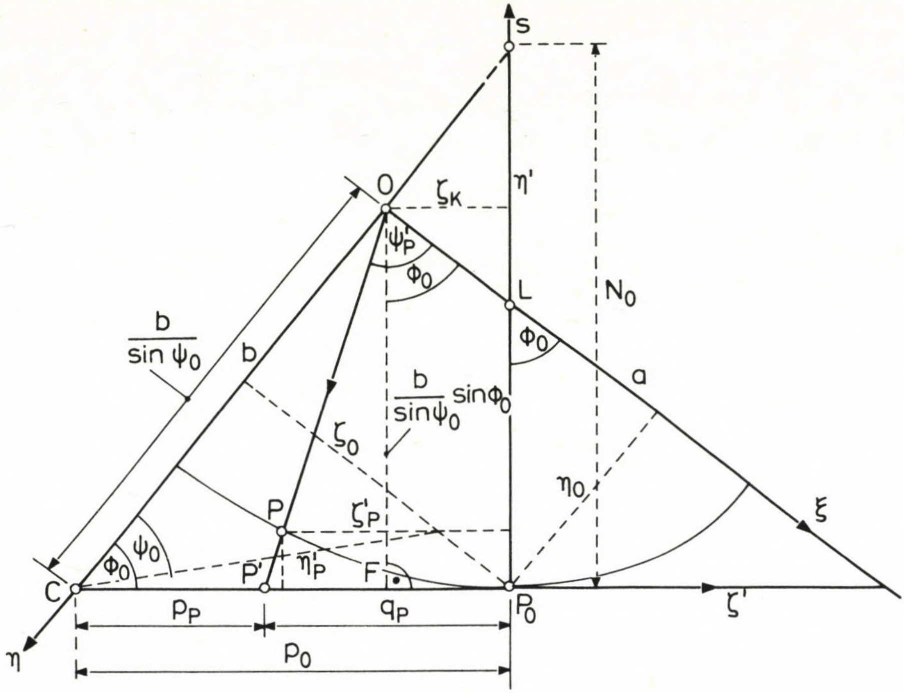

Fig. 2

further

$$p_P = \overline{CT} - \overline{OT} \tan (\psi'_P - \Phi_0)$$

$$p_P = b \left[\frac{\cos \Phi_0}{\sin \psi_0} - \frac{\sin \Phi_0}{\sin \psi_0} \tan (\psi'_P - \Phi_0) \right]. \tag{13}$$

According to Eq. (5):

$$\tan \psi_P = \kappa \tan \psi'_P$$

and, since

$$\lim_{\psi \to \Delta\psi} \tan \psi = \Delta\psi$$

and

$$\lim_{\psi' \to \Delta\psi'} \kappa \tan \psi' = \kappa \Delta\psi'$$

it follows that

$$\Delta\psi = \kappa \Delta\psi'$$

or

$$\mathrm{d}\psi = \kappa \mathrm{d}\psi'.$$

When taking Eq. (4) into consideration, it will be:

$$\frac{\mathrm{d}m}{\mathrm{d}\psi'} = \kappa \frac{\mathrm{d}M}{\mathrm{d}\psi} = \kappa b E_{\psi}. \tag{14}$$

Since

$$-\frac{\mathrm{d}p}{\mathrm{d}\psi'} = -\kappa \frac{\mathrm{d}p}{\mathrm{d}\psi} = \kappa b \frac{\sin \Phi_0}{\sin \psi_0} \frac{1}{\cos^2 (\psi_P - \psi_0)}$$

the linear modulus in the meridional direction will be

$$l_m = \frac{\mathrm{d}p}{\mathrm{d}m} = \frac{\sin \Phi_0}{E_{\psi} \sin \psi_0 \cos^2 (\psi_P - \Phi_0)} \tag{15}$$

and that along the parallel circle:

$$\begin{gathered} l_p = \frac{\sin \Phi_0}{a \cos \psi_P} p_P = \\ l_p = \frac{\sin \Phi_0}{\kappa \cos \psi_P} \left[\frac{\cos \Phi_0}{\sin \psi_0} - \frac{\sin \Phi_0}{\sin \psi_0} \tan (\psi'_P - \Phi_0) \right]. \end{gathered} \tag{16}$$

Finally, since

$$N_0 \cos \Phi_0 = a \cos \psi_0 = \xi_0$$

and

$$p_0 \gamma_0 = \gamma_0 N_0 \cot \Phi_0 = \gamma a \frac{\cos \psi_0}{\cos \Phi_0} \cot \Phi_0$$

further

$$\gamma_0 p_0 = \xi_0 \Lambda = \Lambda a \cos \psi_0$$

the inclination of the projecting radius will be:

$$\gamma = \Lambda \sin \Phi_0 \tag{17}$$

and the co-ordinates of the projection:

$$x_p = p_0 - p_p \cos \gamma$$

and (18)

$$y_p = p_p \sin \gamma.$$

In case of a sphere:

$$a = b = R$$

$$\kappa = 1 \qquad \text{further} \qquad E_{\psi} = 1$$

$$\psi_P = \psi'_P = \varphi_P$$

$$\psi_0 = \varphi_0$$

therefore Eqs (13), (15) and (16) will be transformed into the known form:

$$p_p = R\cot\varphi_0 - R\cot(\varphi_P - \varphi_0)$$

$$l_m = \frac{1}{\cos^2(\varphi_P - \varphi_0)}$$

and

$$l_p = \frac{\sin\varphi_0}{\cos\varphi_P}\left[\cot\varphi_0 - \tan(\varphi_P - \varphi_0)\right] \tag{19}$$

which was published by Vincze in 1968.

Orthographic conical projection

For this projection the imaginary projecting centre lies in the infinite, in other words the projecting radii are parallel and perpendicular to the projection plane. Here, however, this case will not be discussed, but for sake of simplicity that one will be taken into this group, where the projecting radii are not only parallel to each other, but to the rotation axis, too. This is an equal-length projection with parallel circles and is unknown so far in the literature.

On the basis of Fig. 3 it can be written:

$$p_P = \xi_P \sin\Phi_0 = a\frac{\cos\psi_P}{\sin\varphi_0} = \kappa b\frac{\cos\psi_P}{\sin\Phi_0}. \tag{20}$$

Further

$$-\frac{dp}{d\psi} = -\kappa b\frac{\sin\psi_P}{\sin\Phi_P}$$

and from Eq. (4):

$$\frac{dm}{d\psi} = bE_\psi$$

therefore

$$l_m = \kappa\frac{\sin\psi_P}{E_\psi \sin\Phi_0} \tag{21}$$

and

$$l_P = \frac{\sin\Phi_0}{a\cos\psi_P}\,p_P = 1. \tag{22}$$

The projection co-ordinates are identical with those in Eq. (18) and the co-ordinates given in Eqs (20), (21) and (22) will be transformed by means of the substitutions already applied into the following forms valid for the sphere:

$$p_P = R\frac{\cos\varphi_P}{\sin\varphi_0}, \qquad l_m = \frac{\sin\varphi_P}{\sin\varphi_0} \qquad l_P = 1.$$

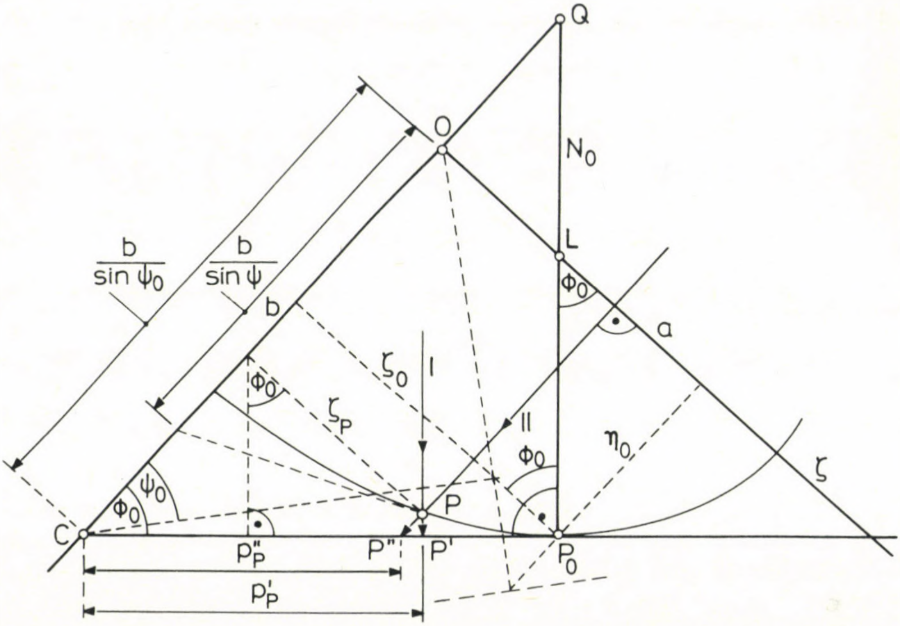

Fig. 3

Cylindrical projections

In case of ellipsoidal cylindrical projection:

$$\Phi_0 = \psi_0 = 0^\circ$$

and

$$\sin \Phi_0 = \sin \psi_0 = 0,$$

$$\cos \Phi_0 = \cos \psi_0 = 1$$

since from Eq. (11) we get:

$$p_0 = \frac{\xi_0}{\sin \Phi_0} \to \infty .$$

From Fig. 1 it follows that, if φ_0 approaches O, one has

$$\lim c \frac{\eta_0}{\sin \Phi_0} \to c \cdot a$$

further from Eq. (9) one gets:

$$\frac{\xi'_P}{ac - \eta'_P} = \frac{b \sin \psi_P}{a(c - 1 + \cos \psi_P)} .$$

Hence, the generalized equation of cylindrical projections will be:

$$p_P = ac\frac{b\sin\psi_P}{a(c-1+\cos\psi_P)} = cb\frac{\sin\psi_P}{c-1+\cos\psi_P}. \tag{23}$$

Perspective cylindrical projections

Equation (23) is valid for this case after the substitution

$$c=k,$$

where k is a constant with positive sign:

$$p_P = kb\frac{\sin\psi_P}{k-1+\cos\psi_P} \tag{24}$$

further

$$\frac{dp}{d\psi} = kb\frac{1+\cos\psi_P-\cos\psi_P}{(k-1+\cos\psi_P)^2}$$

and by taking Eq. (4) into account:

$$l_m = k\frac{1+k\cos\psi_P-\cos\psi_P}{E_\psi(k-1+\cos\psi_P)^2} \tag{25}$$

while the other linear modulus will be:

$$l_p = \frac{a\Lambda}{\xi\Lambda} = \frac{a}{a\cos\psi_P} = \frac{1}{\cos\psi_P}. \tag{26}$$

The projection co-ordinates are:

$$x_P = kb\frac{\sin\psi_P}{k-1+\cos\psi_P}$$

and

$$y_P = a\Lambda_P. \tag{27}$$

In case of a spherical base surface the co-ordinates will be:

$$x_P = kR\frac{\sin\varphi_P}{k-1+\cos\varphi_P} \qquad \text{and} \qquad y = R\lambda_P.$$

Gnomonic cylindrical projections

In case of an ellipsoidal base surface the projecting centre is the centre of the base surface, but one could include here also the projection, where the projecting radius is identical with the normal to the point, since its spherical correspondence is also the gnomonic spherical projection. Here, however, only the first case is dealt with.

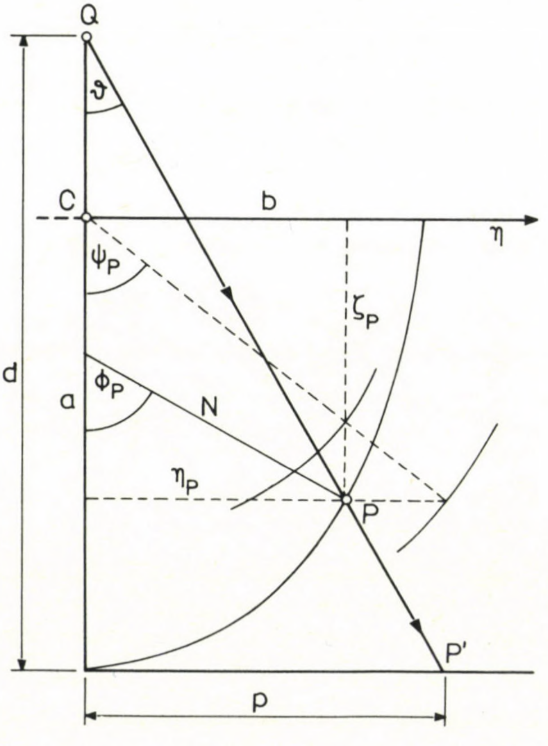

Fig. 4

The projecting centre is, consequently, the centre of the ellipsoid (Fig. 4), and therefore it is a perspective projection where $k=1$. Having made this substitution into Eqs (25), (26) and (27) one gets the connections valid for this case:

$$l_m = \frac{1}{E_\psi \cos^2 \psi_P} \qquad \text{and} \qquad l_P = \frac{1}{\cos \psi_P} \tag{28}$$

further:

$$x_p = b\frac{\sin \psi_P}{\cos \psi_P} = b \tan \psi_P \qquad \text{and} \qquad y_p = a\Lambda_P. \tag{29}$$

Stereographic cylindrical projection

This is again a perspective projection, where

$$k=2.$$

After the substitution the equations of the ellipsoidal stereographic cylindrical projection are:

$$l_m = \frac{2}{E_\psi(1+\cos\psi_P)} \quad \text{and} \quad l_P = \frac{1}{\cos\psi_P} \tag{30}$$

further

$$x_p = 2b\frac{\sin\psi_P}{1+\cos\psi_P} \quad \text{and} \quad y_p = a\Lambda_P. \tag{31}$$

In case of a spherical base surface one gets after substitutions according to Eq. (12) the equations of the stereographic cylindrical projections.

Orthographic cylindrical projection

The projecting centre lies in the infinite and the projecting radii are perpendicular to the projection plane, i.e.:

$$d=\infty \quad \text{and} \quad \vartheta=0°.$$

Corresponding to this it is now (Fig. 4):

$$p_P=\eta_P=x=b\sin\psi_P \tag{32}$$

and the linear moduli will be:

$$l_m = \frac{\cos\psi_P}{E_\psi} \quad \text{and} \quad l_p = \frac{1}{\cos\psi_P}. \tag{33}$$

In case of a spherical base surface this is the Lambertian equal-area cylindrical projection. Since E_ψ is also nearly equal with the unit — at least over a considerable area — this projection can be regarded at least as nearly an equal-area one even in the case of an ellipsoidal base surface.

Conformal cylindrical projection

The generalized equation (23) of the cylindrical projection was:

$$p_P = cb\frac{\sin\psi_P}{c-1+\cos\psi_P}$$

further

$$\frac{\mathrm{d}p}{\mathrm{d}\psi} = cb\frac{(c-1+\cos\psi_P)\cos\psi_P+\sin^2\psi_P}{(c-1+\cos\psi_P)^2} =$$

$$= cb\frac{1+(c-1)\cos\psi_P}{(c-1+\cos\psi_P)^2}$$

and after using Eq. (4):

$$l_m = \frac{\mathrm{d}p}{\mathrm{d}m} = c\frac{1+(c-1)\cos\psi_P}{E_\psi(c-1+\cos\psi_P)^2} \tag{34}$$

and

$$l_P = \frac{a\Delta\Lambda}{N\cos\Phi_P\Delta\Lambda} = \frac{a}{a\cos\psi_P} = \frac{1}{\cos\psi_P}. \tag{35}$$

In case of an equal-angle projection:

$$l_m = l_p,$$

consequently the equation:

$$c\frac{(c-1)\cos\psi_P+1}{E_\psi(c-1+\cos\psi_P)^2} = \frac{1}{\cos\psi_P}$$

must hold.

Having carried out the operations and the necessary reductions we get the following equation:

$$Ac^2+Bc+C=0$$

where

$$\begin{aligned} A &= \cos^2\psi_P - E_\psi \\ B &= \cos\psi_P - \cos^2\psi_P - 2E_\psi\cos\psi_P + 2E_\psi \end{aligned} \tag{36}$$

and

$$C = 2E_\psi\cos\psi_P - E_\psi\cos^2\psi - E_\psi.$$

It follows from that said above:

$$c = \frac{-B\pm\sqrt{B^2-4AC}}{2A}$$

and the projection equations are:

$$x_p = cb\frac{\sin\psi_P}{c-1+\cos\psi_P} \qquad y_p = a\Lambda. \tag{37}$$

These equations are of course valid in case of a spherical base surface after the following substitutions:

$$E=1, \quad \text{and} \quad \psi=\varphi, \quad \text{respectively.}$$

The coefficients in Eq. (36) have the form:

$$A=\cos^2 \varphi_P-1$$

$$B=2-\cos^2 \varphi_P-\cos \varphi_P$$

and

$$C=2\cos \varphi_P-\cos^2 \varphi_P-1.$$

This is the Mercator conformal cylindrical projection in both variants.

Equal-area cylindrical projection

A projection is an equal-area one if:

$$l_m l_p=1,$$

i.e. — with respect to Eqs (34) and (35) — the following equation holds:

$$c\frac{1+(c-1)\cos\psi_P}{E_\psi(c-1+\cos\psi_P)^2\cos\psi_P}=1.$$

Having made the operations and reduced the equation to c, we get the following equation of second order:

$$Ac^2+Bc+C=0$$

where

$$A=(1-E_\psi)\cos\psi_P$$

$$B=1-\cos\psi_P+2E_\psi\cos\psi_P-2E_\psi\cos\psi_P \tag{38}$$

and

$$C=E_\psi(2\cos^2\psi_P-\cos\psi_P-\cos^3\psi_P)$$

and the solution is

$$c=\frac{-B\pm\sqrt{B^2-4AC}}{2A}.$$

In case of sphere

$$E_\psi=1 \qquad \text{and} \qquad A=0$$

since

$$c=\infty$$

which characterizes the Lambertian orthographic equal-area cylindrical projection of spherical base surface.

Concerning the projection equations the connections of (37) are here valid, too, after substituting the corresponding c values.

Azimuthal plane projections

An ellipsoidal plane projection is created, if the following substitutions characteristic for the plane projection are made in the basic equation (11):

$$\Phi_0 = \psi_0 = 0°$$

since

$$\sin \Phi_0 = \sin \psi_0 = 1$$

and

$$\cos \Phi_0 = \cos \psi_0 = 0.$$

Thus, one has:

$$p_0 = \frac{\xi_0}{\sin \Phi_0} = \frac{a \cos \psi_0}{\sin \Phi_0} = 0$$

and

$$c \frac{\eta_0}{\sin \Phi_0} = c \frac{b \sin \psi_0}{\sin \Phi_0} = cb.$$

Further, on the basis of Eq. (9) it can be written:

$$\frac{\xi_P}{cb - \eta'_P} = \frac{a \cos \psi_P}{cb - b + b \sin \psi_P} = \frac{a \cos \psi_P}{b(c - 1 + \sin \psi_P)}.$$

Hence, the generalized equation of the ellipsoidal plane projections is (Fig. 5):

$$p_p = ac \frac{\cos \psi_P}{c - 1 + \sin \psi_P}. \tag{39}$$

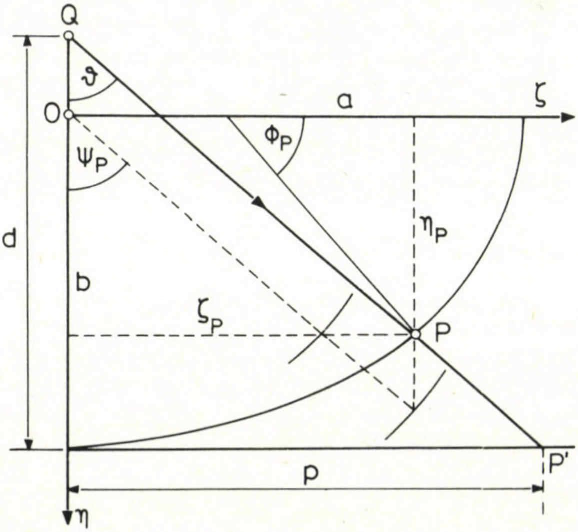

Fig. 5

Perspective plane projections

The factor c in Eq. (39) is in this case constant and is denoted by k. Hence:

$$p_p = ka \frac{\cos \psi_P}{k - 1 + \sin \psi_P} \tag{40}$$

further:

$$-\frac{dp}{d\psi} = ka \frac{(k-1)\sin \psi_P + 1}{(k - 1 + \sin \psi_P)^2}$$

and since:

$$\frac{dm}{d\psi} = aE'_\psi$$

one gets:

$$l_m = k \frac{(k-1)\sin \psi_P + 1}{E'_\psi (k - 1 + \sin \psi_P)^2} \tag{41}$$

and the other linear modulus can be written as:

$$l_p = \frac{k}{k - 1 + \sin \psi_P}. \tag{42}$$

The projection co-ordinates are:

$$x_p = p_p \cos \Lambda_P \qquad \text{and} \qquad y_p = p_p \sin \Lambda_P. \tag{43}$$

Several spherical geographical perspective plane projections are mentioned in the literature (e.g. Hazay 1954, 1964), hereby the factor k varies in our equations from 2.367 to 3.41.

Considering that these numerical values are mostly given with an accuracy of only 2–3 decimals, we suppose that the characteristics of these geographical projections do not change too much, if the same constants are used in case of an ellipsoidal base surface.

Gnomonic plane projection

Similarly to that mentioned for the cylindrical projections, two variants are possible here, too, but we only deal with the case when the projecting centre is identical with the centre of the ellipsoid.

This projection is the variant of perspective projections, where

$$k = 1,$$

and substituting this value into Eq. (40), we get:

$$p_P = a \frac{\cos \psi_P}{\sin \psi_P} = a \cot \psi_P \tag{44}$$

and according to Eqs (41) and (42) the linear moduli are:

$$l_m = \frac{1}{E'_\psi \sin^2 \psi_P} \qquad l_p = \frac{1}{\sin \psi_P}. \tag{45}$$

Stereographic plane projection

This is again a perspective projection, where the constant factor

$$k=2,$$

and consequently Eq. (40) has the form:

$$p_p = 2a \frac{\cos \psi_P}{1+\sin \psi_P} = 2a \tan\left(45^\circ - \frac{\psi_P}{2}\right) \tag{46}$$

or using the complement angle:

$$\beta' = 90^\circ - \psi_P$$

it is

$$p_p = 2a \tan \frac{\beta'_P}{2}$$

and for the linear moduli one gets:

$$l_m = \frac{1+\sin \psi_P}{E'_\psi (1+\sin \psi_P)^2} = \frac{2}{E'_\psi \cos^2 \frac{\beta'}{2}}$$

and

$$l_p = \frac{2}{(1+\sin \psi_P)^2} = \frac{2}{\cos^2 \frac{\beta'}{2}}. \tag{47}$$

In case of a spherical base surface this is the known conformal projection, because here

$$E_\psi = 1.$$

Conformal plane projection

According to the generalized equation for plane projections (Eq. (39)):

$$p_P = ca \frac{\cos \psi_P}{c-1+\sin \psi_P} \tag{48}$$

further

$$-\frac{\mathrm{d}p}{\mathrm{d}\psi} = c \cdot b\kappa \frac{(c-1)\sin \psi_P + 1}{(c-1+\sin \psi_P)^2}$$

and according to Eq. (4):

$$\frac{\mathrm{d}m}{\mathrm{d}\psi} = bE_\psi$$

hence

$$l_m = \frac{\mathrm{d}p}{\mathrm{d}m} = c\kappa \frac{(c-1)\sin\psi_P + 1}{E_\psi(c-1+\sin\psi_P)^2}$$

and (49)

$$l_p = \frac{p_P}{\xi_P} = \frac{c}{c-1+\sin\psi_P}.$$

The projection is conformal, if:

$$l_m = l_p$$

i.e., if:

$$c\kappa \frac{(c-1)\sin\psi_P + 1}{E_\psi(c-1+\sin\psi_P)^2} = \frac{c}{c-1+\sin\psi_P}.$$

Having done the operations noted:

$$c = \frac{(\kappa + E_\psi)(\sin\psi_P - 1)}{\kappa\sin\psi_P - E_\psi}. \tag{50}$$

If the base surface is a sphere:

$$\kappa = 1 \qquad \text{and} \qquad E_\psi = 1$$

consequently

$$c = 2,$$

being the criterion — as known — of the stereographic spherical equal-angle plane projection on the area, naturally, where the ellipsoid is properly substituted by the sphere.

Orthographic plane projection

The projecting centre is in the infinite and the projecting radius perpendicular to the projection plane (Fig. 5). Thus:

$$p_p = \xi_P = a\cos\psi_P \tag{51}$$

and its linear moduli:

$$l_m = \frac{\sin\psi_P}{E_\psi} \qquad \text{and} \qquad l_p = 1. \tag{52}$$

It can be seen that the discussed deduction method of the real projections has the advantage that a fundamental equation (11) of general validity can be introduced, which holds good for all real ellipsoidal projections of normal position, but at the same time the equation (12) valid for all real spherical projections can be deduced from it, too. In this deduction the circumstance can be well used that the sphere is a special variant of the rotation ellipsoid, it was therefore possible to introduce equations of general validity which hold for all real projections irrespective, whether the base surface is an ellipsoid or a sphere.

From this recognition follows the further advantage that it is possible to integrate the whole of the projective geometry, as a discipline, into a well arranged and logical system.

References

Hazay I 1954: Terrestrial projections. (In Hungarian) Akadémiai Kiadó, Budapest

Hazay I 1964: Projective Geometry. (In Hungarian) Tankönyvkiadó, Budapest

Vincze V 1968: Einheitliche Ableitung und allgemeingültige Grundgleichungen der reellen Projektionen. *Acta Geod. Geoph. Mont. Hung.*, 3, 69–103.

Acta Geodaet., Geophys. et Montanist. Hung. Volume 18 (4), pp. 403—419 (1983)

A COMPARISON OF PC MAGNETIC PULSATIONS ON THE GROUND AND AT SYNCHRONOUS ORBIT

J VERŐ[1]—L HOLLÓ[1]

[Manuscript received June 5, 1982]

The paper presents a summary of results on the comparison of pulsations data from the satellite ATS 6 (Takahashi et al. 1981) and the surface station Nagycenk for a year in 1973–74. In spite of the difference in position and L-value, strong similarities were observed, and even a part of the existing differences could be explained in terms of the afternoon-activity unobservable on ground.

Keywords: ATS 6; correlation of pulsations; geomagnetic pulsations; interplanetary magnetic field; magnetospheric-surface connection; Pc 3; solar wind

Introduction

The first comprehensive statistical study of Pc 3 pulsations at a synchronous orbit was carried out by Takahashi et al. (1981) using data of the UCLA fluxgate magnetometer on ATS 6. They could show that a number of pulsation characteristics, determined on the basis of ground observations, can also be found in satellite data. The effect of the solar wind velocity, V_{SW}, and that of direction of the interplanetary magnetic field, Θ_{XB}, were found as the main controlling factors of the pulsation activity, complicated by the local time dependence of the occurrence and amplitude of the pulsation activity. They refer to an agreement of their data with ground-based observations, but for many results of their investigations, no comparable ground-based data are available, or at least they are not from the same time interval. The continuous pulsation recording of the Nagycenk observatory ($\varphi = 47°\ 38'$, $\lambda = 16°\ 43'$, $\Phi = 47.2°$) offer an opportunity to compare nearly all results by Takahashi et al. with similar ground-based data. Such a comparison is presented in this paper.

The differences between the two sets of data lie in the geomagnetic position (L values 4.4 and 1.9) of the observing sites and in the selection of the data. Instead of the binary occurrence index used for the ATS satellite data, in Nagycenk two kinds of values were used: a similar binary index, indicating regular waveform of the existing Pc 3–4 pulsations, and the average hourly amplitudes of all pulsations with periods shorter than 2 min. A comparison of the two Nagycenk data sets enables to clarify certain points. It should be also remarked that regular pulsations have mostly greater than average amplitudes, but maximum amplitudes are found for irregular pulsations. The differences due to the different data bases should be kept in mind when comparing results.

[1] Geodetic and Geophysical Research Institute of the Hungarian Academy of Sciences, H-9401 Sopron, Pf. 5

Pulsation data of the Nagycenk observatory

The Nagycenk observatory has been existing since the International Geophysical Year, IGY, 25 years ago. Earth currents recording has been nearly continuous since the very beginning, moreover the amplitudes of the pulsations in the earth current field have been determined during this time always by the same person. This continuity ensured a stability unusual for subjective indices for these pulsations amplitudes. Thus e.g. the coefficients of the regression equation between solar wind velocity and pulsations amplitudes changed less than 10% during the interval of in situ solar wind measurements. Therefore the hourly pulsation amplitudes of the more disturbed component, telluric E_y (E—W), corresponding nearly to geomagnetic H, are used throughout this comparison. In case of any exceptions, these are especially mentioned. The amplitudes are determined in units of 0.18 mV/km, and in these units the daytime maximum of the amplitudes corresponds to about 2 units. Unit 1 indicates a rather low pulsation activity.

The determination of the pulsation amplitudes is made from records with a chart spead of 25 mm/hour, therefore no distinction can be made from these records between Pc 3 or Pc 4 pulsations, Pc 1 and 2 have very low amplitudes. It is, however, clear that the majority of Pc 3 events surpasses in amplitude Pc 4 events, at least at our latitudes, and the Pc 4 activity has more or less a noise-character. Thus the inclusion of Pc 4 pulsations does not exclude a comparison of the two data sets.

Occurrence frequencies and amplitudes were compared several times in different kinds of records of the Nagycenk observatory, with the result that the main factor governing the amplitude level in case of a given occurrence frequency is geomagnetic activity. That means that for a certain level of occurrence (e.g. for a certain daily occurrence frequency index) the amplitude index is the higher, the greater the geomagnetic activity is. Thus for comparisons not including the geomagnetic activity as a variable, occurrence frequencies and amplitudes can be substituted by each other.

A better comparison can be made with a binary occurrence index indicating the presence of regular Pc 3–4 type variations. It is determined from the pulsation catalogue of the observatory, based on the quick-run earth-current records (6 mm/min) with a similar scale value (0.15 mV/km). The regularity is a subjective term; in a "regular" pulsation event, however, the maximum and minimum apparent periods must not differ by more than 50%. The criterion used in selection of these "regular" events is a more rigorous one than used by Takahashi et al., as around local noon their average occurrence probability is 40–50%, while in case of the Nagycenk data it is around 20%. Thus the two values used in this paper "flank" Takahashi et al.'s index, thus the reliability of a comparison and generally of the data can also be estimated.

Differences in the response of Pc 3 and Pc 4 pulsations to interplanetary changes

The connection between interplanetary field parameters and activities of the pulsations in a number of frequency bands has been already discussed in earlier papers (Verő and Holló 1978, Verő 1980) based on the material of the Nagycenk observatory. Here only some effects should be mentioned which are of importance for the connections studied in this paper.

1. Connection with V_{SW}: the formula is for all period bands $A = c \cdot V_{SW}^{x}$, the exponent x being a function of the period. It is around 2 or somewhat more for pulsations with periods less than 30 s, for pulsations with longer periods it is less than 2 or even around 0 (at 90 s).

2. The maximum activity is found for the short period range if Θ_{XB} is around 30°, for longer periods (longer than 30 s) the maximum is at 0°.

3. The diurnal variation of the average amplitudes or occurrence frequencies has a single peak somewhat before noon for the short period range, and a double peak, with higher morning activities for the longer period range.

4. The wave-form in the shorter period range is quite often regular, that in the longer period range is never as regular as that in the shorter period range.

It follows from these that a boundary of different type pulsations, identifiable with the Pc 3 and Pc 4 types is at our latitude near to 30 s, but this period changes quickly with the latitude, and in the subauroral latitudes it lies near to the generally accepted 45 s.

Diurnal variation of the activity

The diurnal variation of the pulsation activity changes rather significantly during different seasons. During maxima of the solar activity, if the sunspot relative number, R is more than about 100, the activity of the pulsations is severely damped in local winter or in December (Verő 1981). The years 1974–75 were years with low solar activity, therefore such an anomalous change did not appear. Nevertheless there are changes in the diurnal distribution of the pulsations which are evident in all years and which are not connected with the seasonal change of the solar height (e.g. sunrise or sunset). Figure 1 shows the daily distribution of the pulsation activity in Nagycenk, for the Northern summer and winter months of the year 1974, and for June and December in average of the years 1957–1980. The long time average shows that in summer the activity begins and dies out earlier than in winter, and therefore the pulsation activity before noon is in summer greater than in winter, while afternoon the winter activity is higher. In a particular year, the situation can be slightly different. This is just opposite to the ATS 6-results, but neither of them corresponds to the change of the solar height.

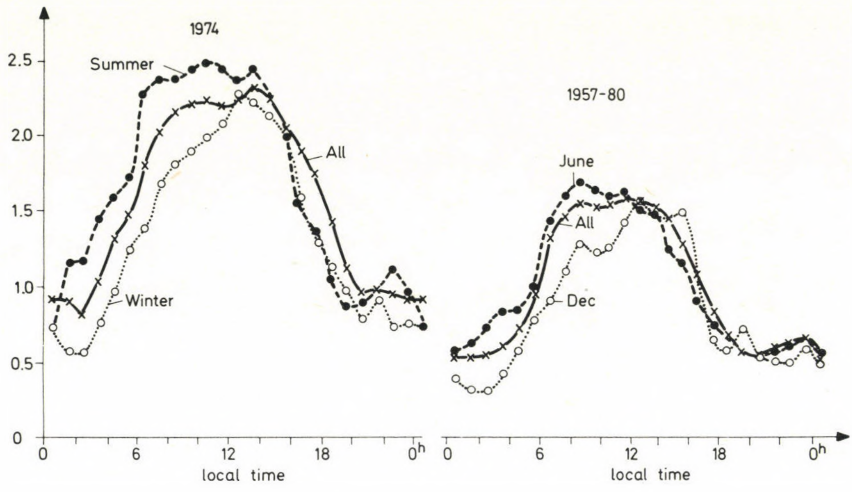

Fig. 1. Diurnal variation of the amplitude of short period pulsations in different seasons in 1974 and in average of the years 1957–1980. Amplitude values in all figures are in units of 0.18 mV/km, and the represented component is E_y (similar to geomagnetic H), if not otherwise stated

In accordance with the different shape of the diurnal variations, the change of the amplitudes with season at two fixed local times are also different. The changes in Nagycenk are by far less important than in the magnetosphere. Here the inclusion of the less regular events may play a certain role, the fractional distribution of the regular events, however, does not change as much as to explain this difference (see e.g. Fig. 3*b*–*d*). For comparison, Fig. 2 shows also the long-time average of the seasonal change of the predawn and mid-afternoon activities, separately for the E—W (*H*) and N—S (*D*) components. It is clear that the character of this seasonal change is similar in both cases, only its amplitude is greater in the *D*-component.

As no similar data are known from the Southern hemisphere, it is not clear if this effect is local or global. ATS 6 data show an opposite tendency, therefore only a mechanism could explain the observed facts which acts inversely in winter and in summer, morning and afternoon, and its effect is reversed even at different latitudes (or below and above the ionosphere). In all cited cases the common element is the pre-noon peak and a double maximum, with changing intensities. The morning activities are greater even in Takahashi et al.'s summer and in our winter season when the differences between morning and afternoon are the smallest.

According to Parker's spiral, this pre-noon peak of the pulsation activity could be explained, if in case of abnormal IMF directions (0–90°, 180–270°) the maximum would be shifted towards later times. This shift was not present (or only its slight trace could be found) in ATS-data, similarly in our data (Fig. 3*a*) the maximum is somewhat shifted in case of abnormal IMF directions towards later local times.

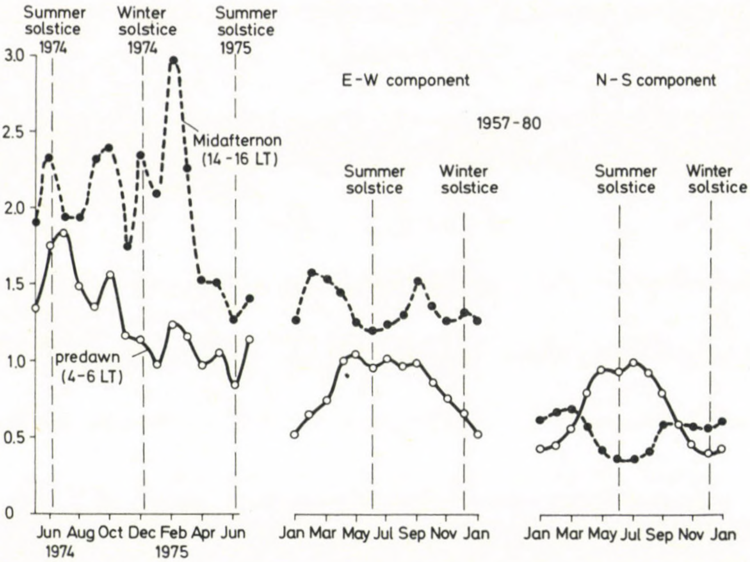

Fig. 2. Seasonal changes in predawn and midafternoon amplitude of short period pulsations in 1974–1975 and in average of the years 1957–1980, separately for the components E_y(E—W) and E_x (N—S, geomagnetic D)

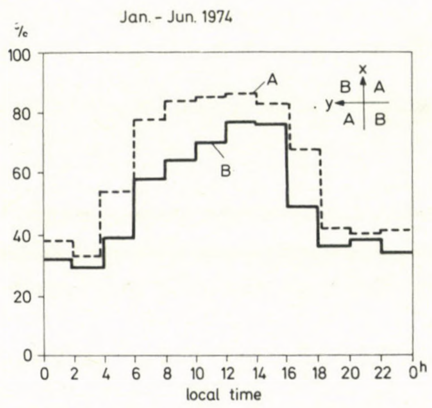

Fig. 3a. Occurrence probability of short period pulsations with greater than average amplitudes, a) for normal, b) for abnormal interplanetary magnetic field directions

Similar data on the regular variations can be seen in Figs 3*b*–*d*. Figure 3*b* shows the seasonal distribution of regular events for the years 1974–75. The lower activity in 1975 is at least partly due to subjective causes and possibly also to artificial noises, which reduced the number of the selected regular cases. There is no recurrent seasonal

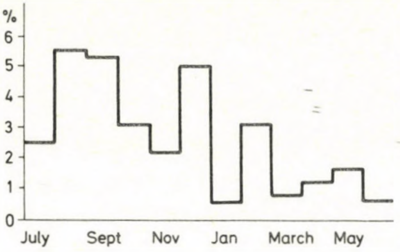

Fig. 3b. Seasonal distribution of regular pulsations in (different months of the year) 1974–1975 (occurrence in percents)

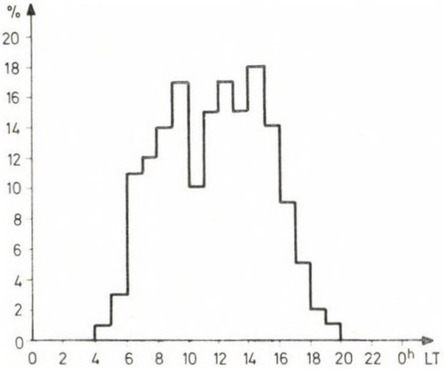

Fig. 3c. Average diurnal change of regular pulsations in 1974

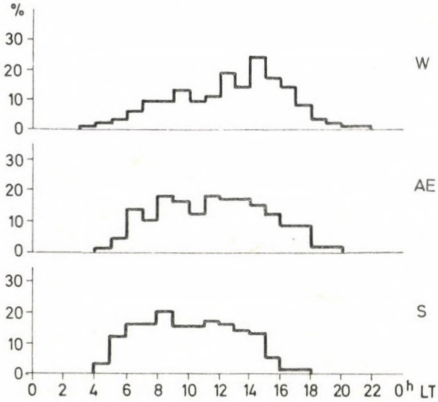

Fig. 3d. Monthly average occurrences of regular pulsations

change, at least the earlier occurrence of these events in summer can be significant. The average daily distribution (Fig. 3*c*) shows a somewhat different diurnal change of the regular cases, with relatively stable occurrence frequencies between 06 and 16 h LT, but the maximum is shifted towards afternoon hours. This can be of a purely random origin, nevertheless it deserves further attention. The shift towards the afternoon hours is most pronounced in winter months (Fig. 3*d*) in accordance with the distribution of pulsation amplitudes (Fig. 1). On the basis of the satellite and ground data, the most reliable conclusion is that the maximum of the pulsation activity appears in case of abnormal IMF directions somewhat later than in case of normal IMF directions, but the maximum does not occur during afternoon, it is at most around local noon.

We remind here to the fact that according to Verő (1980) the Pc 3 activity has a single peak not very far from local noon, and the Pc 4 activity has two peaks early in the morning and later in afternoon, with the first one being the main maximum. Thus it is clear that the exclusion of the (less regular) Pc 4 events shifts the maximum somewhat nearer to local noon, and this is really what we find comparing Figs 1 and 3. The existence of a difference between the diurnal variation of the Pc-activity at different IMF-directions was confirmed among others by Potapov (1974) and Verő (1980), too.

Effect of V_{SM} and Θ_{XB} on pulsation amplitudes

Figure 4 shows a comparison of the correlation coefficients between some interplanetary parameters and pulsation activities on ATS 6 and in Nagycenk. First of all, there is a rather good coincidence in case of the average correlations between the pulsation activity and V_{SW} and Θ_{XB}. In case of B, the majority of the Nagycenk data have reversed sign in comparison to the ATS 6 data. The morning correlations are generally somewhat higher for V_{SW} and Θ_{XB} for the ATS 6 data, while in the afternoon, there is a significant drop in the ATS-correlations which is absent from the Nagycenk data. Here the appearance of the afternoon activity in the magnetosphere which cannot be observed on the ground, plays very likely the most important role. These pulsations in the Pc 4 range were discussed by Hughes et al. (1978). He supposed them to be due to bounce resonance of waves with hot protons. If the spectrum of these waves has a short-period (high frequency) tail, and they do not appear on the surface records, then the difference in the correlation coefficients can be explained. An alternative explanation would be, at least partly, that offered by Takahashi et al. (1981) who supposed that the non-linear connection between solar wind velocity and pulsation activity may play a role here. In our opinion, however, this decrease of the occurrence probability of Pc 3 pulsations can be an artificial one due to the selection criterion. The "noise" (i.e. variations with white spectrum in a rather broad band) increase in intensity very quickly at high geomagnetic activities, roughly from a value of Kp about 6. In such cases the solar wind velocity is most likely also high, and regular pulsations which appear nearly with the same frequency might be veiled by the high noise level.

Just this strong noise in case of high geomagnetic activity makes it rather difficult to use the same selection criteria for regular pulsations in quiet and disturbed times, and this was one of the causes why we compared both overall average pulsation

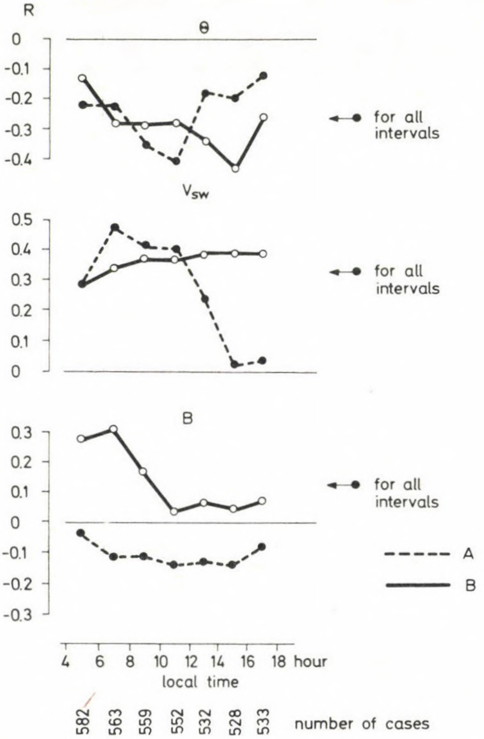

Fig. 4. Correlation coefficients between pulsations measured by ATS (broken line, *A*) and in Nagycenk (continuous line, *B*) and some interplanetary parameters at different local times

amplitudes and occurrences of regular pulsations. It should be added that short period variations have in the earth current field generally greater amplitudes, therefore the problem of the natural "noises" is here even more difficult than in geomagnetic records.

This conclusion is supported by Fig. 5, where the occurrence frequencies of regular pulsations are shown in function of the solar wind velocity. There is a rapid increase till velocities of 600 km/s, then the frequency drops (from 20 to 13%). The fact that the drop of the occurrence frequency begins here already at a lower velocity value than in case of the magnetic satellite data, can be a consequence of the mentioned higher sensibility of the electric field for short period noises. A similar effect might appear in Fig. 5, where the occurrence frequencies of regular pulsations are expressed also in function of the interplanetary magnetic field. Here again at high scalar magnitudes, the occurrence frequency is much lower than at medium values of the IMF (this is statistically significant even if the number of cases with high IMF is less than that of values around 5–10 nT).

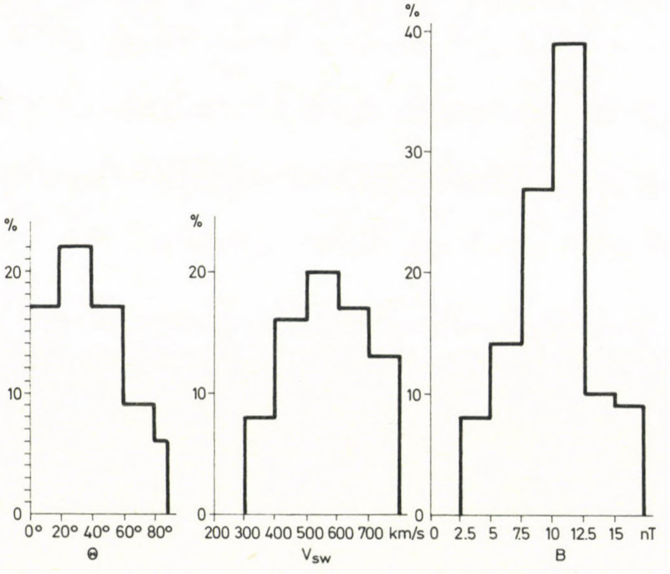

Fig. 5. Occurrence probability of short period regular pulsations (oscillations) in function of Θ, V_{SW} and B, 04–06 h LT in the year 1974

Figure 6 in this paper corresponds to Takahashi et al.'s Fig. 6, with the differences already mentioned. It is evident that the shift of the activity toward earlier hours in case of higher solar wind velocities cannot be observed here. The maximum is in all cases somewhat before local noon; in case of the highest solar wind velocities, $V_{SW} > > 700$ km/s, a secondary maximum appears at 06–09 h LT, which corresponds roughly to the maximum in the same case in Takahashi et al.'s material. Figure 7 shows that the dependence of the pulsation amplitudes has no specific difference between morning and afternoon hours; there are slight changes, but generally the increase with increasing solar wind velocity is continuous (the possible exception is 9–12 h LT, but these are morning hours, while Takahashi et al. found the decrease in afternoon hours).

Figure 8 summarizes the effect of V_{SW} and LT, similarly to Fig. 8 in the cited paper. The general trends are rather similar, but the mentioned differences are naturally reflected here again.

As a summary of these figures, we think that there is a real difference in the afternoon pulsation activity on satellites and at the surface. In addition to this

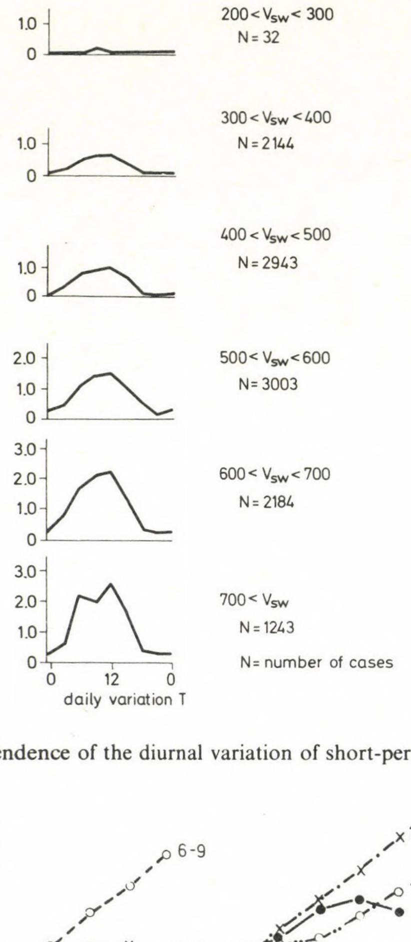

Fig. 6. Solar wind velocity dependence of the diurnal variation of short-period pulsation amplitudes

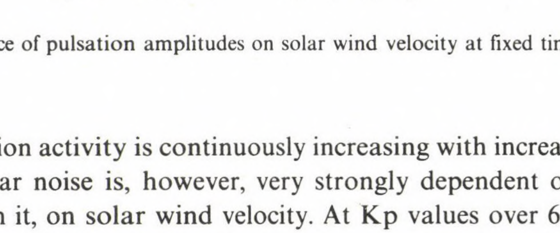

Fig. 7. Dependence of pulsation amplitudes on solar wind velocity at fixed times (in LT)

difference, the pulsation activity is continuously increasing with increasing solar wind velocity. The irregular noise is, however, very strongly dependent on geomagnetic activity, and through it, on solar wind velocity. At Kp values over 6, this noise can suppress any regular pulsations, that is why the number of regular pulsations is (apparently) decreasing in case of high geomagnetic activity (high solar wind velocity).

Figure 9 does not exactly cover the content of Takahashi et al.'s Figs 9 and 10, it is somewhere between the both figures. It expresses the daily pulsation index (based on

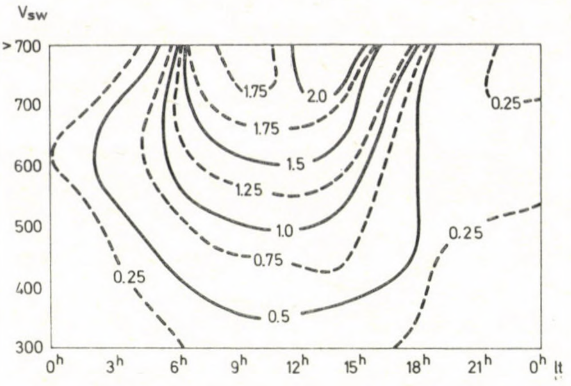

Fig. 8. Summary of the dependence of the Pc 3–4 amplitudes on LT and solar wind velocity

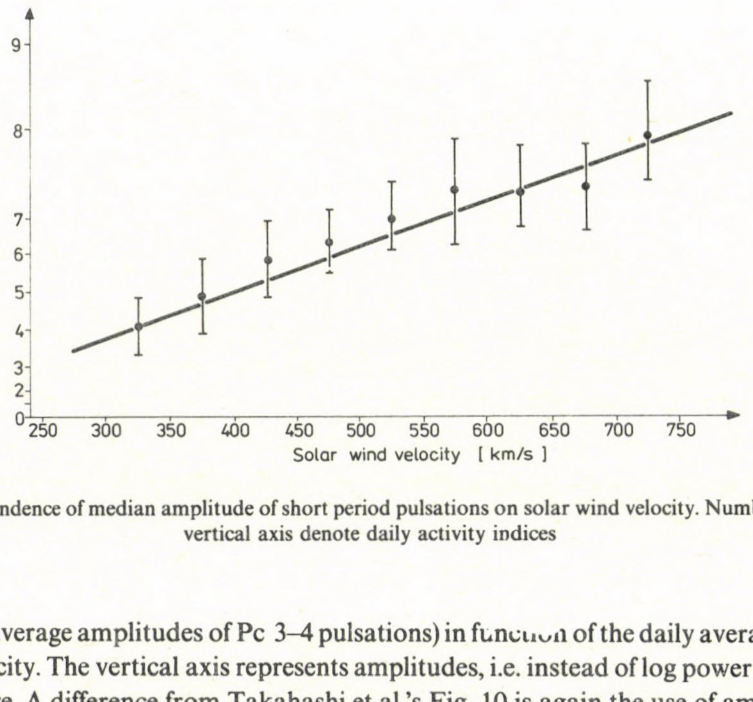

Fig. 9. Dependence of median amplitude of short period pulsations on solar wind velocity. Numbers on the vertical axis denote daily activity indices

the daily average amplitudes of Pc 3–4 pulsations) in function of the daily average solar wind velocity. The vertical axis represents amplitudes, i.e. instead of log power we have power here. A difference from Takahashi et al.'s Fig. 10 is again the use of amplitudes instead of occurrence frequencies. The linear connection between P and V_{SW} is due to the inclusion of Pc 4, which can have rather important amplitudes at low solar wind velocities. The main point is here, however, that no decline can be observed at high V_{SW} values, even if the quite unstable median at the end is omitted. For a more realistic form of the connection between pulsation amplitudes and solar wind velocities, we refer to

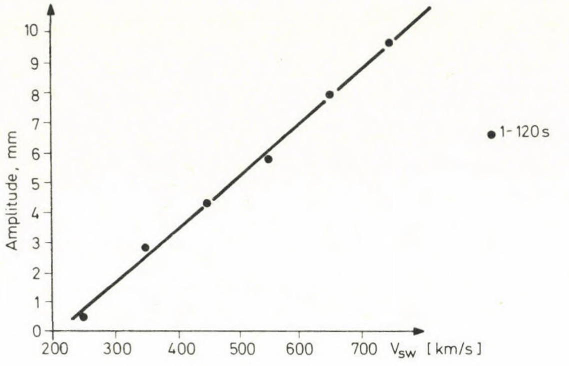

Fig. 10. Dependence of the Pc 3–4 amplitudes (sums of all period ranges) on the solar wind velocity

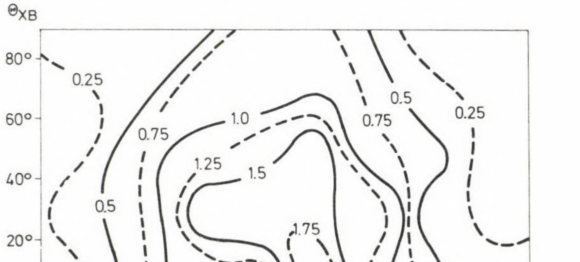

Fig. 11. Summary of the dependence of the Pc 3–4 amplitudes on LT and cone angle, Θ_{XB}

Fig. 11 in Verő (1980) where the functional form of these connections is also given in different period ranges. Similar connections were found later from the material of the year 1973, with some minor modifications. In Figure 10 we give the sum of all period ranges from this study, which gives a result not very far from the present one.

Connection of the pulsation amplitudes with Θ_{XB}

The simultaneous effect of the daily variation and of the cone angle effect is presented in Fig. 11. It should be mentioned that from the material of earlier years (1972–74) we found a constant peak of the pulsation activity around Θ_{XB} around 30°. This maximum can be seen in this figure in form of a bulge of the 1.25 and 1.5 isolines between 20–40°. From 40° on, there is a rather steep decrease in the amplitudes.

The 30° maximum can be found also in Fig. 6*b*, where the occurrence frequency of pulsations is shown in function of the cone angle (Θ_{XB}). Here this maximum is the most significant among all results, the occurrence frequency is for Θ_{XB} between 20–40° at 22‰, for the previous and subsequent direction groups at 17‰.

Figure 12 shows the joint amplitude dependence of pulsation amplitudes as a contour plot in the $\Theta_{XB}-V_{SW}$-plane (as Takahashi et al.'s Fig. 12). In this case the

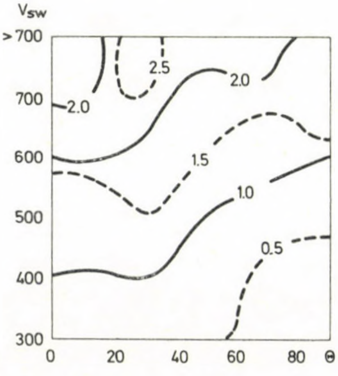

Fig. 12. Solar wind velocity and IMF angle dependence of Pc 3–4 amplitudes

general decrease of the amplitudes with decreasing solar wind velocity is superimposed on a rather complex Θ_{XB}-dependence. The 30° maximum can be seen at very high solar wind velocities and in the 500 km/s range; in Takahashi et al.'s figure, there is only a slight indication for the 30° maximum at the lowest solar wind velocities, below 400 km/s.

This 30° maximum appeared in our data now in the material of three independent, even not consecutive years. It should be added that according to detailed investigations, it is really characteristic only for Pc 3-type pulsations, in the Pc 4-range the maximum is at 0°. This earlier result is proved again by the present results, where the maximum appears very clearly in the regular oscillations which have mostly shorter periods, while they are much less significant in the whole pulsation activity.

It would be too speculative to reflect on the cause of this difference between the Nagycenk and the ATS data. Most of the authors dealing with this question found the maximum at 0°, but in most cases Pc 3 and 4 were not separated. In Takahashi et al.'s data this is not the case; we can only state that we cannot see any artificial source for our 30° maximum which returned now in three different years.

Solar wind stream structure and Pc occurrence

The correspondence between the stream structure of the solar wind and the pulsation activity was also present in our surface data. Figure 13 is a modified representation of Takahashi et al.'s Fig. 13. The variations of the pulsation activity are quite similar in space and on the surface, both are well correlated with the changes of the interplanetary medium, first of all, of the solar wind velocity.

A few numerical data in Takahashi et al.'s figure enabled a comparison of their occurrence index with the Nagycenk amplitude index. The result of this comparison is shown in Fig. 14. It seems that in case of any space pulsation index (P_{sp}) there is a lowest

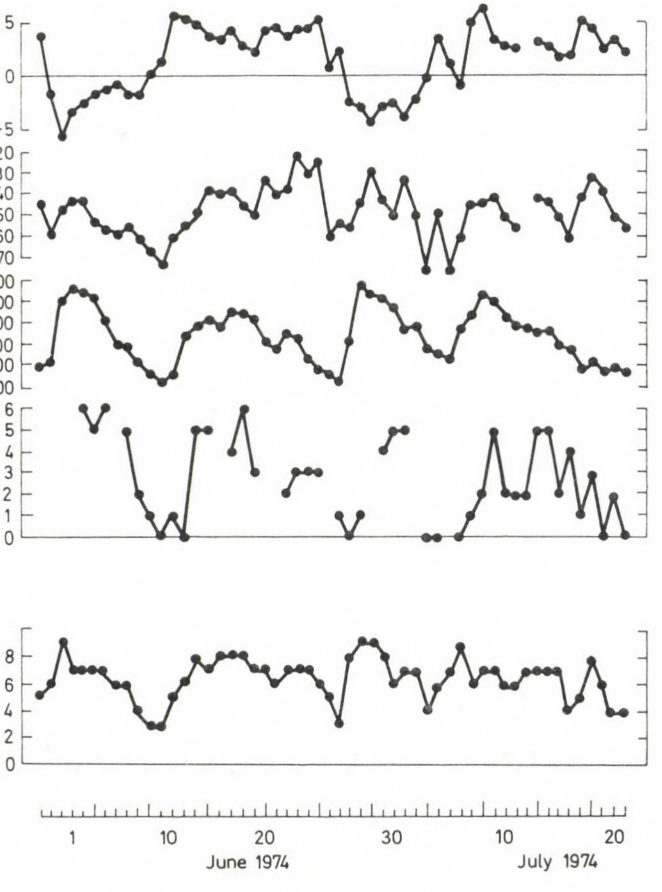

Fig. 13. Takahashi et al.'s data supplemented by the Nagycenk (surface) pulsation indices (bottom) of the interval June—July, 1974. From top to bottom: B_{XSE}, Θ_{XB}, solar wind velocity and daily pulsation indices ATS and Nagycenk

possible surface pulsation activity (P_{Nc}) which can be expressed by the following formula:

$$P_{Nc,\,min} \geq 0.75\, P_{sp} + 2.$$

Any value of P_{Nc} above this lower limit is possible for a given P_{sp}. If this connection could be verified on a greater amount of data, it would be an additional proof of the effectivity of the field line resonance mechanism, even this effectivity could be followed on the basis of the ratio of the actual and minimum possible pulsation activities.

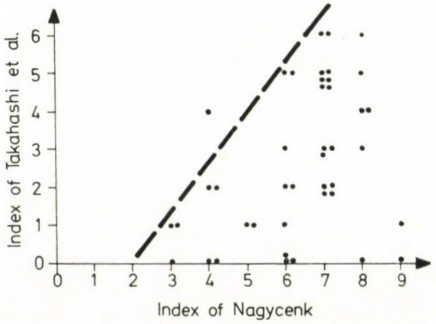

Fig. 14. Connection between the daily pulsation indices by Takahashi et al. and in Nagycenk

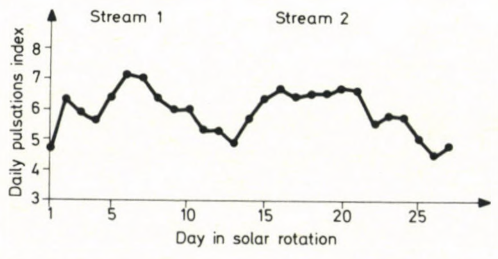

Fig. 15. Average recurrence pattern of the pulsation activity

Figures 15 and 16 are generally consistent with the spacecraft data. In connection with the sector boundaries it should be reminded to the fact that there is no extra sector boundary effect in the pulsations, at least not in the Nagycenk data. If one corrects the actual values of the pulsation activity for the momentaneous values of the interplanetary medium, first of all for the minimum solar wind velocity appearing simultaneously with the sector boundary, the effect disappears, or it least it is no more significant. So no additional source of pulsations must be supposed to be active at sector boundaries.

Summarizing the results of the comparison of the ATS 6 and the Nagycenk surface data, there is a general correspondence between the two data sets. The main

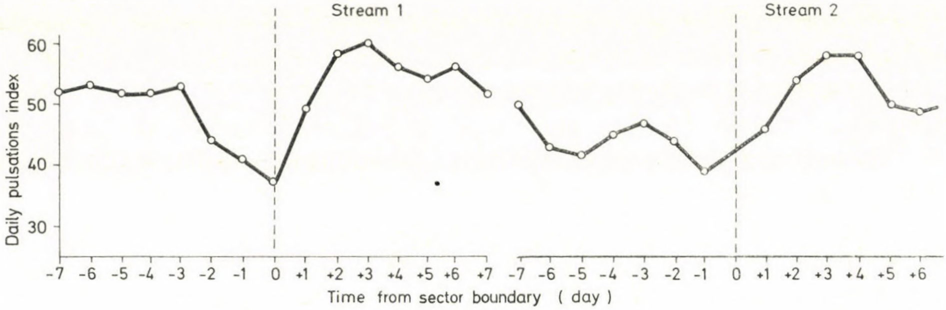

Fig. 16. Superposed epoch analysis of short period pulsation occurrence (same cases, as in Fig. 14 by Takahashi et al. (1981))

effects of the interplanetary medium on the pulsations are similar in both cases in spite of very different data bases and different selection criteria. The effect of the solar wind velocity is the most important one, increasing solar wind velocity means increasing pulsation activity. The interplanetary magnetic field has also a significant effect on the pulsation activity, small cone angles (Θ_{XB}) are favourable for the excitation of the pulsations. The IMF scalar magnitude influences more the period of the pulsations, its effect on the pulsation activity is not unambiguous.

In spite of this general similarity there is a number of points in which ATS and Nagycenk data yielded different results. These differences may be partly due to physical differences between pulsations in space and on the surface, and at different L-values. A part may be due to the different data bases and processing methods. A third part remains unexplained at present and needs further verification.

These differences between the Nagycenk and the ATS data are the following:

The seasonal change of the Pc 3 activity has an earlier peak in (Northern) winter than in sommer in the ATS data, while in Nagycenk the situation is either opposite, or at least this variation cannot be found. As the change includes not only the afternoon, but also the predawn hours, the cause cannot lie in the afternoon activity which can be observed in the magnetosphere, and is absent on the surface. The surface trend is rather uniform in all years, therefore an explanation should have a quite continuous character in time. At present such an explanation is not known.

The shift of the pulsation activity toward afternoon hours in case of abnormal IMF directions is more evident in the Nagycenk data, but even there it is not a completely symmetrical change of the daily variation in comparison to "normal" directions observable. A slight shift is vice versa present in the ATS data, too. This is therefore no contradiction, it could be stated that there is some difference between the two cases but it is not very important.

The decrease of the occurrence frequencies of pulsations in case of very high solar wind velocities is in all probability due to a rapidly increasing noise level. This is shown by a comparison of the Nagycenk pulsation amplitudes, ATS occurrence frequencies and Nagycenk occurrence of regular pulsations, where the sequence indicates both the increasing sensibility for noises and the appearance of the activity increase at high velocities.

The maximum occurrence of pulsations is according to ATS data at cone angles between 0–30°, while in case of the Nagycenk data there is a clear maximum at 30°. In this case the difference can be due to the magnetospheric afternoon activity, which is unobservable at the surface, or due to the processing and display method, as our Fig. 11 is rather similar to Takahashi et al.'s Fig. 12, and shows only traces of this maximum, while Fig. 6*a* indicates very clearly the 30° maximum. It should be noted that we found this maximum in both longitudinal and latitudinal directions independently from each other, too.

At last it seems that a certain magnetospheric pulsation activity level determines only the minimum possible level of the pulsation activity at the surface. The actual surface activity is very likely to be strongly influenced by the efficiency of the field line resonance mechanism.

In conclusion in case of the short-term variations of the pulsation activity we do not see any difference of importance between surface and magnetospheric data, save the afternoon activity in magnetosphere which is due to the bounce-resonance mechanism. In long-term (seasonal, annual etc.) variations there are greater differences, and there are much less data which would confirm and disprove the differences found in this case. Verő (1981) has shown that in solar maximum years there is a damping of pulsations either in December or in (local) winter season. This damping is at least partly due to an ionospheric damping. As 1974–75 were no years with very high solar activity and magnetospheric-ionospheric particle concentrations, this effect was likely absent, and it cannot be traced in surface data at this time.

References

Hughes W J, McPherron R L, Barfield J N 1978: Geomagnetic pulsations observed simultaneously on three geostationary satellites. *J. Geophys. Res.*, 83, 1109–1116.

Potapov A S 1974: Возбуждение геомагнитных пульсаций типа Pc 3 перед фронтом околоземной ударной волны пучком отраженных протонов. *Issl. Geomagn. Aeron. Irkutszk*, 34, 3–8.

Takahashi K, McPherron L, Greenstadt E W, Neely C A 1981: Factors controlling the occurrence of Pc 3 magnetic pulsations at synchronous orbit. *J. Geophys. Res.*, 86, 5472–5484.

Verő J 1980: Geomagnetic pulsations and parameters of interplanetary medium. *J. Atmos. Terr. Phys.*, 42, 371–379.

Verő J 1981: Changes of pulsation activity during two solar cycles. *J. Atmos. Terr. Phys.*, 43, 919–926.

Verő J, Holló L 1978: Connections between interplanetary magnetic field and geomagnetic pulsations. *J. Atmos. Terr. Phys.*, 40, 857–865.

Acta Geodaet., Geophys. et Montanist. Hung. Volume 18 (4), pp. 421—429 (1983)

RELATIONSHIP BETWEEN THE AMPLITUDE OF GEOMAGNETIC Pc 3 PULSATIONS AND PARAMETERS OF THE INTERPLANETARY MEDIUM

G V KUKLIN[1], V A PARKHOMOV[1], P A VINOGRADOV[1]

[Manuscript received September 20, 1982]

The dependence of Pc 3 amplitudes ($T = 10$–45 s) on solar wind velocity (V), particle density (N), components of the interplanetary magnetic field (IMF) (B_φ, B_r, B_T, B_Z) and on the Mach-Alfven number (M_A) are discussed.

By means of a statistical multivariate analysis of experimental data it has been shown that the pulsation amplitude is most closely connected with the solar wind velocity. A significant but less close correlation was found between Pc 3 amplitudes and the components of the interplanetary magnetic field vector in the ecliptic plane (B_r and B_T). The nature of the relationship of Pc 3 with solar wind and IMF parameters are discussed.

Keywords: geomagnetic pulsations; interplanetary magnetic field; Pc 3; principal components analysis; solar wind

1. Introduction

The study of the influence of the interplanetary medium on continuous geomagnetic pulsations (Pc 2–4) led to the discovery of a number of significant connections. Correlations of the pulsation amplitude (mostly of Pc 3) were found with solar wind velocity (Saito 1964, Vinogradov and Parkhomov 1971, Frey et al. 1971), solar wind flux (Gringauz et al., 1971), absolute value (Frey et al., 1971, Vinogradov and Parkhomov, 1972b) and orientation in the ecliptic plane of the interplanetary magnetic field (IMF) (Bolshakova and Troitskaya 1968, Vinogradov and Parkhomov, 1972a). The difficulty of the interpretation is that the interplanetary parameters are intercorrelated (Kovalevsky 1971) and it is not easy to find which of the interplanetary parameters plays a determining role in the excitation mechanism of the pulsations if we use only correlations for pairs. At the same time it is quite possible that amplitude variations are caused by some more general properties of the interplanetary medium which cannot be considered directly. Therefore in order to study the relationship between the pulsations and interplanetary parameters it is obvious to use the statistical multivariate analysis.

In this paper one method of the statistical multivariate analysis is used, namely, the principal component method (expansion in series by natural orthogonal functions)

[1] Siberian Institute of Terrestrial Magnetism, Ionosphere and Radio Wave Propagation Irkutsk, USSR

(Vertlieb et al. 1971, Nalimov 1971). This method permits to reveal (in the frame of a linear model) the most general properties of the considered phenomenon, i.e. to obtain all parameters which cause maximum changes of the pulsation amplitudes and to construct regressions for some more general combinations of the considered parameters.

2. Data and their analysis

In order to study the connection of Pc 3 amplitudes with parameters of the solar wind and of the interplanetary magnetic field, time series of eight parameters were transformed into series of principal components. As initial data we used normalized hourly values of Pc 3 amplitudes, A as observed in Irkutsk, of the solar wind velocity V and density N, of IMF components in the solar ecliptic coordinate system B_φ (horizontal), B_r (radial), B_T (azimuthal), B_Z (vertical) and of the computed Mach-Alfven number $M_A=\beta=\dfrac{4\pi N V^2}{B^2}$ for the period from 23. 12. 67 till 07. 05. 68 (interplanetary data from Explorer 33 and 35 measurements; Obayashi 1970). For every day the parameters were determined and compared in the time interval 08–18 h LT. Altogether 588 hourly sets of the 8 parameters were used. In a first step the source array was divided into four subarrays of 147 sets each, and later the connections were computed for six high-speed and two low-speed streams separately. All parameters were used in a standardized form i.e. they were expressed as differences from the averages in units of RMS deviations.

3. Results and Computations

The computations yielded matrices of the correlation coefficients between pairs of the parameters, coordinated and conjugated time functions, which describe the typical series of the parameters within the considered time interval. In our case, "coordinate" means the serial number of the parameter and the number of functions is equal to the dimension of the set, i.e. eight. The significance of the correlation coefficients and of separate values of the functions was estimated using Fisher's criterion taking as the degrees of freedom $v=n-2$. Results of the computations are presented in Tables I, II and Fig. 1.

In Tables I and II, the values of the correlation coefficients r_n beween the hourly values of Pc 3 amplitudes and corresponding values of the parameters V, N, B_φ, B_T, B_z, M_A and the confidence limits ρ_n for the correlation coefficients at a level of significance 0.95 are given (if the correlation coefficients do not differ significantly from zero, no value is given for ρ_n). The size of the sample (or the number of sets) n, the degrees of freedom v, the relative contributions of the two first coordinate functions of the

Table I

No		V	N	B_φ	B_r	B_T	B_z	M_A	n	v	λ_1/λ_2	σ_A/σ_V
1	r_1	0.49	−0.007	−0.11	0.09	−0.39	0.13	−0.08	147	145	29%	0.52
	ρ_1	0.30−0.65	–	–	–	0.25−0.55	–	–			22%	72
2	r_2	0.57	−0.20	0.02	0.19	−0.16	0.19	−0.11	147	145	29%	0.71
	ρ_2	0.45−0.72	0.05−0.38	–	0.025−0.35	–	0.025−0.35	–			24%	105
3	r_3	0.60	−0.20	−0.005	−0.14	−0.14	0.32	−0.7	147	145	36%	0.84
	ρ_3	0.48−0.73	0.03−0.40	–	–	–	0.13−0.45	–			23%	78
4	r_4	0.37	−0.16	0.29	0.26	0.17	−0.03	0.23	147	145	29%	0.79
	ρ_4	0.23−0.52	–	0.17−0.43	0.10−0.47	–	–	0.05−0.37			24%	100

Table II

No		V	N	B_φ	B_r	B_T	B_z	M_A	n	v	λ_1/λ_2	σ_A/σ_V
I	r_1	+0.32	−0.06	−0.40	0.63	−0.68	−0.53	0.12	35	33	42%	0.51
	ρ_1	0.05÷0.55	–	−0.75÷0.05	0.43÷0.80	−0.45÷0.78	−0.24÷0.73	–			20%	16
II	r_2	+0.44	−0.02	0.29	0.49	0.26	0.03	−0.29	38	36	37%	0.47
	ρ_2	0.15÷0.72	–	–	0.22÷0.72	–	–	–			23%	65
III	r_3	0.39	−0.26	0.02	0.21	−0.34	−0.24	−0.28	27	25	37%	1.06
	ρ_3	0.05÷0.65	–	–	–	−0.05÷0.63	–	–				73
IV	r_4	0.60	−0.52	−0.06	0.41	0.19	0.35	0.08	22	20	33%	0.31
	ρ_4	0.18÷0.80	−0.1÷0.8	–	–	–	–	–			37%	50
V	r_5	0.77	−0.25	0.01	0.66	−0.75	0.01	0.23	27	25	41%	1.04
	ρ_5	0.58÷0.88	–	–	0.36÷0.83	−0.93÷0.52	–	–				76
VI	r_6	0.61	−0.20	0.16	−0.10	−0.24	−0.31	0.11	22	20	48%	0.63
	ρ_6	0.22÷0.80	–	–	–	–	–	–			23%	46
VII	r_7	0.06	−0.35	0.22	0.09	−0.28	0.07	−0.10	22	20	44%	0.23
	ρ_7	–	–	–	–	–	–	–			22%	39
VIII	r_8	0.14	0.18	0.28	0.04	0.10	0.30	0.27	27	25	46%	1.00
	ρ_8	–	–	–	–	–	–	–				76

expansion λ_1 and λ_2 and RMS deviations of Pc 3 amplitudes and of the solar wind velocity σ_A/σ_V are also presented here.

In each of the 4 sets (designated by indices 1, 2, 3, 4) of Table I the results of computations are presented for subarrays of the data (147 points each) into which the initial 588 values were divided.

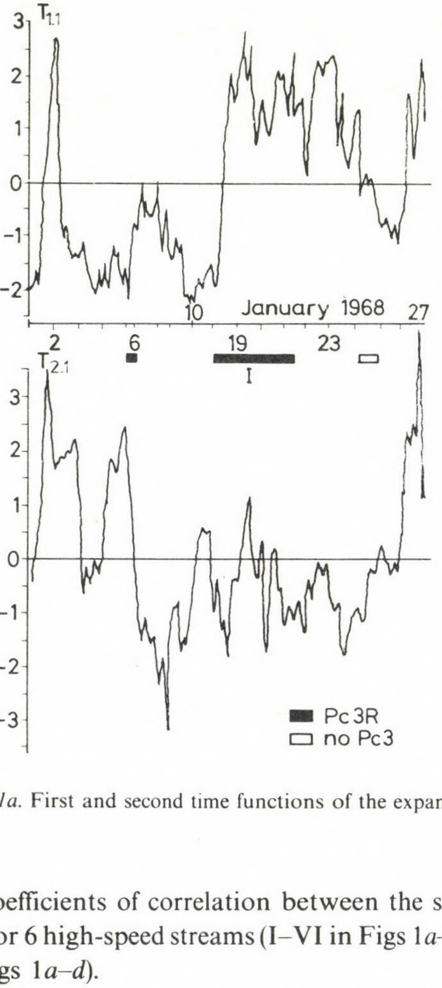

Fig. 1a. First and second time functions of the expansion

In Table II the coefficients of correlation between the same parameters as in Table I are represented for 6 high-speed streams (I–VI in Figs 1*a–d*) and for 2 low-speed streams (VII–VIII in Figs 1*a–d*).

Considering Tables I and II, one can conclude that quite close correlations exist between A and V, B_r, B_T; the most stable and significant correlation coefficient is found for the pair Pc 3 amplitudes and solar wind velocity. Typically the correlation coefficient has positive sign for Pc 3 amplitudes on the one hand and the solar wind velocity or the radial component of the interplanetary magnetic field on the other and it has negative sign for Pc 3 amplitudes and the tangential component of the interplanetary magnetic field. In some time intervals, there are significant correlations with other parameters (B_φ, B_Z, N, M_A) but these correlations are unstable both in value and in sign.

Let us analyse the coordinate and conjugate time functions. We limit ourselves to the first two functions because of their maximum contributions in the expansion. The coordinated functions contain the information about the influence of each parameter on Pc 3 amplitudes. This contribution is determined by the coefficient of any

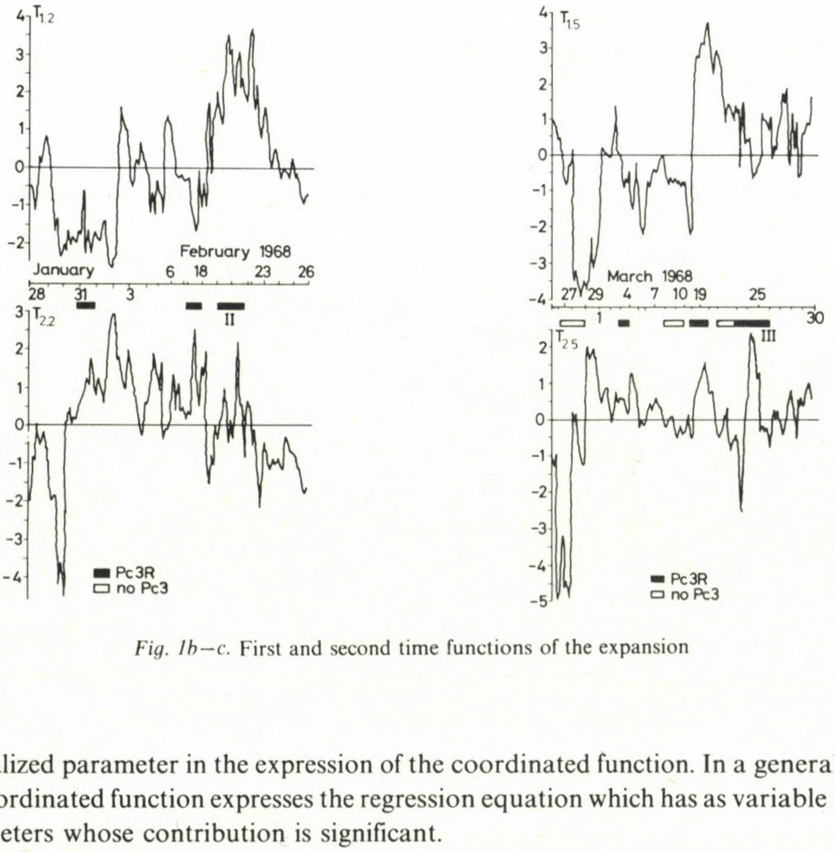

Fig. 1b–c. First and second time functions of the expansion

normalized parameter in the expression of the coordinated function. In a general case the coordinated function expresses the regression equation which has as variable those parameters whose contribution is significant.

In order to obtain quantitative estimates time intervals are chosen during which the corresponding time function has no large and sharp changes and may be taken as constant in a rough approximation. So by solving a linear equation the expression is got which connects Pc 3 amplitudes and all other parameters of the interplanetary medium. This linear relationship is valid only for the selected time interval.

The equations for each subarray are the following:

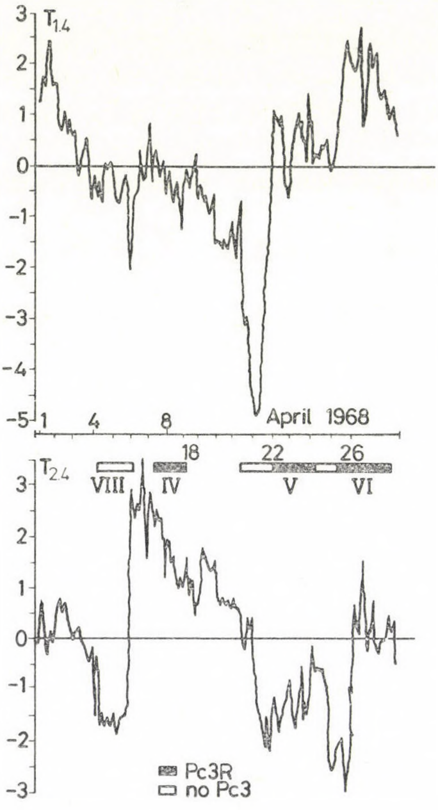

Fig. 1d. First and second time functions of the expansion

The 1st coordinated functions

$$A_1^1 = 0.99 - 1.12V + 1.23B_T$$

$$A_2^1 = 5.85 - 1.35V + 1.07N + 1.05B_T$$

$$A_3^1 = 7.82 - 1.36V + 0.84N + 1.27B_r - 1.48B_T$$

$$A_4^1 = 4.49 - 0.84V + 1.08N + 0.98B_r - 0.89B_T - 1.48M_A$$

The 2nd coordinated functions

$$-0.82 = 0.52N + 0.55B_r - 0.49M_A$$

$$-1.06 = 0.54B_r - 0.58M_A$$

$$0.12 = 0.37V - 0.42N + 0.40B_r - 0.65M_A$$

$$-1.45 = 0.5V - 0.49B_T + 0.51B_z.$$

Let us consider these results. The general property of the first coordinated functions for all subarrays is that the regression equation contains the solar wind velocity V and the interplanetary magnetic field components B_r and B_T as the most significant parameters.

The second coordinated functions practically describe some relationship between parameters of the interplanetary medium as the contribution of the Pc 3 amplitudes is less than the critical value of the significance limit.

4. Discussion

Our results show that the Pc 3 amplitudes are connected most closely with the solar wind velocity V and with the components B_r and B_T of the interplanetary magnetic field. The relationship of A with B_r and B_T is a qualitatively new information.

It should be noted that the dependence of Pc 3 amplitudes on the orientation of the interplanetary magnetic field in the ecliptic plane was observed first by Bolshakova and Troitskaya (1968).

The time function conjugated with the first coordinated function (Fig. 1) changes significantly within the considered time intervals. The first time function T_n^1 changes rather regularly after sharp breaks, some kind of stabilization takes place and in a first approximation the function T_n^1 may be considered as constant one in these intervals. Such changes correspond to sharp increases of the solar wind velocity. It is very typical that at the same time regular continuous pulsations Pc 3R are recorded (Vinogradov 1964) (black boxes in Fig. 1). Computations made for such time intervals of strong T_n^1 changes detect increased correlation coefficients for the three parameters V, B_r, B_T. This fact can be seen from Table II and Fig. 2. In this figure the dependence of the

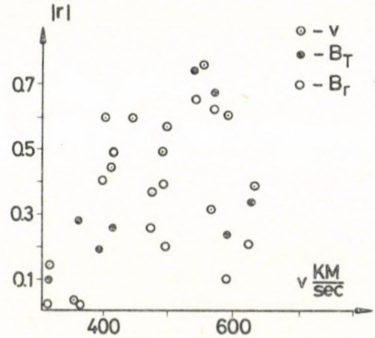

Fig. 2. The dependence of the absolute value of some coefficients on the solar wind velocity: between Pc 3 amplitudes and solar wind velocity, resp. the radial and tangential components of the interplanetary magnetic field

absolute values of the correlation coefficients for the pairs $A-V$, $A-B_r$, $A-B_T$ on V are presented. This result shows the significant role of the high-speed streams in the Pc 3 excitation mechanism on the one hand, and is an evidence of a stronger functional relation between the considered parameters in high-speed streams on the other. The changes (instability) of the time function during time intervals without high-speed streams may be interpreted as a weakening of the connection and a change of the type of the function.

An other interesting information is contained in the sign of the correlation for A and $B_r - B_T$. If one takes into account that in the positive sector of the interplanetary magnetic field $B_r < 0$, $B_T > 0$ and in the negative one the signs are opposite, then the positive correlation between A and B_r and the negative one between A and B_T shows dominating activity in the negative sector of the interplanetary magnetic field at least for the considered time interval.

Up to now there is no unambiguous physical interpretation of the dependence of the Pc 3 amplitudes on the parameters of the interplanetary medium. There is a number of viewpoints about the Pc 3 excitation mechanism. According to Dungey's hypothesis (1964), pulsations are generated as resonant oscillations by the flow of solar wind at the magnetospheric flanks. Gul'elmi and Troitskaya (1973) suppose that the source of Pc 3 is upstream waves generated by the protons reflected before the shock-wave front. Vinogradov and Parkhomov (1975) identify the source of Pc 3 with Alfven waves observed on the background of high-speed streams. Results above (Sections 2, 3) seem to confirm this supposition. The probability to observe such waves in the interplanetary medium depends on the solar wind velocity: the waves are observed at the leading edges of high-speed streams (Burlaga 1972).

5. Conclusions

1. The application of the principal component method enabled to determine the dependence of Pc 3 amplitudes on the parameters of the interplanetary medium and led to a confirmation of a primary role of solar wind velocity V and the components B_r and B_T of the interplanetary magnetic field.

2. The type and strength of the relationship change in dependence on the solar wind velocity and are most sharply expressed for the high-speed streams.

References

Bolshakova O V, Troitskaya V A 1968: Connection between the direction of the interplanetary magnetic field and the continuous pulsations (in Russian). Doklady AN SSSR, 180, 343.

Burlaga L F 1972: Solar Wind. Washington.

Dungey J W 1964: Structure of Exosphere. In: *Geophysics (Earth Space) Moscow, Mir*, 383.

Frey J H, Fisher W L, Maple E, Chernosky E J 1971: Broad band micropulsation activity at a geomagnetic midlatitude station. *J. Geomagn. Geoelectr.*, 23, 61.

Gringauz K J, Solomatine E K, Troitskaya V A, Shepetnov R V 1971: Variations of solar wind flux observed by several space craft and related pulsations of the Earth's electromagnetic field. *J. Geophys. Res.*, 76, 1065.

Gul'elmi A V, Trotskaya V A 1973: Geomagnetic Pulsation and Diagnostics of Magnetosphere. Moscow, Nauka, 133.

Kovalevsky J V 1971: The interplanetary medium and its interaction with the Earth's magnetosphere. *Space Sci. Rev.*, 12, 187.

Nalimov V V 1971: Theory of Experiment. Moscow, Nauka, 81.

Obayashi T 1970: Solar-Terrestrial Activity Charts. STAC-B, No. 6–7.

Saito T 1964: A new index of geomagnetic pilsation and its relation to solar M-regions. Part I. *Space Res. Japan*, 18, 260.

Vertlieb A B, Kuklin G V, Kopecki M 1971: Experiences with the splitting of some indexes of the solar activity into natural orthogonal functions (in Russian). *Issled. po Geomagnetizmu, Aeronomii i Fizike Solntsa*, 2, 194.

Vinogradov P A 1964: Some regularities of the occurrence oc Pc pulsations (in Russian). *Geomagnitnie Issledovaniya*, No. 6.

Vinogradov P A, Parkhomov V A 1971: Velocity of the solar wind and activity of the electromagnetic pulsations (in Russian). *Issled po Geomagnetizmu, Aeronomii i Fizike Solntsa*, 6, 27.

Vinogradov P A, Parkhomov V A 1972a: On the connection of the Pc3 pulsations with the direction of the interplanetary magnetic field. *Issled po Geomagnetizmu, Aeronomii i Fizike Solntsa*, 24, 227.

Vinogradov P A, Perkhamov V A 1972b: Great-sclae structure of the interplanetary magnetic field and the activity of Pc3 pulsations (in Russian). *Issled. po Geomagnetizmu, Aeronomii i Fizike Solntsa*, 24, 249.

Vinogradov P A, Parkhomov V A 1975: MHD waves in solar wind is the possible source of Pc 3 geomagnetic pulsations. *Geomagnetizm i Aeronomiya*, 15, 134.

Acta Geodaet., Geophys. et Montanist. Hung. Volume 18 (4), pp. 431—442 (1983)

ENGINEERING HYDROGEOLOGY AND AQUIFER PROTECTION

C N GARAGUNIS[1] and P S KOLLIAS[2]

[Manuscript received January 2, 1983]

Groundwater becomes more and more an important water source for drinking and irrigation purposes. The factors polluting the waterbearing horizons (sewage, agricultural wastes, livestock wastes, percolation of fertilizers, etc.) also increase nowadays. Thus the importance of the protection of subsurface waters against pollution increases, too.

Based on subsurface hydraulics, formulas are given for the calculation of the protection necessary around a borehole.

The Larissa plain in Greece was selected as a test area for water protection studies.

Keywords: aquifer protection; engineering hydrogeology; Larissa plain water protection; subsurface water; water pollution

Introduction

The amount of the actual daily water consumption pro person is the following:

in rural settlements:	150 l/person (without the consumption of cattles of 50 l/cattle)
in provincial towns:	200–250 l/person
in industrial towns:	300–400 l/person
in highly urbanized areas:	up to 1500 l/person (e.g. New York).

The need for water supply in both rural and urban areas increases constantly. The consumption in the big cities of Greece also increases rapidly.

The groundwater having been estimated as 6.3% of our planet's total fresh water reserve is considered sufficient to cover a greater part of the increased water demand, by a multifarious utilization. Groundwater of highest quality must be used as drinking water, while that of minor quality can be used for irrigation and industrial purposes.

To demonstrate the application of subsurface water protection principles, the Larissa plain in Greece was selected as example (Fig. 1), because the authors were engaged with hydrogeological problems in this area during three years.

[1] National Technical University of Athens 42, 28th October Str., Athens, Greece
[2] 21, Naxou Str., Athens, Greece

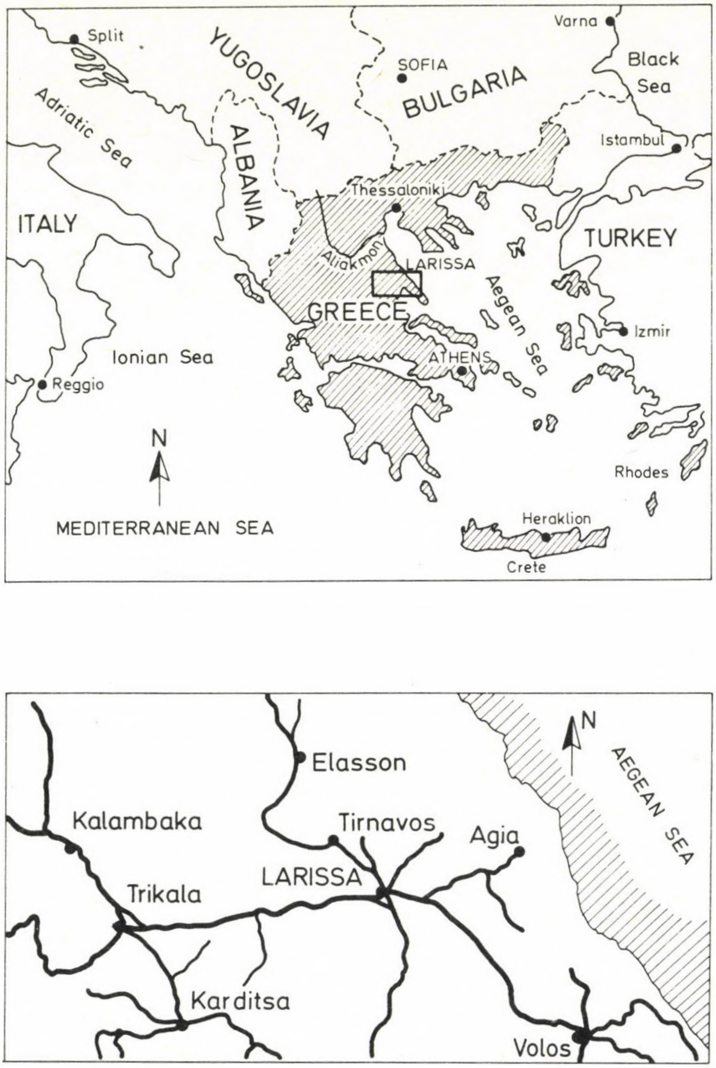

Fig. 1. Location map of Larissa area (Greece)

Water quality

Drinking water

In order to be potable the water must meet certain chemical and microbiological standards. Some standards of the chemical composition of potable water in Greece are listed in Table I. Most of the countries have their own State Health Act, and WHO, also worked out norms. If e.g. the metals are found in higher concentrations than listed in Table I the water has either to be treated in order to meet the standards or to be rejected, if the costs of treatment are high, and less polluted water occurs in the vicinity.

Among the physical characteristics turbidity should not exceed 10 p.p.m. while colour, in the Cobalt Range, should not exceed 20 p.p.m. Finally, the water should not taste and smell.

Table I. Quality standards of drinking water (Greece)

Component	p. p. m. (=mg/l)
As	0.05
Se	0.05
Pb	0.1
F	1.5
Cr	0.05
Zn	15.0
Cu	3
Fe and Mn	0.3
Mg	12.5
Cl	2.5
SO_3	2.5

Irrigation water

Water suitable for irrigation purposes should meet a definite quality, e.g. a high concentration of dissolved salts is an adverse factor to the growth of plants since it increases the osmotic pressure. Metals transported by irrigation-water modify the soil properties either favourably (soil neutralization, $CaCO_3$-sedimentation) or unfavourably (soil alkalinization).

Considering that such an impact is of additive nature, special attention should be paid to the quality of the irrigation-water which must meet the standards given in Tables II, III and IV. Table III takes into consideration the so-called sodium absorption ratio

$$SAR = \frac{Na^{+}}{\sqrt{\dfrac{Ca^{++} + Mg^{++}}{2}}}$$

where Na, Mg and Ca are expressed in ME/l.

Table II. Quality standards of irrigation water

Water quality	Conductivity at 25 °C (mho/cm)	Dissolved salts (mg/l)
Good	<0.25	<160
With slight salt content	0.25 – 0.75	160 – 500
With medium salt content	0.75 – 2.25	500 – 1500
With high salt content	>2.25	>1500

Table III. Alkalinization hazard of irrigation waters

Alkalinization hazard	SAR indicative values		
Slight	<2.2	<6.1	<4.0
Medium	2.2 – 15.4	6.1 – 12.2	4.0 – 9.0
High	15.4 – 22.6	12.2 – 18.3	9.0 – 14.0
Very high	>22.6	>18.3	>14.0

Table IV. Chemical standards for irrigation waters

	Water used continuously in all kinds of soil mg/l	Water used in fine-grained soils, pH 6 – 8.5 mg/l
Al	5	20
As	0.10	2
Be	0.10	0.5
B	0.75	2
Cd	0.01	0.05
Cr	0.10	1
Co	0.05	5
Cu	0.2	5
F	1	15
Fe	5	20
Pb	5	10
Li	2.5	2.5
Mn	0.2	10
Mo	0.01	0.05
Ni	0.2	2
Se	0.02	0.02
V	0.1	1
Zn	2	10

Groundwater pollution sources

Shallow groundwater tables are open to several pollution factors. As primary factor the individual household sewage disposal systems (cesspools) can be considered which affect the groundwater directly by uncontrolled chemical and microbiological contamination. In many cases — generally common in rural areas — there is a fluctuation in the contamination loading of groundwater, reaching its maximum during the summer period. Such a phenomenon has also been observed in touristic areas where the population highly increases in the summer. In coastal areas, where every little village has been transformed to a tourist resort this problem has became extremely acute. Another major contaminating factor has arisen in Greece by the extensive use of agricultural fertilizers. Table V shows some parameters for the water supply in the rural areas of Greece. An expressed increase of nitrates has been observed in regions of intensive agricultural exploitation.

As a first step in the protection of tne groundwater of a certain area, the pollution sources, as remnants of vegetation and of nitrate fertilizers, cesspools, small cattle breeding units (pig farms, stalling), agricultural industry (cheese dairies, tanneries), etc., should be summed up.

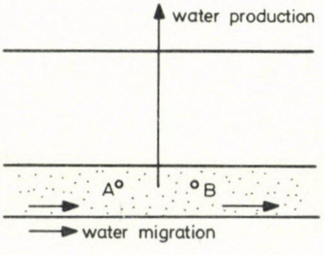

Fig. 2. Water produced by a well is more endangered by source *A* than by source *B*, because of the horizontal water flow

Groundwaters often move horizontally, due to a hydraulic gradient. This subsurface migration, controlled mostly by topographic differences, is of fundamental importance for the spreading of pollution. For example, in Fig. 2, the well is more endangered by the pollution source *A* than by source *B*, although the latter is nearer to the well. For that reason the topographic map of the area should play an important role in the judgement of the pollution sources. They can be divided into two categories: *a)* direct pollution sources, located opposite to the direction of water flow, in a short distance from the well; and *b)* indirect pollution sources, where a long time is necessary for the contamination to reach the well.

Table V. Water quality parameter values in the investigated rural area in Larissa (Greece)

a/a	Community	Turbidity	Hardness	Conductivity micromhos	pH	Dry solids mg/l	Ignitions residue mg/l	Amonium salts as NH_4 mg/l	Nitrite as NO_2^- mg/l	Nitrate NO_3^- mg/l	Chloride mg/l	Organic matter mg/l	Conditions of water intake
1	Kipselohori	none	15.7	592	7.1	384	338	0	0	11.2	13	3.16	Ground water supply from well in agricultural area
2	Omorfohori	none	8.5	567	7.5	458	402	0	0	8.2	8.2	0.2	Ground water supply from well in agricultural area
3	Nikea	none	14.1	608	7.4	408	206	0	0.001	32.5	38	9.6	Ground water supply from well in intensively cultivated agricultural area
4	N. karies	none	16.5	360	7.8	–	–	0	0	0	98	–	Water supply from surface spring
5	Zapio	none	18	568	7.6	384	180	0	0.1	14	24	3.6	Ground water supply from well in intensively cultivated agricultural area
6	Kiparisos	none	12.1	289	7.0	190	32	0	0.001	7.8	8	8.6	Ground water supply from well near agricultural area
7	Kipseli	none	14	506	8.0	340	187	0	0	0.2	164	1.6	Ground water supply from well in protected area
8	Tempi	none	11.2	460	7.7	301	152	0	0	0.2	13	0.8	Ground water supply from well in protected area
9	Ktia	none	15.2	306	7.2	207	235	0.1	0	1.2	12	1.4	Water supply from surface spring
10	Tirnavos	none	12.9	365	7.3	255	223	0	0	–	11.3	2.4	Water supply from surface spring
11	Gianouli	none	6.7	328	7.2	288	170	0	0	7.5	10.8	–	Ground water supply in agricultural area
12	Standards	<10 mg/l	<18		7.0 8.5	<500		<0.2	<0.001	<10	<250	<200	

Greek Standards

Determination of the protection perimeter

As long as the water table is undisturbed from pumping the flow lines follow more or less permanent directions (Fig. 3, left side). During continuous pumping, however, the flow lines partly converge toward the well, and the more distant ones are diverted (Fig. 3 right side).

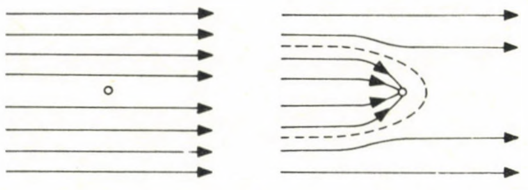

Fig. 3. Flow lines in groundwater without (left) and during pumping (right)

Two areas of water flow can be distinguished around a well: the first provides the yield of the well while in the second the water passes by. Those two areas are separated by a boundary line (dashed line in Fig. 3), which must be determined in order to define the necessary protective area.

Downstream limit of the boundary line

The maximum distance of the depression (the downstream limit) is given by the σ distance of the vertex point of the boundary line. If H is the width of the flow, q_0 the yield of the undisturbed aquifer and Q_0 the yield drawn up by pumping, if it is taken into account that a motionless point in the groundwater flow is possible only at a zero gradient, we find (Fig. 4) that the hydraulic slope of the initial flow is:

$$\frac{\mathrm{d}h}{\mathrm{d}x} = \xi = \frac{q_0}{kH},$$

the hydraulic slope due to pumping is:

$$\frac{\mathrm{d}h}{\mathrm{d}r} = \frac{Q}{2r\pi kH}.$$

At the vertex point

$$v_q = v_Q, \quad \text{but} \quad v_q = k\frac{\mathrm{d}h}{\mathrm{d}x}$$

and

$$v_Q = k\frac{\mathrm{d}h}{\mathrm{d}r}.$$

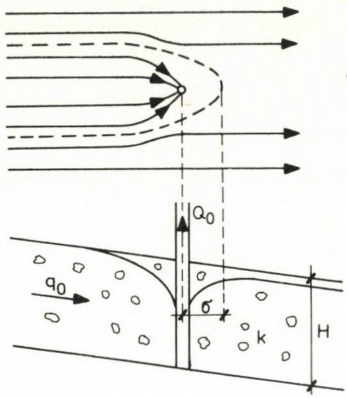

Fig. 4. Determination of downstream limit σ of the perimetric line

Then

$$\frac{dh}{dx} = \frac{dh}{dr} = \xi.$$

If this point has a distance $r=\sigma$ from the well, we take $Q=Q_0$ and

$$\xi = \frac{Q_0}{2\sigma\pi kH} \qquad \text{and} \qquad Q_0 = 2\sigma\pi kH\xi$$

or substituting $kH\xi = q_0$

$$Q_0 = 2\sigma\pi q_0.$$

Substituting $Q_0 = Eq_0$ we get finally $2\sigma\pi q_0 = Eq_0$ and

$$\sigma = \frac{E}{2\pi}.$$

Upstream limit of the boundary line

The distance r from the well, where the contribution to the yield Q_0 of the well is negligible (the upstream limit) can be considered as the border of the area to be protected against surface pollution. A protective zone can be created by spreading out a sand layer on the perimetric area. In this case the upstream limit depends on the created protective layer.

We try to explain this as follows:

Let us take a semifinite aquifer (Fig. 5) penetrated by a well. Let us take the notations φ_1 = the piezometric height in the protective layer, φ = the piezometric height into the well. Q_0 = the yield of the well and q_r = the yield at the distance r. From Darcy's law:

$$q = -2\pi r k H \frac{d\varphi}{dr}$$

(H = the thickness of the layer; k = water permeability) and from the continuity law:

$$\frac{d^2\varphi}{dr^2} + \frac{1}{r}\,\frac{d\varphi}{dr} + \frac{\varphi_1 - \varphi}{\lambda^2} = 0$$

where the leakage factor $\lambda = \sqrt{kHC}$ with $C = \frac{H'}{k'}$ (quantities with $'$ refer to the protecting layer).

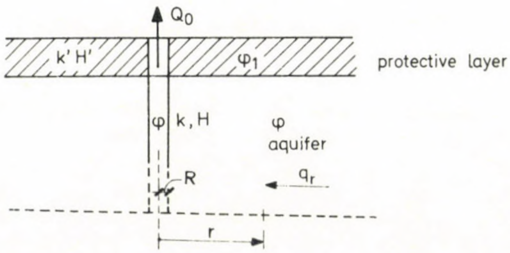

Fig. 5. To calculation of the upstream limit of the perimetric line

This is a modified Bessel equation of zero order. For the boundary conditions

$$r = r \qquad \varphi = \varphi$$

$$r = \infty \qquad \varphi = \varphi'$$

the solution gives

$$\frac{d\varphi}{dr} = \frac{\varphi' - \varphi}{\lambda}\,\frac{K_1\left(\frac{r}{\lambda}\right)}{K_0\left(\frac{r}{\lambda}\right)},$$

where $K_1\left(\frac{r}{\lambda}\right)$ and $K_0\left(\frac{r}{\lambda}\right)$ are functions taken from the Bessel function tables. By introducing this to Darcy's equation, we have at a distance r:

$$\varphi' - \varphi = \frac{-q_r K_0\left(\frac{r}{\lambda}\right)}{2\pi k H \frac{r}{\lambda} K_1\left(\frac{r}{\lambda}\right)}. \tag{1}$$

For the boundary conditions

$$r = R \qquad \varphi = \varphi$$

$$r = \infty \qquad \varphi = \varphi'$$

it will be:

$$Q_0 = -2\pi kH(\varphi' - \varphi)\frac{R}{\lambda}\frac{K_1\left(\frac{R}{\lambda}\right)}{K_0\left(\frac{r}{\lambda}\right)}. \tag{2}$$

For small values of

$$\frac{R}{\lambda} = x \text{ it will be: } K_1(x) = \frac{1}{x}$$

for $x < 0.02$ within an error of < 1‰.

Using this substitution we get

$$K_1\left(\frac{R}{\lambda}\right) = \frac{\lambda}{R}$$

and

$$\varphi' - \varphi = -\frac{Q_0}{2\pi kH}K_0\left(\frac{r}{\lambda}\right). \tag{3}$$

Combining the formulas (1) and (3) we get:

$$\frac{q_r}{Q_0} = \frac{r}{\lambda}K_1\left(\frac{r}{\lambda}\right).$$

As an example, let us suppose that the surroundings of a water well are continuously protected by a protective layer consisting of fine sand with a permeability coefficient of $k' = 10^{-1}$ m/day and having a width of $H' = 0.20\ m$, then the following calculation can be made:

$$C = \frac{H'}{k'} = \frac{0.20\text{ m}}{10^{-1}\text{ m/day}} = 2 \text{ days}.$$

Supposing that the well is $H = 20$ m deep and the aquifer is consisted of fine gravels ($k = 10$ m/day), we obtain:

$$\lambda = \sqrt{k \cdot H \cdot C} = \sqrt{10 \cdot 20 \cdot 2} = 20\text{ m}.$$

According to Table VI the flow reaching the well over a distance of $r=4\lambda$, is of minimum value if λ is not too small. If no fractures or canals will be developed in the ground which would increase the flow velocity, there would be no significant contamination over this distance.

Table VI. Contribution (q_r) to the water supply Q_0 of a well, at the distance r. λ = leakage factor = 20 m

$r=0.1\lambda=2\ m$	$\frac{q_r}{Q_0}=0.985$
$r=0.5\lambda=10\ m$	$=0.830$
$r=1\ \lambda=20$ m	$=0.600$
$r=1.5\lambda=30$ m	$=0.400$
$r=2.4\lambda=48$ m	$=0.200$
$r=4\ \lambda=80$ m	$=0.050$

Protection range

The boundary line separating the groundwater areas can be used as the limit of protection. As far as the upstream limit is concerned, the distance needed for the protection against microbiological contamination is shorter than the one needed for the protection against chemical contamination. As there is no possibility to supervise the area across its total length, we should define a distance up to which monitoring is requested. The area within this distance around the water well will be called the "protection range".

Partial protection range

An optimum solution would be the protection against all contaminations within the defined area around the water well. This is, however, not possible in each case. Restrictions and compromises must be adopted on the considerations that bacteria are mostly destroyed over a filtration path of approximately one hundred meters, while chemical contaminations can easily be transported over many kilometers. Thus, precautions can primarily be taken to prevent bacteriological contaminations what can be achieved by a protective zone of 100–300 m around the water well.

Full protection range

Some chemical contaminations are not neutralized within the short distances as mentioned above. Measurements which do not require the determination of an extended protection area must be considered in this case. The installation of observation holes (Fig. 6) in a suitable distance from the water well can safeguard the indication of a contamination, giving sufficient time for protective means to be taken for its neutralization.

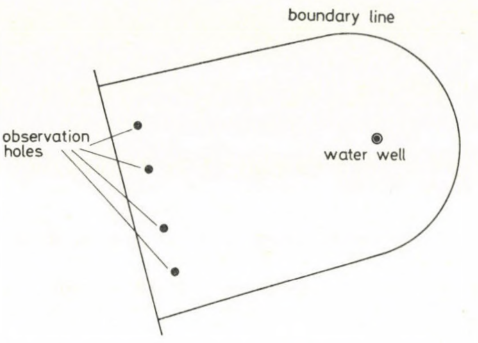

Fig. 6. Position of observation holes, within the partial protection area

Conclusions

The determination of the border of protective areas around water wells is important. The downstream limit of its boundary is defined by the vertex point of the flow lines. The upstream limit allows two alternatives. The first one protects the area against local contaminations and the influence of bacteria, the second takes any contamination due to dissolved substances in the water into consideration. The first protection area can be determined by a 100–300 m circle around the water well.

In order to determine the full protection area, a monitoring zone with observation holes in suitable positions is recommended. The area between the partial protection zone and the monitoring zone should be under intensive control in order to prevent ground water contaminations from any possible pollution.

For the above mentioned reasons, all activities within this area should be supervised and all dangerous permanent contamination sources should be eliminated. In addition, special attention should be paid to casual pollution sources. Last but not least, the control of industrial waste deposits is of great importance in the vicinity of water wells.

References

Feuga B, Vernier J, Sommelet H 1971: Le trace des perimètres de protection autour des captages d'eau. TSM L'EAU, Paris, No. 4.

Garagunis C 1964: Hydrogeologische Untersuchung in der Präfektur Larissa, Griechenland. TYDK 1962–1964

Huisman N 1961: Ground water. Notes from lectures Sanitary Engineering Course, Univ. of Delft, 1960/61

Kollias P S 1976: Water Treatment (In Greek). Athens

Acta Geodaet., Geophys. et Montanist. Hung. Volume 18 (4), pp. 443—452 (1983)

MTS IN CENTRAL KARELIA

I I ROKITYANSKY,[1] M I GOLOD,[2] B N KLABUKOV,[2] A S GRISHIN[2]

[Manuscript received March 22, 1983]

Results of magnetotelluric soundings (MTS) in 21 sites in Central Karelia are presented. The characteristic feature of these results is the high scatter. The MTS have an initial descending branch. The average MTS curve for the North-South polarization and the corresponding phase curve confirm the existence of the asthenosphere in a depth of about 50–170 km. The possibility of distortion in the area studied is discussed.

Keywords: asthenosphere; Baltic shield; Central Karelia; distortion of MTS-curves; global MTS-curve; magnetotellurics

Field observations with digital instruments (DES) have been completed by the Institute of Geology, Karelian Branch of the Academy of Sciences, USSR, at more than 20 sites in Central Karelia (Fig. 1) to cover the area between Geotraverses I and II. Magnetotelluric records were processed by using the programs worked out by Tomchakov at the Geophysical Expedition in Dnepropetrovsk. The consistence of the results provided by the programme in the conditions of the high-resistivity Baltic Shield at a geomagnetic latitude of about 60° has not been examined. The main errors in the impedance tensor determinations are due to industrial noise and to the varying structure of the source of electromagnetic variations, i.e. deviation of the real source structure from the model of a vertically incident plane wave. The effect of the latter is most appreciable in high-resistivity structures, of which the Baltic Shield is the case, and at high latitudes where the source is of the greatest inhomogeneity. The variations of the source structure are illustrated in Fig. 2 where spectra of four eight-hour records of the magnetotelluric field are shown. The magnetic component amplitudes rapidly grow with period, while those of electric components increase slowly, this general tendency holding for all the records. However, local extrema are different for different records which is indicative of considerable variability of the source parameters even when comparing the data obtained in eight hour intervals. Figure 3 shows magnetotelluric parameters, apparent resistivity and impedance phase for the same four records. Although data points show a significant scatter, the following conclusions can be derived: the ρ_{xy}-curve (x being directed to the east, y— to the north) is characterized by a gently sloping descending branch; the ρ_{yx}-curve has a relatively steep descending branch from 25 to 400 s which, at periods more than 600 s, turns into

[1] Institute of Geophysics, Academy of Sciences, UkSSR, Kiev

[2] Institute of Geology, Academy of Sciences, USSR, Karelian Branch, Petrozavodsk

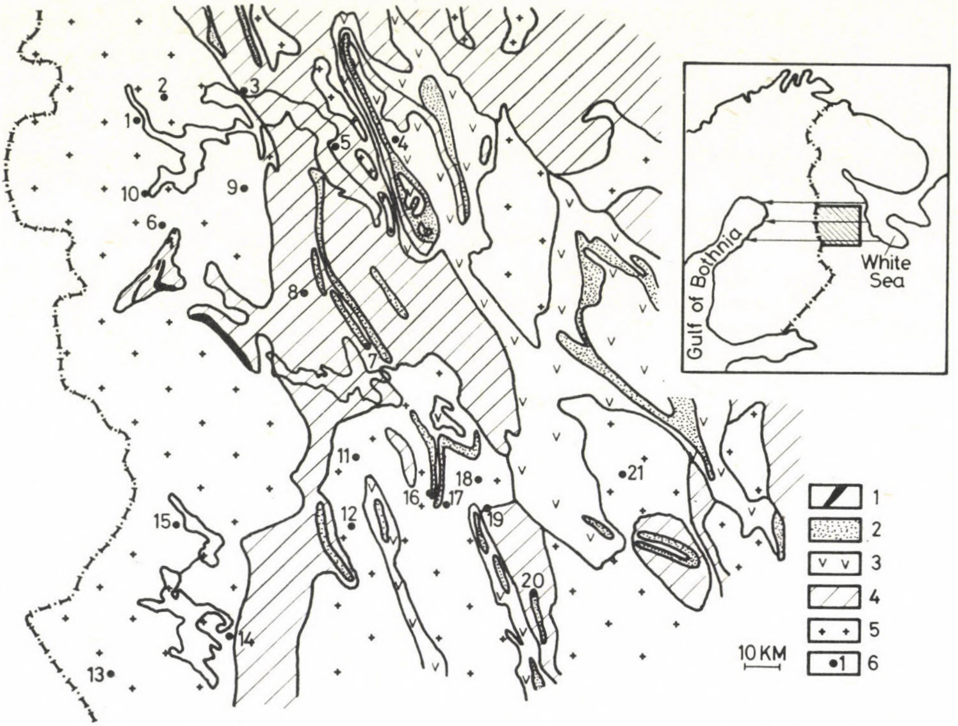

Fig. 1. Electric conductivity scheme for basement rocks in Central Karelia and MTS sites. 1–5 — rocks of specific resistivity to 1000 Ohm · m (1), from 1000 to 3000 (2), from 3000 to 7000 (3), from 7000 to 10000 (4), over 10000 (5); 6 — MTS sites: 1 — Aiguba, 2 — Rivayarvi, 3 — Kalevala, 4 — Kivilampi, 5 — Luusalmi, 6 — Lihanan, 7 — Dlinnoye, 8 — Melgozero, 9 — Kento, 10 — Boknavolok, 11 — Chelmozero, 12 — Tikshozero, 13 — Koroppi, 14 — Chelki, 15 — Konetsostrov, 16 — Chelgozero, 17 — Tiksha, 18 — Puglozero, 19 — Rugozero, 20 — Ondozero, 21 — Khighyarvi

an ascending branch. The data on phases agree with those on amplitudes, hence, confirm them.

The scatter of data points and the discrepancy between the data from different records shown in Fig. 3 are characteristic of the better portion of the processed material. The rest of the data have still greater scatter of the points that sometimes the curves cannot be plotted. Figure 4 shows the MTS amplitude curves that we have managed to obtain by the processing. No error bars are indicated in Fig. 4; their estimation is difficult, too. The curves were deduced by formal averaging the data from different records (over 2 to 5 records at a site) and by subsequent data smoothing. The reliability of any curve in Fig. 4 is not high; therefore, for further interpretation we chose only MTS curves typical for a group of stations.

An analysis of the whole set of amplitude and phase data enables to derive the following conclusions about the MTS curves in the area studied:

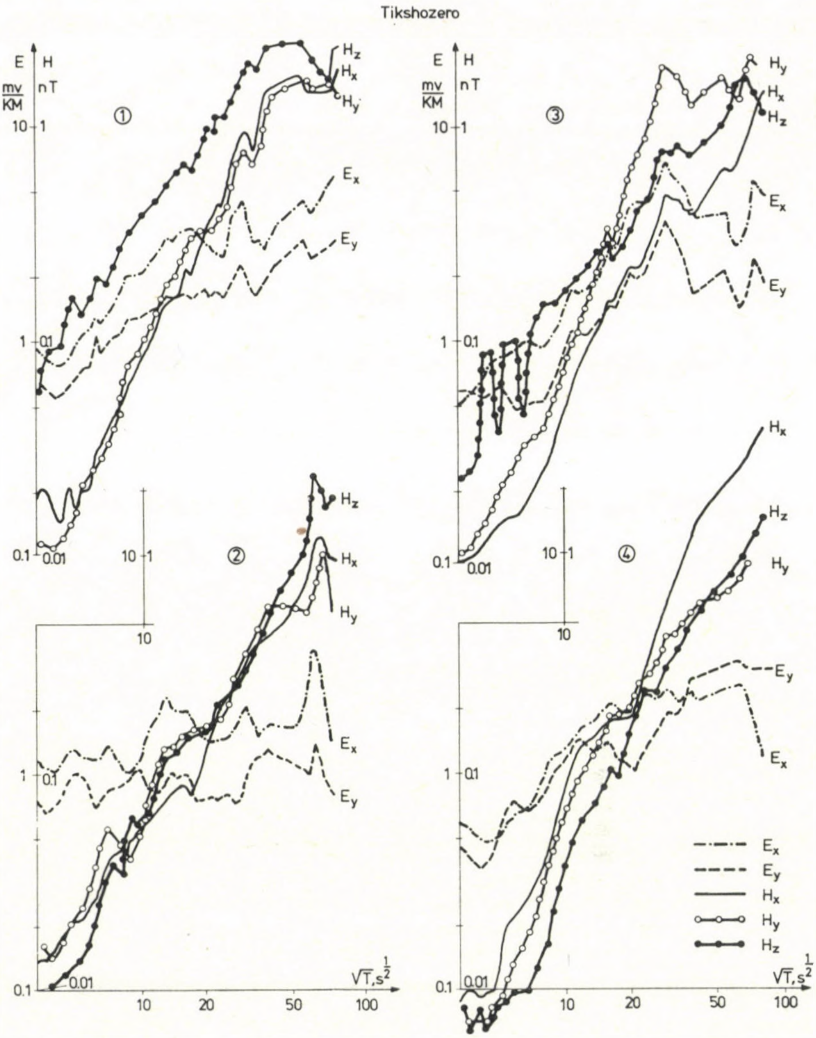

Fig. 2. Amplitude spectra for five components of the magnetotelluric field on eight-hour records obtained at Tikshozero station

1. ρ_{xy}-curves are characterized by a gently descending branch with a slope of 10 to 30°, the phases of the impedances are in average 60–70° and change little with period.

2. ρ_{yx}-curves (with y directed northward) in the range of 40 to 400 s have a descending branch sloping at about 50 to 60°. At periods of more than 400 s, the curves flatten out turning into an ascending branch at some sites. The phase of the impedance φ_{yx} looks like that in Fig. 3 in most points, i.e. it increases from 60° to 80° in the range of 15 to 100 s, then decreases from 80° to 60° in the range of 100 to 700 s, with a hint at a

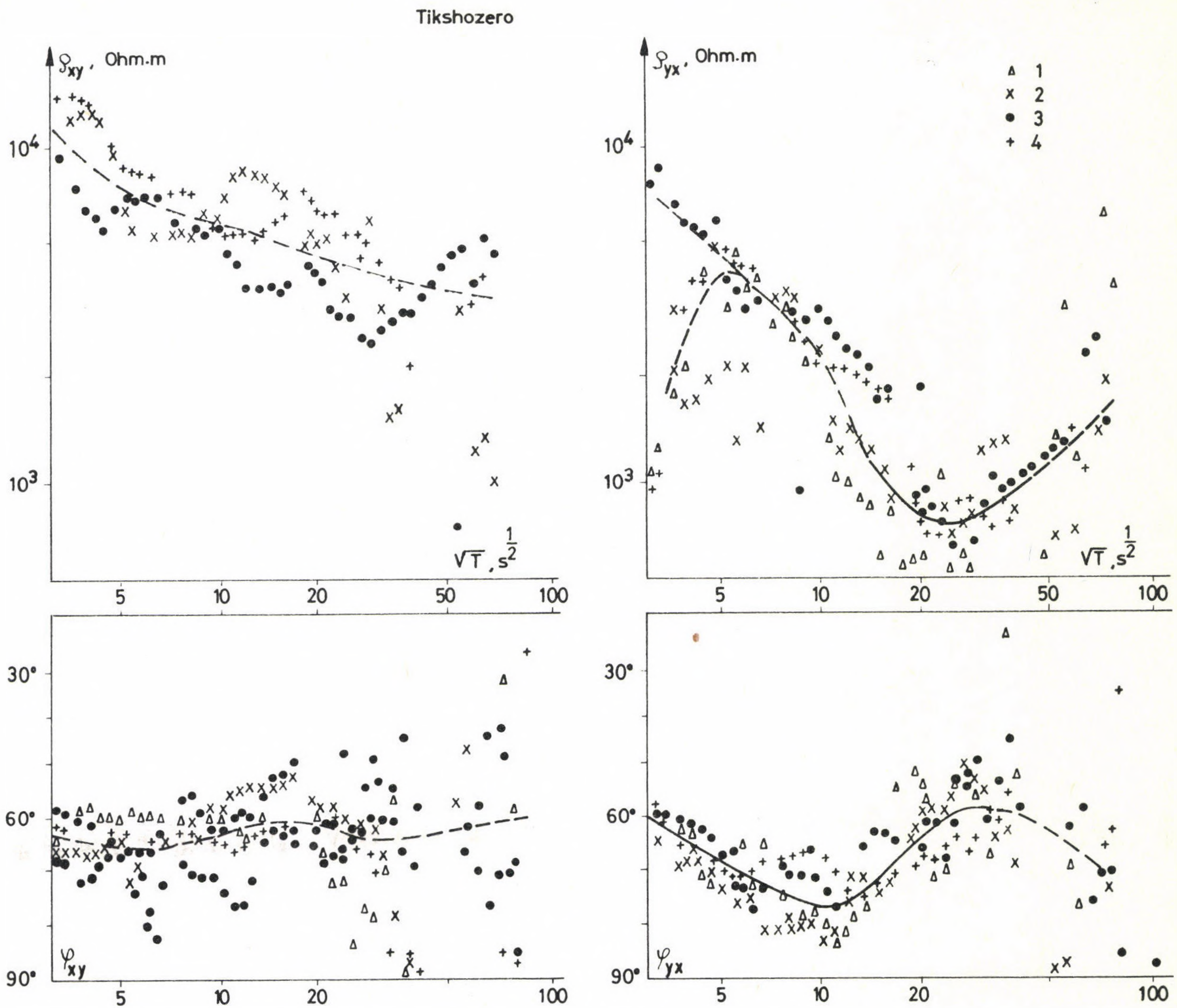

Fig. 3. Apparent resistivities and impedance phases from four records of the magnetotelluric field obtained at Tikshozero station

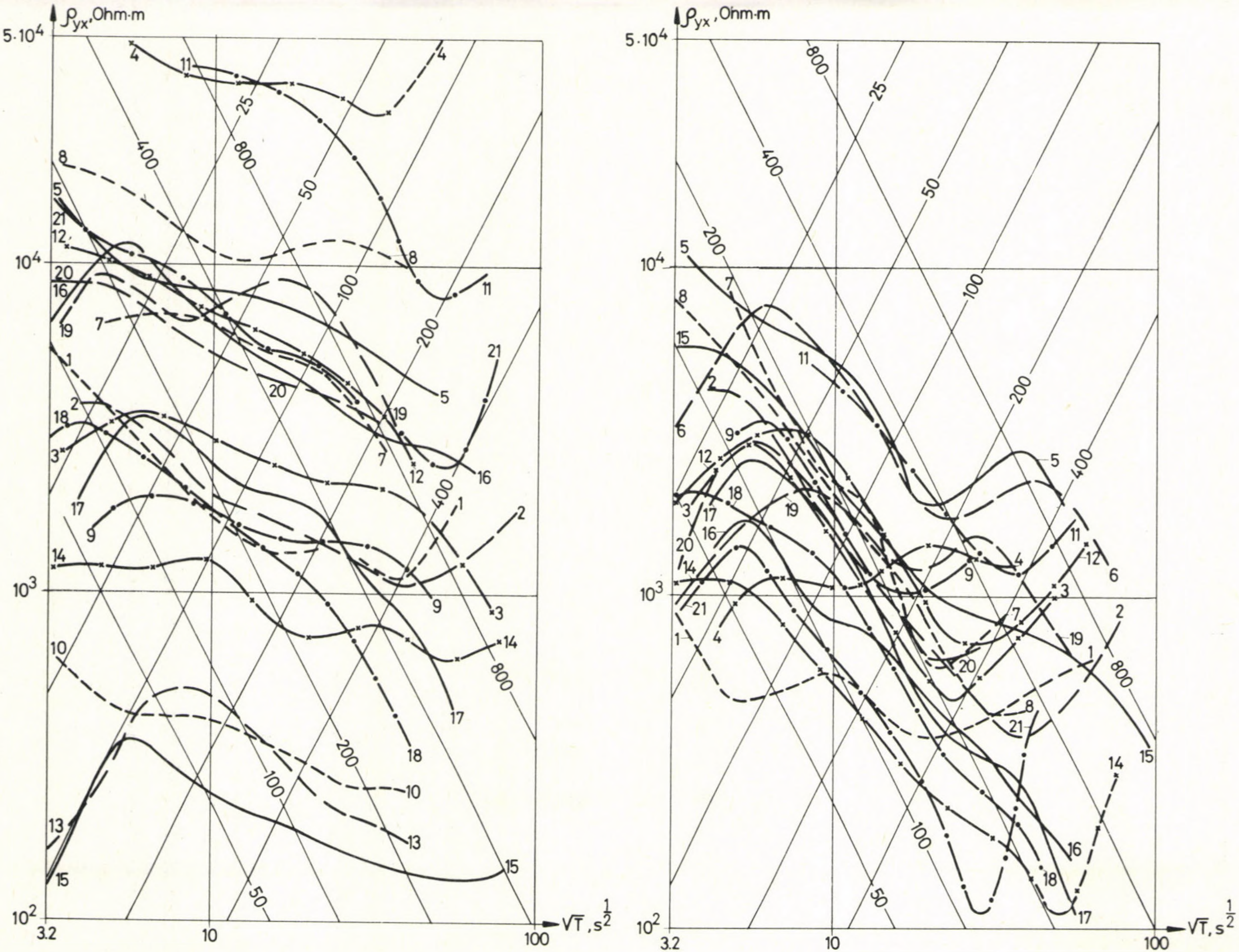

Fig. 4. Amplitude MTS curves in Central Karelia: ρ_{xy} (a) and ρ_{yx} (b), x is directed eastward, y — northward

new increase at even longer periods. The phase data confirm the amplitude curves, particularly, the presence of an ascending part at 500 to 2000 s.

3. The levels of the amplitude curves change within two orders of magnitude. By grouping the curves we can see that, in the western section of the area studied, the amplitude level averages to a half an order of the magnitude observed in the eastern part of the area for both of the components. This is seen from ρ_{yx} in Fig. 5.

Let us consider the geoelectrical conditions in Central Karelia. Here, the sediments have an integral longitudinal conductivity of about 0.01 to 0.02 Ω^{-1}. Such a conductivity does not affect the normal MTS curve in the range of the periods studied ($T > 10$ s), but inhomogeneities in the S-distribution can influence the level of the MTS curves. If S is small like here, the magnetotelluric field essentially depends on the electric conductivity of basement rocks. Taking these into account, a schematic map of the electric conductivity was compiled at the Institute of Geology, Karelian Branch of Academy of Sciences, USSR, shown in Fig. 1. It is based on VES data and data of electric profiling with large AB spacing. The highest resistivity is characteristic for granite widely distributed in the region — more than 10^4 Ohm · m (near to $2 \cdot 10^4$ Ohm · m). Biotite gneisses and amphibole-biotite gneisses have also high resistivities ($\bar{\rho} = 8000$ Ohm · m), as well as gabbro diabases and metaporphyrites ($\bar{\rho} = 6000$ Ohm · m). Much more conductive are metamorphic sediments, such as sandstones, conglomerates, mica quartz schists ($\bar{\rho} = 2000$ Ohm · m). Iron ores in the Kostomuksha region are good conductors ($\bar{\rho} = 300$ Ohm · m). Electron-conducting formations have an insignificant contribution. Horizons of relatively well conducting rocks, as well as geological units in the region, strike mainly northwestward, in the southern part northward.

Let us consider how the MTS curves correlate with the geoelectrical data available. In the western zone, conductivity is the lowest, as the specific resistivity of rocks in the upper part of the basement is the highest there (Fig. 1). This should lead to a higher level of MTS curves compared to that in the eastern zone where subsurface horizons are more conductive. Actually, we have quite the opposite case which suggests the existence of a conducting layer with parameters different in west and east. Two versions of the formal interpretation are possible:

1. The descending branches of ρ_{yx}-curves "mark" the asthenospheric conducting layer (Fig. 5) which is 130 to 170 km deep in the eastern part of the area and 50 to 80 km in the western part. However, considering that the width of the transition zone is only 20–40 km, this version, according to the present physical notions and the data of mathematical modeling, does not seem to be satisfactory.

2. The crust contains a conductor whose integral conductivity does not exceed the values derived from the asymptotes plotted through the left ends of MTS curves. For the eastern zone, the integral conductivity determined from the average curve is 20 Ω^{-1}, while this value for the western zone (Fig. 5) is about 40 Ω^{-1}. The values obtained are about two orders more than the values derived for sediments. If the

integral conductivity of 40 Ω^{-1} were distributed within the whole 40 km thick layer, the average specific conductivity would be 10^3 Ohm · m for the western block and $2 \cdot 10^3$ Ohm · m for the eastern one, i.e. the relation between the values is just opposite to that derived from subsurface VES data (Fig. 1). Another version of interpretation is the suggested existence of a thinner conductor in the crust; such a layer can naturally be assumed below the western block, while below the eastern block the required 20 Ω^{-1}

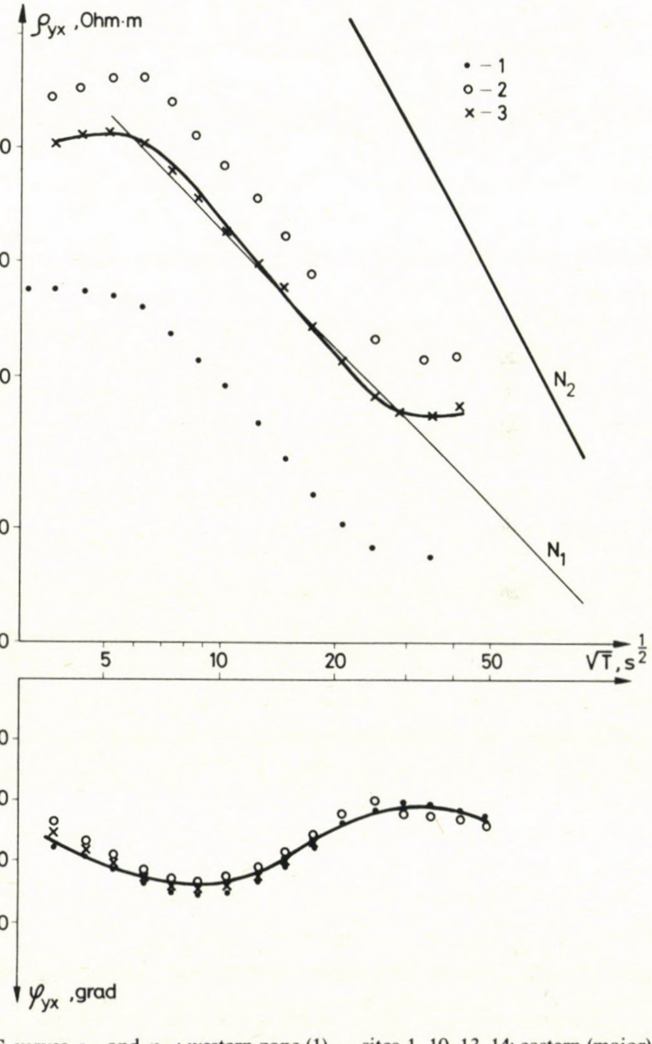

Fig. 5. Average MTS curves ρ_{yx} and φ_{yx}: western zone (1) — sites 1, 10, 13, 14; eastern (major) zone (2) — the rest of the sites; (3) average result for both zones. Thin solid lines show theoretical MTS curves selected for interpretation. Thick solid lines are normal curves: N_1 is plotted on the basis of the descending part of the average curve in Central Karelia in the period range of 40 to 400 s and global data, N_2 is taken from Krasnobayeva et al. (1981)

can be provided by rocks of specific resistivities of about $2 \cdot 10^3$ Ohm · m within a 40 km thick layer. The presence of a local conducting layer below the western block should lead to a lower level of the MTS curves, the drop being the same all over the long-period range. This is indicated by the parallel run of the curves and by the coincidence of the phases. Better motivated speculations about the existence, localization and parameters of the conducting layer would be possible from observations at shorter periods ensured, e.g. by the digital station DES-2.

The deviation of the ρ_{xy} and ρ_{yx}-curves can be qualitatively explained by regional surface conditions, such as the flow of telluric currents from the White Sea into the Gulf of Bothnia (Fig. 1). The distance between these well conducting bodies is 400 km. The three-dimensional effect of the flow which leads to a concentration of the E—W directed telluric currents and an overestimation of ρ_{xy} values appears significantly only at long periods when the wavelength exceeds the above distance (400 km). Assuming $\rho = 10^3$ Ohm · m we see that for variations with periods $T = 10^2$ s, the wavelength $\lambda = \sqrt{10\rho T}$ is longer than 400 km by almost a half order of magnitude; hence, at periods more than 10^2 s, the flow effect can be strong. The "leading" ("concentrating") conductors — the White Sea and the Gulf of Bothnia — are rather extended projections of larger sea basins, which should provide an increase of the concentration of telluric currents as period grows further. This explains qualitatively the milder slope of the ρ_{xy}-curve compared to that of the ρ_{yx}-curve.

Let us assume that the curves ρ_{yx} and φ_{yx} are least distorted by lateral inhomogeneities and, hence, bear information about the vertical distribution of the electric conductivity. Indeed, the S-effect inherent in transverse polarization should occur in the high-resistivity Baltic Shield, but, since the subsurface conducting bodies are many hundreds of kilometers away, the effect can be pronounced only at longer periods. This results in a higher position of the part of the curve containing information about the conducting base of the Earth's mantle; the depths down to the asthenosphere can be assumed to be hardly distorted. Another distortion can be produced by the side induction effect of the conducting waters of the White Sea and, to a lesser extent, of the Gulf of Bothnia (this effect is characteristic for longitudinal polarization). However, the extension of the White Sea from south to north is not great, whereas the sea itself is quite far away. If the influence of the White Sea were strong it could produce the effect of a false conducting layer, then, the "depth" to such a layer would be approximately equal to the distance between the observation point and the coast. However, no dependence of the position of the descending branch of the MTS curve on the distance to the coast is observed; the relation is rather inverse — in the western region the derived depth of the layer is smaller than in the eastern region.

Thus, we have certain reasons for a one-dimensional interpretation of the curves ρ_{yx}, φ_{yx} shown in Fig. 5. The similarity of the average amplitude curves and the coincidence of the phase curves for the two areas (Fig. 5) show that the amplitude curves are displaced parallel to each other by a certain distortion. As first approximation, let us assume the true parameters of the asthenosphere to be unchanged all over the area under study and try to interprete the average curve (designated by crosses in Fig. 5). The fitting to the averaged MTS data presented in Fig. 5 and global sounding data was made at the Institute of Geophysics, Academy of Sciences, UkSSR. The depth of the conducting layer (the asthenosphere) is about 100 km, the integral longitudinal conductivity of the layer is about $300\,\Omega^{-1}$. Informations about specific resistivity of rocks below the asthenosphere are contained only in phase data. As modelling shows, the resistivity of the rocks below the asthenosphere should be not less than 500 Ohm · m to provide a good fit for the phase curve. The error limit of this result is certainly large. It can be estimated firstly by a thorough analysis of the error of the experimental phase curves at long periods and secondly by a conscientious examination of many possible versions of one-dimensional interpretation, thirdly by a comprehensive analysis of distortions through both additional field observations and physical modelling of appropriate two- and three-dimensional problems. All these are for future investigations. Here, we shall present some speculations about the ways of their execution.

1. Figure 3 shows the results of the processing of 4 records. The scatter of the points is sometimes so big that the plotting of the resulting curve becomes problematic, e.g. for ρ_{yx} at short periods and for all parameters at the longest periods. The uncertainty in plotting MTS curves from the results of the processing is a general problem which is especially difficult when sounding is made on shields. The present publication rules for MTS materials require to press the information into a small number of drawings derived from quite a few observation points. This situation is responsible for the fact that resulting curves are generally published without evaluating the confidence limits. Therefore, the results may seem more reliable than they really are and the models derived from the interpretation may be far from the actual geoelectrical structure, or the models close to the real structure may contradict the experimental data. Consequently, experimental data should be always presented with the corresponding confidence limits.

2. When the descending branch of the average ρ_{yx}-curve for Central Karelia is extended by a line to the right until it coincides with the global sounding curve one can obtain a normal curve. In this manner, but from a smaller amount of data, the normal curve was obtained in the work of Vladimirov and Dmitriev (1972) and, later, by Vanyan et al. (1980).

The normal curve is meant to be a high-resistivity envelope of all possible experimental curves after the local distortions of their level have been removed. The normal curve of the region corresponds to the highest-resistivity, with depth monotonously growing electric conductivity compared to which all the other (lower resistivity) distributions in the region may be considered to contain an anomaly. The plotting of the normal MTS curve through experimental points as a line is, actually, identical with denying the asthenosphere, i.e. the low resistivity layer, because the straight line ρ_a suggests that the specific resistivity decreases monotonously with depth. In Central Karelia, the average amplitude curve ρ_{yx} at periods longer than 600 s and the phase curve at periods longer than 200 s lie above the normal curve N_1 in Fig. 5. This behavior refutes the line N_1 as a normal curve and indicates the existence of the low resistivity layer — the asthenosphere. Hence, the normal curve should run higher than N_1. Another version of a normal curve (N_2) is presented by Krasnobaeva et al. (1981). Its slope is $-61°$ in the period range 200 to 10^4 s and is -55–$57°$ at periods longer than a day, as derived from the global sounding data.

The slope of 61° may be too steep, it suggests too high resistivity (in the notion of many scientists) in the rocks below the asthenosphere. However, a slope of the normal curve close to $-60°$ is in good agreement with our data from Central Karelia, from the Kola Peninsula (Krasnobaeva et al. 1981), which, probably, suggests a reappraisal of the notion about a relatively low resistivity below the asthenosphere.

3. The *S*-effect causing a vertical displacement of the MTS curves is revealed almost everywhere. While in Central Karelia, this effect is weak (though, probably, it is the reason for the different levels of ρ_{yx}-curves in the western and eastern part of the area) at periods shorter than several hundred seconds due to the relative regional homogeneity of the electric properties of the Baltic Shield, at longer periods we are right to expect that the influence of the seas and sedimentary basins surrounding the Baltic Shield will cause, through the *S*-effect, an upward bias of MTS curves in the central parts of the shield. Therefore, the long-period branch of the MTS curve may be badly distorted by the regional *S*-effect (the rest of the curve at short and medium periods may remain undistorted by this effect) and cannot be used for tying-in with the normal curve. Therefore, other methods and criteria of tying-in the sounding curves should be used, primarily, those based on grouping.

References

Krasnobaeva A G, Dyakonov B P, Astafyev P F, Batalova O V, Vishnev V S, Gavrilova I E, Zhuravlyova R B, Kirillov S K 1981: Structure of the northeastern part of the Baltic Shield from magnetotelluric data (In Russian). *Izv. AN SSSR, Fizika Zemli*, No 6, 65–73.

Vanyan L L, Berdichevsky M N, Vasin N D, Okulessky B A, Shilovsky P P 1980: On the normal geoelectric depth profile (In Russian). *Izv. AN SSSR, Fizika Zemli*, No 2, 73–76.

Vladimirov N P, Dmitriev V I 1972: Geoelectric depth profile of the earth's crust and upper mantle below the Russian Platform from MTS data (In Russian). *Izv. AN SSSR, Fizika Zemli*, No 6, 100–103.

Acta Geodaet., Geophys. et Montanist. Hung. Volume 18 (4), pp. 453—465 (1983)

COMPUTATION OF GRAVITY AND MAGNETIC FIELDS DUE TO ARBITRARY DENSITY AND MAGNETIZATION DISTRIBUTION

PART I — THEORY

A MESKÓ[1]

[Manuscript received March 15, 1983]

The gravity or magnetic field of a body can be expressed as a convolution of a Green's function with the density distribution or with the magnetization distribution within the body. The convolution can be evaluated rapidly by the fast Fourier transform (FFT) algorithm. These two, well known, features are fully utilized when the body is substituted by a sufficiently large number of mass points or dipoles and the contributions due to these building elements are summed.

The purpose of the paper is to describe the algorithm for effecting such a subdivision and summarize the relevant formulas of the convolutional approach.

In addition to the obvious applications in the solution of the direct and inverse problems the algorithm may be useful in the computation of terrain corrections, isostatic corrections, in the removal of the gravity field of sedimentary basins as well as in the model investigation of various procedures, used in parameter estimation (e.g. depth estimation from spectra).

Keywords: computation of the gravity field; computation of the magnetic field; field of anomalous bodies; gravimetric models

Introduction

Since the introduction of the gravity and magnetic prospection methods considerable efforts have been made to derive methods for the geological interpretation of the anomalies. A direct approach necessarily involves the computation of gravity and magnetic fields. Various algorithms were proposed for the computation of gravity and magnetic effects due to arbitrarily shaped bodies sometimes allowing for varying density or magnetization (Talwani and Ewing 1960, Talwani and Heirztler 1962, Nagy 1966, Botezatu et al. 1971, Mufti 1975, Bhattacharyya and Navolio 1975 etc.).

The mathematical complexity of the formulas, describing gravity and magnetic fields of even simple bodies makes these computations difficult and time consuming. An alternate way of determination is offered by the utilization of the Fourier transform.

A general method has been worked out by the present author (Meskó 1973, 1977) for the computation of gravity fields of arbitrary three-dimensional bodies. Corresponding spectra are also obtained as by-products. Continuations either upward

[1] Geophysics Dept. of Eötvös Loránd University 1083 Budapest, Kun Béla tér 2.

or downward as well as various derivatives of the field can easily be computed. The density distribution or magnetization variations within the body can also be taken into account. The method is useful in modeling or in the iterative solution of inverse problems as well as in the investigation of Fourier spectra.

The main idea is to substitute the body by a sufficiently large number of mass points or dipoles and utilize the simple structure of the Fourier transform of the gravity field due to a point source or that of the magnetic potential of a dipole. The Fourier transforms of the corresponding fields due to a set of mass points or that of the potentials of dipoles at a given depth can easily be computed by two-dimensional Fast Fourier Transform. The contributions from all depth levels are summed up to obtain the integrated effect in the frequency domain. The inverse Fourier transform, computed again by the FFT, gives the gravity field or after some manipulations any components of (or the total field strength of) the magnetic field.

Let us assume that the surface of the irregularly shaped three-dimensional body is described by two sets of digital data $h_1(i, k)$ and $h_2(i, k)$, where h_1 denotes the depth of the upper surface (top) at the (i, k)th point and h_2 denotes the depth of the lower surface (bottom) at the (i, k)th point. We assume that the body is continuous between h_1 and h_2, i.e. there are no holes in it (Fig. 1). Standard interpolation methods could be used to give h_1 and h_2 data at arguments in an arbitrarily dense square grid. Therefore we shall assume that i and k are integers and $x=id$, $y=kd$, where d is the grid spacing.

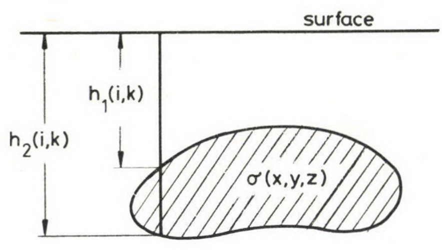

Fig. 1. Notations used in the description of the upper and lower boundaries of the three-dimensional body

Let us assume that the density distribution is given by either a three-dimensional analytical expression $\sigma(x, y, z)$ or a three-dimensional set of discrete data and it can be evaluated for any points within the body. In most practical applications σ_0 is a constant density contrast between the body and its surroundings $\sigma(x, y, z)=\sigma_0$. For modeling purposes, however, the inclusion of varying density may be useful and, as we shall realize it later, it does not appreciably increase computer time.

For simple geometrical bodies such as spheres, prisms, cylinders, cones, etc. the $h_1(i, k)$ and $h_2(i, k)$ can be computed from simple analytical expressions. Most authors (Mufti 1975, Bhattacharyya and Navolio 1975) divide the body into rectangular prisms or cubes and compute first the gravity fields of the prisms. Assuming that the prisms are small compared to the dimensions of the body the sum of their individual gravity fields gives a good approximation to the gravity field of the whole body.

The gravity field due to a rectangular prism can be given analytically. Various formulas have been derived (Nagy 1966, Goodacre 1973, etc.) but none of them is easy to handle. The repeated evaluation of one of these formulas involve time-consuming computations which practically prohibits the use of the exact formulas when the number of prisms are large and the gravity field or magnetic field is to be computed at many points.

The application of the Fourier spectrum of the rectangular prisms (Bhattacharyya and Navolio 1976) looks at first more promising but experiences have shown that it remains still rather tedious mainly because digital handling of continuous spectra.

The gravity field due to a cube, however, can be approximated by the gravity field due to a sphere or a mass point in its center assuming that certain requirements are satisfied (Mufti 1973, 1975, Mufti and Wang 1975). The requirements can always be met by choosing sufficiently small cubes. Without reproducing here the investigations of the cited papers, we merely say that any volume element can be replaced by a point if we are far enough, which is heuristically obvious. The algorithm, on the other hand, can easily take care of the goodness of this approximation.

The two-dimensional Fourier transform of the vertical components of the gravitational attraction due to a point source is known analytically. Consider now all those points which are at the same depth. The total effect of these points is described by convolution. The convolution can be computed very rapidly by two-dimensional FFT.

Let us start at the deepest point of the lower boundary $H_2 = \max h_2(i, k)$. The deepest horizontal slice lies between $H_2 - d$ and H_2. The "empty" volume elements in this slice can easily be determined because then for all lower corners

$$\begin{aligned} &h_2(i, k) && \leqq H_2 - d, \\ &h_2(i+1, k) && \leqq H_2 - d, \\ &h_2(i, k+1) && \leqq H_2 - d, \\ &h_2(i+1, k+1) && \leqq H_2 - d. \end{aligned}$$

When the volume element is not empty its mass is obtained as

$$m(i, k, 1) = \sigma\left(i + \frac{1}{2}, k + \frac{1}{2}, H_2 - \frac{d}{2}\right) V(i, k, 1)$$

where $V(i, k, 1)$ denotes the volume, filled with material (see in Fig. 2). $V(i, k, 1)$ can be approximated by

$$V(i, k, 1) = \frac{d^2}{4}\left[U(i, k, 1) + U(i, k+1, 1) + \right.$$
$$\left. + U(i+1, k, 1) + U(i+1, k+1, 1)\right].$$

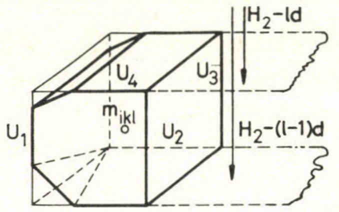

Fig. 2. One of the volume elements $V(i, k, l)$, obtained by the subdivision of the body and the mass point m_{ikl}, substituting it

The side lengths U_i $(i=1, 2, 3, 4)$ depend on the relation of H_2-d and H_2 to the depths of the upper and lower boundaries of the body in the corresponding grid points, as follows

$$\begin{aligned}
U(i, k, 1) &= 0 && \text{when} && h_2(i, k) \leqq H_2-d, \\
&= h_2(i, k)-H_2+d && \text{when} && h_2(i, k) > H_2-d, \\
& && \text{and} && h_1(i, k) < H_2-d, \\
&= H_2-h_1(i, k) && \text{when} && h_2(i, k) = H_2, \\
& && \text{and} && h_1(i, k) \geqq H_2-d, \\
&= h_2(i, k)-h_1(i, k) && \text{when} && h_2(i, k) \leqq H_2, \\
& && \text{and} && h_1(i, k) \geqq H_2-d, \\
&= d && \text{when} && h_2(i, k) = H_2, \\
& && \text{and} && h_1(i, k) \leqq H_2-d,
\end{aligned}$$

see Fig. 3.

The depth of the mass center of the $(i, k, 1)$th volume element is approximated by

$$\frac{1}{4}[W(i, k, 1)+W(i+1, k, 1)+W(i, k+1, 1)+W(i+1, k+1, 1)]=H(i, k, 1),$$

where W values depend again on the relation of H_2-d and H_2 to the depths of the boundaries.

$$\begin{aligned}
W(i, k, 1) &= h_1(i, k, 1)+\frac{1}{2}U(i, k, 1) && \text{for} \quad h_1 \geqq H_2-d, \\
&= H_2-d+\frac{1}{2}U(i, k, 1) && \text{for} \quad h_1 < H_2-d.
\end{aligned}$$

When $U(i, k, 1)$ is equal to zero the mass center of the corresponding volume element is not computed. The depths of mass centers are merely used to approximate the depth of the mass center of the whole slice.

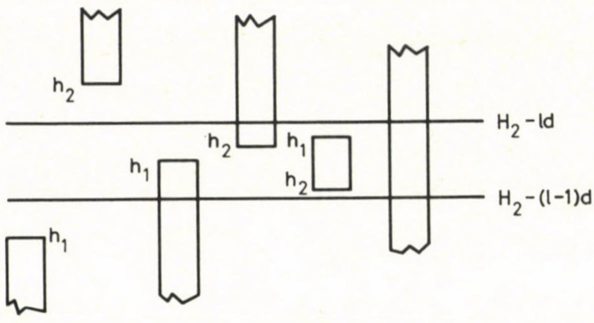

Fig. 3. The possible relations of the boundaries of the body (h_1 and h_2) to the boundaries of the first (bottom) horizontal slice

It is obtained as

$$H(1)=\frac{\sum_i\sum_k m(i,k,1)H(i,k,1)}{\sum_i\sum_k m(i,k,1)},$$

where both sums contain all the volume elements of the slice.

The contribution of the deepest slice to the gravitational attraction of the whole body is then approximated by the gravitational attraction due to mass points in a regular square grid at the depth level $H(1)$. The coordinates of the $(i, k, 1)$th point with mass $m(i, k, 1)$ are $i+\frac{1}{2}$, $k+\frac{1}{2}$, $H(1)$.

Let us consider now the lth intermediate slice $l=2, 3 \dots$. The (i, k, l)th volume element is empty when all the inequalities

$$\begin{aligned}
h_2(i,k) &\leqq H_2-ld,\\
h_2(i,k+1) &\leqq H_2-ld,\\
h_2(i+1,k) &\leqq H_2-ld,\\
h_2(i+1,k+1) &\leqq H_2-ld,
\end{aligned}$$

or all the inequalities

$$\begin{aligned}
h_1(i,k) &\geqq H_2-(l-1)d,\\
h_1(i+1,k) &\geqq H_2-(l-1)d,\\
h_1(i,k+1) &\geqq H_2-(l-1)d,\\
h_1(i+1,k+1) &\geqq H_2-(l-1)d,
\end{aligned}$$

are satisfied. We check again the relation of $h_1(i, k)$ and $h_2(i, k)$ to the upper and lower surfaces of the slice and determine the masses of the volume elements. For the (i, k, l)th volume element one can write again

$$m(i,k,l)=\sigma\left(i+\frac{1}{2},k+\frac{1}{2},H_2-\left(ld-\frac{1}{2}d\right)\right)V(i,k,l),$$

where

$$V(i,k,l)=\frac{d^2}{4}\left[U(i,k,l)+U(i+1,k,l)+U(i,k+1,l)+U(i+1,k+1,l)\right],$$

and

$$\begin{aligned}
U(i,k,l)&=0, && \text{when} && h_2(i,k)\leqq H_2-ld\\
& && \text{or} && h_1(i,k)\geqq H_2-(l-1)d\\
U(i,k,l)&=H_2-(l-1)d-h_1(i,k), && \text{when} && H_2-ld\leqq h_1(i,k)\leqq H_2-(l-1)d\\
& && \text{and} && H_2-(l-1)d\leqq h_2(i,k)\\
&=h_2(i,k)-(H_2-ld), && \text{when} && h_1(i,k)\leqq H-ld\\
& && \text{and} && H_2-ld\leqq h_2(i,k)\leqq H_2-(l-1)d\\
&=h_2(i,k)-h_1(i,k) && \text{when} && H_2-ld\leqq h_2(i,k)\leqq H_2-(l-1)d\\
& && \text{and} && H_2-ld\leqq h_1(i,k)\leqq H_2-(l-1)d\\
&=d, && \text{when} && H_2-(l-1)d\leqq h_2(i,k)\\
& && \text{and} && H-ld\geqq h_1(i,k).
\end{aligned}$$

The possible cases are depicted in Fig. 4.

No approximation is involved when $h_1(i,k)\leqq H_2-ld$ and at the same time $h_2(i,k)\geqq H_2-ld$. For large bodies most volume elements are either "empty" or "full", therefore the whole approximation is usually very good.

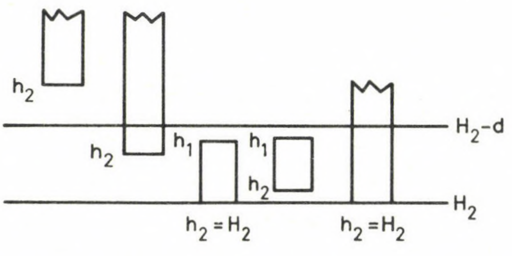

Fig. 4. The possible relations of the boundaries of the body (h_1 and h_2) to the boundaries of an intermediate horizontal slice

The individual mass centers of the volume elements and the mass center of the whole slice is determined as for the first slice and volume elements are substituted again by mass points the depth level $H(l)$ in a regular grid.

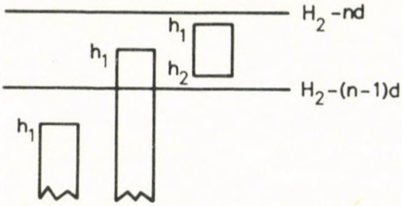

Fig. 5. The possible relations of the boundaries of the body h_1 and h_2 to the boundaries of the uppermost horizontal slice

The uppermost slice is arrived at when

$$H_2-(n-1)d \geqq \min(h_1(i,k)) = H_1 \geqq H_2 - nd.$$

The nth slice is processed similarly. The equations determining the value of $U(i, k, n)$ become

$$\begin{aligned} U(i,k,n) &= 0, && \text{when} \quad h_1(i,k) \geqq H_2-(n-1)d \\ &= H_2-(n-1)d-h_1(i,k), && \text{when} \quad h_1(i,k) \leqq H_2-(n-1)d \\ & && \text{and} \quad h_2(i,k) \geqq H_2-(n-1)d \\ &= h_2(i,k)-h_1(i,k), && \text{when} \quad h_1(i,k) < H_2-(n-1)d \\ & && \text{and} \quad h_2(i,k) \leqq H_2-(n-1)d. \end{aligned}$$

The mass center of the slice is denoted by $H(n)$.

In practical applications the number of points in a slice is more than the number of slices by one or two orders of magnitude. Therefore gravity effects of subsets of points belonging to a given slice are computed separately.

The z component of the gravity field in a point $P(u, v)$ on the surface due to the mass m_{ikl} is equal to

$$g_{ikl} = \frac{Gm_{ikl}H(l)}{[(u-x_i)^2+(v-y_k)^2+H^2(l)]^{3/2}},$$

where $x_i = id$, $y_k = kd$.

The contribution of all mass points in the lth slice is obtained by

$$g_l(u,v) = \sum_i \sum_k \frac{Gm_{ikl}H(l)}{[(u-x_i)^2+(v-y_k)^2+H^2(l)]^{3/2}}.$$

The equation may also be written as a convolution

$$g_l(u, v) = m_{ikl} * \frac{GH(l)}{[x_i^2 + y_i^2 + H^2(l)]^{3/2}}.$$

The first term m_{ikl} contains the shape of, as well the density distribution within the body while the second term is independent of these quantities.

The z component of the gravitational attraction due to the whole body is obtained by summing the contributions of all slices, i.e.

$$g(u, v) = \sum_l (m_{ikl}) * \frac{GH(l)}{[x_i^2 + y_k^2 + H^2(l)]^{3/2}}.$$

The DFT of this equation gives

$$\mathrm{DFT}\{g_l(u, v)\} = \sum_l \mathrm{DFT}\{m_{ikl}\}\, \mathrm{DFT}\left\{\frac{GH(l)}{[x_i^2 + y_k^2 + H^2(l)]^{3/2}}\right\}$$

and the gravity field due the lth slice can be obtained by

$$g_l(u, v) = \mathrm{DFT}^{-1}\left\{\sum_l \mathrm{DFT}\,\{m_{ikl}\}\, \mathrm{DFT}\left\{\frac{GH(l)}{[x_i^2 + y_k^2 + H^2(l)]^{3/2}}\right\}\right\}.$$

When convolution is computed with the aid of the DFT both two-dimensional sequences of samples are treated as being periodic. In order to obtain the non-cyclic convolution the arrays, including mass data m_{ikl} ($l = 1, 2, \ldots n$) have to be augmented by zeros. In most cases, however, the original arrays already contain many zeros. When non-zero data fill less than one quarter of the whole array, augmenting by zeros is not required.

Finer subdivisions with $d = d/2$ or $d = d/4$ can be used to investigate the accuracy of the substitution of volume elements by points.

It is obvious, that the computer time is about the same if the density varies or if it is constant.

We can also include easily the computation of arbitrary linear transforms of the gravity field e.g. horizontal or vertical gradients. Then the discrete transfer function of the corresponding linear operation has to be applied before taking the inverse Fourier transform of the computed spectrum.

Computation of magnetic field vector components

The algorithm based on the utilization of the FFT for the rapid computation of convolution can be used in the determination of magnetic anomalies due to irregularly shaped bodies as well. In the case of gravity anomalies the external gravitational field was considered as the sum of the effects of mass points constituting the body. Similarly, in the computation of magnetic anomalies we may consider the external magnetic field due to the body as the sum of the effects of dipoles that give the body its magnetization. Dipoles, however, may be oriented in any direction. Therefore description of the magnetization of a body requires giving both the magnitudes and directions of the magnetization of the volume elements rather than giving a single magnitude (mass) as in the case of the computation of the gravity field.

Permeable rocks placed in the earth's magnetic field acquire induced magnetization whose strength is determined by the magnetic susceptibility. Other rocks possess a permanent magnetization unrelated to the external field. In either case, however, we may describe the magnetic state of the body by $\bar{M}(x, y, z)$, i.e. by the distribution of the magnetic dipole moment per unit volume within the body.

The magnetic scalar potential at point (x_0, y_0, z_0) outside the body is

$$U(x_0, y_0, z_0) = -\iiint_V \left(\bar{M}, \operatorname{grad} \frac{1}{|\bar{r}-\bar{r}_0|}\right) \mathrm{d}v$$

where V is the volume, filled by the magnetized material and

$$|\bar{r}-\bar{r}_0| = [(x-x_0)^2+(y-y_0)^2+(z-z_0)^2]^{1/2}.$$

The scalar potential can be written as the sum of three components

$$U_1 = \iiint_V M_x(x, y, z) \frac{x-x_0}{((x-x_0)^2+(y-y_0)^2+(z-z_0)^2)^{3/2}} \mathrm{d}x\mathrm{d}y\mathrm{d}z,$$

$$U_2 = \iiint_V M_y(x, y, z) \frac{y-y_0}{((x-x_0)^2+(y-y_0)^2+(z-z_0)^2)^{3/2}} \mathrm{d}x\mathrm{d}y\mathrm{d}z,$$

$$U_3 = \iiint_V M_z(x, y, z) \frac{z-z_0}{((x-x_0)^2+(y-y_0)^2+(z-z_0)^2)^{3/2}} \mathrm{d}x\mathrm{d}y\mathrm{d}z,$$

and $U = U_1 + U_2 + U_3$.

Let us determine now the potential at the surface, where $z_0 = 0$, and consider a thin horizontal slice of the body. The contribution of the kth slice at the depth $z = z_k$ becomes

$$U(x, y, 0) =$$

$$= \Delta z \iint \frac{M_x(x, y, z_k)(x-x_0) + M_y(x, y, z_k)(y-y_0) + M_z(x, y, z_k)(z-z_0)}{((x-x_0)^2+(y-y_0)^2+z_k^2)^{3/2}} \mathrm{d}x\mathrm{d}y.$$

The expression obviously is the sum of three convolutions and each of them can be evaluated by the algorithm utilizing the FFT. The equation may be interpreted as the application of three two-dimensional filters with weight functions M_x, M_y and M_z to the two-dimensional input functions

$$m_1 = \frac{x-x_0}{((x-x_0)^2+(y-y_0)^2+z_k^2)^{3/2}},$$

$$m_2 = \frac{y-y_0}{((x-x_0)^2+(y-y_0)^2+z_k^2)^{3/2}},$$

and

$$m_3 = \frac{z-z_0}{((x-x_0)^2+(y-y_0)^2+z_k^2)^{3/2}},$$

respectively.

The potential is obtained as the sum of the contributions of all horizontal slices. The horizontal and vertical components X, Y and Z of the magnetic field can be obtained by taking the corresponding derivatives of the scalar potential. E.g. the vertical component becomes

$$Z = -\frac{\partial U}{\partial z} = \frac{\partial}{\partial z}\iiint\left(\bar{M}, \operatorname{grad}\frac{1}{|\bar{r}-\bar{r}_0|}\right)\mathrm{d}v.$$

The derivative with respect to the coordinate z can be evaluated numerically. In the point $(x_0, y_0, z_0=0)$ the vertical component becomes

$$Z = \lim_{h\downarrow 0}\frac{U(x_0, y_0, h)-U(x_0, y_0, 0)}{h}.$$

The horizontal component can be determined in a similar way. The total field can then be computed from Z and H.

The derivatives can also be computed by utilizing the transfer functions corresponding to the computation of the derivatives. The transfer functions of the first vertical derivatives are as follows

$$S_{\frac{\partial}{\partial x}}(f_x, f_y) = j2\pi f_x,$$

$$S_{\frac{\partial}{\partial y}}(f_x, f_y) = j2\pi f_y,$$

$$S_{\frac{\partial}{\partial z}}(f_x, f_y) = 2\pi(f_x^2+f_y^2)^{1/2}.$$

In realistic models the direction of magnetization $\bar{M}$ is constant. If we allow for a variation in magnitude but assume that the direction (denoted by $\bar{\kappa}$) is constant the potential can be written as

$$U(x_0, y_0, z_0=0) = -\iiint_V M(x, y, z)\frac{\partial}{\partial\bar{\kappa}}\frac{1}{|\bar{r}-\bar{r}_0|}\mathrm{d}v$$

where M is a scalar function of the x, y, z coordinates while

$$\frac{\partial}{\partial \bar{\kappa}} = A\frac{\partial}{\partial x} + B\frac{\partial}{\partial y} + C\frac{\partial}{\partial z},$$

where

$$A = \cos\tau \sin\eta,$$

$$B = \cos\tau \cos\eta,$$

$$C = \sin\eta,$$

and τ denotes the dip of the magnetization measured clockwise from the horizontal, η is the angle measured counterclockwise from the y axis to the projection of $\bar{M}$ on the horizontal plane Fig. 6.

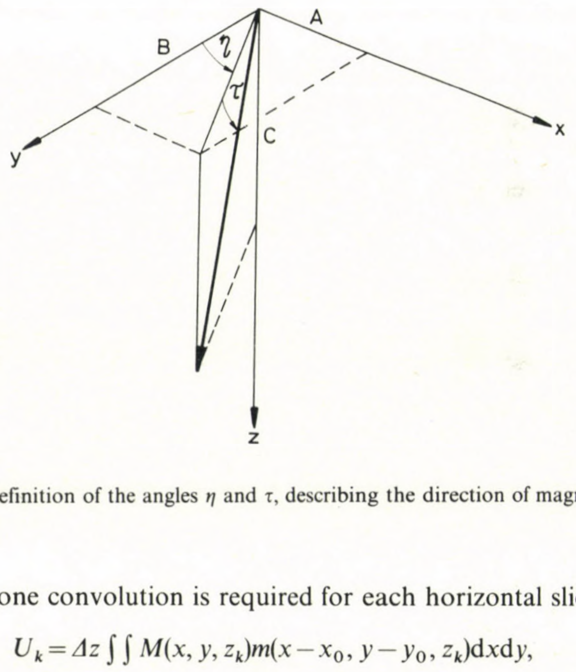

Fig. 6. The definition of the angles η and τ, describing the direction of magnetization

In this case one convolution is required for each horizontal slice because then

$$U_k = \Delta z \int\int M(x, y, z_k) m(x - x_0, y - y_0, z_k) \mathrm{d}x\mathrm{d}y,$$

where

$$m(x - x_0, y - y_0, z_k) = \frac{A(x - x_0) + B(y - y_0) + Cz_k}{((x - x_0)^2 + (y - y_0)^2 + z_k^2)^{3/2}}.$$

If the magnetization $\bar{M}$ is due to the earth's magnetic field, i.e. the body is inductively magnetized and has a negligible permanent magnetic moment, τ becomes equal to the magnetic inclination I, and η becomes equal to the magnetic declination D while $\bar{M} = k\bar{T}_0$ where k is the magnetic susceptibility and $\bar{T}_0$ is the total field intensity of the earth's magnetic field. In this case further simplifications follows from the fact that $\bar{M}$ lies everywhere in the direction of the main magnetic field.

The total field anomaly due to the body is obtained from the scalar potential as

$$T(x_0, y_0, 0) = -\frac{\partial}{\partial \bar{\alpha}} U(x_0, y_0, z_0 = 0),$$

where $\bar{\alpha}$ denotes the direction of $\bar{T}_0$. The directional derivative, which lies in the direction of $\bar{T}_0$ (and $\bar{M}$), becomes

$$\frac{\partial}{\partial \bar{\alpha}} = A_0 \frac{\partial}{\partial x} + B_0 \frac{\partial}{\partial y} + C_0 \frac{\partial}{\partial z},$$

where

$$A_0 = \cos I \sin D,$$

$$B_0 = \cos I \cos D,$$

$$C_0 = \sin I.$$

The expression for the scalar potential becomes

$$U_k = \Delta z T_0 \iint k(x, y, z_k) m(x - x_0, y - y_0, z_k) \mathrm{d}x \mathrm{d}y$$

where

$$m(x - x_0, y - y_0, z_k) = \frac{A_0(x - x_0) + B_0(y - y_0) + C_0 z_k}{((x - x_0)^2 + (y - y_0)^2 + z_k^2)^{3/2}}.$$

The contribution of the kth horizontal slice to the total field anomaly is

$$T_k = \left(A_0 \frac{\partial}{\partial x} + B_0 \frac{\partial}{\partial y} + C_0 \frac{\partial}{\partial z} \right) U_k$$

and can be computed by adding the results of three derivatives.

Further simplification follows when constant magnetization is assumed. For a body with constant permanent magnetization $\bar{M}(x, y, z) = \bar{M}_0$ and for an inductively magnetized body with constant magnetic susceptibility $k(x, y, z) = k_0$ the total field anomaly can be expressed by

$$T(x_0, y_0, 0) = -M_0 \frac{\partial}{\partial \bar{\alpha}} \frac{\partial}{\partial \bar{\kappa}} \iiint \frac{\mathrm{d}v}{|\bar{r} - \bar{r}_0|},$$

and

$$T(x_0, y_0, 0) = -k_0 T_0 \frac{\partial^2}{\partial \bar{\alpha}^2} \iiint \frac{\mathrm{d}v}{|\bar{r} - \bar{r}_0|},$$

respectively. Then the contribution from each horizontal slice of the body can be expressed by one two-dimensional convolution and the total field anomaly is obtained as the sum of these contributions.

The vertical field anomalies can be obtained in a similar way for a body with permanent moment $\bar{M}_0$

$$Z(x_0, y_0, 0) = -M_0 \frac{\partial^2}{\partial z \partial \bar{\kappa}} \iiint \frac{\mathrm{d}v}{|\bar{r} - \bar{r}_0|}$$

and for an inductively magnetized body

$$Z(x_0, y_0, 0) = -kT_0 \frac{\partial^2}{\partial z \partial \bar{\alpha}} \iiint \frac{\mathrm{d}v}{|\bar{r} - \bar{r}_0|}.$$

In both cases the contribution of each horizontal slice can be obtained by one convolution.

References

Bhattacharyya B K, Navolio M E 1975: Digital convolution for computing gravity and magnetic anomalies due to arbitrary bodies. *Geophysics*, 42, 41–50.

Bhattacharyya B K, Navolio M E 1976: A Fast Fourier Transform method for rapid computation of gravity and magnetic anomalies due to arbitrary bodies. *Geophys. Prospect.*, 20, 633–649.

Botezatu R, Visarion M, Scurtu F, Cucu G 1971: Approximation of the gravitational attraction of geological bodies. *Geophys. Prospect.*, 19, 218–227.

Goodacre A K 1973: Some comment on the calculation of the gravitational and magnetic attraction of a homogeneous rectangular prism. *Geophys. Prospect.*, 21, 66–70.

Meskó A 1973: Determination of the depth to the basement rocks from gravity data for Hungarian prospection areas. (in Hungarian) Research report, unpublished

Meskó A 1977: A new algorithm for the computation of gravitational attraction due to irregularly shaped bodies. *Annales Univ. Budapest*, 18, 65–73.

Mufti I R 1973: Rapid determination of the cube's gravity field. *Geophys. Prospect.*, 21, 724–735.

Mufti I R 1975: Iterative modeling by using cubical blocks. *Geophys. Prospect.*, 23, 163–198.

Mufti I R, Wang R 1975: Comments on "Rapid determination of cube's gravity field". *Geophys. Prospect.*, 23, 199–202.

Nagy D 1966: The gravitational attraction of a right rectangular prism. *Geophysics*, 31, 362–371.

Talwani M, Ewing M 1960: Rapid computation of gravitational attraction of three dimensional bodies of arbitrary shape. *Geophysics*, 25, 203–225.

Talwani M, Heirztler J P 1962: The mathematical expression for the magnetic anomaly over a two-dimensional body of polygonal cross-section. Tech. Rep. No. 6. Lamont-Doherty Geol. Observ. Columbia University

Acta Geodaet., Geophys. et Montanist. Hung. Volume 18 (4), pp. 467—488 (1983)

PHYSICAL AND MATHEMATICAL MODELING OF CRUSTAL CONDUCTIVITY ANOMALIES IN THE PANNONIAN BASIN

A ÁDÁM[1], L SZARKA[1], M VARGA[1]

[Manuscript received March 23, 1983]

A new physical modeling technics using a dipole source of 0.1–3 MHz was introduced in the Geodetic and Geophysical Research Institute (GGRI) to help the interpretation of the crustal conductivity anomalies as the sounding curves of dipole and plane wave sources well approximate each other in the wave zone.

For the normalization of measured electromagnetic fields of the dipole source above 2-D conductive structures, a numerical method has been applied using linear filter technics for the basic 1-D layer sequence.

After a short description of the induction problems in the Pannonian Basin to be solved in connection with fracture tectonics, the results of physical modeling are compared with that of numerical calculations using the finite difference method.

Keywords: controlled source magnetotellurics; crustal conducting formation; magnetotellurics; numerical modeling; physical modeling; sounding curves of electric dipole source

Introduction

In the western part of Hungary (Transdanubia) the well conducting crustal formations are mainly connected with linear fracture tectonics, so they are two-dimensional (2-D) structures in a good approximation.

In the interpretation of these formations physical (analogue) and mathematical (numerical) modelings were used. As mathematical modeling the finite difference method (FDM) was applied. In case of the physical modeling, the electromagnetic field generated by an electric dipole was studied over conducting graphite dykes as the frequency sounding curves of electric dipole and plane wave sources well approximate each other if the r/h_1 value is high enough (where r = transmitter-receiver distance, h_1 = depth of the conducting basement) (Goldstein and Strangway 1975). In a one-dimensional (1-D) layered half space this coincidence was numerically studied as a function of the r/h_1 ratio.

After the description of the physical modeling technics and the numerical method used for calculation of the frequency sounding curves of the electric dipole

[1] Geodetic and Geophysical Research Institute of the Hungarian Academy of Sciences, H-9401 Sopron, POB 5, Hungary

source, the results of physical modeling and that calculated by FDM for two characteristic 2-D conducting structures of the Transdanubian anomaly are compared.

An answer was looked for to the practical question: to what extent can be the magnetotelluric sounding curves approximated by controlled source (A)MT technics above conducting formations.

Physical modeling device

The Electromagnetic Modeling Laboratory of the GGRI was built up in Sopron in co-operation with several Hungarian institutions in 1978. Besides the investigation of high conductivity crustal structures it has been used to solve interpretation problems in bauxite and oil explorations of other Hungarian geophysical companies, too.

In this paper only a short description of the laboratory is given. More details can be read in Ádám et al. (1981).

Model experiments are carried out in a NaCl-solution of suitable specific resistivity. The electrolyte is contained in a $4 \times 3 \times 0.5$ m polyester tank. High resistivity structures of the basement are represented by high resistivity model bodies. Conductive embeddings are produced from isotrope graphite bricks. For the conductive measurements a selective measuring system has been developed mainly for dipole-dipole electromagnetic frequency soundings (Fig. 1).

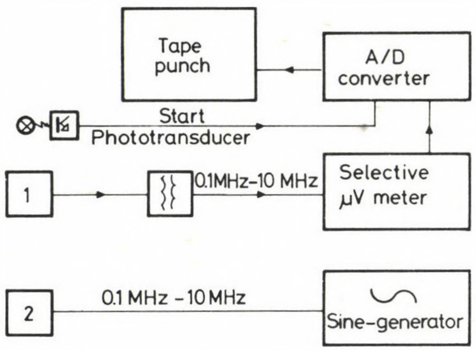

Fig. 1. Simplified block diagram of the measuring device
1: Receiver dipoles and preamplifier
2: Current generator and the transmitting electric dipole

The source of the measuring signal is a sine-generator which gives signals of any frequency between 100 kHz and 10 MHz in 1 kHz steps with a relative accuracy of 10^{-6}. This measuring signal has an amplitude of about 20 mV and is transmitted by cable to a current generator which supplies current of 100 mA intensity (as a peak value) to the salt water (electrolyte) through a dipole.

At the receiver side a low noise amplifier ($U \leqq 300$ nV P.-P.) senses and amplifies the signal appearing at the receiver electrodes (at the same frequency as it was transmitted to the electrolyte). After a 40 dB gain the signal is transmitted through a wide band transformer (for galvanic separation) to the input of a selective μV-meter which should be always tuned to the frequency of the sine-generator. The measured value can be read on the μV meter but at the same time a DC signal proportional to the potential difference on the receiver electrodes will be produced. After an A/D conversion it is punched to tape in BCD code.

The sampling (A/D conversion and tape punch) is controlled by a phototransducer which moves together with the receiver electrodes.

The transmitter and measuring unit can be moved with suitable accuracy along the tank by rolling bridge structures on which carriages can move crosswise. The electrode holding rods are fixed on these carriages.

Most of the mechanical parts of the modeling apparatus are made of different plastic materials.

The determination of the location and resetting to a given point is done by the measuring tapes along the two coordinates with an accuracy of ± 1 mm.

Calculation of theoretical frequency sounding curves in 1-D case

The electromagnetic field of an infinitesimal horizontal current dipole, oriented along the x-axis at the surface of an isotropic, horizontally stratified halfspace can be derived from the solution of Maxwell's equations taking into account the boundary conditions at the interfaces. We summarize only the final result of this solution, because on the one hand the calculation is very lengthy, on the other these formulae (though in a slightly modified form) have been presented by e.q. Keller (1968) and Scriba (1974).

The resulting field component expressions are given in Appendix A.

Because of the complicated structure of the kernel functions for the layered medium, the integrals have to be evaluated numerically, but these kernels are very slowly convergent. The rate of the convergence can be improved by substracting from the integrand a term, representing the homogeneous halfspace and then adding the analytic expression of the integral of this term to the numerically computed value of the modified integral. In this manner we get expressions presented in Appendix B.

Evaluation of the integrals used in these formulae were carried out by use of the digital linear filtering method (Koefoed et al. 1972, Anderson 1979). The essence of this method is that the integrals are transformed into a convolution type integral, and the latter, using suitable filter coefficients, can be replaced with a sum containing only a finite number of terms, and so one can get the value of the integrals in a relatively easy and quick way.

We compute the apparent resistivity curves from the components of the electromagnetic field in the usual manner (Appendix C) and then these curves were compared with the computed magnetotelluric curves and with the results of the analogue modeling.

The MT curves were computed for 1-D structures in the traditional manner.

Comparison of FRS and MT sounding curves above homogeneous and two-layered half spaces

To decide whether the MTS measurements can be substituted by FRS measurements the master curves of Goldstein and Strangway (1975) were studied. They examined the behaviour of the apparent resistivity curves ρ_{FRS} derived from components E_x and H_y for two layered models in case of large values of the parameter r/h_1 in dipole equatorial position and compared them to the ρ_{MT} curves. ("r" is the distance between the transmitter and the receiver, "h_1" is the thickness of the top layer.) On base of Fig. 2 which shows the corresponding ρ_{FRS} and ρ_{MT} curves further conclusions can be made.

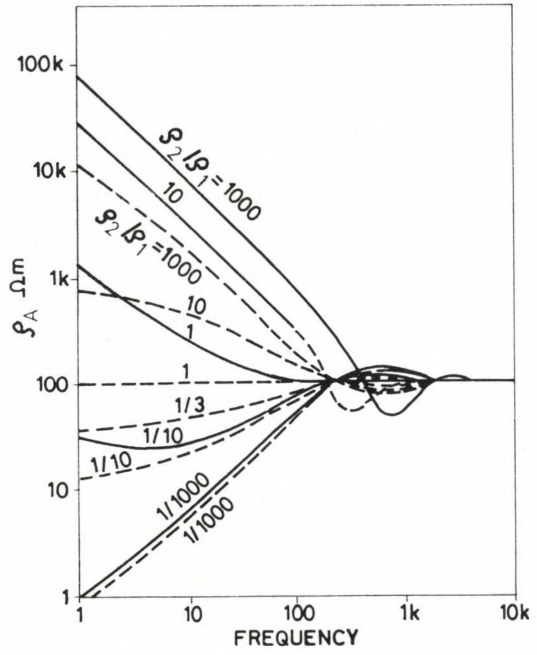

Fig. 2. Apparent resistivity profiles calculated for the case of a layer over a half-space. The top layer is 250 m thick and has a resistivity of 100 Ohm · m. The dashed lines give the results for magnetotellurics. The solid lines are the sounding curves derived using the E_x/H_y ratio for an electric dipole source at a distance of 2000 m along the y-axis (after Goldstein and Strangway 1975)

The homogeneous half space and the two limiting cases of two layered half spaces, $\rho_2 \gg \rho_1$ and $\rho_2 \ll \rho_1$, were examined and the ρ_{FRS}/ρ_{MT} ratios were calculated in the wave zone $|k_1 r| \gg 1$, in the intermediate zone and in the quasi-static zone $|k_1 r| \ll 1$. These ratios are shown in Fig. 3.

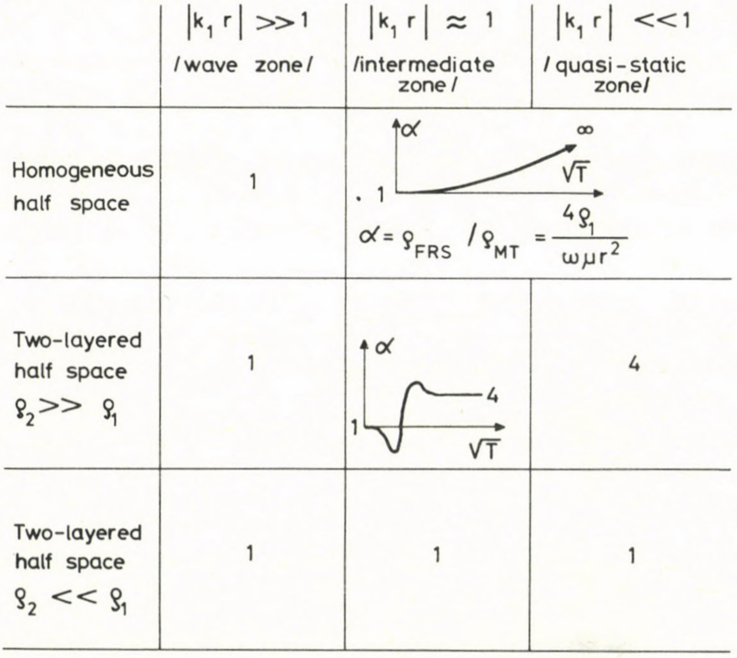

Fig. 3. ρ_{FRS}/ρ_{MT} ratios at large r/h_1 in dipole equatorial position as a function of $|k_1 r|$

It is well known that in the wave zone the ratio ρ_{FRS}/ρ_{MT} equals to 1 and it does not depend on ρ_2.

Above a homogeneous half space, ρ_{FRS}/ρ_{MT} tends to the infinity with decreasing $|k_1 r|$ value.

In case of a highly resistive basement in the quasi-static range, $\rho_{FRS}/\rho_{MT} = 4$ as it has been shown by Szarka (1983). In the intermediate zone a difficult transition function exists.

The conducting basement $\rho_2 \ll \rho_1$ represents a very special case: the ratio $\rho_{FRS}/\rho_{MT} = 1$ in the whole range of $|k_1 r|$. It means that the apparent resistivity curves are the same in magnetotellurics and in artificial frequency sounding if $r/h_1 \gg 1$.

Relations between FRS and MT sounding curves in function of r/h_1

If r/h_1 is high enough, the corresponding dipole equatorial FRS and MT sounding curves agree for the same layer over a highly conductive half-space.

To study this agreement in function of r/h_1 and to determine a satisfactory r/h_1 for model measurements mathematical calculations were made using linear filter technics developed by Koefoed et al. (1972).

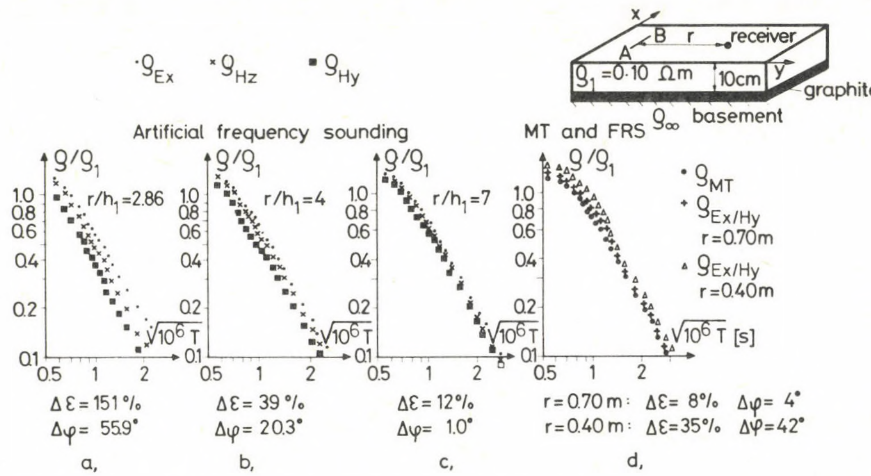

Fig. 4. Comparison of FRS and MT in three layered case, when $\rho_1 \gg \rho_2$ and $\rho_3 \gg \rho_1$ in function of r/h_1
a) ρ_{E_x}, ρ_{H_z} and ρ_{H_y} curves at $r/h_1 = 2.86$
b) ρ_{E_x}, ρ_{H_z} and ρ_{H_y} curves at $r/h_1 = 4$
c) ρ_{E_x}, ρ_{H_z} and ρ_{H_y} curves at $r/h_1 = 7$
d) comparison of ρ_{MT} sounding curves and ρ_{E_x/H_y} FRS sounding curves

Results obtained by the computer program of Varga (1981) are shown in Fig. 4. Figures 4a, b, c show ρ_a curves obtained from the E_x, H_z and H_y components for $r/h_1 = 2.86$, 4 and 7. The three curves approach each other with increasing r/h_1 and approximate the theoretical agreement of the curves. Deviations in amplitude ($\Delta\varepsilon$) and in phase ($\Delta\varphi$) are also disappearing, when r/h_1 increases. According to our conception this agreement exists not only in the wave zone concerning to the first layer, but in the whole range of $|k_1 r|$. (E.g. in case of the lowest frequency $|k_1 r|$ was 2.21 which represents the intermediate zone.) Figure 4d shows the ρ_{MT} curve together with dipole-equatorial ρ_{FRS} curves calculated from E_x and H_y for $r/h_1 = 4$ and 7. It can be seen that ρ_{FRS} at $r/h_1 = 7$ approximates the ρ_{MT} curve with $\Delta\varepsilon = 8\%$ and $\Delta\varphi = 4°$.

A smaller r/h_1 ($r/h_1 = 2.86 - 4$), however, gives only qualitative approximation for the ρ_{MT} curves.

Our model tank has a high resistivity bottom made of plastic, so the $\rho_1 \gg \rho_2 \ll \rho_3$ three layered case also had to be studied to decide whether the above mentioned agreement of FRS and MT sounding curves exists or not. The numerical calculations show that in our model frequency range a graphitic layer of several mm thickness assures this favourable agreement, and all results are the same as in Fig. 4.

Interpretation models of the crustal conductivity anomalies in the Pannonian Basin

As it has been proved by statistical investigations of the distortion of the MT sounding curves measured in the Pannonian Basin, the crustal conductivity anomalies are there in connection with the linear fracture tectonics (Ádám 1981). This relation can be seen on the isoresistivity profile measured above exactly located seismoactive transversal fractures in a shallow basin of the southwestern part of the Bakony Mts. The lowest ρ-values have been got above narrow fracture zones (Fig. 5) and the $Z_{xy\max}$ impedance directions are perpendicular to the fracture strike (Fig. 6).

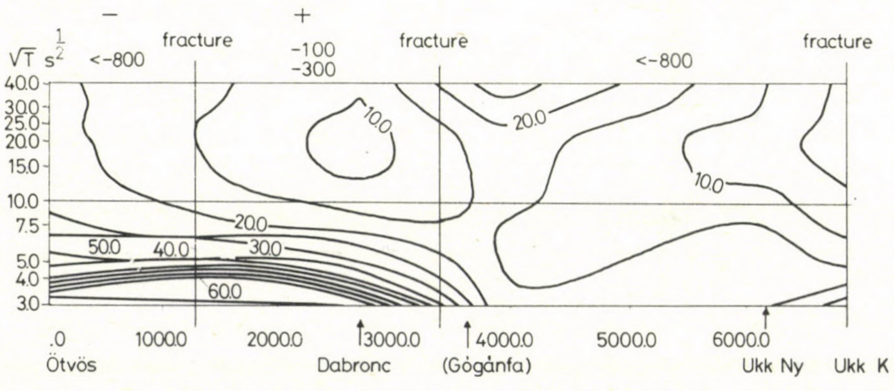

Fig. 5. Isoresistivity profile along a profile between the villages Ukk and Ötvös (W-Hungary)

The 2-D numerical model of a fracture containing a conductive body was calculated by Tátrallyay (1977) using the finite difference method (Fig. 7).

The main characteristics of this model are as follows:

1. The $\rho_{\min}$ curve in the epicentre of the anomaly approximates the parameters of the anomalously conductive body.

2. Above the edges of the body, the MTS curves show an apparent increase of the depth to the top of the body and an apparent decrease of its horizontal (longitudinal) conductivity $\left(S = \dfrac{h}{\rho}\right)$.

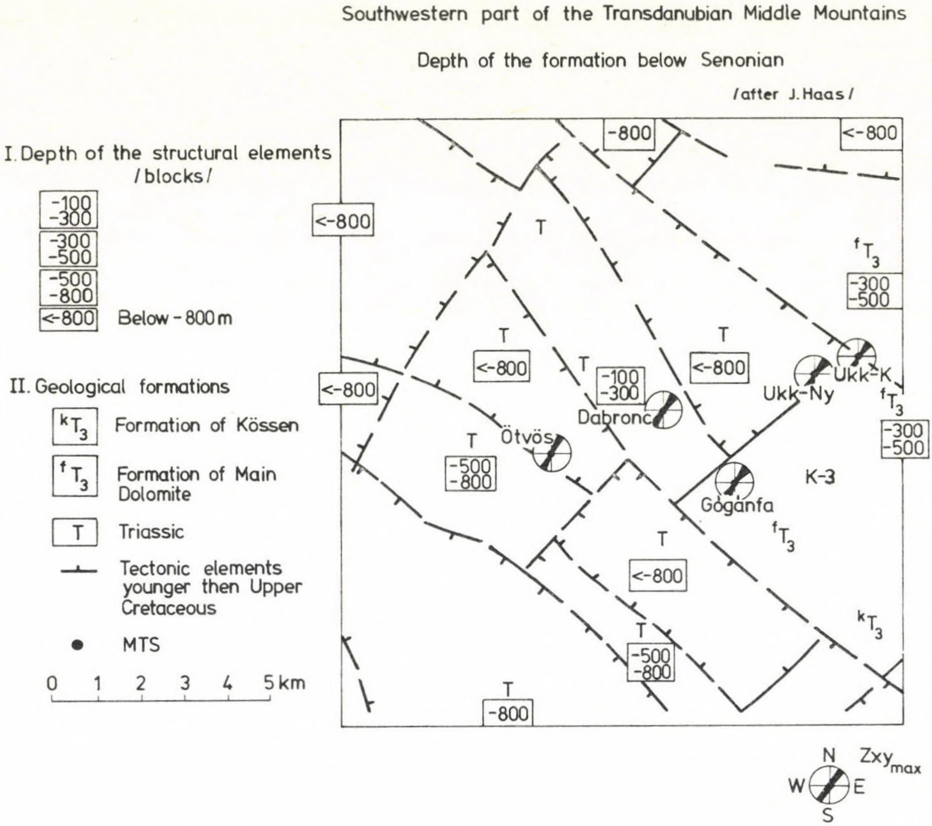

Fig. 6. $Z_{xy\,\max}$ impedance directions at the same area as in Fig. 5

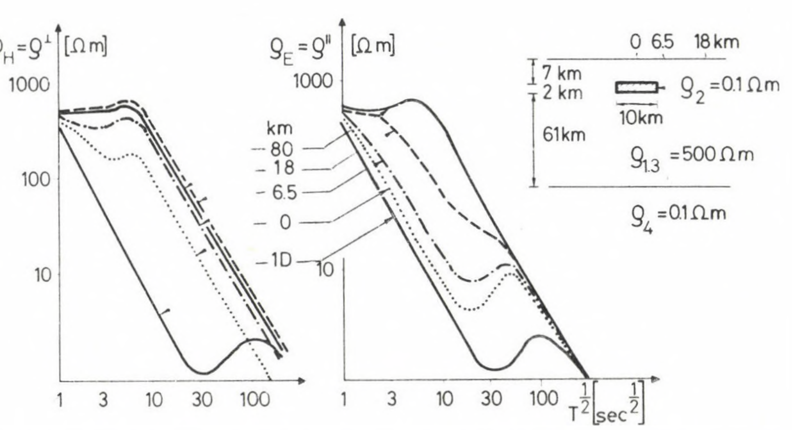

Fig. 7. MT sounding curves of a structure shown on the right upper edge calculated by finite difference method (FDM) (Tátrallyay 1977)

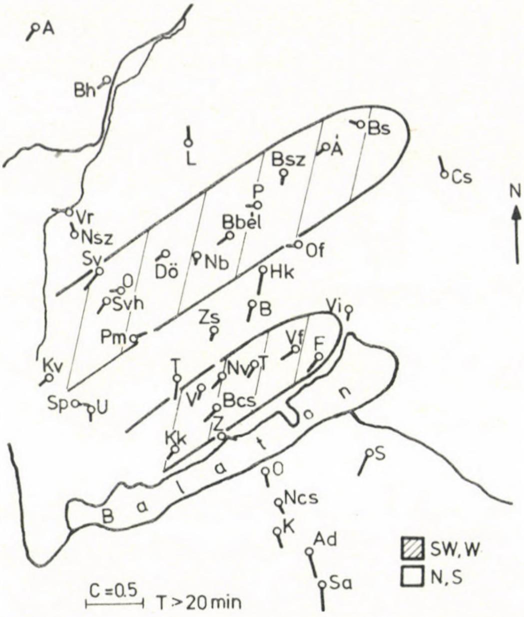

Fig. 8. Anomaly strips of the Wiese arrow map on the area of the Transdanubian crustal conductivity anomaly (Wallner 1977)

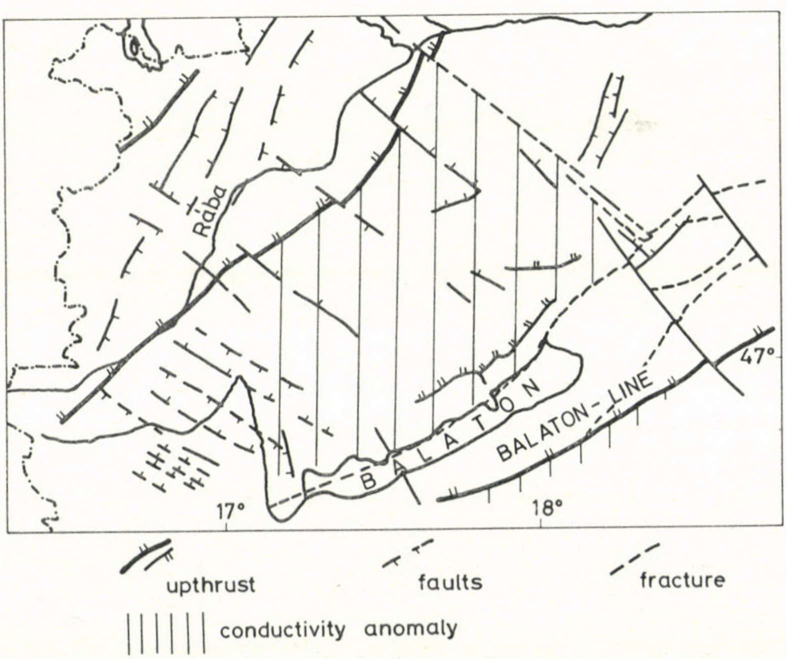

Fig. 9. Crustal conductivity anomaly zones north and south of the Lake Balaton

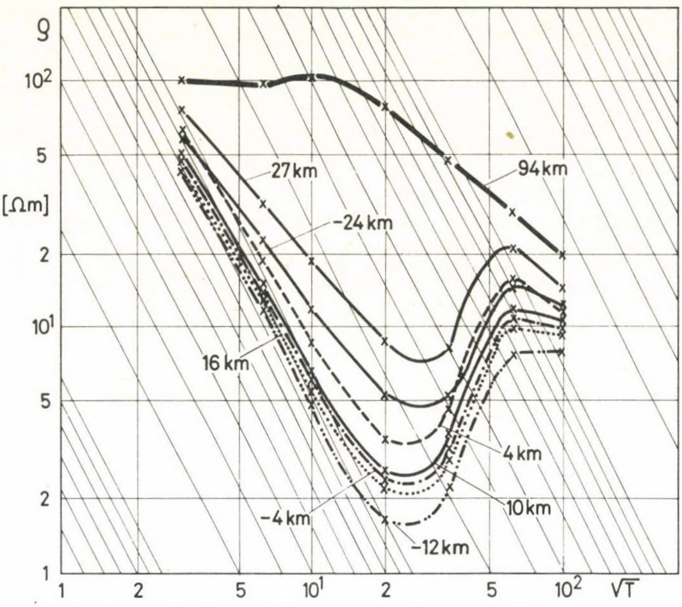
ϱ
[Ωm]
27 km
94 km
-24 km
16 km
4 km
-4 km
10 km
-12 km
√T

a,

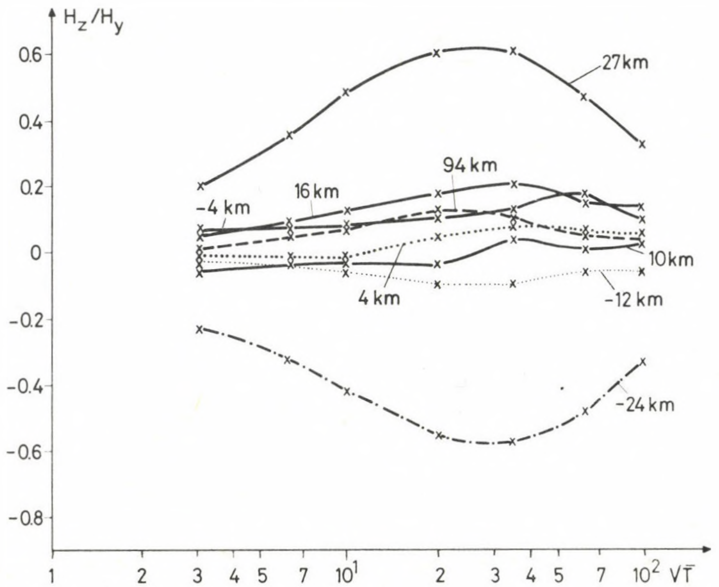
Hz/Hy
27km
94 km
16 km
-4 km
10 km
4 km
-12 km
-24 km
√T

b,

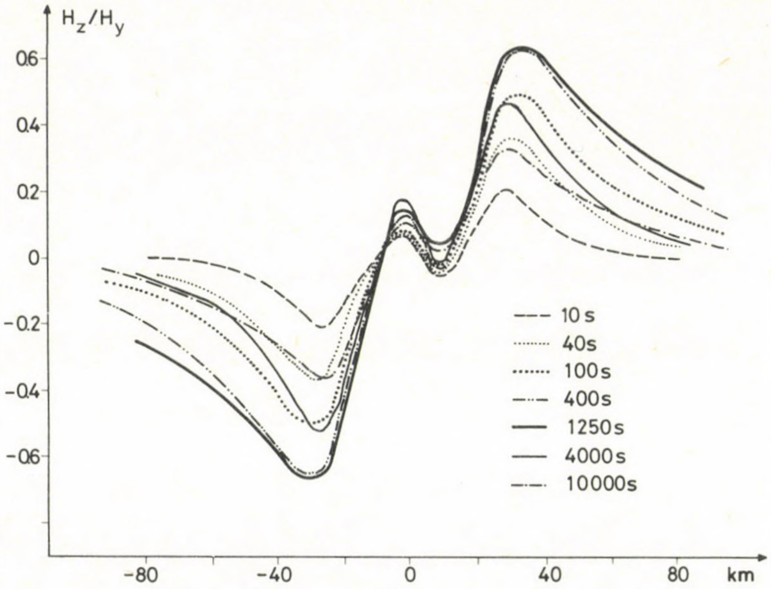

c)

Fig. 10. 2-D model curves of two conductive bodies calculated by FDM (Ádám 1980)
a) MT curves
b) geomagnetic sounding curves
c) H_z/H_r profiles

There is another characteristic feature of the crustal conductivity anomaly zone in the Pannonian Basin: They form quasi-parallel stripes as it can be seen on the Wiese-arrow map of the Transdanubian anomaly (Fig. 8) or on the map of the conductive zones north and south of Lake Balaton bordered by first order longitudinal tectonic lines (Fig. 9).

It is an interesting question how these anomaly stripes modulate each other's induction anomaly.

The 2-D numerical model which approximates these anomaly stripes was also calculated and its results can be seen in Fig. 10.

Analogue models of well conducting crustal anomalies

Two very simple 2-D models of the Transdanubian conductivity anomaly were built in the modeling tank using isotrope graphite bricks. The profiles of these 2-D structures are shown in Fig. 11 both in field and in model dimensions.

On base of the electromagnetic modeling laws the relations between the field periods and the model frequencies are as follows:

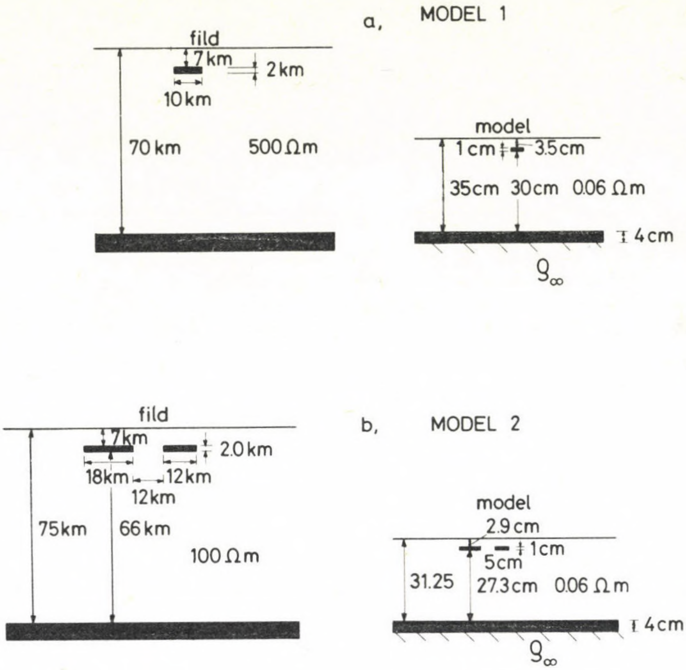

Fig. 11. Well conducting crustal anomalies in Hungary and their analogue models
a) Model 1
b) Model 2

$$T_f[\mathrm{s}] = \frac{4.8}{f_m[\mathrm{MHz}]} \quad \text{for model 1 and}$$

$$T_f[\mathrm{s}] = \frac{34.56}{f_m[\mathrm{MHz}]} \quad \text{for model 2.}$$

The actual model frequencies and field periods for models 1 and 2 are shown in Table I.

The model of the asthenosphere was built of graphite slabs on the bottom of the tank. (As it was mentioned earlier, calculations have shown that in the modeling frequency band a graphite layer of 0.04 m thickness can substitue a thick graphite basement.) The well conducting crustal structures were held in an elevated position by means of a construction toy.

Figure 12 shows the four transmitter-receiver arrangements used. Two of them are "*E*-polarization like" models and the other two represent the "*H*-polarization like" models.

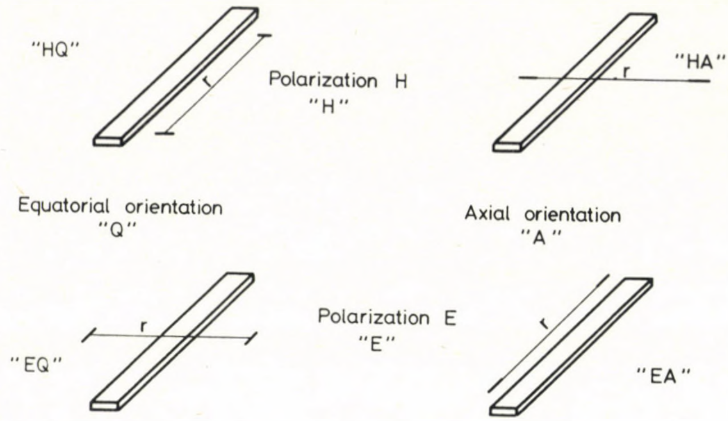

Fig. 12. Transmitter-receiver positions at analogue modeling of well conducting crustal anomalies

Table I. The actual model frequencies f_m and field periods T_f for models 1 and 2

		Model 1		Model 2	
	f_m [MHz]	T_f [sec]	$\sqrt{T_f}$ [$\sqrt{s}$]	T_f [sec]	$\sqrt{T_f}$ [$\sqrt{s}$]
1	3.00	1.60	1.26	11.52	3.39
2	2.40	2.00	1.41	14.40	3.79
3	2.00	2.40	1.55	17.28	4.16
4	1.60	3.00	1.73	21.60	4.65
5	1.40	3.43	1.85	24.69	4.97
6	1.20	4.00	2.00	28.80	5.37
7	1.10	4.36	2.09	31.42	5.61
8	1.00	4.8	2.19	34.56	5.88
9	0.90	5.33	2.31	38.40	6.20
10	0.80	6.00	2.45	43.20	6.57
11	0.70	6.86	2.62	49.37	7.03
12	0.60	8.00	2.83	57.60	7.59
13	0.50	9.60	3.10	69.12	8.31
14	0.40	12.00	3.46	86.40	9.30
15	0.30	16.00	4.00	115.20	10.73
16	0.24	20.00	4.47	144.00	12.00
17	0.20	24.00	4.90	172.80	13.15
18	0.16	30.00	5.48	216.00	14.70
19	0.13	36.92	6.08	265.85	16.30
20	0.10	48.00	6.93	345.60	18.59

Because of the given output power of the current generator, the ratio r/h_1 was only 2.86. In case of $r/h_1 = 2.86$ the ρ_{MT} and ρ_{FRS} sounding curves at dipole equatorial position differ from each other at least by 20%, so the phenomena were studied really qualitatively.

The model measurements were made along a profile which was perpendicular to the strike of the crustal structures using all of the four transmitter-receiver positions shown on Fig. 12.

The distances between measuring points were 2.0 cm (that means 4 km for model 1 and 4.8 km for model 2).

1-D comparison of MT curves and FRS measurements

Figure 13 shows MT and FRS sounding curves for 1-D approximations of Model 1. *AX* means an axial pattern, *EQ* means a dipole equatorial orientation.

Sounding curves above the infinitely extended crustal anomaly (1B) are the same when using the MT method or optional FRS orientations.

The structure without the embedded well conducting layer in the crust produces differing sounding curves as r/h_1 ($r/h_1 = 2.86$) is relatively small.

The measured sounding curves were normalized to theoretical ones.

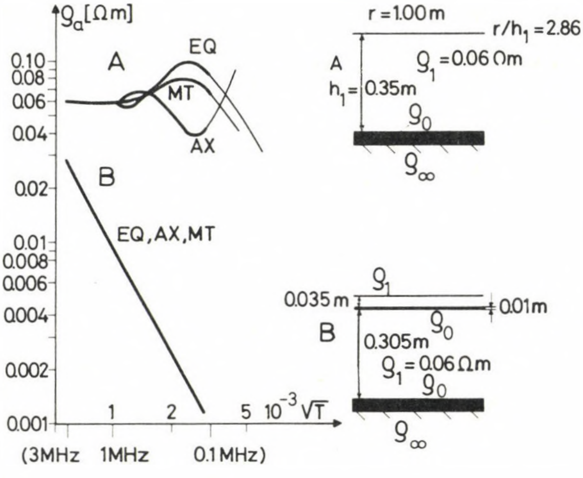

Fig. 13. FRS sounding curves using axial and equatorial orientations and the MT sounding curve above corresponding 1-D structures

a) $\rho(\sqrt{T})$ curves for models 1A and 1B

b) $\rho(\sqrt{T})$ curves for models 2A and 2B

Results of analogue model measurements

Figures 14 and 15 represent $\rho_{||}$ and $\rho_{\perp}$ FRS sounding curves obtained by analogue model experiments over Model 1. Numbers mean distances in kilometres from the epicentre of the conductive embedding.

Figure 7 shows the MT curves over the same structure obtained by Tátrallyay (1977) using the finite difference method.

A comparison of the calculated MT curves with the measured FRS ones indicates a qualitative similarity. Dipole equatorial curves generally have larger apparent resistivity values as the MT sounding curves, as the r/h_1 ratio is relatively small. They could better approximate the MT curves when r/h_1 increases.

In E-polarization the length of the transmitting dipole ($AB = 0.08$ m) itself caused a strong distortion of the electromagnetic field as it reaches earlier the conducting structure than the receiver dipole.

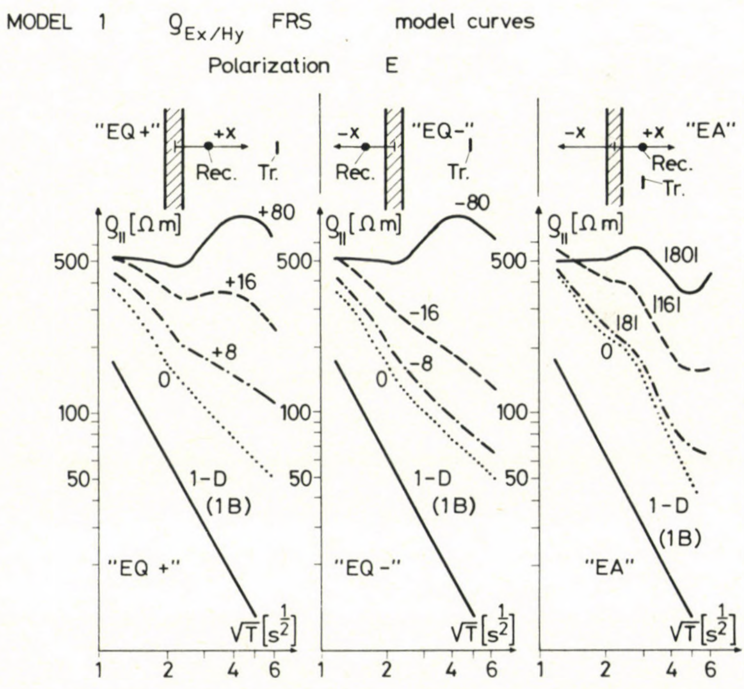

Fig. 14. FRS sounding curves of E-polarization obtained by analogue modeling for Model 1 (in field dimensions):

a) dipole-equatorial orientation, transmitter and receivers are on the same side of the embedding

b) dipole-equatorial orientation, transmitter and receivers are on opposite sides of the embedding

c) axial orientation

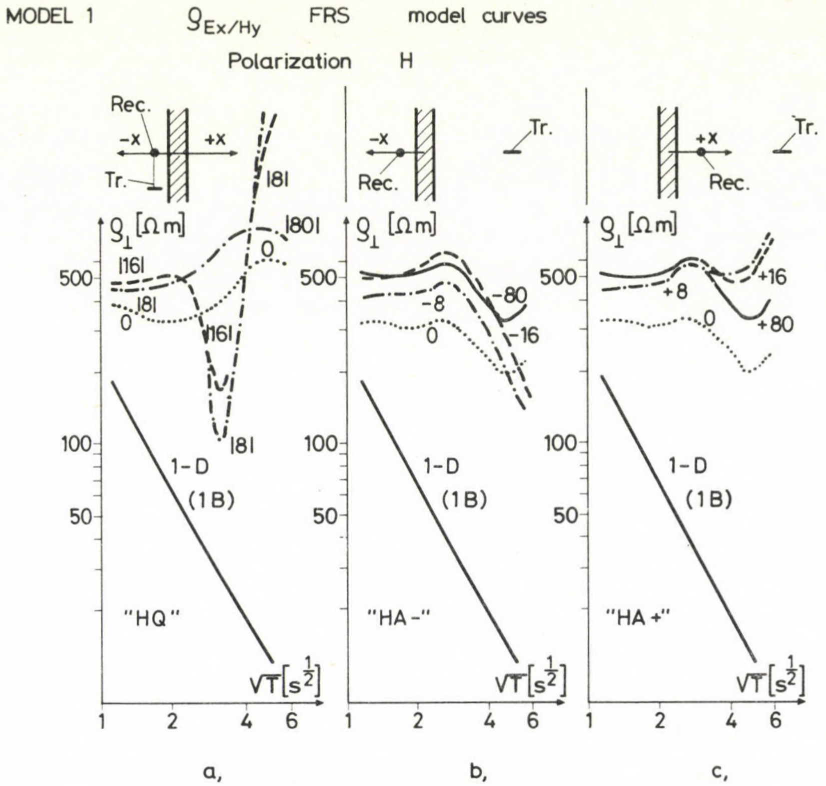

Fig. 15. FRS sounding curves of *H*-polarization obtained by analogue modeling for Model 1 (in field dimensions):

a) dipole-equatorial orientation

b) axial orientation, transmitter and receivers are on opposite sides of the embedding

c) axial orientation, transmitter and receiver are on the same side of the embedding

As for axial orientations the layered normal curves significantly differ from the dipole equatorial and MT ones, the series "HA+" and "HA−" have also unexpected distortions on the basis of MT interpretation.

Figure 16 represents FRS sounding curves in *E*-polarization over Model 2. Only the dipole equatorial orientation gave results somewhat similar to the MT sounding curves.

As it can be seen from this figure, on the basis of 1-D interpretation the region of these dykes would be interpreted as a conducting basement in different depths. This is a general conclusion as it was already drawn from the numerical models.

Figure 17 shows H_z/H_y profiles in *E*-polarization using both dipole equatorial and axial arrangements.

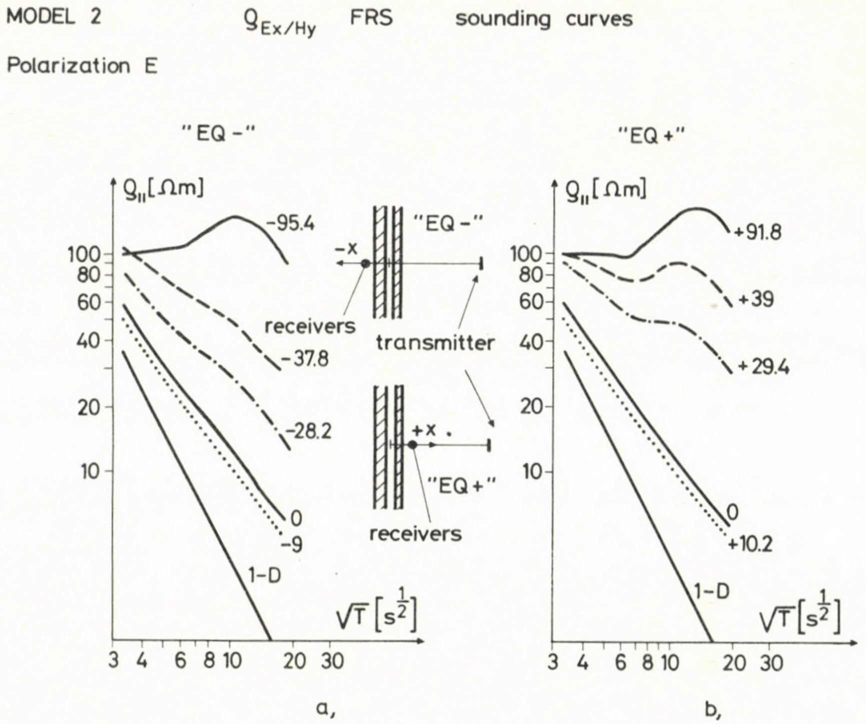

Fig. 16. FRS sounding curves of *E*-polarization obtained by analogue modeling for Model 2 (in field dimensions):

a) dipole-equatorial orientation, embedding is between the moving transmitter and the receivers

b) dipole-equatorial orientation, receivers are between the embedding and the transmitter

It is natural that over a horizontally layered half space in magnetotellurics there is no vertical magnetic component H_z. Using electric dipole sources, in dipole equatorial orientation (Fig. 17a) the component H_z does exist. That is the reason why the asymptotes of these profiles do not approximate zero.

Only the right side of Fig. 17a is similar to the MT profiles. With other words inhomogeneities between the receiver and the transmitter have a very strong effect on the measured H_z/H_y values.

In *E*-polarization using an axial arrangement there is no asymmetry and far off the inhomogeneities the ratios H_z/H_y disappear as in magnetotellurics. Both ends of the profiles run similarly to the MT ones: they have maxima at some ± 30 km and at greater distance they immerse into the noise level.

Measured values between the dykes differ strongly from the magnetotelluric ones and also have a strong period dependence resulting the highest maxima at 346 s.

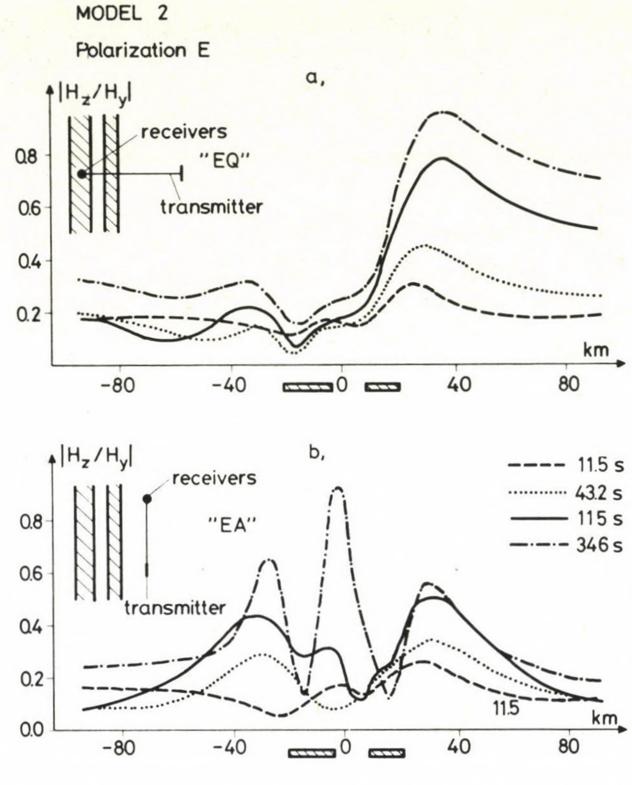

Fig. 17. H_z/H_y profiles of E-polarization obtained by analogue modeling for Model 2
a) dipole-equatorial orientation
b) axial orientation

Conclusions

As it is well known, a dipole-generated and a plane wave electromagnetic field over homogeneous half space agree only in the wave zone. This condition requires an infinite transmitter-receiver distance at low frequencies. It has been shown, in Fig. 3 in case of a well conducting basement that electric dipole-generated and plane-wave fields can also agree using finite transmitter-receiver distances (r) even at low frequencies. This principle can be applied in the physical modeling, too. r/h_1 value larger than 6 or 7 seems to be satisfactory to fulfil the above conditions. The realization of such a modeling meets only technical difficulties.

In case of a smaller value of r/h_1 a good qualitative similarity can be obtained especially in E-polarization and using the dipole equatorial orientation as it has been shown at the Transdanubian models. The characteristics of both E and H polarizations can be produced using different transmitter-receiver orientations.

After increasing the output power of the current generator for larger r/h_1, even closer agreements may be expected between FRS model measurements and MT numerical calculations, i.e. between results obtained by controlled source MT and MT methodes.

Acknowledgements

We thank to J Pongrácz, Gy Märcz and J Turi for supporting these experiments.

Appendix A

Field components at the surface of a stratified halfspace (Fig. 18):

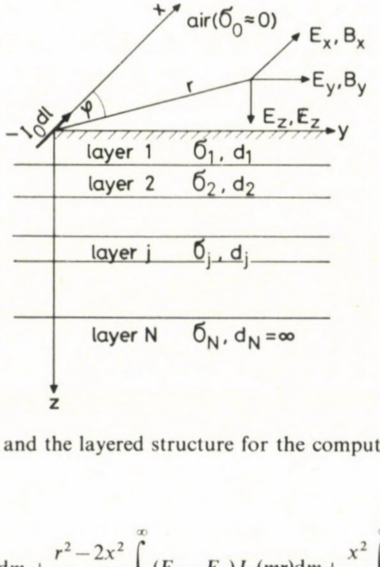

Fig. 18. Coordinate system and the layered structure for the computation of field components

$$E_x = c \cdot i\omega \left[\int_0^\infty F_1 J_0(mr) m \mathrm{d}m + \frac{r^2 - 2x^2}{r^3} \int_0^\infty (F_2 - F_1) J_1(mr) \mathrm{d}m + \frac{x^2}{r^2} \int_0^\infty (F_2 - F_1) J_0(mr) \mathrm{d}m \right]$$

$$E_y = c \cdot i\omega \left[-\frac{2xy}{r^3} \int_0^\infty (F_2 - F_1) J_1(mr) \mathrm{d}m + \frac{xy}{r^2} \int_0^\infty (F_2 - F_1) J_0(mr) \mathrm{d}m \right]$$

$$B_x = c \cdot \left[-\frac{2xy}{r^3} \int_0^\infty F_1 J_1(mr) m \mathrm{d}m + \frac{xy}{r^2} \int_0^\infty F_1 J_0(mr) m^2 \mathrm{d}m \right]$$

$$B_y = -c \cdot \left[\frac{x^2}{r^2} \int_0^\infty F_1 J_0(mr) m^2 \mathrm{d}m + \int_0^\infty F_3 J_0(mr) m n_1 \mathrm{d}m + \frac{r^2 - 2x^2}{r^3} \int_0^\infty F_1 J_1(mr) m \mathrm{d}m \right]$$

$$B_z = c \frac{y}{r} \int_0^\infty F_1 J_1(mr) m^2 \mathrm{d}m$$

where

$$c = \frac{I_0 \mathrm{d}l \mu}{2\pi}$$

$$k_1^2 = i\omega\mu\sigma_1$$

$$n_1 = \sqrt{k_1^2 + m^2}$$

$$F_1 = \frac{r_1}{m r_1 + n_1}$$

$$F_2 = \frac{n_1}{k_1^2 q_1}$$

$$F_3 = \frac{1}{m r_1 + n_1}$$

$$r_1 = r_1(\sigma_i, d_i, \omega)$$

$$q_1 = q_1(\sigma_i, d_i, \omega)$$

and

μ = is the magnetic permeability
ω = angular frequency
r = distance between the transmitter and the receiver
φ = angle between the axis x and the transmitter-receiver line
$x = r \cdot \cos\varphi$
$y = r \cdot \sin\varphi$
I_0 = amplitude of the current in the dipole
$\mathrm{d}l$ = length of the dipole
m = integration parameter (separation constant)
σ_i and d_i are the conductivity and the thickness of the layer i
J_0 and J_1 are Bessel functions of orders zero and one
F_1, F_2, F_3 are kernels of the integrals
r_1 and q_1 take into account the layered structure and can be calculated recursively.

Appendix B

Field components with modified kernels:

$$E_x = c \cdot i\omega \left\{ \int_0^\infty (F_1 - F_1^0) J_0(mr) \mathrm{d}m + \frac{r^2 - 2x^2}{r^3} \int_0^\infty \cdot \right.$$

$$\cdot (F_2 - F_2^0 - F_1 + F_1^0) J_1(mr) \mathrm{d}m + \frac{x^2}{r^2} \int_0^\infty (F_2 - F_2^0 - F_1 + F_1^0) J_0(mr) m \mathrm{d}m +$$

$$\left. + \frac{1}{k_1^2} \left[\frac{k_1}{2r^4} (2r^2 - 3x^2)(I_1 K_0 + I_0 K_1) - \frac{e^{-k_1 r}}{r^3} (1 + k_1 r) \right] \right\}$$

$$E_y=c\cdot i\omega\left\{-\frac{2xy}{r^3}\int_0^\infty (F_2-F_2^0-F_1+F_1^0)J_1(mr)\mathrm{d}m+\right.$$

$$\left.+\frac{xy}{r^2}\int_0^\infty (F_2-F_2^0-F_1+F_1^0)J_0(mr)m\mathrm{d}m-\frac{3}{2}\frac{1}{k_1}\frac{xy}{r^4}(I_1K_0+I_0K_1)\right\}$$

$$B_x=c\cdot\left\{-\frac{2xy}{r^3}\int_0^\infty (F_1-F_1^0)J_1(mr)m\mathrm{d}m+\right.$$

$$\left.+\frac{xy}{r^2}\int_0^\infty (F_1-F_1^0)J_0(mr)m^2\mathrm{d}m-\frac{xy}{r^4}\left[4I_1K_1-\frac{k_1r}{2}(I_0K_1-I_1K_0)\right]\right\}$$

$$B_y=-c\left\{\frac{x^2}{r^2}\int_0^\infty (F_1-F_1^0)J_0(mr)m^2\mathrm{d}m+\int_0^\infty (F_3-F_3^0)J_0(mr)mn_1\mathrm{d}m+\right.$$

$$+\frac{r^2-2x^2}{r^3}\int_0^\infty (F_1-F_1^0)J_1(mr)m\mathrm{d}m+\frac{1}{r^4}\left[(x^2-3y^2)I_1K_1+\right.$$

$$\left.\left.+\frac{k_1r}{2}y^2(I_0K_1-I_1K_0)\right]\right\}$$

$$B_z=c\cdot\left\{\frac{y}{r}\int_0^\infty (F_1-F_1^0)J_1(mr)m^2\mathrm{d}m+\right.$$

$$\left.+\frac{y^2}{k_1^2r^5}\left[\frac{3k_1r}{2}(I_1K_0+I_0K_1)-e^{-k_1r}(3+3k_1r+k_1^2r^2)\right]\right\}$$

where

$$F_1^0=F_3^0=\frac{1}{m+n_1}$$

$$F_2^0=\frac{n_1}{k_1^2}$$

and I_l, K_l are modified Bessel functions of the first and second kind and of the order l with the complex argument $\frac{k_1r}{2}$.

Appendix C

Apparent resistivities computed from the field components

$$\rho_a(E_x)=\frac{2\pi}{I\cdot\mathrm{d}l}\frac{r^5}{3x^2-2r^2}E_x$$

$$\rho_a(E_y)=\frac{2\pi}{I\cdot\mathrm{d}l}\frac{r^5}{3xy}E_y$$

$$\rho_a(H_x)=i\mu\cdot\omega\left(\frac{2\pi}{I\cdot dl}\frac{r^5}{3xy}H_x\right)^2$$

$$\rho_a(H_y)=i\mu\cdot\omega\left(\frac{2\pi}{I\cdot dl}\frac{r^5}{3x^2-r^2}H_y\right)^2$$

$$\rho_a(H_z)=i\mu\omega\frac{2\pi}{I\cdot dl}\frac{r^5}{3y}H_z$$

$$\rho_a(E_x/H_y)=\frac{1}{i\mu\omega}\left(\frac{E_x}{H_y}\right)^2$$

$$\rho_a(E_y/H_x)=\frac{1}{i\mu\omega}\left(\frac{E_y}{H_x}\right)^2$$

$$\rho_a(H_z/H_y)=i\mu\omega\left(\frac{3x^2-2r^2}{3y}\frac{H_z}{H_y}\right)^2$$

References

Ádám A 1980: The change of electrical structure between an orogenic and an ancient tectonic area (Carpathians and Russian Platforms). *J. Geomag. Geoelectr.*, 32, 1–46.

Ádám A 1981: Statistische Zusammenhänge zwischen Elektrischer Leitfähigkeitsverteilung und Bruchtektonik in Transdanubien (Westungarn). *Acta Geod. Geoph. Mont. Hung.*, 16, 97–113.

Ádám A, Pongrácz J, Szarka L, Kardeván P, Szabadváry L, Nagy Z, Zimányi I, Kormos I, Régeni P 1981: Analogue model for studying geoelectric methods in the Geodetic and Geophysical Research Institute of the Hungarian Academy of Sciences. *Acta Geod. Geoph. Mont. Hung.*, 16, 359–380.

Anderson W L 1979: Numerical integration of related Hankel transforms of orders 0 and 1 by adaptive digital filtering. *Geophysics*, 44, 1287–1305.

Goldstein M A, Strangway D W 1975: Audio-frequency magnetotellurics with a grounded electric dipole source. *Geophysics*, 40, 669–683.

Keller G V 1968: Electrical Prospecting for Oil. *Quarterly of the Colorado School of Mines*, 63, 1–261.

Koefoed O, Ghosh D P, Polman G J 1972: Computation of type curves for electromagnetic depth sounding with a horizontal transmitting coil by means of a digital linear filter. *Geophysical Prospecting*, 20, 406–420.

Scriba H 1974: A Numerical Method to Calculate the Electromagnetic Field of a Horizontal Current Dipole. *Pageoph*, 112, 801–809.

Szarka L 1983: Investigation of the high resistivity basement using quasi-static point sources. *Geophysical Prospecting*, 31, 829–839.

Tátrallyay M 1977: On the interpretation of EM sounding curves by numerical modelling using S.O.R. method. *Acta Geod. Geoph. Mont. Hung.*, 12, 279–285.

Varga M 1981: The calculation of the electromagnetic field about a horizontal electrical dipole for a stratified halfspace. (in Hungarian) Research report

Wallner Á 1977: The main features of the induction arrows on the area of the Transdanubian conductivity anomaly. *Acta Geod. Geoph. Mont. Hung.*, 12, 279–285.

Acta Geodaet., Geophys. et Montanist. Hung. Volume 18 (4), pp. 489—499 (1983)

MAGNETOTELLURIC RESULTS ALONG A 1200 KM LONG DEEP PROFILE WITH AN IMPORTANT GEOTHERMAL AREA AT ITS NORTH-WEST END IN THE PROVINCES OF TUCUMAN AND SANTIAGO DEL ESTERO IN ARGENTINA

B BALDIS[1], J DEMICHELI[2], J FEBRER[2], H FOURNIER[3], E GARCIA[4*], J C GASCO[2], M MAMANI[5], M C COMPOSIELLO[6]

[Manuscript received April 6, 1983]

A 1200 km long discontinuous MT profile from Buenos Aires to San Miguel de Tucuman, gives a great diversity of results concerning the structure of the crust, the lithosphere and the upper mantle. At the north-west end of the profile appears a new geodynamic process associated with the Nazca subduction plate, generating an important geothermal area of about 200 km diameter.

Keywords: Argentina; geothermal field; magnetotellurics; Nazca plate; plate collision

Area 1 results

Area 1 of Fig. 1 corresponds to the two soundings made in the region of Buenos Aires (Gasco et al. 1982), upon a cratonic region of approximately 2 billions years (Linares 1979). The site of Zarate has the coordinates lat = 34° 05′ south, long = 59° 10′ west at about 90 km W—NW from Buenos Aires. One of the telluric lines was parallel to the general trend of the regional tectonics (Nm 54° Wm), the other orthogonal. The dispersion of the values of ρ is very small according to the general behaviour of MT results. A unique trace is obtained for the two curves. Figure 2 gives this trace for which the interpretation is very simple: a sedimentary cover of 250 m, highly conducting, then, below a unique resistant layer until 400 km depth having a true resistivity of 10.000 Ωm

[1] Consejo Nacional de Investigaciones Cientificas y Tecnicas, Museo de Ciencias Naturales, Avda Angel Gallardo 470, Buenos Aires, Argentina

[2] Comision Nacional de Investigaciones Espaciales, Seccion Geofisica, Avda Mitre 3100, San Miguel, 1663, Argentina

[3] Laboratoire de Physique de l'École Normale Supérieure, 24 rue Lhomond, Paris (5) France

[4] Observatorio Nacional de Fisica Cosmica, Avda Mitre 3100, San Miguel, 1663, Argentina

[5] Insituto de Investigaciones Aplicadas de Ciencias Espaciales, Seccion Geotermia, cc 131, Mendoza, 5500, Argentina

[6] Consejo Nacional de Investigaciones Cientificas y Tecnicas, Centro Espacial de San Miguel, 1663 Argentina

* Deceased. Eduardo Garcia was tragically killed in a road accident on the 17th June 1977, whilst preparing the Chamical MT campaign

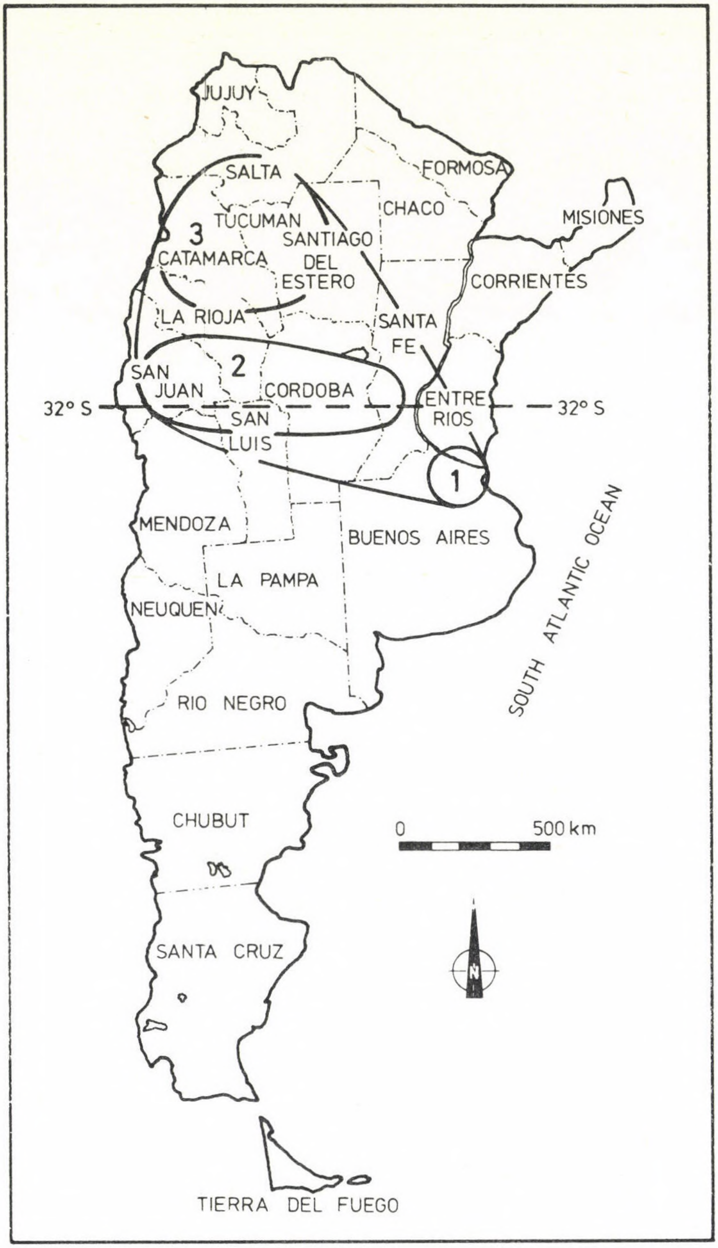

Fig. 1. General map of Argentina delimiting the three regions studied by the MT method in a period of six years (1976–1981).

Area 1: cratonic region. First 400 km of the upper mantle very resistant,

Area 2: Primary and Tertiary perturbed region. Plunging of the Nazca plate below the western part of the continent,

Area 3: region tectonically very complex in the western part. Discovery of an important geothermal field in the eastern part

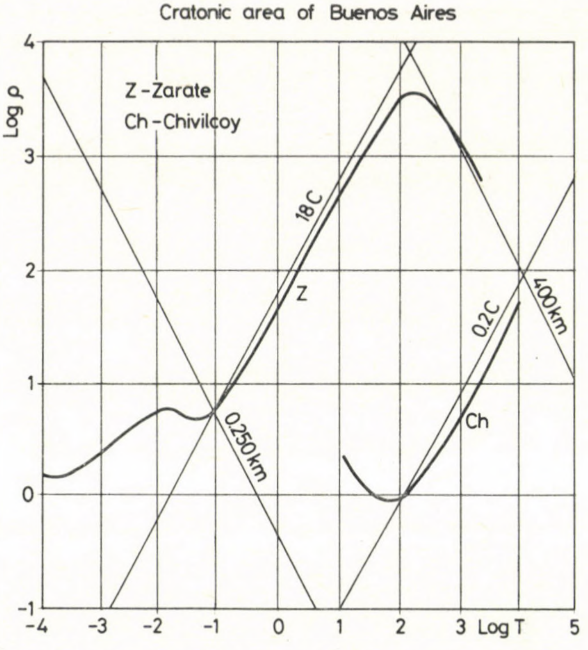

Fig. 2. Preliminary remark: in Fournier (1963) we can see that the following unit is proposed:

$$1 \text{ cagniard} = \frac{1 \text{ mV/km}}{1 \text{ nT}} = 0.001\,256\,6\ldots \text{ ohm} = 1 \text{ C}$$

$$1 \text{ ohm} = 795.774\,88 \ldots \text{ C} \qquad \text{Cagniard (1953)}$$

Z: MT sounding curve for Zarate
Ch: MT sounding curve for Chivilcoy
Cross-section given by the Zarate MT sounding interpretation:

Thickness	Resistivity
0.001 km	10 ohm · m
0.008	1.5
0.140	10
0.100	3.3
400	$\geqq 10\,000$
∞	$\leqq 9$

The thickness of the sedimentary basin — 250 m — was determined by electrical Schlumberger soundings from which the cross section obtained was transformed in an equivalent MT cross section using the method proposed by Benderitter et al. (1978). We think that it is this thin but highly conducting horizontal sedimentary layer covering the craton that is the cause of our high quality results: one unique trace for the two orthogonal sounding directions, with a very small dispersion for the individual values of ρ. This is completely on the contrary to the suggestion in Fournier et al. (1963) to operate MT soundings on crystalline massifs.

The corresponding cross section for Chivilcoy is:

Thickness	Resistivity
3 km	0.7 ohm · m
$\geqq 400$	$\geqq 500$

The screening effect of this sedimentary basin below Chivilcoy, highly conducting, 0.2 C, does not allow us to confirm that there is no intermediate conducting layer in this section of the upper mantle.

One may recall that the MT screening effect of a conducting layer was proposed at the Berkeley University by Fournier et al. (1963) and studied by Fournier (1968) or more, underlain by what we name the ultimate conducting layer — ultimate concerns results obtained by the MT method only (Fournier 1962). An important remark must be given here. If an intermediate conducting layer exists in the lower crust or in the beginning of the upper mantle it must be very negligeable according to the position of the curve on the left on the graph and the straightness of its ascending branch characterised by an asymptotic impedance value of E/H of 18 C (cagniards) in the tetralogarithmic abacus (Fournier 1963, 1965, Fournier et al. 1963). This is not in favour for the presence of a conducting asthenosphere, except if we accept the development given by Shankland and O'Connel (1979), concerning the percentage of melting fraction in the upper mantle. The interpretation of the MT sounding curve of Chivilcoy (lat = 34° 56′ south, long = 60° 06′ west) is not in contradiction with the depth of the ultimate conducting layer found below Zarate.

Area 2 results

Area 2 of Fig. 1 comprises the MT deep soundings of Pilar, Chamical and San Juan along the 32nd south parallel approximately. The coordinates are given in the key of Fig. 3 that presents the curves obtained for the telluric line parallel to the main trend of each local tectonics. The results of the interpretation of these three curves is shown in Fig. 4: top hachures indicate the intermediate conducting layers; two at Pilar and only one at Chamical and San Juan; bottom, the earthquake foci corresponding to the same section, taken from Barazangi and Isacks (1976) and the intermediate conducting layers (hachures) obtained by the MT soundings. We see a good agreement between the results given by the two independent methods, if we accept the fact that the plunging plate is rigid and that it is breaking when it plunges whereby the earthquakes are generated. We conclude that we see by the MT method the Nazca plate diving the depth below the western part of Argentina, above the asthenosphere at San Juan and Chamical and after having cut in, between two slices of it below Pilar, between 120 and 220 km at 750 km east of the Chilean trench. Additionally we see in Fig. 3 the ultimate conducting layer at about 1000 km depth below Chamical and San Juan. This is not yet confirmed by a systematic field study. The ultimate conducting layer does not appear at the site Pilar because the screening effect of the second intermediate conducting layer is too strong near the diurnal band of periods.

Area 3 results

Febrer (1981) has given a description of the results in a preliminary report. Area 3 of Fig. 1 shows the region where 11 deep MT soundings were made in an area of 300 km diameter. The interpretation of 6 of them is at our disposal. The corresponding MT curves to be interpreted are presented in the top of Fig. 5. The interesting fact is the

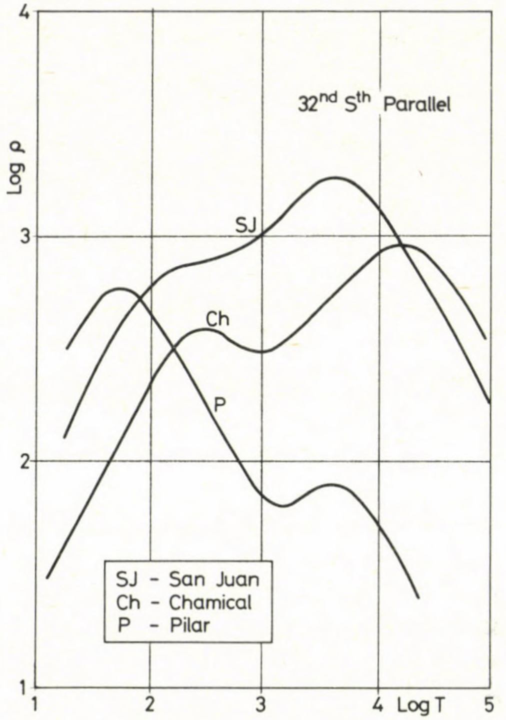

Fig. 3.

MT Curve	Lat. south	Long. west
SJ = San Juan	31° 33′	68° 34′
Ch = Chamical	30° 27′	66° 19′
P = Pilar	31° 40′	65° 53′

Cross-sections given by the three MT sounding interpretations

San Juan		Chamical		Pilar	
unpublished		Febrer Baldis Fournier (1980)		Febrer Demicheli Garcia Fournier (1977)	
Thickness	Resistivity	Thickness	Resistivity	Thickness	Resistivity
0.3 km	3 ohm · m	0.625 km	3 ohm · m	0.75 km	10 ohm · m
170	3000	210	2000	80	3000
110	500	100	1500	30	10
960	4000	950	4000	100	4000
∞	30	∞	60	∞	1

For the first intermediate conducting layer we have:

$h/\rho = 220\ \mathrm{ohm}^{-1}$ $\qquad$ $660\ \mathrm{ohm}^{-1}$ $\qquad$ $3000\ \mathrm{ohm}^{-1}$

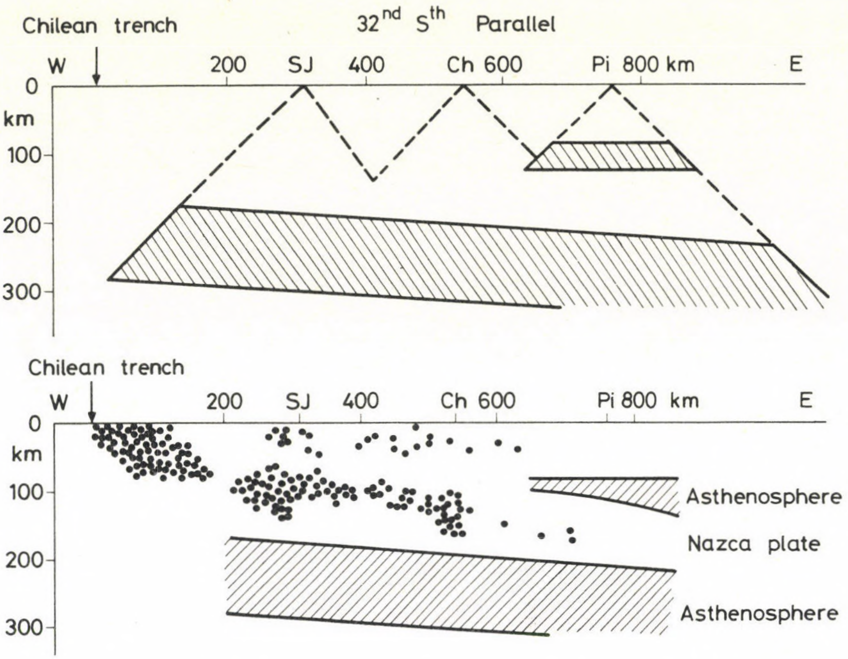

Fig. 4. Top: cross section along the 32nd south parallel from the Chilean trench until Pilar at about 800 km in the centre of Argentina. This section shows the MT sounding results: below San Juan and Chamical, there is one intermediate conducting layer in the range of 200 km depth; below Pilar, on the contrary we see two layers (hachures). Bottom: same cross section with our interpretation of the precendent MT results: the Nazca plate is diving with a dip angle at about 30° over the asthenosphere until 300 km of the Chilean trench and then after having cut in that asthenosphere, gliding between two slices of it below Pilar. The asthenosphere is represented by hachures and the black points represent earthquake foci. The resisting layer containing the descending earthquake foci is interpreted as the Nazca plate

existence of one highly conducting layer situated in the upper crust making a kind of dome. The surface of the dome has in average a dip angle of about 8 to 10% for its external descending zone. The lower part of Fig. 5 represents a cross-section of this dome in NS direction. The map in Fig. 6 indicates the position of the soundings, the general trend of the isodepths of the top of this first intermediate conducting layer forming the dome and the position of a silent triangle — this means a triangle nearly without earthquakes — after Barazangi and Isacks (1976) and after Castanon (1980). At the east of the triangle, the focus of the earthquakes are situated in the range of 500 to 600 km depth.

In more details we can say that below Taco Ralo, the summit of the dome, we find a sedimentary basin, very conducting, 3 km thick followed by a more resistant layer of 4 km, then a highly conducting layer, down to 0.3 ohmm, between 7 and 12 km, then a last layer, more resistant of 8 ohmm or more. Simply, this very conducting layer

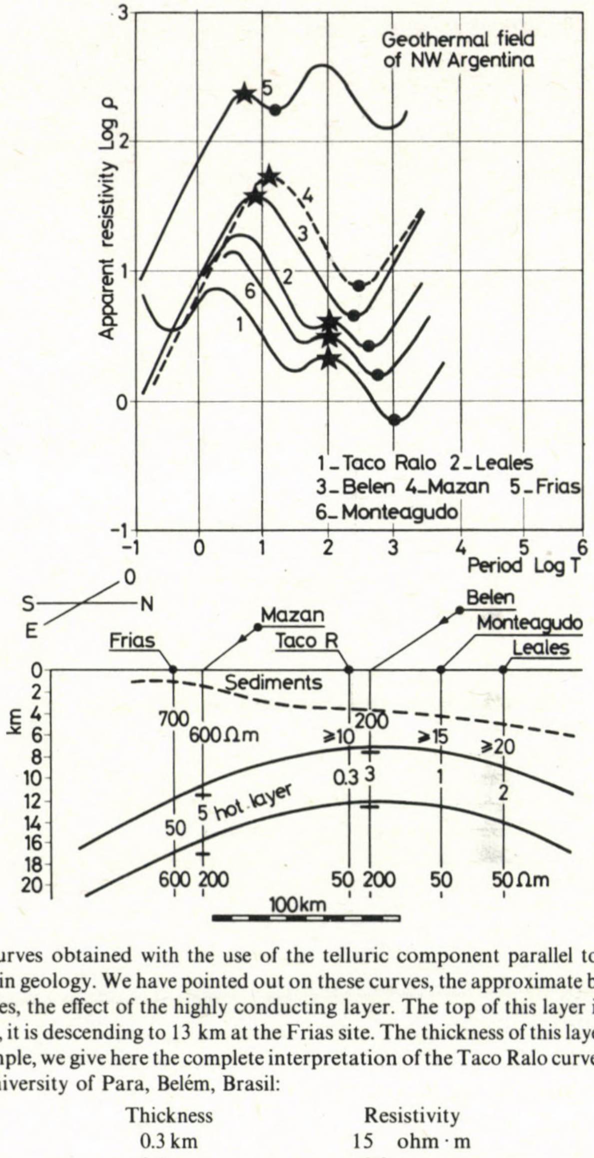

Fig. 5. Top: 6 MT curves obtained with the use of the telluric component parallel to the local tectonic direction well known in geology. We have pointed out on these curves, the approximate beginning with stars and ending with circles, the effect of the highly conducting layer. The top of this layer is at the Taco Ralo station at 7 km depth, it is descending to 13 km at the Frias site. The thickness of this layer has an average of about 6 km. For example, we give here the complete interpretation of the Taco Ralo curve made by Teotonio Ferreira from the University of Para, Belém, Brasil:

Thickness	Resistivity
0.3 km	15 ohm · m
0.1	0.8
1.2	≧ 50
1.7	0.8
3.5	10
4.8	0.3*
∞	50

* layer supposed to be partially molten basalt at a temperature of about 900 to 1000 °C.

Bottom: Cross section along the NS direction passing by Leales, Monteagudo, Taco Ralo and Frias stations. We see the general trend of the section of the dome delimited by the top of this very conducting layer having a dip angle of approximately 8 to 10%. It is impossible to give true values of the resistivity of the underlying layer because the strong screening effect generated by this conducting layer does not permit it

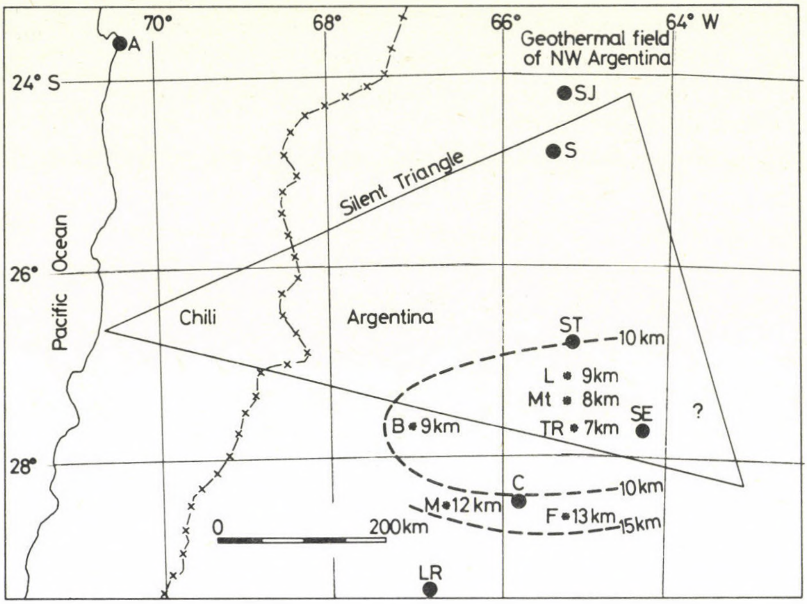

Fig. 6. Map of a part of NW Argentina, with a scale of 1/2.500 000 on the original sheet. The true scale is given with a length of 200 km in the bottom of the figure. This map shows the 6 MT sounding stations: TR: Taco Ralo; L: Leales; B: Belen; M: Mazan; F: Frias; Mt: Monteagudo and also gives the position of the main regional towns: SJ: San Salvador de Jujuy; S: Salta; ST: San Miguel de Tucuman; SE: Santiago del Estero; C: San Teodoro del Valle de Catamarca; LR: La Rioja; A: Antofagasta.

The map indicates the provisionary isodepths of the top of the very conducting layer situated in the upper crust and the silent triangle, after Barazangi and Isacks (1976) and Castanon (1980). We can easily see the importance of this newly found geothermal field and its position according to the silent triangle. It seems probable that the diameter of the workable surface is approximately 100 km. A similar silent triangle exists in Peru

situated in the upper crust plunges further around Taco Ralo until a depth of about 15 km for its top in an area of 250 km diameter. The results given by the review of Haak (1980) permit us to suggest that this highly conducting layer situated in the upper crust is composed of partially molten basalt having a temperature of about 900 to 1000 °C in the central zone of the dome at least. Below this very conducting and supposedly very hot layer our actual results do not permit us to know if the other layers are also at a very high temperature because of the strong screaning effect of the conducting layer and the fact that our range of period used to do the soundings is too short at high temperatures. This high temperature is however possible according to the results proposed in the review of Haak (1980).

The value of the gradient of the temperature given by the water wells is generally 100° per km. The deepest well is 800 m and gives artesian water at 80 °C. Many hot springs are known in this region and thermal stations are built in particular at the Taco Ralo site in which we are invited to make the sounding.

Consequently to the facts described, i.e. the layer at 0.3 ohmm in the upper crust, the strong temperature gradient — three times the normal value — plus in the region of Belen mineral deposits corresponding to this general phenomenon — after a United Nations report for Argentina (1973) — we think that there is around Taco Ralo — 200 km in diameter — a very important geothermal field. We think also that this geothermal field must be very workable because this region seems to be a quiet Tertiary continental sedimentary basin forming a plane of 100 km diameter at least.

One remark must be given here: for this region we have not yet obtained sufficient results concerning the existence of a second intermediate conducting layer situated in the asthenospheric range of depth. Only at the Frias site, at the southern border of the zone, outwards of the silent triangle, where the screening effect of the first conducting layer is not too strong because there is not a first screening effect of sedimentary conducting layer, we found a conducting layer beginning in the range of 60 km.

Conclusion

We have illustrated above the existence of three kinds of very different structures in the upper part of the earth, below Argentina.

The region of Buenos Aires is over an upper mantle layer of 400 km thick having a true resistivity of 10.000 ohmm or more. We have found no previous reference for such a high value of true resistivity for the whole unique resistant layer of the upper mantle.

Along the 32nd south parallel, approximately, we have shown the Nazca plate, to be resistant, descending with a dip angle of about 30° from west to east over and after having cut in, between two slices of the conducting asthenosphere. We may think that it is the first time that we have a so complete identity between the results given by the seismology and the magnetotelluric methods in the case of a plunging oceanic plate below a continent.

In the province of Tucuman, in the NW of Argentina, we have briefly described what we shall name an apparent upwelling of the hot zone of the topmost part of the upper mantle, at least, it seems, for the studied stations situated over the southern part of the silent triangle. Possibly it is the continental prolongation of the W—E hot line (or zone) Eastern Islands, . . . San Ambrosio Island near the coast of Chile, proposed by Bonatti et al. (1977). This continental region has been structurally studied by Baldis and Vaca (1979). The interesting fact in the conjunction of the descending Nazca plate and the trace of this hot line seems to be the regional destruction of a part of the plate yielding the seismological silent zone and a very high geothermic gradient in the cover, making this an important geothermal workable field. It resembles to what, at our knowledge we see for the first time, and what we may name a "continental hot spot" (Barszcus 1982).

We have no idea what are the contacts or separation zones between these three areas with different deep structures. This will be a subject for the next MT campaigns. We shall try to see how it changes in the northern half of Argentina between one extreme structure to the other. See also Fig. 7 that groups the most representative MT curves of each of the three areas.

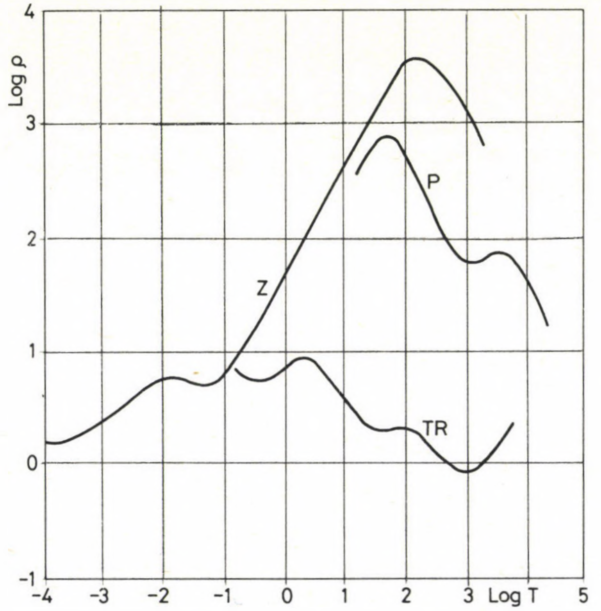

Fig. 7. Groups the most attractive MT curves of each of the three areas studied:

Area 1. Z: Zarate	province of Buenos Aires
Area 2. P: Pilar	province of Cordoba
Area 3. TR: Taco Ralo	province of Tucuman

Using the MT imbricated tetralogarithmic abacus of Fournier (1962, 1963, 1965) we may see easily the surprising fact that for the period of 1000 s the MT soundings of Zarate, Pilar, Taco Ralo give respectively a depth of about 450, 80 and 11 km. This is regular because there is 3.2 decades difference between the extreme values of $\log \rho$, that means consequently 1.6 decade difference between the corresponding values of $\log h - x$ 40 approximately — according to the system of two non linear equations with four parameters of the theory. This is one of the interesting properties of the MT method of Louis Cagniard (1953).

All the MT soundings curve described in this note were obtained by the use of different kinds of magnetic variometers — mumetal core coiled barres — and a Canadian fluxgate three-components magnetometer. All these apparatus were described by Febrer et al. (1977), Febrer et al. (1980), and Gasco (1980)

Acknowledgements

We are indebted to the "Secretaria de Estado de Energia" that has supported this research, associated with the "Comision Nacional de Investigaciones Espaciales" that gave us the logistic support coming from the "Centro Espacial de San Miguel" near Buenos Aires.

We thank the Professor of Geophysics Hugo Posse from the University of Tucuman for his help in the field in the province of Tucuman.

Thanks to Carl Heron from the University of Bradford for his English correction.

References

Baldis B, Vaca A 1979: El sistema preandino de Sudamerica central como zona antitetica de respuesta a la deriva continental. VIII Congreso de Geologia Argentina

Barazangi M, Isacks B 1976: Spatial distribution of earthquakes and subduction of the Nazca plate beneath South America. *Geology*, 4, 686–692.

Barszcus H 1982: Personal communication. Paris

Benderitter Y, Dupis A, Febrer J, Fournier H 1978: Comparaison de mesures de résistivité obtenues par les méthodes de sondages électrique et magnétotellurique en des sites communs situés sur terrain sédimentaire et sur des massifs de granite. Mémoire du B.R.G.M., no 91, Paris

Bonatti E, Harrison C G A, Fischer D E, Honnorez J, Schilling J-G, Stipp J J, Zentilli M 1977: Easter Volcanic chain (Southeast Pacific): A mantle hot line. Jl. *Geophys. Res.*, 82, 2457–2478.

Cagniard L 1953: Basic theory of magnetotelluric method of geophysical prospecting. *Geophysics*, 18, 605–635.

Castanon W 1980: Personal communication. San Juan

Febrer J 1981: La anomalia geotermica del area central del Noroeste Argentino. Abril. Departamento de Geofisica, Grupo Tecnico Cientifico. Centro Espacial, San Miguel. 1663, Argentina

Febrer J, Demicheli J, Garcia E, Fournier H 1977: Magnetotelluric sounding in Pilar, Cordoba, Argentina. *Acta Geod. Geoph. Mont. Hung.*, 12, 29–31.

Febrer J, Baldis B, Fournier H 1980: Sondaje magnetotelurico profundo en Chamical, La Rioja. *Geoacta*, 10.

Fournier H 1962: Position relative des courbes d'investigation magnétotellurique, essentiellement directionnelles, obtenues à la Station Géophysique du Nivernais à Garchy. Bul d'Inf. de l'A.I.Ms. No 10, Mons, Belgique

Fournier H 1963: Concernant l'intervalle de variation du rapport E/H dans l'investigation expérimentale magnéto-tellurique. Garchy-Suilly la Tour, Nièvre. D.L. 9385-63; (4° S.6677) Bibliothèque Nationale, Paris

Fournier H 1965: Abaque des solutions du système $\rho = 0.2\,T\,(E/H)^2$; $h = \sqrt{10 \cdot \rho \cdot T}/8$ (établies en suivant la méthode L. Cagniard). Institut de Physique du Globe de Paris, note No 9. Dépôt Légal Bibliothèque Nationale ler Trim. 9. 2. 1965; 01967bus

Fournier H 1968: Proposition d'une méthode pour déterminer la structure du premier millier de kilomètres de la Terre d'après la résistivité apparente. *Acta Geophysica Polonica*, 16, 215–248.

Fournier H, Ward S H, Morrison H F 1963: Magneto-telluric evidence for the low velocity layer. Tech. Rep. on Contract Nonr 222 (89), Series No 4, Issue No 76. Space Sciences Laboratory, Univ. of Califor., Berkeley

Gasco J C 1980: Deteccion de senales magnetotelluricas en la banda de 0.1 a 10 Hz. Tesis de licenciatura en Ciencias Fisicas; Faculted de Ciencias Exactas y Naturales; Universidad de Buenos Aires

Gasco J C, Febrer J, Demicheli J, Fournier H 1982: Zarate MT sounding and upper mantle resistivity. *Acta Geod. Geoph. Mont. Hung.*, 17, 307–309.

Haak V 1980: Relations between electrical conductivity and petrological parameters of the crust and upper mantle. *Geophysical surveys*, No 4, 57–69.

Linares E 1979: Personal communication. Buenos Aires.

Shankland T J, O'Connell R J 1979: Electrical and elastic anomalies in the upper mantle. XVII General Assembly of I.U.G.G., Canberra

United Nations 1973: Exploracion minera de la region noroeste, Argentina. Nueva York. DP/SF/UN/101 — Technical report

Acta Geodaet., Geophys. et Montanist. Hung. Volume 18 (4), pp. 501—511 (1983)

DETERMINATION OF COEFFICIENTS FOR THE COMPUTATION OF DERIVATIVES OF POTENTIAL FIELDS WITH RESPECT TO *X*, *Y* AND *Z*

K Kis[1]

[Manuscript received April 6, 1983]

The present paper includes the derivation of several sets of coefficients which can be used in the approximation of the derivatives of potential fields with respect to x, y and z. The coefficients form two-dimensional weight functions of digital filters and they are to be convolved with the input data. Due to this approach the sets of coefficients can be derived from the truncated transfer functions of the corresponding operations. The truncation removes the undesirable high amplification of the high frequency components of the input. The paper gives several sets of coefficients (Tables I–III) obtained by truncation with a Gaussian low-pass filter. The application of the coefficients are illustrated by models as well as by the derivatives of measured Bouguer anomaly data.

Keywords: computation of 2-D derivatives; derivatives of potential fields; gravity field derivatives; two dimensional weight function

Introduction

In due course of various computations with potential fields the determination of derivatives with respect to the x, y or z coordinates are often required. The derivatives are to be computed from digital data, representing the gravity or magnetic fields at discrete points. E.g. the reduction to the (north) magnetic pole requires the direction of the magnetic polarization and it can be estimated by Poisson's equation (Ross and Lavin 1966, Chandler et al. 1981). The estimation, in turn, requires the determination of various derivatives of the Bouguer anomaly field over the same area.

The determination of the sets of coefficients for the computation of various derivatives

The purpose of the derivation is the determination of two-dimensional sets of coefficients which, when convolved with the input data, give good approximations to certain derivatives of the input. In accordance with general usage in geophysics the coordinate axes x and y are directed towards North and East, respectively, while the z axis points downwards.

[1] Department of Geophysics Eötvös Loránd University H-1083 Budapest, Kun Béla tér 2, Hungary

The theoretical transfer functions have long been known (e.g. Erdélyi et al. 1954) and they read

$$S_{dx}(f_x, f_y) = j2\pi f_x, \tag{1}$$

$$S_{dy}(f_x, f_y) = j2\pi f_y, \tag{2}$$

$$S_{dz}(f_x, f_y) = 2\pi(f_x^2 + f_y^2)^{1/2}, \tag{3}$$

where f_x and f_y denote spatial frequencies, measured along the x and y axes, respectively. We may introduce dimensionless spatial frequencies by the definitions

$$f'_x = f_x \tau \quad \text{and} \quad f'_y = f_y \tau, \tag{4}$$

where τ denotes the grid spacing.

The imaginary part of the transfer function (1) is shown on the left of Fig. 1. The imaginary part of the transfer function (2) can be seen on the upper part of Fig. 2, and the real part of the transfer function (3) is presented on the left of Fig. 3. All three theoretical transfer functions are depicted as functions of the dimensionless frequency variables f'_x and f'_y.

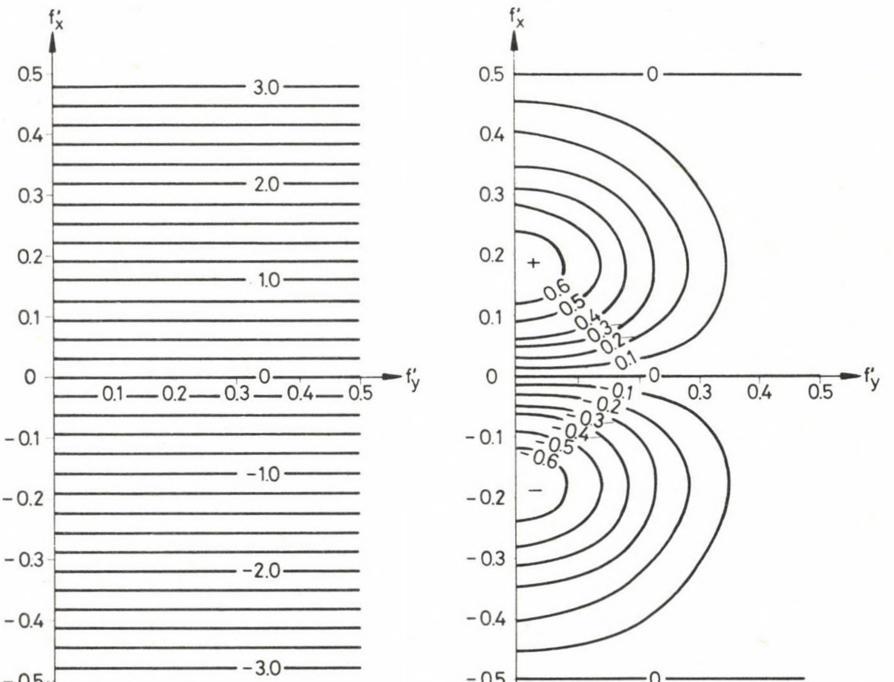

Fig. 1. The imaginary parts of the theoretical and actual transfer functions of the computation of the derivatives with respect to x (left and right). The independent variables are the dimensionless frequencies f'_x and f'_y

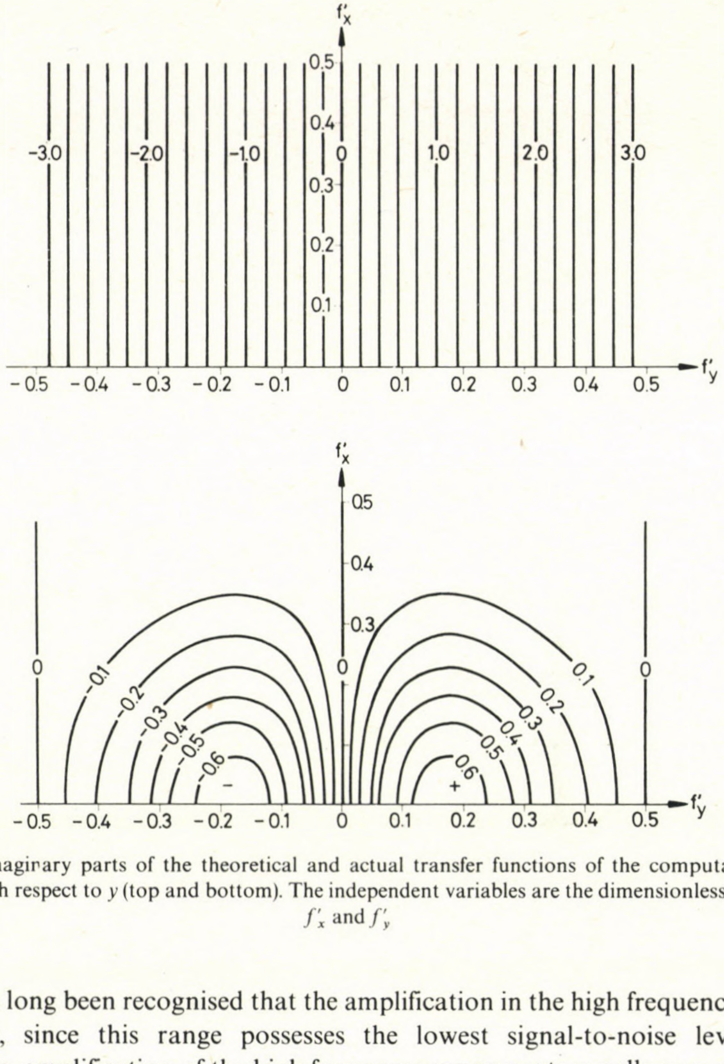

Fig. 2. The imaginary parts of the theoretical and actual transfer functions of the computation of the derivatives with respect to y (top and bottom). The independent variables are the dimensionless frequencies f'_x and f'_y

It has long been recognised that the amplification in the high frequency range is undesirable, since this range possesses the lowest signal-to-noise level. As a consequence, amplification of the high frequency components usually corresponds to the amplification of the high frequency noise. In order to remove this undesirable property the theoretical transfer function is multiplied with a two-dimensional window. In the present paper we use the window function

$$S_{LP}(f_x, f_y) = e^{-\left(\frac{36}{m}\right)^2 (f_x^2 + f_y^2)}. \tag{5}$$

The windowing corresponds to low-pass filtering of the input (Meskó 1967). The parameter m in Eq. (5) is used to modify the cut-off frequency of the filter. If m is small, e.g. $m=2$, the pass-band becomes narrow, while for greater m's, $m=8$ or $m=9$, the pass-band becomes wider. The advantages and practical aspects of the application

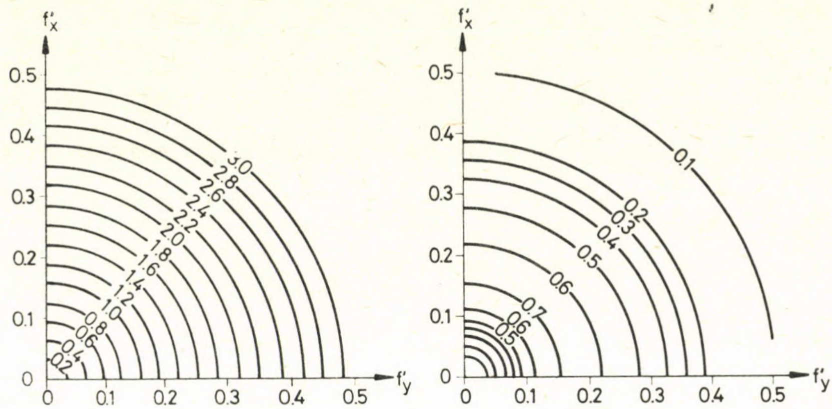

Fig. 3. The theoretical and actual transfer functions of the computation of the derivatives with respect to z (left and right). The independent variables are the dimensionless frequencies f'_x and f'_y

of this particular type of low-pass filter with transfer function (5) is discussed in details by Meskó (1983).

Let us denote any of the theoretical transfer functions (1)–(3) by $S(f_x, f_y)$. Then the transfer function after truncation reads

$$S_T(f_x, f_y) = S(f_x, f_y) S_{LP}(f_x, f_y). \tag{6}$$

In the following computation we choose $m=9$ for the parameter of the low-pass (wide pass-band).

The digital weight function is obtained by inverse Fourier transformation as follows

$$s(x, y) = \frac{1}{M^2} \sum_{p=-\frac{M}{2}}^{\frac{M}{2}} \sum_{r=-\frac{M}{2}}^{\frac{M}{2}} S_T\left(\frac{p}{M}, \frac{r}{M}\right) e^{j\frac{2\pi}{M}(xp+yr)} \tag{7}$$

where x and y are discrete variables

$$\begin{aligned} x &= -\frac{N}{2}, -\frac{N}{2}+1, \ldots, 0, \ldots, \frac{N}{2} \\ y &= -\frac{N}{2}, -\frac{N}{2}+1, \ldots, 0, \ldots, \frac{N}{2} \end{aligned} \tag{8}$$

(the sampling distance is considered unity). Equation (7) has been evaluated with $M=32$ for the range of the variables x and y from -5 to 5.

Results are given in Tables I, II and III. Due to the symmetry properties of the digital weight functions one quadrant determines the whole set of coefficients. Thus each Table contains essentially one quadrant of the corresponding sets of coefficients.

Table I

−0.001 229	−0.000 670	−0.000 102	−0.000 006	0.000 000	0.000 000
0.001 382	0.000 753	0.000 115	0.000 007	0.000 000	0.000 000
−0.004 397	−0.002 394	−0.000 365	−0.000 022	0.000 002	0.000 000
−0.039 418	−0.021 467	−0.003 272	−0.000 198	0.000 014	0.000 002
−0.131 262	−0.071 486	−0.010 897	−0.000 658	0.000 047	0.000 007
0.000 000	0.000 000	0.000 000	0.000 000	0.000 000	0.000 000

Table II

0.000 000	0.000 007	0.000 002	0.000 000	0.000 000	0.000 000
0.000 000	0.000 047	0.000 014	0.000 002	0.000 000	0.000 000
0.000 000	−0.000 658	−0.000 198	−0.000 022	0.000 007	−0.000 006
0.000 000	−0.010 897	−0.003 272	−0.000 365	0.000 115	−0.000 102
0.000 000	−0.071 486	−0.021 467	−0.002 394	0.000 753	−0.000 670
0.000 000	−0.131 262	−0.039 418	−0.004 397	0.001 382	−0.001 229

Table III

−0.002 988	−0.002 852	−0.002 575	−0.002 296	−0.002 059	−0.001 878
−0.005 016	−0.004 529	−0.003 640	−0.002 903	−0.002 390	−0.002 059
−0.011 448	−0.009 837	−0.006 520	−0.004 106	−0.002 903	−0.002 296
−0.022 938	−0.023 120	−0.014 766	−0.006 520	−0.003 640	−0.002 575
0.097 600	0.021 882	−0.023 120	−0.009 837	−0.004 529	−0.002 852
0.266 837	0.097 600	−0.022 938	−0.011 448	−0.005 016	−0.002 988

The first columns give the coefficients along the positive x axis, the last rows give the coefficients along the positive y axis. The central coefficient of each set of coefficients is given in the first place (first column) of the last row.

The whole set of coefficients for approximate digital computation of the derivative with respect to x is obtained by reflecting the values in the first quadrant to the coordinate axes and multiplying with (-1) the values in the third and fourth quadrants, as shown in Fig. 4.

The whole set of coefficients for the approximate digital computation of the derivative with respect to y is obtained by reflecting the values in the first quadrant to the coordinate axes and then multiplying with (-1) the values in the second and third quadrants, as shown in Fig. 5.

The whole set of coefficients for approximate digital computation of the derivative with respect to z is obtained, again, by reflecting the values in the first quadrant to the coordinate axes. Now, however the signs do not change.

If we want to obtain the derivatives in s^{-2} units the results of the convolution with the corresponding sets of coefficients should be multiplied a constant whose

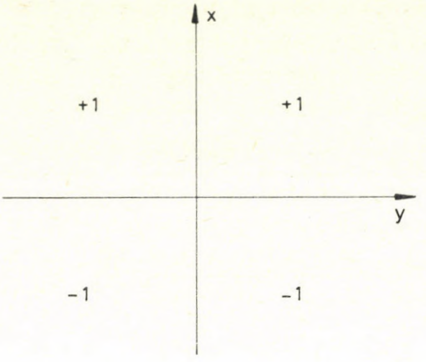

Fig. 4. The multipliers to be used in the derivation of the whole set of coefficients, corresponding to the computation of the derivatives with respect to x from the coefficients in the first quadrant

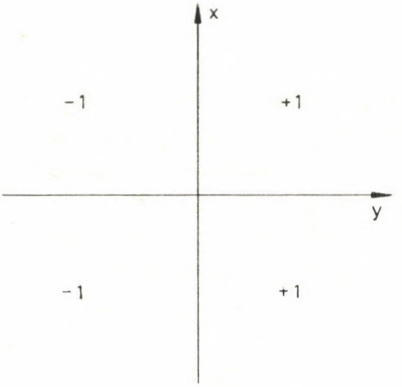

Fig. 5. The multipliers to be used in the derivation of the whole set of coefficients, corresponding to the computation of the derivatives with respect to y from the coefficients in the first quadrant

numerical value depends on the sampling distance. The constants are summarised in Table IV.

The actual transfer functions have been determined by taking the digital Fourier transform of the computed sets of coefficients. These are shown in Figs 1–3 besides the corresponding theoretical transfer functions. The actual and theoretical transfer functions should be close to each other in the neighbourhood of the origin, i.e. in the pass-band of the low-pass filter (5). For the medium and high-frequency range the derivations become significant since the application of the low-pass filter introduces continuously increasing attenuation. The phase-characteristics of the theoretical and actual transfer functions are identical to each other. The actual transfer functions are periodic.

Table IV

Sampling distance	Factor if data are obtained in mgal units	Factor if data are obtained in μms^{-2} units
100 m	$1 \cdot 10^{-7}$	$1 \cdot 10^{-8}$
250 m	$4 \cdot 10^{-8}$	$4 \cdot 10^{-9}$
500 m	$2 \cdot 10^{-8}$	$2 \cdot 10^{-9}$
1 000 m	$1 \cdot 10^{-8}$	$1 \cdot 10^{-9}$
2 000 m	$5 \cdot 10^{-9}$	$5 \cdot 10^{-10}$
5 000 m	$2 \cdot 10^{-9}$	$2 \cdot 10^{-10}$
10 000 m	$1 \cdot 10^{-9}$	$1 \cdot 10^{-10}$

The illustration of the method by a simple model

The approximate digital determination of derivatives is illustrated by the computation of the derivatives of the gravity field due to a sphere. The radius, the specific density, depth of the center and the mass of the sphere be denoted by R, ρ, d, and m, respectively. The origin of the coordinate system (x, y) is placed above the center of the sphere, the z coordinate axis is directed vertically downwards and it goes through the center of the sphere. Then the z-component of the gravity field due to the sphere becomes

$$g_z(x, y) = Gm \frac{d}{(x^2+y^2+d^2)^{3/2}}, \quad m = \frac{4R^3\pi}{3}\rho \tag{9}$$

where G is the gravitational constant.

Due to the simplicity of the analytical expression, describing the field of the sphere, the derivatives with respect to x, y, and z can be easily (and analytically) determined. They are

$$\frac{\partial}{\partial x} g_z(x, y) = -3Gm \frac{xd}{(x^2+y^2+d^2)^{5/2}} \tag{10}$$

$$\frac{\partial}{\partial y} g_z(x, y) = -3Gm \frac{yd}{(x^2+y^2+d^2)^{5/2}} \tag{11}$$

and

$$\frac{\partial}{\partial z} g_z(x, y) = -Gm \left(\frac{3d}{(x^2+y^2+d^2)^{5/2}} + \frac{1}{(x^2+y^2+d^2)^{3/2}} \right). \tag{12}$$

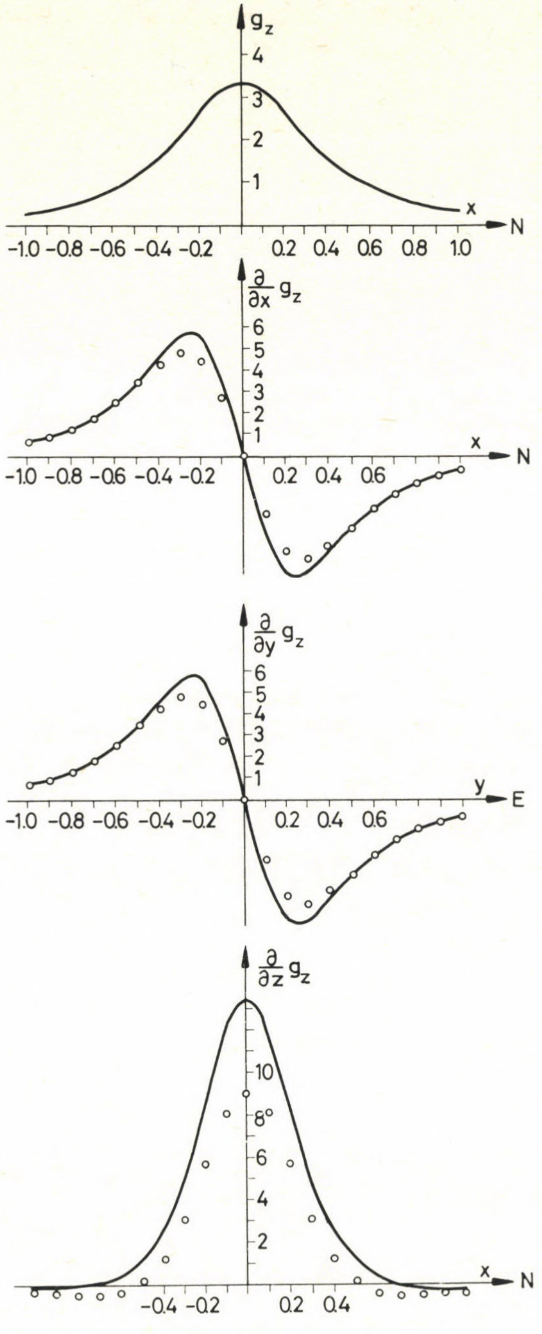

Fig. 6. The z-component of the gravity field due to a sphere g_z and its derivatives (continues lines) compared to the values of derivatives obtained digitally (open circles) ($\rho = 3 \cdot 10^3$ kg m^{-3}, $d = 50$ m, $R = 0.2 \cdot d$, the independent variables $0.1 \cdot dx$ or $0.1 \cdot dy$, the units μms^{-2} and 10^{-9}s^{-2} respectively)

The z component of the gravity field along the x axis is shown in Fig. 6 (top), together with its derivatives. The derivatives with respect to x and z are shown along the x axis, the derivative with respect to y is shown along the y axis. The type of the derivatives is indicated. Values determined by the application of the sets of coefficients are shown along the same axes (x, y and x, respectively). The derivatives, obtained digitally are depicted by circles.

Application to measured data

Figure 7 shows the Bouguer anomaly field over the Vése prospection area. The sampling distance is 1000 m. The x, y and z derivatives of the fields, obtained by convolving original data with the derived sets of coefficients, are given as Figs 8–10 respectively.

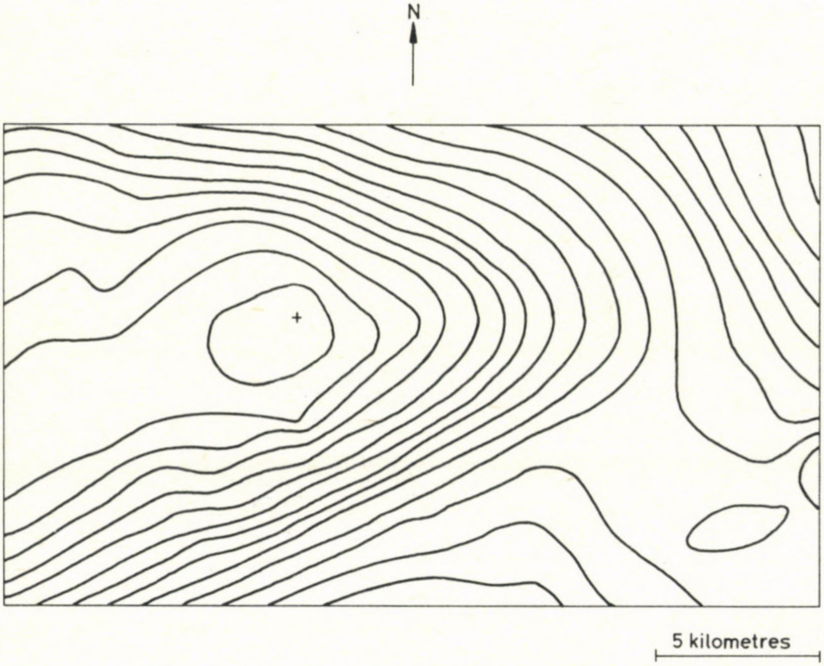

Fig. 7. Bouguer anomaly field over the Vése prospection area. Anomalies are contured at 10 μms^{-2}

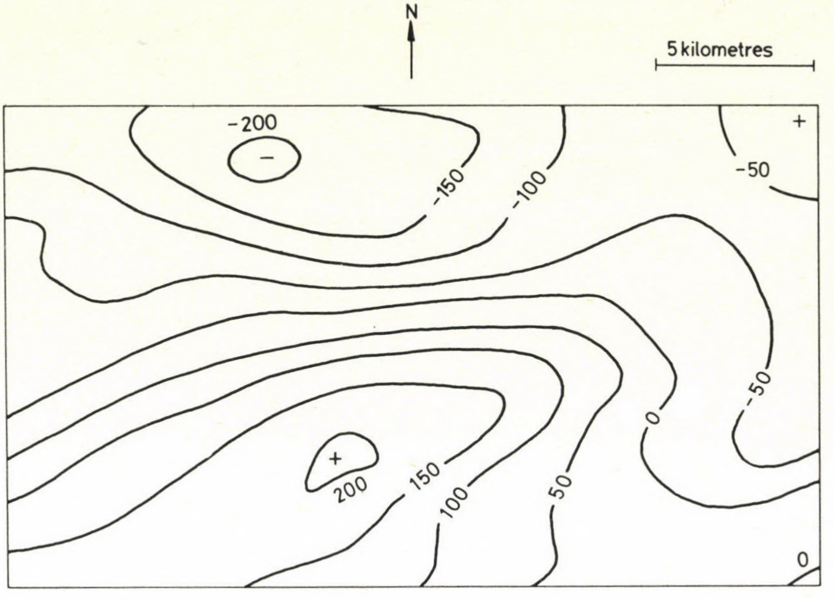

Fig. 8. The derivatives with respect to x of the Bouguer gravity (shown in Fig. 7), obtained by the set of coefficients in Table I (Isolines are $10^{-9}\ s^{-2}$ apart)

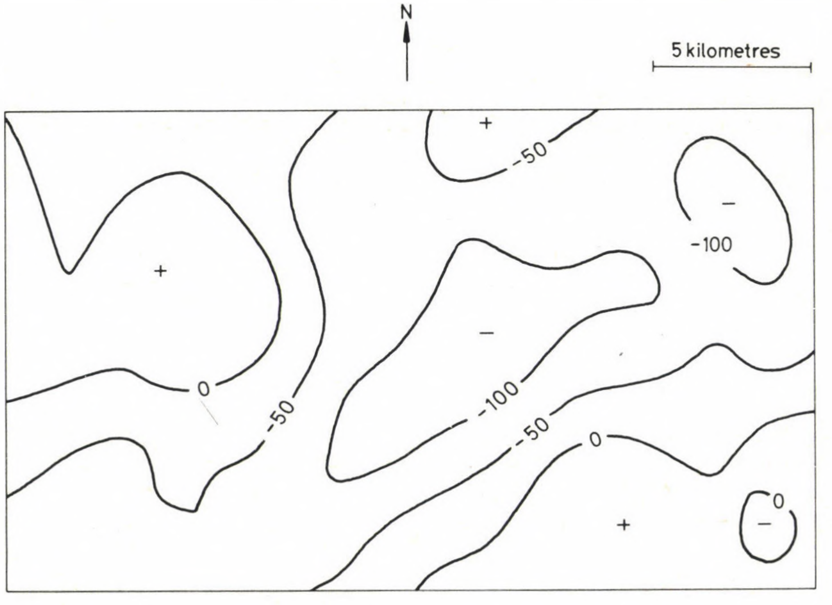

Fig. 9. The derivatives with respect to y of the Bouguer gravity (shown in Fig. 7), obtained by the set of coefficents in Table II (Isolines are $10^{-9}\ s^{-2}$ apart)

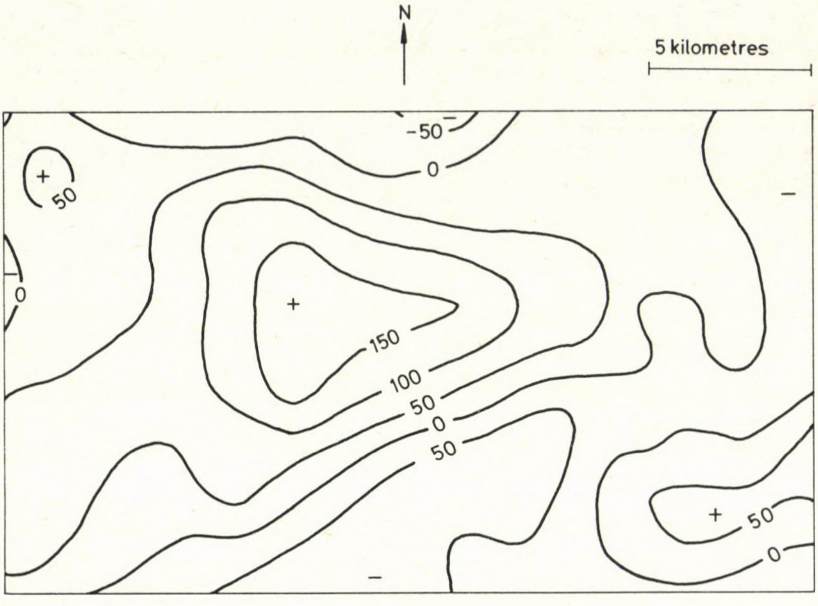

Fig. 10. The derivatives with respect to z of the Bouguer gravity (shown in Fig. 7), obtained by the set of coefficients in Table III (Isolines are $10^{-9}\,s^{-2}$ apart)

Acknowledgements

The author would like to thank Prof. A Meskó for the discussions and Mr. F Kovács for the permission to use gıavity data measured by the Geophysical Prospecting Company.

References

Chandler V W, Koski J S, Hinze W J, Braile L W 1981: Analysis of multisource gravity and magnetic anomaly data sets by moving-window application of Poisson's theorem. *Geophysics*, 46, 30–39.
Erdelyi A et al. 1954: Tables of Integral Transforms. McGraw-Hill Book Co. New York.
Kovács F 1982: Private communication.
Meskó A 1967: Gravity interpretation and information theory II. Smoothing and computation of regionals. *Annales Univ. Sci.*, 10, 15–27.
Meskó A 1983: Regional Bouguer gravity maps of Hungary. *Acta Geod. Geoph. Mont. Hung.*, 18 (in press)
Ross H P, Lavin P M 1966: In situ determination of the remanent vector of two-dimensional tabular bodies. *Geophysics*, 31, 948–962.

Acta Geodaet., Geophys. et Montanist. Hung. Volume 18 (4), pp. 513—516 (1983)

Book reviews

E Bisztricsány and Gy Szeidovitz eds: *Proceedings of the 17th Assembly of the European Seismological Commission.* Akadémiai Kiadó, Budapest, 1982 (Joint edition with Elsevier, Amsterdam) 689 p.

This volume contains about 120 papers presented at the 17th Assembly of ESC in Budapest, 1980, being the majority of all papers presented there. The papers are divided into chapters covering main areas of seismology, giving a colourful picture of this field of science at a given moment. That means that events being recent at the time of the symposium are well documented in the volume.

After Professor Ritsema's Presidential Address, the first part deals with the European Digital Seismic Network (EDS NET). Two papers discuss the Bulgarian part of the system, the others (4) different problems (processing, accuracy, instrumentation) connected with it.

Earthquake Hazard and Prediction is represented by 9 papers, including most hopeful methods of prediction (geoelectric Vp/Vs, geologic factors etc.) and give also a general survey about Europe, Anatolia and Czechoslovakia from this point of view.

Seismicity is one of the best represented sections (21 papers), including 5 papers on the April 15, 1979 quake in Yugoslavia and Albania. Other papers describe seismicity of the GDR, Mexico, Finland, Bulgaria, or generally Central and Eastern Europe (4 papers). The remaining part of the sections deal with problems connected with seismicity (magnitude and intensity determination, rock behaviour, analysis of historical data etc.).

Data Acquisition contains papers on the new Hungarian and GDR teleseismic systems, as well as a paper on coordinated geodetic measurements.

The section Focal Mechanism and Earthquake Prediction contains 6, Microseisms and Seismic Noise 5 papers closely related to the title.

Theory and Interpretation includes 10 papers e.g. on synthetic seismograms, propagation, new arrival-types, atmospheric pressure waves due to the St. Helens eruption etc.

Deep Seismic Sounding is represented by 2 papers, Physical and Chemical Properties of the Mantle by 11, including topics like ferroelectricity, electric properties of garnets, electromagnetic sounding with submarine cables, phase transitions, core anelasticity, fragmentation of the Farallon plate and rheology of subducted slabs.

Recent Crustal Movements and Associated Seismology are described in the Fennoscandian uplift zone, Phlegrean fields, Rumania, Switzerland, Great Hungarian Plain, Rhinegraben, and Bohemian Massif among others, altogether 9 papers.

Crustal structure in Europe consists of 21 papers, 4 on the Iberian Peninsula, 3 on Fennoscandia (Fennolora project), 2 each on the Bohemian Massif, on the Hercynian belt, on Eastern Europe, one each on the North Atlantic, Italy, Aquitany and the Tien-Shan region, the other papers discuss regional or general questions.

A special feature of this assembly was the discussion of problems of Plate Tectonics in Eastern Europe. 7 papers deal with the Carpathians and the Pannonian Basin, 6 with problems of adjacent regions. The volume is supplemented by 2 papers on other fields.

As this short summary shows, a characteristic feature of the assembly was a strong participation of seismologists from Eastern Europe, so a high number of papers is devoted to this part of the continent, representing a certain guideline in the wide variety of topics discussed. Welcome addition to the book is a copy of the first isoseismal map of the world, that of the Mór earthquake, January 14, 1810, made by the Hungarian Pál Kitaibel.

J Verő

Geodesia Universalis Festschrift Karl Rinner zum 70. Geburtstag. Mitteilungen der Geodätischen Institute der Technischen Universität Graz, Folge 40. Graz, 1982 p. 382

For the 70th birthday of Prof. K Rinner the Technical University of Graz published this proceedings in 1982. The book contains 39 articles from Austrian and foreign authors. They are all well known experts in the field of Geodesy.

About the life and scientific activity of Prof. Rinner we can read a review written by Prof. H Moritz. The articles can be divided in the following topics: physical geodesy, surveying, computation and adjustment, measurement technique, photogrammetry.

The proceedings printed at the Technical University of Graz contains 382 pages with a number of figures and tables. The papers deal with up-to-date problems of geodesy and so it seems to be very useful for many readers.

J Somogyi

H W Georgii and J Pankrath: *Deposition of Atmospheric Pollutants.* D. Reidel Publishing Company, Dordrecht, Holland, 1982. 217 pp., 100 figs., Dfl 85.00/US $37.00

This book contains the papers presented at a colloquium held at Oberursel/Taunus, West Germany, 9–11 November 1981. The papers discuss the results of investigations of processes opposite to atmospheric pollution. The proceedings are divided on the basis of these processes in two groups, dry and wet deposition. Most of the papers deals with the results of research work done in West Germany, but scientists from Great Britain, France, the Netherlands and Hungary contributed also to the discussion.

On the basis of the papers the main results of the investigations of dry deposition can be summarized as follows: The values of deposition velocity measured in wind tunnels may be applied in field conditions with an uncertainty of a factor of ~ 3 (Garland). Both field and wind tunnel experiments show deviations from the deposition velocities predicted by the model of Sehmel and Hodgson up to one order of magnitude (Markgrander and Flothmann). Recent experimental work confirms that deposition velocity is dependent on atmospheric stability and surface conditions (Davies and Nicholson). Measuring the mass size distribution, the atmospheric residence time can be determined and substances classified into local, regional and long-range pollutants (Müller). The atmospheric ammonia level generally exceeds the equilibrium concentration, which is determined by the chemical composition of the soil (Horváth).

The wet deposition of atmospheric pollutants has been discussed by eleven papers and the main results are as follows: The global distribution of the acidity in precipitation shows a maximum in North Europe and a minimum in Central Asia (Georgii). Rain acidity is due with decreasing pH to increasing acid concentration and limited removal capability of rain causes the spread of pollutants to large areas (Winkler). The wet deposition pattern is mainly determined by the precipitation pattern (Perseke). Concentrations of substances show a larger variation during rain from convective clouds, than in precipitation from stratiform clouds (Kins). Sulphate concentrations show a variation—parallel to the seasonal variation of pH values with high concentrations in winter and lower values in summer (Kuttler). It has been shown that the acid in rain associated with maritime air masses does not differ much from that in rain associated with continental air masses due to the higher degree of neutralization of acid by NH_3 in the latter case (Asman, Jonker, Slanina and Baard). The immediate deep freezing of rain samples assures the contamination free preservation resulting in a reduced diffusion to walls and diminished chemical, as well as bacteriological activity (Müller, Aheimer and Gravenhorst). The insoluble fractions of polycyclic aromatic hydrocarbons are much higher in the city than the soluble fractions (Schmitt). More than 90% of toxic metals as Pb, Cd, Cu, Zn and Se are dissolved in the rain, the toxic metal concentration being substantially higher during the initial two hours of rainfalls (Nürnberg, Valenta and Nguyen). Metals bound on submicron aerosol particles are removed primarily by wet deposition, while that on coarse particles by dry deposition (Rohbock). Many elements, which have greater soluble fractions, are associated with smaller aerosol particles (Pattenden, Branson and Fisher).

The aerosol concentrations, depending on the size and the sort of tree showed much lower values beneath the canopies, than above it (Gravenhorst and Höfken). The concentration of ions and elements is much higher in the throughfall, than in the precipitation above the forest (Höfken and Gravenhorst). Dry deposition to forests in rural areas may even exceed wet deposition (Mayer and Ulrich). The knowledge of the deposition mechanism can be used also to predict corrosion effects on man-made materials (Lanting).

P Bencze

A Nishida ed.: *Magnetospheric Plasma Dynamics.* Developments in earth and planetary sciences 04. Lectures presented at the Autumn College of Plasma Physics, International Center for Theoretical Physics, Trieste, Italy, Center for Academic Publications, Japan, Reidel, 1982 p. 348, US $ 49.50

The present book includes five review papers presented at the Autumn College of Plasma Physics, held at the International Center for Theoretical Physics in Trieste, Italy in 1979. This occasion offered a possibility to discuss results of magnetospheric plasma physics with other branches of plasma physics, and accordingly, the reviews intend to give a possibly full picture of the phenomena to be explained. This character of the book makes it a really valuable collection of different points of view, which give at the end nevertheless a uniform picture. This is then the greatest advantage, in addition to being really a review, that means it indicates further sources of informations concerning processes and phenomena described shortly here.

In Chapter I, the editor, Nishida, discusses the origin of not only terrestrial magnetospheric plasmas, but also that of the plasma in the magnetosphere of other planets, with special emphasis on the Jovian plasma from Io. Here as in the following the rich and well chosen pictorial part strongly enhances the understanding of the text. Both atmospheric and extra-planetary origins of the plasmas are elucidated.

In Chapter 2, Haerendel and Paschman deals with the interaction of the solar wind with the dayside magnetosphere. Here beginning from the solar wind, and continuing by the bow shock and the boundary layer, the effects and processes are outlined which at the end determine the state of the magnetosphere. Special emphasis is given to the long-discussed process of field line reconnection at the magnetopause, and the most recent results at the time of the presentation are also explained. In the last part, some microprocesses related to reconnection are surveyed, including e.g. different wave phenomena.

Chapter 3 continues the discussion of the solar wind-magnetosphere interaction on the opposite, night-side of the magnetosphere. A number of instabilities, as the lower-hybrid-drift instability and the tearing instability are explained in their respective magnetospheric application. Galeev concludes the Chapter with the description of the macroscopic consequences of the ion tearing mode instability.

Auroral physics, i.e. special situations arising in the polar zones, in the cusp region of the magnetosphere are treated in Chapter 4 by Sato. The main sections deal with the primary energy sources of the auroras and substorms, with the role of double layers in the acceleration, including several laboratory experiments of the author about these double layers. The magnetosphere-ionosphere coupling, i.e. the cause for the spectacular auroral arcs and the kilometric radiation, being an important factor in the energy balance of the auroras are reviewed in the subsequent sections.

In the last Chapter 5, Kennel and Ashour-Abdalla review electrostatic waves and the strong diffusion of magnetospheric electrons. This review can include only a part of the wave phenomena observed in the magnetosphere, however, it picks out the most exciting ones, such as e.g. electron cyclotron harmonic instabilities. It gives also a comprehensive section on observational facts, followed by a comparison of the most important theoretical points with observations.

Summarizingly, the present book is an excellent review of the magnetospheric plasma physics at the time of the end of the International Magnetospheric Studies.

J Verő

A E Scheidegger: *Principles of Geodynamics.* 3rd completely new ed. Berlin–Heidelberg–New York: Springer Verlag 1982, ISBN 3-540-11323-1. 126 figs XVII, 395 pages. Cloth DM 165.—; approx. US $ 73.30

The main subject of GEODYNAMICS is "to provide the basis for understanding the origin of the visible surface features of the Earth", as the author has written in the Preface of the present treatise on theoretical geology. (It should be noted that Springer Verlag published an other book by the same author on Theoretical Geomorphology as the "antagonistic pair" of this one on geodynamic processes.)

This is the third *completely revised* edition of this book. "Although the headings of the chapters and sections are much the same as in the previous editions, it will be found that most of the material is, in fact, new." The author has explained this change by the entirely new philosophy of the plate tectonics coming into its own since the last edition of this book at the end of sixties. This book is first of all a compilation of the writer's ideas on the subject of geodynamics (more than 50 of the author's own scientific papers are referred among some hundreds of others).

The book consists of the following eight chapters:

1. Physiographic and Geological Data Regarding the Earth
2. Geophysical Data Regarding the Earth
3. The Mechanics of Deformation
4. Geodynamic Effects of the Rotation of the Earth
5. Planetary Problems
6. Orogenesis
7. Geotectonics
8. Theory of Some Local Features.

It is admirable how many problems of different and apparently independent branches of geosciences are condensed into this book showing their multilateral relations realized in the Earth. Beside the principles of the theory of the deformation of continuous material the book summarizes the physical facts about the Earth and gives a very comprehensive review on various aspect of geodynamics as they are covered by the titles of the chapters.

A special merit of the book is its concise, and at the same time very clear style which is needed to catch the essence of scientific results multiplying from day to day. The rapid progress in sciences can explain that in some special questions the author's treatment is no more up-to-date. Nevertheless, it is an advantage that there is a lot of geodynamic problems on which the author can report on the results of his own researches and on his views.

The clear mathematical treatment of the problems, the well-collected figures help the readers to reach a higher level in their theoretical and practical knowledge on geodynamics.

The book is warmly recommended not only to geoscientists who are interested in geodynamics but to those also who want to get a systematic overview on different branches of geosciences and their interconnections.

A Ádám

PRINTED IN HUNGARY
Akadémiai Kiadó és Nyomda, Budapest

— treble underlining: bold-face italics
— red underlining: Greek letters
— green underlining: script letters.

Rules for mathematical-physical notations:

— trigonometric, logarithmic, analytic symbols, symbols for units and functions are in roman type (not underlined)
— letter symbols in mathematical and physical formulas, scalars, and subscripts of algebraic and physical quantities are in italics (underlined)
— vectors, matrices, operators in probability theory are in bold-face roman type (double underlining)
— tensors, operators and some special functions are in script letters (green underlining). These cannot be bold.
— Greek letters (red underlining) cannot be bold or extra bold type (thus they cannot be used for vectors or tensors)
— void upper lines e.g. for vectors
— avoid possible confusion between o (letter) and 0 (zero), l (letter) and 1 (one), ν (Greek nu) and v, u (letters) etc.
— explain ambiguous or uncommon symbols by making marginal notes in pencil
— be careful about superscripts and subscripts
— formulae must be numbered consecutively with the number in parentheses to the right of the formula. References in text to the equations may then usually be made by the number in parenthesis. When the word equation is used with a number, it is to be abbreviated, Eq. or Eqs in the plural
— the International System of Units (SI) should be used.

Authors are liable for the cost of alteration in the *proofs.* It is, therefore, the responsibility of the author to check the text for errors of facts before submitting the paper for publication.

3. *References* are accepted only in the Harvard system. Citations in the text should be as:

...(Bomford 1971)...or Bomford (1971)

...(Brosche and Sündermann 1976)...

...(Gibbs et al. 1976b)...

The list of references should contain names and initials of all authors (the abbreviation et al. is not accepted here); for *journal articles* year of publication, the title of the paper, title of the journal abbreviated, volume number, first and last page.

For *books* or *chapters in books,* the title is followed by the publisher and place of publication.

All items must appear both in the text and references.

Examples:

Bomford G 1971: Geodesy. Clarendon Press, Oxford

Brosche P, Sündermann J 1976: Effects of oceanic tides on the rotation of the earth. Manuscript. Univ. of Bonn

Buntebarth G 1976: Temperature calculations on the Hungarian seismic profile-section NP-2. In: *Geoelectric and Geothermal Studies (East-Central Europe, Soviet Asia), KAPG Geophysical Monograph.* Akadémiai Kiadó, Budapest, 561–566.

Gibbs N E, Poole W G, Stockmeyer P K 1976a: An algorithm for reducing the bandwidth and profile of a sparse matrix. *SIAM J. Number. Anal.,* 13, 236–250.

Gibbs N E, Poole W G, Stockmeyer P K 1976b: A comparison of several bandwidth and profile reduction algorithms. *ACM Trans. on Math. Software,* 2, 322–330.

Szarka L 1980: Potenciáltérképezés analóg modellezéssel (Analogue modeling of potential mapping). *Magyar Geofizika,* 21, 193–200.

4. *Footnotes* should be typed on separate sheets.

5. *Legends* should be short and clear. The place of the tables and figures should be indicated in the text, on the margin.

6. *Tables* should be numbered serially with Roman numerals. Vertical lines are not used.

All the illustrations should contain the figure number and author's name in pencil on the reverse.

Figures will be redrawn. Therefore the most important point is clearness of the figures, even pencil-drawings are accepted (with a duplicate).

Photographs and *half-tone* illustrations should be sharp and well contrasted.

If a specific reduction or enlargement is required, please indicate this in blue pencil on the figure.

The editors will send information to the first author about the *arrival* and acceptance of the papers. A galley proof is also sent to the first author for *correction.* Hundred *offprints* are supplied free of charge.

Periodicals of the Hungarian Academy of Sciences are obtainable at the following addresses:

AUSTRALIA
C.B.D. LIBRARY AND SUBSCRIPTION SERVICE
Box 4886, G.P.O., *Sydney N.S.W. 2001*
COSMOS BOOKSHOP, 145 Ackland Street
St. Kilda (Melbourne), Victoria 3182

AUSTRIA
GLOBUS, Höchstädtplatz 3, *1206 Wien XX*

BELGIUM
OFFICE INTERNATIONAL DE LIBRAIRIE
30 Avenue Marnix, *1050 Bruxelles*
LIBRAIRIE DU MONDE ENTIER
162 rue du Midi, *1000 Bruxelles*

BULGARIA
HEMUS, Bulvar Ruszki 6, *Sofia*

CANADA
PANNONIA BOOKS, P.O. Box 1017
Postal Station "B", *Toronto, Ontario M5T 2T8*

CHINA
CNPICOR, Periodical Department, P.O. Box 50
Peking

CZECHOSLOVAKIA
MAD'ARSKÁ KULTURA, Národní třida 22
115 66 Praha
PNS DOVOZ TISKU, Vinohradská 46, *Praha 2*
PNS DOVOZ TLAČE, *Bratislava 2*

DENMARK
EJNAR MUNKSGAARD, Norregade 6
1165 Copenhagen K

FEDERAL REPUBLIC OF GERMANY
KUNST UND WISSEN ERICH BIEBER
Postfach 46, *7000 Stuttgart 1*

FINLAND
AKATEEMINEN KIRJAKAUPPA, P.O. Box 128 *SF- 00101 Helsinki 10*

FRANCE
DAWSON-FRANCE S. A., B. P. 40, *91121 Palaiseau*
EUROPÉRIODIQUES S. A., 31 Avenue de Versailles, *78170 La Celle St. Cloud*
OFFICE INTERNATIONAL DE DOCUMENTATION ET LIBRAIRIE, 48 rue Gay-Lussac
75240 Paris Cedex 05

GERMAN DEMOCRATIC REPUBLIC
HAUS DER UNGARISCHEN KULTUR
Karl Liebknecht-Straße 9, *DDR-102 Berlin*
DEUTSCHE POST ZEITUNGSVERTRIEBSAMT Straße der Pariser Kommüne 3-4, *DDR-104 Berlin*

GREAT BRITAIN
BLACKWELL'S PERIODICALS DIVISION
Hythe Bridge Street, *Oxford OXI 2ET*
BUMPUS, HALDANE AND MAXWELL LTD.
Cowper Works, *Olney, Bucks MK46 4BN*
COLLET'S HOLDINGS LTD., Denington Estate *Wellingborough, Northants NN8 2QT*
WM. DAWSON AND SONS LTD., Cannon House *Folkstone, Kent CT19 5EE*
H. K. LEWIS AND CO., 136 Gower Street
London WCIE 6BS

GREECE
KOSTARAKIS BROTHERS INTERNATIONAL BOOKSELLERS, 2 Hippokratous Street, *Athens-143*

HOLLAND
MEULENHOFF-BRUNA B. V., Beulingstraat 2, *Amsterdam*
MARTINUS NIJHOFF B.V.
Lange Voorhout 9-11, *Den Haag*
SWETS SUBSCRIPTION SERVICE
347b Heereweg, *Lisse*

INDIA
ALLIED PUBLISHING PRIVATE LTD., 13/14
Asaf Ali Road, *New Delhi 110001*
150 B-6 Mount Road, *Madras 600002*
INTERNATIONAL BOOK HOUSE PVT. LTD.
Madame Cama Road, *Bombay 400039*
THE STATE TRADING CORPORATION OF INDIA LTD., Books Import Division, Chandralok 36 Janpath, *New Delhi 110001*

ITALY
INTERSCIENTIA, Via Mazzé 28, *10149 Torino*
LIBRERIA COMMISSIONARIA SANSONI, Via Lamarmora 45, *50121 Firenze*
SANTO VANASIA, Via M. Macchi 58
20124 Milano
D. E. A., Via Lima 28, *00198 Roma*

JAPAN
KINOKUNIYA BOOK-STORE CO. LTD.
17-7 Shinjuku 3 chome, Shinjuku-ku, *Tokyo 160-91*
MARUZEN COMPANY LTD., Book Department, P.O. Box 5050 Tokyo International, *Tokyo 100-31*
NAUKA LTD. IMPORT DEPARTMENT
2-30-19 Minami Ikebukuro, Toshima-ku, *Tokyo 171*

KOREA
CHULPANMUL, *Phenjan*

NORWAY
TANUM-TIDSKRIFT-SENTRALEN A.S., Karl Johansgatan 41-43, *1000 Oslo*

POLAND
WĘGIERSKI INSTYTUT KULTURY, Marszalkowska 80, *00-517 Warszawa*
CKP-I W, ul. Towarowa 28, *00-958 Warszawa*

ROUMANIA
D. E. P., *Bucuresti*
ILEXIM, Calea Grivitei 64-66, *Bucuresti*

SOVIET UNION
SOJUZPECHAT — IMPORT, *Moscow*
and the post offices in each town
MEZHDUNARODNAYA KNIGA, *Moscow G-200*

SPAIN
DIAZ DE SANTOS, Lagasca 95, *Madrid 6*

SWEDEN
GUMPERTS UNIVERSITETSBOKHANDEL AB
Box 346, *401 25 Göteborg 1*

SWITZERLAND
KARGER LIBRI AG, Petersgraben 31, *4011 Basel*

USA
EBSCO SUBSCRIPTION SERVICES
P.O. Box 1943, *Birmingham, Alabama 35201*
F. W. FAXON COMPANY, INC.
15 Southwest Park, *Westwood Mass. 02090*
READ-MORE PUBLICATIONS, INC.
140 Cedar Street, *New York, N. Y. 10006*

YUGOSLAVIA
JUGOSLOVENSKA KNJIGA, Terazije 27, *Beograd*
FORUM, Vojvode Mišića 1, *21000 Novi Sad*

Index: 26.031